

# **QCD and Collider Physics**

**R.K. ELLIS, W.J. STIRLING  
AND B.R. WEBBER**

**CAMBRIDGE MONOGRAPHS  
ON PARTICLE PHYSICS, NUCLEAR PHYSICS  
AND COSMOLOGY**

# **QCD and Collider Physics**

**R. K. ELLIS**

Fermi National Accelerator Laboratory

**W. J. STIRLING**

University of Durham

**B. R. WEBBER**

University of Cambridge



PUBLISHED BY THE PRESS SYNDICATE OF THE UNIVERSITY OF CAMBRIDGE  
The Pitt Building, Trumpington Street, Cambridge, United Kingdom

CAMBRIDGE UNIVERSITY PRESS  
The Edinburgh Building, Cambridge CB2 2RU, UK  
40 West 20th Street, New York NY 10011-4211, USA  
477 Williamstown Road, Port Melbourne, VIC 3207, Australia  
Ruiz de Alarcón 13, 28014 Madrid, Spain  
Dock House, The Waterfront, Cape Town 8001, South Africa

<http://www.cambridge.org>

© R. K. Ellis, W. J. Stirling and B. R. Webber 1996

This book is in copyright. Subject to statutory exception  
and to the provisions of relevant collective licensing agreements,  
no reproduction of any part may take place without  
the written permission of Cambridge University Press.

First published 1996  
First paperback edition 2003

*A catalogue record for this book is available from the British Library*

*Library of Congress Cataloguing in Publication data*

Ellis, R. K. (R. Keith)  
QCD and collider physics / R. K. Ellis, W. J. Stirling, B. R. Webber.  
p. cm Includes index.  
ISBN 0 521 58189 3 hardback  
1. Quantum chromodynamics 2. Colliders (Nuclear physics)  
I. Stirling, W. J., 1953-. II. Webber, B. R., 1943-.  
III. Title.  
QC793.3.Q35E44 1996  
539.7'548-dc20 96-31560 CIP

ISBN 0 521 58189 3 hardback  
ISBN 0 521 54589 7 paperback

Transferred to digital printing 2003

# Contents

<b>Preface</b>	<b>xii</b>
<b>1 Fundamentals of QCD</b>	<b>1</b>
1.1 Colour SU(3)	1
1.2 Lagrangian of QCD	5
1.3 Local gauge invariance	7
1.4 Feynman rules	8
1.5 Choice of gauge	11
1.6 Exact symmetries	12
1.7 Approximate symmetries	14
1.7.1 Light quark symmetries	14
1.7.2 Heavy quark symmetries	17
References	20
<b>2 Asymptotic freedom and confinement</b>	<b>22</b>
2.1 The running coupling constant	22
2.2 The $\beta$ function	24
2.3 Asymptotic freedom	27
2.4 Quark masses	29
2.5 The $\Lambda$ parameter	34
2.6 Lattice QCD	39
References	51
<b>3 QCD in electron-positron annihilation</b>	<b>53</b>
3.1 The total hadronic cross section	53
3.2 Heavy quark production	62
3.3 Jet cross sections	63
3.4 Event shape variables	71
3.5 The triple-gluon vertex	76
3.6 Gluon emission from heavy quarks	78

<b>3.7</b>	<b>Summary and outlook</b>	<b>81</b>
	<b>References</b>	<b>84</b>
<b>4</b>	<b>Deep inelastic scattering</b>	<b>86</b>
<b>4.1</b>	Deep inelastic scattering and the parton model	86
<b>4.2</b>	The parton model from field theory	93
<b>4.3</b>	The parton model and QCD	98
	<b>4.3.1 Contribution from one-gluon emission</b>	99
	<b>4.3.2 Factorization</b>	104
	<b>4.3.3 Scaling violations and the GLAP equation</b>	108
	<b>4.3.4 Solution of the leading-order GLAP equations</b>	116
<b>4.4</b>	QCD fits to deep inelastic data	122
<b>4.5</b>	Sum rules	126
	<b>4.5.1 Gross–Llewellyn Smith sum rule</b>	126
	<b>4.5.2 Adler sum rule</b>	127
	<b>4.5.3 Gottfried sum rule</b>	128
<b>4.6</b>	Deep inelastic scattering at small $x$	128
	<b>4.6.1 Regge theory</b>	130
	<b>4.6.2 The double asymptotic limit <math>Q^2 \rightarrow \infty, x \rightarrow 0</math></b>	132
	<b>4.6.3 Higher-order corrections to the GLAP equation at small <math>x</math></b>	136
	<b>4.6.4 The BFKL description of <math>F_2</math></b>	138
	<b>4.6.5 The BFKL equation</b>	139
	<b>4.6.6 Parton saturation</b>	147
<b>4.7</b>	Polarized scattering	147
	<b>4.7.1 Parton model interpretation</b>	148
	<b>4.7.2 Perturbative QCD corrections</b>	151
	<b>References</b>	<b>154</b>
<b>5</b>	<b>Parton branching and jet simulation</b>	<b>157</b>
<b>5.1</b>	Parton branching	158
<b>5.2</b>	Evolution equations	165
<b>5.3</b>	Monte Carlo method	173
<b>5.4</b>	Backward evolution	175
<b>5.5</b>	Coherent branching	178
<b>5.6</b>	Hadronization models	184
	<b>5.6.1 Independent fragmentation</b>	186
	<b>5.6.2 String model</b>	187
	<b>5.6.3 Cluster model</b>	188
<b>5.7</b>	QCD event generators	191
	<b>References</b>	<b>191</b>

<b>6</b>	<b>Jet properties beyond fixed order</b>	<b>193</b>
6.1	Jet fragmentation	193
6.1.1	Scaling violation	195
6.1.2	Average multiplicity	200
6.1.3	Small- $x$ fragmentation	204
6.1.4	Longitudinal fragmentation	207
6.1.5	Fragmentation in deep inelastic scattering	211
6.2	Generating function method	213
6.3	Multiplicity distributions	216
6.4	Quark and gluon jet differences	219
6.5	Resummation of event shapes	220
6.5.1	Exponentiation and resummation	223
6.5.2	Combining with fixed-order predictions	226
6.6	Resummation of jet rates	228
6.7	Average jet multiplicity	231
	References	234
<b>7</b>	<b>Hadroproduction of jets and photons</b>	<b>237</b>
7.1	The QCD improved parton model	237
7.2	Factorization of the cross section	240
7.3	Luminosities	242
7.4	Kinematics and jet definition	246
7.5	Two-jet cross sections	247
7.6	Comparison with experiment	250
7.7	Multijet production	255
7.8	Jet profiles	260
7.9	Direct photon production	264
	References	268
<b>8</b>	<b>Electroweak interactions</b>	<b>270</b>
8.1	Gauge boson interactions	270
8.2	The Higgs mechanism	272
8.2.1	Boson couplings	276
8.2.2	The $\rho$ parameter	278
8.3	Fermion multiplets and interactions	280
8.3.1	Anomaly cancellation	281
8.3.2	Fermion masses and couplings	283
8.3.3	The CKM matrix	288
8.4	$W$ and $Z$ decay properties	290
8.5	Vector boson scattering	291
8.6	Vector boson pair production	295
	References	299

<b>9</b>	<b>The production of vector bosons</b>	<b>301</b>
9.1	The Drell-Yan mechanism	303
9.2	Perturbative QCD corrections	307
9.3	Comparison with experiment	310
9.4	<i>W</i> and <i>Z</i> boson production	313
9.4.1	Production cross sections	313
9.4.2	<i>W</i> rapidity asymmetry	315
9.4.3	<i>W</i> transverse mass	319
9.4.4	<i>W</i> and <i>Z</i> transverse momentum distributions	321
9.4.5	Multijet production with <i>W</i> and <i>Z</i>	327
References		330
<b>10</b>	<b>Heavy quarks</b>	<b>332</b>
10.1	Charm and bottom quark decays	333
10.1.1	Semi-leptonic decays	334
10.1.2	Hadronic decays	338
10.2	Top quark decays	340
10.2.1	Conventional decays	340
10.2.2	Unconventional decays	345
10.3	Heavy quark production	347
10.3.1	Leading order	347
10.3.2	Higher-order corrections	350
10.4	Charm and bottom quark production	357
10.5	Top quark production	362
10.5.1	Top cross section	364
10.5.2	Prospects for top studies	368
10.6	Heavy quarks in jets	370
10.6.1	Fragmentation functions for heavy quarks	370
10.6.2	Heavy quarks in gluon jets	372
10.7	Quarkonium	375
10.7.1	Quarkonium spectrum	375
10.7.2	Quarkonium decays	378
10.7.3	Quarkonium production	380
References		385
<b>11</b>	<b>Higgs bosons at high-energy colliders</b>	<b>388</b>
11.1	Higgs mass constraints	389
11.2	Decay channels and branching ratios	391
11.3	Higgs search at LEP2	394
11.4	Higgs production at the LHC	397
11.4.1	Production mechanisms	397
11.4.2	Gluon-gluon fusion	397
11.4.3	<i>WW</i> , <i>ZZ</i> fusion	399
11.4.4	Associated production with <i>W</i> , <i>Z</i> bosons	401
11.4.5	Associated production with <i>t</i> <i>t</i>	401

11.4.6	Theoretical uncertainties in the cross sections	402
11.5	Search strategies and backgrounds	403
11.6	Summary	408
	References	409
<b>12</b>	<b>Measurements of the strong coupling constant</b>	<b>411</b>
12.1	Summary of $\alpha_S$ measurements	413
12.2	Deep inelastic scattering	415
12.2.1	Sum rules	415
12.2.2	Scaling violation in structure functions	415
12.2.3	Jets in deep inelastic scattering	416
12.3	$\tau$ lepton decay	416
12.4	Quarkonium	418
12.4.1	Lattice spectroscopy	418
12.4.2	Quarkonium decays	420
12.5	$e^+e^-$ annihilation	421
12.5.1	Hadronic cross section	421
12.5.2	Event shapes	422
12.5.3	Scaling violation in fragmentation	422
12.6	Hadron-hadron scattering	423
12.7	Conclusions	424
	References	426
<b>Index</b>		<b>428</b>

# Preface

Quantum Chromodynamics (QCD) is the theory of the strong interaction, one of the four fundamental forces in nature. It describes the interactions between quarks and gluons, and in particular how they bind together to form the class of particles called hadrons, of which the proton and neutron are familiar examples. QCD emerged as a mathematically consistent theory in the 1970s, and nowadays is regarded as one of the cornerstones of the ‘Standard Model’ of the elementary particles and their interactions.

Collider physics has grown from a small part of the subject in the 1960s to the position it now holds as the principal method of high-energy physics research. Particle colliders provide the highest available centre-of-mass energies and permit us to probe the structure of matter at the shortest distances. On these scales, all of the known fundamental interactions except gravity can be studied in unprecedented detail. In this book, in order to limit the scope, and not stray too far from our field of expertise, we concentrate mainly on the strong interaction aspects of collider physics, which are described by QCD.

One of the triumphs of modern particle physics has been the extent to which QCD has successfully accounted for the strong interaction processes observed at colliders, most notably the dramatic phenomena of hadronic jet and heavy quark production. Our aim here is to show what has been achieved in this area, while indicating the directions that need further development. Increasingly the study of QCD also has an ‘engineering’ aspect. In order to exploit the potential of high-energy colliders to study other physics, especially at machines with circulating hadron beams, one needs a quantitative understanding of QCD.

After a general description of the QCD Lagrangian and its symmetries in the first Chapter, we concentrate in Chapter 2 on the crucial properties of asymptotic freedom and colour confinement. Because of the asymptotic freedom of QCD, the appropriate calculational technique at the short

distances probed by colliders is perturbation theory. The treatment of perturbative QCD is developed in analogy with perturbative Quantum Electrodynamics, with which we assume the reader has some familiarity. In subsequent chapters we describe how short-distance cross sections are calculated, and how the results of these calculations compare with experiment. In Chapters 3 and 4, this is done in detail for the ‘classic’ QCD processes of high-energy electron-positron annihilation and deep inelastic lepton-hadron scattering. Chapters 5 and 6 then deal with the properties of hadronic jets, while Chapter 7 discusses the production of jets and photons in hadron-hadron collisions.

A large part of collider physics is concerned with the production of massive particles: the gauge and Higgs bosons of the electroweak interaction, and heavy quarks. The relevant properties of electroweak interactions are reviewed in Chapter 8, and then, in Chapters 9 – 11, the production and decays of these particles are discussed, with emphasis on their QCD aspects. Finally in Chapter 12 we summarize the various ways of measuring the one fundamental parameter of QCD: the strong coupling constant  $\alpha_s$ .

Much of the theoretical challenge of perturbative QCD derives from extending the well-tried methods of QED to the novel and more complicated context of a non-Abelian gauge theory. There are, however, important differences between the two theories, primarily because the quanta of QCD, quarks and gluons, the analogues of electrons and photons in QED, are confined inside hadrons and not observed as free particles. At long distances, confinement effects predominate, and non-perturbative methods become more appropriate. The most developed of these is lattice QCD, which we review briefly in Chapter 2. Even in the shortest-distance processes, one cannot avoid confinement effects, because the asymptotic incoming and/or outgoing states consist of hadrons. At present, the lattice technique cannot predict such effects in dynamical scattering processes. For certain quantities, however, factorization theorems permit the short- and long-distance dynamics to be separated, and the latter can be treated by parametrizations or model calculations. This has led to the ‘industries’ of fitting and modelling structure functions (for incoming hadrons) and hadronization or fragmentation distributions (for outgoing ones), which we also review in the appropriate places.

Our intention in writing this book has been to provide an introduction to the physics of high-energy colliders with special emphasis on the study of QCD. We wanted to produce a book which would give an overview of the subject as it stands today while providing a firm basis for understanding future developments. The resulting work is therefore neither a textbook nor a research monograph, but something of each. Above all, we wanted to stress the relationship between theory and experiment.

This book is an outgrowth of lectures which we have given over the

years in many different places. The level of treatment is suitable for a graduate student who has followed a first course in quantum field theory. At the same time, since we have attempted to give a fuller set of references than is usual in such a book, including references to original work, the book will be a suitable point of departure for researchers who wish to find out about aspects of the subject with which they are not so familiar. For the same reason we have chosen to group the references at the end of each chapter rather than at the end of the book. Although we have tried to ascribe credit correctly, the principal criterion in our choice of references has been to refer to readily accessible published works which we judge will be of use to the reader.

We would like to thank the American Physical Society, publishers of *Physical Review* and *Physical Review Letters*, for permission to reproduce Figs. 1.2, 4.28, 7.12, 9.8, 9.9, 9.10, 9.14, 10.31; the Director General of CERN for permission to reproduce Figs. 3.14, 11.11, 11.12; Elsevier Science, Sara Burgerhartstraat 25, 1055 KV Amsterdam, Netherlands, publishers of *Nuclear Physics*, *Nuclear Physics Supplements* and *Physics Letters*, for permission to reproduce Figs. 2.7, 2.8, 3.7, 3.11, 4.19, 6.1, 6.3, 6.4, 6.11, 6.15, 7.19, 10.13, 10.15, 10.20, 12.2; IOP Publishing for permission to reproduce Figs. 5.13, 8.4; the Royal Swedish Academy of Sciences, publishers of *Physica Scripta*, for permission to reproduce Fig. 6.2; Springer Verlag, publishers of *Zeitschrift für Physik*, for permission to reproduce Figs. 6.5, 6.6, 6.7, 6.8, 6.9, 6.10, 6.12, 6.13; World Scientific, publishers of *International Journal of Modern Physics*, for permission to reproduce Fig. 2.9. The source of each figure is given in the caption, and we are most grateful to the authors for permission to reproduce or adapt them.

We are happy to acknowledge the invaluable help of J. Berryhill, S. Bethke, A. Bodek, E. Braaten, H. Budd, C. Davies, A. De Ridder, A. De Roeck, L. del Pozo, M. Demarteau, E. Eichten, H. Frisch, S. Frixione, T. Gehrmann, F. Gianotti, T. Hebbeker, P. Jenni, Z. Kunszt, A. Milsztajn, G. Martinelli, H. Montgomery, S. Moretti, P. Nason, M. Neubert, R. Roberts, J. Rosner, D. Ross, C. Sachrajda, G. Salam, K. Schilling, M. Schmelling, T. Takeuchi, D. Treille, D. Ward and H. Weerts in helping us locate the figures which we have included in the text or for their comments on the manuscript.

In conclusion, we would like to thank our families for their support and encouragement, and the many colleagues and collaborators, too numerous to mention, who have contributed to our understanding of this field.

R.K.E., W.J.S. and B.R.W.  
April, 1996.

# 1

## Fundamentals of QCD

The genesis of the theory which we now call Quantum Chromodynamics was the result of the assembling of many ideas and experimental results. In this chapter we start by reviewing the main evidence for the colour degree of freedom, which lies at the heart of the theory. We then write down the QCD Lagrangian and the Feynman rules which follow from it. We go on to discuss the exact and approximate symmetries of the theory.

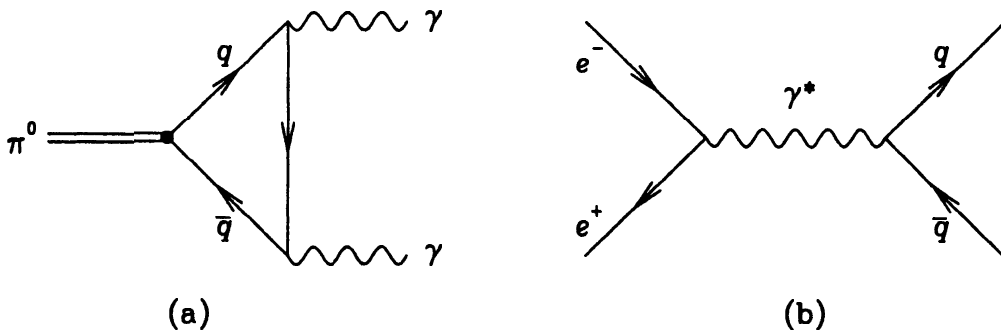
### 1.1 Colour SU(3)

The most fundamental tenet of QCD is that hadronic matter is made of quarks. The idea of quarks arose from the need to have a physical manifestation for the SU(3) of flavour [SU(3)<sub>f</sub>] observed in the spectrum of the lowest-mass mesons and baryons. The properties of the six known quarks are shown in Table 1.1. The observed baryons are interpreted as three-quark states. The quark constituents of the baryons are forced to have half-integral spin in order to account for the spins of the low-mass baryons. The quarks in the spin- $\frac{3}{2}$  baryons are then in a symmetrical state of space, spin and SU(3)<sub>f</sub> degrees of freedom. However the requirements of Fermi-Dirac statistics imply the total antisymmetry of the wave function. The resolution of this dilemma was the introduction of the colour degree of freedom: a colour index  $a$  with three possible values (usually called red, green, blue for  $a = 1, 2, 3$ ) is carried by each quark. The baryon wave functions are totally antisymmetric in this new index.

Of course the introduction of the colour degree of freedom could lead to a proliferation of states, and so the colour hypothesis has to be supplemented by a requirement that only colour singlet states can exist in nature. If the group of colour transformations is SU(3), with the quarks

Quark	Charge	Mass	Baryon Number	Isospin
$u$	$+\frac{2}{3}$	$\sim 4$ MeV	$\frac{1}{3}$	$+\frac{1}{2}$
$d$	$-\frac{1}{3}$	$\sim 7$ MeV	$\frac{1}{3}$	$-\frac{1}{2}$
$c$	$+\frac{2}{3}$	$\sim 1.5$ GeV	$\frac{1}{3}$	0
$s$	$-\frac{1}{3}$	$\sim 135$ MeV	$\frac{1}{3}$	0
$t$	$+\frac{2}{3}$	$\sim 175$ GeV	$\frac{1}{3}$	0
$b$	$-\frac{1}{3}$	$\sim 5$ GeV	$\frac{1}{3}$	0

Table 1.1. The properties of the six quarks.

Fig. 1.1. (a)  $\pi^0$  decay, (b)  $e^+e^-$  annihilation to quarks.

$q_a$  transforming according to the fundamental ( $3 \times 3$  unitary matrix) representation and the antiquarks  $\bar{q}^a$  according to the complex conjugate representation, then the basic colour singlet states are precisely the mesons  $q_a \bar{q}^a$  and the baryons  $\epsilon^{abc} q_a q_b q_c$ , where  $\epsilon^{abc}$  is the totally antisymmetric tensor.

There now exists resounding proof of the validity of colour SU(3). In this section we shall briefly describe some experimental results which were historically important. One early experimental test of the correctness of the three colour idea<sup>1</sup> was provided by the rate for the decay  $\pi^0 \rightarrow \gamma\gamma$ . This decay proceeds by the coupling of the pion to a quark loop as shown in Fig. 1.1(a). The rate is determined by the matrix element

$$\langle 0 | J_\alpha(x) J_\beta(y) \varphi(0) | 0 \rangle = \frac{1}{f_\pi m_\pi^2} \langle 0 | J_\alpha(x) J_\beta(y) \partial_\mu A^\mu(0) | 0 \rangle \quad (1.1)$$

where  $J_\alpha$  is the electromagnetic current. The interpolating field for the neutral pion  $\varphi$  can be replaced by the divergence of the axial current  $A$

<sup>1</sup> For a personal historical perspective on the discovery of QCD we refer the reader to ref. [1].

using the Goldberger-Treiman relation [2]. The parameter  $f_\pi \simeq 93$  MeV is the decay constant of the pion as measured in the decay  $\pi^- \rightarrow \mu^- \bar{\nu}_\mu$ ,

$$\langle 0 | A^\mu(0) | \pi(p) \rangle = i f_\pi p^\mu. \quad (1.2)$$

Remarkably enough, the rate for the decay is exactly calculable using the quark diagram shown in Fig. 1.1(a). This leads to an absolute prediction for the decay rate,

$$\Gamma(\pi^0 \rightarrow \gamma\gamma) = \xi^2 \left( \frac{\alpha}{\pi} \right)^2 \frac{1}{64\pi} \frac{m_\pi^3}{f_\pi^2} = 7.6 \xi^2 \text{ eV}. \quad (1.3)$$

The experimental value is  $7.7 \pm 0.6$  eV [3]. The electric charge and colour factor  $\xi$  for three colours of fractionally charged quarks is

$$\xi = 3 \left[ \left( \frac{2}{3} \right)^2 - \left( \frac{1}{3} \right)^2 \right] = 1 \quad (1.4)$$

where the overall factor 3 represents the number of colours. Note however that the original calculation of this decay rate [4], performed before the discovery of quarks, used the proton and neutron as constituents yielding

$$\xi = \left[ (1)^2 - (0)^2 \right] = 1. \quad (1.5)$$

So the measured decay rate is suggestive of the existence of three colours of fractionally charged quarks, but not conclusive.

Another test of the number of charged fundamental constituents is provided by the ratio  $R$  of the  $e^+e^-$  total hadronic cross section to the cross section for the production of a pair of point-like, charge-one objects such muons. The virtual photon emitted by the annihilating electron and positron will excite all electrically charged constituent-anticonstituent pairs from the vacuum as shown in Fig. 1.1(b). At low energy the virtual photon excites only the  $u$ ,  $d$  and  $s$  quarks, each of which occurs in three colours. The result for the ratio  $R$  is therefore

$$R = 3 \left[ \left( \frac{2}{3} \right)^2 + \left( -\frac{1}{3} \right)^2 + \left( -\frac{1}{3} \right)^2 \right] = 2. \quad (1.6)$$

For centre-of-mass energies  $E_{\text{cm}} \geq 10$  GeV one is above the threshold for the production of pairs of  $c$  and  $b$  quarks, and so

$$R = 3 \left[ 2 \times \left( \frac{2}{3} \right)^2 + 3 \times \left( -\frac{1}{3} \right)^2 \right] = \frac{11}{3}. \quad (1.7)$$

The data on  $R$  shown in Fig. 1.2 are in reasonable agreement with the prediction of the three colour model. This ratio will be considered in more detail in Chapter 3.

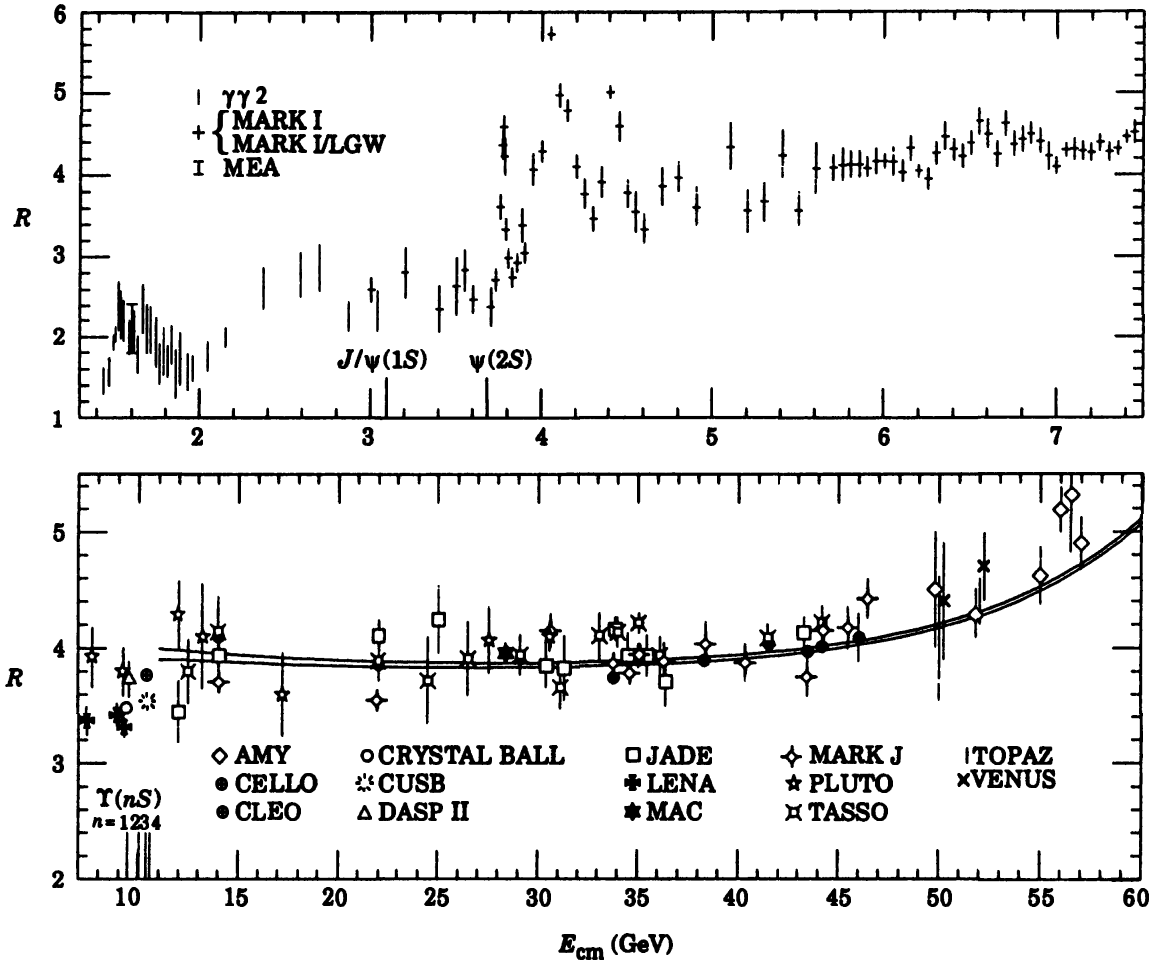


Fig. 1.2. Compilation of values of  $R$  in  $e^+e^-$  annihilation. Figure from ref. [3].

The existence of approximately point-like constituents inside hadrons was demonstrated by the classic electron deep inelastic scattering experiments performed at SLAC [5]. The surprising result was that the measured cross sections did not fall off exponentially as the inelasticity of the reaction increased. Rather, they had a scaling behaviour which was indicative of point-like structure inside the target nucleons. This gave rise to the ‘parton’ model, in which the constituents of hadrons were identified with partons, which we now know to be the coloured quarks and gluons.

The final step in this chain of argument was provided by the discovery of asymptotic freedom. Before this discovery, the outstanding question was why quarks appeared to be free particles when probed by a deep inelastic photon. Since quarks are not observed as free entities they evidently have strong interactions which bind them together to form hadrons. Asymptotic freedom predicts that the coupling of quarks and gluons is large at large distances so as to confine quarks; at the same time the coupling is predicted to be small at short distances so that the quarks behave as free particles at asymptotic energies. However, the approach to asymptotia is

very slow. At any finite energy there are calculable corrections to the free quark result which are unambiguous predictions of the theory.

## 1.2 Lagrangian of QCD

We begin with a brief description of the QCD Lagrangian and the Feynman rules which can be derived from it. This is a practical guide which does little more than introduce notation and certainly does not do justice to the elegant structure of quantum field theory. For more details, the reader is referred to the standard texts, for example refs. [6-9]. Treatments of QCD can be found in refs. [10-16].

Just as in Quantum Electrodynamics, the perturbative calculation of any process requires the use of Feynman rules describing the interactions of quarks and gluons. The Feynman rules required for a perturbative analysis of QCD can be derived from a Lagrangian density which is given by

$$\mathcal{L}_{\text{classical}} + \mathcal{L}_{\text{gauge-fixing}} + \mathcal{L}_{\text{ghost}}. \quad (1.8)$$

The expression for the classical Lagrangian density is

$$\mathcal{L}_{\text{classical}} = -\frac{1}{4}F_{\alpha\beta}^A F_A^{\alpha\beta} + \sum_{\text{flavours}} \bar{q}_a (iD - m)_{ab} q_b. \quad (1.9)$$

These terms describe the interaction of spin- $\frac{1}{2}$  quarks of mass  $m$  and massless spin-1 gluons.  $D$  in Eq. (1.9) is a symbolic notation for  $\gamma_\mu D^\mu$  and the spinor indices of  $\gamma_\mu$  and  $q_a$  have been suppressed. We follow the notation of Bjorken and Drell [6], with metric given by  $g^{\alpha\beta} = \text{diag}(1, -1, -1, -1)$  and set  $\hbar = c = 1$ . The gamma matrices satisfy the anticommutation relations,

$$\{\gamma^\mu, \gamma^\nu\} = 2g^{\mu\nu}. \quad (1.10)$$

$F_{\alpha\beta}^A$  is the field strength tensor derived from the gluon field  $A_\alpha^A$ ,

$$F_{\alpha\beta}^A = [\partial_\alpha A_\beta^A - \partial_\beta A_\alpha^A - g f^{ABC} A_\alpha^B A_\beta^C] \quad (1.11)$$

and the indices  $A, B, C$  run over the eight colour degrees of freedom of the gluon field. It is the third ‘non-Abelian’ term on the right-hand-side of Eq. (1.11) which distinguishes QCD from QED, giving rise to triplet and quartic gluon self-interactions and ultimately to the property of asymptotic freedom. Note that each term in the Lagrangian has mass dimension four, in order to give the correct dimensions for the action when integrated over all space-time. It follows that the dimensions of the fields  $q_\alpha$  and  $A_\alpha^A$  are  $3/2$  and  $1$ , respectively.

The explicit sum in Eq. (1.9) runs over the  $n_f$  different flavours of quarks,  $g$  in Eq. (1.11) is the coupling constant which determines the strength of the interaction between coloured quanta, and  $f^{ABC}$  ( $A, B, C = 1, \dots, 8$ ) are the structure constants of the SU(3) colour group. The quark fields  $q_a$  are in the triplet representation of the colour group, ( $a = 1, 2, 3$ ) and  $D$  is the covariant derivative. Acting on triplet and octet fields the covariant derivative takes the form

$$(D_\alpha)_{ab} = \partial_\alpha \delta_{ab} + ig (t^C A_\alpha^C)_{ab}, \quad (D_\alpha)_{AB} = \partial_\alpha \delta_{AB} + ig (T^C A_\alpha^C)_{AB}, \quad (1.12)$$

where  $t$  and  $T$  are matrices in the fundamental and adjoint representations of SU(3) respectively:

$$[t^A, t^B] = if^{ABC} t^C, \quad [T^A, T^B] = if^{ABC} T^C, \quad (T^A)_{BC} = -if^{ABC}. \quad (1.13)$$

A representation for the generators  $t^A$  is provided by the eight Gell-Mann matrices, which are hermitean and traceless,

$$t^A = \frac{1}{2} \lambda^A \quad (1.14)$$

$$\begin{aligned} \lambda^1 &= \begin{pmatrix} 0 & 1 & 0 \\ 1 & 0 & 0 \\ 0 & 0 & 0 \end{pmatrix}, \quad \lambda^2 = \begin{pmatrix} 0 & -i & 0 \\ i & 0 & 0 \\ 0 & 0 & 0 \end{pmatrix}, \quad \lambda^3 = \begin{pmatrix} 1 & 0 & 0 \\ 0 & -1 & 0 \\ 0 & 0 & 0 \end{pmatrix}, \\ \lambda^4 &= \begin{pmatrix} 0 & 0 & 1 \\ 0 & 0 & 0 \\ 1 & 0 & 0 \end{pmatrix}, \quad \lambda^5 = \begin{pmatrix} 0 & 0 & -i \\ 0 & 0 & 0 \\ i & 0 & 0 \end{pmatrix}, \quad \lambda^6 = \begin{pmatrix} 0 & 0 & 0 \\ 0 & 0 & 1 \\ 0 & 1 & 0 \end{pmatrix}, \\ \lambda^7 &= \begin{pmatrix} 0 & 0 & 0 \\ 0 & 0 & -i \\ 0 & i & 0 \end{pmatrix}, \quad \lambda^8 = \frac{1}{\sqrt{3}} \begin{pmatrix} 1 & 0 & 0 \\ 0 & 1 & 0 \\ 0 & 0 & -2 \end{pmatrix}. \end{aligned} \quad (1.15)$$

By convention the normalization of the SU( $N$ ) matrices is chosen to be

$$\text{Tr } t^A t^B = T_R \delta^{AB}, \quad T_R = \frac{1}{2}. \quad (1.16)$$

With this choice, the colour matrices obey the following relations:

$$\sum_A t_{ab}^A t_{bc}^A = C_F \delta_{ac}, \quad C_F = \frac{N^2 - 1}{2N} \quad (1.17)$$

$$\text{Tr } T^C T^D = \sum_{A,B} f^{ABC} f^{ABD} = C_A \delta^{CD}, \quad C_A = N. \quad (1.18)$$

Thus for the specific case of SU(3) we have

$$C_F = \frac{4}{3}, \quad C_A = 3. \quad (1.19)$$

For the anticommutator of the fundamental representation  $t$  matrices we also have

$$\begin{aligned}\{t^A, t^B\} &= \frac{1}{N} \delta^{AB} I + d^{ABC} t^C \\ \sum_{A,B} d^{ABC} d^{ABD} &= \frac{N^2 - 4}{N} \delta^{CD}, \quad d^{AAC} \equiv 0.\end{aligned}\quad (1.20)$$

### 1.3 Local gauge invariance

Eq. (1.9) has the property that it is invariant under local gauge transformations. That is, one can perform a redefinition of the quark fields independently at every point in space and time, without changing the physical content of the theory. The behaviour of the quark field under such a local transformation is

$$q_a(x) \rightarrow q'_a(x) = \exp(it \cdot \theta(x))_{ab} q_b(x) \equiv \Omega(x)_{ab} q_b(x). \quad (1.21)$$

The covariant derivative is so called because it transforms under a local gauge transformation in the same way as the field itself:

$$D_\alpha q(x) \rightarrow D'_\alpha q'(x) \equiv \Omega(x) D_\alpha q(x). \quad (1.22)$$

In this and following equations we have omitted the colour labels of the quark fields. We can use this equation to derive the transformation property of the gauge field  $A$

$$\begin{aligned}D'_\alpha q'(x) &= (\partial_\alpha + igt \cdot A'_\alpha) \Omega(x) q(x) \\ &\equiv (\partial_\alpha \Omega(x)) q(x) + \Omega(x) \partial_\alpha q(x) + igt \cdot A'_\alpha \Omega(x) q(x) \\ t \cdot A_\alpha &\equiv \sum_A t^A A_\alpha^A.\end{aligned}\quad (1.23)$$

Thus we find that the transformation property of the gluon field is given by

$$t \cdot A'_\alpha = \Omega(x) t \cdot A_\alpha \Omega^{-1}(x) + \frac{i}{g} (\partial_\alpha \Omega(x)) \Omega^{-1}(x). \quad (1.24)$$

Using this equation it is straightforward to show that the transformation property of the non-Abelian field strength tensor is

$$t \cdot F_{\alpha\beta}(x) \rightarrow t \cdot F'_{\alpha\beta}(x) = \Omega(x) t \cdot F_{\alpha\beta}(x) \Omega^{-1}(x). \quad (1.25)$$

Alternatively we may derive the same result using the relation

$$[D_\alpha, D_\beta] = igt \cdot F_{\alpha\beta}, \quad (1.26)$$

which follows from Eqs. (1.11) and (1.12).

The behaviour of the field strength tensor under a local gauge transformation should be contrasted with that of the electromagnetic field

strength in QED. The QCD field strength is not gauge invariant because of the self-interaction of the gluons. The carriers of the colour force are themselves coloured, unlike the electrically neutral photon.

Note that there is no gauge invariant way of including a mass for the gluon. A term such as

$$m^2 \mathcal{A}^\alpha \mathcal{A}_\alpha \quad (1.27)$$

is not gauge invariant. This is very similar to the QED requirement of a massless photon. On the other hand the mass term for the quarks given in Eq. (1.9) is gauge invariant.

#### 1.4 Feynman rules

We cannot perform perturbation theory with the Lagrangian of Eq. (1.8) without the gauge fixing term. For a discussion of gauge fixing we refer again to the standard texts, for example refs. [6-9]. The key point is that it is impossible to define the propagator for the gluon field without making a choice of gauge. The choice

$$\mathcal{L}_{\text{gauge-fixing}} = -\frac{1}{2\lambda} (\partial^\alpha \mathcal{A}_\alpha^A)^2, \quad (1.28)$$

fixes the class of *covariant gauges* with gauge parameter  $\lambda$ . In a non-Abelian theory such as QCD this covariant gauge fixing term must be supplemented by a ghost Lagrangian, which is given by

$$\mathcal{L}_{\text{ghost}} = \partial_\alpha \eta^A \dagger (D_{AB}^\alpha \eta^B). \quad (1.29)$$

Here  $\eta^A$  is a complex scalar field which obeys Fermi statistics. The derivation of the form of the ghost Lagrangian is best provided by the path integral formalism [17] and the procedures due to Faddeev and Popov [18]. The ghost fields cancel unphysical degrees of freedom which would otherwise propagate in covariant gauges. For an explanation of the physical role played by ghost fields, the reader is referred to ref. [19].

Eqs. (1.9), (1.28) and (1.29) are sufficient to derive the Feynman rules of the theory in a covariant gauge. The Feynman rules are defined from the operator

$$S = i \int \mathcal{L} d^4x \quad (1.30)$$

which gives the phase of transition amplitudes, rather than from the Lagrangian density. We can separate the Lagrangian density into a free piece  $\mathcal{L}_0$ , which normally contains all the terms bilinear in the fields, and an interaction piece,  $\mathcal{L}_I$ , which contains all the rest:

$$S = S_0 + S_I$$

$$S_0 = i \int d^4x \mathcal{L}_0(x), \quad S_I = i \int d^4x \mathcal{L}_I(x). \quad (1.31)$$

The practical recipe to determine the Feynman rules is that the inverse propagator is derived from  $-S_0$ , whereas the Feynman rules for the interacting parts of the theory which are treated as perturbations are derived from  $S_I$ .

This recipe (including the extra minus sign) can be understood [20] by considering the following two different approaches to the quantization of a theory. For simplicity, consider a theory which contains only a complex scalar field  $\phi$  and an action which contains only bilinear terms,  $S = \phi^* (K + K') \phi$ . In the first approach, both  $K$  and  $K'$  are included in the free Lagrangian,  $S_0 = \phi^* (K + K') \phi$ . Using the above rule the propagator  $\Delta$  for the  $\phi$  field is given by

$$\Delta = \frac{-1}{K + K'}. \quad (1.32)$$

In the second approach  $K$  is regarded as the free Lagrangian,  $S_0 = \phi^* K \phi$ , and  $K'$  as the interaction Lagrangian,  $S_I = \phi^* K' \phi$ . Now  $S_I$  is included to all orders in perturbation theory by inserting the interaction term an infinite number of times:

$$\begin{aligned} \Delta &= \frac{-1}{K} + \left(\frac{-1}{K}\right) K' \left(\frac{-1}{K}\right) + \left(\frac{-1}{K}\right) K' \left(\frac{-1}{K}\right) K' \left(\frac{-1}{K}\right) + \dots \\ &= \frac{-1}{K + K'} \end{aligned} \quad (1.33)$$

Note that with the choice of signs described above the full propagator of the  $\phi$  field is the same in both approaches, demonstrating the internal consistency of the recipe.

Using the free piece  $\mathcal{L}_0$  of the QCD Lagrangian given in Eq. (1.8) one can readily obtain the quark and gluon propagators. Thus, for example, the inverse fermion propagator in momentum space can be obtained by making the identification  $\partial^\alpha = -ip^\alpha$  for an incoming field. In momentum space the two-point function of the quark field depends on a single momentum  $p$ . It is found to be

$$\Gamma_{ab}^{(2)}(p) = -i\delta_{ab} (\not{p} - m), \quad (1.34)$$

which is the inverse of the propagator given in Fig. 1.3. The  $i\varepsilon$  prescription for the pole of the propagator is added to preserve causality, in exactly the same way as in QED [6]. Similarly the inverse propagator of the gluon field is found to be

$$\Gamma_{\{AB, \alpha\beta\}}^{(2)}(p) = i\delta_{AB} \left[ p^2 g_{\alpha\beta} - (1 - \frac{1}{\lambda}) p_\alpha p_\beta \right]. \quad (1.35)$$

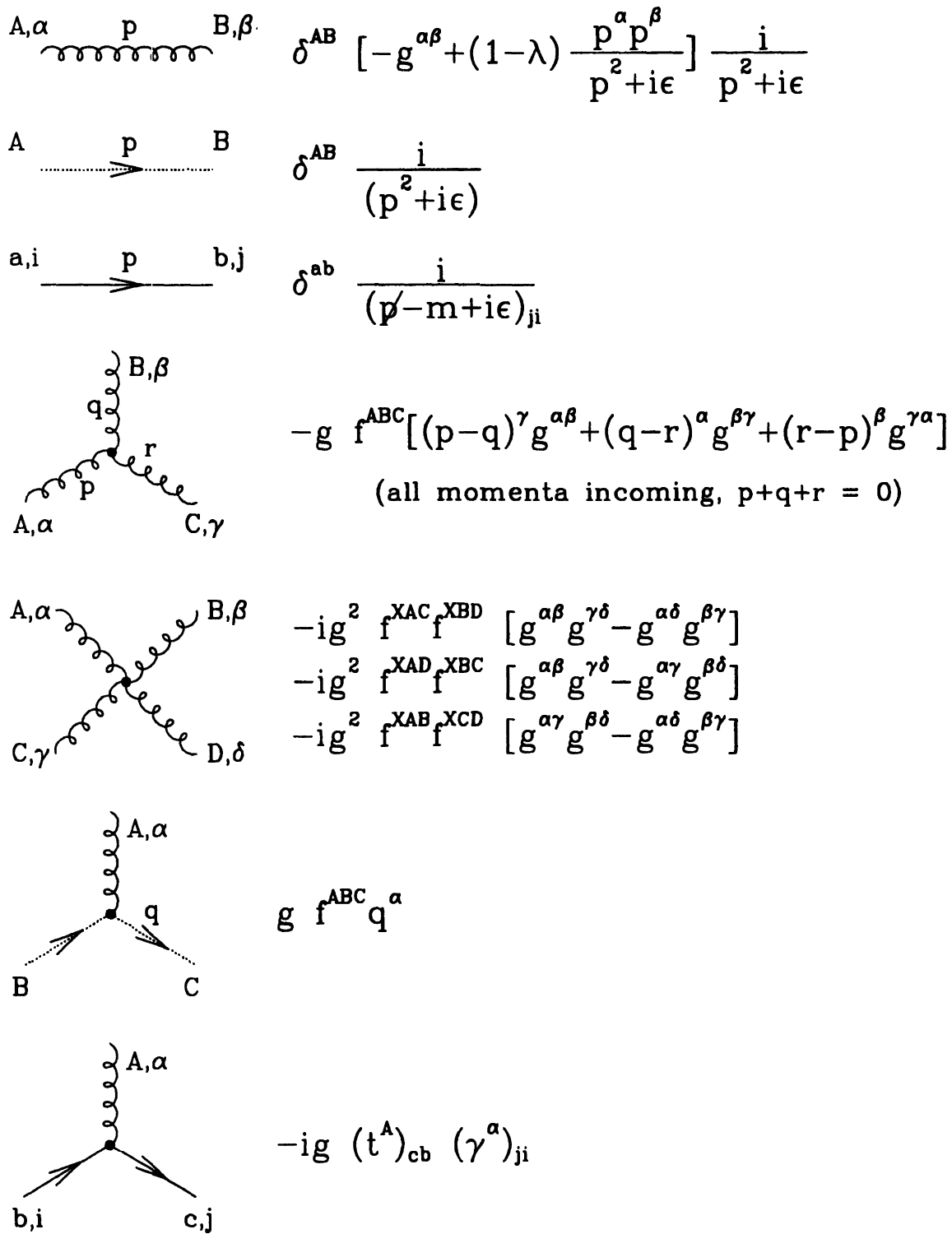


Fig. 1.3. Feynman rules for QCD in a covariant gauge for gluons (curly lines), fermions (solid lines) and ghosts (dotted lines).

It is straightforward to check that without the gauge fixing term this function would have no inverse. The result for the gluon propagator  $\Delta$  is as given in Fig. 1.3:

$$\Gamma_{\{AB, \alpha\beta\}}^{(2)}(p) \Delta^{(2)\{BC, \beta\gamma\}}(p) = \delta_A^C g_\alpha^\gamma \quad (1.36)$$

$$\Delta_{\{BC, \beta\gamma\}}^{(2)}(p) = \delta_{BC} \frac{i}{p^2} \left[ -g_{\beta\gamma} + (1 - \lambda) \frac{p_\beta p_\gamma}{p^2} \right]. \quad (1.37)$$

Replacing derivatives with the appropriate momenta, Eqs.(1.9), (1.28) and (1.29) can be used to derive all the rules in Fig. 1.3.

## 1.5 Choice of gauge

The introduction of the gauge fixing term Eq. (1.28) explicitly breaks gauge invariance. The form of the breaking depends on the parameter  $\lambda$ . However, in the end, physical results (technically, S-matrix elements) will be independent of  $\lambda$ . Thus it does not really matter for physics which choice one makes for the gauge fixing term, although the calculation may look very different at intermediate stages. Setting  $\lambda = 1$  ( $\lambda = 0$ ) in Eq. (1.37) we obtain the Feynman gauge (Landau gauge). The Feynman gauge is convenient for many purposes, because the simplicity of the gluon propagator reduces the number of terms to be computed.

An alternative choice of gauge fixing is provided by the *axial gauges* which are fixed in terms of another vector which we denote by  $n$

$$\mathcal{L}_{\text{gauge-fixing}} = -\frac{1}{2\lambda} (n^\alpha A_\alpha^A)^2, \quad (1.38)$$

The advantage of the axial class of gauge is that ghost fields are not required. However one pays for this simplicity because the gluon propagator is more complicated. The inverse propagator is

$$\Gamma_{\{AB, \alpha\beta\}}^{(2)}(p) = i\delta_{AB} \left[ p^2 g_{\alpha\beta} - p_\alpha p_\beta + \frac{1}{\lambda} n_\alpha n_\beta \right]. \quad (1.39)$$

The inverse of this matrix gives the gauge boson propagator,

$$\Delta_{\{BC, \beta\gamma\}}^{(2)}(p) = \delta_{BC} \frac{i}{p^2} \left[ -g_{\beta\gamma} + \frac{n_\beta p_\gamma + p_\beta n_\gamma}{n \cdot p} - \frac{(n^2 + \lambda p^2)p_\beta p_\gamma}{(n \cdot p)^2} \right]. \quad (1.40)$$

Notice the larger number of terms in the numerator of the propagator and in addition the new singularities at  $n \cdot p = 0$ .

What are the properties of these gauges which make them interesting? Let us specialize to the case  $\lambda = 0$ ,  $n^2 = 0$ . This is called the light-cone gauge. The propagator becomes

$$\Delta_{\{BC, \beta\gamma\}}^{(2)}(p) = \delta_{BC} \frac{i}{p^2} d_{\beta\gamma}(p, n) \quad (1.41)$$

where

$$d_{\beta\gamma} = -g_{\beta\gamma} + \frac{n_\beta p_\gamma + p_\beta n_\gamma}{n \cdot p}. \quad (1.42)$$

In the limit  $p^2 \rightarrow 0$  we find that

$$n^\beta d_{\beta\gamma}(p, n) = 0, \quad p^\beta d_{\beta\gamma}(p, n) = 0. \quad (1.43)$$

Only two physical polarization states, orthogonal to  $n$  and  $p$ , propagate. For this reason these classes of gauges are called physical gauges. In fact in the  $p^2 \rightarrow 0$  limit we may decompose the numerator of the propagator into a sum over two polarizations:

$$d_{\alpha\beta} = \sum_i \varepsilon_\alpha^{(i)}(p) \varepsilon_\beta^{(i)}(p). \quad (1.44)$$

In addition to the constraint  $\varepsilon_\beta^{(i)}(p)p^\beta = 0$ , which is always true, in an axial gauge we have the further constraint  $\varepsilon_\beta^{(i)}(p)n^\beta = 0$ . For further information on non-covariant gauges see ref. [21].

## 1.6 Exact symmetries

The most important of the exact symmetries of the Lagrangian of QCD is local gauge invariance which has already been described in Section 1.3. Local gauge invariance is responsible for the renormalizability of the theory. In addition to this symmetry, the Lagrangian of Eq. (1.9) possesses several other discrete global symmetries. These are the operation of parity, charge conjugation invariance and time reversal. These discrete symmetries are in agreement with the observed properties of the strong interactions. Tests of the discrete symmetries C, P and T in processes mediated by the strong interactions are discussed in ref. [3].

The analysis of the behaviour of the QCD Lagrangian under these discrete symmetries is considerably complicated at the quantum level by the fact that there is another gauge invariant operator of mass dimension four which can be added to the Lagrangian,

$$\mathcal{L}_\theta = \frac{\theta g^2}{32\pi^2} F_{\alpha\beta}^A \tilde{F}_A^{\alpha\beta}, \quad (1.45)$$

where  $\tilde{F}$  is the dual of the gluon field strength tensor,

$$\tilde{F}_A^{\alpha\beta} = \frac{1}{2} \epsilon_{\alpha\beta\gamma\delta} F_A^{\gamma\delta}. \quad (1.46)$$

The normalization of  $\mathcal{L}_\theta$  is chosen conventionally. A term of the form in Eq. (1.45) corresponds to an interaction  $E \cdot B$  in QED. Such an interaction would violate both parity and time reversal symmetry, in contradiction to the observed properties of the strong interactions. We therefore have

a dilemma. The coefficient  $\theta$  in Eq. (1.45) is required to be small. Of course we could set it to zero by fiat, but it could still be regenerated by CP-violating effects that are known to exist in weak interactions.

At first sight it appears that the term in Eq. (1.45) is innocuous since it can be written as a total divergence,

$$\begin{aligned} F_{\alpha\beta}^A \tilde{F}_A^{\alpha\beta} &= \partial_\alpha K^\alpha \\ K^\alpha &= 2\epsilon^{\alpha\beta\gamma\delta} A_\beta^A \{ \partial_\gamma A_\delta^A - \frac{2}{3} g f^{ABC} A_\gamma^B A_\delta^C \}. \end{aligned} \quad (1.47)$$

A total divergence contributes only a surface term to the action (1.30) and can therefore be neglected in the context of perturbation theory. This explains why such a term is absent from the Feynman rules and why it plays no role in our description of perturbative QCD. For the purposes of most of this book the term given by Eq. (1.45) can simply be ignored.

A much more sophisticated non-perturbative analysis [22,23] shows that  $\mathcal{L}_\theta$  can give rise to real physical effects, despite the fact that it is a total divergence. The vacuum of QCD can have non-trivial topological structure and in this case the surface term in the action integral cannot be neglected. Since the operator  $K^\alpha$  is not gauge invariant it can have singular behaviour at infinity without implying similar behaviour in physical gauge invariant quantities. The existence of this term  $\mathcal{L}_\theta$  gives rise to a violation of CP with a magnitude dictated by the strong interactions. In fact the limit [24] on the size of the parameter  $\theta$  coming from the measurements of the dipole moment of the neutron is  $\theta < 10^{-9}$  and it is plausible to assume that it is exactly zero. The unexplained smallness of the parameter  $\theta$  is referred to as the strong CP problem.

Several solutions to the strong CP problem exist in the literature [23,25]. The first mechanism exploits the fact that the phase which gives rise to physical effects ( $\bar{\theta}$ ) is the sum of a CP-violating phase in the quark mass matrix and the QCD phase  $\theta$ . If the mass of the up quark were exactly zero the net physical effect could be rotated away<sup>2</sup>. However, an up quark with zero mass appears not to be acceptable phenomenologically [26]. Another mechanism is to convert  $\theta$  into a parameter which is dynamically chosen to be small, rather than fixed *a priori*. This is the Peccei-Quinn mechanism [25], which has the further consequence that it requires the existence of axions. Axions are hypothetical particles which couple to scalar and pseudoscalar fermion currents. There is as yet no definitive solution to the strong CP problem. However as emphasized above, this problem has no relevance for the development of perturbative QCD.

---

<sup>2</sup> The relationship between the mass matrix and the  $\theta$  term is beyond the scope of this book. Suffice it to say that it is related to anomalies in the axial vector current.

## 1.7 Approximate symmetries

The Lagrangian of the QCD also possesses a number of approximate symmetries which are related to properties of the quark mass matrix. Such symmetry principles are extremely important because they provide relationships between masses and matrix elements, which are valid even in strong coupling regimes in which perturbation theory is not applicable.

For the most part we shall be concerned with symmetries of the classical action which are preserved once quantum effects are included. However it is important to remember that this is not always the case. The most famous example of this is the violation of scale invariance, which in QCD without quark masses is true at the classical level. Quantum effects lead to violation of scale invariance. The mechanism by which quantum effects violate scale invariance will be extensively discussed in Chapter 2. In the following sections we will discuss the symmetries which follow from properties of the quark mass matrix.

### 1.7.1 Light quark symmetries

Let us now specialize to the quark sector of the Lagrangian given in Eq. (1.9) and consider first only the  $u$  and  $d$  fields:

$$\mathcal{L} = \sum_{j=u,d} \bar{q}_j (i\mathcal{D} + m) q_j . \quad (1.48)$$

If we perform a global phase re-definition of the up and down fields separately the Lagrangian (1.48) remains invariant. This invariance corresponds to the conservation of quark number.

Since we also want to consider approximate invariances which couple different flavours, it is convenient to introduce a matrix notation for the quark field

$$q = \begin{pmatrix} u \\ d \end{pmatrix} . \quad (1.49)$$

With this notation the Lagrangian may be written in the form

$$\mathcal{L} = \bar{q} (i\mathcal{D} + M) q \quad (1.50)$$

where

$$M = \begin{pmatrix} m_u & 0 \\ 0 & m_d \end{pmatrix} . \quad (1.51)$$

Let us assume that that  $m_u - m_d$  is very much less than the hadronic mass scale so that we can approximate the matrix  $M$  by a multiple of the unit matrix. In this case the symmetry of the Lagrangian is increased. It

is now invariant under a  $2 \times 2$  unitary transformation acting on the quark fields. The general form of such a transformation is

$$q' = \exp \left( \sum_0^3 \alpha_i \sigma_i \right) q \quad (1.52)$$

where  $\sigma_i$ , ( $i = 1, 2, 3$ ) are the Pauli matrices and  $\sigma_0$  is the unit matrix. This symmetry  $U(2)_V$  can be decomposed into the product  $U(1)_V \otimes SU(2)_V$ . The  $U(1)$  symmetry is the quark number symmetry mentioned above. The new approximate symmetry  $SU(2)_V$  is isospin symmetry, which becomes exact in the limit that the up quark is degenerate in mass with the down quark. According to Noether's theorem, there is a conserved current corresponding to each symmetry:

$$J_\mu^i = \bar{q} \gamma_\mu \sigma^i q . \quad (1.53)$$

The subscript  $V$  on the symmetry group is to remind us that it is associated with vector currents.

This approximate flavour symmetry can be further enhanced by considering the strange quark also to be degenerate in mass with the up and the down. Examination of Table 1.1 shows that this symmetry will be less reliable than isospin. In this case we obtain the approximate  $SU(3)_V$  flavour symmetry which gives the classification of the mesons and baryons into flavour octets and decuplets.

If we now take the limit in which we consider the masses of the up and down quarks to be negligible ( $M=0$ ) the symmetry becomes even larger. To explain this it is convenient to introduce the left- and right-handed projectors

$$\gamma_L = \frac{1}{2}(1 - \gamma_5), \quad \gamma_R = \frac{1}{2}(1 + \gamma_5), \quad (1.54)$$

which satisfy the relations  $\gamma_L^2 = \gamma_L$ ,  $\gamma_R^2 = \gamma_R$  and  $\gamma_L \gamma_R = 0$ . We may decompose the quark fields into left- and right-handed components,  $q_L = \gamma_L q$ ,  $q_R = \gamma_R q$ . In the massless limit, these correspond to the positive and negative helicity states. The quark sector of the Lagrangian becomes

$$\mathcal{L} = \bar{q}_L i \not{D} q_L + \bar{q}_R i \not{D} q_R . \quad (1.55)$$

There is now no term which connects left- and right-handed fields, and so independent left and right rotations are permitted, yielding a  $U(2)_L \otimes U(2)_R$  symmetry:

$$q'_L = \exp \left( \sum_0^3 \alpha_i \sigma_i \right) q_L , \quad q'_R = \exp \left( \sum_0^3 \beta_i \sigma_i \right) q_R . \quad (1.56)$$

A symmetry which acts separately on left- and right-handed fields is called a *chiral* symmetry. In this case, we have chiral  $SU(2)$ . The currents

generated by this symmetry group are

$$\begin{aligned} L_\mu^i &= \bar{q}\gamma_\mu\gamma_L\sigma^i q, \\ R_\mu^i &= \bar{q}\gamma_\mu\gamma_R\sigma^i q. \end{aligned} \quad (1.57)$$

Once again, if we also neglect the mass of the strange quark, the symmetry is extended to chiral SU(3).

Chiral symmetry is not apparent in the observed spectrum of QCD. If it were, every hadron would be accompanied by a partner of opposite parity with the same mass. Instead, chiral SU(2) is *spontaneously broken*, leaving only the  $SU(2)_V \otimes U(1)_V$  symmetry of isospin and baryon number conservation mentioned previously.

Spontaneous breaking of a symmetry occurs when the symmetry group of the solutions to a theory is dynamically determined to be less than the symmetry of the original Lagrangian. This will be the case if the ground state of the theory (the vacuum) is not invariant under the full group of symmetry transformations. In QCD, it is believed that the vacuum has a non-zero expectation value of the light-quark operator  $\bar{q}q$ :

$$\langle 0 | \bar{q}q | 0 \rangle = \langle 0 | (\bar{u}u + \bar{d}d) | 0 \rangle \simeq (250 \text{ MeV})^3. \quad (1.58)$$

This vacuum expectation value is referred to as a quark condensate. Since the condensate connects left- and right-handed fields,

$$\langle 0 | \bar{q}q | 0 \rangle \equiv \langle 0 | \bar{q}_L q_R + \bar{q}_R q_L | 0 \rangle, \quad (1.59)$$

it breaks the chiral symmetry, while remaining invariant under the subgroup  $SU(2)_V \otimes U(1)_V$ .

If an exact symmetry of the Lagrangian is spontaneously broken, the theory will contain massless spin-zero particles called Goldstone bosons. The Goldstone theorem [27] states that the number of such particles will be equal to the number of spontaneously broken symmetry generators. In the case of chiral SU(2) breaking to  $SU(2)_V$ , this implies three pseudoscalar bosons, which are identified with the three pions  $\pi^+$ ,  $\pi^-$  and  $\pi^0$  in the massless quark limit. The  $U(1)_L \otimes U(1)_R$  symmetry is also broken down to  $U(1)_V$ , but the lost  $U(1)_A$  is spoilt by quantum effects and does not give rise to a Goldstone boson. This is related to the existence of the contribution to the Lagrangian in Eq. (1.45).

In the real world, the light quark masses are not precisely zero, and therefore the chiral symmetry of the QCD Lagrangian is not exact. Nevertheless the masses are small on the scale of strong interactions ( $m_u \simeq 4$  MeV,  $m_d \simeq 7$  MeV), and may be treated as a perturbation. Correspondingly, the pions are not precisely massless Goldstone bosons, but their masses are much smaller than those of other hadrons. In fact the above values of the quark masses are deduced from those of the pions, and other low-energy data, via a perturbative approach. This *chiral perturbation*

*theory* leads to a remarkably consistent picture of strong interactions at energies that are small compared with the typical hadronic mass scale (about 1 GeV) [28].

Similarly, neglecting the strange quark mass ( $m_s \simeq 135$  MeV) yields a chiral  $SU(3)$  symmetry spontaneously broken to  $SU(3)_V$ , with eight pseudoscalar Goldstone bosons corresponding to the flavour  $SU(3)$  octet ( $\pi^\pm, \pi^0, K^\pm, K^0, \bar{K}^0$  and  $\eta$ ). These are in fact the lightest hadrons, so chiral  $SU(3)$  perturbation theory is still applicable. However, the masses of the heavier quarks are too large for chiral  $SU(N)$  with  $N > 3$  to be a useful starting point. In this case there are other approximate symmetries that can be exploited, as discussed below.

### 1.7.2 Heavy quark symmetries

The heavy quark symmetries of the QCD Lagrangian are most easily illustrated by considering the properties of bound states containing heavy quarks such as the  $B$  and  $D$  mesons. Such a hadron at rest consists of an almost static heavy quark  $Q$  coupled to light degrees of freedom (light quarks, antiquarks and gluons) to give a colour singlet state. We consider a quark to be heavy when its Compton wavelength is much smaller than the radius of the hadronic state ( $\sim 1$  fm, so that  $m_Q \gg 200$  MeV). As far as the light degrees of freedom are concerned the heavy quark acts only as a static source of colour charge. The details of the spectrum and matrix elements are almost independent of its mass and spin orientation. We therefore have an  $SU(2N_f)$  symmetry of the matrix elements where  $N_f$  is the number of possible heavy quark flavours. In practice the heavy quarks of interest will be the charm and bottom quarks, since the top quark is expected to decay via the weak interaction too rapidly to form bound states.

The basic idea of heavy quark symmetry is familiar from atomic physics. The properties of an atom depend only weakly on the particular isotope of the element one is considering. The nuclear mass is not relevant since the dynamics of the atom operate at the scale of the Bohr radius, where the nucleus can be regarded for most purposes as a static point charge.

Corrections to this picture will typically be of order  $1/m_Q$ , and are suppressed since  $m_Q$  is much bigger than the inverse hadronic size which sets the scale. For example, the mass difference between the  $Q\bar{q}$  pseudoscalar and vector mesons is due to interactions involving the heavy quark spin, which couples via the colour magnetic moment, which like the ordinary magnetic moment is proportional to  $1/m_Q$ . Hence

$$M_V - M_P \propto 1/m_Q . \quad (1.60)$$

On the other hand, to leading order in  $1/m_Q$

$$M_V + M_P \propto m_Q , \quad (1.61)$$

and hence we expect

$$M_V^2 - M_P^2 \simeq \text{constant} . \quad (1.62)$$

This relation is quite well satisfied by the relevant bottom and charm quark states:

$$\begin{aligned} M_{B^*}^2 - M_B^2 &= 0.49 \text{ GeV}^2 \\ M_{D^*}^2 - M_D^2 &= 0.55 \text{ GeV}^2 . \end{aligned} \quad (1.63)$$

The formal approach to heavy quark symmetries is via the construction of an effective field theory. Consider a bound state  $H$  moving with four-velocity  $v^\mu$  and containing a heavy quark  $Q$  together with light degrees of freedom. The momentum of the heavy quark will be of the form

$$p_Q^\mu = m_Q v^\mu + k^\mu \quad (1.64)$$

where  $k^\mu$  is of the order of the inverse size of the bound state. Since  $v^2 = 1$  the heavy quark propagator can be written as

$$\frac{i}{p_Q - m_Q} = \frac{i}{v \cdot k} \left( \gamma + \frac{1}{2} \right) + O(k/m_Q) . \quad (1.65)$$

We now define a projector onto positive energy states:

$$P_+ = \frac{1}{2} (\gamma + 1) , \quad (1.66)$$

$$P_+ P_+ = P_+, \quad \gamma P_+ = P_+ . \quad (1.67)$$

Since a gluon interaction with the heavy quark always appears sandwiched by heavy quark propagators or on-shell spinors, the vertex may then be simplified to

$$P_+ \gamma^\mu P_+ = \frac{1}{2} P_+ \left( \gamma \gamma^\mu + \gamma^\mu \gamma \right) P_+ \equiv P_+ v^\mu P_+ \quad (1.68)$$

and all Dirac matrices disappear, because the spin of the heavy quark is no longer relevant. The corresponding Feynman rules are as shown in Fig. 1.4. These Feynman rules follow from the heavy quark effective Lagrangian

$$\mathcal{L} = \bar{h}_v i v \cdot D h_v \equiv \bar{h}_v (i v^\mu \partial_\mu - g t^A v^\mu A_\mu^A) h_v \quad (1.69)$$

where the heavy quark field operator  $h_v$  is related to the one in the corresponding term of the original QCD Lagrangian, viz.

$$\bar{Q} (i \not{D} - m_Q) Q , \quad (1.70)$$

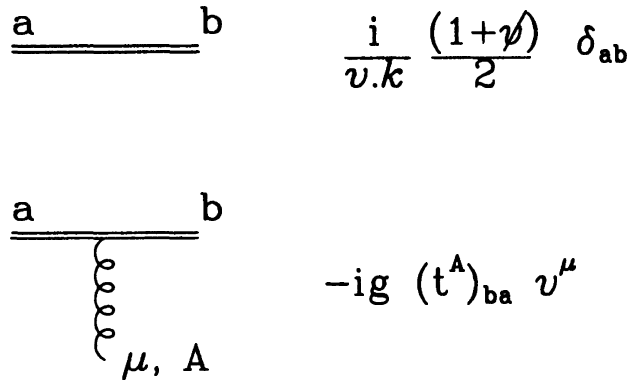


Fig. 1.4. Feynman rules of the heavy quark effective theory.

by

$$Q(x) \approx h_v \exp(-im_Q v \cdot x). \quad (1.71)$$

The Dirac equation for the heavy quark becomes

$$\not{v} h_v = h_v. \quad (1.72)$$

The part of  $Q(x)$  which is thrown away in writing Eq. (1.71) creates a heavy antiquark, and so it contributes only to the creation of virtual heavy quark-antiquark pairs in the bound state  $H$ . Such contributions involve energy fluctuations of the order of  $2m_Q$  and are therefore suppressed by powers of  $1/m_Q$ .

The mass, flavour and spin of the heavy quark do not appear in the effective Lagrangian (1.69), and therefore heavy quarks moving at the same velocity are related by a spin-flavour symmetry  $SU(2N_f)$ .

How does the weak decay of a heavy-light quark bound state look from the standpoint of the heavy quark effective theory? Let us consider a heavy meson  $H$ , such as a  $B$ , travelling with velocity  $v$  and decaying because of the action of a flavour-changing weak current into another heavy meson  $H'$ , such as a  $D^*$ , plus leptons. The action of the current instantaneously replaces a colour source travelling with velocity  $v$  with another moving at a velocity  $v'$ . If  $v = v'$  then as far as the light degrees of freedom are concerned nothing happens. If on the other hand the velocity of the heavy quark changes, the light degrees of freedom must re-arrange themselves to reconstitute the heavy meson now travelling with velocity  $v'$ . This re-arrangement of the light degrees of freedom leads to a form factor suppression. Because of the heavy flavour symmetry and Lorentz invariance, the form factor must be a universal function of  $v \cdot v'$ . It is called the Isgur-Wise function [29] and is usually denoted by  $\xi(v \cdot v')$ .

All matrix elements of the form

$$\langle H'(v', \epsilon') | \bar{h}_v \Gamma h_v | H(v, \epsilon) \rangle, \quad (1.73)$$

where  $\Gamma$  represents any combination of Dirac matrices and  $\epsilon, \epsilon'$  are polarization vectors, can be expressed in terms of the Isgur-Wise function and kinematic factors. For example, when  $H$  and  $H'$  are pseudoscalar mesons and  $\Gamma = \gamma^\mu$  we find

$$\langle P(v') | \bar{h}_{v'} \gamma^\mu h_v | P(v) \rangle = \xi(v \cdot v')(v + v')^\mu \quad (1.74)$$

where the normalization convention for the hadronic states is

$$\langle P(v') | P(v) \rangle = 2v^0(2\pi)^3 \delta^3(\vec{v} - \vec{v}') . \quad (1.75)$$

No term proportional to  $v - v'$  is possible in Eq. (1.74), since the Dirac equation (1.72) implies that the matrix element must vanish when multiplied by  $v - v'$ . The normalization of the Isgur-Wise function is fixed by Eqs. (1.74) and (1.75) as

$$\xi(v \cdot v') = 1 \text{ at } v \cdot v' = 1 . \quad (1.76)$$

For flavour-changing decays such as  $b \rightarrow c\ell\nu$  we have

$$v \cdot v' = \frac{m_b^2 + m_c^2 - q^2}{2m_b m_c} \quad (1.77)$$

where  $q^\mu$  is the momentum transfer to the leptons. Thus the Isgur-Wise function is normalized at the point of maximum momentum transfer. At the minimum momentum transfer

$$v \cdot v' = \frac{m_b^2 + m_c^2}{2m_b m_c} \simeq 1.6 . \quad (1.78)$$

In the region  $1.0 < v \cdot v' < 1.6$  it is found that

$$\xi(v \cdot v') \simeq 1 - 0.7(v \cdot v' - 1) . \quad (1.79)$$

The above brief description of heavy quark effective theory has concentrated on the extreme limit in which all mass-dependent terms are neglected. It is possible to extend the treatment to include corrections systematically order-by-order in  $1/m_Q$ . To first order in  $1/m_Q$ , it turns out that four additional form factors, each a function of  $v \cdot v'$ , are needed. We refer the interested reader to the review by Neubert [30] for further details.

## References

- 1) M. Gell-Mann, in *QCD, 20 years later*, P.M. Zerwas and H.A. Kastrup (eds.), World Scientific (1993).
- 2) H. Georgi, *Weak Interactions and Modern Particle Theory*, Addison-Wesley (1984).
- 3) Particle Data Group, L. Montanet et al., *Review of Particle Properties*, *Phys. Rev. D* **50** (1994) 1173.
- 4) J. Steinberger, *Phys. Rev.* **76** (1949) 1180.

- 5) R.E. Taylor, *Rev. Mod. Phys.* **63** (1991) 573;  
H.W. Kendall, *Rev. Mod. Phys.* **63** (1991) 597;  
J.I. Friedman, *Rev. Mod. Phys.* **63** (1991) 615.
- 6) J.D. Bjorken and S.D. Drell, *Relativistic Quantum Fields*, McGraw Hill, New York (1964).
- 7) C. Itzykson and J.B. Zuber, *Quantum Field Theory*, McGraw Hill, New York (1980).
- 8) G. Sterman, *Introduction to Quantum Field Theory*, Cambridge (1993).
- 9) M.E. Peskin and D.V. Schroeder, *An Introduction to Quantum Field Theory*, Addison-Wesley (1995).
- 10) F. Yndurain, *Quantum Chromodynamics*, Springer-Verlag (1983).
- 11) T. Muta, *Foundations of Quantum Chromodynamics*, World Scientific (1987).
- 12) Yu.L. Dokshitzer et al., *Basics Of Perturbative QCD*, Editions Frontières (1991).
- 13) A.H. Mueller, *Phys. Rep.* **73** (1981) 237.
- 14) G. Altarelli, *Phys. Rep.* **81** (1982) 1.
- 15) D.W. Duke and R.G. Roberts, *Phys. Rep.* **120** (1985) 275.
- 16) G. Sterman et al., *Rev. Mod. Phys.* **67** (1995) 157.
- 17) E. Abers and B.W. Lee, *Phys. Rep.* **9** (1973) 1.
- 18) L. Faddeev and V.N. Popov, *Phys. Lett.* **B25** (1967) 29.
- 19) R.K. Ellis, Proceedings of the 1987 Theoretical Advanced Study Institute in Elementary Particle Physics, World Scientific, R. Slansky and G. West (eds.).
- 20) G. t'Hooft and M.J.G. Veltman, Diagrammar, CERN Yellow Report 73-9, published in the proceedings of the summer school, *Particle Interactions At Very High Energies, Part B*, Louvain (1973);  
M. Veltman, *Diagrammatica: The Path to Feynman Diagrams*, Cambridge (1994).
- 21) G. Leibbrandt, *Rev. Mod. Phys.* **59** (1987) 1067;  
A. Bassetto, G. Nardelli and R. Soldati, *Yang-Mills theory in algebraic non-covariant gauges: canonical quantization and renormalization*, World Scientific (1991).
- 22) S. Coleman, Proceedings of the 15th course of the International School of Subnuclear Physics, August 1977, Erice, Italy. A. Zichichi (ed.).
- 23) F. Wilczek, Proceedings of the 21st course of the International School of Subnuclear Physics, August 1983, Erice, Italy. A. Zichichi (ed.).
- 24) H-Y. Cheng, *Phys. Rep.* **158** (1988) 1.
- 25) R.D. Peccei and H. Quinn, *Phys. Rev.* **D16** (1977) 1791.
- 26) H. Leutwyler, *Phys. Lett.* **B374** (1996) 163;  
Bern preprint BUTP 94/8, to be published in the proceedings of 2nd IFT Workshop, *Yukawa interactions and the origin of mass*, International Press, Cambridge, MA 1995, P. Ramond (ed.).
- 27) J. Goldstone, *Nuovo Cimento* **19** (1961) 154.
- 28) H. Leutwyler, Proceedings of the 1991 Theoretical Advanced Study Institute in Elementary Particle Physics;  
J. Donoghue, Proceedings of the 1993 Theoretical Advanced Study Institute in Elementary Particle Physics.
- 29) N. Isgur and M.B. Wise, *Phys. Lett.* **B232** (1989) 113; *ibid.* **B237** (1990) 527.
- 30) M. Neubert, *Phys. Rep.* **245** (1994) 259.

# 2

## Asymptotic freedom and confinement

This chapter introduces the two concepts of asymptotic freedom and confinement. Confinement explains why the quark and gluon degrees of freedom are not observed as states which propagate over macroscopic distances. Asymptotic freedom explains why the methods of perturbation theory are useful at high energy; the coupling constant is said to run, being large at low energy and becoming smaller at high energy.

### 2.1 The running coupling constant

In order to introduce the concept of a running coupling, consider as an example a dimensionless physical observable  $R$  which depends on a single energy scale  $Q$ . By assumption the scale  $Q$  is much bigger than all other dimensionful parameters such as quark masses and we shall therefore set the masses to zero. This step requires the additional assumption that  $R$  has a sensible zero-mass limit – we discuss this point in more detail in Section 2.4.

Naive scaling would suggest that because there is a single large scale,  $R$  should have a constant value independent of  $Q$ . This result is not however true in a renormalizable quantum field theory. When we calculate  $R$  as a perturbation series in the coupling  $\alpha_s = g^2/4\pi$ , (defined in analogy with the fine structure constant of QED), the perturbation series requires renormalization to remove ultraviolet divergences. Because this renormalization procedure introduces a second mass scale  $\mu$  – the point at which the subtractions which remove the ultraviolet divergences are performed –  $R$  depends in general on the ratio  $Q^2/\mu^2$  and is therefore not constant. It follows also that the renormalized coupling  $\alpha_s$  depends on the choice made for the subtraction point  $\mu$ .

However  $\mu$  is an arbitrary parameter. The Lagrangian of QCD makes no mention of the scale  $\mu$ , even though a choice of  $\mu$  is required to define the theory at the quantum level. Therefore, if we hold the bare coupling fixed, physical quantities such as  $R$  cannot depend on the choice made for  $\mu$ . Since  $R$  is dimensionless, it can only depend on the ratio  $Q^2/\mu^2$  and the renormalized coupling  $\alpha_s$ . Mathematically, the  $\mu$  independence of  $R$  may be expressed by

$$\mu^2 \frac{d}{d\mu^2} R(Q^2/\mu^2, \alpha_s) \equiv \left[ \mu^2 \frac{\partial}{\partial \mu^2} + \mu^2 \frac{\partial \alpha_s}{\partial \mu^2} \frac{\partial}{\partial \alpha_s} \right] R = 0 . \quad (2.1)$$

To rewrite this equation in a more compact form we introduce the notations

$$t = \ln \left( \frac{Q^2}{\mu^2} \right), \quad \beta(\alpha_s) = \mu^2 \frac{\partial \alpha_s}{\partial \mu^2} . \quad (2.2)$$

The derivative of the coupling in the definition of the  $\beta$  function is performed at fixed bare coupling. We rewrite Eq. (2.1) as

$$\left[ -\frac{\partial}{\partial t} + \beta(\alpha_s) \frac{\partial}{\partial \alpha_s} \right] R(e^t, \alpha_s) = 0 . \quad (2.3)$$

This first order partial differential equation is solved by implicitly defining a new function – the *running coupling*  $\alpha_s(Q^2)$  – as follows:

$$t = \int_{\alpha_s}^{\alpha_s(Q^2)} \frac{dx}{\beta(x)}, \quad \alpha_s(\mu^2) \equiv \alpha_s . \quad (2.4)$$

By differentiating Eq. (2.4) we see that

$$\frac{\partial \alpha_s(Q^2)}{\partial t} = \beta(\alpha_s(Q^2)), \quad \frac{\partial \alpha_s(Q^2)}{\partial \alpha_s} = \frac{\beta(\alpha_s(Q^2))}{\beta(\alpha_s)} \quad (2.5)$$

and hence that  $R(1, \alpha_s(Q^2))$  is a solution of Eq. (2.3). The above analysis shows that all of the scale dependence in  $R$  enters through the running of the coupling constant  $\alpha_s(Q^2)$ . It follows that knowledge of the quantity  $R(1, \alpha_s)$ , calculated in fixed-order perturbation theory, allows us to predict the variation of  $R$  with  $Q$  if we can solve Eq. (2.4). In the next section, we shall show that QCD is an *asymptotically free* theory. This means that  $\alpha_s(Q^2)$  becomes smaller as the scale  $Q$  increases. For sufficiently large  $Q$ , therefore, we can always solve Eq. (2.4) using perturbation theory.

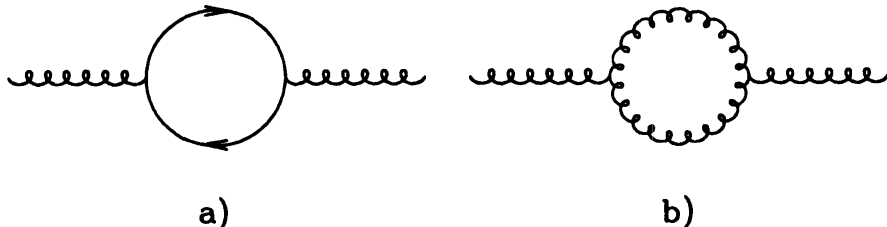


Fig. 2.1. Graphs which contribute to the  $\beta$  function in the one loop approximation.

## 2.2 The $\beta$ function

The running of the coupling constant  $\alpha_s$  is determined by the renormalization group equation,

$$Q^2 \frac{\partial \alpha_s}{\partial Q^2} = \beta(\alpha_s). \quad (2.6)$$

In QCD, the  $\beta$  function has the perturbative expansion [1,2,3]

$$\beta(\alpha_S) = -b\alpha_S^2(1 + b'\alpha_S + b''\alpha_S^2 + O(\alpha_S^3)) , \quad (2.7)$$

where

$$\begin{aligned}
b &= \frac{(11C_A - 2n_f)}{12\pi} = \frac{(33 - 2n_f)}{12\pi} \\
b' &= \frac{(17C_A^2 - 5C_A n_f - 3C_F n_f)}{2\pi(11C_A - 2n_f)} = \frac{(153 - 19n_f)}{2\pi(33 - 2n_f)}, \\
b'' &= \frac{(2857C_A^3 + (54C_F^2 - 615C_F C_A - 1415C_A^2)n_f + (66C_F + 79C_A)n_f^2)}{288\pi^2(11C_A - 2n_f)} \\
&= \frac{(77139 - 15099n_f + 325n_f^2)}{288\pi^2(33 - 2n_f)}
\end{aligned} \tag{2.8}$$

and  $n_f$  is the number of active light flavours.<sup>1</sup> We shall define this concept more precisely in Section 2.4. The  $\beta$  function coefficients are extracted from the higher-order (loop) corrections to the bare vertices of the theory, as in QED. Fig. 2.1 shows some of the diagrams which contribute to the  $\beta$  function of QCD in the one-loop approximation. Here we see for the first time the effect of the non-Abelian interactions in QCD. In QED (with one fermion flavour) the  $\beta$  function is

$$\beta_{\text{QED}}(\alpha) = \frac{1}{3\pi}\alpha^2 + \dots \quad (2.9)$$

<sup>1</sup> The three-loop coefficient  $b''$  depends on the scheme used for the renormalization of the theory. The result given here is for the  $\overline{\text{MS}}$  scheme. See Section 2.5 for a discussion of scheme dependence.

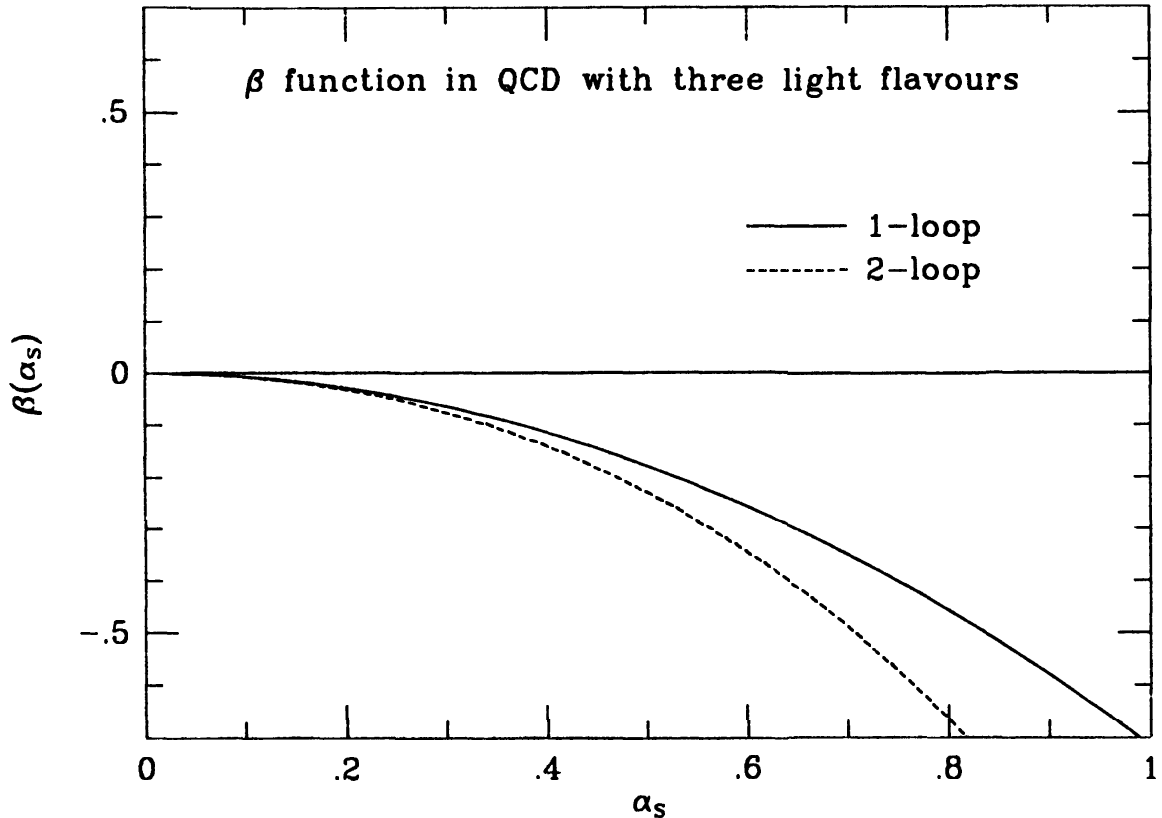


Fig. 2.2. The  $\beta$  function in the one- and two-loop approximations.

and thus the  $b$  coefficients in QED and QCD have the opposite sign for  $n_f \leq 16$ .

Fig. 2.2 shows the beta function with three light flavours, when only the first (one-loop) term, or the first and second (two-loop) terms in the perturbative expansion in Eq. (2.7) are retained. So far, the three-loop coefficient  $b''$  has not been generally used for phenomenology, because most other quantities are not known to this order, and so we shall neglect it. The curve including the three-loop coefficient has not been shown in Fig. 2.2 because it would be indistinguishable from the two-loop curve. An alternative notation which is sometimes used is

$$\begin{aligned} \beta(\alpha_s) &= -\alpha_s \sum_{n=0}^{\infty} \beta_n \left( \frac{\alpha_s}{4\pi} \right)^{(n+1)} \\ \beta_0 &= 4\pi b = 11 - \frac{2}{3}n_f, \quad \beta_1 = 16\pi^2 bb' = 102 - \frac{38}{3}n_f, \\ \beta_2 &= 64\pi^3 bb'' = \frac{2857}{2} - \frac{5033}{18}n_f + \frac{325}{54}n_f^2, \quad \dots \end{aligned} \quad (2.10)$$

From Eqs. (2.6,2.7) we may write

$$Q^2 \frac{\partial \alpha_s(Q^2)}{\partial Q^2} = -b \alpha_s^2(Q^2) [1 + b' \alpha_s(Q^2) + O(\alpha_s^2(Q^2))]. \quad (2.11)$$

If both  $\alpha_s(\mu^2)$  and  $\alpha_s(Q^2)$  are in the perturbative region it makes sense to truncate the series on the right-hand-side and solve the resulting differential equation for  $\alpha_s(Q^2)$ . For example, neglecting the  $b'$  and higher coefficients in Eq. (2.11) gives the solution

$$\alpha_s(Q^2) = \frac{\alpha_s(\mu^2)}{1 + \alpha_s(\mu^2)bt}, \quad t = \ln \frac{Q^2}{\mu^2}. \quad (2.12)$$

This gives the relation between  $\alpha_s(Q^2)$  and  $\alpha_s(\mu^2)$ , if both are in the perturbative region. Evidently as  $t$  becomes very large, the running coupling  $\alpha_s(Q^2)$  decreases to zero. This is the property of *asymptotic freedom*. The approach to zero is rather slow since  $\alpha_s$  only decreases like an inverse power of  $\ln Q^2$ . Notice that the sign of  $b$  is crucial. With the opposite sign of  $b$  the coupling would *increase* at large  $Q^2$ , as it does in QED.

It is relatively straightforward to show that including the next-to-leading order coefficient  $b'$  yields the solution

$$\frac{1}{\alpha_s(Q^2)} - \frac{1}{\alpha_s(\mu^2)} + b' \ln \left( \frac{\alpha_s(Q^2)}{1 + b'\alpha_s(Q^2)} \right) - b' \ln \left( \frac{\alpha_s(\mu^2)}{1 + b'\alpha_s(\mu^2)} \right) = bt. \quad (2.13)$$

Note that this is now an implicit equation for  $\alpha_s(Q^2)$  as a function of  $t$  and  $\alpha_s(\mu^2)$ . In practice, given values for these parameters,  $\alpha_s(Q^2)$  can easily be obtained numerically to any desired accuracy. We discuss in Section 2.5 the expressions for  $\alpha_s$  that are normally used in practice.

Returning to the physical quantity  $R$ , we can now demonstrate the type of terms which the renormalization group resums. Assume that in perturbation theory  $R$  has the expansion

$$R = R_1 \alpha_s + \dots \quad (2.14)$$

where  $\dots$  represents terms of order  $\alpha_s^2$  and higher. The solution of Eq. (2.3),  $R(1, \alpha_s(Q^2))$ , can be re-expressed in terms of  $\alpha_s(\mu^2)$  using Eq. (2.12):

$$\begin{aligned} R(1, \alpha_s(Q^2)) &= R_1 \alpha_s(\mu^2) \sum_{j=0}^{\infty} [-\alpha_s(\mu^2)bt]^j \\ &= R_1 \alpha_s(\mu^2) [1 - \alpha_s(\mu^2)bt + \alpha_s^2(\mu^2)(bt)^2 + \dots] \end{aligned} \quad (2.15)$$

Thus order by order in perturbation theory there are logarithms of  $Q^2/\mu^2$  which are automatically resummed by using the running coupling. Higher-order terms in  $R$  – represented by the dots in Eq. (2.14) – when expanded give terms with fewer logarithms per power of  $\alpha_s$ . For example, a term  $R_2 \alpha_s^2$  would give  $R_2 \alpha_s(\mu^2)^2 [1 - 2\alpha_s(\mu^2)bt + \dots]$ , with one less logarithm in each term. An example of how this works in practice will be discussed in the next chapter.

### 2.3 Asymptotic freedom

There is no simple intuitive explanation of the property of asymptotic freedom in QCD. This is in contrast to QED, where the idea that the observed charge of the electron is smaller at large distances because of screening of its electric charge by vacuum polarization is quite intuitive. It would be nice to be able to extend this argument to QCD. The new feature in QCD is the presence of the gluons, which are spin one particles that carry colour charge.

There are two types of arguments which aim to give a simple explanation of asymptotic freedom [4,5]. They describe the phenomenon either as a dielectric or a paramagnetic effect. The first line of argument [4] calculates the dielectric properties of the vacuum and ascribes the asymptotic freedom of the theory to the self-interaction of the gluon field. The basic idea is that the emission of virtual gluons by static colour sources causes their colour charges to ‘leak out’ into the surrounding vacuum. The interaction between distributed charges is weaker than that between point charges when the charge distributions overlap, leading to a reduction of the colour force at short distances, which is the essence of asymptotic freedom.

Here we sketch in more detail an argument of the second type [5] which describes asymptotic freedom as a paramagnetic effect due to the spin of the gluons. The appealing feature of the magnetic explanation is that polarizable materials that are attracted towards a magnetic field (paramagnetism) and repelled from one (diamagnetism) are both familiar. This is in contrast to electric polarization effects in matter which are always attractive (dielectric).

We start by reviewing the situation in QED. Here the effective charge grows at small distances (large momenta) as one probes more of the unshielded central charge. This can be represented by a scale-dependent dielectric constant. One can define a running charge at scale  $q^2$  in terms of the charge at the ultraviolet cut-off scale  $\Lambda_{\text{UV}}^2 \gg q^2$  as

$$\alpha(q^2) = \frac{\alpha(\Lambda_{\text{UV}}^2)}{\varepsilon(q^2)} \quad (2.16)$$

where

$$\frac{1}{\varepsilon(q^2)} = 1 - \frac{\beta(\alpha)}{\alpha} \ln \frac{\Lambda_{\text{UV}}^2}{q^2} \quad (2.17)$$

and the running charge satisfies the equation

$$\frac{d\alpha(q^2)}{d \ln q^2} = \beta(\alpha). \quad (2.18)$$

Electric		Magnetic		
Screening	$\epsilon > 1$	$\mu < 1$	$\chi < 0$	diamagnetism
Anti-screening	$\epsilon < 1$	$\mu > 1$	$\chi > 0$	paramagnetism

Table 2.1. Relationship between the dielectric and paramagnetic explanation of asymptotic freedom.

If the  $\beta$  function is positive, as in QED, then  $\epsilon(q^2) > 1$ , which corresponds to a screening of the central charge.

We now assume that the vacuum of a relativistic quantum field theory can be treated as a polarizable medium. For this special medium the dielectric constant  $\epsilon(q^2)$  and the magnetic permeability  $\mu(q^2)$  must satisfy the relation

$$\mu(q^2)\epsilon(q^2) = 1 \quad (2.19)$$

(in units in which  $c = 1$ ) for all  $q$ . This is a consequence of the Lorentz invariance of the vacuum. We are free to exploit this relationship by considering the properties of the QCD vacuum in a background colour magnetic field, rather than a colour electric field, if it is simpler to do so. We choose to consider the behaviour of the magnetic susceptibility,  $\chi$  related to the permeability by the relation  $\mu = 1 + \chi$ . From Eq. (2.17) we have

$$\chi(q^2) = -\frac{\beta(\alpha)}{\alpha} \ln \frac{\Lambda_{UV}^2}{q^2}. \quad (2.20)$$

The relationship between electric and magnetic properties is summarized in Table 2.1.

Before we go on to describe the paramagnetic properties of the vacuum, a brief reminder of the magnetic properties of a free electron quantum gas may be useful [6]. The magnetic susceptibility of a free electron gas may be divided into two parts. The first term, known as Pauli paramagnetism, represents the effect of electrons coupling to the magnetic field through their spin magnetic moments. It therefore describes a gas of particles with magnetic moments but no charges. The second term, known as Landau diamagnetism, describes the coupling of the field to the orbital motion of the electrons. It can be shown that the two contributions are related by

$$\chi_{\text{Landau}} = -\frac{1}{3} \chi_{\text{Pauli}}. \quad (2.21)$$

In this case the system is paramagnetic because the Pauli paramagnetism is larger in magnitude than the Landau diamagnetism.

Returning to the case of the vacuum of a relativistic field theory, we find that both paramagnetic and diamagnetic contributions are present. The Pauli term has to be generalized slightly to take into account particles of spin  $S$  different from one half: it becomes proportional to  $S^2$ . The final result is given by Eq. (2.20) where

$$\beta(\alpha) = -b\alpha^2 \quad (2.22)$$

and the contribution to  $b$  from particles of spin  $S$  is

$$b = \frac{(-1)^{2S}}{2\pi} \left[ (2S)^2 - \frac{1}{3} \right]. \quad (2.23)$$

For spins 0,  $\frac{1}{2}$  and 1 the result from Eq. (2.23) is

$$b = -\frac{1}{6\pi}, -\frac{1}{3\pi}, \frac{11}{6\pi} \quad \text{for } S = 0, \frac{1}{2}, 1. \quad (2.24)$$

We see that Eq. (2.23) can be considered as a generalization of Eq (2.21) to arbitrary spin. As expected, the Pauli paramagnetic term grows with the spin of the particle. The overall sign  $(-1)^{2S}$  is due to the fact that the fermionic vacuum energy, including the energy due to an external magnetic field, is negative, whereas that for bosons is positive. This is a consequence of the anticommutation and commutation relations, respectively, of the field operators. Because of this overall sign, spin- $\frac{1}{2}$  particles give a diamagnetic contribution to the  $\beta$  function (unlike the case of the free electron gas), while spin-1 particles make a larger paramagnetic contribution.

Inserting the appropriate colour factors of  $C_A/2$  for gluons with  $S = 1$  and  $n_f/2$  for quarks with  $S = \frac{1}{2}$ , we obtain

$$b = \frac{1}{12\pi} (33 - 2n_f), \quad (2.25)$$

which exhibits asymptotic freedom as long as  $n_f < 17$ , because the colour paramagnetic contribution of the gluons overcomes the colour diamagnetic quark contribution.

## 2.4 Quark masses

In the discussion up to now we have ignored the masses of the quarks. We shall now investigate the theoretical basis for this assumption. Note that from the point of view of the Lagrangian the quark mass is just another parameter like the coupling. Let us consider for simplicity the case where we have one flavour of quark with renormalized mass  $m$ . As before the  $\mu$  independence of the physical result implies a renormalization group equation for  $R$  which is now a function of the renormalized mass

*m.* The form of the equation depends on the choice of renormalization procedure. In the following we shall use the scheme of Weinberg [7] which ensures that the  $\beta$  function and the mass anomalous dimension  $\gamma_m$  are only functions of the renormalized coupling  $\alpha_s$ .

In this scheme the renormalization group equation including the mass parameter is of the form

$$\left[ \mu^2 \frac{\partial}{\partial \mu^2} + \beta(\alpha_s) \frac{\partial}{\partial \alpha_s} - \gamma_m(\alpha_s) m \frac{\partial}{\partial m} \right] R(Q^2/\mu^2, \alpha_s, m/Q) = 0. \quad (2.26)$$

The partial derivatives in Eq. (2.26) are taken at fixed values of the other two parameters. The function  $\gamma_m$  is the mass anomalous dimension, a perturbatively calculable quantity:

$$\gamma_m(\alpha_s) = c\alpha_s(1 + c'\alpha_s + \dots). \quad (2.27)$$

The coefficients of the mass anomalous dimension are also dependent on the renormalization scheme: in the scheme that is most often used (the  $\overline{\text{MS}}$  scheme – see Section 2.5), they are [8]

$$c = \frac{1}{\pi}, \quad c' = \frac{(303 - 10n_f)}{72\pi}. \quad (2.28)$$

Since  $R$  is a dimensionless function we have the result

$$\left[ Q^2 \frac{\partial}{\partial Q^2} + \mu^2 \frac{\partial}{\partial \mu^2} + m^2 \frac{\partial}{\partial m^2} \right] R(Q^2/\mu^2, \alpha_s, m/Q) = 0. \quad (2.29)$$

Subtracting Eq.(2.26) from Eq.(2.29) we obtain an equation which fixes the dependence of  $R$  on  $Q$ :

$$\left[ Q^2 \frac{\partial}{\partial Q^2} - \beta(\alpha_s) \frac{\partial}{\partial \alpha_s} + (\frac{1}{2} + \gamma_m(\alpha_s)) m \frac{\partial}{\partial m} \right] R(Q^2/\mu^2, \alpha_s, m/Q) = 0. \quad (2.30)$$

This equation is solved by introducing a running mass  $m(Q^2)$  in analogy with the running coupling, such that

$$Q^2 \frac{\partial m}{\partial Q^2} = -\gamma_m(\alpha_s)m(Q^2). \quad (2.31)$$

The solution of this equation is

$$\begin{aligned} m(Q^2) &= m(\mu^2) \exp \left[ - \int_{\mu^2}^{Q^2} \frac{dQ^2}{Q^2} \gamma_m(\alpha_s(Q^2)) \right] \\ &= m(\mu^2) \exp \left[ - \int_{\alpha_s(\mu^2)}^{\alpha_s(Q^2)} d\alpha_s \frac{\gamma_m(\alpha_s)}{\beta(\alpha_s)} \right]. \end{aligned} \quad (2.32)$$

In terms of the running mass and running coupling, the solution of the renormalization group equation is the same as before. All of the non-

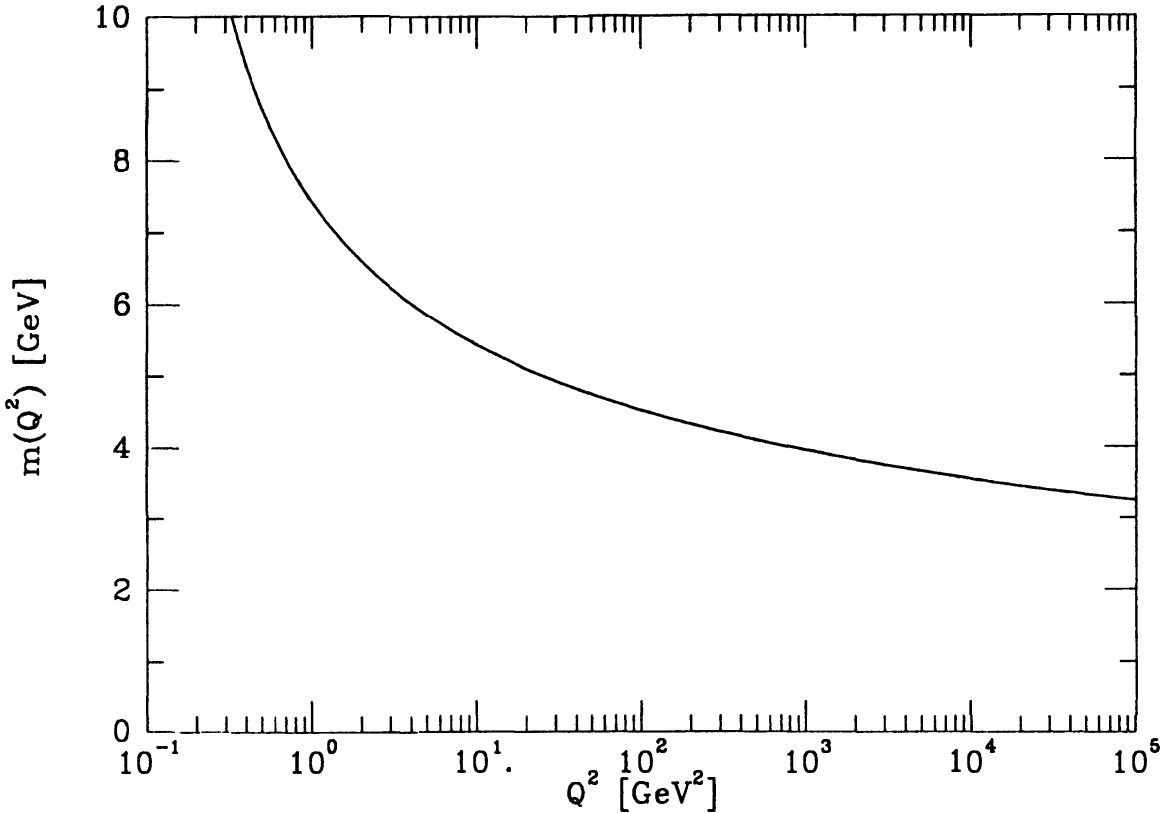


Fig. 2.3. Running of the bottom quark mass.

trivial scale dependence of  $R$  can be included in the running of the mass and the coupling:

$$R(Q^2/\mu^2, \alpha_s, m/Q) \rightarrow R(1, \alpha_s(Q^2), m(Q^2)/Q). \quad (2.33)$$

Using the asymptotic freedom of the theory at large  $Q$ , we can calculate the running mass in perturbation theory. From Eq. (2.31) we obtain

$$m(Q^2) = \hat{m} [\alpha_s(Q^2)]^{c/b} \left[ 1 + \frac{c(c' - b')}{b} \alpha_s(Q^2) + O(\alpha_s^2) \right]. \quad (2.34)$$

The mass  $\hat{m}$  is a renormalization-group invariant constant of integration (similar to  $\Lambda$ ). The running of the  $b$  quark mass is illustrated in Fig. 2.3. We see from Eqs. (2.33) and (2.34) that the effect of the mass is suppressed at high  $Q^2$ , both by its ‘engineering dimension’ which leads to a suppression of  $1/Q$  and by its anomalous dimension  $\gamma_m$  ( $c/b > 0$ ), which leads to a further logarithmic suppression.

To investigate mass effects more quantitatively, consider the case in which  $R$  and its first  $N$  derivatives are finite at  $m = 0$ . We can write

$$\begin{aligned} R(1, \alpha_s(Q^2), m(Q^2)/Q) &\sim R(1, \alpha_s(Q^2), 0) \\ &+ \sum_{n=1}^N \frac{1}{n!} \left[ \frac{m(Q^2)}{Q} \right]^n R^{(n)}(1, \alpha_s(Q^2), 0) \end{aligned} \quad (2.35)$$

where  $R^{(n)}$  denotes the  $n$ th derivative of  $R$  with respect to its third argument. The derivative terms are suppressed by at least an inverse power of  $Q$ . At large  $Q$  we therefore have a theoretical justification to drop the mass. The important point is that in an asymptotically free theory the anomalous dimension leads to a change of the mass with  $Q$  which varies like a power of  $\ln Q$ . This can never overcome the inverse power of  $Q$  from the engineering dimension, and in fact leads to a further suppression when  $Q \gg m(Q^2)$ .

Consider now the opposite case, of a heavy quark with mass much greater than the relevant scale  $Q$ . An example would be the influence of the top quark on physics at scales well below  $m_t$ . In this case it can be shown that the effects of the heavy quark on cross sections are suppressed by inverse powers of  $m$  and can therefore be ignored for  $Q \ll m$  [9]. That is why we specified that  $n_f$  in Eq. (2.7) represents the number of ‘active’ light flavours, i.e. the number with masses much smaller than the characteristic scale  $Q$  at which  $\alpha_s(Q^2)$  is required.

When  $Q$  is neither much smaller nor much larger than a particular quark mass, but still large enough to be in the perturbative domain (for example,  $Q \sim m_b$ ), then the mass of that quark has to be taken into account explicitly in calculations. We shall see examples of this in Chapter 10. There remains, however, the problem of relating the values of  $\alpha_s$  measured in the two domains  $Q \ll m$  and  $Q \gg m$ . Technically this is achieved by matching the coupling of the full theory which includes the heavy quark with an effective theory which involves only the light degrees of freedom. In particular, the value of  $n_f$  increases by one unit as we pass from the effective theory to the full theory and so the  $\beta$  function changes, altering the running of  $\alpha_s$ .

The simplest prescription is to require that  $\alpha_s(Q^2)$  should be continuous at  $Q = m$ , the heavy quark mass scale. In this approach,  $\alpha_s$  is simply regarded as the solution of the first-order differential equation (2.11), with a step-function discontinuity in the right-hand side at  $Q = m$ . Writing the solutions above and below the discontinuity as  $\alpha_+$  and  $\alpha_-$ , respectively, and expanding the  $\beta$  function to leading order, we have

$$\frac{1}{\alpha_+(Q^2)} - b_+ \ln \frac{Q^2}{m^2} = \frac{1}{\alpha_-(Q^2)} - b_- \ln \frac{Q^2}{m^2} = \frac{1}{\alpha_s(m^2)}, \quad (2.36)$$

where  $b_- - b_+ = 1/6\pi$  from Eq. (2.7), and hence

$$\alpha_+(Q^2) = \alpha_-(Q^2) \left[ 1 - \frac{1}{6\pi} \alpha_-(Q^2) \ln \frac{Q^2}{m^2} \right]^{-1}. \quad (2.37)$$

The same approach can be carried through to any order; for example, Eq. (2.13) yields an implicit next-to-leading order relation between  $\alpha_+$  and  $\alpha_-$ .

At this point one might wonder why we should match the two expressions for  $\alpha_s$  at  $Q^2 = m^2$  rather than, say,  $4m^2$ , which might even seem more natural in terms of the energy required to create a heavy quark-antiquark pair. It should be recalled, however, that our expressions for  $\alpha_+(Q^2)$  and  $\alpha_-(Q^2)$  are only valid for  $Q^2 \gg m^2$  and  $Q^2 \ll m^2$  respectively, and so a physical argument about what should happen at  $Q \sim m$ , or even whether  $\alpha_s$  should be continuous in that region, is not strictly relevant. What matters is the consistency of the calculation in the full theory including the heavy quark, (appropriate when  $Q \gg m$ ) and the calculation performed in an effective theory with only light degrees of freedom, (appropriate when  $Q \ll m$ ). This is enforced by computing the coefficient functions  $C_k$  in the generalized version of Eq. (2.37):

$$\alpha_+(Q^2) = \alpha_-(Q^2) + \sum_{k=1}^{\infty} C_k \left( \ln \frac{Q^2}{m^2} \right) [\alpha_-(Q^2)]^{k+1}. \quad (2.38)$$

One finds [10] that in the usual renormalization scheme (the  $\overline{\text{MS}}$  scheme – see the discussion in Section 2.5)

$$C_1(x) = \frac{1}{6\pi} x \quad (2.39)$$

$$C_2(x) = \frac{1}{72\pi^2} (2x^2 + 33x - 7). \quad (2.40)$$

Taking into account that  $m = m(Q^2)$  is a running mass, this is almost equivalent to the prescription of matching at the quark mass, defined implicitly by  $m_q = m(m_q^2)$  [11]. At this point Eq. (2.38) becomes

$$\alpha_+(m_q^2) = \alpha_-(m_q^2) - \frac{7}{72\pi^2} [\alpha_-(m_q^2)]^3, \quad (2.41)$$

a difference that is negligible for all practical purposes. Eq. (2.39) explains the choice of performing the matching of the  $\overline{\text{MS}}$  coupling at  $Q = m$ . The absence of a constant term in Eq. (2.39) indicates that at one loop order the coupling  $\alpha_+$  is equal to  $\alpha_-$  if the matching is performed at  $Q = m$ . If the matching were performed at another scale, such as  $Q = 2m$ , the  $\overline{\text{MS}}$  coupling of the full theory including the heavy quark would differ at the matching point from the coupling of the effective theory with only the light degrees of freedom. As emphasized above, the continuity of the coupling at the matching point is not in itself a requirement of the theory. The choice of matching at  $Q = m$  leads to approximate continuity of the running coupling and hence an appealing physical picture for  $\alpha_s$ .

## 2.5 The $\Lambda$ parameter

Perturbative QCD tells us how the coupling constant varies with the scale, not the absolute value itself. The latter has to be obtained from experiment. Thus we can choose as ‘the’ fundamental parameter of the theory the value of the coupling constant at a convenient reference scale which is large enough to be in the perturbative domain,  $M_Z^2$  for example. Setting  $\mu = M_Z$  in Eq. (2.13), we can then deduce the value at any other large scale  $Q^2$ . This has become the standard approach: when we review the measurements of  $\alpha_s$  in Chapter 12, we shall compare them mainly in terms of  $\alpha_s(M_Z^2)$ .

An alternative approach, which was adopted historically and is still convenient for many purposes, is to introduce a dimensionful parameter directly into the definition of  $\alpha_s(Q^2)$ . By convention this parameter is called  $\Lambda$  and is the constant of integration defined by

$$\ln \frac{Q^2}{\Lambda^2} = - \int_{\alpha_s(Q^2)}^{\infty} \frac{dx}{\beta(x)} = \int_{\alpha_s(Q^2)}^{\infty} \frac{dx}{bx^2(1 + b'x + \dots)}. \quad (2.42)$$

$\Lambda$  represents the scale at which the coupling would diverge, if extrapolated outside the perturbative domain. More qualitatively, it indicates the order of magnitude of the scale at which  $\alpha_s(Q^2)$  becomes strong. Depending on the precise definition, to be discussed below, its value is in the neighbourhood of 200 MeV. Thus  $\alpha_s(Q^2)$  becomes large, and perturbation theory breaks down, for scales comparable with the masses of the light hadrons, *i.e.*  $Q \simeq 1$  GeV. This could be an indication that the *confinement* of quarks and gluons inside hadrons is actually a consequence of the growth of the coupling at low scales, which is a corollary of the decrease at high scales that leads to asymptotic freedom.

The introduction of  $\Lambda$  allows us to write the asymptotic solution for  $\alpha_s$  in terms of this parameter. In leading order (LO), *i.e.* retaining only the  $b$  coefficient in the  $\beta$  function, we can perform the integration in Eq. (2.42) to obtain

$$\alpha_s(Q^2) = \frac{1}{b \ln(Q^2/\Lambda^2)}. \quad (2.43)$$

Note that for large  $Q^2$  this solution agrees with Eq. (2.12) as it must. The definition of  $\Lambda$  is extended to next-to-leading order (NLO) by including also the  $b'$  coefficient in the integral:

$$\frac{1}{\alpha_s(Q^2)} + b' \ln \left( \frac{b' \alpha_s(Q^2)}{1 + b' \alpha_s(Q^2)} \right) = b \ln \left( \frac{Q^2}{\Lambda^2} \right). \quad (2.44)$$

Again, this allows a numerical determination of  $\alpha_s(Q^2)$  for a given value of  $\Lambda$ . Alternatively, we can obtain an approximate solution of Eq. (2.44)

	$\alpha_s(n_f = 4)$	$\alpha_s(n_f = 5)$
LO	0.234	0.255
NLO	0.184	0.206

Table 2.2.  $\alpha_s(Q^2)$  for  $Q = 5$  GeV and  $\Lambda = 200$  MeV.

in terms of inverse powers of  $\ln(Q^2/\Lambda^2)$ :

$$\alpha_s(Q^2) = \frac{1}{b \ln(Q^2/\Lambda^2)} \left[ 1 - \frac{b'}{b} \frac{\ln \ln(Q^2/\Lambda^2)}{\ln(Q^2/\Lambda^2)} + \dots \right]. \quad (2.45)$$

Note, however, that this expression corresponds to a slightly different definition of  $\Lambda$  to Eq. (2.44). The *true* expansion of  $\alpha_s(Q^2)$  in inverse powers of  $\ln(Q^2/\Lambda^2)$  would contain a term of order  $k/\ln^2(Q^2/\Lambda^2)$  where  $k$  is a constant. To this order, the two definitions differ by a constant factor. Specifically, if we call Eqs. (2.44) and (2.45) definitions 1 and 2 respectively, then for the *same* value of  $\alpha_s(Q^2)$  the two  $\Lambda$ 's are related by

$$\Lambda_1 \simeq \left( \frac{b}{b'} \right)^{\frac{b'}{b}} \Lambda_2 \simeq 1.1 \Lambda_2 \quad (n_f = 5). \quad (2.46)$$

In this book we shall follow the convention of using Eq. (2.45) as described in ref. [12].

It will be clear from the above discussion that the use of  $\Lambda$  as the fundamental parameter of QCD presents a number of traps which can ensnare the unwary. First,  $\Lambda$  can be defined to leading or next-to-leading order and in each case multiplying  $\Lambda$  by a constant gives an equally acceptable definition. The differences induced in  $\alpha_s(Q^2)$  are one order higher in perturbation theory. Nowadays, all precision QCD phenomenology is performed at next-to-leading order. Either Eq. (2.44) or Eq. (2.45) can be used to define  $\Lambda$  in this case, and both definitions are used in the literature. Since in practice it is usually  $\alpha_s$  which is measured experimentally, it is important when comparing  $\Lambda$  values to check that the same equation has been used to determine  $\Lambda$  from the coupling constant. Differences between the results obtained using different conventions – although small – can be comparable to present-day measurement errors.

A second difficulty with the above definitions is that  $\Lambda$  depends on the number of active flavours. At two loop order values of  $\Lambda$  for different numbers of flavours are defined by imposing the continuity of  $\alpha_s$  at the scale  $\mu = m$ , where  $m$  is the mass of the heavy quark, as described in the previous section. This is illustrated in Table 2.2 where the LO and NLO couplings are calculated using Eqs.(2.43) and (2.45) respectively. The matching prescription is determined by the conditions that for all

values of the momenta the coupling constant must be both a solution of the renormalization group equation and also a continuous function. From Eq. (2.45) for  $\mu > m_b$  we have

$$\alpha_s(Q^2, 5) = \frac{1}{b(5) \ln(Q^2/\Lambda(5)^2)} [1 - \dots]. \quad (2.47)$$

For  $m_c < Q < m_b$ , the coupling evolves with four active flavours, and the form to use is

$$\frac{1}{\alpha_s(Q^2, 4)} = \frac{b(4) \ln(Q^2/\Lambda(5)^2)}{[1 - \dots]} + \text{constant} \quad (2.48)$$

where the square bracket is the same as in Eq. (2.47). The constant is fixed by the continuity condition,

$$\alpha_s(m_b^2, 4) = \alpha_s(m_b^2, 5). \quad (2.49)$$

Using the next-to-leading order form for  $\alpha_s(Q^2)$  one can show then that

$$\Lambda(4) \approx \Lambda(5) \left( \frac{m_b}{\Lambda(5)} \right)^{\frac{2}{25}} \left[ \ln \left( \frac{m_b^2}{\Lambda(5)^2} \right) \right]^{\frac{963}{14375}}. \quad (2.50)$$

Fig. 2.4 shows the relation between  $\Lambda(4)$  and  $\Lambda(5)$ . In summary, it is important when comparing different  $\Lambda$  values to establish the number of light quark flavours assumed and also whether the LO or NLO expressions have been used. The change in the value of  $\alpha_s$  at  $Q = 5$  GeV with the different definitions of  $\Lambda$  is illustrated in Table 2.2. An error can lead to a substantial change in  $\alpha_s$ .

The third troubling property of  $\Lambda$  is that it depends on the renormalization scheme. Consider two calculations of the renormalized coupling constant which start from the same bare parameters,

$$\begin{aligned} \alpha_s^A &= Z^A \alpha_s^0, \\ \alpha_s^B &= Z^B \alpha_s^0. \end{aligned} \quad (2.51)$$

The two schemes start from the same bare coupling  $\alpha_s^0$ . The infinite parts of the renormalization constants  $Z^A$  and  $Z^B$  must be the same in all orders of perturbation theory. Therefore the two renormalized coupling constants must be related by a finite renormalization:

$$\alpha_s^B = \alpha_s^A (1 + c_1 \alpha_s^A + \dots). \quad (2.52)$$

Note that the first two coefficients of the  $\beta$  function,  $b$  and  $b'$ , are unchanged by such a transformation. They are therefore independent of the renormalization scheme. From Eq. (2.42) we see that the two values of  $\Lambda$  are related by,

$$\ln \frac{\Lambda^B}{\Lambda^A} = \frac{1}{2} \int_{\alpha_s^A(Q^2)}^{\alpha_s^B(Q^2)} \frac{dx}{bx^2(1 + \dots)} = \frac{c_1}{2b}. \quad (2.53)$$

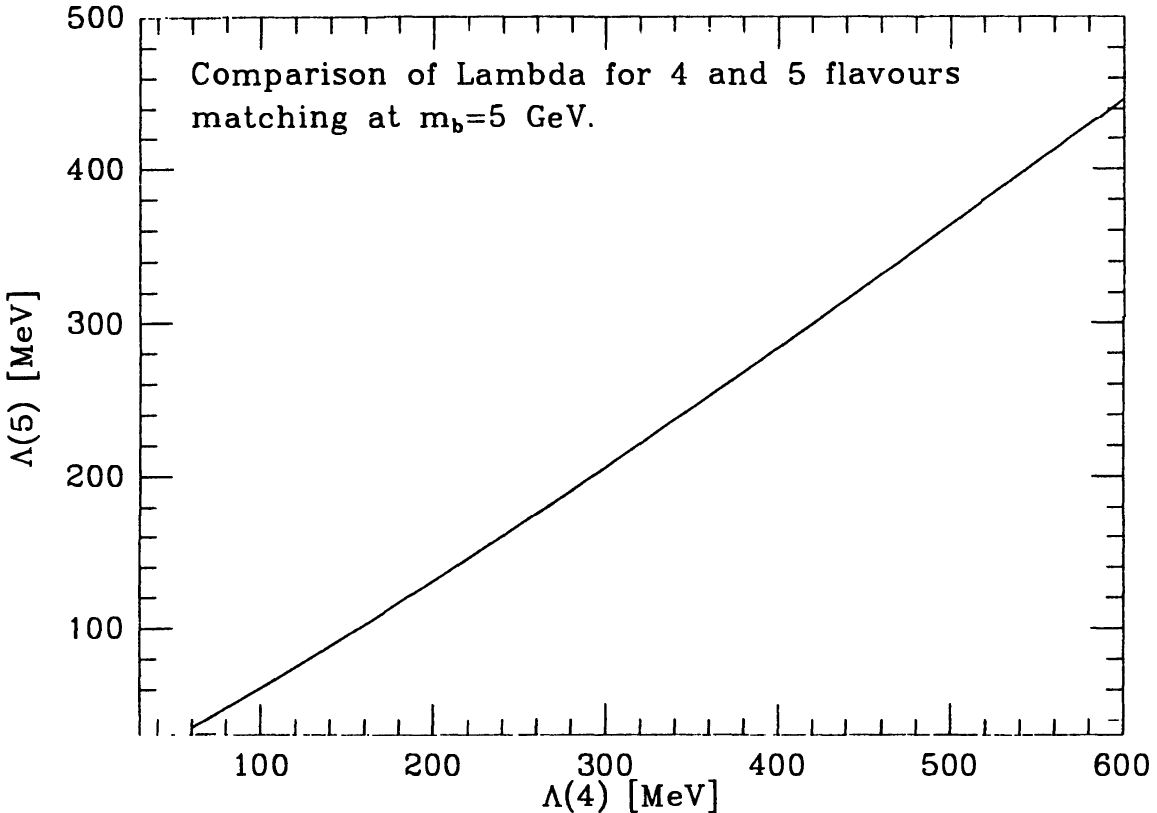


Fig. 2.4. Comparison of  $\Lambda$  for 4 and 5 light quark flavours, with matching at  $m_b = 5$  GeV.

The last equality follows from taking the limit  $Q \rightarrow \infty$ , because the relation must be true for all values of  $Q^2$ . Therefore relations between different definitions of  $\Lambda$  are always determined by the one loop calculation which fixes  $c_1$ :

$$\Lambda^B = \Lambda^A \exp \frac{c_1}{2b} . \quad (2.54)$$

Nowadays, most calculations in fixed-order QCD perturbation theory are performed in the *modified minimal subtraction* renormalization scheme. In this approach, ultraviolet loop divergences are regulated by reducing the number of space-time dimensions to  $n < 4$ :

$$\frac{d^4 k}{(2\pi)^4} \longrightarrow (\mu)^{2\epsilon} \frac{d^{4-2\epsilon} k}{(2\pi)^{4-2\epsilon}} \quad (2.55)$$

where  $\epsilon = 2 - \frac{n}{2}$ . For a detailed discussion of renormalization and dimensional regularization we refer the reader to ref. [13]. Note that the renormalization scale  $\mu$  preserves the dimensions of the couplings and the fields. Loop integrals of the form  $d^n k / [k^2 + m^2]^2$  then lead to poles at  $\epsilon = 0$ . The *minimal subtraction* renormalization prescription is to subtract off these poles and to replace the bare coupling by the renormalized

coupling  $\alpha_s(\mu^2)$ . In practice the poles always appear in the combination

$$\frac{\Gamma(1+\epsilon)}{\epsilon} (4\pi)^\epsilon = \frac{1}{\epsilon} + \ln(4\pi) - \gamma_E + O(\epsilon). \quad (2.56)$$

The  $\Gamma$  function is defined as

$$\Gamma(z) = \int_0^\infty dt e^{-t} t^{z-1}, \text{ Re } z > 0, \quad (2.57)$$

and has the properties

$$\Gamma(1+z) = z\Gamma(z) \quad (2.58)$$

$$\Gamma(1+\epsilon) = 1 - \gamma_E \epsilon + \left(\frac{\pi^2}{12} + \frac{1}{2}\gamma_E^2\right) \epsilon^2 + O(\epsilon^3) \quad (2.59)$$

where  $\gamma_E = 0.5772\dots$  is the Euler constant. In the *modified minimal subtraction* scheme the additional constants in Eq. (2.56) which accompany the pole are subtracted off as well. These two schemes are therefore examples of schemes A and B introduced above, and it is straightforward to show using Eqs.(2.52) and (2.54) that

$$\Lambda_{\overline{\text{MS}}}^2 = \Lambda_{\overline{\text{MS}}}^2 e^{(\ln(4\pi)-\gamma_E)}. \quad (2.60)$$

Lastly, the expression of the experimentally measured coupling  $\alpha_s$  in terms of  $\Lambda$  leads to an error which is both exponentially magnified and asymmetric. This is mathematically correct but depressing for an experimenter since most experiments actually measure  $\alpha_s$ . A compilation of measurements is shown in Fig. 2.5. The data points will be described in detail in Chapter 12. The errors in Fig. 2.5 are too large to measure the slope of the logarithmic dependence of  $1/\alpha_s$  on  $Q$  precisely, but the coupling constant clearly decreases with increasing scale. An analysis of jet data in  $e^+e^-$  annihilation demonstrates that  $\alpha_s$  decreases with scale using a single reaction type (see Chapter 3).

Guided by Fig. 2.5, for the purpose of making phenomenological predictions one may assume that

$$100 \text{ MeV} < \Lambda_{\overline{\text{MS}}}(5) < 400 \text{ MeV}. \quad (2.61)$$

Using Eq. (2.45), this corresponds to

$$0.105 < \alpha_s(M_Z^2) < 0.129. \quad (2.62)$$

i.e.  $\alpha_s \simeq 0.117$ , with about a  $\pm 10\%$  uncertainty, at the mass of the  $Z$ . As we shall see in Chapter 12, the current world average value of  $\alpha_s(M_Z^2)$  is  $0.116 \pm 0.005$ . The wider range of uncertainty in Eq. (2.62) is chosen to cover all the highest-precision measurements. The uncertainty in  $\alpha_s$  translates directly into an uncertainty in the prediction of the size of QCD cross sections. Thus we should expect errors of the order of  $\pm 10\%$  in the prediction of cross sections that begin in order  $\alpha_s$ .

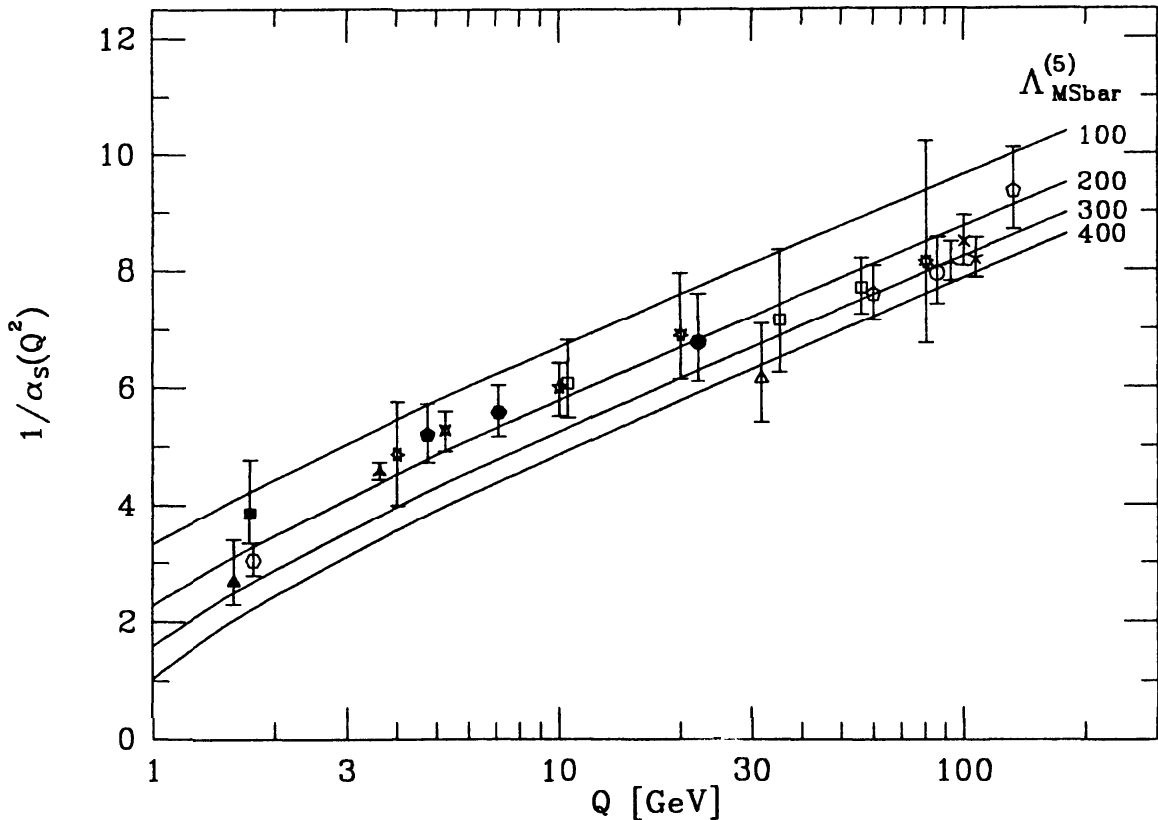


Fig. 2.5. Measurements of  $\alpha_s$  compared with predictions for various values of  $\Lambda(5)$ .

## 2.6 Lattice QCD

We have seen in the preceding section that at high momenta (or equivalently small distances) the coupling constant of QCD becomes small. On the other hand at large distances (of about 1 fermi), it becomes large. In this latter regime perturbation theory is not useful. Furthermore, when we actually calculate amplitudes in perturbation theory using quarks and gluons we find collinear and infra-red singularities which indicate the inapplicability of the perturbative method. Another signal of the inadequacy of perturbation theory is the failure to observe the free quarks and gluons which are used as asymptotic states. The physical asymptotic states are the hadrons observed in detectors.

Although the principal tool which we shall use in this book is the method of perturbation theory, there are clearly situations in which this method is inapplicable. It is therefore important to have a non-perturbative formulation of the theory determined by the QCD Lagrangian. One of the most developed and systematic methods is the method of lattice QCD, which has been extensively used to study hadronic masses and matrix elements.

The Lagrangian of QCD does not make sense without an ultraviolet cut-off, because of divergences which occur at high momenta or equivalently at short distances. In order to perform calculations with the theory one has to introduce a regulator. A description of the regulation procedure used in perturbation theory was given briefly in Section 2.5 and will be amplified in the next chapter. In this section we will describe a regulation of the Euclidean version of QCD implemented by defining the theory on a four-dimensional hypercubic lattice [14,15,16,17,18]. The continuation to the Euclidean region gives a real, positive action for the gauge fields. This allows one easily to identify the most important field configurations, which give the smallest action.

The basic idea is to separate the field operators by discretizing Euclidean space-time into hypercubes with sides of length  $a$ . Full Lorentz invariance is reduced to a hypercubic symmetry by this procedure, but the lattice version of the theory preserves local gauge invariance. We are ultimately interested in the limit of small lattice spacing when the full symmetry should be restored. The lattice spacing provides a cut-off of order  $\pi/a$  on all momenta so that ultraviolet divergences are no longer present. As long as the lattice spacing  $a$  is small compared to the physical extent of the hadrons one is studying, the discrete version of the theory should be an adequate approximation at that scale.

The continuum Euclidean action can be calculated from the corresponding expression in Minkowski space, Eq. (1.9). Performing the Wick rotation  $x^4 = ix^0, \partial^4 = -i\partial^0$  we find that

$$i \int d^4x \mathcal{L}(x) \rightarrow -S_E \quad (2.63)$$

where

$$S_E = \int d^4x_E \left[ \sum_{\mu, \nu} \frac{1}{2} \text{Tr}\{t \cdot F^{\mu\nu}(x) t \cdot F^{\mu\nu}(x)\} + \bar{q}(x) \left( \sum_{\mu} \hat{\gamma}^{\mu} \partial^{\mu} + m \right) q(x) \right]. \quad (2.64)$$

The indices  $\mu$  and  $\nu$  run from 1 to 4 and the four gamma matrices used in the Euclidean version of the theory satisfy the anticommutation relation

$$\{\hat{\gamma}^{\mu}, \hat{\gamma}^{\nu}\} = 2\delta^{\mu\nu}. \quad (2.65)$$

They are related to the gamma matrices used in Minkowski space by the transformation,

$$\hat{\gamma}^4 = \gamma^0, \hat{\gamma}^k = i\gamma^k, k = 1, 2, 3. \quad (2.66)$$

To motivate the structure of the discrete version of this theory we will first describe the construction of a gauge-invariant operator made from two quark fields at different space-time points. Consider a quark field which belongs to the fundamental representation of SU(3). If we form a

composite operator for two separated points  $x$  and  $y$ , gauge invariance may be preserved by linking the two fields by a *parallel transporter* which we denote by  $\mathcal{U}$ ,

$$O = \bar{q}_j(y) \mathcal{U}(y, x)_{ji} q_i(x) \quad (2.67)$$

where the parallel transporter is expressed in terms of the gauge field  $A$  as

$$\mathcal{U}(y, x)_{ji} = \mathcal{P} \left\{ \exp \left[ -ig \int_x^y dz_\mu t \cdot A^\mu(z) \right] \right\}_{ji}. \quad (2.68)$$

The line integral is along a path connecting  $x$  with  $y$  and  $\mathcal{P}$  defines a path ordering. Each choice of path defines a different gauge-invariant operator. The path ordering is defined by the power series expansion of the exponential.

$$\begin{aligned} \mathcal{U}(y, x) &= 1 - ig \int_x^y dz_\mu t \cdot A^\mu(z) \\ &\quad - g^2 \int_x^y dz_\mu t \cdot A^\mu(z) \int_z^y dw_\mu t \cdot A^\mu(w) + \dots \end{aligned} \quad (2.69)$$

If  $s$  denotes the position along the path, fields with larger  $s$  stand to the left of those with smaller  $s$ .

We may investigate the gauge transformation properties of the parallel transporter by considering the infinitesimal version for  $y = x + dx$ . Using Eq. (1.24) we find that under a gauge transformation the infinitesimal parallel transport transforms as

$$\begin{aligned} \mathcal{U}(x + dx, x) &= 1 - ig dx_\mu t \cdot A^\mu(x) \\ &\rightarrow 1 - ig dx_\mu \Omega(x) t \cdot A^\mu(x) \Omega^{-1}(x) \\ &\quad + dx_\mu (\partial^\mu \Omega(x)) \Omega^{-1}(x) \end{aligned} \quad (2.70)$$

and hence for the infinitesimal transporter we derive

$$\mathcal{U}(x + dx, x) \rightarrow \Omega(x + dx) \mathcal{U}(x + dx, x) \Omega^{-1}(x). \quad (2.71)$$

Under a gauge transformation  $\Omega$  the parallel transporter over a finite path transforms as

$$\mathcal{U}(y, x) \rightarrow \Omega(y) \mathcal{U}(y, x) \Omega^{-1}(x). \quad (2.72)$$

When combined with the gauge transformation property of the quark fields, Eq. (1.21), this is sufficient to demonstrate the gauge invariance of Eq. (2.67).

The formulation of QCD on the lattice uses a link variable  $U$  which is a discretized version of the parallel transporter as the fundamental quantity to represent the gauge fields. Fig. 2.6 shows a two-dimensional lattice with spacing  $a$  and linear size  $L = na$ , where for the case illustrated  $n = 5$ .

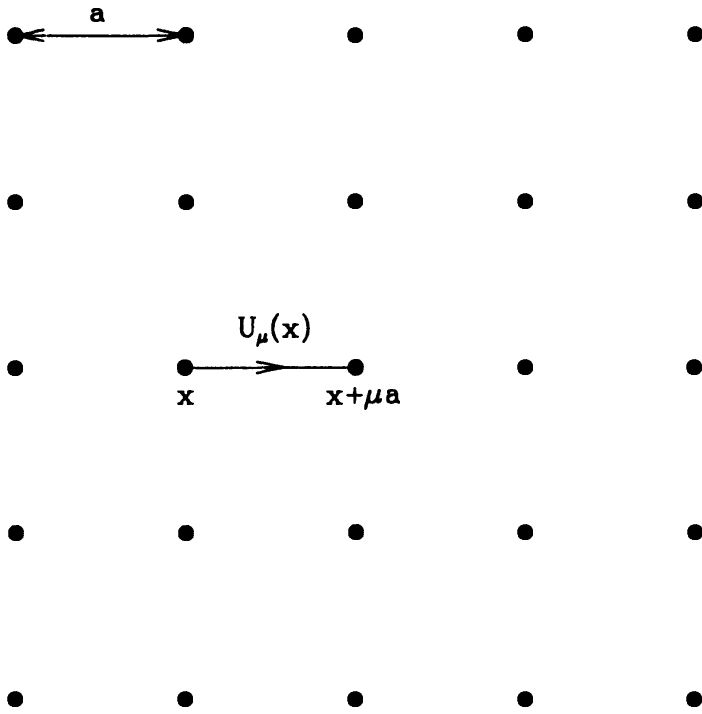


Fig. 2.6. Two-dimensional lattice showing a link variable.

The link variables are the parallel transporters between adjacent lattice sites as shown,

$$U_\mu(x) \equiv U(x, x + \mu a) \quad (2.73)$$

where  $\mu$  is a unit vector directed along one of the links of the lattice. In the lattice implementation of QCD the quark fields reside on the lattice sites and the gauge fields are associated with the links between lattice sites. Because of the gauge transformation property, Eq. (2.72), the product of matrices along a closed path or along a path terminated at the ends by quark and antiquark fields is gauge invariant.

We begin by considering the lattice action for the gauge field alone. The simplest action for the gauge field is determined by the product of link variables around a square path of side length  $a$ , called a plaquette.

$$\begin{aligned} U_{\square} &= U_\mu(x)U_\nu(x + a\mu)U_{-\mu}(x + a\mu + a\nu)U_{-\nu}(x + a\nu) \\ &\equiv U_\mu(x)U_\nu(x + a\mu)U_\mu^\dagger(x + a\nu)U_\nu^\dagger(x). \end{aligned} \quad (2.74)$$

The total action for SU(3) pure gauge theory is given by a sum over plaquettes,

$$S_G = \beta \sum_{\square} \left[ 1 - \frac{1}{3} \text{ReTr} U_{\square}(x) \right] \quad (2.75)$$

where  $\beta$  is a constant related to the gauge coupling. The sum over pla-

quettes includes every plaquette with only one orientation:

$$\sum_{\square} \equiv \sum_x \sum_{1 \leq \mu < \nu \leq 4} \equiv \frac{1}{2} \sum_x \sum_{\mu, \nu=1}^4. \quad (2.76)$$

To show the correspondence of Eq. (2.75) with the continuum Euclidean action we take the limit  $a \rightarrow 0$  and replace the link variable by

$$U_\mu(x) = 1 - ig_L a t \cdot \mathcal{A}_\mu(x) - \frac{1}{2} g_L^2 a^2 t \cdot \mathcal{A}_\mu(x) t \cdot \mathcal{A}_\mu(x) + O(a^3). \quad (2.77)$$

The displaced gauge field may also be expanded about  $x$ :

$$\mathcal{A}_\nu(x + a\mu) = 1 + a\partial_\mu \mathcal{A}_\nu(x) + O(a^2). \quad (2.78)$$

We find that the plaquette variable may be written as

$$\begin{aligned} U_\square(x) &\approx 1 - ia^2 g_L t \cdot F_{\mu\nu}(x) - \frac{1}{2} a^4 g^2 t \cdot F_{\mu\nu}(x) t \cdot F_{\mu\nu}(x) \\ \text{Tr} U_\square(x) &\approx 3 - \frac{1}{2} a^4 g^2 \text{Tr}\{t \cdot F_{\mu\nu}(x) t \cdot F_{\mu\nu}(x)\}, \end{aligned} \quad (2.79)$$

where the field strength tensor is

$$t \cdot F_{\mu\nu}(x) = t \cdot \partial_\mu \mathcal{A}_\nu(x) - t \cdot \partial_\nu \mathcal{A}_\mu(x) + ig_L [t \cdot \mathcal{A}_\mu(x), t \cdot \mathcal{A}_\nu(x)]. \quad (2.80)$$

The action for the pure gauge theory in the continuum limit is thus

$$\begin{aligned} S_G &\rightarrow a^4 \frac{\beta g_L^2}{6} \sum_{\square} \text{Tr}\{t \cdot F^{\mu\nu} t \cdot F^{\mu\nu}\} \\ &= a^4 \sum_x \left\{ \frac{\beta g_L^2}{12} \sum_{\mu, \nu} \text{Tr}\{t \cdot F^{\mu\nu} t \cdot F^{\mu\nu}\} \right\}, \end{aligned} \quad (2.81)$$

in agreement with Eq. (2.64) provided we interpret  $\beta = 6/g_L^2$  and replace  $a^4 \sum_x$  by an integral over  $x$ . The  $a \rightarrow 0$  limit of the quantum theory is more subtle than the formal limit given in Eq. (2.81) because of the phenomenon of renormalization and will be considered below.

We have therefore constructed a regulated version of Euclidean QCD without quarks on a space-time lattice. Gauge invariance has been preserved, although the full Lorentz invariance has been reduced to a hypercubic symmetry. Note also that there is considerable ambiguity in the formulation of the action of QCD on the lattice. For example, any action which differs from Eq. (2.75) only by terms which vanish as  $a \rightarrow 0$  would also be acceptable.

The construction of an action for quark fields follows the pattern of the above. The quark fields are placed on the sites of the lattice. A Euclidean action for the free quark fields on the lattice can be obtained by replacing the derivative in the action by a finite difference, and the integral over  $x$  by a sum over sites. The simplest prescription, which we shall call the

'naive fermion' action, is

$$\begin{aligned} S_{\text{NF}} &= \int d^4x_E \bar{q}(x)(\hat{\gamma}_\mu \partial_\mu + m)q(x) \\ &\rightarrow a^4 \sum_x \left\{ \frac{1}{2a} \sum_{\mu=1}^4 \bar{q}_x(t_\mu - t_{-\mu}) \hat{\gamma}_\mu q_x + m \bar{q}_x q_x \right\} \end{aligned} \quad (2.82)$$

where  $t$  is a displacement operator,  $t_\mu q_x = q_{x+a\mu}$ .

If we take the Fourier transform of the inverse propagator derived from Eq. (2.82) we obtain

$$S_{\text{NF}}(p) = \sum_{\mu=1}^4 \frac{i}{a} \sin(ap_\mu) \hat{\gamma}_\mu + m. \quad (2.83)$$

We must examine all values of this inverse propagator which are of order  $a^0$  in the limit  $a \rightarrow 0$ . The range of momenta is restricted to an interval of length  $2\pi/a$  which we can take to be  $-\pi/(2a) < p_\mu < 3\pi/(2a)$ . Terms which are more singular than  $a^0$  lead to a vanishing propagator. There are 16 contributions which lead to terms of order  $a^0$ , corresponding to choosing each of the four components of  $p_\mu$  to be either in the vicinity of zero or in the vicinity of  $\pi/a$ . Therefore rather than representing one fermion, Eq. (2.82) actually represents 16 fermions. This is referred to as the fermion doubling problem; it is a consequence of the fact that the Dirac equation is first order. The solution to the fermion doubling problem advocated by Wilson [14] is to add another term to the fermionic action to remove the degeneracy of the unwanted states,

$$S_{\text{WF}} = S_{\text{NF}} - a^4 \sum_x \left\{ \frac{a}{2} \sum_{\mu=1}^4 \bar{q}_x \Delta q_x \right\} \quad (2.84)$$

where  $\Delta = (t_\mu + t_{-\mu} - 2)/a^2$ . The inverse propagator is now given by

$$S_{\text{WF}}(p) = \sum_{\mu=1}^4 \frac{i}{a} \sin(ap_\mu) \hat{\gamma}_\mu + m + \frac{1}{a} \sum_{\mu=1}^4 (1 - \cos(ap_\mu)). \quad (2.85)$$

The propagator is of order  $O(a^0)$  only for  $p_\mu \approx 0$ ; in the vicinity of  $p_\mu = 0$  the Wilson term is of order  $a$  and therefore innocuous in the naive continuum limit. It is only important for  $p_\mu \approx 1/a$ . As a consequence the Wilson prescription gives all but one of the fermions a mass  $m + 2j/a$  where  $j = 1, 2, 3$  or  $4$  and the degeneracy is lifted. Combining terms in the action we find that

$$S_{\text{WF}} = a^4 \sum_x \left\{ \left( m + \frac{4}{a} \right) \bar{q}_x q_x - \frac{1}{2a} \sum_{\mu=1}^4 \bar{q}_x \left[ (1 - \hat{\gamma}_\mu) t_\mu + (1 + \hat{\gamma}_\mu) t_{-\mu} \right] q_x \right\}. \quad (2.86)$$

This Lagrangian is conventionally re-written by changing the normalization of the quark fields to simplify the coefficient of the mass term. Including the link variables we obtain the full gauge-invariant expression for the quark terms in the action,

$$S_F = a^4 \sum_x \left\{ \bar{q}_x q_x - K \sum_{\mu=1}^4 [\bar{q}_x (1 - \hat{\gamma}_\mu) U_\mu(x) q_{x+a\mu} + \bar{q}_x (1 + \hat{\gamma}_\mu) U_\mu^\dagger(x) q_{x-a\mu}] \right\}. \quad (2.87)$$

The coefficient of the term connecting adjacent lattice sites,  $K$ , is called the hopping parameter and is given by

$$K = \frac{1}{2(ma + 4)}. \quad (2.88)$$

Note that chiral symmetry has been destroyed by the introduction of the  $\Delta$  term in the action, Eq. (2.84), even in the absence of an explicit mass term  $m$ .

In the above discussion of the fermion lattice action we have followed the treatment by Wilson. An alternative solution to the fermion doubling problem is provided by Kogut-Susskind fermions [19].

Physical predictions are made by evaluating the integral over all configurations of the fields, weighted by the complete action. The fermion fields normally appear as a bilinear term in the action and can be integrated out

$$\begin{aligned} & \int \{dU_\mu\} d\bar{q} d\bar{q} \exp[-S_G(U) + \bar{q} M(U) q] \\ &= \int \{dU_\mu\} \det M(U) \exp[-S_G(U)]. \end{aligned} \quad (2.89)$$

The above integral is a functional integral which is approximated by integrating over all the fields and links at all points of the lattice. Although several techniques have been used to obtain numerical evaluation of the lattice integrals, the most frequently used is direct Monte Carlo evaluation of the integral with importance sampling. The computation of the fermion determinant is very costly in computer time. As a result most calculations are currently performed in the *quenched approximation* [20] which replaces the determinant in Eq. (2.89) by a constant independent of the link variables  $U$ . Replacing  $M$  by a constant is equivalent to the neglect of closed fermion loops and leads to an enormous saving in computer time since the probability of any configuration of the gauge field is calculated with the pure gauge theory action alone. Note that the quenched approximation is made only to save computing time. Its validity will not be the same for all physical quantities and can only be established *a posteriori*.

In the quenched approximation the expectation value of any operator  $O(U)$  is

$$\langle O \rangle = \frac{\int \{dU_\mu\} O(U) \exp[-S_G(U)]}{\int \{dU_\mu\} \exp[-S_G(U)]}. \quad (2.90)$$

In order for the lattice theory to be an adequate representation of the continuum theory we must satisfy two conditions. The lattice must be large enough that the object which we wish to describe fits on it. If this not the case the result obtained will be subject to effects from the boundaries called finite size effects. In addition the lattice spacing must be small enough that the physical quantity to be calculated is insensitive to the granularity of the lattice.

Calculations proceed by evaluating the integral in Eq. (2.90) by Monte Carlo methods. The two variables that one has at one's disposal are the bare lattice coupling  $g_L$  and the number of lattice sites. As we shall see, the value of the coupling controls the physical size of the lattice spacing. As an ideal one would like to have a large number of sites so that the system being modelled fits comfortably on to the lattice. On the other hand one would like to have a small value of the coupling so that the granularity of the lattice is small compared to the object under study. Therefore for a hadron of radius  $R$  we require that

$$a \ll R \ll L = na. \quad (2.91)$$

The relationship between the value of the coupling and the size of lattice spacing cannot be determined *a priori*.

Consider any physical quantity such as the mass of a hadron,  $m$ , which is measured on the lattice. If we assume that quarks are massless, the mass of the hadron is fixed by the inverse lattice spacing which is the only parameter with dimension

$$m = \frac{1}{a} f(g_L). \quad (2.92)$$

In order to yield a sensible answer the  $a \rightarrow 0$  limit must clearly be taken with some care. The proper continuum limit is achieved when we take  $a$  to zero holding the physical quantities fixed. In practice this means that as  $a \rightarrow 0$

$$\lim_{a \rightarrow 0} \frac{1}{a} f(g_L) \rightarrow \text{constant}. \quad (2.93)$$

This means that  $g_L$  must also be changed as  $a$  goes to zero so that a sensible continuum theory is reached. The continuum limit of the theory cannot be approached at fixed  $g_L$ . Fortunately the behaviour of the coupling of the theory at small distances is predicted in QCD as we discussed

earlier in this chapter. That this should happen is a consequence of the renormalizability of the theory.

We shall now use our knowledge of the short-distance behaviour of the coupling to determine the relationship between the coupling and the lattice spacing which leads to a sensible continuum limit. In the limit  $a \rightarrow 0$  we must have that

$$\frac{d}{da} m = 0 \quad (2.94)$$

since a physical quantity cannot depend on the cut-off. Differentiating Eq. (2.92) using the chain rule,

$$\left\{ a \frac{\partial}{\partial a} \Big|_{g_L} + \left( a \frac{\partial g_L}{\partial a} \right) \frac{\partial}{\partial g_L} \Big|_a \right\} m = 0 , \quad (2.95)$$

we get

$$f(g_L) = \left( a \frac{\partial g_L}{\partial a} \right) \frac{\partial}{\partial g_L} f(g_L) . \quad (2.96)$$

The scale dependence of the bare coupling is determined by the QCD  $\beta$  function (not to be confused with the  $\beta$  of Eq. (2.75)),

$$a \frac{\partial g_L}{\partial a} = \frac{b}{4\pi} g_L^3 \left( 1 + b' \frac{g_L^2}{4\pi} + \dots \right) \quad (2.97)$$

where the coefficients  $b$  and  $b'$  are given in Eq. (2.7). We therefore find that all dimensionful quantities are proportional to a fixed scale  $\Lambda_L$ :

$$m = c \Lambda_L \quad (2.98)$$

where

$$\Lambda_L = \frac{1}{a} \exp \left( -\frac{2\pi}{bg_L^2} \right) \left( \frac{4\pi + b'g_L^2}{4\pi g_L^2} \right)^{b'/(2b)} . \quad (2.99)$$

Despite the fact that we start with a theory which is scale free (if we ignore quark masses) we end up with a theory which has one scale, to which all other dimensionful quantities are related. This is the phenomenon of *dimensional transmutation*. The lattice spacing goes to zero exponentially in  $1/g_L^2$  as  $g_L$  tends to zero. This relationship, which is known as *asymptotic scaling*, serves two functions. As the output of a Monte Carlo simulation one obtains the mass in lattice units as a function of the coupling. One can then check that the Monte Carlo data satisfy Eq. (2.99). It can also be used to determine  $\Lambda_L$  which is related to the  $\Lambda$  parameter measured in the continuum.

How does a practical Monte Carlo simulation proceed? We shall use as an illustration the calculation of hadronic masses. The first step is to

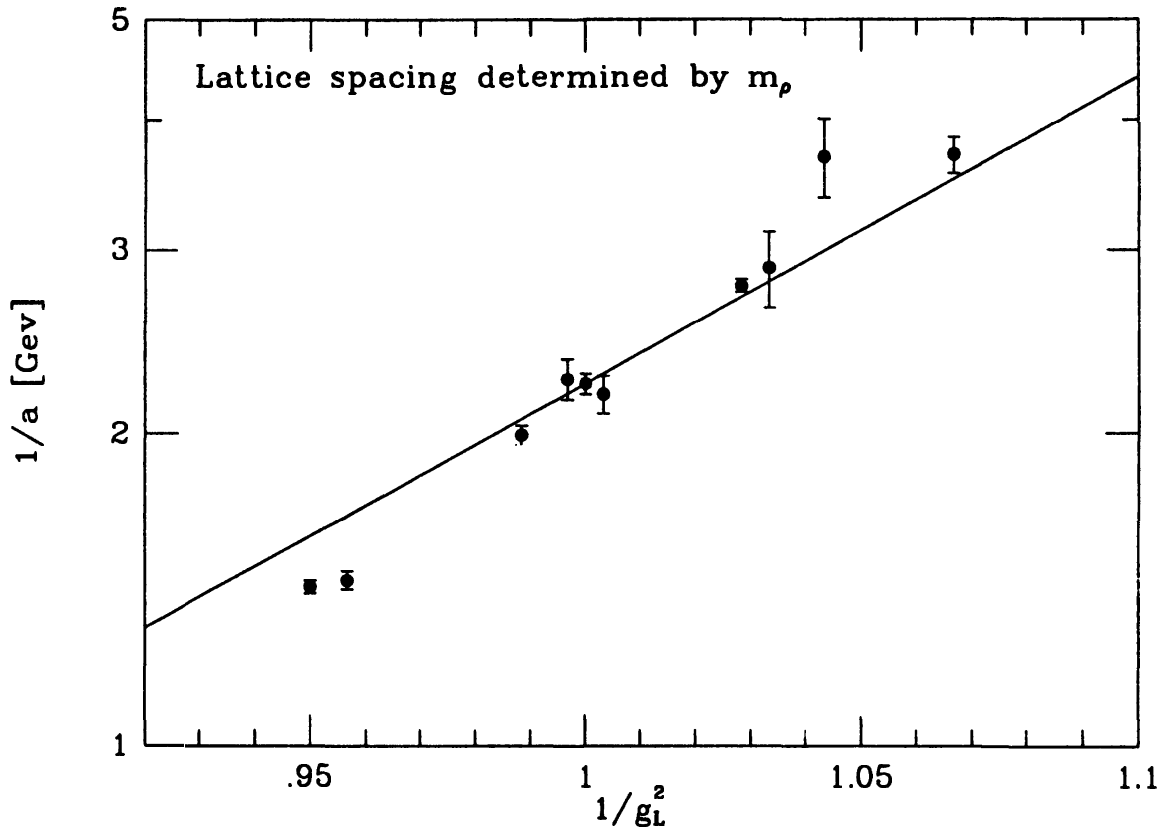


Fig. 2.7. Lattice spacing as a function of coupling. Adapted from ref. [21].

calculate the masses in lattice units at several values of the bare coupling and to verify that the relationship between the masses and the couplings is as predicted by asymptotic scaling, Eq. (2.99). Fig. 2.7 shows a compilation of data points which are the result of Monte Carlo measurements of the lattice spacing  $a$  as a function of the lattice coupling. The quantity measured on the lattice is the mass of the  $\rho$  meson. The value of the  $\rho$  mass measured by experiment and given in the particle data tables is used to transform this measurement into GeV. The curve in Fig. 2.7 shows the prediction of Eq. (2.99) with the value of the intercept adjusted to the data (corresponding to  $\Lambda_L = 1.74$  MeV). The data are in fair agreement with the slope predicted by asymptotic scaling, which gives assurance that the results are indeed close to the continuum limit.

Having chosen the mass of the  $\rho$  to fix the scale, one can then go on to make predictions for other physical quantities. In the quenched approximation it is found that  $g_L^2 = 1$  corresponds to  $a^{-1} \approx 2$  GeV, or equivalently  $a \approx 1/10$  fermi. This lattice spacing should be much less than the size of the hadron whose mass one is computing. If this condition is satisfied it makes sense to predict the other hadron masses in terms of the first.

Fig. 2.8 shows the results of a lattice calculation of the hadron masses

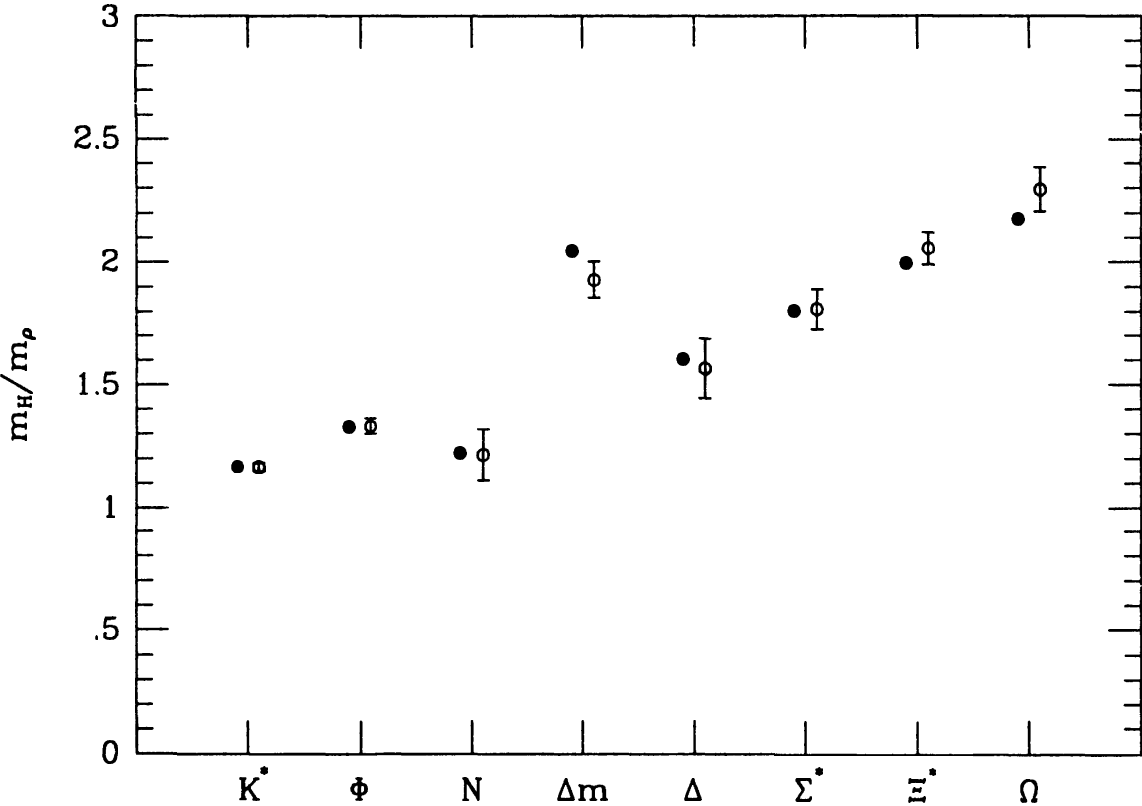


Fig. 2.8. Hadron masses in units of the  $\rho$  mass from the lattice (open points) compared with experiment (solid points).

[22] performed with Wilson fermions in the quenched approximation. The open points, which are the lattice predictions, have been obtained from calculations performed at values of  $\beta = 6/g_L^2$  between 5.70 and 6.17. The quantity  $\Delta m$  refers to the combination of masses  $m_\Xi + m_\Sigma - m_N$ . The lattice results have been extrapolated to zero lattice spacing at finite volume and subsequently extrapolated to infinite volume. The details of the procedure can be found in ref. [22]. For comparison Fig. 2.8 also shows the measured values for hadron masses (solid points). The agreement between theory and experiment is extremely good. This indicates that the quenched approximation is reliable for the calculation of hadron masses.

As a second example of the precision now available from lattice gauge theory, we present in Fig. 2.9 a lattice calculation of the static  $q\bar{q}$  potential [23], performed again in the quenched approximation. At small distances the potential is expected to be of the form

$$V(R) = V_0 - \alpha_s(aR)/R. \quad (2.100)$$

At large distances we have a linearly rising potential of the form,

$$V(R) = V_0 + KR. \quad (2.101)$$

The constant  $K$  is known as the string tension. Fig. 2.9 shows the poten-

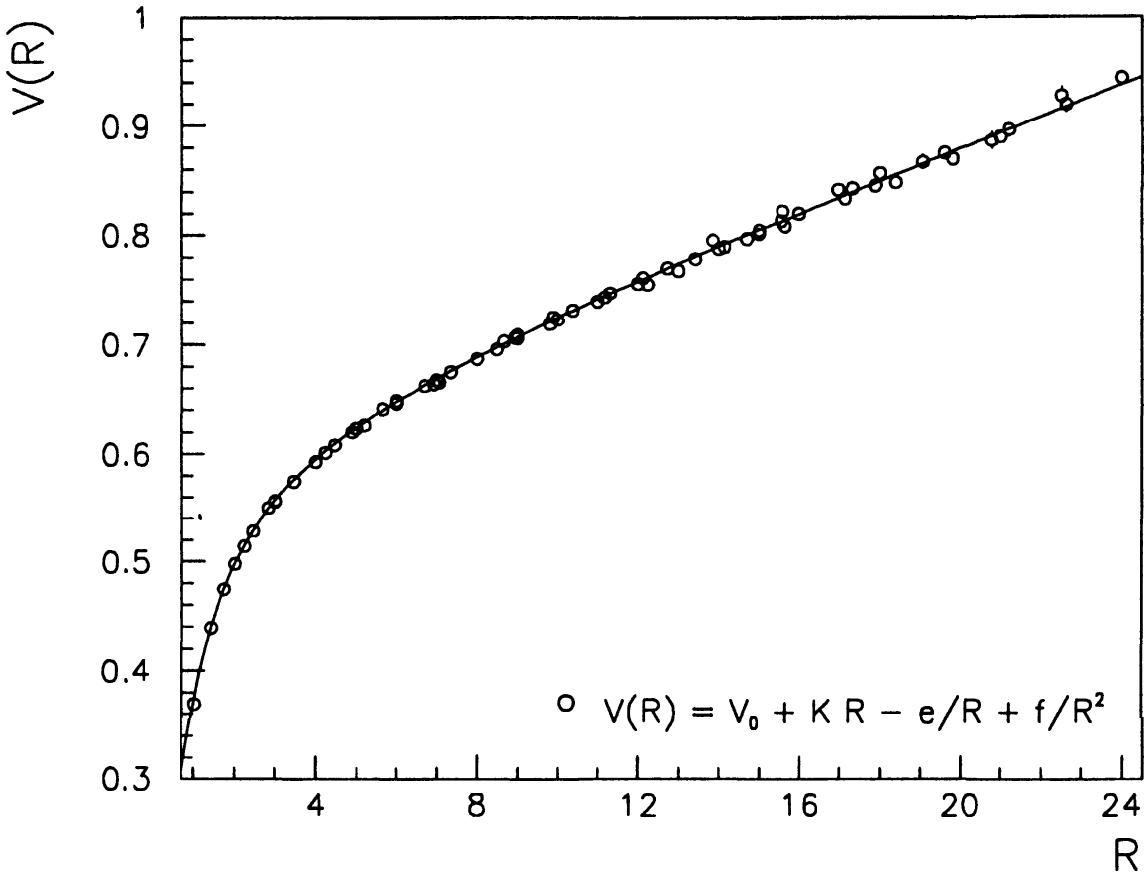


Fig. 2.9. QCD potential *vs.*  $R$  (in lattice units) from lattice QCD. Figure from ref. [23].

tial as calculated in lattice QCD with  $\beta \equiv 6/g_L^2 = 6.4$  as a function of the distance  $R$  measured in lattice units. The curve is a fit to the Monte Carlo data and the fitted value of  $Ka^2 \approx 0.0147$ . Using the value of the string tension determined from experiment [24], which is  $(440 \text{ MeV})^2$ , we can determine the lattice spacing in physical units to be  $a = 0.0544$  fermi. The existence of the linearly rising term with  $K > 0$  is a signal for confinement, since it costs infinite energy to separate quarks an infinite distance. The linearly rising term alone is not sufficient to demonstrate confinement, since it refers to a calculation performed at finite lattice spacing in the quenched approximation. However the observation that the string tension varies as we change the coupling in accordance with the renormalization group scaling relation, Eq. (2.99), makes it plausible that confinement survives in the continuum limit.

For reasons of simplicity we have described only the calculation of hadron masses and the string tension in the above discussion. If this were all that one could accomplish with lattice gauge theory it would be of limited utility, since both of these quantities are well determined by experiment. In fact much of the modern research on lattice QCD is devoted

to the calculation of quantities of great interest which are not so directly measured by experiment. Examples of this latter type of quantities are the parameters of the Lagrangian (such as quark masses and the running coupling) and the hadronic matrix elements of quark fields, which are important to calculate weak decays. The hadronic matrix elements of quark operators are poorly known and therefore even the relatively crude information which is presently available from lattice gauge theory is of great importance.

## References

- 1) H.D. Politzer, *Phys. Rev. Lett.* **30** (1973) 1346;  
D.J Gross and F. Wilczek, *Phys. Rev. Lett.* **30** (1973) 1343.
- 2) W.A. Caswell, *Phys. Rev. Lett.* **33** (1974) 244.
- 3) O.V. Tarasov, A.A. Vladimirov and A.Yu. Zharkov, *Phys. Lett.* **B93** (1980) 429;  
S.A. Larin and J.A.M. Vermaasen, *Phys. Lett.* **B303** (1993) 334.
- 4) V.N. Gribov, Lectures at the 12th Winter School of the Leningrad Nuclear Physics Institute, SLAC-TRANS-176 (1977);  
S. D. Drell, in a *Festschrift for Maurice Goldhaber*, Trans. NY Acad. Sci., Series II, **40** (1980) 76.
- 5) N.K. Nielsen, *Am. J. Phys.* **49** (1981) 1171;  
R.J. Hughes, *Phys. Lett.* **B97** (1980) 246; *Nucl. Phys.* **B186** (1981) 376;  
K. Johnson, in *Asymptotic Realms of Physics*, edited by A. Guth, K. Huang and R.L. Jaffe, MIT press, Cambridge, Mass. (1983).
- 6) R. E. Peierls, *Quantum Theory of Solids*, Oxford (1955).
- 7) S. Weinberg, *Phys. Rev.* **D8** (1973) 3497.
- 8) R. Tarrach, *Nucl. Phys.* **B183** (1981) 384;  
O. Nachtmann and W. Wetzel, *Nucl. Phys.* **B187** (1981) 333.
- 9) T. Appelquist and J. Carazzone, *Phys. Rev.* **D11** (1975) 2856.
- 10) W. Bernreuther and W. Wetzel, *Nucl. Phys.* **B197** (1982) 228;  
W. Bernreuther, *Ann. Phys. (NY)* **151** (1983) 127.
- 11) W. Marciano, *Phys. Rev.* **D29** (1984) 580.
- 12) Particle Data Group, L. Montanet et al., *Review of Particle Properties*, *Phys. Rev.* **D50** (1994) 1173.
- 13) J.C. Collins *Renormalization*, Cambridge University Press (1984).
- 14) K. Wilson, *Phys. Rev.* **D10** (1974) 2445;  
K. Wilson in *New Phenomena in Subnuclear Physics*, edited by A. Zichichi, Plenum, New York (1977).
- 15) M. Creutz, *Quarks, gluons and lattices*, Cambridge University Press (1983).
- 16) C. Rebbi, *Lattice gauge theories and Monte Carlo simulations*, World Scientific (1983).
- 17) I. Montvay and G. Munster, *Quantum Fields on a Lattice*, Cambridge University Press (1994).
- 18) A.S. Kronfeld and P.B. Mackenzie, *Ann. Rev. Nucl. Part. Sci.* **43** (1993) 793.
- 19) L. Susskind, *Phys. Rev.* **D16** (1977) 3031;  
T. Banks, J.B. Kogut and L. Susskind, *Phys. Rev.* **D13** (1976) 1043.
- 20) D. Weingarten, *Phys. Lett.* **B109** (1982) 57.
- 21) C.R. Allton, *Nucl. Phys.* **B437** (1995) 641.
- 22) F. Butler et al., *Nucl. Phys.* **B430** (1994) 179.

- 23) G.S. Bali and K. Schilling, *Phys. Rev.* **D47** (1993) 661, *Intl. J. Mod. Phys.* **C4** (1993) 1167.
- 24) E.J. Eichten *et al.*, *Phys. Rev.* **D21** (1980) 203;  
P. Goddard *et al.*, *Nucl. Phys.* **B56** (1973) 109.

# 3

## QCD in electron-positron annihilation

Many of the basic ideas and properties of perturbative QCD can be illustrated by considering the production of hadrons in electron-positron annihilation. In this chapter we will discuss a variety of ways in which the theory can be tested. We begin by discussing the *total cross section* for  $e^+e^- \rightarrow$  hadrons: we show how the order  $\alpha_s$  corrections are calculated, and how renormalization scheme dependence enters at order  $\alpha_s^2$ . Because of its inclusive nature, this is one of the few quantities for which the first three terms in the QCD perturbation series are known, and for which non-perturbative corrections are expected to be small. As a result it provides potentially one of the most precise measurements of the strong coupling.

Perturbative QCD also predicts a rich ‘jet’ structure for the final-state hadrons in electron-positron annihilation. We discuss the various ways in which jet cross sections can be defined, how such cross sections are calculated in perturbation theory, and how the predictions compare with experiment. Jet cross sections can also be used to measure  $\alpha_s$ , and to test the basic interactions in the theory, in particular the triple-gluon vertex.

### 3.1 The total hadronic cross section

The production of a muon pair in electron-positron annihilation,  $e^+e^- \rightarrow \mu^+\mu^-$ , is one of the fundamental processes of QED. The same annihilation process can also produce hadrons in the final state. As we have seen in the previous chapter, the formation of these hadrons is not governed by perturbation theory. Why then would one expect a perturbative approach to give an accurate description of the hadronic cross section? The answer can be understood by visualizing the event in space-time. The electron

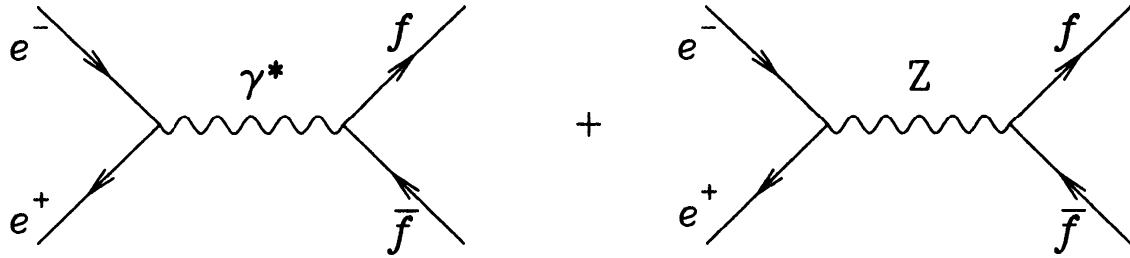


Fig. 3.1. Feynman diagrams for the process  $e^+e^- \rightarrow f\bar{f}$ .

and positron form a photon (or  $Z$ ), of virtuality  $Q$  equal to the collision energy  $\sqrt{s}$ , which fluctuates into a quark and an antiquark. By the uncertainty principle, this fluctuation occurs on a distance scale of order  $1/Q$ , and if  $Q$  is large the production rate for this short-distance process should be predicted by perturbation theory. Subsequently, the quarks and gluons form themselves into hadrons. This process is called *hadronization*. Hadronization occurs at a much later time scale characterized by  $1/\Lambda$ , where  $\Lambda$  is the scale in  $\alpha_s$ , *i.e.* the scale at which the coupling becomes strong. The interactions which change quarks and gluons into hadrons certainly modify the outgoing state, but they occur too late to modify the original probability for the event to happen, which can therefore be calculated in perturbation theory.

At lowest order, the total hadronic cross section is obtained by simply summing over all kinematically accessible flavours and colours of quark-antiquark pairs,  $e^+e^- \rightarrow \sum q\bar{q}$ . Real and virtual gluon corrections to this basic process will generate higher-order contributions to the perturbation series. Since it is convenient to compare the hadronic cross section to that for  $\mu^+\mu^-$  production, and to include the possibility of both photon and  $Z$  exchange, we begin by considering the general high-energy  $2 \rightarrow 2$  process  $e^+e^- \rightarrow f\bar{f}$ , with  $f$  a light charged fermion,  $f \neq e$ . At lowest order, this is mediated by either a virtual photon or a  $Z$  in the  $s$ -channel, Fig. 3.1. With  $\theta$  the centre-of-mass scattering angle of the final-state fermion, the differential cross section is

$$\begin{aligned} \frac{d\sigma}{d\cos\theta} = & \frac{\pi\alpha^2}{2s} \left[ (1 + \cos^2\theta) \left\{ Q_f^2 - 2Q_f V_e V_f \chi_1(s) \right. \right. \\ & + (A_e^2 + V_e^2)(A_f^2 + V_f^2)\chi_2(s) \Big\} \\ & \left. + \cos\theta \left\{ -4Q_f A_e A_f \chi_1(s) + 8A_e V_e A_f V_f \chi_2(s) \right\} \right], \quad (3.1) \end{aligned}$$

where

$$\chi_1(s) = \kappa \frac{s(s - M_Z^2)}{(s - M_Z^2)^2 + \Gamma_Z^2 M_Z^2}$$

$$\begin{aligned}\chi_2(s) &= \kappa^2 \frac{s^2}{(s - M_Z^2)^2 + \Gamma_Z^2 M_Z^2} \\ \kappa &= \frac{\sqrt{2} G_F M_Z^2}{16\pi\alpha}.\end{aligned}\quad (3.2)$$

Here  $G_F$  is the Fermi constant,  $\alpha$  is the electromagnetic coupling, and  $M_Z$  and  $\Gamma_Z$  are the mass and total decay width of the  $Z$  boson respectively. The vector and axial couplings of the fermions to the  $Z$  are (see Chapter 8)

$$V_f = T_f^3 - 2Q_f \sin^2 \theta_W, \quad A_f = T_f^3, \quad (3.3)$$

with  $T_f^3 = +\frac{1}{2}$  for  $f = \nu, u, \dots$  and  $T_f^3 = -\frac{1}{2}$  for  $f = e, d, \dots$ . The  $\chi_2$  term comes from the square of the  $Z$ -exchange amplitude and the  $\chi_1$  term from the photon- $Z$  interference. At centre-of-mass scattering energies ( $\sqrt{s}$ ) far below the  $Z$  peak, the ratio  $s/M_Z^2$  is small and so  $1 \gg \chi_1 \gg \chi_2$ . This means that the weak effects — manifest in the terms involving the vector and axial couplings — are small and can be neglected. Eq. (3.1) then reduces to

$$\frac{d\sigma}{d\cos\theta} = \frac{\pi\alpha^2 Q_f^2}{2s} (1 + \cos^2\theta). \quad (3.4)$$

Integrating over  $\theta$  gives the total cross section,

$$\sigma_0 = \frac{4\pi\alpha^2}{3s} Q_f^2. \quad (3.5)$$

On the  $Z$  pole,  $\sqrt{s} = M_Z$ , the  $\chi_2$  term in (3.1) dominates and the corresponding (peak) cross section is

$$\sigma_0 = \frac{4\pi\alpha^2 \kappa^2}{3\Gamma_Z^2} (A_e^2 + V_e^2) (A_f^2 + V_f^2). \quad (3.6)$$

We next introduce the ratio  $R$  of the total  $e^+e^-$  hadronic cross section to the muon pair production cross section. As we have argued, the hadronic cross section is obtained at leading order simply by counting the possible  $q\bar{q}$  final states. Thus, at energies far below the  $Z$  pole, we have (cf. Eq. (1.7))

$$R = \frac{\sigma(e^+e^- \rightarrow \text{hadrons})}{\sigma(e^+e^- \rightarrow \mu^+\mu^-)} = \frac{\sum_q \sigma(e^+e^- \rightarrow q\bar{q})}{\sigma(e^+e^- \rightarrow \mu^+\mu^-)} = 3 \sum_q Q_q^2, \quad (3.7)$$

where the factor 3 comes from the sum over quark colours. On the  $Z$  pole, the analogous quantity is the ratio of the partial decay widths of the  $Z$  to hadrons and to muon pairs:

$$R_Z = \frac{\Gamma(Z \rightarrow \text{hadrons})}{\Gamma(Z \rightarrow \mu^+\mu^-)} = \frac{\sum_q \Gamma(Z \rightarrow q\bar{q})}{\Gamma(Z \rightarrow \mu^+\mu^-)} = \frac{3 \sum_q (A_q^2 + V_q^2)}{A_\mu^2 + V_\mu^2}. \quad (3.8)$$

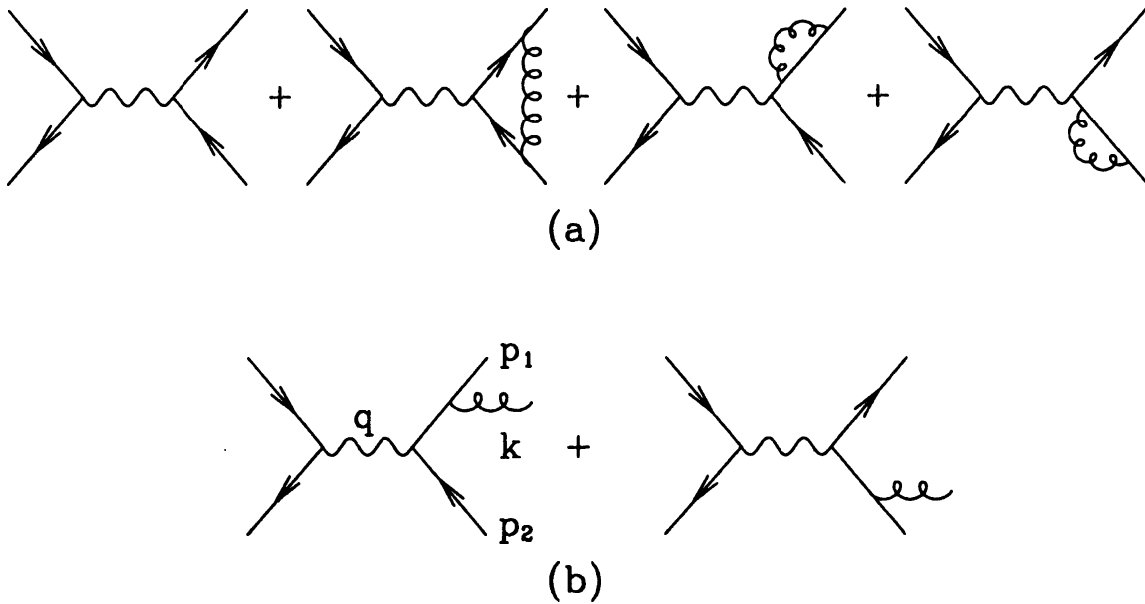


Fig. 3.2. Feynman diagrams for the  $O(\alpha_s)$  corrections to the total hadronic cross section in  $e^+e^-$  annihilation.

These results are valid for massless quarks; the effect of a non-zero quark mass will be discussed in Section 3.2.

With  $q = u, \dots, b$ , Eq. (3.7) gives  $R = 11/3 = 3.67$  and (with  $\sin^2 \theta_W = 0.23$ )  $R_Z = 20.09$ . For the latter, the measured value at LEP is  $20.79 \pm 0.04$  [1], some 3.5% higher than the lowest-order prediction. In fact the difference is largely due to higher-order QCD corrections, and the comparison between theory and experiment provides a determination of the strong coupling constant, as we shall see in Chapter 12.

The  $O(\alpha_s)$  corrections to the total hadronic cross section are calculated from the real and virtual gluon diagrams shown in Fig. 3.2. For simplicity, we shall consider only the photon-exchange contribution in detail. For the real gluon diagrams, Fig. 3.2(b), it is convenient to write the three-body phase space integration as

$$d\Phi_3 = \frac{1}{(2\pi)^5} \frac{s}{32} d\alpha d\cos\beta d\gamma dx_1 dx_2 , \quad (3.9)$$

where  $\alpha, \beta, \gamma$  are Euler angles, and  $x_1 = 2E_q/\sqrt{s}$  and  $x_2 = 2E_{\bar{q}}/\sqrt{s}$  are the energy fractions of the final-state quark and antiquark. The matrix element squared for  $e^+(q_1) + e^-(q_2) \rightarrow q(p_1) + \bar{q}(p_2) + g(k)$  is obtained using the Feynman rules given in Chapter 1:

$$\frac{1}{4} \sum |\mathcal{M}|^2 = 24C_F e^4 Q_q^2 g_s^2 \frac{(p_1 \cdot q_1)^2 + (p_1 \cdot q_2)^2 + (p_2 \cdot q_1)^2 + (p_2 \cdot q_2)^2}{q_1 \cdot q_2 \ p_1 \cdot k \ p_2 \cdot k} , \quad (3.10)$$

where the sum is over spins and colours. If we integrate out the Euler angles then the matrix element depends only on  $x_1$  and  $x_2$ . The contribution

to the total cross section is then

$$\sigma^{q\bar{q}g} = \sigma_0 3 \sum_q Q_q^2 \int dx_1 dx_2 C_F \frac{\alpha_s}{2\pi} \frac{x_1^2 + x_2^2}{(1-x_1)(1-x_2)} \quad (3.11)$$

where  $\sigma_0 = 4\pi\alpha^2/(3s)$  and the integration region is:  $0 \leq x_1, x_2 \leq 1$ ,  $x_1 + x_2 \geq 1$ . Unfortunately, the integrals in Eq. (3.11) are divergent along the boundaries at  $x_i = 1$ . Since  $1 - x_1 = x_2 E_g (1 - \cos \theta_{2g})/\sqrt{s}$  and  $1 - x_2 = x_1 E_g (1 - \cos \theta_{1g})/\sqrt{s}$ , where  $E_g$  is the gluon energy and  $\theta_{ig}$  ( $i = 1, 2$ ) the angles between the gluon and the quarks, we see that the singularities come from regions of phase space where the gluon is *collinear* with the quark or antiquark,  $\theta_{ig} \rightarrow 0$ , or where the gluon is *soft*,  $E_g/\sqrt{s} \rightarrow 0$ . These singularities are not of course physical; they simply indicate a breakdown of the perturbative approach. Quarks and gluons are never on-mass-shell particles, as this calculation assumes. When we encounter gluon energies and quark-gluon invariant masses which are of the same order as hadronic mass scales ( $\sim 1$  GeV or less) then we cannot ignore the effects of confinement. We will discuss in later chapters various ways to model these effects. In the meantime, we can regard the singular behaviour on the boundaries of the phase space diagram as signifying physics beyond perturbation theory.

The key point is that we have not yet demonstrated that these ‘dangerous’ regions actually make an important contribution to the total cross section. The way to proceed is to introduce a temporary ‘regularization procedure’ for making the integrals finite, both for the real- and virtual-gluon diagrams, and then to see whether we can remove the regulator at the end of the calculation and obtain a finite result. Several methods are suitable. We can give the gluon a small mass, or take the final-state quark and antiquark off mass-shell by a small amount (which one might argue had some physical relevance). With either of these procedures, the singularities in the contributions from individual diagrams are avoided, being manifest instead as logarithms of the regulating mass scale.

A mathematically more elegant regularization procedure is to use dimensional regularization, with the number of space-time dimensions now  $n > 4$ . Recall that this was encountered in the previous chapter as a method for performing ultraviolet regularization in the context of renormalization. Here the method is being extended to *real* gluon emission in addition to loop diagrams. Going to  $n \neq 4$  dimensions affects both the phase space and the traces of the Dirac matrices in the  $q\bar{q}g$  cross-section calculation. As a result, Eq. (3.11) becomes

$$\sigma^{q\bar{q}g}(\epsilon) = \sigma_0 3 \sum_q Q_q^2 H(\epsilon) \int dx_1 dx_2 \frac{2\alpha_s}{3\pi} \frac{x_1^2 + x_2^2 - \epsilon(2 - x_1 - x_2)}{(1-x_1)^{1+\epsilon}(1-x_2)^{1+\epsilon}} \quad (3.12)$$

with  $\epsilon = \frac{1}{2}(4 - n)$ , and

$$H(\epsilon) = \frac{3(1-\epsilon)^2}{(3-2\epsilon)\Gamma(2-2\epsilon)} = 1 + O(\epsilon), \quad (3.13)$$

where  $\Gamma$  is the Euler gamma function given in Eq. (2.57). With the three-body phase space integrals recast in  $n$  dimensions, the soft and collinear singularities are regulated, appearing instead as *poles* at  $n = 4$ . Performing the integrations in Eq. (3.12) gives

$$\sigma^{q\bar{q}g}(\epsilon) = \sigma_0 3 \sum_q Q_q^2 \frac{\alpha_s}{2\pi} H(\epsilon) \left[ \frac{2}{\epsilon^2} + \frac{3}{\epsilon} + \frac{19}{2} + O(\epsilon) \right]. \quad (3.14)$$

The virtual gluon contribution can be calculated in a similar fashion, with dimensional regularization again used to control the infra-red divergences in the loops. The result is

$$\sigma^{q\bar{q}(g)}(\epsilon) = \sigma_0 3 \sum_q Q_q^2 \frac{C_F \alpha_s}{2\pi} H(\epsilon) \left[ -\frac{2}{\epsilon^2} - \frac{3}{\epsilon} - 8 + O(\epsilon) \right]. \quad (3.15)$$

When the two contributions Eqs. (3.14) and (3.15) are added together, the poles exactly cancel and the result is *finite* in the limit  $\epsilon \rightarrow 0$ :

$$R = 3 \sum_q Q_q^2 \left\{ 1 + \frac{\alpha_s}{\pi} + O(\alpha_s^2) \right\}. \quad (3.16)$$

At this order and for massless quarks, the QCD correction is independent of the nature of the exchanged weak boson, *i.e.* the  $1 + \alpha_s/\pi$  result is valid also for  $R_Z$ . Notice also that the next-to-leading-order correction is positive, and with a value for  $\alpha_s$  of about 0.11, can accommodate the experimental measurement of  $R_Z$  given above. In contrast, the corresponding correction would be negative in a theory with a scalar gluon.

The cancellation of the soft and collinear singularities between the real and virtual gluon diagrams is not accidental. There are theorems — the Bloch, Nordsieck [2] and Kinoshita, Lee, Nauenberg [3] theorems — which state that suitably defined inclusive quantities will indeed be free of singularities in the massless limit. The total hadronic cross section is an example of such a quantity, whereas the cross section for the exclusive  $q\bar{q}$  final state, *i.e.*  $\sigma(e^+e^- \rightarrow q\bar{q})$  with no gluon emission, is not.

In the above result, the coupling  $\alpha_s$  is understood to be evaluated at a renormalization scale  $\mu$ . Since the ultraviolet divergences in the loop diagrams in Fig. 3.2 cancel, the coefficient of the coupling is independent of  $\mu$  at this order. At  $O(\alpha_s^2)$  and higher, we encounter the ultraviolet divergences associated with the renormalization of the strong coupling. The coefficients are therefore renormalization scheme dependent, and we

can write (see Chapter 2)

$$R = K_{QCD} 3 \sum_q Q_q^2,$$

$$K_{QCD} = 1 + \frac{\alpha_s(\mu^2)}{\pi} + \sum_{n \geq 2} C_n \left( \frac{s}{\mu^2} \right) \left( \frac{\alpha_s(\mu^2)}{\pi} \right)^n. \quad (3.17)$$

The  $O(\alpha_s^2)$  and  $O(\alpha_s^3)$  corrections have been calculated. In the  $\overline{MS}$  scheme with the renormalization scale choice  $\mu = \sqrt{s}$ , the values are

$$C_2(1) = \left( \frac{2}{3} \zeta(3) - \frac{11}{12} \right) n_f + \left( \frac{365}{24} - 11\zeta(3) \right)$$

$$\simeq 1.986 - 0.115 n_f$$

$$C_3(1) = \left( \frac{87029}{288} - \frac{1103}{4} \zeta(3) + \frac{275}{6} \zeta(5) \right)$$

$$- \left( \frac{7847}{216} - \frac{262}{9} \zeta(3) + \frac{25}{9} \zeta(5) \right) n_f$$

$$+ \left( \frac{151}{162} - \frac{19}{27} \zeta(3) \right) n_f^2$$

$$- \frac{\pi^2}{432} (33 - 2n_f)^2 + \eta \left( \frac{55}{72} - \frac{5}{3} \zeta(3) \right)$$

$$\simeq -6.637 - 1.200 n_f - 0.005 n_f^2 - 1.240 \eta, \quad (3.18)$$

where  $\eta = (\sum_q Q_q)^2 / 3 \sum_q Q_q^2$  and the sum extends over the ( $n_f$ ) quarks which are effectively massless at the energy scale  $\sqrt{s}$ . The Riemann  $\zeta$  function,

$$\zeta(s) = \sum_{k=1}^{\infty} \frac{1}{k^s}, \quad (3.19)$$

has the values  $\zeta(3) = 1.202\,057$ ,  $\zeta(5) = 1.036\,928$ . The expression for  $C_3$  is taken from ref. [4]. For massless quarks, the QCD corrections to the ratio  $R_Z$  of hadronic to leptonic  $Z$  decay widths are again the same at this order, except that  $\eta$  changes to <sup>1</sup>

$$\eta = \frac{(\sum_q V_q)^2}{3 \sum_q (V_q^2 + A_q^2)}. \quad (3.20)$$

The  $\mu^2$  dependence of the coefficients  $C_2$ ,  $C_3 \dots$  is fixed by the requirement that order-by-order, the series should be independent of the choice of scale:

$$C_2 \left( \frac{s}{\mu^2} \right) = C_2(1) - \pi b \ln \frac{s}{\mu^2}$$

---

<sup>1</sup> This result assumes complete isodoublets of massless quarks, see Section 3.2.

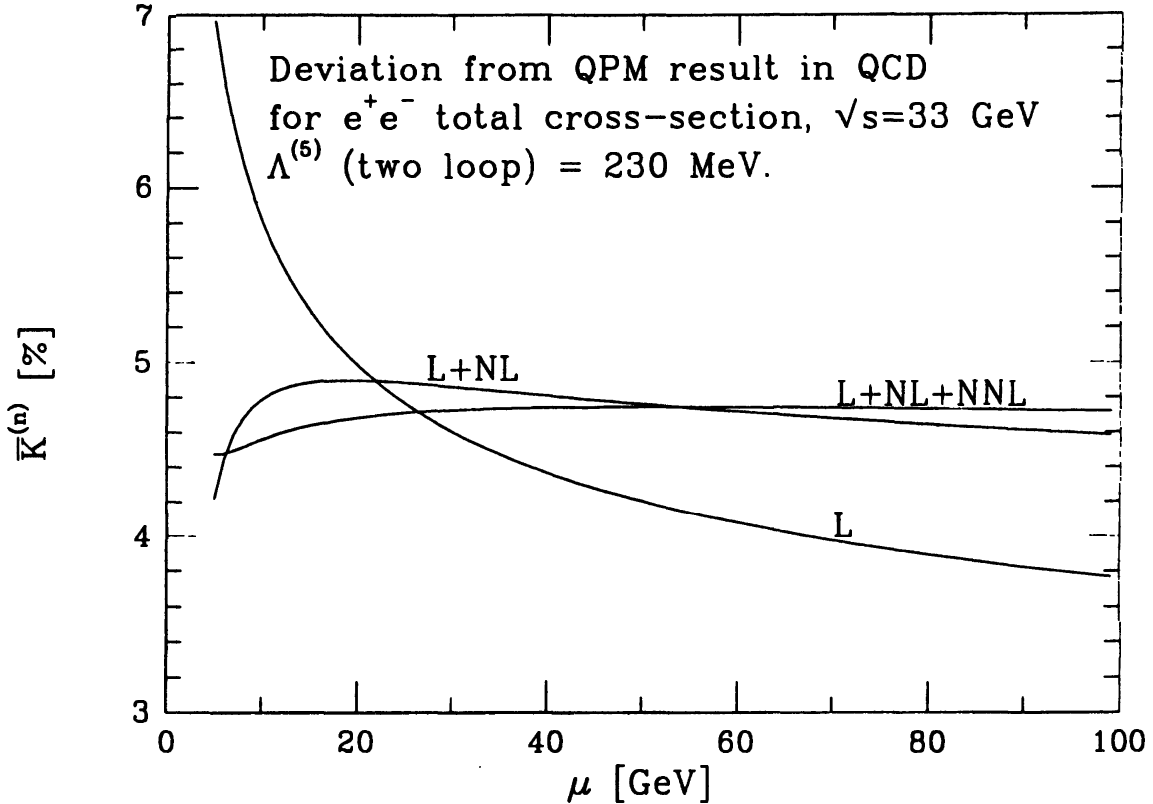


Fig. 3.3. The quantity  $\bar{K}^{(n)} = K^{(n)} - 1$ , where  $K^{(n)}$  denotes the QCD prediction for  $K_{QCD}$  truncated at  $O(\alpha_s^n)$ , as a function of the renormalization scale  $\mu$ .

$$\begin{aligned} C_3 \left( \frac{s}{\mu^2} \right) &= C_3(1) + C_1(1) \left( \pi b \ln \frac{s}{\mu^2} \right)^2 \\ &\quad - (\pi b' + 2C_2(1)) \pi b \ln \frac{s}{\mu^2}, \end{aligned} \quad (3.21)$$

where  $b$  and  $b'$  are defined in Eq. (2.8). The above result provides an explicit example of how the coefficients of any QCD perturbative expansion depend on the choice made for the renormalization scale  $\mu$ , in such a way that as  $\mu$  is varied, the change in the coefficients exactly compensates the change in the coupling  $\alpha_s(\mu^2)$ . However this  $\mu$ -independence breaks down whenever the series is *truncated*. One can show by differentiating the above expression for  $K_{QCD}$  with respect to  $\mu$  that the result is  $O(\alpha_s^4)$ . More generally, changing the scale in a physical quantity which has been calculated to  $O(\alpha_s^n)$  induces changes which are  $O(\alpha_s^{n+1})$ . This is illustrated in Fig. 3.3, which shows  $K_{QCD}$  defined in Eq. (3.17) as a function of  $\mu$ , as the higher-order terms are added in. As expected, the more terms are added, the more stable the prediction.

In the absence of higher-order corrections, one can try to guess the ‘best’ choice of scale (more generally, renormalization scheme), defined as

the scale which makes the truncated and all-orders predictions equal.<sup>2</sup> In the literature, various particular choices have been advocated. Suppose that the perturbation series for  $R$  has been calculated to order  $\alpha_S^n$ . In the *fastest apparent convergence* (FAC) approach, one chooses the scale  $\mu = \mu_{FAC}$ , where

$$R^{(1)}(\mu_{FAC}) = R^{(n)}(\mu_{FAC}). \quad (3.22)$$

On the other hand, the *principle of minimal sensitivity* (PMS) [5] imposes the known renormalization-scheme independence of the all-orders result on the truncated calculation. Within the  $\overline{\text{MS}}$  renormalization prescription, this suggests a scale choice  $\mu = \mu_{PMS}$ , where

$$\mu \frac{d}{d\mu} R^{(n)}(\mu) \Big|_{\mu_{PMS}} = 0. \quad (3.23)$$

A third approach (BLM [6]) argues that the  $n_f$  dependent terms in the coefficients indicate which parts should be associated with the the QCD  $\beta$  function, and that the appropriate scale is the one which absorbs all these terms into  $\alpha_S$ . To  $O(\alpha_S^2)$ , it is straightforward to calculate these three special scales from Eq. (3.21):

$$\begin{aligned} \mu_{FAC} &= \sqrt{s} \exp \left( -\frac{C_2(1)}{2\pi b} \right) \simeq 0.692 \sqrt{s}, \\ \mu_{PMS} &= \sqrt{s} \exp \left( -\frac{\pi b' + 2C_2(1)}{4\pi b} \right) \simeq 0.587 \sqrt{s}, \\ \mu_{BLM} &= \sqrt{s} \exp \left( 2\zeta(3) - \frac{11}{4} \right) \simeq 0.708 \sqrt{s}, \end{aligned} \quad (3.24)$$

where  $C_2(1)$  is given in Eq. (3.18) and five massless flavours have been assumed. In the present context, these three scales are numerically rather close (the first two can be identified directly in Fig. 3.3), indicating that the scale dependence of  $R$  is rather weak, and that the  $\alpha_S$  value obtained from fitting the above expressions to the  $e^+e^-$  total cross section or the  $Z$  hadronic decay width should be reliable. The results of such fits will be discussed in Chapter 12. It is, however, important to remember that there are no theorems that *prove* that any of the above scale-fixing schemes are correct. All one can say is that the theoretical error on a quantity calculated to  $O(\alpha_S^n)$  is always  $O(\alpha_S^{n+1})$ . Fixing a special scale does *not* remove this theoretical error on the prediction. One can vary the scale over some ‘physically reasonable range’ (for example, the range of momentum scales flowing through the Feynman diagrams) to try to quantify this uncer-

---

<sup>2</sup> We do not address here the meaning of an ‘all-orders’ summation of what is an asymptotic rather than a convergent series.

tainty, but ultimately there is no substitute for actually performing the higher-order calculations.

### 3.2 Heavy quark production

The results presented in the previous section for the cross sections for  $e^+e^- \rightarrow q\bar{q}, q\bar{q}g, \dots$  are valid only for massless quarks,  $m_q = 0$ . This is a reasonable approximation for the  $u, d, s$  and  $c$  quarks at high-energy colliders such as LEP and SLC. For  $b$  and  $t$  quarks, however, the expressions must be modified to take the non-negligible quark mass into account. In this section we present some basic results for massive quarks. We use the notation  $Q$  for the field of a heavy quark of mass  $m$ .

We begin with the lowest-order process,  $e^+e^- \rightarrow Q\bar{Q}$ . There are two sources of mass effects — the matrix element and the phase space integration. Energy conservation embodied in the latter causes the cross section to vanish for  $\sqrt{s} \leq 2m$ .<sup>3</sup> It is convenient to introduce the quark *velocity*

$$\beta = \sqrt{1 - \frac{4m^2}{s}}, \quad (3.25)$$

so that  $\beta = 0$  corresponds to the heavy quark threshold, and the results for massless quarks are recovered in the relativistic limit  $\beta \rightarrow 1$ .

A straightforward calculation gives the analogues of Eqs. (3.7,3.8) for massive quarks,

$$\begin{aligned} R(\beta) &= 3Q_Q^2 \beta \frac{3 - \beta^2}{2} \\ R_Z(\beta) &= \frac{3\beta}{A_\mu^2 + V_\mu^2} \left( \beta^2 A_Q^2 + \frac{3 - \beta^2}{2} V_Q^2 \right) \\ &\equiv R_{ZA}(\beta) + R_{ZV}(\beta). \end{aligned} \quad (3.26)$$

Notice that the dependence on the mass is *different* for the vector and axial-vector parts of  $R_Z$ , since the quark mass breaks chiral invariance. For the same reason, the higher-order QCD corrections are also different:<sup>4</sup>

$$\begin{aligned} R_Z(\beta) &= R_{ZV}(\beta) \left[ 1 + c_1 \frac{\alpha_S}{\pi} + c_2 \left( \frac{\alpha_S}{\pi} \right)^2 + \dots \right] \\ &+ R_{ZA}(\beta) \left[ 1 + d_1 \frac{\alpha_S}{\pi} + d_2 \left( \frac{\alpha_S}{\pi} \right)^2 + \dots \right]. \end{aligned} \quad (3.27)$$

---

<sup>3</sup> We shall consider only the idealized case of *stable* heavy quarks. Otherwise the behaviour near threshold is influenced by finite decay width effects.

<sup>4</sup> We use the notation of ref. [7].

The higher-order coefficients contain logarithms of  $s/m^2$  which originate in the running of the quark mass, as described in Section 2.4. These can be removed by replacing the ‘bare’ mass  $m$  by the running mass  $m(s)$  in, say, the  $\overline{\text{MS}}$  renormalization scheme.

The  $\mathcal{O}(\alpha_s)$  correction coefficients  $c_1$  and  $d_1$  are known for arbitrary quark mass [8], but the expressions are too unwieldy to present here. For small quark masses, a good approximation is [7]

$$\begin{aligned} c_1 &= 1 + 12\epsilon + \dots \\ d_1 &= 1 - 22\epsilon + \dots , \end{aligned} \quad (3.28)$$

where  $\epsilon = m^2(s)/s \ll 1$ . Note that setting  $\epsilon = 0$  reproduces the massless quark results  $c_1 = d_1 = 1$ . The coefficients  $c_2$  and  $d_2$  are also known in the small-quark-mass approximation [9]:

$$\begin{aligned} c_2 &= 1.4092 + 104.83\epsilon + \dots \\ d_2 &= 1.4092 - 85.72\epsilon + \dots \end{aligned} \quad (3.29)$$

in the  $\overline{\text{MS}}$  scheme with  $n_f = 5$  and  $\alpha_s = \alpha_s(s)$  in (3.27). In  $e^+e^-$  annihilation at the  $Z$  pole the precision of the  $R_Z$  measurement is such that the effects due to the finite  $b$  quark mass ( $\epsilon \approx 10^{-3}$ ) must be taken into account in the coefficients to  $\mathcal{O}(\alpha_s^2)$ .

The result for  $d_2$  in Eq. (3.29) is strictly only valid for mass-degenerate weak isospin quark doublets. When the mass difference between the quarks in the same doublet becomes large, there is an additional large contribution. This is related to the triangle anomaly for axial currents. In particular, for  $m_t > M_Z \gg m_b$  [10],

$$\delta d_2 \approx \ln \left( \frac{M_Z^2}{m_t^2} \right) - \frac{37}{12} + \mathcal{O} \left( \frac{M_Z^2}{m_t^2} \right) . \quad (3.30)$$

### 3.3 Jet cross sections

The expression given for the total hadronic cross section in Section 3.1 is very concise, but it tells us nothing about the kinematic *distribution* of hadrons in the final state. If the hadronic fragments of a fast moving quark have limited transverse momentum relative to the quark momentum (collinear fragmentation), then the lowest-order contribution to the cross section,  $e^+e^- \rightarrow q\bar{q}$ , can naively be interpreted as the production of two back-to-back jets. Experimentally, it *does* appear to be true that most events are ‘two-jet-like’, with a smaller fraction containing three jets, an even smaller fraction containing four jets, and so on. At first sight, this seems consistent with our intuition that each jet after the first two should correspond to the emission of a gluon off the quark lines, each emission

'costing' a power of  $\alpha_s \ll 1$ . However, this simple picture, although essentially correct, masks a much more complicated situation, which involves both perturbative and non-perturbative aspects of the theory. In this section we will attempt to construct a theory of jets based on the lowest orders in perturbation theory. In subsequent chapters, we will extend this to higher orders and describe how to include the non-perturbative transition from a final state involving quarks and gluons to one involving the hadrons which are measured by experiment.

We begin by considering the next-to-leading process  $e^+e^- \rightarrow q\bar{q}g$ . From the previous section (Eq. (3.11)), we have

$$\frac{1}{\sigma} \frac{d^2\sigma}{dx_1 dx_2} = C_F \frac{\alpha_s}{2\pi} \frac{x_1^2 + x_2^2}{(1-x_1)(1-x_2)}. \quad (3.31)$$

Recall that this cross section becomes (infinitely) large when one or both of the  $x_i$  approach 1, which corresponds to the gluon being collinear with one of the quarks, or soft (*i.e.* its energy is small compared to  $\sqrt{s}$ ) respectively. If we again assume that quarks and gluons fragment collinearly into hadrons, then this preference for the gluon to be soft or collinear means that the two-jet-like structure of the lowest order is maintained at  $O(\alpha_s)$ . If, on the other hand, the gluon is *required* to be well-separated in phase space from the quarks — a configuration which we might identify as a 'three-jet event' — then the singular regions of the matrix element are avoided and the cross section is suppressed relative to lowest order by one power of  $\alpha_s$ . In fact, this qualitative result holds to *all* orders of perturbation theory. The amplitudes for multiple gluon emission contain the same type of singularities as those which appear at first order, which leads to a final state which is predominantly 'two-jet-like', with a smaller probability (determined by  $\alpha_s$ ) for three or more distinguishable jets.

To make all this more quantitative, we need to introduce the concept of a *jet measure*, *i.e.* a procedure for classifying a final state of hadrons (experimentally) or quarks and gluons (theoretically) according to the number of jets it contains. To be useful, a jet measure should give cross sections which, like the total cross section, are free of soft and collinear singularities when calculated in perturbation theory, and should also be relatively insensitive to the non-perturbative fragmentation of quarks and gluons into hadrons.

One of the first attempts to define jet cross sections in perturbation theory was by Sterman and Weinberg [11]. In their picture, a final state is classified as two-jet-like if all but a fraction  $\epsilon$  of the total available energy is contained in a pair of cones of half-angle  $\delta$ . The two-jet cross section is then obtained by integrating the matrix elements for the various quark and gluon final states over the appropriate region of phase space determined by  $\epsilon$  and  $\delta$ . At lowest order, the two-jet and total cross sections

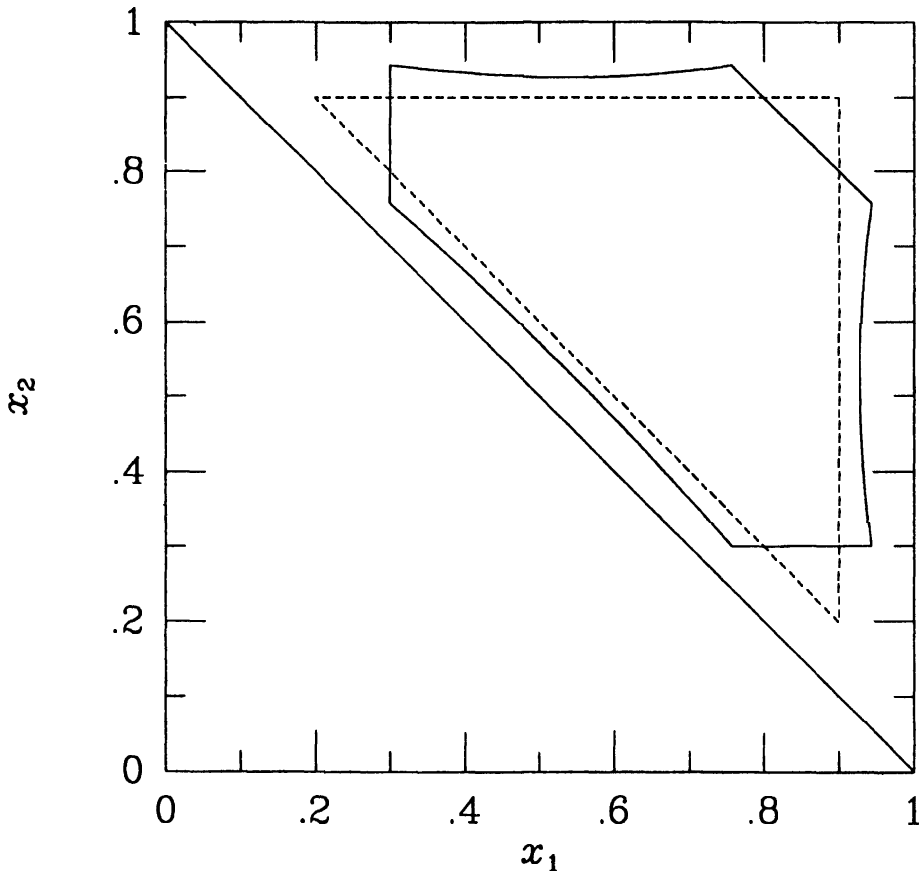


Fig. 3.4. Boundaries between the two- and three-jet regions in the  $(x_1, x_2)$  plane for Sterman-Weinberg jets with  $(\epsilon, \delta) = (0.3, 30^\circ)$  (solid lines), and JADE algorithm jets with  $y = 0.1$  (dashed lines).

obviously coincide, for any values of the parameters. At  $O(\alpha_s)$ , the two-jet cross section is obtained by integrating the right-hand side of Eq. (3.31) over the appropriate range of  $x_1$  and  $x_2$ . Fig. 3.4 shows the boundaries (solid lines) for the specific choice of parameters  $\epsilon = 0.3$  and  $\delta = 30^\circ$ . The two-jet region is the narrow band between these boundaries and the edges of the triangle. Note that the  $\delta$  constraint corresponds to the curved portions of the boundary, while the  $\epsilon$  constraint gives the straight line segments at the corners.

Rather than calculating the two-jet cross section directly, integrating the  $q\bar{q}g$  matrix element (in  $n$  dimensions) over this region and adding the contribution from the virtual gluon diagrams, it is easier to use the fact that at this order  $\sigma = \sigma_2 + \sigma_3$ . The two-jet cross section can therefore be obtained by subtracting the three-jet cross section from the total cross section already obtained in Section 3.1. The advantage of this is that the calculation of  $\sigma_3$  can be performed in four dimensions, since the matrix element singularities are outside the three-jet region at this order. Defining

the two- and three-jet fractions by  $f_i = \sigma_i/\sigma$  ( $i = 2, 3$ ) we obtain<sup>5</sup>

$$\begin{aligned} f_2 &= 1 - 8C_F \frac{\alpha_s}{2\pi} \left\{ \ln \frac{1}{\delta} \left[ \ln \left( \frac{1}{2\epsilon} - 1 \right) - \frac{3}{4} + 3\epsilon \right] \right. \\ &\quad \left. + \frac{\pi^2}{12} - \frac{7}{16} - \epsilon + \frac{3}{2}\epsilon^2 + O(\delta^2 \ln \epsilon) \right\}, \\ f_3 &= 1 - f_2. \end{aligned} \quad (3.32)$$

Notice that when the parameters  $\epsilon$  and  $\delta$  are small, the  $O(\alpha_s)$  correction becomes logarithmically large. This is simply the vestige of the soft and collinear singularities. We shall discuss in Chapter 6 techniques for resumming terms analogous to the  $\alpha_s \ln \delta$  terms in Eq. (3.32) to all orders in perturbation theory; when  $\delta$  is small this should improve on the first-order result. On the other hand, as the parameters become large, the three-jet region in Fig. 3.4 shrinks and the three-jet fraction decreases, as expected.

At higher orders in perturbation theory, we can have events with more than three jets. For example, the  $O(\alpha_s^2)$   $q\bar{q}q\bar{q}$  and  $q\bar{q}gg$  production processes can give rise to two, three or four jet events, depending on the separation in phase space and energy of the outgoing partons. It turns out that from an experimental and theoretical point of view, the Sterman-Weinberg jet definition based on cones is not well-suited to analysing multijet final states. One of the reasons is that fixed-angle cones give an inefficient ‘tiling’ of the phase space  $4\pi$  solid angle. For this reason, various alternatives have been proposed, the most important of which is the ‘minimum invariant mass’ or JADE algorithm [12], which we shall now describe.

Consider  $q\bar{q}g$  production at  $O(\alpha_s)$ , i.e. with three partons in the final state. A three-jet event is defined as one in which the minimum invariant mass of the parton pairs is larger than some fixed fraction  $y$  (sometimes called  $y_{\text{cut}}$ ) of the overall centre-of-mass energy:

$$\min (p_i + p_j)^2 = \min 2E_i E_j (1 - \cos \theta_{ij}) > ys, \quad i, j = q, \bar{q}, g, \quad (3.33)$$

for massless partons in the  $e^+e^-$  centre-of-mass frame. It is easily shown that this region of phase space avoids the soft and collinear singularities of the matrix element. In fact in terms of the energy fractions, Eq. (3.33) is equivalent to

$$0 < x_1, x_2 < 1 - y, \quad x_1 + x_2 > 1 + y \quad (y \leq \frac{1}{3}). \quad (3.34)$$

The corresponding boundary (for  $y = 0.1$ ) is shown by the dashed lines in Fig. 3.4. Just as for the Sterman-Weinberg jets, the two- and three-

---

<sup>5</sup> We show here only those terms which are important when  $\delta$  is small. The full expression is rather unwieldy.

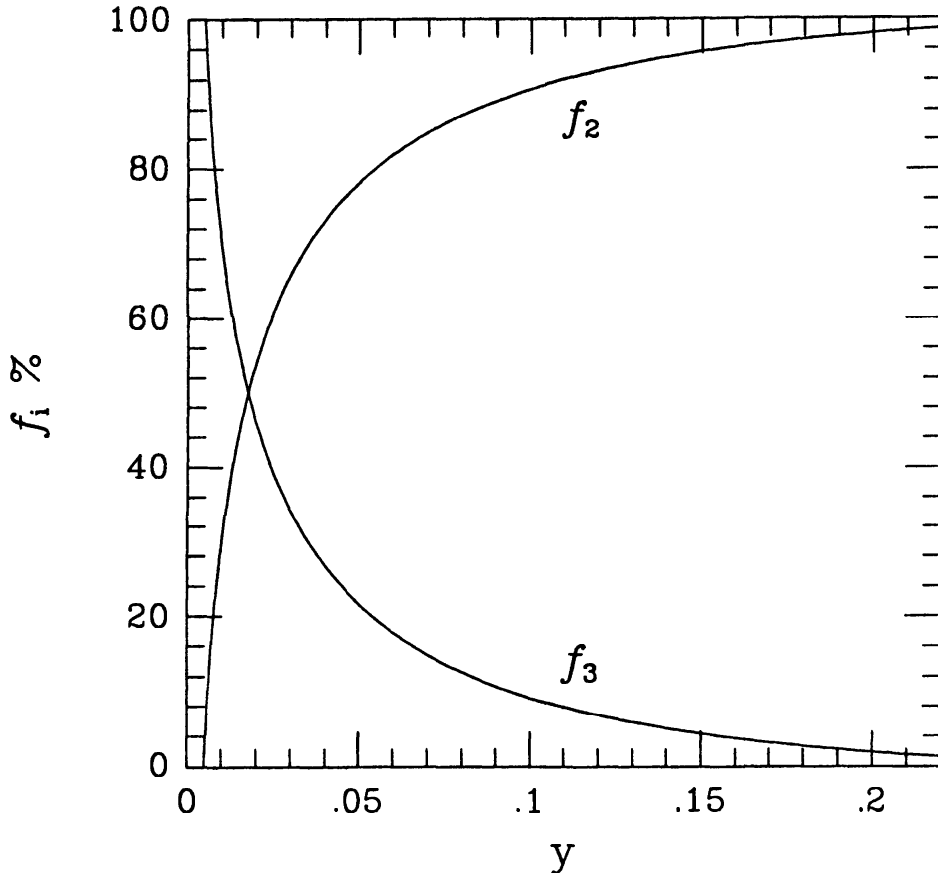


Fig. 3.5. The functions  $f_2$  and  $f_3$  from Eq. (3.35).

jet fractions to  $O(\alpha_S)$  are obtained by integrating the right-hand side of Eq. (3.11) over the appropriate region:

$$\begin{aligned} f_3 &= C_F \frac{\alpha_S}{2\pi} \left[ (3 - 6y) \ln \left( \frac{y}{1 - 2y} \right) + 2 \ln^2 \left( \frac{y}{1 - y} \right) \right. \\ &\quad \left. + \frac{5}{2} - 6y - \frac{9}{2}y^2 + 4 \operatorname{Li}_2 \left( \frac{y}{1 - y} \right) - \frac{\pi^2}{3} \right], \\ f_2 &= 1 - f_3, \end{aligned} \tag{3.35}$$

where  $\operatorname{Li}_2$  is the dilogarithm function,

$$\begin{aligned} \operatorname{Li}_2(x) &= - \int_0^x dy \frac{\ln(1-y)}{y} \\ &= \frac{x}{1^2} + \frac{x^2}{2^2} + \frac{x^3}{3^2} + \dots \text{ for } |x| \leq 1. \end{aligned} \tag{3.36}$$

The soft and collinear singularities again appear as large logarithms in the limit  $y \rightarrow 0$ . Clearly the result in Eq. (3.35) only makes sense for  $y$  values large enough such that  $f_2 \gg f_3$ , so that the  $O(\alpha_S)$  correction to  $f_2$  is perturbatively small. Fig. 3.5 shows the functions  $f_2(y)$  and  $f_3(y)$  from Eq. (3.35) for  $\alpha_S = 0.118$ .

The generalization to multijet fractions is straightforward, using the following algorithm. Starting from an  $n$ -parton final state, identify the pair with the minimum invariant mass squared. If this is greater than  $ys$  then the number of jets is  $n$ . If not, combine the minimum pair into a single ‘cluster’. Then repeat for the  $(n - 1)$ -parton/cluster final state, and so on until all partons/clusters have a relative invariant mass squared greater than  $ys$ . The number of clusters remaining is then the number of jets in the final state. According to this definition, an  $n$ -parton final state can give any number of jets between  $n$  (all partons well-separated) and 2 (for example, two energetic quarks accompanied by soft and collinear gluons).

Since a soft or collinear gluon emitted from a quark line does not change the multiplicity of jets, the cancellation of the corresponding singularities that was evident in the total cross section calculation can still take place, and the jet fractions defined this way are ‘infra-red safe’, *i.e.* free of such singularities to all orders in perturbation theory. We shall discuss other examples of infra-red safe jet variables below.

Now in general we have

$$\begin{aligned} f_{n+2}(\sqrt{s}, y) &= \left( \frac{\alpha_s(\mu^2)}{2\pi} \right)^n \sum_{j=0}^{\infty} C_{nj} \left( y, \frac{s}{\mu^2} \right) \left( \frac{\alpha_s(\mu^2)}{2\pi} \right)^j, \quad n \geq 0, \\ \sum_{n=2}^{\infty} f_n &= 1. \end{aligned} \tag{3.37}$$

We follow the convention in the literature of expanding the perturbation series for the total cross section and jet cross sections in powers of  $(\alpha_s/\pi)$  and  $(\alpha_s/2\pi)$  respectively. In (3.37) we have assumed some particular renormalization prescription ( $\overline{\text{MS}}$  is almost always used in practice) and introduced  $\mu$  as the renormalization scale. Since the jet parameter  $y$  is dimensionless, with the choice  $\mu = \sqrt{s}$  all the energy dependence of the jet fractions is contained in the coupling  $\alpha_s(s)$ . One can therefore exhibit, at least in principle, the *running* of the strong coupling by measuring, for example, a decrease in  $f_3$  as  $\sqrt{s}$  increases, see Fig. 3.6.

In experiments, the JADE algorithm is applied to final-state *hadrons* rather than *partons*.<sup>6</sup> However studies using hadronization models to describe the transition from partons to hadrons have shown that — at least at high energy — the hadronization corrections are small and therefore the QCD parton-level predictions can be reliably compared with the experimental data. This will be discussed further in Chapter 5.

The next-to-leading-order corrections to  $f_3$  have been calculated [14].

---

<sup>6</sup> There are in fact several slight variants of the JADE algorithm which are used in practice, see ref. [13].

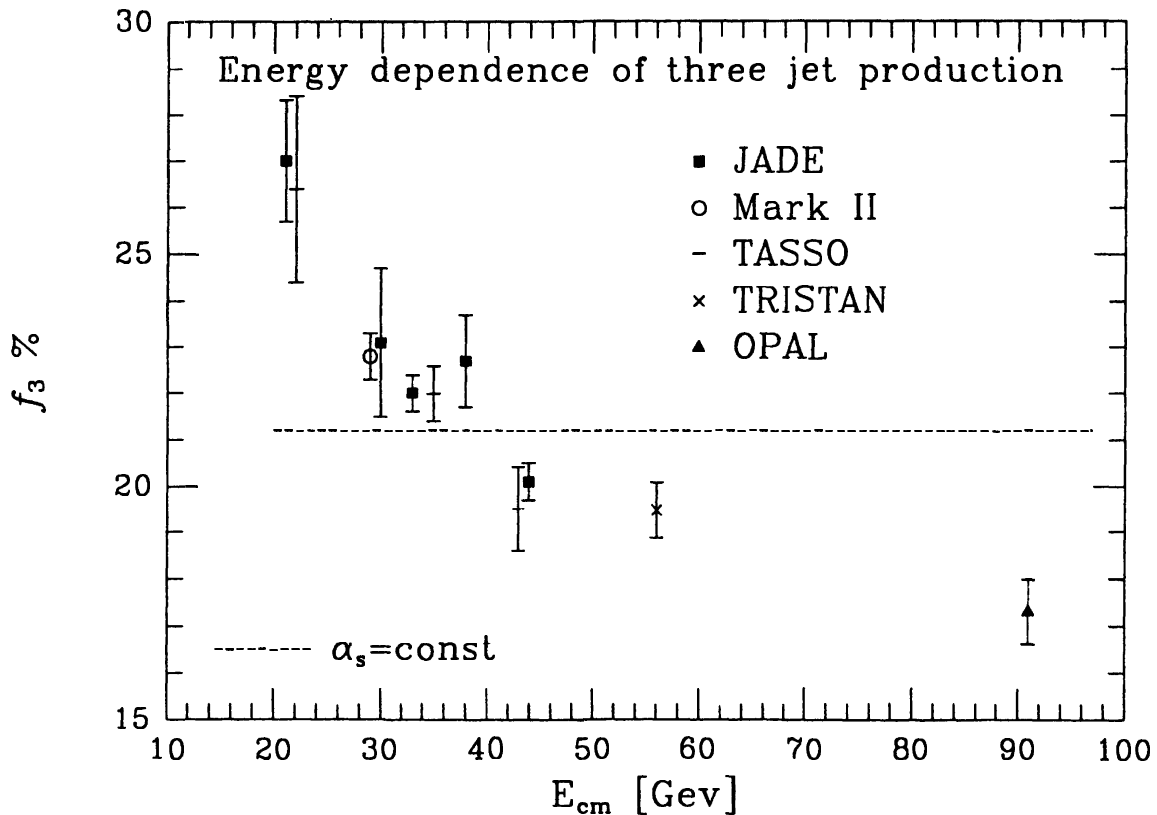


Fig. 3.6. A compilation of three-jet fractions at different  $e^+e^-$  annihilation energies. Adapted from ref. [15].

Because the hadronization corrections to  $f_3$  are small, the three-jet rate provides one of the most precise measurements of  $\alpha_s$  at  $e^+e^-$  colliders. A typical fit is shown in Fig. 3.7 [15]. The curves correspond to the perturbative predictions calculated in the  $\overline{\text{MS}}$  prescription with two different choices of scale. At large  $y$ , the events are mostly classified as two (broad) jets. As  $y$  decreases, and the jets are allowed to be narrower, fewer events are two-jet and the number of multijet events increases. Notice that at medium and large  $y$ , where these calculations should be most reliable, both scale choices give equally acceptable fits, *but with different values of  $\Lambda_{\overline{\text{MS}}}$* . This is an example of the scale-dependence uncertainty discussed above. At smaller  $y$ , there appears to be some preference for the curve corresponding to the smaller scale. However, some care must be taken with this interpretation. We have already seen (Eq. (3.35)) that when  $y$  is so small that  $\alpha_s \ln^2 y \sim 1$ , the perturbation series for  $f_2$  breaks down. In fact one can show that all the jet fractions have higher-order corrections which contain terms like  $\alpha_s^n \ln^{2n} y$  at small  $y$ . Before concluding anything about which renormalization scales are ‘preferred’, we should make sure that these large corrections are correctly taken into account. We shall see in Chapter 6 that when this is done, there is no longer any preference in the data for a small scale, and indeed the overall scale-dependence

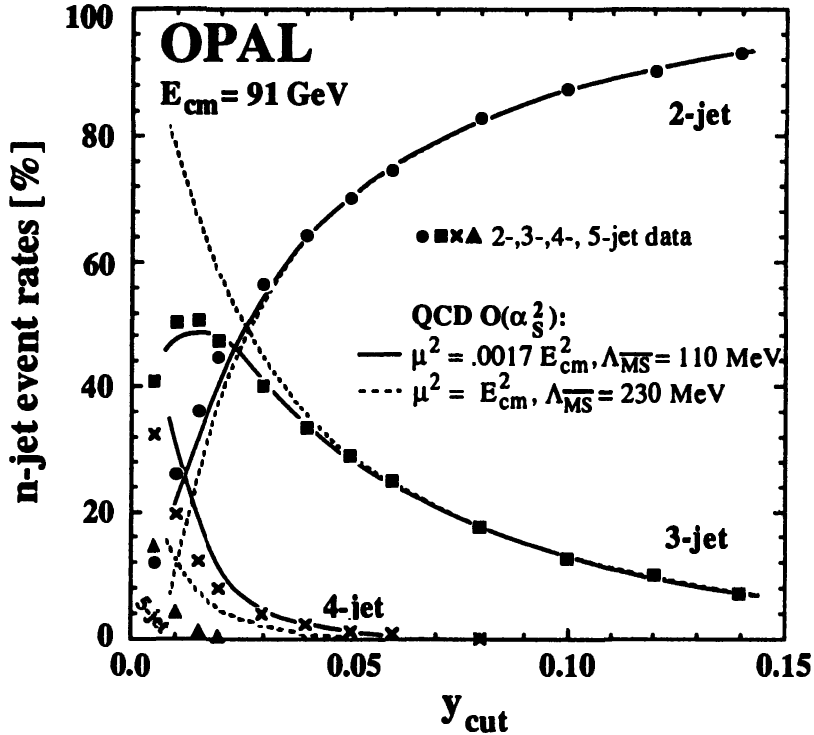


Fig. 3.7. QCD fits to the jet rates at LEP, as measured by the OPAL collaboration. Figure from ref. [15].

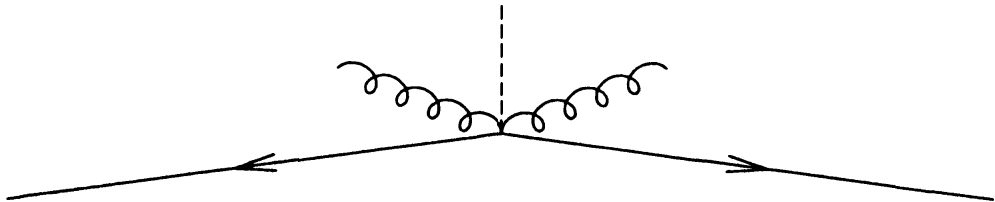


Fig. 3.8. An example of a configuration which the JADE algorithm classifies as a three-jet event.

uncertainty in the extracted value of the coupling is reduced.

While the JADE algorithm is well suited to experimental jet measurements, it is not quite optimal from a theoretical point of view. We have already remarked that when  $y$  is small, the  $O(\alpha_S^n \ln^{2n} y)$  terms must be resummed to all orders to obtain a reliable prediction. Unfortunately, the algorithm is not readily amenable to this type of resummation [16]. This reflects a tendency for the algorithm to reconstruct ‘spurious’ jets, *i.e.* clusters of hadrons or partons whose net momentum does not obviously coincide with any approximately collinear set of particles in the actual event. An example is provided by the configuration shown in Fig. 3.8, where two soft gluons are emitted close to the quark and antiquark. Even though the two gluons have a large relative angle, their invariant mass is the smallest in the event. If this is smaller than  $y$ , the algorithm combines

them into a single cluster, whose direction is indicated by the dashed line in the figure. If after this clustering all remaining invariant masses exceed the critical value determined by  $y$ , the event is classified as three jet, even though the direction of the third ‘cluster’ jet does not coincide with any of the original partons in the event.

To overcome these problems, a variant of the JADE algorithm — the  $k_T$  or ‘Durham’ algorithm — has been proposed [17]. In this new algorithm, the invariant mass measure of two partons (hadrons), defined in Eq. (3.33), is replaced by a quantity which, when the angle between the partons is small, is the minimum of the relative transverse momenta:

$$2 \min(E_i^2, E_j^2) (1 - \cos \theta_{ij}) > ys, \quad (3.38)$$

in the  $e^+e^-$  centre-of-mass frame. Notice that with this new definition, the configuration in Fig. 3.8 is classified, more naturally, as a two-jet event, since the relative transverse momentum of the gluons is larger than that of the two pairs of quarks and gluons. Using this modified algorithm, the jet fractions can be calculated in perturbation theory as before. At  $O(\alpha_s)$ , the conditions for two- and three-jet events implied by Eq. (3.38) again define a boundary in the  $(x_1, x_2)$  plane. Analogous expressions for  $f_2$  and  $f_3$  to those in Eq. (3.35) can then be obtained. As we shall see in Chapter 6, with this new definition of the jet measure resummation of the large logarithms can be performed [17], and the range of applicability can be extended to smaller values of  $y$  where comparison with data can be made. The next-to-leading-order corrections for the  $k_T$  algorithm have also been calculated [13] and comparisons of theory and experiment have been performed, as for the JADE algorithm. The corresponding  $\alpha_s$  values for the various algorithms, with and without resummation, will be presented in Chapter 12.

### 3.4 Event shape variables

Another approach to studying the jet-like characteristics of hadronic final states in  $e^+e^-$  annihilation is to use ‘shape variables’. The idea is to define a quantity which characterizes the ‘shape’ of an event, for example whether the distribution of hadrons is pencil-like, planar, spherical etc. This is more general than the jet cross section approach discussed above, since a jet-finding algorithm will *always* find jets in a hadronic final state even when none existed in the first place, for example in the limiting case when the hadronic energy is distributed uniformly over the  $4\pi$  solid angle.

The procedure, then, is to define a quantity  $X$  which measures some particular aspect of the shape of the hadronic final states. The distribution  $d\sigma/dX$  can be measured and compared with the theoretical predic-

tion. For the latter to be calculable in perturbation theory, the variable should be infra-red safe, *i.e.* insensitive to the emission of soft or collinear gluons. In particular, if  $\mathbf{p}_i$  is any momentum<sup>7</sup> occurring in its definition, it must be invariant under the branching

$$\mathbf{p}_i \rightarrow \mathbf{p}_j + \mathbf{p}_k \quad (3.39)$$

whenever  $\mathbf{p}_j$  and  $\mathbf{p}_k$  are parallel or one of them is small. Quantities made out of *linear* sums of momenta meet this requirement. Some widely-used examples are

(i) thrust [18]

$$T = \max_{\mathbf{n}} \frac{\sum_i |\mathbf{p}_i \cdot \mathbf{n}|}{\sum_i |\mathbf{p}_i|} \quad (3.40)$$

(ii) spherocity [19]

$$S = \left(\frac{4}{\pi}\right)^2 \min_{\mathbf{n}} \left( \frac{\sum_i |\mathbf{p}_i \times \mathbf{n}|}{\sum_i |\mathbf{p}_i|} \right)^2 \quad (3.41)$$

(iii)  $C$ -parameter [20]

$$C = \frac{3}{2} \frac{\sum_{i,j} [|\mathbf{p}_i| |\mathbf{p}_j| - (\mathbf{p}_i \cdot \mathbf{p}_j)^2 / |\mathbf{p}_i| |\mathbf{p}_j|]}{(\sum_i |\mathbf{p}_i|)^2}. \quad (3.42)$$

In these definitions,  $\mathbf{p}_i$  are the final-state hadron (or parton) momenta and  $\mathbf{n}$  is an arbitrary unit vector. If the  $\mathbf{p}_i$  form an almost collinear jet, then after the specified maximization or minimization  $\mathbf{n}$  will lie along the jet in the case of  $T$  or  $S$  (defining the thrust or spherocity axes, respectively). The values of the above shape variables for the idealized cases of perfectly pencil-like and spherical events are given in Table 3.1.

At lowest order in perturbation theory,  $e^+e^- \rightarrow q\bar{q}$ , the event shape variables have the values listed in the first row in Table 3.1. At  $O(\alpha_S)$ , the distribution in the the shape variable  $d\sigma/dX$  ( $X = T, S, \dots$ ) is obtained by integrating the right-hand side of Eq. (3.11) over  $x_1$  and  $x_2$  with the constraint

$$\delta(X - f_X(x_1, x_2, x_3 = 2 - x_1 - x_2)), \quad (3.43)$$

*i.e.* along a contour in the  $(x_1, x_2)$  plane. The functions  $f_X$  are listed in the third row in Table 3.1. Note that as long as the variables are not

---

<sup>7</sup> Boldface quantities denote three-momenta.

Quantity	$T$	$S$	$C$
pencil-like event	1	0	0
spherical event	$\frac{1}{2}$	1	1
$q\bar{q}g$	$\max\{x_i\}$	$\frac{16}{\pi^2} \frac{\prod_i (1-x_i)}{\max\{x_i^2\}}$	$6 \frac{\prod_i (1-x_i)}{x_1 x_2 x_3}$

Table 3.1. Values of the shape variables for different event types. The third row gives the constraint functions  $f_X$  of Eq. (3.43).

equal to their pencil-like limits, *e.g.*  $T < 1$ , then these distributions are finite, since the soft and collinear configurations are excluded from the integration range.

For the thrust distribution, the function  $f_T$  gives exactly the same integration contour as the two-jet/three-jet boundary for the JADE algorithm, Fig. 3.4. A straightforward calculation gives

$$\frac{1}{\sigma} \frac{d\sigma}{dT} = C_F \frac{\alpha_s}{2\pi} \left[ \frac{2(3T^2 - 3T + 2)}{T(1-T)} \ln \left( \frac{2T-1}{1-T} \right) - \frac{3(3T-2)(2-T)}{(1-T)} \right]. \quad (3.44)$$

As expected, the distribution diverges as  $T \rightarrow 1$ , reflecting the soft and collinear gluon singularities in the matrix element. The virtual gluon contribution at this order gives a singular contribution proportional to  $\delta(T-1)$ , such that (with a suitable regularization procedure) the correct result for the total cross section is obtained when  $d\sigma/dT$  is integrated over  $\frac{1}{2} \leq T \leq 1$ .

The thrust distribution for  $T \simeq 1$  is dominated by two-jet configurations. In fact we can use the distribution integrated over  $T_0 < T < 1$  to define a two-jet measure analogous to  $f_2$ , with  $1-T_0$  playing the role of  $y$ . The tail of the distribution away from  $T = 1$  is, on the other hand, dominated by multijet final states. In this region we have a direct test of the QCD matrix elements, through the shape of the distribution, and also a measurement of the strong coupling  $\alpha_s$ , through the normalization. This can be done with high precision, since the next-to-leading corrections for the ( $T < 1$ ) thrust distribution (and indeed the other shape variables) are known [21]. The results of such measurements will be presented in Chapter 12. Care must be taken near  $T = 1$  where (a) hadronization corrections become large, and (b) terms of order  $[\alpha_s \ln^2(1-T)]^n$  appear in the perturbation series. This will be discussed further in Chapter 6.

It was quantities like the thrust distribution which provided the first indications that gluons are *vector* particles. For *scalar* gluons (in the adjoint representation of SU(3)), the distribution in  $x_1$  and  $x_2$  for  $q\bar{q}g$

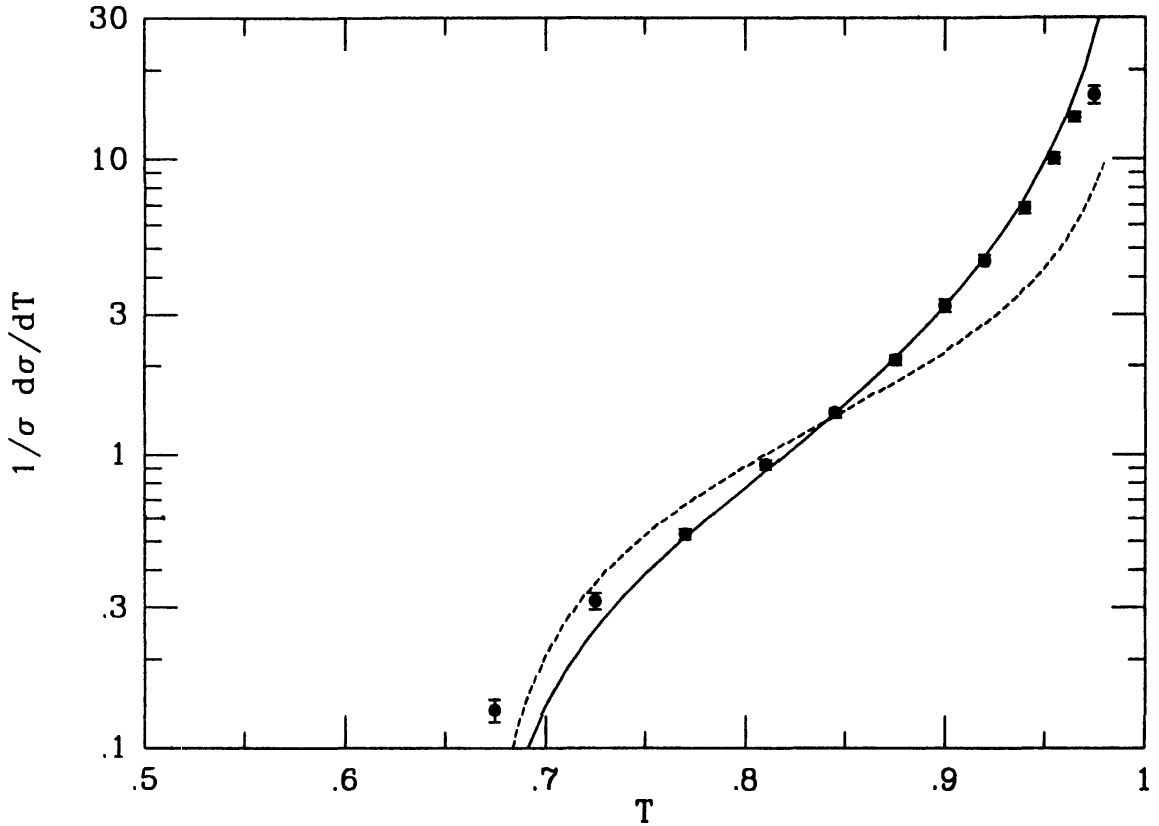


Fig. 3.9. The thrust distribution measured at LEP, showing data from the DELPHI collaboration [22] for  $T < 0.98$ , together with predictions of scalar gluon (dashed line) and vector gluon (solid line) theories.

production is obtained from Eq. (3.11) by the replacement

$$x_1^2 + x_2^2 \rightarrow \frac{1}{2}x_3^2 = \frac{1}{2}(2 - x_1 - x_2)^2 \quad (3.45)$$

in the numerator. Fig. 3.9 shows a comparison of data on the thrust distribution measured at LEP with the predictions of the  $O(\alpha_s)$  vector and scalar gluon theories. The values of  $\alpha_s$  (0.265 and 1.59 respectively) are chosen to give the best fit to the distribution away from  $T = 1$ . The scalar gluon theory is evidently ruled out. Note the slight discrepancy between the vector gluon prediction and the data at both large and small  $T$ . For the former, this is precisely the region where higher-order, logarithmic contributions become important. At small  $T$ , on the other hand, contributions from higher-order multiparton production are important. In fact a more complete calculation, with resummation of large logarithms and higher-order contributions included, gives good agreement over the whole range, see Fig. 6.12.

Finally, we mention briefly the *energy-energy correlation function* (EEC) [23], another quantity which is related to the shape variables already discussed and which is also widely used to test QCD at  $e^+e^-$  colliders. The

EEC is a dimensionless angular distribution defined by

$$\frac{1}{\sigma} \frac{d\Sigma}{d \cos \chi} = \sum_{i,j} \int \frac{d^3 p_i}{E_i} \frac{d^3 p_j}{E_j} \left( \frac{2E_i E_j}{s} \right) E_i E_j \frac{d^6 \sigma}{d^3 p_i d^3 p_j} \delta(\hat{n}_i \cdot \hat{n}_j - \cos \chi) + \sum_i \int \frac{d^3 p_i}{E_i} \left( \frac{E_i^2}{s} \right) E_i \frac{d^3 \sigma}{d^3 p_i} \delta(1 - \cos \chi), \quad (3.46)$$

where  $E_1 E_2 d^6 \sigma / d^3 p_1 d^3 p_2$  is the two-hadron inclusive cross section. The first sum on the right-hand side is over all distinct pairs of hadrons —  $n(n - 1)/2$  terms for an  $n$ -hadron final state. The second sum is a self-correlation ( $n$  terms) which guarantees the sum rule

$$\int_{-1}^1 d \cos \chi \frac{1}{\sigma} \frac{d\Sigma}{d \cos \chi} = 1, \quad (3.47)$$

since  $\sum E_i = \sqrt{s}$ . Eq. (3.46) represents the standard integrated version of the EEC, in the sense that the information concerning the orientation of the final state with respect to the beam direction has been integrated out. A related quantity is the *asymmetry* of the energy-energy correlation function (EECA), defined by

$$\frac{1}{\sigma} \frac{d\Sigma^A}{d \cos \chi} = \frac{1}{\sigma} \frac{d\Sigma}{d \cos \chi} \Big|_{180^\circ - \chi} - \frac{1}{\sigma} \frac{d\Sigma}{d \cos \chi} \Big|_\chi, \quad (3.48)$$

for  $0 \leq \cos \chi \leq 1$ , which, at least in principle, has smaller hadronization corrections (see Chapter 5). The EEC, therefore, measures the correlation of hadronic energy flow in an event. In a ‘two-jet’ event, for example, the function is strongly peaked at  $\chi = 0^\circ$  and  $\chi = 180^\circ$ . In contrast, the more isotropic (spherical) the event, the flatter the distribution.

The energy-energy correlation function is straightforward to measure in experiments, relatively insensitive to hadronization and, most important from a theoretical point of view, infra-red safe. The cancellation of the singular contributions from soft and collinear real gluon emission and from virtual gluons can take place, since the net energy weighting and angular distribution is the same for both. At lowest order,  $e^+ e^- \rightarrow q\bar{q}$ , the EEC is simply

$$\frac{1}{\sigma} \frac{d\Sigma}{d \cos \chi} = \frac{1}{2} \delta(1 - \cos \chi) + \frac{1}{2} \delta(1 + \cos \chi). \quad (3.49)$$

For  $\chi \neq 0^\circ, 180^\circ$  the perturbation series starts at order  $\alpha_s$  with the process  $e^+ e^- \rightarrow q\bar{q}g$ , i.e.

$$\frac{1}{\sigma} \frac{d\Sigma}{d \cos \chi} = \frac{\alpha_s(\mu^2)}{2\pi} A_1(\chi) + \left( \frac{\alpha_s(\mu^2)}{2\pi} \right)^2 A_2 \left( \chi, \frac{s}{\mu^2} \right) + \dots \quad (3.50)$$

The first two terms in this series have been calculated [21]. In fact,  $A_1$

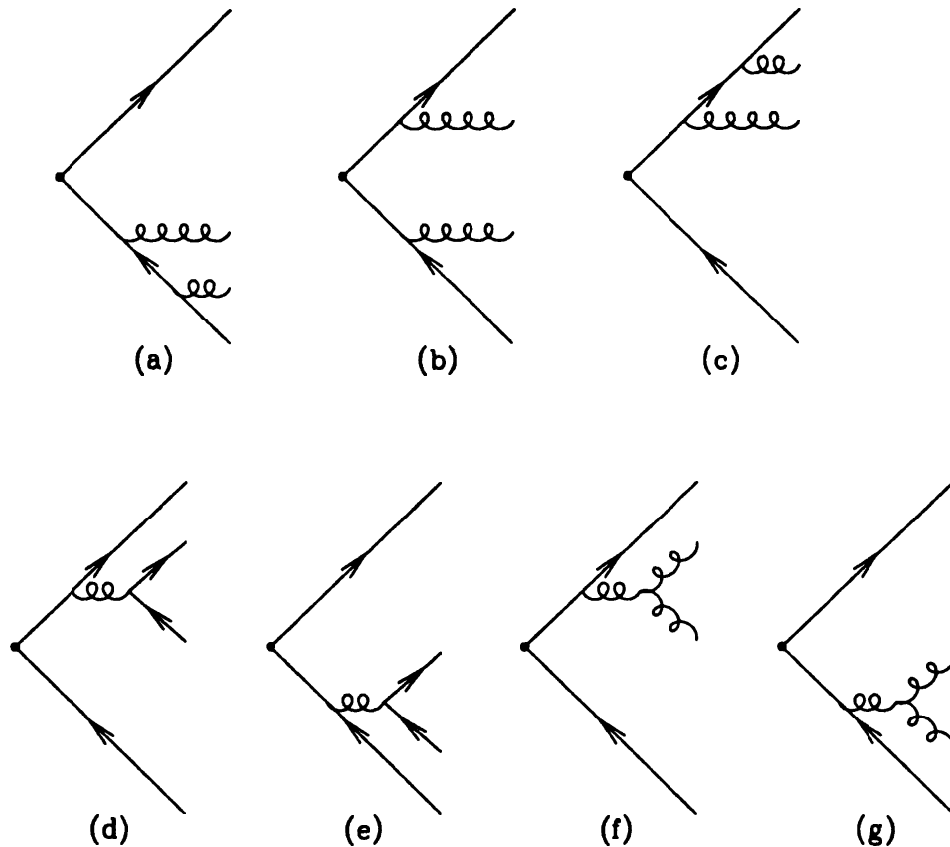


Fig. 3.10. Feynman diagrams for the  $e^+e^- \rightarrow q\bar{q}gg$ ,  $q\bar{q}q\bar{q}$  contributions to four-jet production in  $e^+e^-$  annihilation.

is obtained from the differential cross section given in Eq. (3.11) by including an appropriate  $\delta$ -function expressing the angle  $\chi$  in terms of the energy fractions  $x_i$ . The functions  $A_i(\chi)$  are singular at  $\chi = 0^\circ, 180^\circ$  but well away from these regions the series appears to converge satisfactorily. As for the other shape variables, resummation of large logarithmic contributions can extend the region of applicability into the singular regions.

### 3.5 The triple-gluon vertex

In the previous sections we have seen how cross sections can be defined for an arbitrary number of jets in the final state. We have seen in Fig. 3.7 that events containing as many as five jets have been identified at LEP. The four-jet rate is particularly interesting, since this is the lowest-order cross section in  $e^+e^-$  annihilation which is sensitive to the triple-gluon vertex, see Fig. 3.10.<sup>8</sup>

---

<sup>8</sup> The triple-gluon vertex also plays an important role in large  $p_T$  jet production at hadron colliders, through the  $gg \rightarrow gg$  subprocess, see Chapter 7.

Within the context of jet production in  $e^+e^-$  annihilation, we have seen how the three-jet cross section is consistent with a spin-one gluon. We could, however, imagine an alternative ‘Abelian QCD’ theory, in which  $SU(3)$  is replaced by  $[U(1)]^3$ , and the coupling is adjusted to be  $\tilde{\alpha}_S = C_F \alpha_S$ , so that the correct three-jet rate is obtained.<sup>9</sup> It is then the four-jet rate that allows this to be distinguished from QCD, since only a subset ((a) – (e)) of the Feynman diagrams shown in Fig. 3.10 contribute in the Abelian case.

The matrix elements corresponding to the diagrams in Fig. 3.10 were first calculated in ref. [24]. The general structure is

$$d\sigma^{(4)} = \left(\frac{\alpha_S}{2\pi}\right)^2 [C_F^2 \mathcal{A} + C_F C_A \mathcal{B} + C_F T_R n_f \mathcal{C}] , \quad (3.51)$$

where  $\mathcal{A}$ ,  $\mathcal{B}$  and  $\mathcal{C}$  are functions of the parton-parton invariant masses squared,  $s_{ij} = (p_i + p_j)^2$ . The last term on the right-hand side of Eq. (3.51) corresponds to the  $q\bar{q}q\bar{q}$  final state, and is common to both the Abelian and non-Abelian theories. The first two terms correspond to the  $q\bar{q}gg$  final state: the second term receives contributions from the triple-gluon vertex diagrams and is absent in the Abelian theory.

With the overall couplings already fixed by the three-jet rate, the four-jet rates are therefore different in the two theories, and one could in principle discriminate between them on the basis of overall event rate alone. In particular, the rate is much smaller for the Abelian theory, where the  $q\bar{q}q\bar{q}$  final state is relatively more important than in QCD. The problem with this is that the magnitude of the cross section is quite sensitive to the choice of scale in the strong coupling which appears in Eq. (3.51), and this freedom would allow the overall rates to be adjusted to fit the measured rate in each case. In principle, the fraction of four-quark events would also provide a discrimination. However, as we shall see in Chapter 6, it is very difficult to distinguish light-quark and gluon jets with the necessary efficiency. The only realistic possibility appears to be to tag at least three  $b$  quarks in the final state (using vertex detectors or semi-leptonic decays) to estimate the fraction of  $q\bar{q}q\bar{q}$  events, but the efficiency is again very low.

A much more powerful and illuminating method makes use of the different *correlations* among the final-state particles induced by the various contributions to the cross section. These correlations have their origin in the different angular momentum properties of the final state, and will be discussed in more detail in Chapter 5. Several event shape variables have been proposed for using angular correlations to quantify the differences

---

<sup>9</sup> Such a theory is not, of course, asymptotically free, and is therefore already ruled out by data such as those shown in Fig. 3.6.

between the Abelian and non-Abelian theories [25]. The basic idea is to measure the relative orientation of the planes containing the primary  $q\bar{q}$  jets and the secondary  $gg$  or  $q\bar{q}$  jets. Of course in practice one cannot distinguish primary and secondary jets on an event-by-event basis, but on average the secondary jets are less energetic, in the same way that the gluon in  $q\bar{q}g$  production is the least energetic jet on average.

In practice, the most widely-used variables are the Nachtmann-Reiter angle  $\theta_{NR}$ , defined by

$$\cos \theta_{NR} = \frac{(\mathbf{p}_1 - \mathbf{p}_3) \cdot (\mathbf{p}_2 - \mathbf{p}_4)}{|\mathbf{p}_1 - \mathbf{p}_3| |\mathbf{p}_2 - \mathbf{p}_4|}, \quad (3.52)$$

where the  $\mathbf{p}_i$  are the jet three-momenta, ordered according to energy, and the Bengtsson-Zerwas angle  $\chi_{BZ}$ , defined as the angle between the planes defined by the two lowest and two highest energy jets:

$$\cos \chi_{BZ} = \frac{(\mathbf{p}_1 \times \mathbf{p}_2) \cdot (\mathbf{p}_3 \times \mathbf{p}_4)}{|\mathbf{p}_1||\mathbf{p}_2||\mathbf{p}_3||\mathbf{p}_4|}. \quad (3.53)$$

Fig. 3.11 shows the  $\chi_{BZ}$  distribution measured by the L3 collaboration at LEP [26]. The curves correspond to the Abelian and non-Abelian QCD theories, and the data exhibit a clear preference for the former.

### 3.6 Gluon emission from heavy quarks

The results for jet cross sections and shape variables presented so far have been derived assuming the quarks are massless. In this section we extend some of the previous  $O(\alpha_s)$  results to heavy quarks. For pure vector  $s$ -channel exchange<sup>10</sup>, e.g.  $e^+e^- \rightarrow \gamma^* \rightarrow Q\bar{Q}g$ , the cross section differential in the quark and antiquark energy fractions is, for a quark of mass  $m$ , (cf. Eq. (3.31))

$$\begin{aligned} \frac{1}{\sigma} \frac{d^2\sigma}{dx_1 dx_2} = & \frac{1}{\beta} C_F \frac{\alpha_s}{2\pi} \left[ \frac{2(x_1 + x_2 - 1 - 2\gamma)}{(1-x_1)(1-x_2)} \right. \\ & - 2\gamma \left\{ \frac{1}{(1-x_1)^2} + \frac{1}{(1-x_2)^2} \right\} \\ & \left. + \frac{1}{1+2\gamma} \frac{(1-x_1)^2 + (1-x_2)^2}{(1-x_1)(1-x_2)} \right], \end{aligned} \quad (3.54)$$

where

$$\gamma = \frac{m^2}{s} \leq \frac{1}{4}, \quad \beta = \sqrt{1 - 4\gamma}. \quad (3.55)$$

---

<sup>10</sup> Unlike for massless quarks, the  $e^+e^- \rightarrow Q\bar{Q}g$  matrix element is different for  $s$ -channel vector and axial exchange, see ref. [27] for a full discussion.

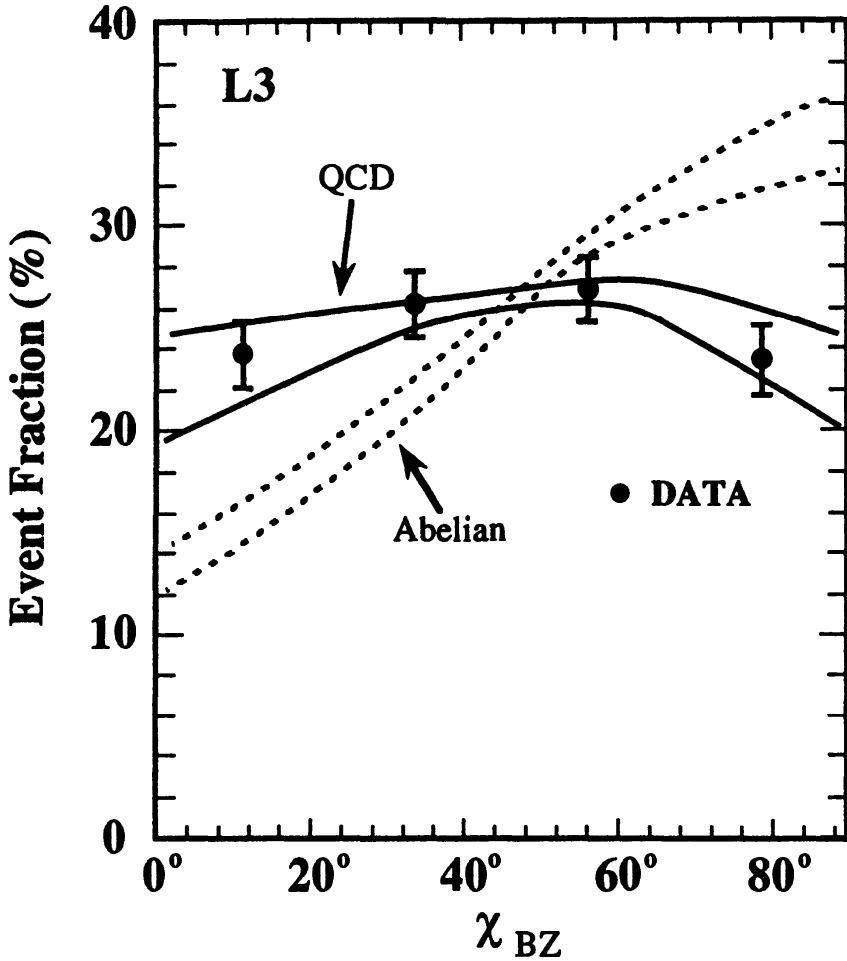


Fig. 3.11. Distribution in the Bengtsson-Zerwas angle at LEP. Figure from ref. [26].

Because the quarks have mass, the phase space available for gluon emission is reduced. As an illustration, the phase space boundary for the case  $\gamma = 1/25$  ( $m = \sqrt{s}/5$ ) is shown in Fig. 3.12. In the limit  $\gamma \rightarrow 0$ , the boundary expands to become the usual massless-quark triangle,  $x_1 = 1$ ,  $x_2 = 1$ ,  $x_1 + x_2 = 1$ , while for  $\gamma \rightarrow 1/4$  — the heavy-quark threshold — the phase space shrinks to a point at  $x_1 = x_2 = 1$ . An important feature of the cross section in Eq. (3.54) is that the collinear divergences are regularized by the non-zero quark mass. From Fig. 3.12, we see that the singularities along the lines  $x_1 = 1$  and  $x_2 = 1$  are outside the phase space region. There is still, however, a single-logarithmic infra-red divergence when the gluon momentum approaches zero, *i.e.* at  $x_1 = x_2 = 1$ . Another interesting feature, not immediately apparent from Eq. (3.54), is that the cross section is suppressed near the phase space boundary, which corresponds to gluons approximately collinear with the heavy quarks. This is called the ‘dead-cone’ effect [28]. It is simply a reflection of the fact that angular momentum conservation suppresses the emission, via a helicity-

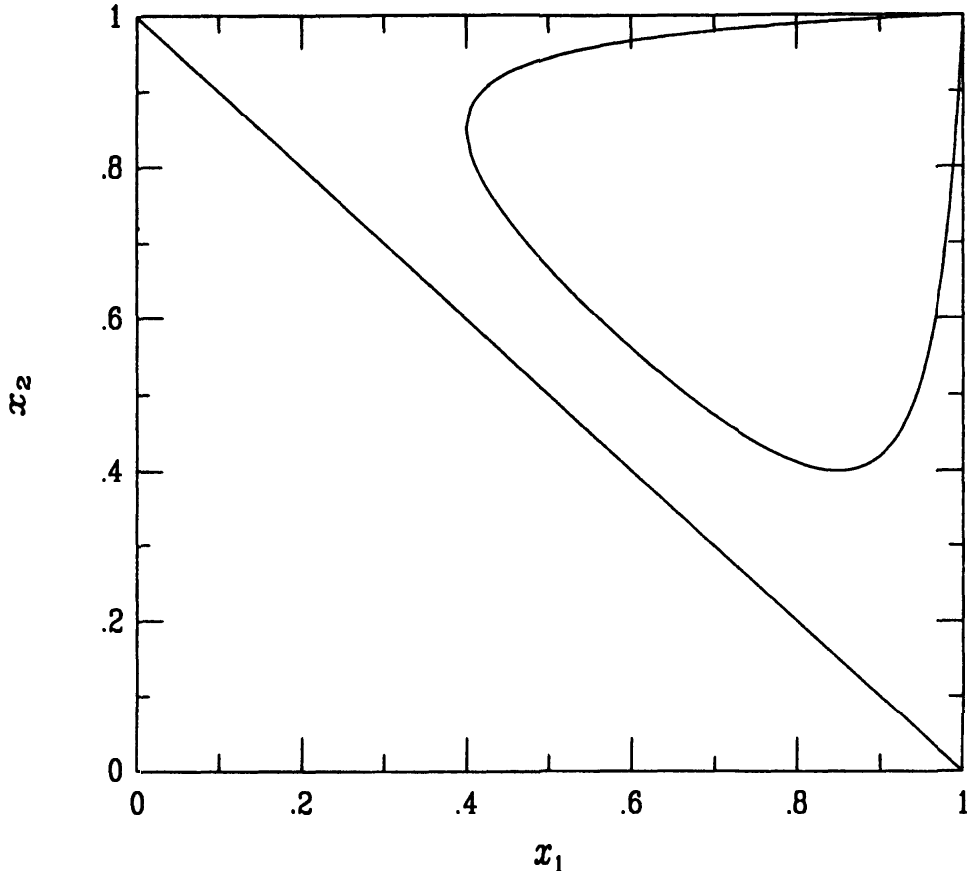


Fig. 3.12. The phase space boundary for  $Q\bar{Q}g$  production in  $e^+e^-$  annihilation. The quark mass is  $m = \sqrt{s}/5$ .

conserving interaction, of a spin-one gluon in the same direction as a spin- $\frac{1}{2}$  quark. In fact for gluons which are soft ( $z = 2 - x_1 - x_2 \ll 1$ ) and close in angle ( $\theta$ ) to the direction of motion of a heavy quark with  $\gamma \ll 1$ , the differential cross section in Eq. (3.54) can be approximated by

$$\frac{1}{\sigma} \frac{d^2\sigma}{dz d\theta^2} \approx C_F \frac{\alpha_s}{\pi} \frac{1}{z} \frac{\theta^2}{(\theta^2 + 4\gamma)^2}. \quad (3.56)$$

This shows that the gluon radiation is suppressed in an angular cone of size  $\theta \sim 2\sqrt{\gamma} = 2m/\sqrt{s}$ . In other words, the heavier the quark, the broader the dead cone.

The above results are derived under the assumption that the heavy quark is *stable*. In practice, heavy quarks like  $c, b, t, \dots$  decay weakly after a finite length of time,  $Q \rightarrow qW^{(*)} \rightarrow q\bar{q}\bar{q}, ql\nu$ , and a complete analysis of gluon radiation associated with such quarks should also take into account the possibility of emitting gluons from the decay products. Further details can be found, for example, in ref. [29].

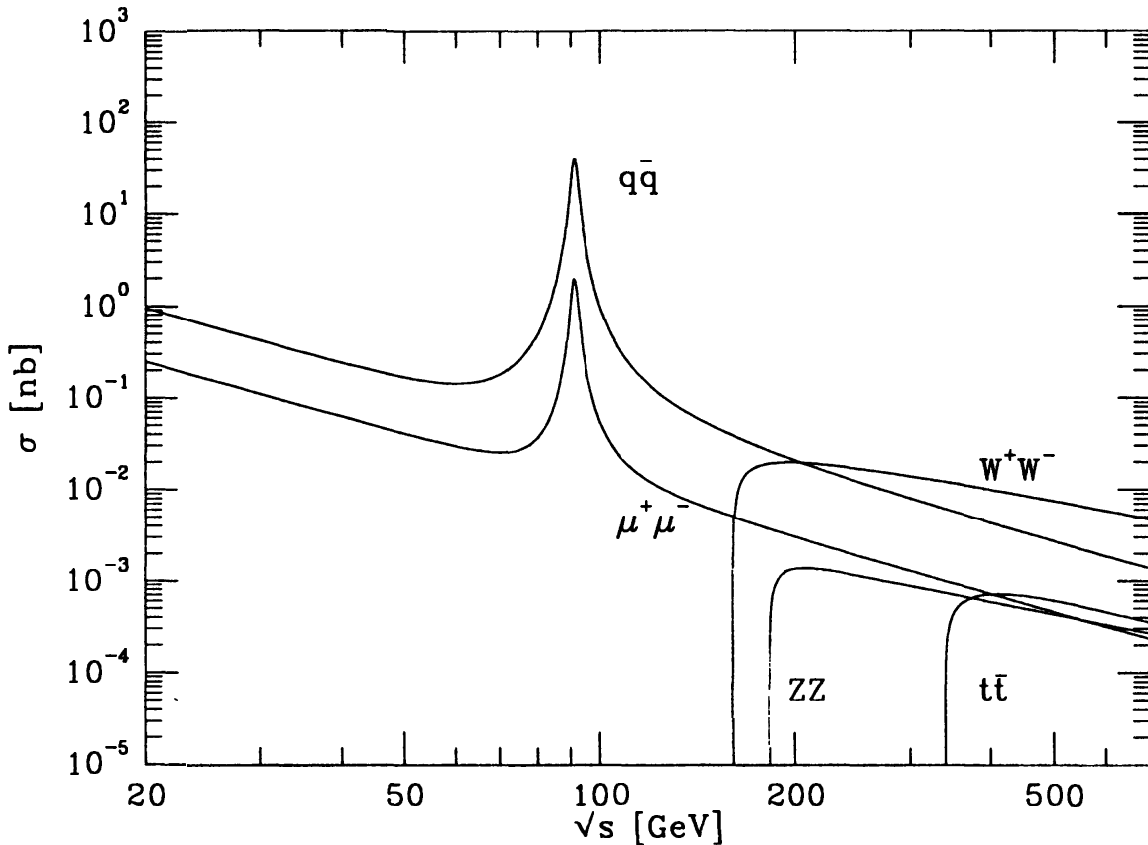


Fig. 3.13. Cross sections in  $e^+e^-$  annihilation.

### 3.7 Summary and outlook

Electron-positron annihilation into hadrons at high energy provides a particularly clean environment in which to test perturbative QCD. At the LEP and SLC colliders, for example, the energy is sufficiently high that for many quantities of interest, the corrections due to hadronization are small. Jet final states then give direct insight into the production and properties of the quarks and gluons. In such a way, the basic  $q\bar{q}g$  and  $ggg$  interactions of the theory have been verified. The precision on measurements of  $\alpha_s(M_Z^2)$  from the total hadronic cross section and from jet cross sections and shape variables is of order 5% (see Chapter 12).

The success of QCD studies at LEP and SLC is due in part to the fact that the peak hadronic cross section is so large, of order 40 nb, as shown in Fig. 3.13. Above the  $Z$  peak, the  $e^+e^-$  annihilation hadronic cross section falls away rapidly, ultimately regaining the  $1/s$  fall-off of lower energies. This means that a future high-energy  $e^+e^-$  collider would find it difficult to match the precision of QCD studies at  $\sqrt{s} = M_Z$ . However, there would be other hadronic production processes with larger cross sections. Examples are the electroweak processes  $e^+e^- \rightarrow W^+W^- \rightarrow$  jets and  $\gamma\gamma \rightarrow$  jets. In fact, at the LEP2 collider ( $\sqrt{s} = 160 - 200$  GeV) the QCD

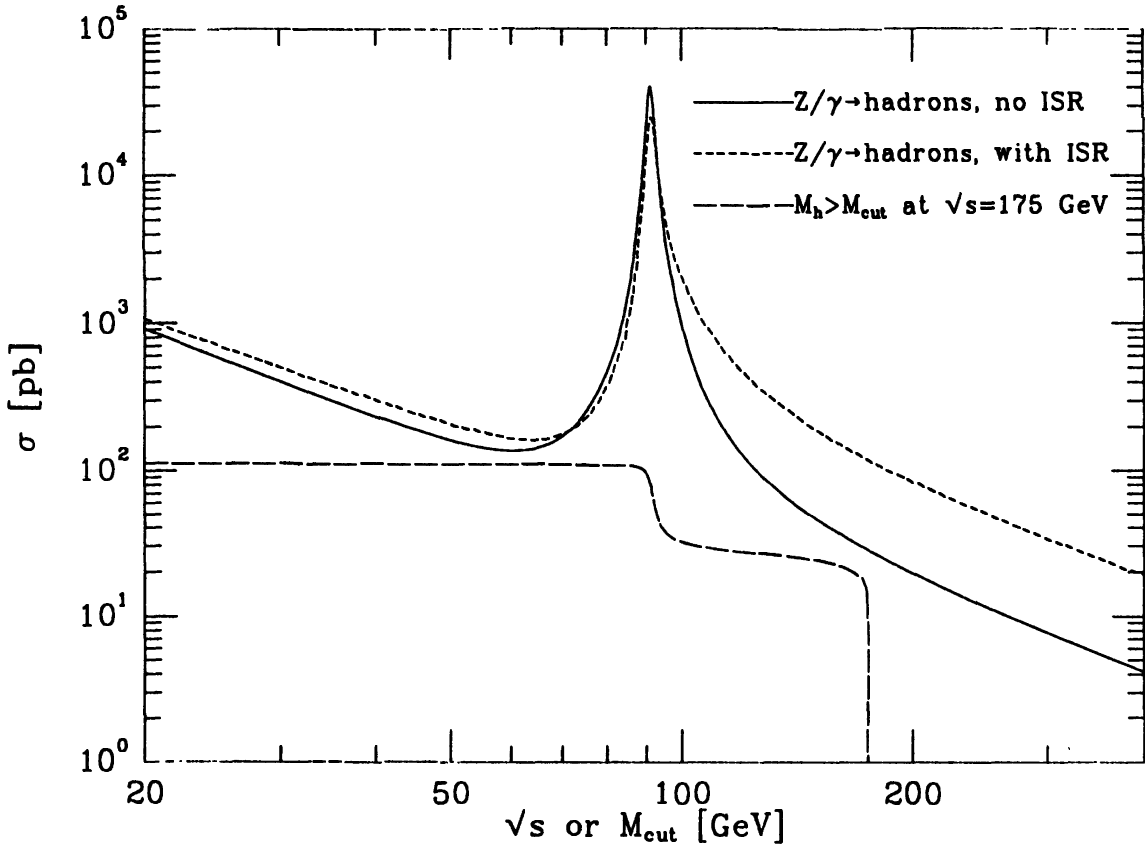


Fig. 3.14. Hadronic cross section with initial-state radiation. Adapted from ref. [31].

annihilation process  $e^+e^- \rightarrow \sum q\bar{q} \rightarrow \text{jets}$  is a non-negligible *background* to the  $W$  mass determination from the  $e^+e^- \rightarrow W^+W^- \rightarrow q\bar{q}q\bar{q}$  final state [30].

Another feature of the annihilation cross section which is relevant to LEP2 physics is the phenomenon known as ‘radiative return to the  $Z$  pole’. By radiating one or more hard collinear photons, the incoming electron and/or positron can lose enough energy that the hadronic invariant mass  $M_h$  is close to the pole of the  $Z$  propagator, *i.e.*  $\sqrt{s} > M_h \sim M_Z$ . The enhancement of the cross section thus obtained more than compensates the additional powers of the electromagnetic coupling, so that  $\sigma(e^+e^- \rightarrow \sum q\bar{q} + n\gamma) > \sigma(e^+e^- \rightarrow \sum q\bar{q})$ . This may be seen by comparing the solid and short-dashed curves in Fig. 3.14.

Even though the radiated photons are usually too close to the beam direction to be detectable, events with hard initial-state radiation are relatively easy to eliminate by means of a lower cut on the hadronic invariant mass  $M_h$ . The long-dashed curve in Fig. 3.14 shows the cross section at fixed  $\sqrt{s} = 175$  GeV, as a function of such a cut,  $M_h > M_{\text{cut}}$ . For  $M_{\text{cut}} = 0$ , the cross section coincides with the value on the dashed curve at  $\sqrt{s} = 175$  GeV. As the cut is increased above the  $Z$  mass, the cross

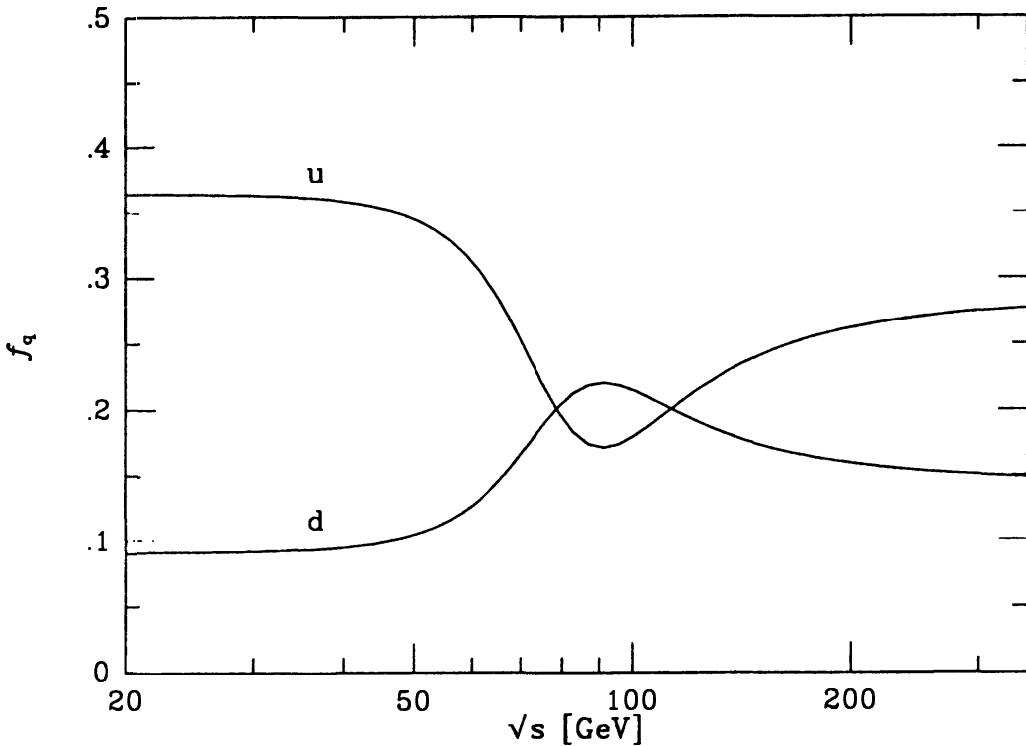


Fig. 3.15.  $u$  and  $d$  quark contributions as a fraction of the total  $e^+e^- \rightarrow \sum q\bar{q}$  cross section, with  $q = u, d, s, c, b$ .

section drops suddenly, as a consequence of the ‘radiative return’ effect discussed above. It then remains fairly constant before falling sharply to zero at  $M_{cut} = \sqrt{s}$ . Thus, in the region  $M_{cut} > M_Z$ , the cross section remains close to the Born value, *i.e.* the value on the solid curve at  $\sqrt{s} = 175$  GeV, provided one allows for at least a few GeV of initial-state radiation.

For two-photon induced hadronic events,  $e^+e^- \rightarrow e^+e^- + \sum q\bar{q}$ , the hadronic invariant mass is strongly peaked at small values, again making them relatively easy to distinguish from annihilation events by means of an invariant mass cut.

A final point concerns the relative proportions of  $u$ - and  $d$ -type quarks in the  $e^+e^- \rightarrow \sum q\bar{q}$  annihilation cross section shown in Fig. 3.13. Because of the differences between the quarks’ electric and weak (neutral current) charges, these proportions change as the energy of the collider increases. Fig. 3.15 shows the  $u$  and  $d$  quark contributions as a fraction of the total light-quark (*i.e.*  $(u, d, s, c, b)$ ) cross section. At low energies ( $\sqrt{s} \ll M_Z$ ) the fractions are essentially determined by the electric charges, and so  $f_u \approx 4/11$ ,  $f_d \approx 1/11$ . As the energy increases, the  $Z$ -exchange contribution becomes more important (see Eq. (3.1)). The maximum value of  $f_d$  occurs at the  $Z$  peak, where  $f_d > f_u$ . Since above the  $b\bar{b}$  threshold  $f_b \approx f_d$ , we see that the  $b$  quark fraction is also maximal at  $\sqrt{s} \simeq M_Z$ . At

very high energies ( $\sqrt{s} \gg M_Z$ ) the  $f_q$  fractions become constant again, with the values given by combinations of the electromagnetic and weak couplings.

## References

- 1) D. Schaile, Proc. XXVII Int. Conf. on High Energy Physics, Glasgow, July 1994, eds. P.J. Bussey and I.G. Knowles, Institute of Physics Publishing, Bristol (1995), Vol. I, p. 27.
- 2) F. Bloch and A. Nordsieck, *Phys. Rev.* **52** (1937) 54.
- 3) T. Kinoshita, *J. Math. Phys.* **3** (1962) 650;  
T.D. Lee and M. Nauenberg, *Phys. Rev.* **133B** (1964) 1549.
- 4) M.A. Samuel and L.R. Surguladze, *Phys. Rev. Lett.* **66** (1991) 560;  
S.G. Gorishny, A.L. Kataev and S.A. Larin, *Phys. Lett.* **B259** (1991) 144.
- 5) P.M. Stevenson, *Phys. Lett.* **B100** (1981) 61; *Phys. Rev.* **D23** (1981) 2916.
- 6) S.J. Brodsky, G.P. Lepage and P.B. MacKenzie, *Phys. Rev.* **D28** (1983) 228.
- 7) A. Djouadi, J.H. Kühn and P.M. Zerwas, *Zeit. Phys.* **C48** (1990) 411.
- 8) J. Schwinger, *Particles, Sources and Fields*, Addison-Wesley, New York (1973);  
J. Jersak, E. Laermann and P.M. Zerwas, *Phys. Rev.* **D25** (1982) 1218;  
L. Reinders, H. Rubenstein and S. Yazaki, *Phys. Rep.* **127** (1985) 1;  
T.H. Chang, K.J.F. Gaemers and W.L. van Neerven, *Nucl. Phys.* **B202** (1982) 407.
- 9) S.G. Gorishny, A.L. Kataev and S.A. Larin, *Nuovo Cimento* **92A** (1986) 117;  
K.G. Chetyrkin, J.H. Kühn and A. Kwiatkowski, *Phys. Lett.* **B282** (1992) 221.
- 10) B.A. Kniehl and J.H. Kühn, *Phys. Lett.* **B224** (1989) 229; *Nucl. Phys.* **B329** (1990) 547.
- 11) G. Sterman and S. Weinberg, *Phys. Rev. Lett.* **39** (1977) 1436.
- 12) JADE collaboration, S. Bethke *et al.*, *Phys. Lett.* **B213** (1988) 235.
- 13) S. Bethke, Z. Kunszt, D.E. Soper and W.J. Stirling, *Nucl. Phys.* **B370** (1992) 310.
- 14) G. Kramer and B. Lampe, *Fortschr. Phys.* **37** (1989) 161.
- 15) OPAL collaboration, M.Z. Akrawy *et al.*, *Phys. Lett.* **B235** (1990) 389.
- 16) N. Brown and W.J. Stirling, *Phys. Lett.* **B252** (1990) 657.
- 17) S. Catani, Yu.L. Dokshitzer, M. Olsson, G. Turnock and B.R. Webber, *Phys. Lett.* **B269** (1991) 432.
- 18) S. Brandt, Ch. Peyrou, R. Sosnowski and A. Wroblewski, *Phys. Lett.* **12** (1964) 57;  
E. Farhi, *Phys. Rev. Lett.* **39** (1977) 1587.
- 19) H. Georgi and M. Machacek, *Phys. Rev. Lett.* **39** (1977) 1237.
- 20) R.K. Ellis, D.A. Ross and A.E. Terrano, *Nucl. Phys.* **B178** (1981) 421.
- 21) Z. Kunszt *et al.*, *Z Physics at LEP1*, CERN Report 89-08 (1989), Vol. 1, p. 373.
- 22) DELPHI collaboration, P. Abreu *et al.*, *Zeit. Phys.* **C54** (1992) 55.
- 23) C.L. Basham, L.S. Brown, S.D. Ellis and S.T. Love, *Phys. Rev. Lett.* **41** (1978) 1585.
- 24) A. Ali, J.G. Körner, G. Kramer, Z. Kunszt, E. Pietarinen, G. Schierholz and J. Willrodt, *Phys. Lett.* **B82** (1979) 285; *Nucl. Phys.* **B167** (1980) 454.
- 25) J.G. Körner, G. Schierholz and J. Willrodt, *Nucl. Phys.* **B185** (1981) 365;  
O. Nachtmann and A. Reiter, *Zeit. Phys.* **C14** (1982) 47; *ibid.* **C16** (1982) 45;  
M. Bengtsson and P.M. Zerwas, *Phys. Lett.* **B208** (1988) 306;  
M. Bengtsson, *Zeit. Phys.* **C42** (1989) 75.
- 26) L3 collaboration, B. Adeva *et al.*, *Phys. Lett.* **B248** (1990) 227.
- 27) Yu.L. Dokshitzer, V.A Khoze and W.J. Stirling, *Nucl. Phys.* **B428** (1994) 3.

- 28) Yu.L. Dokshitzer, V.A. Khoze, and S.I. Troyan, *Proc. 6th Int. Conf. on Physics in Collision*, ed. M. Derrick, World Scientific (1987), p. 417.
- 29) G. Jikia, *Phys. Lett.* **B257** (1991) 196;  
V.A. Khoze, L.H. Orr and W.J. Stirling, *Nucl. Phys.* **B378** (1992) 413.
- 30) Report of the  $W$  Mass Working Group, in *Physics at LEP2*, eds. G. Altarelli, T. Sjöstrand and F. Zwirner, CERN Report 96-01 (1996).
- 31) P. Nason, in *Physics at LEP2*, eds. G. Altarelli, T. Sjöstrand and F. Zwirner, CERN Report 96-01 (1996).

# 4

## Deep inelastic scattering

The original, and still the most powerful, test of perturbative QCD is the breaking of Bjorken scaling in deep inelastic lepton-hadron scattering (DIS). Nowadays, deep inelastic structure function analyses not only provide some of the most precise tests of the theory but also determine the momentum distributions of partons in hadrons, for use as input in predicting cross sections in high-energy hadron collisions. In this chapter we begin by discussing deep inelastic scattering and the ‘naive’ parton model. We then show how QCD modifies the simple Bjorken scaling property of the parton model, and discuss how these scaling violations can be calculated in perturbation theory. We compare the theoretical predictions with experimental data, and consider the behaviour of the parton distributions in various kinematic limits.

### 4.1 Deep inelastic scattering and the parton model

We begin with an overview of how deep inelastic lepton-hadron scattering has a natural interpretation in terms of the parton picture of quarks and gluons in hadrons. In this section our derivation of the parton model will be rather heuristic. In the following section we will present a more rigorous derivation.

Consider the scattering of a high-energy charged lepton off a hadron target. If we label the incoming and outgoing lepton four-momenta by  $k^\mu$  and  $k'^\mu$  respectively, the momentum of the target hadron (assumed hereafter to be a proton) by  $p^\mu$  and the momentum transfer by  $q^\mu = k^\mu - k'^\mu$ , then the standard deep inelastic variables are defined by:

$$Q^2 = -q^2$$

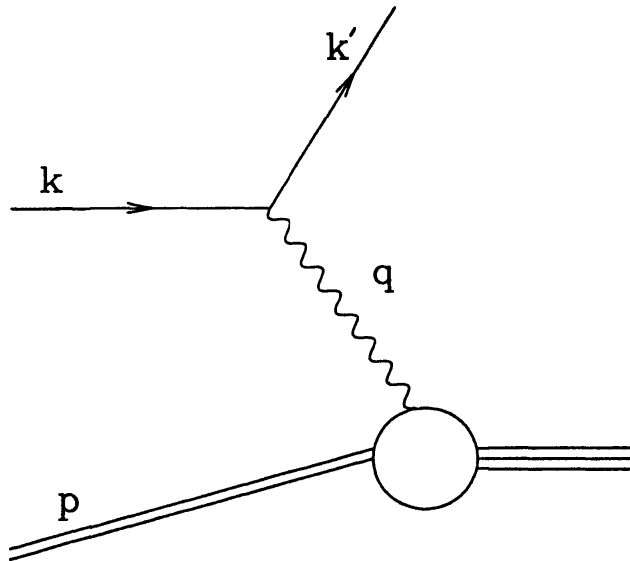


Fig. 4.1. Deep inelastic charged lepton-proton scattering.

$$\begin{aligned}
 M^2 &= p^2 \\
 \nu &= p \cdot q = M(E' - E) \\
 x &= \frac{Q^2}{2\nu} = \frac{Q^2}{2M(E - E')} \\
 y &= \frac{q \cdot p}{k \cdot p} = 1 - E'/E,
 \end{aligned} \tag{4.1}$$

where the energy variables refer to the target rest frame and  $M$  is the proton mass. If the lepton is an electron or muon, then the scattering is mediated by the exchange of a virtual photon, Fig. 4.1.

*Structure functions*  $F_i(x, Q^2)$  — which parametrize the structure of the target as ‘seen’ by the virtual photon — are defined in terms of the lepton scattering cross sections. For charged lepton scattering,  $lp \rightarrow lX$ ,<sup>1</sup>

$$\begin{aligned}
 \frac{d^2\sigma^{em}}{dxdy} &= \frac{8\pi\alpha^2 ME}{Q^4} \left[ \left( \frac{1 + (1 - y)^2}{2} \right) 2xF_1^{em} \right. \\
 &\quad \left. + (1 - y)(F_2^{em} - 2xF_1^{em}) - (M/2E)xyF_2^{em} \right], \tag{4.2}
 \end{aligned}$$

and for neutrino (antineutrino) scattering,  $\nu p \rightarrow lX$ ,

$$\begin{aligned}
 \frac{d^2\sigma^{\nu(\bar{\nu})}}{dxdy} &= \frac{G_F^2 ME}{\pi} \left[ (1 - y - \frac{M}{2E}xy)F_2^{\nu(\bar{\nu})} \right. \\
 &\quad \left. + y^2xF_1^{\nu(\bar{\nu})} + (-) y(1 - \frac{1}{2}y)xF_3^{\nu(\bar{\nu})} \right]. \tag{4.3}
 \end{aligned}$$

<sup>1</sup> This expression is strictly valid only for  $Q^2 \ll M_Z^2$ , see below.

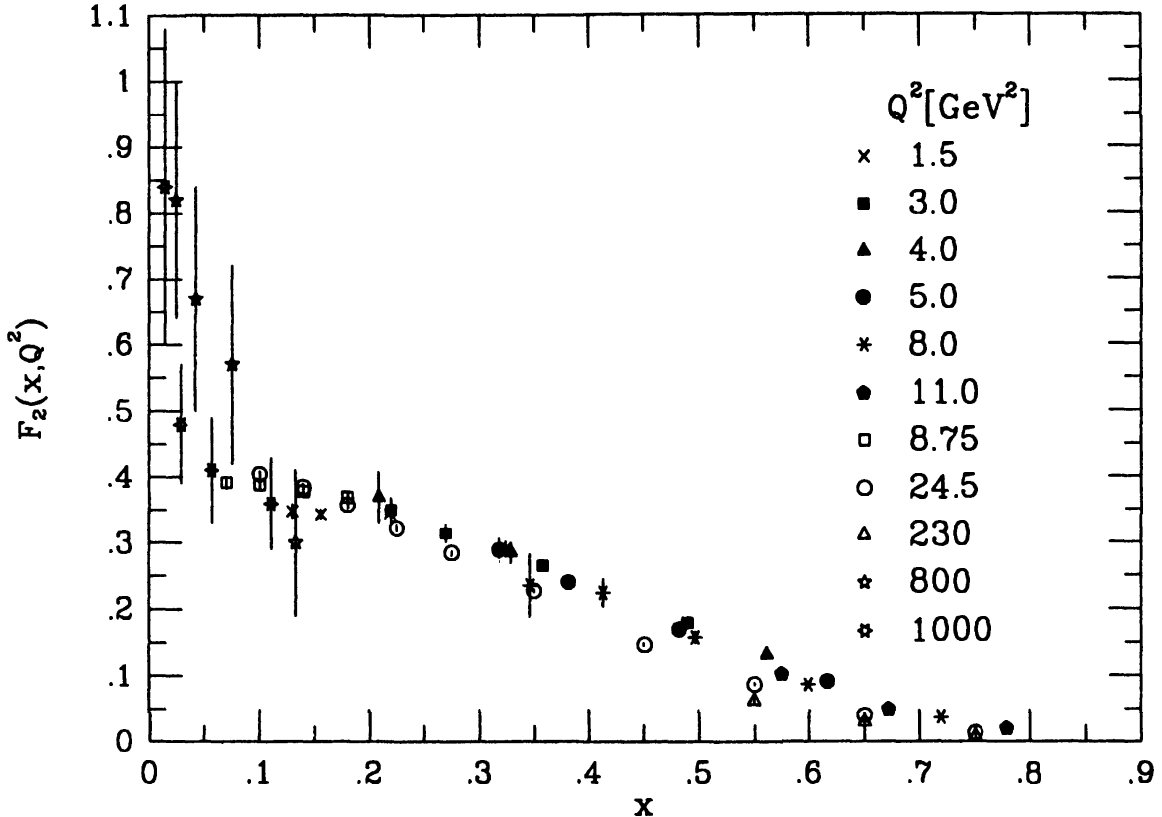


Fig. 4.2. The  $F_2$  structure function from the SLAC-MIT, BCDMS, H1 and ZEUS collaborations.

We will explain the structure of these equations in the next section. The *Bjorken limit* is defined as  $Q^2, \nu \rightarrow \infty$  with  $x$  fixed. In this limit the structure functions are observed to obey an approximate *scaling* law [1,2], i.e. they depend only on the dimensionless variable  $x$ :

$$F_i(x, Q^2) \longrightarrow F_i(x) . \quad (4.4)$$

This is illustrated in Fig. 4.2, where data on the electromagnetic structure function  $F_2$ , measured with a proton target, are displayed. The data span two decades of experiments, from the original SLAC-MIT measurements [3] to the high precision fixed-target measurements from the BCDMS collaboration [4] and the recent high-energy electron-proton collider measurements from the H1 [5] and ZEUS [6] experiments at HERA. Only a representative sample of data points is shown. Note that even though the  $Q^2$  values vary by three orders of magnitude, to a good approximation the data lie on a universal curve.

Bjorken scaling implies that the virtual photon scatters off *pointlike constituents*, since otherwise the dimensionless structure functions would depend on the ratio  $Q/Q_0$ , with  $1/Q_0$  some length scale characterizing the size of the constituents. The parton model picture of deep inelastic scattering is most easily formulated in the ‘infinite momentum frame’ in

which the proton is moving very fast,  $p^\mu \approx (P, 0, 0, P)$  with  $P \gg M$ . In this frame, we can consider a simple model where the photon scatters off a pointlike quark constituent which is moving parallel with the proton and carrying a fraction  $\xi$  of its momentum, i.e.  $p_q^\mu = \xi p^\mu$ . Neglecting the proton mass  $M$ , we can rewrite Eq. (4.2) as

$$\frac{d^2\sigma}{dxdQ^2} = \frac{4\pi\alpha^2}{Q^4} \left[ [1 + (1 - y)^2]F_1 + \frac{(1 - y)}{x}(F_2 - 2xF_1) \right]. \quad (4.5)$$

Now the spin-averaged matrix element squared for massless  $e^- q \rightarrow e^- q$  scattering can be obtained from the corresponding matrix element for  $e^+ e^- \rightarrow q\bar{q}$  considered in Chapter 3. The two amplitudes are related by crossing symmetry, which requires that the amplitude for a process with a particle of momentum  $k$  in the initial state is equal to the amplitude for the process with an antiparticle of momentum  $-k$  in the final state. Thus the amplitudes for the two processes

$$e^-(k) + q(p_q) \rightarrow e^-(k') + q(p'_q) \quad (4.6)$$

$$e^+(-k') + e^-(k) \rightarrow \bar{q}(-p_q) + q(p'_q) \quad (4.7)$$

are equal. In terms of the usual Mandelstam variables  $\hat{s} = (k + p_q)^2$ ,  $\hat{t} = (k - k')^2$  and  $\hat{u} = (p_q - k')^2$ , the matrix element squared for amplitude (4.6) is

$$\overline{\sum} |\mathcal{M}|^2 = 2e_q^2 e^4 \frac{\hat{s}^2 + \hat{u}^2}{\hat{t}^2}. \quad (4.8)$$

The notation  $\overline{\sum}$  denotes the average (sum) over initial (final) colours and spins. Using Eq. (4.1) we can substitute for the deep inelastic variables:  $\hat{t} = -Q^2$ ,  $\hat{u} = \hat{s}(y - 1)$  and  $\hat{s} = \xi Q^2 / xy$ . Using the standard result for the cross section for massless  $2 \rightarrow 2$  scattering,

$$\frac{d\hat{\sigma}}{d\hat{t}} = \frac{1}{16\pi\hat{s}^2} \overline{\sum} |\mathcal{M}|^2, \quad (4.9)$$

and substituting for the kinematic variables in the matrix element squared, gives

$$\frac{d\hat{\sigma}}{dQ^2} = \frac{2\pi\alpha^2 e_q^2}{Q^4} [1 + (1 - y)^2]. \quad (4.10)$$

The mass-shell constraint for the outgoing quark,

$$p_q'^2 = (p_q + q)^2 = q^2 + 2p_q \cdot q = -2p \cdot q(x - \xi) = 0, \quad (4.11)$$

implies  $x = \xi$ . By writing  $\int_0^1 dx \delta(x - \xi) = 1$ , we obtain the double differential cross section for the quark scattering process:

$$\frac{d^2\hat{\sigma}}{dxdQ^2} = \frac{4\pi\alpha^2}{Q^4} [1 + (1 - y)^2] \frac{1}{2} e_q^2 \delta(x - \xi). \quad (4.12)$$

By comparing Eqs. (4.5) and (4.12) we see that the structure functions in this simple model are:

$$\hat{F}_2 = xe_q^2 \delta(x - \xi) = 2x\hat{F}_1. \quad (4.13)$$

This result suggests that the structure function  $F_2(x)$  ‘probes’ a quark constituent with momentum fraction  $\xi = x$ . From Fig. 4.2, the measured structure function is evidently a *distribution* in  $x$  rather than a delta function, which indicates that the quark constituents carry a range of momentum fractions.

The above ideas are incorporated in what is now known as the ‘naive parton model’ [2]:

- $q(\xi)d\xi$  represents the probability that a quark  $q$  carries momentum fraction between  $\xi$  and  $\xi + d\xi$ , where  $0 \leq \xi \leq 1$ ,
- the virtual photon scatters incoherently off the quark constituents.

Thus the proton structure functions are obtained by weighting the quark structure functions with the probability distribution  $q(\xi)$ ,

$$\begin{aligned} F_2(x) = 2xF_1(x) &= \sum_{q,\bar{q}} \int_0^1 d\xi q(\xi) xe_q^2 \delta(x - \xi) \\ &= \sum_{q,\bar{q}} e_q^2 xq(x). \end{aligned} \quad (4.14)$$

In particular, for the scattering of a charged lepton off a proton target by virtual photon exchange,  $lp \rightarrow lX$ , with four quark flavours,

$$\begin{aligned} F_2^{em}(x) &= x \left[ \frac{4}{9} (u(x) + \bar{u}(x) + c(x) + \bar{c}(x)) \right. \\ &\quad \left. + \frac{1}{9} (d(x) + \bar{d}(x) + s(x) + \bar{s}(x)) \right]. \end{aligned} \quad (4.15)$$

For neutrino scattering,  $\nu p \rightarrow lX$ , the virtual  $W^+$  probe measures the quark distributions weighted by the corresponding *weak charge*:

$$F_2^\nu(x) = 2x [d(x) + s(x) + \bar{u}(x) + \bar{c}(x)]. \quad (4.16)$$

A list of the most commonly encountered parton-model deep inelastic structure functions for scattering off an unpolarized proton target is given below:

$$\begin{aligned} F_2^\nu &= 2x[d + s + \bar{u} + \bar{c}] \\ xF_3^\nu &= 2x[d + s - \bar{u} - \bar{c}] \\ F_2^\nu &= 2x[u + c + \bar{d} + \bar{s}] \\ xF_3^\nu &= 2x[u + c - \bar{d} - \bar{s}] \\ F_2^{em} &= x \left[ \frac{4}{9}(u + \bar{u} + c + \bar{c}) + \frac{1}{9}(d + \bar{d} + s + \bar{s}) \right] \end{aligned}$$

$$2xF_1 = F_2. \quad (4.17)$$

This last result (the *Callan-Gross relation*) is a direct consequence of the spin- $\frac{1}{2}$  property of the quarks. To understand this, we note that the two terms in the square brackets on the right-hand side of Eq. (4.5) correspond to the absorption of transversely ( $F_1$ ) and longitudinally ( $F_2 - 2xF_1$ ) polarized virtual photons. In fact the combination

$$F_L(x, Q^2) = \left(1 + \frac{4M^2x^2}{Q^2}\right) F_2(x, Q^2) - 2xF_1(x, Q^2) \xrightarrow{Q^2 \rightarrow \infty} F_2 - 2xF_1, \quad (4.18)$$

called the *longitudinal structure function*, is sometimes used instead of  $F_1$  or  $F_2$ . The Callan-Gross relation follows from the fact that a spin- $\frac{1}{2}$  quark cannot absorb a longitudinally polarized vector boson. In contrast, spin-0 (scalar) quarks cannot absorb transversely polarized vector bosons and so would have  $F_1 = 0$ , i.e.  $F_L = F_2$ , in the Bjorken limit. Structure function measurements show that  $F_L \ll F_2$ , confirming the spin- $\frac{1}{2}$  property of quarks. Note that in the QCD-improved parton model  $F_L$  is only non-zero at leading order in perturbation theory, i.e.  $F_L = O(\alpha_s)$ , see Section 4.3.1.

At very high energies, in particular for  $Q^2 \sim M_Z^2$ , the contribution to  $ep \rightarrow eX$  scattering from  $Z$  exchange cannot be ignored. The calculation of the  $Z$ -exchange and the  $Z - \gamma$  interference contributions proceeds in a similar way to the corresponding calculation of high-energy  $e^+e^-$  annihilation discussed in Chapter 3. The generalization of Eq. (4.5) which incorporates the complete *neutral current* ( $\gamma$  and  $Z$ ) exchange for  $e^-p \rightarrow e^-X$  scattering is

$$\frac{d^2\sigma_{NC}}{dx dQ^2} = \frac{4\pi\alpha^2}{xQ^4} [xy^2 F_1^{NC} + (1-y)F_2^{NC} + y(1-\frac{1}{2}y)F_3^{NC}(x, Q^2)], \quad (4.19)$$

where

$$\begin{aligned} F_2^{NC}(x) &= 2xF_1^{NC}(x) = \sum_q x[q(x) + \bar{q}(x)] C_q(Q^2) \\ xF_3^{NC}(x) &= \sum_q x[q(x) - \bar{q}(x)] D_q(Q^2), \end{aligned} \quad (4.20)$$

with

$$\begin{aligned} C_q(Q^2) &= e_q^2 - 2e_q V_e V_q P_Z + (V_e^2 + A_e^2)(V_q^2 + A_q^2)P_Z^2 \\ D_q(Q^2) &= -2e_q A_e A_q P_Z + 4V_e A_e V_q A_q P_Z^2 \\ P_Z &= \frac{Q^2}{Q^2 + M_Z^2}. \end{aligned} \quad (4.21)$$

Note the appearance of an additional parity-violating structure function  $F_3$ . The vector and axial couplings of the fermions to the  $Z$  boson are

defined in Chapter 8, Table 8.3. The *charged-current* ( $W$ -exchange) contribution,  $e^- p \rightarrow \nu_e X$  also becomes significant at high  $Q^2$ . The corresponding parton-distribution decomposition of the cross section is

$$\frac{d^2\sigma_{CC}}{dx dQ^2} = \frac{(1 - \lambda_e)\pi\alpha^2}{8\sin^4\theta_W(Q^2 + M_W^2)^2} \times \sum_{i,j} [|V_{u,d_i}|^2 u_i(x) + (1 - y)^2 |V_{u,d_i}|^2 d_i(x)] , \quad (4.22)$$

where  $\lambda_e$  is the helicity of the electron,  $u_i$  and  $d_i$  refer to up- and down-type quarks respectively, and the  $V_{u,d_i}$  are the elements of the CKM matrix, which describes the couplings of the quarks to the charged weak current (see Chapter 8).

The above relations can in principle be inverted to give the individual quark distribution functions in terms of the measured structure functions. From such an analysis, the following picture emerges. The proton consists of three *valence* quarks ( $uud$ ) which carry its electric charge and baryon quantum numbers, and an infinite *sea* of light  $q\bar{q}$  pairs. When probed at momentum scale  $Q$ , the sea contains all quark flavours with mass  $m_q \ll Q$ . Thus at a scale of  $O(1 \text{ GeV})$ , and assuming the sea to be symmetric in the quark flavours, we would have

$$\begin{aligned} u(x) &= u_V(x) + S(x) \\ d(x) &= d_V(x) + S(x) \\ S(x) &= \bar{u}(x) = \bar{d}(x) = s(x) = \bar{s}(x) , \end{aligned} \quad (4.23)$$

with the sum rules

$$\begin{aligned} \int_0^1 dx u_V(x) &= 2 , & \int_0^1 dx d_V(x) &= 1 , \\ \sum_q \int_0^1 dx x [q(x) + \bar{q}(x)] &= \int_0^1 dx x [u_V(x) + d_V(x) + 6S(x)] \approx 0.5 . \end{aligned} \quad (4.24)$$

The last of these is an experimental result. It indicates that the quarks only carry about 50% of the proton's momentum. The rest is attributed to *gluon* constituents. Although the electroweak-neutral gluons are not directly measured in deep inelastic lepton hadron scattering, their presence is evident in other high-energy processes such as large transverse momentum jet, prompt photon and heavy quark production (see Chapters 7 and 10). Fig. 4.3 shows a typical set of quark and gluon distributions [7] extracted from fits to deep inelastic data, when probed at a momentum scale  $\mu^2 = 10 \text{ GeV}^2$ . Notice the differences compared to the naive expectations of Eq. (4.23). The sea is *not* SU(3) flavour symmetric, rather the strange quark distribution is roughly a factor of two smaller than the average of

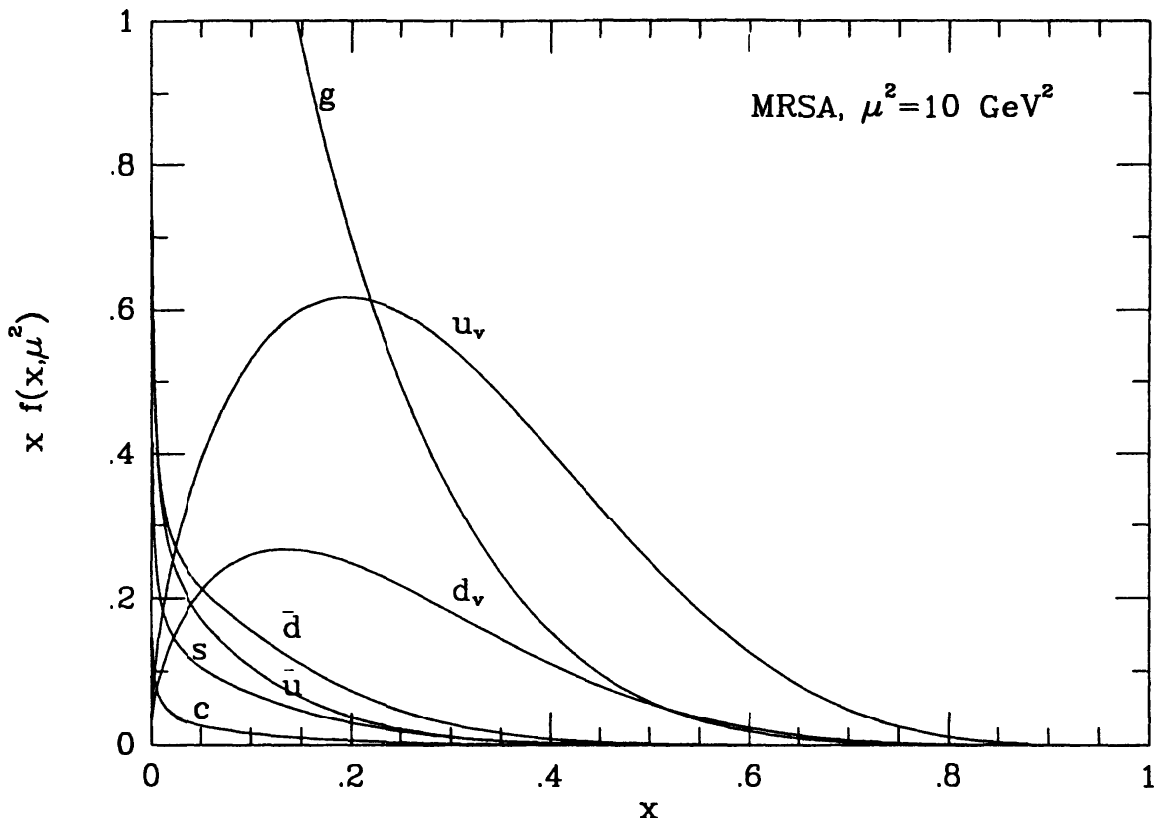


Fig. 4.3. Quark and gluon distribution functions at  $\mu^2 = 10 \text{ GeV}^2$ , from ref. [7].

the light quark distributions, and there is an asymmetry between the  $\bar{u}$  and  $\bar{d}$  quarks in the sea. Neither of these features is quantitatively understood at present. Notice also that at this scale a small charm quark component is observed, consistent with the expectation that the virtual photon should be able to resolve  $c\bar{c}$  pairs in the quark sea when  $Q^2 \gtrsim m_c^2$ .

Closer examination of Fig. 4.2 reveals a systematic deviation from exact Bjorken scaling: the structure function decreases with increasing  $Q^2$  at large  $x$  and has the opposite behaviour at small  $x$ . In Section 4.3 we will show that these scaling violations arise naturally in perturbative QCD. First, however, we give a more rigorous formulation of the parton model.

## 4.2 The parton model from field theory

The ‘naive’ parton model introduced in the previous section existed before the invention of QCD. It has a special status as a model because much of the motivation comes from field theory, with additional assumptions added from the phenomenology of hadronic interactions.

The basic assumption of the naive parton model is that the interactions of hadrons are due to the interactions of partons; in certain types of reactions the structure of the hadrons may be described by an instantaneous

distribution of partons. A necessary condition for such a picture to make sense is that changes in the number and momenta of the partons should be negligible during the time which they are probed. An analogy with diffraction studies of a crystal may be useful. An X-ray diffracted by a crystal reveals its detailed structure, because the atoms in the crystal lattice can be considered to be at rest during the transit time of the X-ray across the crystal. In hadronic systems we ensure that the transit time across the target is less than the timescale of internal motion by moving to an infinite momentum frame.

Although the simplest description makes use of the infinite momentum frame, the model can be formulated covariantly. To see how this is achieved, we return to the basic deep inelastic scattering diagram, Fig. 4.1. The amplitude for this process is<sup>2</sup>

$$\mathcal{A} = e\bar{u}(k')\gamma^\alpha u(k) \frac{1}{q^2} \langle X | j_\alpha(0) | P \rangle , \quad (4.25)$$

where  $j_\alpha$  is the electromagnetic current. The key point is that the cross section, which is proportional to the amplitude squared, can be factored into a leptonic and a hadronic piece,

$$\frac{d^2\sigma}{dx dy} \propto L_{\alpha\beta} W^{\alpha\beta} . \quad (4.26)$$

The structure of the leptonic tensor, assuming photon exchange only, is completely determined by QED:

$$L_{\alpha\beta} = e^2 \text{Tr}[\not{k}' \gamma_\alpha \not{k}' \gamma_\beta] = 4e^2 \left( k_\alpha k'_\beta + k_\beta k'_\alpha - g_{\alpha\beta} k \cdot k' \right) . \quad (4.27)$$

In contrast, the hadronic tensor contains all the information about the interaction of the electromagnetic current  $j_\alpha$  with the target proton  $P$ :

$$\begin{aligned} W_{\alpha\beta}(p, q) &= \frac{1}{4\pi} \sum_X \langle P | j_\beta^\dagger(0) | X \rangle \langle X | j_\alpha(0) | P \rangle (2\pi)^4 \delta^4(q + p - p_X) \\ &= \frac{1}{4\pi} \int d^4 z e^{iq \cdot z} \langle P | j_\beta^\dagger(z) j_\alpha(0) | P \rangle \\ &= \frac{1}{4\pi} \int d^4 z e^{iq \cdot z} \langle P | [j_\beta^\dagger(z), j_\alpha(0)] | P \rangle . \end{aligned} \quad (4.28)$$

In deriving this result we have used the completeness of the final states  $X$  and introduced an integral representation for the four-dimensional delta function. Energy-momentum conservation implies that the second term in the current commutator gives no contribution. Because the electro-

---

<sup>2</sup> In what follows we omit spin labels and sums.

magnetic current is conserved,  $q \cdot W = 0$ , we may write

$$W^{\alpha\beta}(p, q) = \left(g^{\alpha\beta} - \frac{q^\alpha q^\beta}{q^2}\right) W_1(x, Q^2) + \left(p^\alpha + \frac{1}{2x} q^\alpha\right) \left(p^\beta + \frac{1}{2x} q^\beta\right) W_2(x, Q^2) \quad (4.29)$$

where the information about the structure of the hadron as ‘seen’ by the virtual photon is contained in the two functions  $W_1$  and  $W_2$ . The scattering cross section is then obtained by multiplying the leptonic and hadronic tensors and substituting into the right-hand side of Eq. (4.26). Comparing the resulting expression with that given in Eq. (4.2) allows us to relate the functions  $W_i$  to the electromagnetic structure functions defined in the previous section,

$$\begin{aligned} F_1(x, Q^2) &= W_1(x, Q^2) \\ F_2(x, Q^2) &= \nu W_2(x, Q^2). \end{aligned} \quad (4.30)$$

To analyse the hadronic tensor  $W$  it is convenient to introduce two light-like vectors  $p$  and  $n$ , with  $n \cdot p = 1$  so that  $n$  has the dimensions of an inverse mass. Any four-vector can then be written in terms of  $p$ ,  $n$  and a spacelike two-dimensional transverse vector:

$$k^\mu = ap^\mu + bn^\mu + k_T^\mu, \quad (4.31)$$

where

$$p^2 = n^2 = n \cdot k_T = p \cdot k_T = 0. \quad (4.32)$$

In particular, we can identify  $p$  with the four-momentum of the target in the approximation in which we ignore its mass. The kinematic four-vectors for deep inelastic scattering can then be written as

$$\begin{aligned} P^\mu &= p^\mu + \frac{M^2}{2} n^\mu \\ q^\mu &= \nu n^\mu + q_T^\mu, \end{aligned} \quad (4.33)$$

where  $q_T^2 = -q^2 = Q^2$ . In the frame in which the struck proton is moving very fast along the positive  $z$ -axis, an explicit representation for the vectors  $p$  and  $n$  is<sup>3</sup>

$$\begin{aligned} p^\mu &= (P, 0, 0, P) \\ n^\mu &= \left(\frac{1}{2P}, 0, 0, -\frac{1}{2P}\right). \end{aligned} \quad (4.34)$$

For simplicity, in what follows we will ignore the mass  $M$  so that  $p^\mu \equiv P^\mu$ . Using the representation Eq. (4.33) the functions  $W_{1,2}$  can be projected

---

<sup>3</sup> Our notation for four-vectors is  $(E, p_x, p_y, p_z)$ .

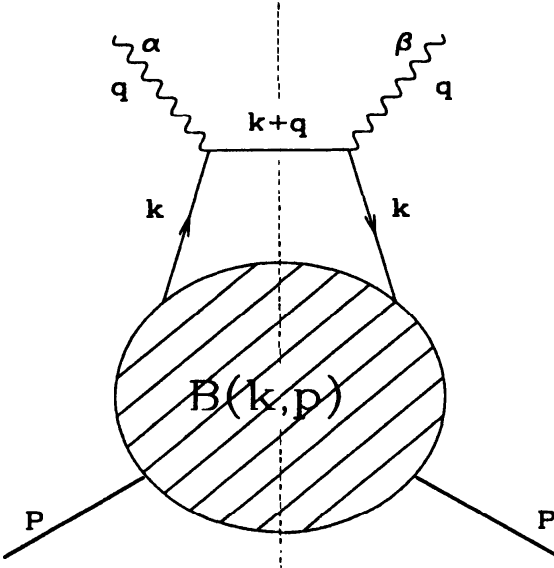


Fig. 4.4. Handbag diagram.

out of the hadronic tensor by

$$\begin{aligned} \nu n^\alpha n^\beta W_{\alpha\beta} &= \nu W_2 = F_2 , \\ \frac{4x^2}{\nu} p^\alpha p^\beta W_{\alpha\beta} &= \nu W_2 - 2x W_1 = F_L = F_2 - 2x F_1 . \end{aligned} \quad (4.35)$$

We next make the important assumption<sup>4</sup> that the photon scatters incoherently off the individual partons. The hadronic tensor  $W$  is then obtained from the simple ‘handbag’ diagram shown in Fig. 4.4:

$$W^{\alpha\beta}(p, q) = e_q^2 \int \frac{d^4 k}{(2\pi)^4} [\gamma^\alpha (k + q) \gamma^\beta]_{ij} [B(k, p)]_{ji} \delta((k + q)^2) . \quad (4.36)$$

The quark four-momentum  $k$  can be decomposed in terms of  $p$ ,  $n$  and a transverse vector  $k_T$ ,

$$k^\mu = \xi p^\mu + \frac{k^2 + k_T^2}{2\xi} n^\mu + k_T^\mu . \quad (4.37)$$

The assumption of the parton model is that the structure of the amplitude  $B(k, p)$  is such that it is strongly damped when the transverse momentum  $k_T^2$  and the virtuality  $k^2$  are large. Thus the integral in (4.36) is dominated by small values of these variables and the delta function may be simplified to give

$$\delta((k + q)^2) = \delta(k^2 + 2\xi\nu - 2q_T \cdot k_T + q^2) \approx \delta(2\xi\nu - Q^2) = \frac{1}{2\nu} \delta(\xi - x) . \quad (4.38)$$

---

<sup>4</sup> This can be justified by considering the general behaviour of parton-proton scattering amplitudes.

This gives

$$\begin{aligned} \nu W_2 \equiv F_2 &= \frac{e_q^2}{2} \int \frac{d^4 k}{(2\pi)^4} [\not{k}(\not{k} + \not{q}) \not{n}]_{ij} B_{ji}(k, p) \delta(\xi - x) \\ &= e_q^2 x \int \frac{d^4 k}{(2\pi)^4} [\not{k}]_{ij} B_{ji}(k, p) \delta(\xi - x) \\ &\equiv e_q^2 x q(x), \end{aligned} \quad (4.39)$$

where the quark distribution is

$$q(x) = \int \frac{d^4 k}{(2\pi)^4} \text{Tr}[\not{k} B(k, p)] \delta(n \cdot k - x). \quad (4.40)$$

We therefore see that the structure function *scales*, i.e. it depends only on the dimensionless variable  $x$ :

$$F_2(x, Q^2) \longrightarrow F_2(x). \quad (4.41)$$

We can project out the longitudinal structure function in a similar way by multiplying the hadronic tensor  $W_{\alpha\beta}$  by  $p_\alpha p_\beta$ . In this case we find  $F_L = O(\nu^{-1})$  which vanishes in the Bjorken limit. We therefore derive the Callan-Gross relation  $F_2 = 2x F_1$  characteristic of the spin- $\frac{1}{2}$  nature of the constituents.

It is also possible to give an operator representation for the quark distribution  $q(x)$ . In the light-cone gauge,  $n \cdot A = 0$ , the matrix element of the gauge-invariant operator product (2.67) of two quark fields separated by a light-like distance along the  $n^\mu$  direction is independent of the gauge field  $A^\mu$ . The quark distribution is given by the Fourier transform of this correlation function,

$$q(x) = \int \frac{d\lambda}{2\pi} e^{i\lambda x} \langle P | \bar{\psi}(0) \not{\psi}(\lambda n) | P \rangle, \quad (4.42)$$

where  $\psi$  represents the quark field operator. Notice that the identification of  $q(x)$  with a quark number density is only valid in the infinite momentum frame. To see this, we take the first moment of the quark distribution with respect to  $x$  to obtain

$$\int dx q(x) = \langle P | \bar{\psi}(0) \not{\psi}(0) | P \rangle \approx \langle P | \bar{\psi}^\dagger(0) \psi(0) | P \rangle, \quad (4.43)$$

where the approximation is valid only in a fast moving frame in which

$$\bar{\psi} \gamma^0 \psi \approx \bar{\psi} \gamma^3 \psi. \quad (4.44)$$

How does a proton look in the infinite momentum frame? Because of the Lorentz contraction, the longitudinal size of the proton is contracted by a factor  $M/P$  with respect to its size in the rest frame. Partons with finite values of  $x$  and fixed transverse size are distributed on this disc, as shown

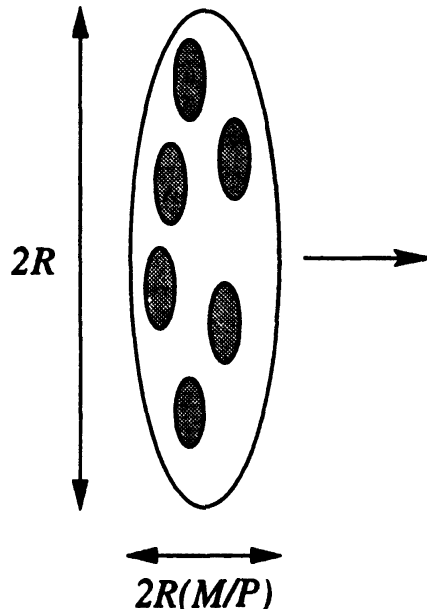


Fig. 4.5. The proton as viewed in the infinite momentum frame.

in Fig. 4.5, and the number of partons per unit of longitudinal phase space  $dx/x$  is rather small. Partons with very small values of  $x$  such that  $x \sim 1 \text{ GeV}/P$  are sometimes called ‘wee’ partons [2]. Because of their very small momentum they are not confined to the Lorentz contracted disc. Their spatial extent is rather determined by the uncertainty principle,

$$\Delta z \sim \frac{1}{xP} . \quad (4.45)$$

### 4.3 The parton model and QCD

In the ‘naive’ parton model the structure functions *scale*, i.e.  $F(x, Q^2) \rightarrow F(x)$  in the asymptotic (Bjorken) limit:  $Q^2 \rightarrow \infty$ ,  $x$  fixed. In QCD, this scaling is *broken* by logarithms of  $Q^2$ . The key point is that the parton’s transverse momentum (in the frame defined in the previous section) is *not* in fact restricted to be small. As we shall see below, a quark can emit a gluon and acquire large transverse momentum  $k_T$  with probability proportional to  $\alpha_s dk_T^2/k_T^2$  at large  $k_T$ . The integral extends up to the kinematic limit  $k_T^2 \sim Q^2$ , and gives rise to contributions proportional to  $\alpha_s \log Q^2$  which break scaling. These logarithmic scaling violations are a particular property of renormalizable gauge theories with point-like fermion–vector boson interactions. In contrast, one could imagine a different theory in which the probability for a parton to acquire large  $k_T$  was proportional to  $dk_T^2(m^2/k_T^4)$ , with  $m$  some mass scale in the theory.

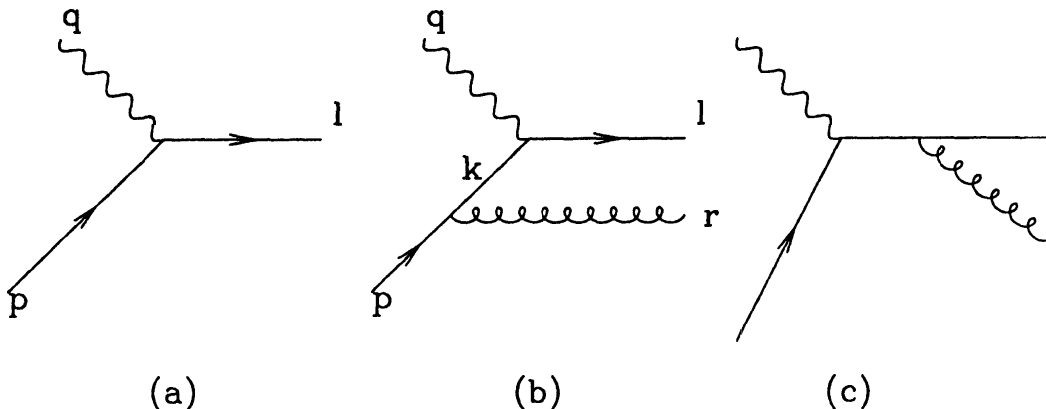


Fig. 4.6. Amplitudes for deep inelastic scattering off a quark.

In this case, the transverse momentum would be effectively cut off at  $k_T^2 \sim m^2$ , giving rise to Bjorken scaling for  $Q^2 \gg m^2$ .

In this section we will calculate the structure function of a quark which can emit a gluon, *i.e.* the  $O(\alpha_s)$  correction to the parton model result  $\hat{F}_2 = e_q^2 x \delta(x - \xi)$  obtained in Section 4.1.

### 4.3.1 Contribution from one-gluon emission

To establish the normalization we first calculate the scattering of a virtual photon off a free quark with momentum  $p$  (i.e.  $\xi = 1$ ), represented by Fig. 4.6(a):

$$\gamma^*(q) + q(p) \rightarrow q(l) . \quad (4.46)$$

The four-momenta of the lines are shown in brackets. The invariant matrix element for this process is

$$\mathcal{M}_\alpha = -ie_q \bar{u}(l) \gamma^\alpha u(p), \quad (4.47)$$

leading to a squared matrix element (summed and averaged over spins and colours and with the  $F_2$  contribution projected out)

$$n^\alpha n^\beta \sum |M|_{\alpha\beta}^2 = 4e_g^2. \quad (4.48)$$

The one-dimensional phase space is

$$d\Phi_1 = 2\pi \delta((p+q)^2) . \quad (4.49)$$

Inserting the ‘flux factor’ of  $1/4\pi$  from Eq. (4.28) we obtain

$$\hat{F}_2(x) = e_g^2 \delta(1 - x) \quad (4.50)$$

which is the naive parton model result with  $\xi = 1$ . The ‘‘’ indicates that the structure function refers to a quark, rather than proton, target. We next investigate the more complicated parton process, Fig. 4.6(b,c),

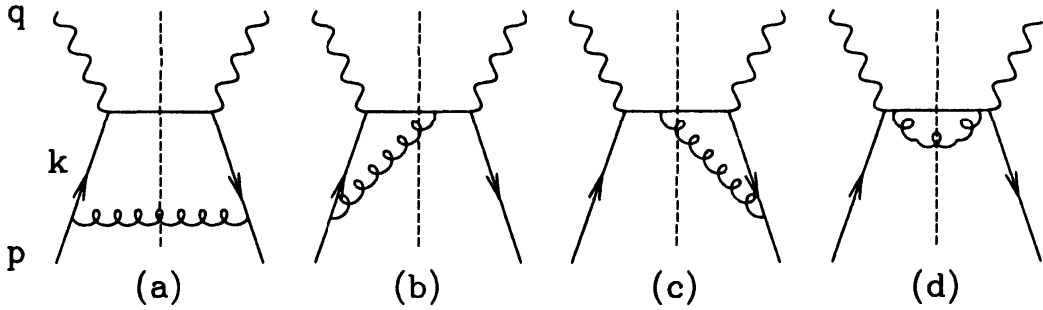


Fig. 4.7. Real gluon emission diagrams contributing to deep inelastic scattering.

in which the quark emits a gluon:

$$\gamma^*(q) + q(p) \rightarrow g(r) + q(l). \quad (4.51)$$

The squares of the Feynman diagrams involving real radiation are shown in Fig. 4.7. We begin by considering the diagram of Fig. 4.7(a). Notice that this has the same topology as the hadron-quark amplitude of the previous section, where here the amplitude  $B$  in Fig. 4.4 is represented by single gluon exchange. The Lorentz invariant phase space for this contribution is

$$d\Phi_2 = \int \frac{d^4 r}{(2\pi)^3} \frac{d^4 l}{(2\pi)^3} \delta^+(r^2) \delta^+(l^2) (2\pi)^4 \delta^4(p + q - r - l). \quad (4.52)$$

Introducing  $k^\mu$  to denote the momentum of the struck parton line we obtain

$$d\Phi_2 = \frac{1}{4\pi^2} \int d^4 k \delta^+((p - k)^2) \delta^+((k + q)^2). \quad (4.53)$$

The four-vector  $k^\mu$  can be written in terms of  $n$ ,  $p$  and a transverse vector  $k_T^\mu$ :

$$k^\mu = \xi p^\mu + \frac{k_T^2 - |k^2|}{2\xi} n^\mu + k_T^\mu \quad (4.54)$$

$$d^4 k = \frac{d\xi}{2\xi} dk^2 d^2 k_T \quad (4.55)$$

which gives

$$(p - k)^2 = (1 - \xi) \frac{|k^2|}{\xi} - \frac{k_T^2}{\xi}, \quad (4.56)$$

$$(k + q)^2 = 2\xi\nu - Q^2 - |k^2| - 2q_T \cdot k_T. \quad (4.57)$$

In terms of the components of  $k^\mu$ , the phase space becomes

$$d\Phi_2 = \frac{1}{16\nu\pi^2} \int d\xi dk^2 dk_T^2 d\theta \delta(k_T^2 - (1 - \xi)|k^2|)$$

$$\times \delta\left(\xi - x - \frac{|k^2| + 2q_T \cdot k_T}{2\nu}\right) \quad (4.58)$$

with  $0 < \theta < \pi$ . The corresponding matrix element is

$$\mathcal{M}^\alpha = -ig_e q \bar{u}(l) \gamma^\alpha \frac{1}{k} \not{k} t^A u(p) \quad (4.59)$$

where  $t^A$  is the SU(3) colour matrix introduced in Eq. (1.14). Squaring and averaging over colours and spins gives

$$\overline{\sum} |\mathcal{M}|_{\alpha\beta}^2 = \frac{1}{2} e_q^2 g^2 \sum_{\text{pol}} C_F \text{Tr}[\gamma^\beta (\not{k} + \not{q}) \gamma^\alpha \not{k} \not{p} \not{q}^* \not{k}] \frac{1}{k^4}, \quad (4.60)$$

where we have used the colour-matrix identity (1.17).

To perform the sum over the polarization of the real gluon we use the projector

$$\sum_{\text{pol}} \epsilon_\mu(r) \epsilon_\nu^*(r) = -g_{\mu\nu} + \frac{n_\mu r_\nu + n_\nu r_\mu}{n \cdot r}. \quad (4.61)$$

Thus in addition to the Lorentz condition  $\epsilon \cdot r = 0$ , the gluon satisfies the (light-cone) gauge condition  $\epsilon \cdot n = 0$ . This ensures that only two physical (*i.e.* transverse) polarizations propagate.

We can again project out the contribution to  $\hat{F}_2$  by using the vector  $n$  as in Eq. (4.35). Using the kinematic relations implicit in the phase space terms we find

$$\frac{1}{4\pi} n^\alpha n^\beta \overline{\sum} |\mathcal{M}|_{\alpha\beta}^2 = \frac{8e_q^2 \alpha_s}{|k^2|} \xi P(\xi), \quad (4.62)$$

where the function  $P(\xi)$  is known as the *splitting function*:

$$P(\xi) = C_F \frac{1 + \xi^2}{1 - \xi}. \quad (4.63)$$

Its form is specific to the  $q\bar{q}g$  vertex of QCD. Note that the  $1/k^4$  factor in Eq. (4.60) has been reduced to  $1/k^2$  by terms in the numerator coming from the trace over the Dirac matrices. Putting everything together and performing the  $k_T^2$  and  $\theta$  integrations gives

$$\hat{F}_2 = e_q^2 \frac{\alpha_s}{2\pi^2} \int_0^{2\nu} \frac{d|k^2|}{|k^2|} \int_{\xi_-}^{\xi_+} d\xi \frac{\xi P(\xi)}{\sqrt{(\xi_+ - \xi)(\xi - \xi_-)}} \quad (4.64)$$

where

$$\xi_\pm(z, x) = x + z - 2zx \pm \sqrt{4x(1-x)z(1-z)}. \quad (4.65)$$

In order to simplify the notation we have introduced the variable  $z = |k^2|/(2\nu)$ . Requiring real roots for the quadratic gives the limits  $0 < z < 1$ .

As anticipated at the start of this section, the transverse momentum (equivalently, the virtuality  $|k^2|$ ) is *not* restricted to small values.<sup>5</sup> In addition, we see that the  $|k^2|$  integral is logarithmically divergent at small  $|k^2|$ . The origin and treatment of this singularity will be discussed below, but in the meantime we can introduce a small cut-off  $\kappa^2$  in the integral and calculate the coefficient of the resulting logarithm. Noting that  $\xi_{\pm} \rightarrow x$  as  $z \rightarrow 0$ , and using the result

$$\int_{\xi_-}^{\xi_+} d\xi \frac{1}{\sqrt{(\xi_+ - \xi)(\xi - \xi_-)}} = \pi \quad (4.66)$$

we obtain

$$\hat{F}_2 \Big|_{\text{div}} = e_q^2 \frac{\alpha_s}{2\pi} x P(x) \int_{\kappa^2}^{2\nu} \frac{d|k^2|}{|k^2|} = e_q^2 \frac{\alpha_s}{2\pi} x P(x) \ln \left( \frac{2\nu}{\kappa^2} \right). \quad (4.67)$$

So far we have only considered the diagram of Fig. 4.7(a). In fact in the light-cone gauge (4.61) this is the only diagram which gives a logarithmic divergence — the other diagrams give finite corrections to the structure function. Consider for example Fig. 4.7(b). Instead of the  $1/k^4$  present in Fig. 4.7(a), this diagram contains only one propagator which can diverge. The other propagator involves  $1/(p + q)^2$ . The numerator factors at the  $qgg$  vertex contribute another factor of  $k_T \sim \sqrt{|k^2|}$ , in the light-cone gauge, and so this diagram gives only a finite contribution to the structure function.

In summary, the four diagrams of Fig. 4.7, together with the leading-order diagram, give a structure function

$$\hat{F}_2(x, Q^2) = e_q^2 x \left[ \delta(1-x) + \frac{\alpha_s}{2\pi} \left( P(x) \ln \frac{Q^2}{\kappa^2} + C(x) \right) \right], \quad (4.68)$$

where  $P$  is given by Eq. (4.63) and  $C$  is a calculable function. Note that in deriving Eq. (4.68) we have used  $\ln(2\nu) = \ln Q^2 - \ln x$  and absorbed the latter logarithm into the function  $C(x)$ .

Our calculation shows that *beyond leading order the structure function is  $Q^2$  dependent*, with Bjorken scaling broken by logarithms of  $Q^2$ . The corresponding quark distribution function to this order in perturbation theory is

$$q(x, Q^2) = \delta(1-x) + \frac{\alpha_s}{2\pi} \left( P(x) \ln \frac{Q^2}{\kappa^2} + C(x) \right). \quad (4.69)$$

This is not quite the complete answer for  $q$ . The full result requires the inclusion of virtual gluon radiation, specifically the inclusion of self-energy

<sup>5</sup> This is to be expected since there is no small scale in the calculation which could provide such a limit.

insertions on the quark legs and the photon vertex correction. The calculation of these diagrams is straightforward using standard loop-integral methods.<sup>6</sup> The ultraviolet divergences which appear in individual loop diagrams cancel in the sum. In fact, a physical argument provides a useful short-cut to the answer [8]. First we note that because the delta function  $\delta((p+q)^2)$  is common to all the virtual diagrams, their contribution to the structure function is proportional to  $\delta(1-x)$ . Thus, for example, the splitting function becomes

$$P(x) \longrightarrow P(x) + K\delta(1-x). \quad (4.70)$$

Second, in order to conserve quark (*i.e.* baryon) number, the integral of the quark distribution cannot vary with  $Q^2$ . This implies that the function on the right-hand side of Eq. (4.70) must integrate to 0. This is achieved with

$$P(x) = C_F \left[ \frac{1+x^2}{(1-x)_+} + \frac{3}{2}\delta(1-x) \right], \quad (4.71)$$

where the ‘plus’ distribution is defined so that its integral with any sufficiently smooth distribution  $f$  is

$$\int_0^1 dx \frac{f(x)}{(1-x)_+} = \int_0^1 dx \frac{f(x) - f(1)}{1-x}, \quad (4.72)$$

and

$$\frac{1}{(1-x)_+} = \frac{1}{1-x} \quad \text{for } 0 \leq x < 1. \quad (4.73)$$

The one-gluon contribution to the longitudinal structure function can be calculated in a similar way. In this case, following Eq. (4.35), the projection of the matrix element in Eq. (4.62) is replaced by

$$\frac{x^2}{\pi\nu^2} p^\alpha p^\beta \sum |{\mathcal M}|_{\alpha\beta}^2. \quad (4.74)$$

Once again the leading contribution comes from Fig. 4.7(a), since it is the only diagram to give non-zero transverse momentum to the struck quark. However in this case there is no logarithmic singularity: the integral over the quark virtuality is  $\nu^{-1} \int^{2\nu} d|k^2| = O(1)$ . The result is (*cf.* Eq. (4.68))

$$\hat{F}_L(x, Q^2) = e_q^2 x \left[ 0 + \frac{\alpha_s}{2\pi} C_F 2x \right]. \quad (4.75)$$

---

<sup>6</sup> In fact the treatment of these graphs in the light-cone gauge is somewhat delicate, and so in practice it is simpler to use a covariant gauge for these diagrams.

### 4.3.2 Factorization

Our procedure for regulating the singularity at  $|k^2| = 0$  by introducing a small cut-off  $\kappa^2$  was completely *ad hoc*. One could in fact have performed a regularization in other ways. For example, dimensional regularization, which is a convenient method for handling *ultraviolet* divergences, can be used in the present context as well. The idea is to change the number of space-time dimensions from 4 to  $n = 4 - 2\epsilon$ , whereupon the divergent integral becomes  $d|k^2|/|k^2|^{1+\epsilon}$ . The result is then finite for any  $\epsilon < 0$ , and the analogue of Eq. (4.67) is

$$\hat{F}_2 \Big|_{\text{div}} = e_q^2 \frac{\alpha_s}{2\pi} x P(x) \left( -\frac{1}{\epsilon} \right). \quad (4.76)$$

How should we interpret the divergence in the structure function at  $O(\alpha_s)$ ? Notice that the singularity arises when the gluon is emitted parallel to the quark ( $k_T = 0$ ), and for this reason is often called a collinear divergence. This divergence is not subject to the theorems for cancellation of singularities discussed in Chapter 3, because the virtual photon *can* distinguish between a quark and a collinear quark-gluon pair carrying the same overall momentum. The key to understanding what is happening is to realize that the limit  $k_T^2 \rightarrow 0$  corresponds to a long-range ('soft') part of the strong interaction which is not calculable in perturbation theory. In order to obtain a proton structure function we must convolute the quark structure function  $\hat{F}_2$  of Eq. (4.68) with a 'bare' distribution  $q_0$  of a quark in a proton and sum over quark flavours, as we did in Section 4.1 for the naive parton model. This gives

$$F_2(x, Q^2) = x \sum_{q,\bar{q}} e_q^2 \left[ q_0(x) + \frac{\alpha_s}{2\pi} \int_x^1 \frac{d\xi}{\xi} q_0(\xi) \left\{ P\left(\frac{x}{\xi}\right) \ln \frac{Q^2}{\kappa^2} + C\left(\frac{x}{\xi}\right) \right\} + \dots \right], \quad (4.77)$$

where the ellipsis represents contributions from higher orders in perturbation theory.

Exactly as for the renormalization of the coupling constant, we can regard  $q_0(x)$  as an unmeasurable, *bare* distribution. The collinear singularities are absorbed into this bare distribution at a 'factorization scale'  $\mu$ , which plays a similar role to the renormalization scale. In other words, we define a 'renormalized' distribution  $q(x, \mu^2)$  by

$$q(x, \mu^2) = q_0(x) + \frac{\alpha_s}{2\pi} \int_x^1 \frac{d\xi}{\xi} q_0(\xi) \left\{ P\left(\frac{x}{\xi}\right) \ln \frac{\mu^2}{\kappa^2} + C\left(\frac{x}{\xi}\right) \right\} + \dots, \quad (4.78)$$

in terms of which

$$\begin{aligned} F_2(x, Q^2) &= x \sum_{q,\bar{q}} e_q^2 \int_x^1 \frac{d\xi}{\xi} q(\xi, \mu^2) \\ &\times \left\{ \delta(1 - \frac{x}{\xi}) + \frac{\alpha_s}{2\pi} P\left(\frac{x}{\xi}\right) \ln \frac{Q^2}{\mu^2} + \dots \right\}. \quad (4.79) \end{aligned}$$

The distribution  $q(x, \mu^2)$  cannot be calculated from first principles in perturbation theory, since it receives contributions from the long-distance (non-perturbative) part of the strong interaction. It can of course be determined from structure function data at any particular scale, since  $F_2(x, Q^2) = x \sum e_q^2 q(x, Q^2)$ .

The ability to separate or factorize the long- and short-distance contributions to the structure function (or more generally, to any physical cross section involving large momentum transfers) in this way is a fundamental property of the theory. Although we have only demonstrated factorization to  $O(\alpha_s)$ , proofs to all orders in perturbation theory exist. A more complete discussion will be given in Chapter 7.

It is interesting to note that while factorization provides a prescription for dealing with the logarithmic singularities, there is an arbitrariness in how the *finite* (non-logarithmic) contributions are treated. In the example given above, all of the finite contribution  $C$  was absorbed into the quark distribution  $q(x, \mu^2)$ . We could, however, have factored out an arbitrary finite term,  $C'$  say, which would have left behind an additional finite contribution  $C - C'$  in the expression for the structure function. How much finite contribution is factored out defines what is called the ‘factorization scheme’. The example above, in which  $F_2(x, Q^2) = x \sum_{q,\bar{q}} e_q^2 q(x, Q^2)$  with no finite  $O(\alpha_s)$  corrections, is called the DIS (Deep Inelastic Scattering) scheme [9]. A more common choice in practice is the  $\overline{\text{MS}}$  scheme, in which in addition to the divergent piece only a ubiquitous  $\ln(4\pi) - \gamma_E$  contribution is absorbed into the quark distribution. In this case one has

$$F_2(x, Q^2) = x \sum_{q,\bar{q}} e_q^2 \int_x^1 \frac{d\xi}{\xi} q(\xi, Q^2) \left\{ \delta(1 - \frac{x}{\xi}) + \frac{\alpha_s}{2\pi} C_{\overline{\text{MS}}} \left( \frac{x}{\xi} \right) + \dots \right\}. \quad (4.80)$$

It might at first sight appear that the arbitrariness in defining a factorization scheme removes any predictive power from the theory. This is not the case, since once a scheme has been fixed, say in deep inelastic scattering, it must be used in *all* other cross section calculations. For example, the higher-order corrections to the cross section for lepton pair production in hadron-hadron collisions will depend on the factorization scheme used to define the parton distributions (see Chapter 9).

In order to obtain a complete description of the deep inelastic structure functions in terms of parton distributions, there is one further contribu-

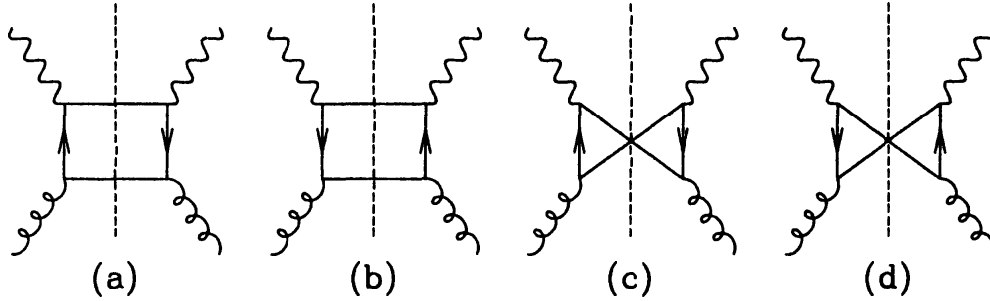


Fig. 4.8. Deep inelastic scattering with initial gluons.

tion that we must include, the  $O(\alpha_s)$  contribution from the  $\gamma^*g \rightarrow q\bar{q}$  process shown in Fig. 4.8. The calculation of this contribution, which we denote by  $\hat{F}_2^g$ , proceeds in the same way as the  $\gamma^*q \rightarrow qg$  calculation described in Section 4.3.1. The result is

$$\hat{F}_2^g(x, Q^2) = x \sum_{q,\bar{q}} e_q^2 \frac{\alpha_s}{2\pi} \left( P_{qg}(x) \ln \frac{Q^2}{\kappa^2} + C_g(x) \right). \quad (4.81)$$

Note the similarity between this result and that for the quark contribution, Eq. (4.68). There is again a logarithmic singularity from vanishing quark virtuality,  $|k^2| \rightarrow 0$ . The splitting function coefficient is now

$$P_{qg}(x) = T_R[x^2 + (1-x)^2]. \quad (4.82)$$

The colour factor  $T_R = \frac{1}{2}$  is obtained from Eq. (1.16). The sum in Eq. (4.81) is over the  $n_f$  massless quark and antiquark flavours which contribute, *i.e.* the quark contributions from Figs. 4.8(a,c) and the identical antiquark contributions from Figs. 4.8(b,d).

To obtain the physical structure function, the contribution (4.81) must be folded with a bare gluon distribution  $g_0(x)$  and added to the result obtained in Eq. (4.77). Exactly as for the  $O(\alpha_s)$  quark contribution, the logarithmic singularity in (4.81) can then be absorbed into the bare quark distribution at the factorization scale  $\mu$ , so that Eq. (4.78) becomes

$$\begin{aligned} q(x, \mu^2) &= q_0(x) + \frac{\alpha_s}{2\pi} \int_x^1 \frac{d\xi}{\xi} g_0(\xi) \left\{ P_{qg} \left( \frac{x}{\xi} \right) \ln \frac{\mu^2}{\kappa^2} + C_g \left( \frac{x}{\xi} \right) \right\} + \\ &\quad + \frac{\alpha_s}{2\pi} \int_x^1 \frac{d\xi}{\xi} g_0(\xi) \left\{ P_{qg} \left( \frac{x}{\xi} \right) \ln \frac{\mu^2}{\kappa^2} + C_g \left( \frac{x}{\xi} \right) \right\} + \dots . \end{aligned} \quad (4.83)$$

By absorbing *all* the gluon contribution into the quark distribution — the DIS factorization scheme — we still have  $F_2(x, Q^2) = x \sum_{q,\bar{q}} e_q^2 q(x, Q^2)$ . In the  $\overline{\text{MS}}$  scheme, only the divergent part is absorbed into the renormalized

quark distribution, so that

$$\begin{aligned} F_2(x, Q^2) &= x \sum_{q,\bar{q}} e_q^2 \int_x^1 \frac{d\xi}{\xi} q(\xi, Q^2) \left\{ \delta(1 - \frac{x}{\xi}) + \frac{\alpha_s}{2\pi} C_q^{\overline{\text{MS}}} \left( \frac{x}{\xi} \right) + \dots \right\} \\ &\quad + x \sum_{q,\bar{q}} e_q^2 \int_x^1 \frac{d\xi}{\xi} g(\xi, Q^2) \left\{ \frac{\alpha_s}{2\pi} C_g^{\overline{\text{MS}}} \left( \frac{x}{\xi} \right) + \dots \right\}. \end{aligned} \quad (4.84)$$

The functions  $C_q(x)$  and  $C_g(x)$  are called *coefficient functions*. They depend on the factorization and renormalization schemes, and also on the structure function under consideration (*i.e.* they are different in general for  $F_1$ ,  $F_2$  and  $F_3$ ). In the DIS scheme these functions for  $F_2$  are zero at all non-leading orders in perturbation theory. The  $\overline{\text{MS}}$   $O(\alpha_s)$  coefficient functions for  $F_2$  are [10]

$$\begin{aligned} C_q^{\overline{\text{MS}}}(z) &= C_F \left[ 2 \left( \frac{\ln(1-z)}{1-z} \right)_+ - \frac{3}{2} \left( \frac{1}{1-z} \right)_+ - (1+z) \ln(1-z) \right. \\ &\quad \left. - \frac{1+z^2}{1-z} \ln z + 3 + 2z - \left( \frac{\pi^2}{3} + \frac{9}{2} \right) \delta(1-z) \right], \\ C_g^{\overline{\text{MS}}}(z) &= T_R \left[ ((1-z)^2 + z^2) \ln \left( \frac{1-z}{z} \right) - 8z^2 + 8z - 1 \right]. \end{aligned} \quad (4.85)$$

For the longitudinal structure function, the leading-order coefficient functions are scheme independent:

$$\begin{aligned} F_L(x, Q^2) &= x \sum_{q,\bar{q}} e_q^2 \int_x^1 \frac{d\xi}{\xi} q(\xi, Q^2) \left\{ \frac{\alpha_s}{2\pi} \left[ 2C_F \frac{x}{\xi} \right] + \dots \right\} \\ &\quad + x \sum_{q,\bar{q}} e_q^2 \int_x^1 \frac{d\xi}{\xi} g(\xi, Q^2) \left\{ \frac{\alpha_s}{2\pi} \left[ 4T_R \frac{x}{\xi} \left( 1 - \frac{x}{\xi} \right) \right] + \dots \right\}. \end{aligned} \quad (4.86)$$

We have already stated that the first-principles calculation of the parton distributions is beyond the scope of perturbation theory. Attempts to use non-perturbative methods, for example numerical calculations based on lattice gauge theory, have been so far been unable to achieve a level of precision necessary to make a meaningful comparison with the experimental measurements, see for example ref. [11]. However what *can* be calculated perturbatively is how they depend on the factorization scale  $\mu^2$ . To see how this is achieved, we simply have to notice that the right-hand side of Eq. (4.79) must be independent of  $\mu^2$ . Taking the derivative  $\partial/\partial \ln \mu^2$  of both sides will give us a differential equation for the  $\mu^2$  dependence of  $q(x, \mu^2)$ , and hence for the  $Q^2$  dependence (scaling violations) of the deep inelastic structure function.

### 4.3.3 Scaling violations and the GLAP equation

If we define  $t = \mu^2$  and take the  $\ln t$  partial derivative of Eq. (4.79) we obtain

$$t \frac{\partial}{\partial t} q(x, t) = \frac{\alpha_s(t)}{2\pi} \int_x^1 \frac{d\xi}{\xi} P\left(\frac{x}{\xi}\right) q(\xi, t). \quad (4.87)$$

This equation — known as the (Dokshitzer)-Gribov-Lipatov-Altarelli-Parisi (GLAP) equation [12] — is the analogue of the  $\beta$  function equation describing the variation of  $\alpha_s(t)$  with  $t$  and is one of the most important equations of perturbative QCD.

The above derivation is not completely rigorous, for example we have introduced  $t$  as the argument of the running coupling, but a more exact treatment based on the operator product expansion and the renormalization group equation [13,14] confirms Eq. (4.87) and extends the result to higher orders in perturbation theory. The full prediction of the theory is

$$t \frac{\partial}{\partial t} q(x, t) = \frac{\alpha_s(t)}{2\pi} \int_x^1 \frac{d\xi}{\xi} P_{qq}\left(\frac{x}{\xi}, \alpha_s(t)\right) q(\xi, t). \quad (4.88)$$

The function  $P_{qq}$  has a perturbative expansion in the running coupling,

$$P_{qq}(z, \alpha_s) = P_{qq}^{(0)}(z) + \frac{\alpha_s}{2\pi} P_{qq}^{(1)}(z) + \dots \quad (4.89)$$

Retaining only the first term in this expansion gives precisely the result of Eq. (4.87), with  $P \equiv P_{qq}^{(0)}$ .

In fact the above equation is strictly only correct for ‘non-singlet’ distributions, defined as differences between quark distributions, e.g.  $q_{NS} = q_i - q_j$ . More generally, the GLAP equation is a  $(2n_f + 1)$ -dimensional matrix equation in the space of quarks, antiquarks and gluons,

$$\begin{aligned} t \frac{\partial}{\partial t} \begin{pmatrix} q_i(x, t) \\ g(x, t) \end{pmatrix} &= \frac{\alpha_s(t)}{2\pi} \sum_{q_j, \bar{q}_j} \int_x^1 \frac{d\xi}{\xi} \\ &\times \begin{pmatrix} P_{q_i q_j}\left(\frac{x}{\xi}, \alpha_s(t)\right) & P_{q_i g}\left(\frac{x}{\xi}, \alpha_s(t)\right) \\ P_{g q_j}\left(\frac{x}{\xi}, \alpha_s(t)\right) & P_{gg}\left(\frac{x}{\xi}, \alpha_s(t)\right) \end{pmatrix} \begin{pmatrix} q_j(\xi, t) \\ g(\xi, t) \end{pmatrix}, \end{aligned} \quad (4.90)$$

where each splitting function (or ‘evolution kernel’) is again calculable as a power series in  $\alpha_s$ ,

$$\begin{aligned} P_{q_i q_j}(z, \alpha_s) &= \delta_{ij} P_{qq}^{(0)}(z) + \frac{\alpha_s}{2\pi} P_{q_i q_j}^{(1)}(z) + \dots \\ P_{q g}(z, \alpha_s) &= P_{qg}^{(0)}(z) + \frac{\alpha_s}{2\pi} P_{qg}^{(1)}(z) + \dots \\ P_{g q}(z, \alpha_s) &= P_{gq}^{(0)}(z) + \frac{\alpha_s}{2\pi} P_{gq}^{(1)}(z) + \dots \end{aligned}$$

$$P_{gg}(z, \alpha_s) = P_{gg}^{(0)}(z) + \frac{\alpha_s}{2\pi} P_{gg}^{(1)}(z) + \dots \quad (4.91)$$

Note that because of charge conjugation invariance and  $SU(n_f)$  flavour symmetry we have

$$\begin{aligned} P_{q_i q_j} &= P_{\bar{q}_i \bar{q}_j} \\ P_{q_i \bar{q}_j} &= P_{\bar{q}_i q_j} \\ P_{q_i g} &= P_{\bar{q}_i g} \equiv P_{qg} \\ P_{g q_i} &= P_{g \bar{q}_i} \equiv P_{gq}, \end{aligned} \quad (4.92)$$

i.e. the splitting functions  $P_{qg}$  and  $P_{gq}$  are independent of the quark flavour and the same for quarks and antiquarks. The leading-order  $P_{q_i q_j}$  splitting function is zero unless  $q_i = q_j$ . This allows the matrix equation to be considerably simplified at this order (see below).

The leading-order GLAP splitting functions  $P_{ab}^{(0)}(x)$  have an attractive physical interpretation as the probabilities of finding a parton of type  $a$  in a parton of type  $b$  with a fraction  $x$  of the longitudinal momentum of the parent parton and a transverse momentum squared much less than  $\mu^2$  [8]. The interpretation as probabilities implies that the splitting functions are positive definite for  $x < 1$ , and satisfy the sum rules

$$\begin{aligned} \int_0^1 dx P_{qq}^{(0)}(x) &= 0 \\ \int_0^1 dx x [P_{qq}^{(0)}(x) + P_{gq}^{(0)}(x)] &= 0 \\ \int_0^1 dx x [2n_f P_{qg}^{(0)}(x) + P_{gg}^{(0)}(x)] &= 0, \end{aligned} \quad (4.93)$$

which correspond to quark number conservation and momentum conservation in the splittings of quarks and gluons respectively.

Both the leading-order [8] and  $O(\alpha_s)$  [15,16,17] contributions to the GLAP splitting functions have been calculated. The leading-order contributions are

$$\begin{aligned} P_{qq}^{(0)}(x) &= C_F \left[ \frac{1+x^2}{(1-x)_+} + \frac{3}{2} \delta(1-x) \right], \\ P_{qg}^{(0)}(x) &= T_R \left[ x^2 + (1-x)^2 \right], \quad T_R = \frac{1}{2}, \\ P_{gq}^{(0)}(x) &= C_F \left[ \frac{1+(1-x)^2}{x} \right], \\ P_{gg}^{(0)}(x) &= 2C_A \left[ \frac{x}{(1-x)_+} + \frac{1-x}{x} + x(1-x) \right] \\ &\quad + \delta(1-x) \frac{(11C_A - 4n_f T_R)}{6}, \end{aligned} \quad (4.94)$$

where the ‘plus prescription’ on the singular parts of the functions has been defined in Eq. (4.72). Beyond leading order, the flavour structure of the  $P_{q_i q_k}$  function is non-trivial. Using  $SU(n_f)$  flavour symmetry, we can write this in terms of flavour singlet ( $S$ ) and non-singlet ( $V$ ) quantities:

$$\begin{aligned} P_{q_i q_k} &= \delta_{ik} P_{qq}^V + P_{qq}^S \\ P_{q_i \bar{q}_k} &= \delta_{ik} P_{q\bar{q}}^V + P_{q\bar{q}}^S \\ P^\pm &= P_{qq}^V \pm P_{q\bar{q}}^V. \end{aligned} \quad (4.95)$$

At next-to-leading order, the functions  $P_{qq}^S$  and  $P_{q\bar{q}}^S$  are non-zero, but we have the additional relation

$$P_{qq}^S = P_{q\bar{q}}^S. \quad (4.96)$$

which simplifies the treatment of the non-singlet pieces.

An efficient method for calculating the evolution of the individual quark distributions is to introduce a sequence of non-singlet combinations:

$$\begin{aligned} V_i &= q_i^- \\ T_3 &= u^+ - d^+ \\ T_8 &= u^+ + d^+ - 2s^+ \\ T_{15} &= u^+ + d^+ + s^+ - 3c^+ \\ T_{24} &= u^+ + d^+ + s^+ + c^+ - 4b^+ \\ T_{35} &= u^+ + d^+ + s^+ + c^+ + b^+ - 5t^+ \end{aligned} \quad (4.97)$$

where

$$q_i^\pm = q_i \pm \bar{q}_i \quad (4.98)$$

and  $u, d, s, c, b, t$  are the distributions of the various flavours of quarks. It is then straightforward to show that (at next-to-leading order) the combinations  $V_i$  and  $T_j$  evolve according to Eq. (4.88) with  $P_{qq}^{(1)} \equiv P^-$  and  $P_{qq}^{(1)} \equiv P^+$  respectively.

The one remaining combination of quark distributions is the *singlet* distribution,

$$\Sigma(x, t) = \sum_i q_i^+(x, t) \equiv \sum_i [q_i(x, t) + \bar{q}_i(x, t)] \quad (4.99)$$

whose evolution is coupled with that of the gluon distribution:

$$\begin{aligned} t \frac{\partial}{\partial t} \begin{pmatrix} \Sigma(x, t) \\ g(x, t) \end{pmatrix} &= \frac{\alpha_s(t)}{2\pi} \int_x^1 \frac{d\xi}{\xi} \\ &\times \begin{pmatrix} P_{qq} \left( \frac{x}{\xi}, \alpha_s(t) \right) & 2n_f P_{qg} \left( \frac{x}{\xi}, \alpha_s(t) \right) \\ P_{gg} \left( \frac{x}{\xi}, \alpha_s(t) \right) & P_{gg} \left( \frac{x}{\xi}, \alpha_s(t) \right) \end{pmatrix} \begin{pmatrix} \Sigma(\xi, t) \\ g(\xi, t) \end{pmatrix}, \end{aligned} \quad (4.100)$$

where now

$$P_{qq} = P^+ + n_f (P_{qq}^S + P_{q\bar{q}}^S) . \quad (4.101)$$

Knowing the 6  $V_i$  combinations, the 5  $T_j$  combinations and  $\Sigma$  one can solve for each of the 12 individual quark and antiquark distributions.

For completeness, we give here the full set of next-to-leading-order splitting functions in the  $\overline{\text{MS}}$  factorization/renormalization scheme. We first introduce the notation

$$T_f = T_R n_f = \frac{1}{2} n_f \quad (4.102)$$

$$p_{qq}(x) = \frac{2}{1-x} - 1 - x \quad (4.103)$$

$$p_{qg}(x) = x^2 + (1-x)^2 \quad (4.104)$$

$$p_{gq}(x) = \frac{1+(1-x)^2}{x} \quad (4.105)$$

$$p_{gg}(x) = \frac{1}{1-x} + \frac{1}{x} - 2 + x(1-x) . \quad (4.106)$$

Then for  $x \neq 1$ , the non-singlet functions are [15]

$$\begin{aligned} P_{qq}^{V(1)} &= C_F^2 \left\{ - \left[ 2 \ln x \ln(1-x) + \frac{3}{2} \ln x \right] p_{qq}(x) \right. \\ &\quad \left. - \left( \frac{3}{2} + \frac{7}{2}x \right) \ln x - \frac{1}{2}(1+x) \ln^2 x - 5(1-x) \right\} \\ &\quad + C_F C_A \left\{ \left[ \frac{1}{2} \ln^2 x + \frac{11}{6} \ln x + \frac{67}{18} - \frac{\pi^2}{6} \right] p_{qq}(x) \right. \\ &\quad \left. + (1+x) \ln x + \frac{20}{3}(1-x) \right\} \\ &\quad + C_F T_f \left\{ - \left[ \frac{2}{3} \ln x + \frac{10}{9} \right] p_{qq}(x) - \frac{4}{3}(1-x) \right\} , \end{aligned} \quad (4.107)$$

$$\begin{aligned} P_{q\bar{q}}^{V(1)} &= C_F \left( C_F - \frac{C_A}{2} \right) \left\{ 2p_{qq}(-x) S_2(x) \right. \\ &\quad \left. + 2(1+x) \ln x + 4(1-x) \right\} , \end{aligned} \quad (4.108)$$

and for the singlet functions [16],

$$\begin{aligned} P_{qq}^{(1)} &= C_F^2 \left\{ -1 + x + \left( \frac{1}{2} - \frac{3}{2}x \right) \ln x - \frac{1}{2}(1+x) \ln^2 x \right. \\ &\quad \left. - \left[ \frac{3}{2} \ln x + 2 \ln x \ln(1-x) \right] p_{qq}(x) + 2p_{qq}(-x) S_2(x) \right\} \\ &\quad + C_F C_A \left\{ \frac{14}{3}(1-x) + \left[ \frac{11}{6} \ln x + \frac{1}{2} \ln^2 x + \frac{67}{18} - \frac{\pi^2}{6} \right] p_{qq}(x) \right. \end{aligned}$$

$$\begin{aligned} & -p_{qq}(-x)S_2(x) \Big\} \\ & +C_F T_f \left\{ -\frac{16}{3} + \frac{40}{3}x + \left( 10x + \frac{16}{3}x^2 + 2 \right) \ln x \right. \\ & \left. - \frac{112}{9}x^2 + \frac{40}{9x} - 2(1+x) \ln^2 x - \left[ \frac{10}{9} + \frac{2}{3} \ln x \right] p_{qq}(x) \right\} \quad (4.109) \end{aligned}$$

$$\begin{aligned} P_{qg}^{(1)} = & C_F T_f \left\{ 4 - 9x - (1 - 4x) \ln x - (1 - 2x) \ln^2 x + 4 \ln(1 - x) \right. \\ & + \left[ 2 \ln^2 \left( \frac{1-x}{x} \right) - 4 \ln \left( \frac{1-x}{x} \right) - \frac{2}{3}\pi^2 + 10 \right] p_{qg}(x) \Big\} \\ & +C_A T_f \left\{ \frac{182}{9} + \frac{14}{9}x + \frac{40}{9x} + \left( \frac{136}{3}x - \frac{38}{3} \right) \ln x \right. \\ & - 4 \ln(1 - x) - (2 + 8x) \ln^2 x + 2p_{qg}(-x)S_2(x) \\ & + \left[ -\ln^2 x + \frac{44}{3} \ln x - 2 \ln^2(1 - x) + 4 \ln(1 - x) \right. \\ & \left. \left. + \frac{\pi^2}{3} - \frac{218}{9} \right] p_{qg}(x) \right\} \quad (4.110) \end{aligned}$$

$$\begin{aligned} P_{gq}^{(1)} = & C_F^2 \left\{ -\frac{5}{2} - \frac{7x}{2} + \left( 2 + \frac{7}{2}x \right) \ln x - \left( 1 - \frac{1}{2}x \right) \ln^2 x \right. \\ & - 2x \ln(1 - x) - \left[ 3 \ln(1 - x) + \ln^2(1 - x) \right] p_{gq}(x) \Big\} \\ & +C_F C_A \left\{ \frac{28}{9} + \frac{65}{18}x + \frac{44}{9}x^2 - \left( 12 + 5x + \frac{8}{3}x^2 \right) \ln x \right. \\ & + (4 + x) \ln^2 x + 2x \ln(1 - x) + S_2(x)p_{gq}(-x) \\ & + \left[ \frac{1}{2} - 2 \ln x \ln(1 - x) + \frac{1}{2} \ln^2 x + \frac{11}{3} \ln(1 - x) \right. \\ & \left. \left. + \ln^2(1 - x) - \frac{\pi^2}{6} \right] p_{gq}(x) \right\} \\ & +C_F T_f \left\{ -\frac{4}{3}x - \left[ \frac{20}{9} + \frac{4}{3} \ln(1 - x) \right] p_{gq}(x) \right\} \quad (4.111) \end{aligned}$$

$$\begin{aligned} P_{gg}^{(1)} = & C_F T_f \left\{ -16 + 8x + \frac{20}{3}x^2 + \frac{4}{3x} \right. \\ & - (6 + 10x) \ln x - (2 + 2x) \ln^2 x \Big\} \\ & +C_A T_f \left\{ 2 - 2x + \frac{26}{9} \left( x^2 - \frac{1}{x} \right) - \frac{4}{3}(1 + x) \ln x - \frac{20}{9} p_{gg}(x) \right\} \\ & +C_A^2 \left\{ \frac{27}{2}(1 - x) + \frac{67}{9} \left( x^2 - \frac{1}{x} \right) - \left( \frac{25}{3} - \frac{11}{3}x + \frac{44}{3}x^2 \right) \ln x \right. \end{aligned}$$

$$+4(1+x)\ln^2 x + 2p_{gg}(-x)S_2(x) \\ + \left[ \frac{67}{9} - 4\ln x \ln(1-x) + \ln^2 x - \frac{\pi^2}{3} \right] p_{gg}(x) \Big\} . \quad (4.112)$$

The function  $S_2(x)$  is defined by

$$S_2(x) = \int_{\frac{x}{1+x}}^{\frac{1}{1-x}} \frac{dz}{z} \ln \left( \frac{1-z}{z} \right) . \quad (4.113)$$

In terms of the dilogarithm function defined in Eq. (3.36), we have

$$S_2(x) = -2\text{Li}_2(-x) + \frac{1}{2} \ln^2 x - 2\ln x \ln(1+x) - \frac{\pi^2}{6} . \quad (4.114)$$

The above results for the  $P^{(1)}$  functions in Eqs. (4.107, 4.109, 4.112) can be extended to all values of  $x$  by using sum rules to fix the endpoint ( $x = 1$ ) contributions: *i.e.* from the conservation of fermion number,

$$\int_0^1 dx (P_{qq}(x) - P_{q\bar{q}}(x)) \equiv \int_0^1 dx P^-(x) = 0 , \quad (4.115)$$

and momentum fraction,

$$\int_0^1 dx x (P_{qq}(x) + P_{gq}(x)) = 0 , \quad (4.116)$$

$$\int_0^1 dx x (P_{qg}(x) + P_{gg}(x)) = 0 . \quad (4.117)$$

These results for the integral of the splitting functions are satisfied if one makes the substitution

$$\frac{1}{1-x} \rightarrow \frac{1}{(1-x)_+} \quad (4.118)$$

in Eqs. (4.103, 4.106), and adds the following endpoint contributions to Eqs. (4.107), (4.109) and (4.112):

$$\delta P_{qq}^{V(1)} = \delta P_{qq}^{(1)} = \left[ C_F^2 \left\{ \frac{3}{8} - \frac{\pi^2}{2} + 6\zeta(3) \right\} \right. \\ \left. + C_F C_A \left\{ \frac{17}{24} + \frac{11\pi^2}{18} - 3\zeta(3) \right\} \right. \\ \left. - C_F T_f \left\{ \frac{1}{6} + \frac{2\pi^2}{9} \right\} \right] \delta(1-x) , \quad (4.119)$$

$$\delta P_{gg}^{(1)} = \left[ C_A^2 \left\{ \frac{8}{3} + 3\zeta(3) \right\} - C_F T_f - \frac{4}{3} C_A T_f \right] \delta(1-x) . \quad (4.120)$$

The values of the Riemann zeta functions are given in Eq. (3.19).

In the small- $x$  limit (see Section 4.6), Eq. (4.113) for  $S_2$  gives

$$S_2 = \frac{1}{2} \ln^2 x - \frac{\pi^2}{6} + O(x) . \quad (4.121)$$

The small- $x$  limit of the leading- and next-to-leading-order splitting functions for the evolution of the singlet quark and gluon distributions according to Eq. (4.100) is then

$$\begin{aligned} P_{qq} &\rightarrow \frac{\alpha_s}{2\pi} \frac{40C_F T_f}{9x} \\ P_{qg} &\rightarrow \frac{\alpha_s}{2\pi} \frac{40C_A T_f}{9x} \\ P_{gq} &\rightarrow \frac{2C_F}{x} + \frac{\alpha_s}{2\pi} \frac{9C_F C_A - 40C_F T_f}{x} \\ P_{gg} &\rightarrow \frac{2C_A}{x} + \frac{\alpha_s}{2\pi} \frac{12C_F T_f - 46C_A T_f}{9x} . \end{aligned} \quad (4.122)$$

The large- $x$  limit is dominated by the diagonal terms of the splitting function matrix:

$$\begin{aligned} P_{qq} &\rightarrow \frac{2C_F}{(1-x)_+} \left( 1 + \frac{\alpha_s}{2\pi} \kappa \right) \\ P_{gg} &\rightarrow \frac{2C_A}{(1-x)_+} \left( 1 + \frac{\alpha_s}{2\pi} \kappa \right) , \end{aligned} \quad (4.123)$$

where

$$\kappa = C_A \left( \frac{67}{18} - \frac{\pi^2}{6} \right) - T_f \frac{10}{9} . \quad (4.124)$$

An alternative formulation of the evolution equations is in terms of the *moments* (Mellin transforms) of the parton distributions:

$$f(j, t) = \int_0^1 dx x^{j-1} f(x, t) , \quad f = q_i, g . \quad (4.125)$$

In terms of these moments, the  $t$  dependence of a non-singlet quark distribution function is given by

$$t \frac{\partial}{\partial t} q_{NS}(j, t) = \frac{\alpha_s(t)}{2\pi} \gamma_{qq}(j, \alpha_s(t)) q_{NS}(j, t) , \quad (4.126)$$

where the ‘anomalous dimension’  $\gamma_{qq}$  is given by

$$\gamma_{qq}(j, \alpha_s) = \int_0^1 dx x^{j-1} P_{qq}(x, \alpha_s) . \quad (4.127)$$

Similar equations hold for the evolution of the singlet quark and gluon

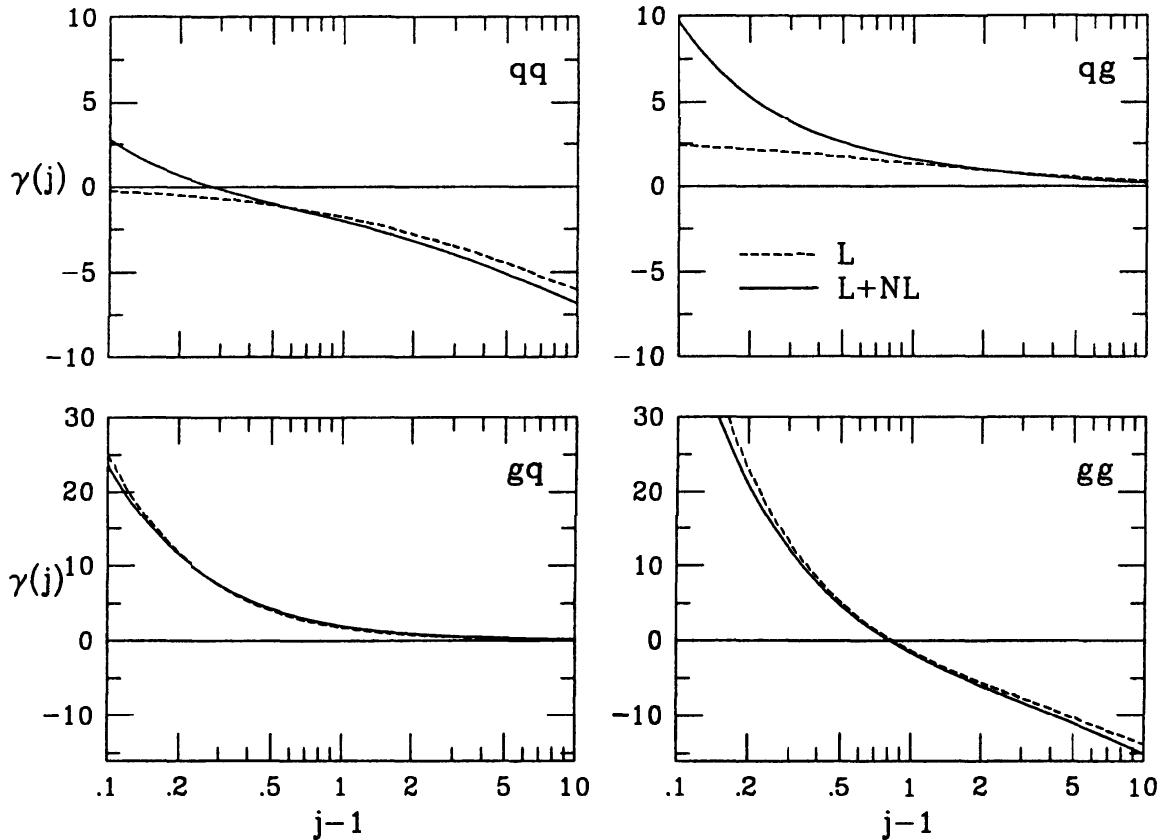


Fig. 4.9. The leading-order and next-to-leading-order singlet anomalous dimensions of Eq. (4.128) in the  $\overline{\text{MS}}$  scheme as a function of the moment number  $j$ , with  $n_f = 4$  and  $\alpha_s/(2\pi) = 1/30$ .

distributions:

$$t \frac{\partial}{\partial t} \begin{pmatrix} \Sigma(j, t) \\ g(j, t) \end{pmatrix} = \frac{\alpha_s(t)}{2\pi} \begin{pmatrix} \gamma_{qq}(j, \alpha_s(t)) & 2n_f \gamma_{qg}(j, \alpha_s(t)) \\ \gamma_{gg}(j, \alpha_s(t)) & \gamma_{gg}(j, \alpha_s(t)) \end{pmatrix} \begin{pmatrix} \Sigma(j, t) \\ g(j, t) \end{pmatrix} \quad (4.128)$$

where  $\Sigma(j, t)$  and  $g(j, t)$  are the moments of the singlet quark and gluon distributions respectively. Notice that by taking moments we have reduced the convolution integral on the right-hand side of the evolution equations to a simple product. In the next section we shall see how this enables us to solve the equations analytically.

The complete set of leading-order anomalous dimensions is

$$\begin{aligned} \gamma_{qq}^{(0)}(j) &= C_F \left[ -\frac{1}{2} + \frac{1}{j(j+1)} - 2 \sum_{k=2}^j \frac{1}{k} \right], \\ \gamma_{qg}^{(0)}(j) &= T_R \left[ \frac{(2+j+j^2)}{j(j+1)(j+2)} \right], \\ \gamma_{gg}^{(0)}(j) &= C_F \left[ \frac{(2+j+j^2)}{j(j^2-1)} \right], \end{aligned}$$

$$\gamma_{gg}^{(0)}(j) = 2C_A \left[ -\frac{1}{12} + \frac{1}{j(j-1)} + \frac{1}{(j+1)(j+2)} - \sum_{k=2}^j \frac{1}{k} \right] - \frac{2}{3} n_f T_R . \quad (4.129)$$

The dependence of the leading- and next-to-leading-order anomalous dimensions of Eq. (4.128) on the moment number  $j$  is illustrated in Fig. 4.9. Using the results

$$\begin{aligned} \int_0^1 dx x^{j-1} \frac{1}{x} &= \frac{1}{j-1} \\ \int_0^1 dx x^{j-1} \frac{1}{(1-x)_+} &= - \int_0^1 dx \frac{x^{j-1} - 1}{(x-1)} \sim -\ln j , \quad \text{for } j \rightarrow \infty , \end{aligned} \quad (4.130)$$

we see that all the anomalous dimensions have poles at  $j = 1$ , and that the diagonal anomalous dimensions grow as  $\ln j$  at large  $j$ . Notice from Fig. 4.9 that fixed-order perturbation theory appears to break down as  $j \rightarrow 1$ . This has important implications for the small- $x$  behaviour of structure functions, and will be discussed in more detail in Section 4.6.

#### 4.3.4 Solution of the leading-order GLAP equations

The solution of the GLAP equation is simplest for (flavour) non-singlet combinations of quark distributions, e.g.  $V = q_i - q_j$ . In such combinations the mixing with the flavour singlet gluon distribution drops out and we have simply

$$t \frac{\partial}{\partial t} V(x, t) = \frac{\alpha_s(t)}{2\pi} [P_{qq}(\xi) \otimes V(z, t)] , \quad (4.131)$$

where we have introduced  $\otimes$  as a shorthand notation for the convolution integral of Eq. (4.88). In terms of moments, this equation becomes

$$t \frac{\partial}{\partial t} V(j, t) = \frac{\alpha_s(t)}{2\pi} \gamma_{qq}^{(0)}(j) V(j, t) , \quad (4.132)$$

with  $\gamma_{qq}^{(0)}(j)$  given in Eq. (4.129). Inserting the lowest-order form (2.43) for the running coupling, we obtain the solution for the moments of the non-singlet distribution,

$$V(j, t) = V(j, t_0) \left( \frac{\alpha_s(t_0)}{\alpha_s(t)} \right)^{d_{qq}(j)} , \quad d_{qq}(j) = \frac{\gamma_{qq}^{(0)}(j)}{2\pi b} \quad (4.133)$$

where  $b = (33 - 2n_f)/12\pi$ . Finally, the distribution in  $x$  space can be obtained using the inverse Mellin transform integral,

$$V(x, t) = \frac{1}{2\pi i} \int_C dj x^{-j} V(j, t) , \quad (4.134)$$

where the integration contour in the complex  $j$  plane is parallel to the imaginary axis and to the right of all singularities of the integrand. Except in very special cases, the inverse transformation can only be performed by numerical integration.

It is straightforward to show that  $d_{qq}(1) = 0$  and that  $d_{qq}(j) < 0$  for  $j \geq 2$ . This in turn implies that as  $\mu^2$  increases the non-singlet distribution function *decreases* at large  $x$  and *increases* at small  $x$ . Physically, this can be understood as an increase in the phase space for gluon emission by the quarks as  $\mu^2$  increases, with a corresponding reduction in quark momentum. The trend is clearly visible in the data. Fig. 4.10 shows data on the structure function  $F_2^{\mu p}$  from the BCDMS [4] and NMC [18] collaborations. The slope  $\partial F_2 / \partial \ln Q^2$  is negative at large  $x$  and positive at small  $x$  respectively. In the limits  $x \rightarrow 0$  and  $x \rightarrow 1$  it is in fact possible to derive analytic approximations to the solution of the evolution equation. The small- $x$  behaviour is determined by the rightmost singularities of the anomalous dimensions  $\gamma_{ab}(j)$  on the positive real axis, and will be discussed in detail in Section 4.6. The large- $x$  behaviour, on the other hand, is controlled by the form of the anomalous dimensions at large, real  $j$ . In particular, suppose that we look for a large- $x$  solution of the form  $V(x, t) \sim (1 - x)^{a(t)}$ . The large- $j$  moments of such a solution are  $V(j, t) \sim j^{-a(t)}$ . From Eq. (4.129) we have also that

$$\gamma_{qq}(j) \sim -2C_F \ln j, \quad j \gg 1, \quad (4.135)$$

so that the large- $j$  limit of the right-hand side of the solution (4.133) is

$$j^{-a(t_0)} \left( \frac{\alpha_s(t_0)}{\alpha_s(t)} \right)^{-C_F \ln j / \pi b} = j^{-a(t_0) - C_F \ln(\alpha_s(t_0)/\alpha_s(t)) / \pi b}. \quad (4.136)$$

The solution of the evolution equation in the  $x \rightarrow 1$  limit is therefore

$$V(x, t) \sim (1 - x)^{a_0 + C_F \ln(\alpha_s(t_0)/\alpha_s(t)) / \pi b}, \quad (4.137)$$

where  $a_0$  is the exponent at the starting scale  $t_0$ . As  $t$  increases, the exponent grows linearly with  $\ln \ln t$ , confirming that the distribution decreases at large  $x$  as the scale increases.

We now turn to the flavour singlet combination of quark distributions. At leading order we have

$$\begin{aligned} t \frac{\partial \Sigma}{\partial t} &= \frac{\alpha_s(t)}{2\pi} \left[ P_{qq}^{(0)} \otimes \Sigma + 2n_f P_{qg}^{(0)} \otimes g \right] + O(\alpha_s^2(t)) \\ t \frac{\partial g}{\partial t} &= \frac{\alpha_s(t)}{2\pi} \left[ P_{gq}^{(0)} \otimes \Sigma + P_{gg}^{(0)} \otimes g \right] + O(\alpha_s^2(t)). \end{aligned} \quad (4.138)$$

These equations are most easily solved by direct numerical integration in  $x$  space starting with input distributions obtained from data. The analytic solution in moment space, which requires finding the eigenvectors

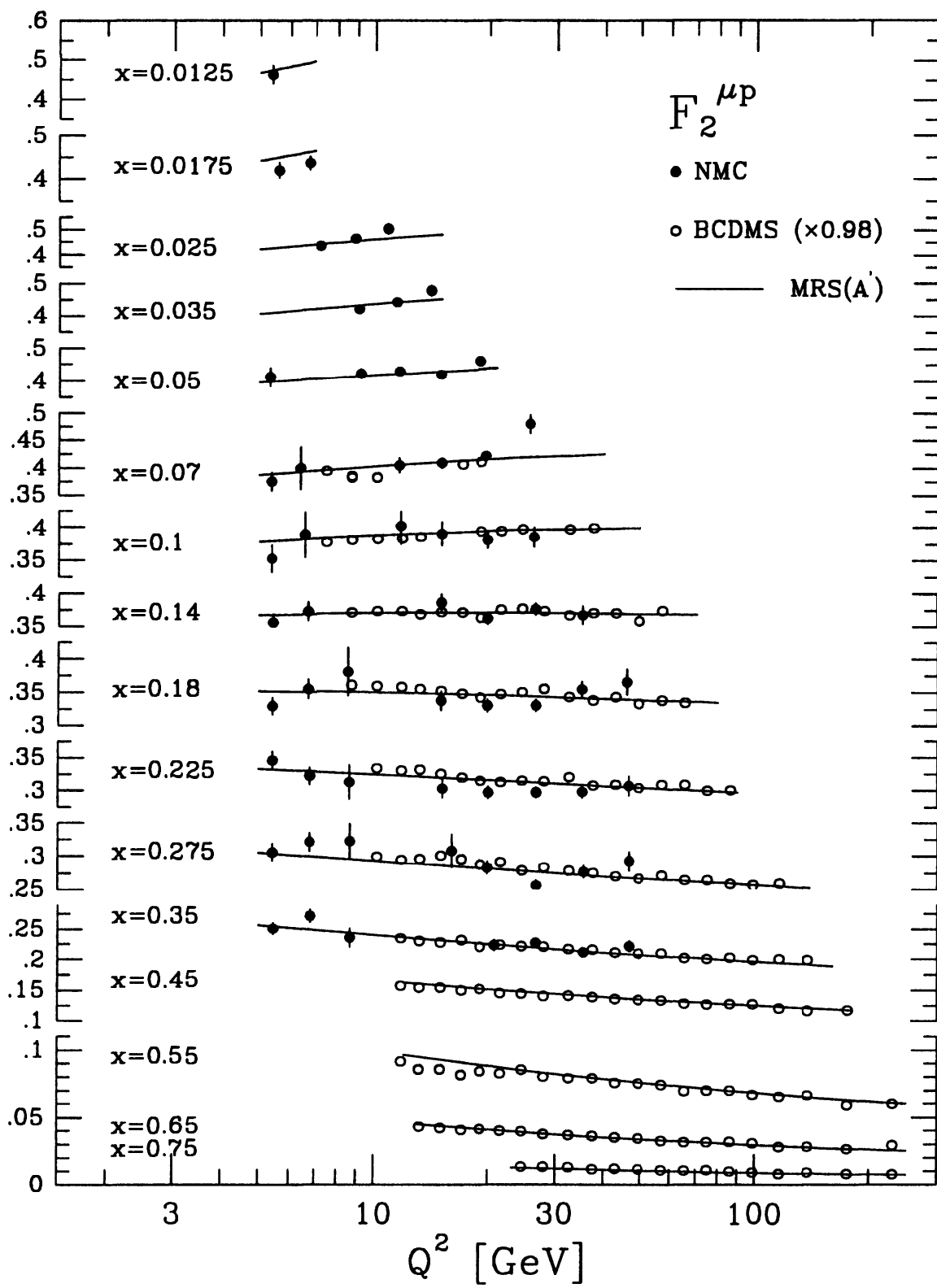


Fig. 4.10. Data on the structure function  $F_2$  in muon-proton deep inelastic scattering, from BCDMS [4] and NMC [18]. The curves are QCD fits [7] as described in the text.

and eigenvalues of the  $2 \times 2$  matrix of anomalous dimensions, is rather cumbersome. The eigenvalues  $\gamma_{\pm}$  are the solutions of the quadratic equation given by

$$\begin{vmatrix} \gamma_{qq} - \gamma & 2n_f \gamma_{qg} \\ \gamma_{gq} & \gamma_{gg} - \gamma \end{vmatrix}, \quad (4.139)$$

i.e.

$$\gamma_{\pm} = \frac{1}{2} \left[ \gamma_{gg} + \gamma_{qq} \pm \sqrt{(\gamma_{gg} - \gamma_{qq})^2 + 8n_f \gamma_{gq} \gamma_{qg}} \right]. \quad (4.140)$$

The moment method can be used to illustrate some simple analytic properties of the solutions. For the second ( $j = 2$ ) moment we have

$$t \frac{\partial}{\partial t} \begin{pmatrix} \Sigma(2, t) \\ g(2, t) \end{pmatrix} = \frac{\alpha_s(t)}{2\pi} \begin{pmatrix} -\frac{4}{3}C_F & \frac{1}{3}n_f \\ \frac{4}{3}C_F & -\frac{1}{3}n_f \end{pmatrix} \begin{pmatrix} \Sigma(2, t) \\ g(2, t) \end{pmatrix}. \quad (4.141)$$

The eigenvectors and associated eigenvalues of this system of equations are

$$\begin{aligned} O^+(2, t) &= \Sigma(2, t) + g(2, t) \quad \text{with eigenvalue } 0, \\ O^-(2, t) &= \Sigma(2, t) - \frac{n_f}{4C_F} g(2, t) \quad \text{with eigenvalue } -\left(\frac{4}{3}C_F + \frac{n_f}{3}\right). \end{aligned} \quad (4.142)$$

Note that the combination  $O^+$ , which corresponds to the total momentum carried by the quarks and gluons, is independent of  $t$ . The eigenvector  $O^-$  vanishes in the limit  $t \rightarrow \infty$ :

$$O^-(2, t) = \left( \frac{\alpha_s(t_0)}{\alpha_s(t)} \right)^{d^-(2)} \rightarrow 0, \quad \text{with } d^-(2) = \frac{\gamma_-(2)}{2\pi b} = -\frac{\left(\frac{4}{3}C_F + \frac{1}{3}n_f\right)}{2\pi b}, \quad (4.143)$$

so that asymptotically we have

$$\frac{\Sigma(2, t)}{g(2, t)} \rightarrow \frac{n_f}{4C_F} = \frac{3}{16}n_f. \quad (4.144)$$

The momentum fractions  $f_q$  and  $f_g$  carried by the quarks and gluons in the  $\mu^2 = t \rightarrow \infty$  limit are therefore

$$f_q = \frac{3n_f}{16 + 3n_f}, \quad f_g = \frac{16}{16 + 3n_f}. \quad (4.145)$$

Note, however, that the approach to this asymptotic limit is controlled by  $\ln t$  and is therefore quite slow. Expressions for the eigenvectors and eigenvalues of the moments of Eq. (4.138) can be found in ref. [19].

From the solution of the evolution equations for the moments of non-singlet and singlet combinations of quark distributions, the evolution of

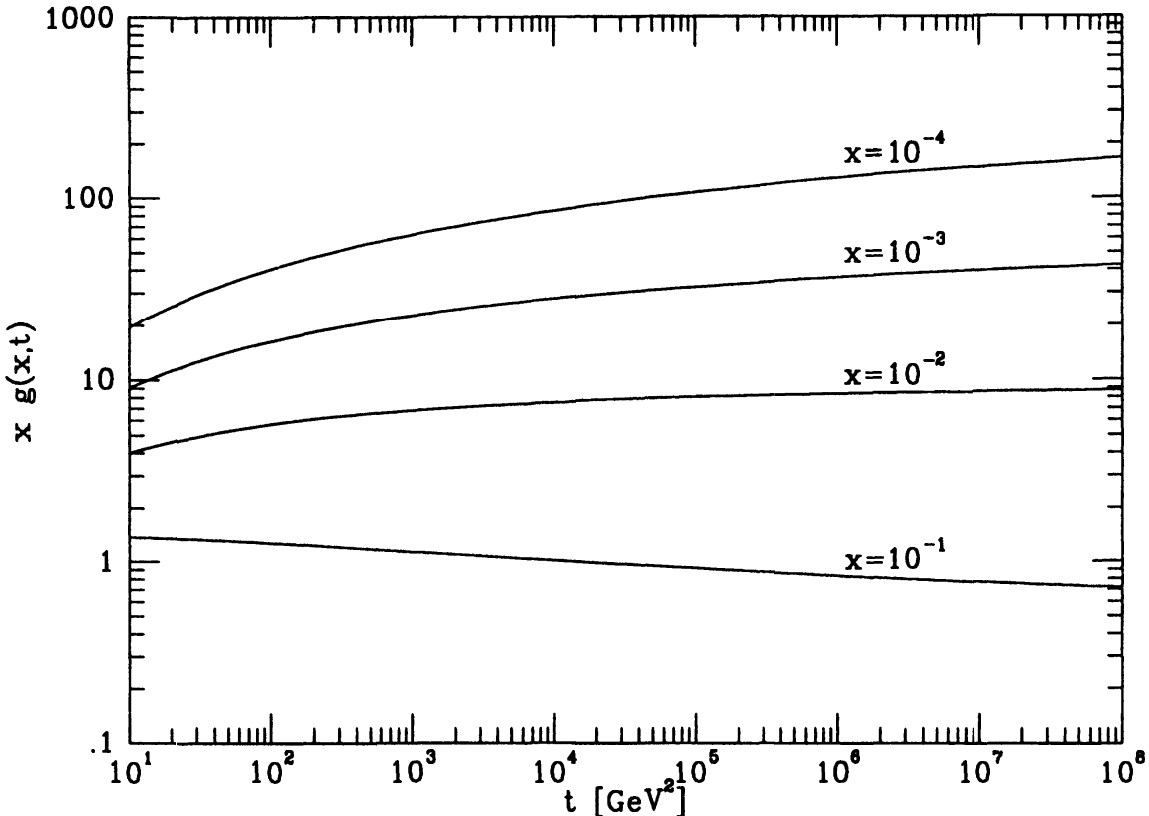


Fig. 4.11. The scale dependence of the gluon distribution.

the moments of any individual flavour of quark distribution can be determined. The  $x$  distributions themselves are then obtained by an inverse Mellin transformation, *cf.* Eq. (4.134),

$$f_a(x, \mu^2) = \frac{1}{2\pi i} \int_C dj x^{-j} f_a(j, \mu^2), \quad a = q_i, g. \quad (4.146)$$

An alternative method of solution, which avoids a numerical integration in the complex plane, is to solve the integro-differential evolution equations directly in  $x$  space by a numerical procedure. This is particularly convenient if a simultaneous solution for all  $(2n_f + 1)$  parton distributions is required, given a set of starting distributions  $f_a(x, \mu_0^2)$  at some reference scale  $\mu_0$ . In either the moment or direct integration method, the inclusion of higher-order contributions to the splitting function, Eq. (4.91), is relatively straightforward.

Figs. 4.11, 4.12 and 4.13 illustrate the scale dependence of the gluon, valence up-quark and up-antiquark distributions [7] respectively. In each case, the distributions decrease with increasing scale at large  $x$ , and increase at small  $x$ . Fig. 4.14 shows the momentum fractions carried by the individual quarks and gluons as functions of the scale.

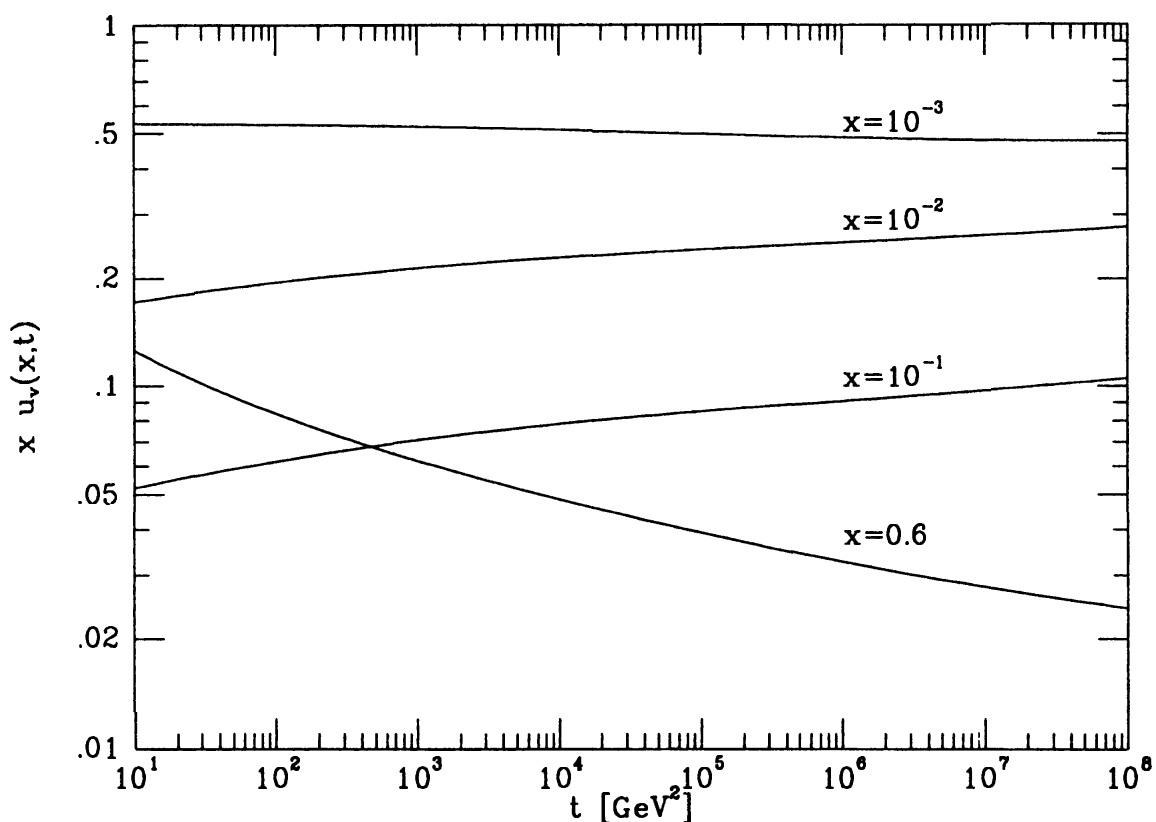


Fig. 4.12. The scale dependence of the valence up-quark distribution.

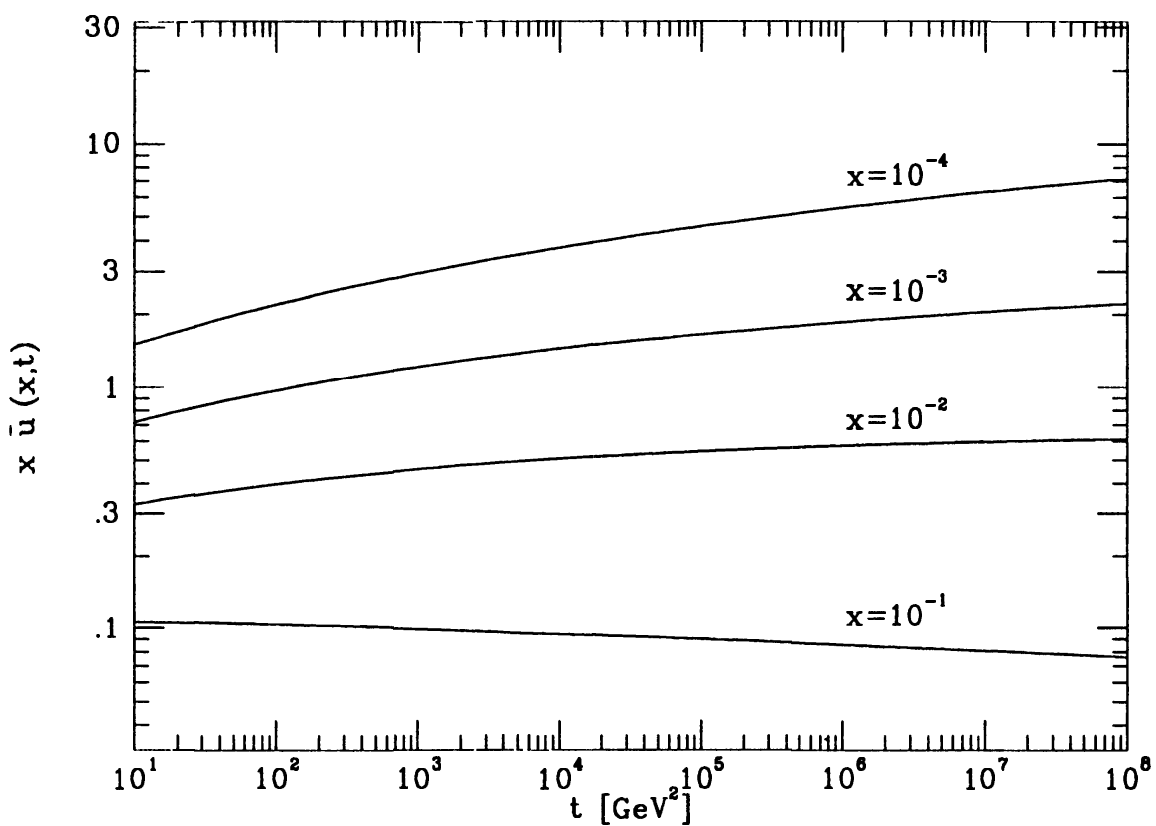


Fig. 4.13. The scale dependence of the up-antiquark distribution.

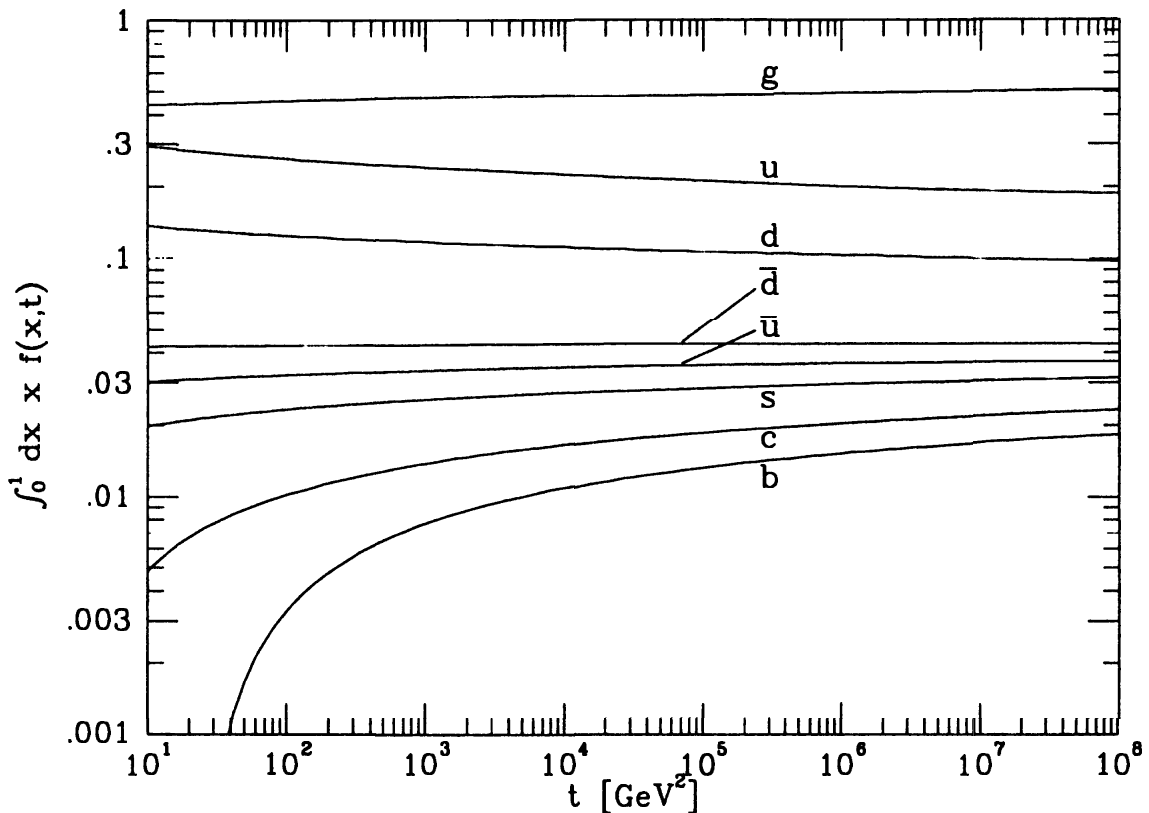


Fig. 4.14. Momentum fractions carried by the quarks and gluons as functions of the scale.

#### 4.4 QCD fits to deep inelastic data

In the previous section we saw that perturbative QCD predicts the  $Q^2$  evolution of the structure functions, rather than the size and shape of the functions themselves. In particular, for non-singlet structure functions ( $F_2^{\mu p} - F_2^{\mu n}$  and  $xF_3^{\nu N}$  are examples in practice — see Eq. (4.17)) the variation with  $Q^2$  is comparatively simple,

$$Q^2 \frac{\partial}{\partial Q^2} F_{\text{NS}}(x, Q^2) = \frac{\alpha_s(Q^2)}{2\pi} \int_x^1 \frac{d\xi}{\xi} F_{\text{NS}}(\xi, Q^2) \frac{x}{\xi} P\left(\frac{x}{\xi}\right). \quad (4.147)$$

For structure functions like  $F_2^{\mu p}$ , which is a linear combination of singlet and non-singlet pieces, the differential equation has an additional term on the right-hand side proportional to the gluon distribution. Quantitatively, the strength of the scaling violation is controlled by  $\alpha_s(Q^2)$  and hence by the QCD scale parameter  $\Lambda$ . Deep inelastic scattering data of the type shown in Fig. 4.10, therefore, provide one of the precision tests of QCD and one of the most accurate determinations of  $\alpha_s$ .

Although the theoretical predictions appear simplest when expressed in terms of structure function moments, it is difficult to extract such moments from the data. This is because the measurements do not extend

to very large and very small  $x$ , and some form of *ad hoc* extrapolation is required to construct the moment integrals. A more practical and accurate method is to choose a reference value  $Q_0$  and parametrize the parton distributions at that value, *e.g.*  $q(x, Q_0^2) = Ax^a(1 + c\sqrt{x} + dx)(1 - x)^b$ . These distributions are then evolved numerically, using the GLAP equations, to obtain values for the  $F_i(x, Q^2)$  in the kinematic regions where they are measured. Note that in this approach the rate of change with  $Q^2$  of the structure function at a given  $x$  manifestly depends only on the structure function evaluated at  $\xi > x$ . Finally, a global numerical fit is performed to determine the ‘best’ values for the parameters, including  $\Lambda$ . The extent to which the measured value of  $\Lambda$  depends on the other parameters can also be quantified and used to derive a systematic error.

The above procedure is not, however, without problems. In QCD, the structure functions have ‘higher-twist’ power corrections, which are much more difficult to estimate quantitatively:

$$F(x, Q^2) = F^{(2)}(x, Q^2) + \frac{F^{(4)}(x, Q^2)}{Q^2} + \dots, \quad (4.148)$$

where the superscripts on the right-hand side refer to the ‘twist’ = (dimension – spin) of the contributing operators. Such power corrections are indeed visible in the structure function data — a phenomenological fit to both low- and high- $Q^2$   $F_2^{lp}$  data [20] of the form  $F^{(4)} = C(x)F^{(2)}$  yields

$$C(x) \approx 0.5 \text{ GeV}^2 \Theta(x - \tfrac{1}{3}) \left( \frac{1}{1-x} - \frac{3}{2} \right), \quad (4.149)$$

where  $\Theta(z) = 1$  for  $z > 0$  and 0 for  $z < 0$ . The term proportional to  $(1-x)^{-1}$  is expected on general theoretical grounds — there are  $j$  times more operators which contribute to the  $j$ th moment of  $F^{(4)}$  than to  $F^{(2)}$ . Therefore at large  $j$  the moments are expected to differ by a factor of  $j$ , corresponding to a factor  $(1-x)^{-1}$  difference in the contributions to the structure function. To avoid complications from higher-twist contributions in extracting parton distributions and a value of  $\Lambda$ , the analysis must be performed at large  $(1-x)Q^2$  where such contributions are expected to be negligible.

A second problem is that the most precise data are for  $F_2$  measured in fixed-target electron, muon and neutrino scattering on nucleon and nuclear targets. Except at large  $x$ , the  $Q^2$  variation of these is sensitive to the *a priori* unknown gluon distribution and there is potentially a strong  $\Lambda$ -gluon correlation. Although the evolution of *non-singlet* structure functions does not suffer from this problem, see Eq. (4.147), these are only measurable experimentally by constructing differences between cross sections, *e.g.*  $\sigma^{\mu p} - \sigma^{\mu n}$ . This inevitably introduces additional systematic

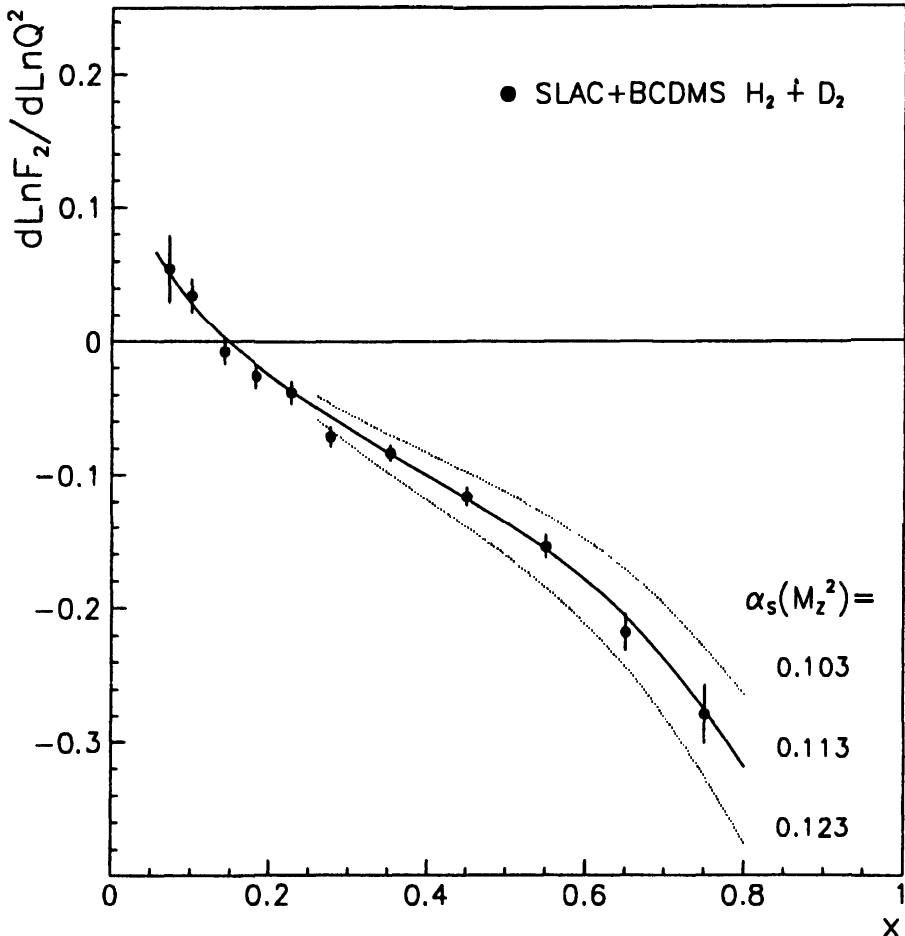


Fig. 4.15. Logarithmic  $Q^2$  derivative of the  $F_2$  structure function measured on hydrogen and deuterium together with QCD fits. Figure from ref. [20].

and statistical uncertainties.

The most recent generation of fixed-target deep inelastic experiments partially solve these problems by collecting high statistics data at large  $x$  and  $Q^2$ . In fact the precision of contemporary data demands that the next-to-leading-order QCD corrections are incorporated in the fits. Beyond leading order a specific renormalization scheme must be chosen, in addition to the factorization scheme discussed in the previous section, and in practice this is usually the  $\overline{\text{MS}}$  scheme. For this reason the results quoted in the literature almost always refer to  $\Lambda_{\overline{\text{MS}}}$ .

Some of the most precise data come from the BCDMS collaboration [4,21]. As an example, Fig. 4.10 shows the structure function  $F_2$  measured by BCDMS in deep inelastic muon-hydrogen scattering, together with similar data from the NMC collaboration [18]. The measurements extend up to  $x$  values of 0.75 and  $Q^2$  values of several hundred  $\text{GeV}^2$ . Fig. 4.15 shows the  $\ln Q^2$  derivative of  $\ln F_2$  as a function of  $x$ , obtained from a combined analysis [20] of BCDMS [4,21] and SLAC [22] data. Note that the derivatives in the high- $x$  (low- $x$ ) region are negative (positive),

consistent with a structure function which decreases (increases) with increasing  $Q^2$ . The solid line in Fig. 4.15 is a next-to-leading-order QCD fit, which gives [20]

$$\Lambda_{\overline{\text{MS}}}^{(4)} = 263 \pm 42 \text{ MeV}. \quad (4.150)$$

Using the formulae given in Section 2.5, it is straightforward to convert this to a value of  $\alpha_s(M_Z^2)$ :

$$\alpha_s(M_Z^2) = 0.113 \pm 0.003. \quad (4.151)$$

Note that four light quark flavours are generally appropriate for the range of  $Q^2$  probed by fixed-target deep inelastic scattering experiments. In ref. [20] an additional theoretical uncertainty in  $\alpha_s(M_Z^2)$  is estimated by varying the values of the renormalization and factorization scales in the fit about the nominal choice  $\mu_R^2 = \mu_F^2 = Q^2$ . This gives  $\Delta\alpha_s(M_Z^2)(\text{theory}) = \pm 0.004$ , which when combined with the experimental error in (4.151) gives

$$\alpha_s(M_Z^2) = 0.113 \pm 0.005, \quad (4.152)$$

one of the most precise measurements of the strong coupling constant. This value is compared with determinations from other processes in Chapter 12. Note that the broken lines in Fig. 4.15 correspond to  $\Delta\alpha_s(M_Z^2) = \pm 0.010$ .

Fixed-target experiments measure quark distributions very accurately over a broad range in  $x$  ( $\sim 0.01 - 0.8$ ) up to scales of order  $\mu^2 \sim 200 \text{ GeV}^2$ . (The HERA high-energy  $ep$  collider is able to extend the  $x$  range down to very small values — see below.) Knowing  $\Lambda_{\overline{\text{MS}}}$ , one can then evolve these to higher  $\mu^2$  and use them for hadron collider phenomenology. Instead of laboriously integrating the GLAP equations each time a parton distribution is required, it is useful to have an analytic approximation, valid to a sufficient accuracy over a prescribed  $(x, \mu^2)$  range. Such parametrizations are widely available. An analytic form which is commonly used is

$$\begin{aligned} q(x, \mu^2) &= Ax^a(1 + c\sqrt{x} + dx)(1 - x)^b \\ A &= A_0 + A_1 s + A_2 s^2 \\ a &= a_0 + a_1 s + a_2 s^2 \quad \text{etc.} \\ s &= \ln\left(\frac{\ln(\mu^2/\Lambda^2)}{\ln(\mu_0^2/\Lambda^2)}\right) > 0, \end{aligned} \quad (4.153)$$

with the parameters  $A_0, A_1, \dots$  fitted to an exact numerical solution of the leading-order or next-to-leading-order evolution equations, to an accuracy at the per cent level. Because deep inelastic scattering data do not significantly constrain the gluon distribution, it is necessary to include in the parton distribution fit data from other processes where the gluon distribution plays a more leading role. An example of such a process is the

production of large transverse momentum photons in hadron-hadron collisions, where the leading-order  $qg \rightarrow \gamma q$  scattering process is important. In this way data from high precision fixed-target direct photon experiments are able to constrain the gluon distribution, particularly in the medium  $x$  ( $\sim 0.2 - 0.4$ ) range. This will be discussed in more detail in Chapter 7.

A recent set of parton distributions [7] resulting from a global next-to-leading-order QCD fit to deep-inelastic scattering, prompt photon and other data is shown in Fig. 4.3, at scale  $\mu^2 = 10 \text{ GeV}^2$ . Distributions like these cover a wide range in  $x$  and  $\mu^2$ , and are invaluable for making quantitative predictions for present and future hadron-hadron and lepton-hadron colliders.

## 4.5 Sum rules

In Section 4.1 we saw how the integrals over certain combinations of parton distributions had particular values in the parton model. Several examples were given in Eq. (4.24). Such integrals are called sum rules. In QCD these sum rules remain valid, up to perturbative corrections, because of the vanishing of the first moment of the non-singlet anomalous dimensions to all orders in perturbation theory. At lowest order in  $\alpha_s$  this property is evident in Eqs. (4.129,4.133). In practice the sum rules provide a variety of information, from constraints on parton distributions and tests of conservation laws to precision measurements of  $\alpha_s$ . In this section we shall describe some of the more important sum rules.

### 4.5.1 Gross-Llewellyn Smith sum rule

The Gross–Llewellyn Smith sum rule [23] applies to the  $F_3$  structure function measured in neutrino– and antineutrino–proton scattering:

$$I_{GLS} = \frac{1}{2} \int_0^1 dx (F_3^{\nu p} + F_3^{\bar{\nu} p}) . \quad (4.154)$$

In the parton model, we can substitute for the structure functions using (4.17) to obtain

$$\begin{aligned} I_{GLS} &= \int_0^1 dx (d - \bar{u} + u - \bar{d}) \\ &= \int_0^1 dx (u_V + d_V) \\ &= 3 . \end{aligned} \quad (4.155)$$

In perturbative QCD there are finite  $O(\alpha_s)$  corrections, so that the parton model value is only attained in the  $Q^2 \rightarrow \infty$  limit:

$$I_{GLLS}(Q^2) = 3 \left[ 1 + d_1 \frac{\alpha_s}{\pi} + d_2 \left( \frac{\alpha_s}{\pi} \right)^2 + d_3 \left( \frac{\alpha_s}{\pi} \right)^3 + \dots \right] \quad (4.156)$$

where  $\alpha_s \equiv \alpha_s(\mu^2)$  and the coefficients are functions of  $Q^2/\mu^2$ . In the  $\overline{\text{MS}}$  renormalization scheme with  $\mu^2 = Q^2$ ,

$$\begin{aligned} d_1 &= -1 \quad [9, 10] \\ d_2 &= -\frac{55}{12} + n_f \frac{1}{3} \quad [24] \\ d_3 &= -\frac{13841}{216} - \frac{44}{9} \zeta(3) + \frac{55}{2} \zeta(5) \\ &\quad + n_f \left( \frac{10009}{1296} + \frac{91}{54} \zeta(3) - \frac{5}{3} \zeta(5) \right) - n_f^2 \frac{115}{648} \quad [25] \end{aligned} \quad (4.157)$$

where  $C_F = 4/3$  and  $C_A = 3$  have been substituted. The values of the Riemann zeta functions are given in Eq. (3.19). The CCFR collaboration [26] have measured the Gross–Llewellyn Smith sum in (anti)neutrino–nucleon scattering at  $\langle Q^2 \rangle \sim 3 \text{ GeV}^2$ . This has been used to measure  $\alpha_s$ , as will be discussed in Chapter 12.

#### 4.5.2 Adler sum rule

The Adler sum rule [27] applies to the  $F_2$  structure function measured in neutrino– and antineutrino–proton scattering:

$$\begin{aligned} I_A &= \int_0^1 \frac{dx}{x} (F_2^{\nu p} - F_2^{\bar{\nu} p}) \\ &= 4 \langle I_3 \rangle = 2 \end{aligned} \quad (4.158)$$

where  $I_3$  is the third component of the isospin of the target, which for a proton is equal to one half. The value of  $I_A$  is exact and follows from the conservation of the charged weak current. Unlike the Gross–Llewellyn Smith sum rule there are no higher-order perturbative or higher-twist power corrections. Unfortunately the sum rule is not straightforward to measure, since all of the high precision neutrino scattering data is taken on heavy (approximately isoscalar) nuclear targets. (Note that for an isoscalar target  $F_2^{\nu N} = F_2^{\bar{\nu} N}$ , and so the integral corresponding to Eq. (4.158) vanishes.) The only measurement in the literature is from the BEBC collaboration [28]:

$$I_A = 2.02 \pm 0.40, \quad (4.159)$$

in agreement with the theoretical prediction (4.158).

### 4.5.3 Gottfried sum rule

Important information on the sea quark distributions is provided by the Gottfried sum [29],

$$I_G = \int_0^1 \frac{dx}{x} (F_2^{\mu p} - F_2^{\mu n}) . \quad (4.160)$$

Again using the parton model expressions given in Section 4.1, together with isospin symmetry to relate the distributions in protons and neutrons, we find

$$\begin{aligned} I_G &= \frac{1}{3} \int_0^1 dx (u_V - d_V + \bar{u} - \bar{d}) \\ &= \frac{1}{3} + \int_0^1 dx (\bar{u} - \bar{d}) . \end{aligned} \quad (4.161)$$

In particular, if the quark sea is symmetric under the interchange of  $u$  and  $d$ , then one obtains the Gottfried sum rule  $I_G = 1/3$ . However, the measurement from the NMC collaboration is [30]

$$I_G (0.004 < x < 0.8) = 0.236 \pm 0.008 . \quad (4.162)$$

Note that the measurement, and hence the integral, does not extend either to  $x = 0$  or to  $x = 1$ . This is a problem with all such sum rule measurements. However, with a reasonable extrapolation outside the measured range one finds [30] that the sum rule  $I_G = 1/3$  is badly violated, indicating a strong light quark flavour asymmetry in the sea,

$$\int_0^1 dx (\bar{u} - \bar{d}) \approx -0.1 . \quad (4.163)$$

The constraint from the Gottfried sum is incorporated in the most recent global parton distribution fits. For example, Fig. 4.3 shows a clear difference between the  $\bar{u}$  and  $\bar{d}$  distributions in the MRS(A) partons [7].

## 4.6 Deep inelastic scattering at small $x$

The form of the parton distributions in the small- $x$  region is of considerable theoretical interest. In the parton model, one can show that the  $x$  dependence in the limit  $x \rightarrow 0$  is related by Regge theory to the behaviour of hadronic scattering cross sections at high energy. As these arguments are based on non-perturbative dynamics, they presumably relate to the distributions at a typical hadronic scale,  $\mu^2 \sim 1 \text{ GeV}^2$ . We have already seen that perturbative GLAP evolution causes the distributions to rise with increasing  $\mu^2$  at small  $x$ . In fact, in certain circumstances the behaviour in the double asymptotic limit  $x \rightarrow 0, \mu^2 \rightarrow \infty$  can be determined analytically.

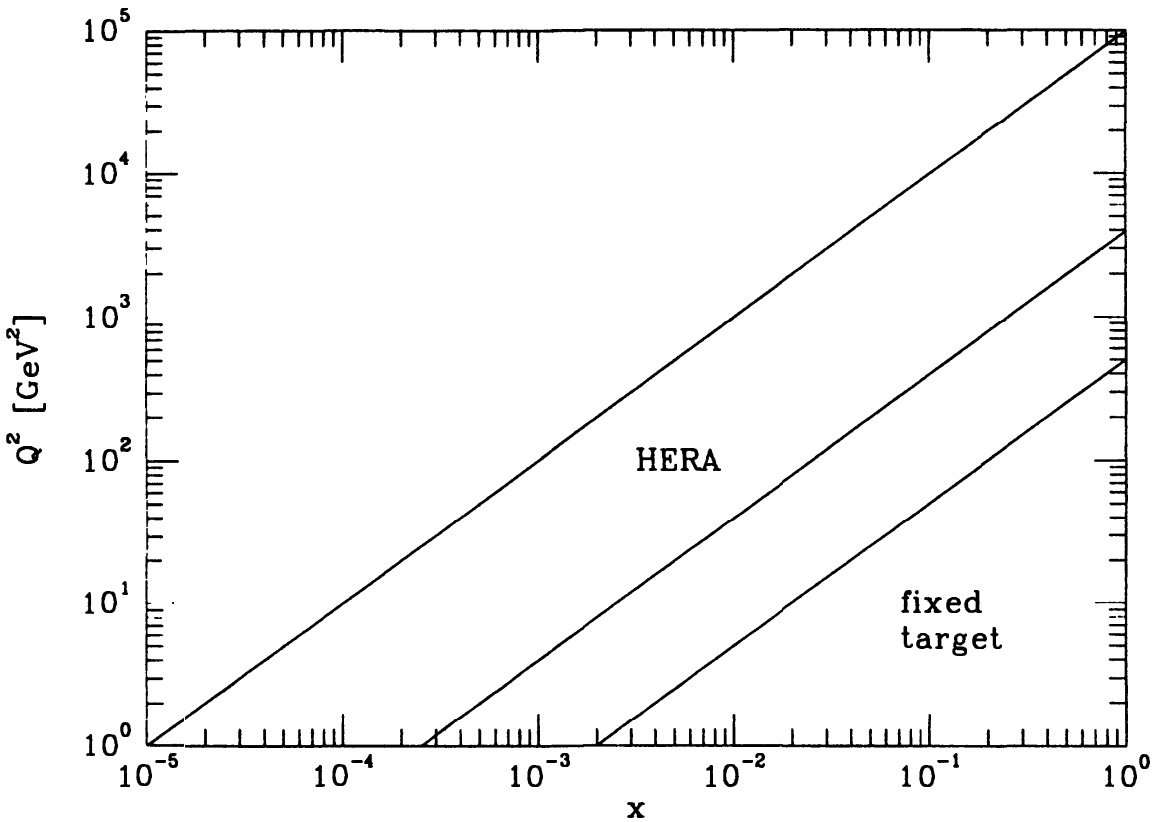


Fig. 4.16. Kinematic region for HERA and fixed-target deep inelastic scattering experiments.

To test these theoretical ideas requires precise structure function measurements at very small  $x$ , and in a range of  $Q^2$  which spans both the perturbative and non-perturbative regimes. The HERA high-energy electron-proton collider ( $\sqrt{s_{ep}} \sim 300$  GeV) provides the ideal kinematic conditions for such measurements. In practice, the range in  $x$  and  $Q^2$  is approximately determined by the limits on the variable  $y$  defined in Eq. (4.1):

$$y_{min} < y = \frac{Q^2}{xs_{ep}} < 1. \quad (4.164)$$

Taking the typical values  $\sqrt{s_{ep}} = 314$  GeV and  $y_{min} = 0.04$  gives the region in the two-dimensional  $x$  and  $Q^2$  plane shown in Fig. 4.16. Also shown is the region corresponding to fixed-target experiments. We see immediately that the HERA kinematics allow (i) tests of GLAP evolution at medium and large  $x$  to very high  $Q^2$  values (but recall from Eq. (4.5) that the cross section at fixed  $x$  decreases rapidly, as  $1/Q^4$ ), and (ii) a test of the small- $x$  behaviour down to  $x \sim 10^{-5}$  in the deep inelastic regime. The crucial point here is that at such small- $x$  values  $\ln(1/x)$  can be regarded as a ‘large logarithm’, and a perturbative treatment which resums these large logarithms to all orders may be applicable. In the sections which follow we will describe several approximations to the small-

$x$  behaviour based on perturbation theory. First, however, we discuss the original non-perturbative Regge arguments for structure functions in the  $x \rightarrow 0$  limit.

#### 4.6.1 Regge theory

In Section 4.2 we saw how in the parton model the deep inelastic structure functions can be extracted from the hadronic tensor  $W^{\alpha\beta}(p, q)$ , which in turn is obtained from the handbag diagram, Fig. 4.4. The invariant mass of the system left behind when the quark is removed from the proton is  $s_0 = (p - k)^2$ . Using the decomposition of the quark four-momentum given in Eq. (4.37), we have (setting the proton mass to zero)

$$s_0 = k^2 - 2p \cdot k = \frac{-k^2(1-x) - k_T^2}{x}, \quad (4.165)$$

and so  $s_0 \rightarrow \infty$  as  $x \rightarrow 0$ . Now according to Regge theory, the high-energy behaviour of an elastic hadron scattering amplitude is controlled by a sequence of Regge trajectories corresponding to the exchange of families of particles with different spin, see for example ref. [31]. Applying this to the quark-proton amplitude  $B$  in the  $s_0 \rightarrow \infty$  limit gives

$$B \sim \beta_P s_0^{\alpha_P - 1} + \beta_R s_0^{\alpha_R - 1} + \dots, \quad (4.166)$$

where the leading trajectories are

$$\begin{aligned} \alpha_P &\simeq 1 && \text{pomeron } \mathcal{P} \\ \alpha_R &\simeq \frac{1}{2} && \rho, \omega, a_2, f_2, \dots \end{aligned} \quad (4.167)$$

Inserting this behaviour into the parton-model calculation of the  $F_2$  structure function, Eq. (4.39), gives the leading small- $x$  behaviour

$$F_2(x) \sim \beta_P x^{1-\alpha_P} + \beta_R x^{1-\alpha_R}. \quad (4.168)$$

We may interpret the two terms in (4.168) as the contributions to the structure function from the flavour-singlet quark sea, with behaviour determined by the leading ‘pomeron’ trajectory  $\alpha_P$ , and from the flavour-non-singlet valence quarks, with behaviour controlled by the ‘reggeon’ trajectory  $\alpha_R$ . We would likewise expect that the behaviour of the gluon distribution at small  $x$  would also be determined by the pomeron trajectory, yielding the predictions

$$S, g \sim x^{-1}, \quad qv \sim x^{-\frac{1}{2}} \quad (4.169)$$

in the  $x \rightarrow 0$  limit, or equivalently

$$F_2^p \sim x^0, \quad F_2^p - F_2^n \sim x^{\frac{1}{2}}. \quad (4.170)$$

A detailed analysis of small- $x$  structure function measurements at fixed-target energies [32] shows that they are indeed approximately consis-

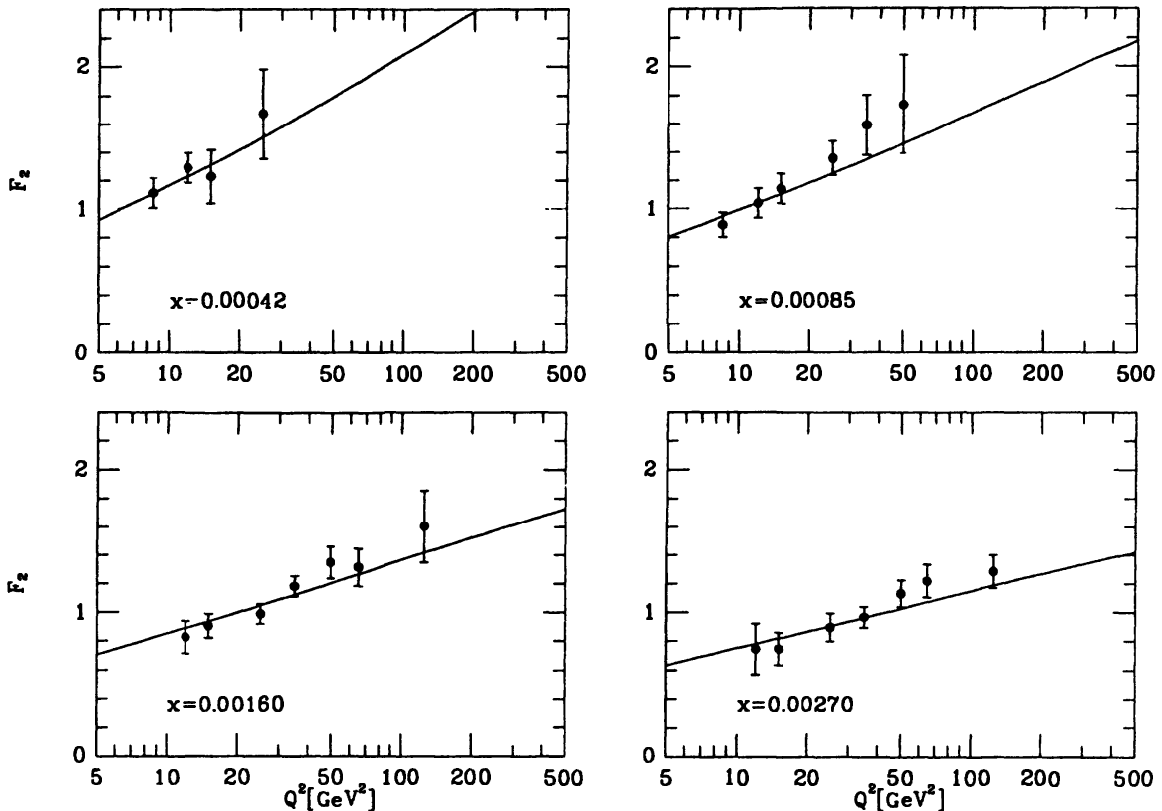


Fig. 4.17. The description of  $F_2$  data from the ZEUS collaboration [6] at HERA by a NLO QCD fit from ref. [33].

tent with the predictions of Regge theory. For example, the behaviour  $F_2 \sim \text{constant}$  at small  $x$  is evident in the fixed-target data shown in Fig. 4.2. However this figure also shows an apparent steepening of the behaviour at small  $x$  as  $Q^2$  increases. An attractive interpretation of this rise is that it is caused by the onset of the perturbative GLAP evolution described in Section 4.3, with the non-perturbative Regge theory describing the form of the starting distributions for the evolution, at a typical hadronic scale of order 1 GeV $^2$ . Indeed the HERA small- $x$   $F_2$  data are very well described by NLO GLAP-based fits. As an example, Fig. 4.17 shows the description of data from the ZEUS collaboration [6] by a NLO QCD fit from ref. [33]. Note that  $F_2$  grows approximately linearly with  $\ln Q^2$  at small  $x$ , consistent with the theoretical prediction. The starting distributions in this fit have

$$S, g \sim x^{-1.17} \quad \text{at } \mu_0^2 = 4 \text{ GeV}^2 , \quad (4.171)$$

in line with Regge theory expectations.

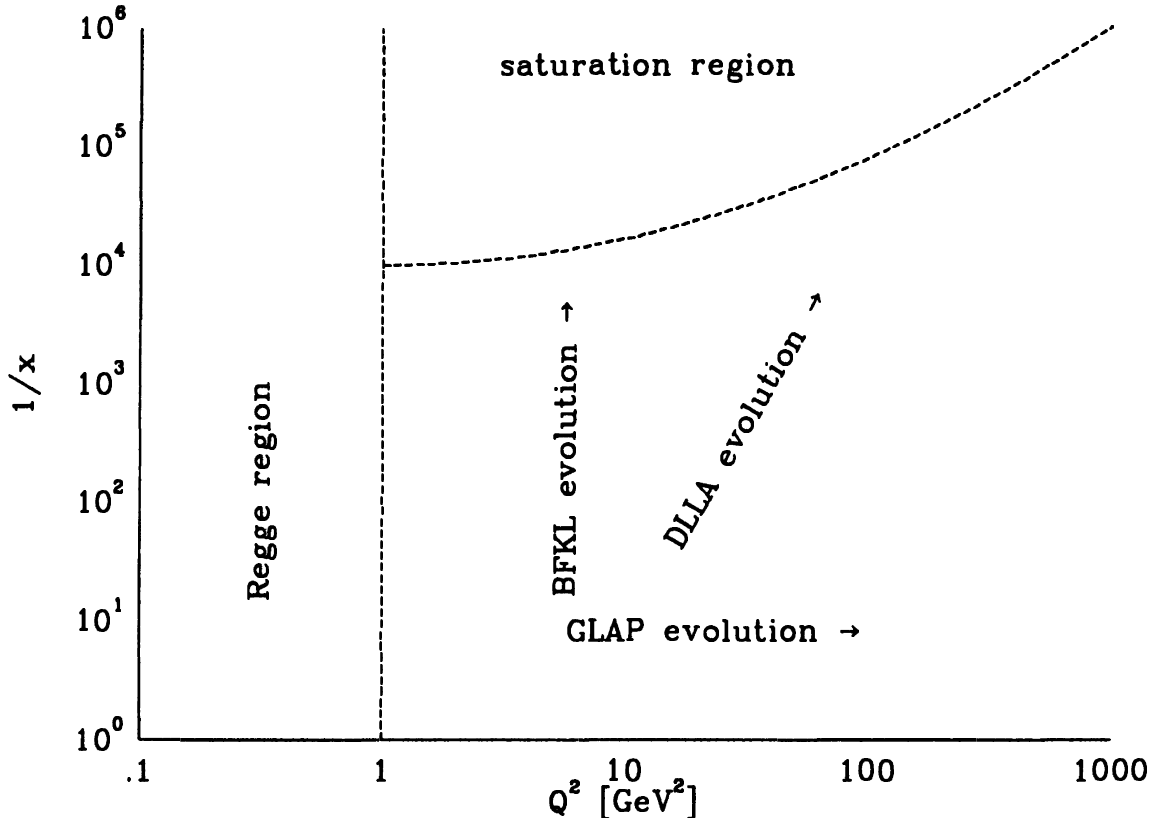


Fig. 4.18. The various regions of the  $1/x$  vs  $Q^2$  plane discussed in the text.

#### 4.6.2 The double asymptotic limit $Q^2 \rightarrow \infty, x \rightarrow 0$

If the parton distributions at the starting scale  $t_0$  ( $= \mu_0^2$ ) are indeed specified by Regge theory, i.e.  $q(x, t_0), g(x, t_0) \sim x^{-1}$  for  $x \ll 1$ , then we see from Figs. 4.11 and 4.17 that the evolution causes the distributions to grow rapidly at small  $x$  with increasing  $t$ . In the asymptotic limit where  $x \rightarrow 0$  and  $t \rightarrow \infty$  it is possible to determine the behaviour of the distributions directly from the GLAP equations [34]. In effect, the leading  $\ln Q^2$  resummation of the GLAP equations is supplemented by an additional approximation in which only the most singular (leading  $\ln(1/x)$ )  $x$ -dependent contributions are retained. This is then called the double-leading-logarithm approximation (DLLA). Fig. 4.18 shows the region in the  $x, Q^2$  plane which corresponds to this limit.

The  $x \rightarrow 0$  limit of the parton distributions is controlled by the behaviour of the anomalous dimensions  $\gamma(j)$  near  $j = 1$ . At leading order, the anomalous dimensions  $\gamma_{gq}^{(0)}$  and  $\gamma_{gg}^{(0)}$  are singular at  $j = 1$  (Eq. (4.129), Fig. 4.9) and it is these that dominate the evolution of the distributions at small  $x$ . To avoid complications due to the mixing under evolution of the quark singlet and gluon distributions, we begin by considering the

evolution in a theory with gluons only:

$$t \frac{\partial}{\partial t} g(j, t) = \frac{\alpha(t)}{2\pi} \gamma_{gg}^{(0)}(j) g(j, t) \quad (4.172)$$

where from Eq. (4.129) (see also Fig. 4.9),

$$\gamma_{gg}^{(0)}(j) \approx \frac{2N}{j-1}. \quad (4.173)$$

In this limit the solution for the moments of the gluon distribution is

$$g(j, t) = g(j, t_0) \exp\left(\frac{\xi}{j-1}\right), \quad (4.174)$$

where  $\xi$  is defined by

$$\xi = \frac{N}{\pi} \int_{t_0}^t \frac{dt'}{t'} \alpha_s(t') = \frac{N}{\pi b} \ln\left(\frac{\ln t/\Lambda^2}{\ln t_0/\Lambda^2}\right). \quad (4.175)$$

To return to  $x$  space we perform the inverse Mellin transform as given by Eq. (4.146):

$$\begin{aligned} xg(x, t) &= \frac{1}{2\pi i} \int dj x^{-(j-1)} g(j, t) \\ &\equiv \frac{1}{2\pi i} \int dj g(j, t_0) \exp[f(j)], \end{aligned} \quad (4.176)$$

where the exponent  $f$  is

$$f(j) = (j-1)Y + \frac{\xi}{j-1}, \quad (4.177)$$

with  $Y \equiv \ln(1/x)$ . In the limit in which both  $Y$  and  $\xi$  become asymptotically large, we can estimate this integral by expanding about the saddle point of the exponential,

$$f(j) = 2\sqrt{\xi Y} + O(j - j_0)^2, \quad j_0 = 1 + \sqrt{\frac{\xi}{Y}}, \quad (4.178)$$

which gives, for the asymptotic solution,

$$xg(x, t) = g(j_0, t_0) \exp(2\sqrt{\xi Y}). \quad (4.179)$$

When expressed in terms of the original variables, this becomes [34]

$$g(x, \mu^2) \sim \frac{1}{x} \exp \sqrt{\frac{4N}{\pi b} \ln \frac{\ln \mu^2/\Lambda^2}{\ln \mu_0^2/\Lambda^2} \ln \frac{1}{x}}, \quad N = 3, \quad b = \frac{(33 - 2n_f)}{12\pi}. \quad (4.180)$$

Notice that the dependence on the starting distribution enters via the  $j_0$ th moment of  $g$ . Therefore at fixed  $\xi/Y$  the initial information enters only as an overall factor. An important point to note is that the above derivation breaks down if the starting distribution is too singular as  $x \rightarrow 0$ .

The contour in the complex  $j$ -plane must be located to the right of all the singularities of  $g(j, t_0)$ . If  $xg(x, t_0) \sim x^{-\lambda}$  as  $x \rightarrow 0$ , then  $g(j, t_0)$  has a pole at  $j = 1 + \lambda$ . If the saddle point  $j_0$ , Eq. (4.178), is to the left of this, i.e.  $\lambda > j_0 - 1$ , then the asymptotic behaviour is more complicated than that given in Eq. (4.179) and, in particular, depends on  $\lambda$ . Physically, if the starting gluon distribution is too steep then there are not enough faster moving gluons to emit the slower gluons which build up the perturbative rise at small  $x$ .

It is straightforward to compute various sub-leading corrections to the asymptotic behaviour given in (4.179). For example, the residual Gaussian saddle-point integral gives an additional overall factor of  $\xi^{1/4}Y^{-3/4}$ . Keeping the next-to-leading (constant) term in the expansion of the anomalous dimension around  $j = 1$ , i.e.

$$\gamma_{gg}^{(0)}(j) = N \left[ \frac{2}{j-1} + \kappa + O(j-1) \right], \quad (4.181)$$

where  $\kappa = -11/6 - n_f/(3N)$ , gives an overall factor of  $\exp(\xi\kappa/2)$ .

Since the evolution of the gluon and quark-singlet distributions is coupled (see Eq. (4.138)), the above asymptotic behaviour also applies to the quark distributions at small  $x$  and large  $t$  and therefore to the structure function  $F_2$ . In this case we must replace  $\gamma_{gg}$  by  $\gamma_+$ , defined in Eq. (4.140), the leading eigenvalue of the anomalous dimension matrix as  $j \rightarrow 1$ . This substitution does not change the leading term in Eq. (4.181) but changes  $\kappa$  to  $-11/6 - n_f/(3N^3)$ . It is interesting to investigate whether the asymptotic behaviour predicted by perturbative QCD is already visible in the HERA  $F_2$  data. In this context, it is convenient to introduce [35] two new variables:

$$\begin{aligned} \sigma &= [\ln(x_0/x) \ln(\ln(Q^2/\Lambda^2)/\ln(Q_0^2/\Lambda^2))]^{1/2} = \gamma^{-1} \sqrt{(Y - Y_0)\xi}, \\ \rho &= \left[ \frac{\ln(x_0/x)}{\ln(\ln(Q^2/\Lambda^2)/\ln(Q_0^2/\Lambda^2))} \right]^{1/2} = \gamma \sqrt{(Y - Y_0)/\xi}, \end{aligned} \quad (4.182)$$

with  $Y_0 = \ln(1/x_0)$  and  $\gamma = \sqrt{N/(\pi b)} = 6(33 - 2n_f)^{-1/2}$ , so that the double asymptotic limit is  $\sigma \rightarrow \infty$ ,  $\rho = O(1)$ . Note that an additional parameter  $x_0$  has been introduced to define the ‘small- $x$ ’ region,  $x < x_0$ , in the same way that  $Q^2 > Q_0^2$  defines the large- $Q^2$  region. In terms of these new variables, the asymptotic result (4.179) for the gluon distribution is simply  $xg \sim \exp(2\gamma\sigma)$ , i.e. the quantity  $\ln(xg)/(2\gamma\sigma)$  becomes independent of  $\sigma$  and  $\rho$  in the  $\sigma \rightarrow \infty$  limit. This behaviour is known as ‘double asymptotic scaling’.

The corresponding result for  $F_2$ , including the sub-leading terms de-

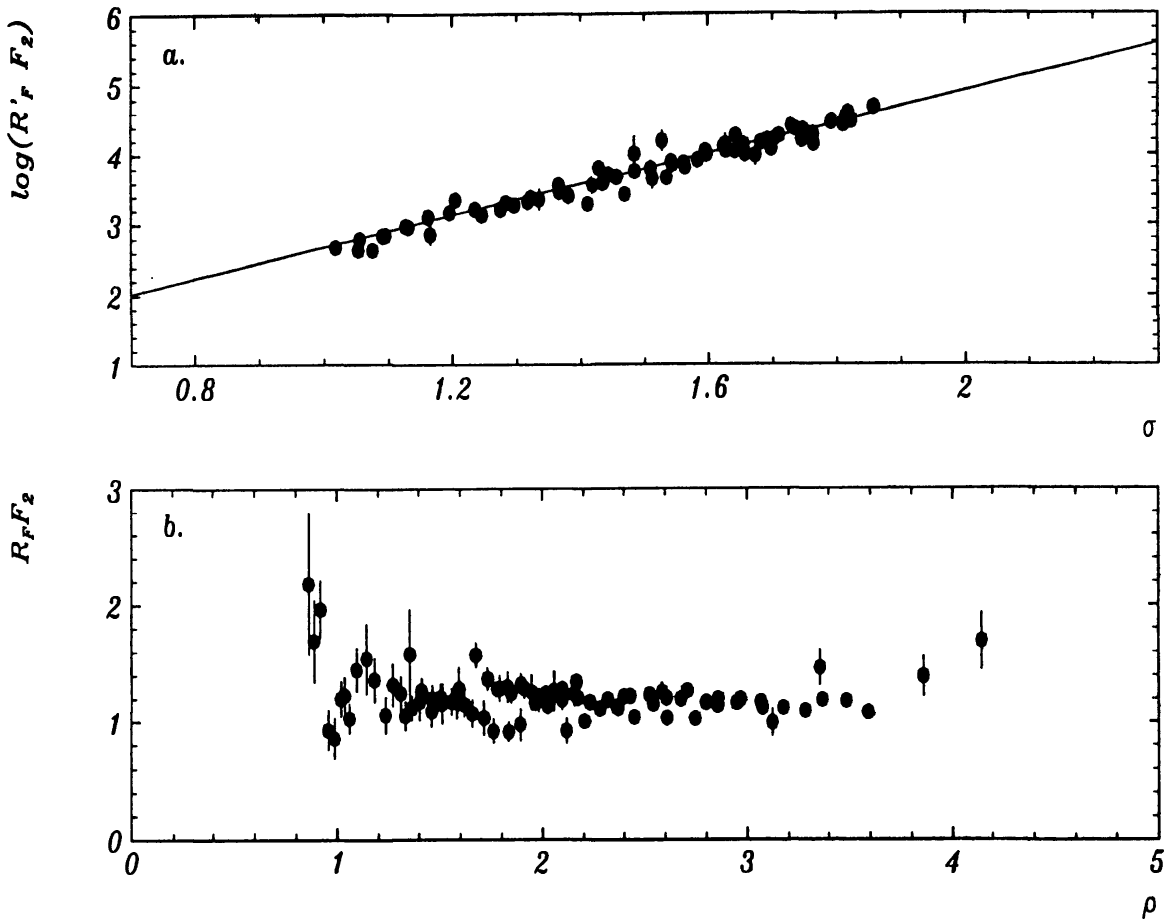


Fig. 4.19.  $F_2$  from the H1 collaboration at HERA, showing evidence for double asymptotic scaling. Figure from ref. [36].

scribed above, is [35]

$$F_2(\sigma, \rho) \approx A_0(\gamma/\rho) \sqrt{\frac{\gamma}{\sigma\rho^2}} \exp(2\gamma\sigma - \delta\sigma/\rho) \left[ 1 + O\left(\frac{1}{\sigma}\right) \right], \quad (4.183)$$

with  $\delta = 61/45$ . For non-singular starting distributions, the overall normalization  $A_0$  becomes constant for large  $\rho$ .

Parameters  $x_0$ ,  $Q_0$  and  $\Lambda$  can be found such that the HERA  $F_2$  data show clear evidence for the asymptotic scaling behaviour predicted by Eq. (4.183). As an illustration, Fig. 4.19(a) shows H1 data [36] for the quantity  $\log(R'_F F_2)$ , where

$$R'_F(\sigma, \rho) = 8.1 \sqrt{\sigma} \frac{\rho}{\gamma} \exp(\delta\sigma/\rho), \quad (4.184)$$

which according to (4.183) is predicted to rise linearly with  $\sigma$ , as a function of  $\sigma$  for different (fixed) values of  $\rho$ . The parameters are  $x_0 = 0.1$ ,  $Q_0 = 1$  GeV, and  $\Lambda_{LO}^{(4)} = 185$  MeV. A clear linear rise is seen, and the measured slope value  $2.22 \pm 0.04(\text{stat.}) \pm 0.10(\text{sys.})$  is consistent with the prediction  $2\gamma = 2.4$ . Fig. 4.19(b) shows  $F_2$  scaled by  $\exp(-2\gamma\sigma)R'_F$ ,

which removes all the model-independent leading behaviour of the asymptotic result (4.183). The observed approximate scaling in  $\rho$  for large  $\rho$  is consistent with a ‘soft’ small- $x$  starting distribution at  $Q_0$  [35].

#### 4.6.3 Higher-order corrections to the GLAP equation at small $x$

The splitting functions which appear on the right-hand side of the GLAP equation have a perturbative expansion in powers of  $\alpha_s$ , Eq. (4.91):

$$P(x, \alpha_s) = P^{(0)}(x) + \frac{\alpha_s}{2\pi} P^{(1)}(x) + \dots, \quad (4.185)$$

for  $P = P_{q;q_j}, P_{q;g}, \dots$ . In the next-to-leading-order (NLO) global parton analyses described in Section 4.4, only the first two terms in the perturbation series (4.185) are retained, together with the next-to-leading contributions to the coefficient functions which relate the parton distributions to the measured structure functions. Away from  $x = 0$  and  $x = 1$  this is a good approximation, in that the NLO correction to the leading-order (LO) evolution is quite small.

However care must be taken at small  $x$ , where large logarithms  $Y = \ln(1/x)$  can appear in the higher-order contributions to the splitting functions (and coefficient functions) and spoil the convergence. The trend can already be seen in the behaviour of the anomalous dimensions as  $j \rightarrow 1$ , equivalent to  $x \rightarrow 0$ , in Fig. 4.9. For  $\gamma_{qg}$ , for example, the NLO contribution exceeds the LO contribution for  $j - 1 \lesssim 0.3$ .

In general one can show that

$$xP^{(n)}(x) = A_n^{(n)}Y^n + A_{n-1}^{(n)}Y^{n-1} + \dots + A_0^{(n)} + x\bar{P}^{(n)}(x), \quad (4.186)$$

where  $\bar{P}^{(n)}$  is finite in the limit  $x \rightarrow 0$ . The full splitting function is then

$$xP(x, \alpha_s) = \sum_{n=0}^{\infty} \left(\frac{\alpha_s}{2\pi}\right)^n \left[ \sum_{m=0}^n A_m^{(n)} Y^m + x\bar{P}^{(n)}(x) \right]. \quad (4.187)$$

This expression holds for all four splitting functions,  $P_{gg}$ ,  $P_{qg}$ ,  $P_{gq}$  and  $P_{qq}$ . Explicit calculation of the leading  $P_{gg}$  coefficients gives, for example,

$$A_0^{(0)} = 6, \quad A_1^{(1)} = A_2^{(2)} = 0, \quad A_3^{(3)} = 518.4, \quad \dots \quad (4.188)$$

The general expansion (4.187) can be used to define various approximations to GLAP evolution:

- ( $n = 0; m = 0$ ) +  $\bar{P}^{(1)}$ : LO.
- ( $n = 0; m = 0$ ): DLLA (Sec. 4.6.2).
- ( $n = 0, 1; m = 0, 1$ ) +  $\bar{P}^{(0,1)}$ : NLO.
- ( $n \geq 0; m = n$ ): leading-log in  $1/x$  (LL $_x$ ).

- ( $n \geq 0; m = n, n - 1$ ): next-to-leading-log in  $1/x$  ( $\text{NL}_x$ ).

Only the  $P_{gg}$  and  $P_{gq}$  splitting functions have non-zero  $\text{LL}_x$  coefficients in general. These leading contributions can be resummed using the BFKL equation [37] (see Section 4.6.5), and eventually give rise to the characteristic behaviour at very small  $x$

$$xg \sim x^{-\lambda}, \quad \lambda = 12 \ln 2 \frac{\alpha_s}{\pi} \approx 0.5, \quad (4.189)$$

i.e. more singular than the double-asymptotic scaling behaviour of the DLLA (Section 4.6.2). The  $\text{NL}_x$  contributions to  $P_{qg}$  and  $P_{qq}$  are also known [38], while those for  $P_{gg}$  and  $P_{gq}$  remain unknown at present.

There are a number of important questions raised by the above observations. Clearly the fixed-order approximation to the evolution equations will break down when  $x$  is sufficiently small that  $\alpha_s \ln(1/x) \sim 1$ . Where and how LO or NLO GLAP evolution breaks down, and whether an ‘improved’ prediction can be obtained by incorporating the known resummed  $\text{LL}_x$  and  $\text{NL}_x$  contributions, are open questions at present. From recent numerical studies [39] it appears that (i) the importance of the higher-order  $\ln(1/x)$  corrections is very dependent on the form of the starting distributions at  $\mu_0^2$  — steep starting distributions are evidently less affected than flat distributions, and (ii) the dominant influence on the evolution of  $F_2$  in the HERA kinematic region comes not from the leading  $P_{gg}$  or  $P_{gq}$   $\text{LL}_x$  contributions, but rather from the formally subleading  $P_{qg}$   $\text{NL}_x$  contribution. The reason for this is that the gluon distribution is much larger than the quark distributions at small  $x$  and so the evolution of the structure function is dominated by the term proportional to  $g$ , i.e.  $\delta F_2 \sim P_{qg} \otimes g$ .

There are, however, several important issues still to be clarified. At any order in perturbation theory, the full splitting functions satisfy momentum conservation sum rule constraints:

$$\int_0^1 dx x \left[ \sum_i P_{q_i g}^{(n)} + P_{gg}^{(n)} \right] = 0, \quad (4.190)$$

$$\int_0^1 dx x \left[ \sum_j P_{q_j q_i}^{(n)} + P_{gq_i}^{(n)} \right] = 0. \quad (4.191)$$

This is *not* satisfied by the  $\text{LL}_x$  or  $\text{NL}_x$  contributions, and it is not clear to what extent momentum conservation is important for small- $x$  GLAP evolution. Another issue concerns the factorization scheme dependence at small  $x$  — changing schemes can move large  $L_x$  contributions from the splitting functions into the coefficient functions, and therefore corrections to the evolution at small  $x$  can be less important in some schemes than in others.

#### 4.6.4 The BFKL description of $F_2$

Traditionally, simple parton model and Regge arguments were used to justify using gluon and sea quark ‘starting distributions’ which behave at small  $x$  as  $x^{-1-\lambda}$  with  $\lambda \approx 0$ . In the previous sections we have seen how perturbative QCD evolution in  $Q^2$  causes the distributions to rapidly develop a steeper shape at small  $x$ . The GLAP equation effectively sums leading powers of  $[\alpha_s \ln Q^2]^n$  generated by multigluon emission in a region of phase space where the gluons have strongly-ordered transverse momenta,  $Q^2 \gg k_{nT}^2 \gg \dots \gg k_{1T}^2$ :

$$\int \frac{dk_{nT}^2}{k_{nT}^2} \dots \int \frac{dk_{2T}^2}{k_{2T}^2} \int \frac{dk_{1T}^2}{k_{1T}^2} \sim \frac{[\ln Q^2]^n}{n!}. \quad (4.192)$$

Such a resummation is appropriate for  $\ln Q^2$  much larger than  $\ln(1/x)$ . When the two logarithms are large and of the same order, the DLLA sums leading powers of  $[\alpha_s \ln(1/x) \ln Q^2]^n$  and the corresponding distributions increase faster than any power of  $\ln(1/x)$  as  $x \rightarrow 0$ .

However, at HERA  $Q^2$  is not so large at very small  $x$  (Fig. 4.16), and so it may be more appropriate to consider the case when  $\ln Q^2 \ll \ln(1/x)$ . GLAP evolution does *not* include all the leading terms in this limit: it neglects those terms which contain the leading power of  $\ln(1/x)$  but which are not accompanied by the leading power of  $\ln Q^2$ . The resummation of terms proportional to  $\alpha_s \ln(1/x)$  to all orders, retaining the full  $Q^2$  dependence and not just the leading  $\ln Q^2$  terms, is accomplished by the Balitsky–Fadin–Kuraev–Lipatov (BFKL) equation [37]. Here the integration is taken over the full  $k_T$  phase space of the gluons, not just the strongly-ordered part as in (4.192).

In the following section the BFKL equation will be derived from first principles. In terms of the small- $x$  behaviour of parton distributions, the result is most conveniently established for the gluon distribution unintegrated over  $k_T$ ,

$$xg(x, Q^2) = \int^{Q^2} dk_T^2 \mathcal{G}(x, k_T^2), \quad (4.193)$$

and is

$$\mathcal{G}(x, k_T^2) \sim h(k_T^2)x^{-\lambda}, \quad (4.194)$$

where  $h \sim (k_T^2)^{-\frac{1}{2}}$  at large  $k_T^2$  and  $\lambda$  is the maximum eigenvalue of the kernel  $K$  of the BFKL equation

$$\frac{\partial \mathcal{G}}{\partial \ln(1/x)} = \int d^2 k'_T K(\vec{k}_T, \vec{k}'_T) \mathcal{G}(x, k'^2_T). \quad (4.195)$$

For fixed  $\alpha_s$ ,  $\lambda$  has the value given in Eq. (4.189). The prediction for  $F_2$

is obtained by using the  $k_T$ -factorization theorem [40]

$$F_2(x, Q^2) = \int_x^1 \frac{dx'}{x'} \int \frac{dk_T^2}{k_T^4} G\left(\frac{x}{x'}, k_T^2\right) \bar{F}_2(x', k_T^2, Q^2), \quad (4.196)$$

where  $\bar{F}_2$  denotes the quark-box contribution  $\gamma g \rightarrow q\bar{q}$  for the scattering of a photon of virtuality  $Q^2$  off a gluon with longitudinal momentum fraction  $x'$  and transverse momentum  $k_T$ .

The BFKL predictions for  $F_2$ , based on the above results, can be obtained by numerical methods, see for example ref. [41]. The result can be summarized as

$$F_2(x, Q^2) = C(Q^2)x^{-\lambda} + F_2^{NP}, \quad (4.197)$$

where  $\lambda \approx 0.5$  and  $F_2^{NP}$  is a non-perturbative background contribution which is constant at small  $x$ . A good description of the HERA data is obtained. However the BFKL-based analysis is not entirely satisfactory: (i) there are infra-red problems associated with integrating  $\int dk_T^2 \alpha_S(k_T^2)$  down to  $k_T^2 = 0$ ,<sup>7</sup> which in practice means that the predictions depend to some extent on an undetermined infra-red cut-off parameter, and (ii) the next-to-leading (in  $\ln(1/x)$ ) corrections to the BFKL equation are as yet unknown. Kinematic constraints such as momentum conservation and the upper limit on transverse momenta, although formally sub-leading, may also be important in the HERA kinematic regime.

Ultimately one would like to achieve a ‘unified’ treatment of the  $x$  and  $Q^2$  dependence of parton distributions and structure functions which incorporates both the GLAP and BFKL dynamics. Progress in this direction has been reported in ref. [42], where a modified evolution equation based on gluon emission with angular ordering (see Chapter 5) has been derived. This reproduces the results of GLAP evolution at large  $x$  and BFKL behaviour at small  $x$  [43].

#### 4.6.5 The BFKL equation

Although the most important phenomenological application of BFKL physics is to the small- $x$  behaviour of deep inelastic structure functions, it is more convenient to derive the equation for the small- $x$  behaviour of the *wave function* of a bound state of a heavy quark-antiquark pair (quarkonium), for which complications from non-perturbative contributions are absent. We shall follow the ‘colour dipole’ formulation of the problem used by Mueller [44]. The wave function can in principle be used to compute the structure functions, and its small- $x$  behaviour is similar.

---

<sup>7</sup> We expect the argument of  $\alpha_S$  to be the transverse momentum-squared  $k_T^2$  (see the discussion in Chapter 5), because of the breakdown of strong ordering of  $k_T$  at small  $x$ . This leads to values of  $k_T^2$  much lower than  $Q^2$  and hence to larger  $\alpha_S$  values.

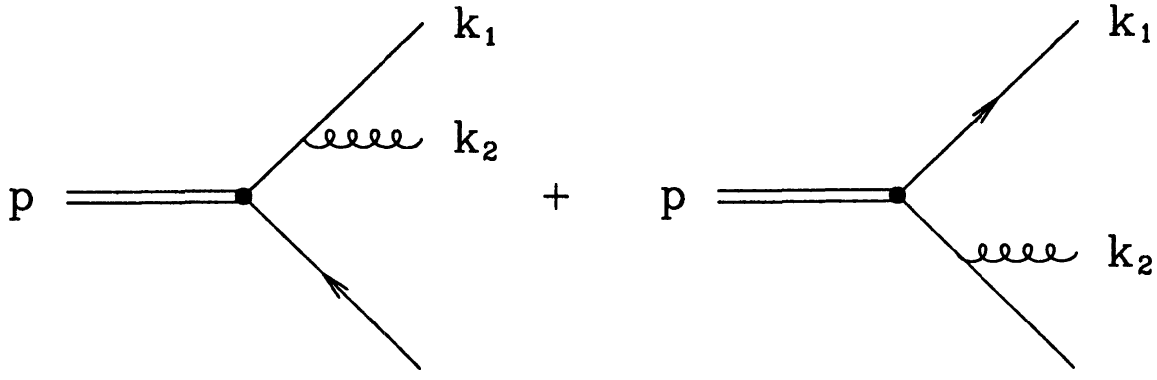


Fig. 4.20. Feynman diagrams for the  $Q\bar{Q}g$  light-cone wave function.

Consider the wave function  $\psi^{(n)}$  of a quarkonium state of momentum  $p$ , consisting of a quark of momentum  $k_1$ ,  $n$  gluons of momenta  $k_2, \dots, k_{n+1}$  and an antiquark of momentum  $k_0 = p - k_1 - \dots$ . Ignoring the spin of the quarks, which is irrelevant when the gluons are soft, the 1-gluon and 0-gluon wave functions are related by the diagrams in Fig. 4.20, which give

$$\psi^{(1)}(k_1, k_2) \sim g t^A \left[ \psi^{(0)}(k_1 + k_2) \frac{k_1 \cdot \epsilon_2}{k_1 \cdot k_2} - \psi^{(0)}(k_1) \frac{k_0 \cdot \epsilon_2}{k_0 \cdot k_2} \right] \quad (4.198)$$

for a gluon with colour index  $A$ .

We use a light-cone representation in which

$$k_i = x_i p + y_i n + k_{Ti}, \quad \epsilon_i = \omega_i n + \epsilon_{Ti} \quad (4.199)$$

with  $p = (P, 0, 0, P)$ ,  $n = (1/(2P), 0, 0, -1/(2P))$ , and  $k_T = (0, k_x, k_y, 0)$ . Note that we choose  $P$  so large that the quarkonium mass is negligible. Writing transverse vectors as  $k = (k_x, k_y)$  etc., we find from the mass-shell and transversality ( $k_i \cdot \epsilon_i = 0$ ) conditions that

$$y_i = k_i^2/x_i, \quad \omega_i = k_i \cdot \epsilon_i/x_i. \quad (4.200)$$

Then for  $x_2 \ll x_1, (1 - x_1)$  Eq. (4.198) becomes

$$\psi^{(1)}(x_1, k_1, x_2, k_2) \sim 2gt^A [\psi^{(0)}(x_1, k_1 + k_2) - \psi^{(0)}(x_1, k_1)] \frac{k_2 \cdot \epsilon_2}{k_2^2}. \quad (4.201)$$

A standard trick for simplifying this type of equation is to perform a two-dimensional Fourier transformation from transverse momenta  $k_i$  to transverse coordinates (*impact parameters*)  $b_i$ :

$$\tilde{\psi}^{(n-1)}(x_1, b_1 \dots x_n, b_n) = \int \prod_{i=1}^n \frac{d^2 k_i}{(2\pi)^2} e^{i k_i \cdot b_i} \psi^{(n-1)}(x_1, k_1 \dots x_n, k_n). \quad (4.202)$$

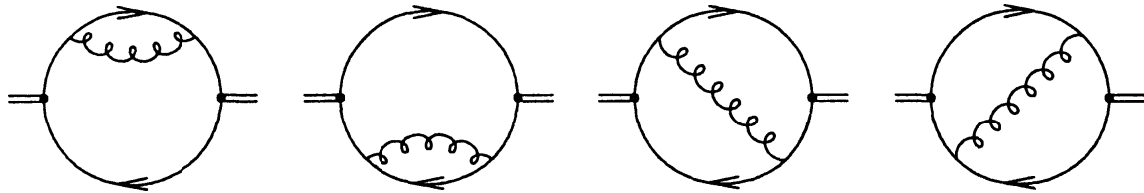


Fig. 4.21. Loop diagrams corresponding to the terms of Eq. (4.205).

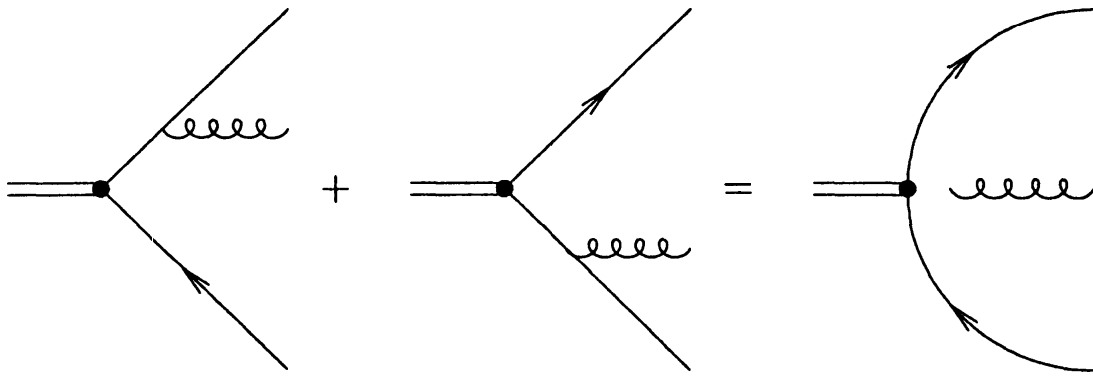


Fig. 4.22. Representation of gluon emission from a dipole.

Then we find that Eq. (4.201) becomes simply

$$\tilde{\psi}^{(1)}(x_1, \mathbf{b}_1, x_2, \mathbf{b}_2) = \frac{ig}{\pi} t^A \tilde{\psi}^{(0)}(x_1, \mathbf{b}_1) \left( \frac{\mathbf{b}_{21}}{\mathbf{b}_{21}^2} - \frac{\mathbf{b}_{20}}{\mathbf{b}_{20}^2} \right) \cdot \epsilon_2 \quad (4.203)$$

where  $\mathbf{b}_{ij} = \mathbf{b}_i - \mathbf{b}_j$  ( $\mathbf{b}_0 = 0$ ). Taking the square modulus and performing the polarization and colour sums gives

$$|\tilde{\psi}^{(1)}|^2 = 4C_F \frac{\alpha_s}{\pi} |\tilde{\psi}^{(0)}|^2 \frac{\mathbf{b}_{10}^2}{\mathbf{b}_{20}^2 \mathbf{b}_{21}^2}. \quad (4.204)$$

In writing Eq. (4.204) we have used the fact that

$$\frac{1}{\mathbf{b}_{21}^2} + \frac{1}{\mathbf{b}_{20}^2} - 2 \frac{\mathbf{b}_{21} \cdot \mathbf{b}_{20}}{\mathbf{b}_{21}^2 \mathbf{b}_{20}^2} = \frac{\mathbf{b}_{10}^2}{\mathbf{b}_{20}^2 \mathbf{b}_{21}^2}. \quad (4.205)$$

The terms on the left-hand side correspond to the four contributions to  $|\tilde{\psi}^{(1)}|^2$  depicted in Fig. 4.21. We represent the whole dipole expression (4.204) symbolically by the diagram on the right-hand side of Fig. 4.22, which is not a Feynman graph but simply a representation of the fact that the gluon is radiated coherently by the quark and antiquark.

Next we compute the 2-gluon contribution to the wave function when one of the gluons is much softer,  $x_3 \ll x_2 \ll x_1, (1 - x_1)$ . This is the relevant configuration because it gives rise to the largest number of factors of  $\ln x$  in the inclusive gluon distribution. There will be contributions corresponding to adding a gluon line to the loops in Fig. 4.21 in all possible ways. At this order it is not difficult to compute all the contributions,

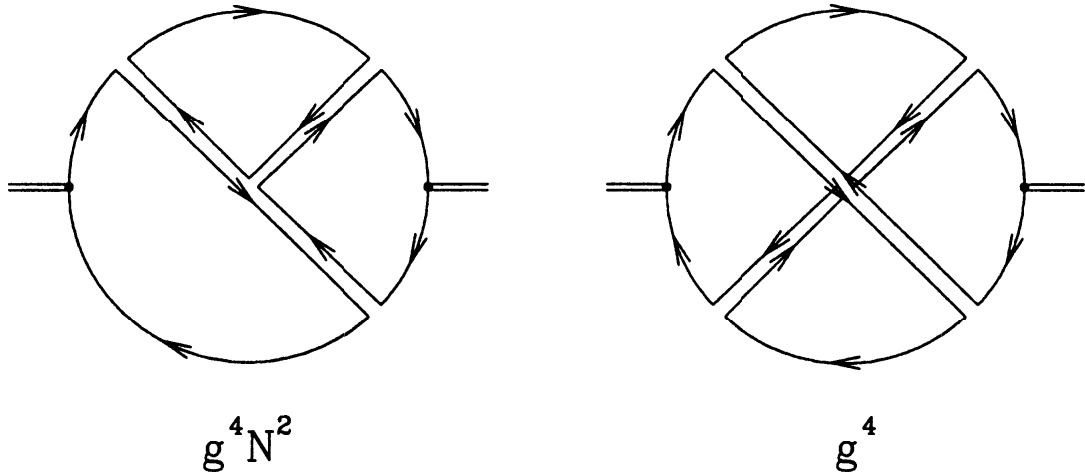


Fig. 4.23. Planar and non-planar diagrams.

but the full calculation becomes too complicated in higher orders, so we shall simplify things by making the *planar approximation*.

All contributions in which additional gluon lines are added to Fig. 4.21 can be classified as *planar* (possible to draw with all gluons inside the quark loop and not overlapping) or *non-planar*. The non-planar graphs are suppressed relative to the planar ones by powers of  $1/N$  where  $N$  is the number of colours [45]. Examples of the two types of contributions are shown in Fig. 4.23, where the gluons are represented by double lines indicating the flow of colour and anticolour. This representation corresponds to the approximation that there are  $N^2$  gluons instead of  $N^2 - 1$  and  $C_A = 2C_F = N$ , so it is valid at large  $N$ .

The two graphs in Fig. 4.23 are of the same order in the coupling  $g$ , but the planar one has three closed colour loops while the non-planar graph has only one. The quarkonium vertices each introduce a normalization factor of  $1/\sqrt{N}$ , since the state must be a colour singlet. Thus the planar graph is  $\mathcal{O}(g^4 N^2)$  while the other is  $\mathcal{O}(g^4)$  with no factors of  $N$ . The planar limit corresponds to taking  $g \rightarrow 0$ ,  $N \rightarrow \infty$  while keeping  $g^2 N$  fixed. In this limit the non-planar graph vanishes like  $1/N^2$ . In fact  $1/N^2 = 1/9$  so the planar approximation is expected to be reasonable at the 10% level.

The two-gluon wave-function-squared in the planar approximation is found to be

$$|\tilde{\psi}^{(2)}|^2 = 2N \frac{\alpha_s}{\pi} |\tilde{\psi}^{(1)}|^2 \left( \frac{b_{21}^2}{b_{31}^2 b_{32}^2} + \frac{b_{20}^2}{b_{30}^2 b_{32}^2} \right). \quad (4.206)$$

This result has a simple interpretation in terms of the dipole picture, represented by Fig. 4.24. In a planar graph, the extra gluon has to be inserted either between the quark and the first gluon (as in Fig. 4.23) or between the gluon and the antiquark. Thus it is either radiated by

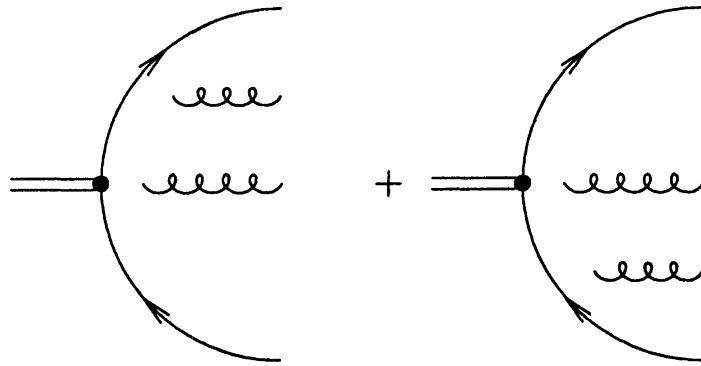


Fig. 4.24. Emission of a second gluon in dipole representation.

the (21) dipole (the first term) or by the (20) dipole (the second term). Similarly in higher orders an additional gluon can be emitted by any of the dipoles corresponding to pairs of partons that are adjacent when the diagram is drawn on a plane. The neglected non-planar graphs correspond to interference between different dipoles.

We next compute the *inclusive* gluon  $\ln x$  distribution  $\tilde{\mathcal{G}}(x, b_{10}^2; x_1)$  in the wave function of a quarkonium state of transverse size  $b_{10}$  with quark momentum fraction  $x_1$ . ‘Inclusive’ means that we sum over all contributions with any number of gluons. We construct a differential equation for this function in a way similar to that used for the (GLAP)  $Q^2$  evolution of parton distributions. The difference is that here we study the evolution in  $x$  rather than  $Q^2$ .

Consider first the change  $\delta\tilde{\mathcal{G}}$  in  $\tilde{\mathcal{G}}$  when the quark momentum fraction is increased by a small amount  $\delta x_1$ . This opens up a new region of phase space for the emission of the hardest gluon (remember that  $x < x_1$  in a leading  $\ln x$  treatment). If a gluon 2 is emitted in the interval  $\delta x_1$ , this creates two dipoles (21) and (20) in place of the original one (10). Thus we have

$$\begin{aligned} \delta\tilde{\mathcal{G}}(x, b_{10}^2; x_1) = & 2N \frac{\alpha_s}{\pi} \frac{\delta x_1}{2x_1} \int \frac{d^2 b_2}{2\pi} \frac{b_{10}^2}{b_{20}^2 b_{21}^2} \\ & \times [\tilde{\mathcal{G}}(x, b_{21}^2; x_1) + \tilde{\mathcal{G}}(x, b_{20}^2; x_1) - \tilde{\mathcal{G}}(x, b_{10}^2; x_1)]. \end{aligned} \quad (4.207)$$

From invariance under longitudinal boosts,  $\tilde{\mathcal{G}}$  can only be a function of  $x/x_1$ . Hence

$$x \frac{\partial \tilde{\mathcal{G}}}{\partial x} = -x_1 \frac{\partial \tilde{\mathcal{G}}}{\partial x_1}, \quad (4.208)$$

which gives (dropping the argument  $x_1$  from now on)

$$x \frac{\partial}{\partial x} \tilde{G}(x, b_{10}^2) = -\frac{N\alpha_s}{2\pi^2} \int d^2 b_2 \frac{b_{10}^2}{b_{20}^2 b_{21}^2} [\tilde{G}(x, b_{21}^2) + \tilde{G}(x, b_{20}^2) - \tilde{G}(x, b_{10}^2)]. \quad (4.209)$$

This is essentially Mueller's form of the BFKL equation, Eq. (4.195).

The quantity  $\tilde{G}$  is the inclusive gluon distribution in the quarkonium wave function, but this does not tell us directly the distribution of gluons relevant to the deep inelastic scattering structure functions. However, the small- $x$  behaviour should be the same. As a check of this, we can calculate the small- $x$  solution in the approximation that transverse momenta  $k_T^2 \sim t_i$  are strongly ordered, which should reproduce the DLLA GLAP form (4.180).

Strong ordering of transverse momenta implies strong ordering of impact parameters, i.e. gluon 2 is either very close to the quark ( $b_{21}^2 \ll b_{10}^2$  and  $b_{20}^2 \simeq b_{10}^2$ ) or to the antiquark ( $b_{20}^2 \ll b_{10}^2$  and  $b_{21}^2 \simeq b_{10}^2$ ). These regions of the impact parameter integration give

$$x \frac{\partial}{\partial x} \tilde{G}(x, b_{10}^2) \sim -\frac{N\alpha_s}{2\pi} \left[ \int^{b_{10}^2} \frac{db_{21}^2}{b_{21}^2} \tilde{G}(x, b_{21}^2) + \int^{b_{10}^2} \frac{db_{20}^2}{b_{20}^2} \tilde{G}(x, b_{20}^2) \right] \quad (4.210)$$

and hence

$$b^2 \frac{\partial}{\partial b^2} x \frac{\partial}{\partial x} \tilde{G}(x, b^2) \sim -\frac{N\alpha_s}{\pi} \tilde{G}(x, b^2). \quad (4.211)$$

The solution of this equation has the asymptotic form

$$\tilde{G}(x, b^2) \sim \tilde{G}(x_0, b_0^2) \exp \sqrt{\frac{4N\alpha_s}{\pi} \ln \frac{x_0}{x} \ln \frac{b_0^2}{b^2}}, \quad (4.212)$$

where  $x_0$  and  $b_0$  here represent arbitrary boundary values. Eq. (4.212) is essentially the fixed- $\alpha_s$  version of Eq. (4.180) in impact-parameter space, obtained by putting  $\xi = (N\alpha_s/\pi) \ln(b_0^2/b^2)$  in Eq. (4.179), and it exhibits the same  $\exp \sqrt{\ln 1/x}$  behaviour at small  $x$ .

In fact there is *no* strong ordering in  $k_T^2$  or  $b^2$  at small  $x$ : the region in which gluon 2 is not close to either the quark or the antiquark gives a significant contribution, which causes the inclusive gluon distribution to rise faster than  $\exp \sqrt{\ln 1/x}$ . To see this we note that after azimuthal integration we have, schematically,

$$\int \frac{d^2 b_2}{b_{21}^2} = \int \frac{b_{20} db_{20} d\phi}{b_{20}^2 + b_{10}^2 - 2b_{20}b_{10} \cos \phi} = \pi \int_0^\infty \frac{db_{20}^2}{|b_{20}^2 - b_{10}^2|}. \quad (4.213)$$

The combination of integrals in Eq. (4.209) is regular, but the part in (4.213) is divergent, so one must be careful about regularization. Writing  $b_{10}^2 = b^2$  and defining  $b_{20}^2 = ub^2$  when  $b_{20}^2 < b^2$  and  $b_{20}^2 = b^2/u$  when

$b_{20}^2 > b^2$ , we find that Eq. (4.209) becomes

$$x \frac{\partial}{\partial x} \tilde{G}(x, b^2) = -\frac{N\alpha_s}{\pi} \int_0^1 \frac{du}{1-u} [\tilde{G}(x, ub^2)/u + \tilde{G}(x, b^2/u) - 2\tilde{G}(x, b^2)] . \quad (4.214)$$

Eq. (4.214) seems to be the simplest form in which the BFKL equation can be written. We can diagonalize it (*i.e.* remove the coupling between different values of  $b^2$ ) by using a Mellin representation

$$\tilde{G}(x, b^2) = \int_{\frac{1}{2}-i\infty}^{\frac{1}{2}+i\infty} \frac{d\gamma}{2\pi i} (b^2)^\gamma \hat{G}(x, \gamma) , \quad (4.215)$$

which gives

$$x \frac{\partial \hat{G}}{\partial x} = -\bar{\alpha}_s \hat{G} \int_0^1 \frac{u}{1-u} (u^{\gamma-1} + u^{-\gamma} - 2) \equiv -\bar{\alpha}_s \hat{G} \chi(\gamma) \quad (4.216)$$

and hence

$$\hat{G}(x, \gamma) = \hat{G}(x_0, \gamma) \left( \frac{x_0}{x} \right)^{\bar{\alpha}_s \chi(\gamma)} \quad (4.217)$$

where  $\bar{\alpha}_s = N\alpha_s/\pi$  and  $\chi$  is the *Lipatov characteristic function*

$$\chi(\gamma) = \int_0^1 \frac{u}{1-u} (u^{\gamma-1} + u^{-\gamma} - 2) = 2\psi(1) - \psi(\gamma) - \psi(1-\gamma) . \quad (4.218)$$

Here  $\psi$  is the digamma function,

$$\psi(z) = \Gamma'(z)/\Gamma(z) , \quad (4.219)$$

with the Euler gamma function  $\Gamma$  defined in Eq. (2.57). Inserting the solution (4.217) into Eq. (4.215) then gives

$$\tilde{G}(x, b^2) = \int \frac{d\gamma}{2\pi i} \hat{G}(x_0, \gamma) \exp[\gamma \ln b^2 + \bar{\alpha}_s \chi(\gamma) \ln(x_0/x)] . \quad (4.220)$$

Given the assumed form of  $\tilde{G}(x_0, b^2)$  at some starting value  $x_0$ , one can Mellin transform to obtain  $\hat{G}(x_0, \gamma)$  using the inverse of Eq. (4.215),

$$\hat{G}(x, \gamma) = \int_0^\infty db^2 (b^2)^{-\gamma-1} \tilde{G}(x, b^2) , \quad (4.221)$$

and then deduce  $\tilde{G}(x, b^2)$  at any  $x < x_0$ . For large values of  $\ln(x_0/x)$  the integral will be dominated by the saddle point of the integrand, *i.e.* the point  $\gamma = \gamma_s$ , at which the derivative of the exponent vanishes. Denoting the exponent by

$$\phi(\gamma) = \gamma \ln b^2 + \bar{\alpha}_s \chi(\gamma) \ln(x_0/x) , \quad (4.222)$$

we have

$$\tilde{G}(x, b^2) \sim \int \frac{d\gamma}{2\pi i} \hat{G}(x_0, \gamma_s) \exp[\phi(\gamma_s) + \frac{1}{2}\phi''(\gamma_s)(\gamma - \gamma_s)^2]$$

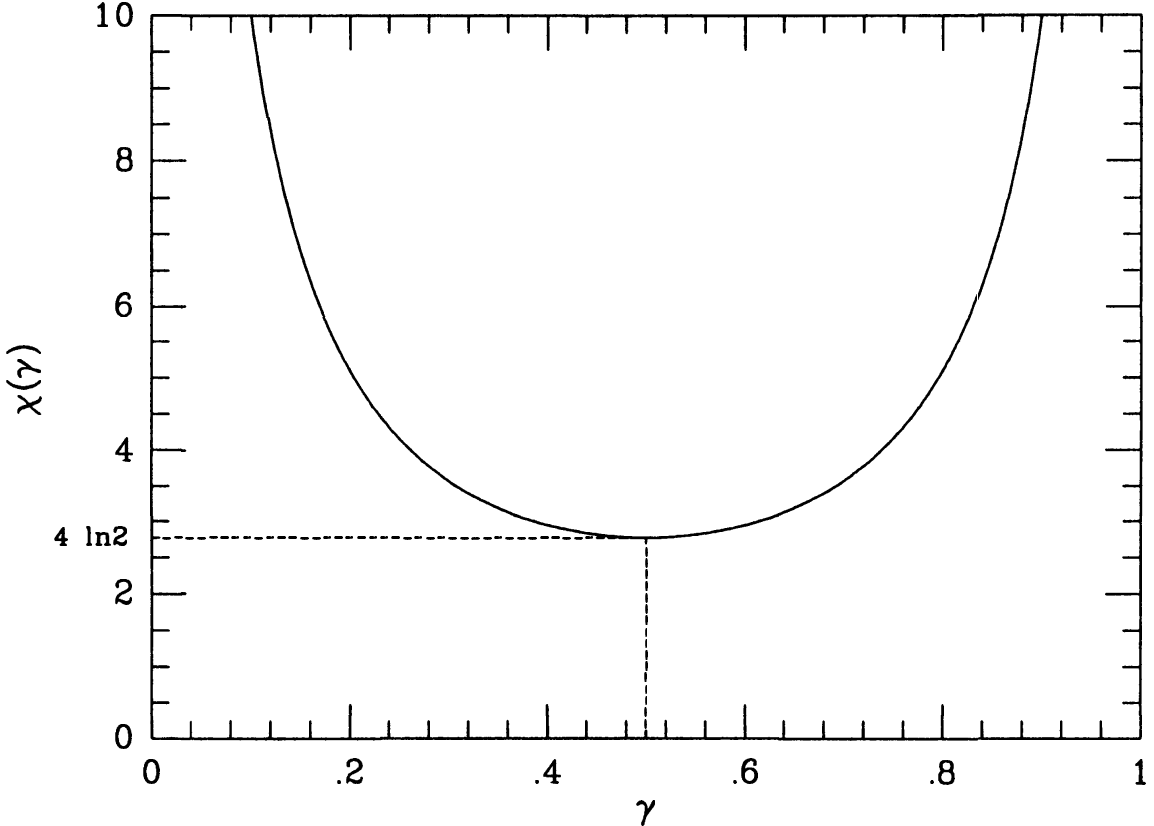


Fig. 4.25. The Lipatov characteristic function.

$$= \frac{1}{\sqrt{2\pi\phi''(\gamma_s)}} \hat{\mathcal{G}}(x_0, \gamma_s) \exp \phi(\gamma_s) \quad (4.223)$$

where

$$\phi'(\gamma_s) = \ln b^2 + \bar{\alpha}_s \chi'(\gamma_s) \ln(x_0/x) = 0. \quad (4.224)$$

The form of the Lipatov characteristic function  $\chi$  is shown in Fig. 4.25. For any fixed value of  $b^2$ , we have  $\gamma_s \rightarrow \frac{1}{2}$  as  $x \rightarrow 0$ , since  $\chi'(\frac{1}{2}) = 0$ . Thus  $\tilde{\mathcal{G}}(x, b^2)$  at small  $x$  is power behaved:

$$\tilde{\mathcal{G}}(x, b^2) \sim \frac{1}{\sqrt{2\pi\phi''(\frac{1}{2})}} \hat{\mathcal{G}}(x_0, \frac{1}{2}) \exp[\phi(\frac{1}{2})] \propto bx^{-\lambda} \quad (4.225)$$

where

$$\lambda = \bar{\alpha}_s \chi(\frac{1}{2}) = 4N \ln 2 \frac{\alpha_s}{\pi}, \quad (4.226)$$

as in Eq. (4.189). Finally, we may take the inverse two-dimensional Fourier transformation to obtain the inclusive gluon distribution as a function of  $x$  and  $k_T$ :

$$\mathcal{G}(x, k_T^2) = \int d^2 \mathbf{k}_i e^{-i \mathbf{k}_i \cdot \mathbf{b}_i} \tilde{\mathcal{G}}(x, b^2) \propto \frac{1}{\sqrt{k_T^2}} x^{-\lambda}, \quad (4.227)$$

which is the result for the gluon distribution function quoted in Eq. (4.194). The parameter  $\lambda$  is about 0.5 for  $\alpha_s \simeq 0.2$ , leading to an approximate  $x^{-3/2}$  divergence in the gluon distribution at small  $x$ .

#### 4.6.6 Parton saturation

In the previous sections we have seen how perturbative QCD predicts a rapid increase of the parton distributions at small  $x$ . However this increase cannot go on indefinitely. If the number density of partons becomes too large inside the proton then they can no longer be treated as free. The effect is evidently most important for gluons, whose distribution at small  $x$  exceeds that of the sea quarks by more than an order of magnitude.

When the number density becomes so large that the gluons ‘saturate’ the proton, we would expect that gluon recombination effects would limit any further growth of the distribution [46]. A simple geometric argument gives an indication as to where in  $x$  and  $\mu^2$  space this saturation may be expected to occur. In the infinite momentum frame the gluon momentum distribution  $xg(x, \mu^2)$  gives the number of gluons per unit of longitudinal phase space  $dx/x$ , with a transverse size greater than  $1/\mu$ , when probed at a deep inelastic scale  $Q^2 = \mu^2$ . Therefore the gluons occupy a transverse area  $\sim xg(x, \mu^2)/\mu^2$  of the disc shown in Fig. 4.5. As  $x$  decreases this area becomes large, and we would expect saturation effects to become important when

$$\frac{\alpha_s(\mu^2)}{\mu^2} xg(x, \mu^2) \gtrsim \pi R^2, \quad (4.228)$$

where  $R \sim 5 \text{ GeV}^{-1}$  is the proton radius. Note the additional factor of  $\alpha_s(\mu^2)$  which enters because the effective gluon-gluon cross section is  $\sigma_{gg} \sim \alpha_s(\mu^2)/\mu^2$ . For a typical gluon distribution, the  $x, \mu^2$  region where the inequality (4.228) is satisfied is shown in Fig. 4.18. From Fig. 4.16, we see that parton saturation is unlikely to play a major role in the HERA kinematic region. Detailed analytic and numerical studies, which go beyond the crude estimate of Eq. (4.228), support this conclusion, see for example refs. [47,48].

## 4.7 Polarized scattering

All the deep inelastic structure functions discussed so far in this chapter correspond to *spin-averaged* scattering. In this section we generalize the discussion to the situation where the lepton beam and nucleon target are polarized in the longitudinal direction. Such scattering processes yield information on the spin content of the nucleon, in particular how the spin of a fast-moving nucleon is distributed among its parton constituents. For

simplicity we shall consider only the electromagnetic (photon exchange) contribution to the cross section.

In deep inelastic scattering experiments where both the beam and target can be longitudinally polarized one can measure the spin asymmetry

$$A(x, Q^2) = \frac{d\sigma^{\uparrow\downarrow}(x, Q^2) - d\sigma^{\uparrow\uparrow}(x, Q^2)}{d\sigma^{\uparrow\downarrow}(x, Q^2) + d\sigma^{\uparrow\uparrow}(x, Q^2)} \quad (4.229)$$

where the cross section  $d\sigma^{\uparrow\uparrow}$  ( $d\sigma^{\uparrow\downarrow}$ ) corresponds to the incoming lepton and nucleon being polarized parallel (anti-parallel) to one another. The denominator in (4.229) is simply twice the spin-averaged cross section discussed in Section 4.1. The numerator can be written in terms of two new structure functions  $g_1$  and  $g_2$  (cf. Eq. (4.2))

$$\begin{aligned} \frac{d^2\sigma^{\uparrow\downarrow}}{dxdy} - \frac{d^2\sigma^{\uparrow\uparrow}}{dxdy} &= \frac{8\pi\alpha^2 ME}{Q^4} \left[ \left( 2y - y^2 - \frac{Mxy^2}{E} \right) 2xg_1(x, Q^2) \right. \\ &\quad \left. - \frac{4M}{E} x^2 y g_2(x, Q^2) \right]. \end{aligned} \quad (4.230)$$

The structure functions  $g_1, g_2$  are the polarized analogues of  $F_1, F_2$ . They represent the two independent contributions to the *antisymmetric* part of the hadronic tensor  $W_{\alpha\beta}(p, q)$  (4.28) allowed by  $P$  and  $T$  invariance. In the kinematic region characteristic of fixed-target experiments, the numerator and denominator in Eq. (4.229) are dominated by the terms proportional to  $g_1$  and  $F_1$  respectively, and

$$A(x, Q^2) \approx \frac{g_1(x, Q^2)}{F_1(x, Q^2)}. \quad (4.231)$$

Thus the polarized structure function can be extracted from a measurement of the longitudinal asymmetry combined with a measurement of the unpolarized structure function. In the current range of  $x$  and  $Q^2$  probed by (fixed-target) experiments the asymmetry is observed to be essentially  $Q^2$  independent, from which we deduce that  $g_1$  also satisfies approximate Bjorken scaling.

#### 4.7.1 Parton model interpretation

To establish the parton model description of the polarized structure functions we may proceed exactly as in Section 4.1. We consider scattering off a pointlike, massless quark constituent of a longitudinally polarized proton in the infinite momentum frame. There are now two probability distributions,  $q^\uparrow(\xi)$  and  $q^\downarrow(\xi)$ , representing the probabilities that the quark spin is respectively parallel and antiparallel to the spin of the parent proton. A straightforward calculation of the spin-dependent  $eq \rightarrow eq$

scattering cross section then gives

$$\begin{aligned} F_1(x) &= \frac{1}{2} \sum_q e_q^2 [q(x) + \bar{q}(x)], \\ g_1(x) &= \frac{1}{2} \sum_q e_q^2 [\Delta q(x) + \Delta \bar{q}(x)], \end{aligned} \quad (4.232)$$

where

$$q = q^\uparrow + q^\downarrow, \quad \Delta q = q^\uparrow - q^\downarrow. \quad (4.233)$$

Note that  $g_2 = 0$  in this simple model. However this is misleading. A more realistic parton model calculation, in which the quark can be both off-shell and have non-zero transverse momentum with respect to the parent proton direction of motion, gives a non-zero  $g_2$  of similar magnitude to  $g_1$ . A more complete discussion can be found, for example, in ref. [49].

In a model with three quark flavours, the structure function  $g_1$  for proton and neutron targets can be written as

$$\begin{aligned} g_1^p(x) &= \frac{2}{9} [\Delta u(x) + \Delta \bar{u}(x)] + \frac{1}{18} [\Delta d(x) + \Delta \bar{d}(x) + \Delta s(x) + \Delta \bar{s}(x)], \\ g_1^n(x) &= \frac{2}{9} [\Delta d(x) + \Delta \bar{d}(x)] + \frac{1}{18} [\Delta u(x) + \Delta \bar{u}(x) + \Delta s(x) + \Delta \bar{s}(x)]. \end{aligned} \quad (4.234)$$

Several important sum rules can be derived for the first moment of  $g_1$ ,  $\Gamma_1 = \int_0^1 dx g_1(x)$ . From Eq. (4.234) it follows that

$$\Gamma_1^{p,n} = \frac{1}{9} a_0 \pm \frac{1}{12} a_3 + \frac{1}{36} a_8 \quad (4.235)$$

where  $a_0$ ,  $a_3$  and  $a_8$  are respectively the SU(3) flavour singlet, octet isotriplet and octet isosinglet combinations of the first moments of the quark distributions:

$$\begin{aligned} a_0 &= \eta_u + \eta_d + \eta_s \\ a_3 &= \eta_u - \eta_d \\ a_8 &= \eta_u + \eta_d - 2\eta_s, \end{aligned} \quad (4.236)$$

with  $\eta_u = \int_0^1 dx [\Delta u(x) + \Delta \bar{u}(x)]$  denoting the net spin carried by the different quark flavours. The triplet combination  $a_3$  is particularly interesting since it corresponds to the matrix element of a current which is directly measured in neutron  $\beta$ -decay. Taking the difference between  $\Gamma_1^p$  and  $\Gamma_1^n$  gives the *Bjorken sum rule* [50]

$$\Gamma_1^p - \Gamma_1^n = \int_0^1 dx (g_1^p - g_1^n) = \frac{1}{6} \left| \frac{g_A}{g_V} \right| = 0.209 \pm 0.001. \quad (4.237)$$

This sum rule, based on current algebra and SU(2) isospin symmetry, provides a fundamental test of the theory. In practice, perturbative QCD

corrections to the right-hand side of (4.237) (see below) must also be taken into account.

More generally, the axial-vector couplings measured in hyperon ( $\Lambda, \Sigma, \Xi$ ) decays give information on other combinations of  $\eta_u$ ,  $\eta_d$  and  $\eta_s$ , assuming SU(3) flavour symmetry. There are two independent parameters,  $F$  and  $D$ , which can be determined for example from  $n \rightarrow p$  and  $\Sigma^- \rightarrow n$  decays and in terms of which

$$\begin{aligned} a_3 &= F + D = 1.257 \pm 0.003 , \\ a_8 &= 3F - D = 0.58 \pm 0.02 , \end{aligned} \quad (4.238)$$

where the numerical values are taken from ref. [51].

The above information is, by itself, insufficient to determine the individual  $\Gamma_1^p$  and  $\Gamma_1^n$ . However with the further assumption that the strange quark sea in the proton is unpolarized ( $\eta_s = 0$ ), we obtain the *Ellis-Jaffe* [52] sum rule:

$$\Gamma_1^p = \int_0^1 dx g^p = \frac{1}{12} \left| \frac{g_A}{g_V} \right| \left[ 1 + \frac{5}{3} \frac{3F - D}{F + D} \right] = 0.185 \pm 0.003 . \quad (4.239)$$

Similarly, for the neutron we have

$$\Gamma_1^n = \int_0^1 dx g_1^n = \frac{1}{12} \left| \frac{g_A}{g_V} \right| \left[ -1 + \frac{5}{3} \frac{3F - D}{F + D} \right] = -0.024 \pm 0.003 . \quad (4.240)$$

A recent experimental measurement of  $\Gamma_1^p$ , which includes all available data, gives [53]

$$\Gamma_1^p = 0.142 \pm 0.008(\text{stat.}) \pm 0.011(\text{sys.}) \quad (Q^2 = 10 \text{ GeV}^2) . \quad (4.241)$$

Even allowing for the perturbative QCD correction  $1 - O(\alpha_s(Q^2)/\pi)$  to the right-hand side of (4.239), the measured value is significantly below the theoretical prediction. A possible explanation for this discrepancy is that the strange quarks do carry some of the proton's spin. In fact by combining the results from hyperon decays and the measured values of  $\Gamma_1^{p,n}$ , and including perturbative QCD corrections, one can deduce that, at  $Q^2 = 10 \text{ GeV}^2$ , [54]

$$\eta_u = +0.83 \pm 0.03, \quad \eta_d = -0.43 \pm 0.03, \quad \eta_s = -0.10 \pm 0.03 , \quad (4.242)$$

and therefore

$$\eta_\Sigma = \eta_u + \eta_d + \eta_s = 0.31 \pm 0.07 . \quad (4.243)$$

These can be compared with the SU(6) constituent quark model predictions [55]

$$\eta_u = \frac{4}{3}, \quad \eta_d = -\frac{1}{3}, \quad \eta_s = 0, \quad \eta_\Sigma = 1 . \quad (4.244)$$

### 4.7.2 Perturbative QCD corrections

The relatively large strange quark polarization and small total spin carried by the quarks, compared to the naive expectations of Eq. (4.244), has been the subject of much theoretical discussion in recent years. Although there is no reason why  $\eta_\Sigma$  should equal 1, since orbital angular momentum also contributes to the total spin of the nucleon, it seems somehow unnatural that the quarks should carry so little of the net spin. One of the more compelling explanations for this result is that a substantial amount of the nucleon's spin is carried by gluons. If we denote the net polarized gluon contribution by  $\eta_g = \int_0^1 dx \Delta g(x)$ , where  $\Delta g = g^\uparrow - g^\downarrow$ , then conservation of angular momentum implies

$$\frac{1}{2} = \frac{1}{2}\eta_\Sigma + \eta_g + \langle L_z \rangle. \quad (4.245)$$

The polarized gluon contributes to  $g_1$  at  $O(\alpha_s)$ , just as in the unpolarized case. In perturbative QCD the parton model result of Eq. (4.232) is replaced by (cf. Eq. (4.84) for  $F_2$ )

$$\begin{aligned} g_1(x, Q^2) &= \frac{1}{2} \sum_q e_q^2 \int_x^1 \frac{d\xi}{\xi} [\Delta q(x/\xi, Q^2) + \Delta \bar{q}(x/\xi, Q^2)] \\ &\times \left\{ \delta(1-\xi) + \frac{\alpha_s(Q^2)}{2\pi} \Delta C_q(\xi) + \dots \right\} \\ &+ \left( \sum_q e_q^2 \right) \int_x^1 \frac{d\xi}{\xi} \Delta g(x/\xi, Q^2) \left\{ \frac{\alpha_s(Q^2)}{2\pi} \Delta C_g(\xi) + \dots \right\}. \end{aligned} \quad (4.246)$$

The leading-order GLAP equations for the evolution of the polarized quark and gluon distributions are

$$\begin{aligned} t \frac{\partial}{\partial t} \begin{pmatrix} \Delta q_i(x, t) \\ \Delta g(x, t) \end{pmatrix} &= \frac{\alpha_s(t)}{2\pi} \sum_j \int_x^1 \frac{d\xi}{\xi} \\ &\times \begin{pmatrix} \Delta P_{q_i q_j} \left( \frac{x}{\xi} \right) & \Delta P_{q g} \left( \frac{x}{\xi} \right) \\ \Delta P_{g q} \left( \frac{x}{\xi} \right) & \Delta P_{g g} \left( \frac{x}{\xi} \right) \end{pmatrix} \begin{pmatrix} \Delta q_j(\xi, t) \\ \Delta g(\xi, t) \end{pmatrix}. \end{aligned} \quad (4.247)$$

The splitting functions are [8]

$$\begin{aligned} \Delta P_{qq}^{(0)}(x) &= C_F \left[ \frac{1+x^2}{(1-x)_+} + \frac{3}{2} \delta(1-x) \right], \\ \Delta P_{qg}^{(0)}(x) &= T_R [2x-1], \quad T_R = \frac{1}{2}, \\ \Delta P_{gg}^{(0)}(x) &= C_F [2-x], \end{aligned}$$

$$\begin{aligned}\Delta P_{gg}^{(0)}(x) &= C_A \left[ \frac{2}{(1-x)_+} - 4x + 2 \right] \\ &\quad + \delta(1-x) \frac{11C_A - 4n_f T_R}{6},\end{aligned}\quad (4.248)$$

where the ‘plus prescription’ on the singular parts of the splitting functions has been defined in Eq. (4.72). The next-to-leading ( $O(\alpha_s^2)$ ) contributions to the polarized splitting functions have also been calculated [56].

The evolution of the first ( $j = 1$ ) moments of the quark flavour singlet and gluon distributions can be obtained from Eqs. (4.247) and (4.248):

$$t \frac{\partial}{\partial t} \begin{pmatrix} \Delta\Sigma(1,t) \\ \Delta g(1,t) \end{pmatrix} = \frac{\alpha_s(t)}{2\pi} \begin{pmatrix} 0 & 0 \\ \frac{3}{2}C_F & 2\pi b \end{pmatrix} \begin{pmatrix} \Delta\Sigma(1,t) \\ \Delta g(1,t) \end{pmatrix}. \quad (4.249)$$

Hence

$$t \frac{\partial}{\partial t} \eta_\Sigma(t) = 0 + O(\alpha_s^2), \quad (4.250)$$

$$t \frac{\partial}{\partial t} \alpha_s(t) \eta_g(t) = 0 + O(\alpha_s^2). \quad (4.251)$$

which implies that the gluon contribution to  $g_1$  ( $\sim \alpha_s \Delta g$ ) is formally of the same order as the quark contribution. The polarized structure function has been separated into two conserved (at leading order) quantities associated with quark and gluon contributions, the former to be identified with the SU(6) ‘constituent’ quarks. If we attribute the difference between the Ellis-Jaffe sum rule prediction (*i.e.* assuming no strange quark polarization at low  $Q^2$ ) and the measured value to the gluon contribution, then we find  $\eta_g(Q_0^2 = 4 \text{ GeV}^2) \approx 2$  [57]. The importance of the polarized gluon contribution to the structure function was first pointed out in refs. [58,59].

In the Bjorken sum (4.237) the gluon contribution cancels, and perturbative QCD corrections simply modify the leading-order result. In fact the corrections are closely related to those for the Gross-Llewellyn Smith sum rule (4.156), and are known to  $O(\alpha_s^3)$  [25]. In the  $\overline{\text{MS}}$  renormalization scheme

$$\begin{aligned}\Gamma_1^p(Q^2) - \Gamma_1^n(Q^2) &= \frac{1}{6} \left| \frac{g_A}{g_V} \right| \left[ 1 - \frac{\alpha_s(Q^2)}{\pi} + \left( \frac{\alpha_s(Q^2)}{\pi} \right)^2 \left( -\frac{55}{12} + n_f \frac{1}{3} \right) \right. \\ &\quad + \left( \frac{\alpha_s(Q^2)}{\pi} \right)^3 \left( -\frac{13841}{216} - \frac{44}{9} \zeta(3) + \frac{55}{2} \zeta(5) \right. \\ &\quad \left. \left. + n_f \left( \frac{10339}{1296} + \frac{61}{54} \zeta(3) - \frac{5}{3} \zeta(5) \right) - n_f^2 \frac{115}{648} \right) \right].\end{aligned}\quad (4.252)$$

Comparison of the theoretical prediction with the measured value gives a measurement of the strong coupling, see Chapter 12.

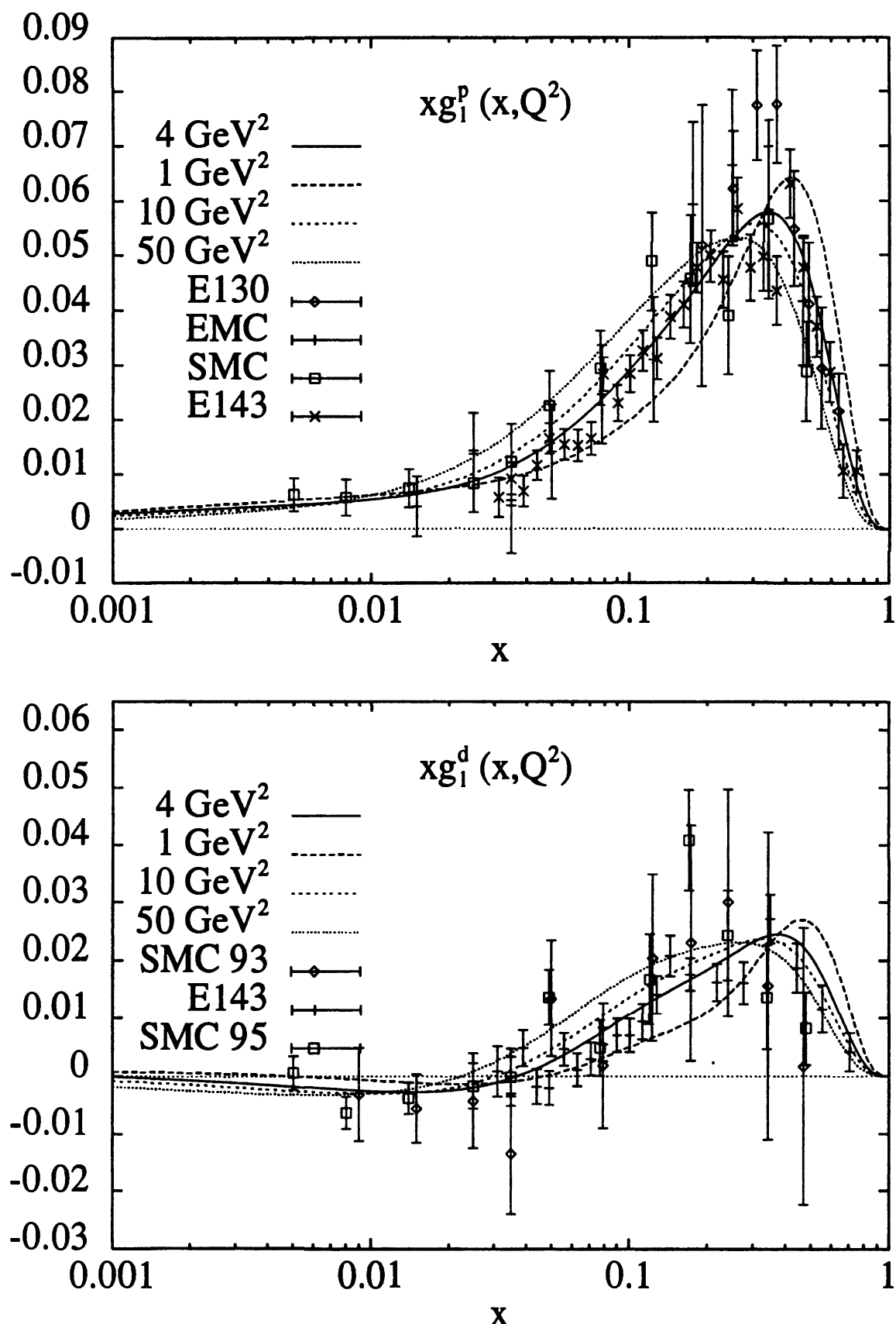


Fig. 4.26. Data on the structure function  $g_1$  for proton and deuteron targets. The curves are NLO QCD fits. Figure from ref. [57].

Concerning the *shape* in  $x$  of the polarized parton distributions, the situation is very different from the unpolarized case, where a combination of structure function measurements with charged lepton and neutrino beams and measurements of gluon-induced processes, such as direct photon and heavy quark production, pin down quite accurately the shape of the individual distributions. Here, the only useful information at present comes from  $g_1(x, Q^2)$  measured with proton, neutron and deuteron targets. These data essentially only determine the shape of the valence  $u$  and  $d$  quark distributions, and the sea and gluon distributions are largely unconstrained. Parton distribution fits, similar to those described in Section 4.4, must therefore be supplemented by model assumptions about the behaviours at large and small  $x$ , the flavour decomposition of the sea, the shape of the gluon distribution etc. Nevertheless, the high- $Q^2$   $g_1$  structure function data *can* be very well described in either leading- or next-to-leading-order fits based on the perturbative QCD evolution equations. This is illustrated in Fig. 4.26, which shows the NLO description [57] of various  $g_1$  measurements [60] using a particular ansatz for the shape of the gluon distribution. The curves correspond to  $Q^2 = 1, 4, 10, 50 \text{ GeV}^2$ , reflecting the spread in  $Q^2$  values of the different data sets. There is a systematic decrease in the  $Q^2$  values of the data points from large  $x$  to small  $x$ .

## References

- 1) J.D. Bjorken, *Phys. Rev.* **179** (1969) 1547.
- 2) R.P. Feynman, *Photon Hadron Interactions*, W.A. Benjamin, New York (1972).
- 3) SLAC-MIT collaboration, G. Miller *et al.*, *Phys. Rev.* **D5** (1972) 528.
- 4) BCDMS collaboration, A.C. Benvenuti *et al.*, *Phys. Lett.* **B223** (1989) 485.
- 5) H1 collaboration, T. Ahmed *et al.*, *Nucl. Phys.* **B439** (1995) 471.
- 6) ZEUS collaboration, M. Derrick *et al.*, *Zeit. Phys.* **C65** (1995) 379.
- 7) A.D. Martin, R.G. Roberts and W.J. Stirling, *Phys. Rev.* **D50** (1994) 6734.
- 8) G. Altarelli and G. Parisi, *Nucl. Phys.* **B126** (1977) 298.
- 9) G. Altarelli, R.K. Ellis and G. Martinelli, *Nucl. Phys.* **B143** (1978) 521; *ibid.* **B146** (1978) 544(erratum).
- 10) W.A. Bardeen, A.J. Buras, D.W. Duke and T. Muta, *Phys. Rev.* **D18** (1978) 3998.
- 11) M. Göckeler *et al.*, *Phys. Rev.* **D53** (1996) 2317.
- 12) L.N. Lipatov, *Sov. J. Nucl. Phys.* **20** (1975) 95;  
V.N. Gribov and L.N. Lipatov, *Sov. J. Nucl. Phys.* **15** (1972) 438;  
G. Altarelli and G. Parisi, ref. [8];  
Yu.L. Dokshitzer *Sov. Phys. JETP* **46** (1977) 641.
- 13) H. Georgi and H.D. Politzer, *Phys. Rev.* **D9** (1974) 416.
- 14) D. Gross and F. Wilczek, *Phys. Rev.* **D9** (1974) 980.
- 15) G. Curci, W. Furmanski and R. Petronzio, *Nucl. Phys.* **B175** (1980) 27.
- 16) W. Furmanski and R. Petronzio, *Phys. Lett.* **B97** (1980) 437.

- 17) E.G. Floratos, D.A. Ross and C.T. Sachrajda, *Nucl. Phys.* **B129** (1977) 66; *ibid.* **B139** (1978) 545(erratum); *ibid.* **B152** (1979) 493;  
 A. Gonzalez-Arroyo, C. Lopez and F.J. Yndurain, *Nucl. Phys.* **B153** (1979) 161;  
 E.G. Floratos, R. Lacaze and C. Kounnas, *Nucl. Phys.* **B192** (1981) 417.
- 18) NMC collaboration, P. Amaudruz *et al.*, *Phys. Lett.* **B295** (1992) 159.
- 19) G. Altarelli, *Phys. Rep.* **81** (1982) 1.
- 20) A. Milsztajn and M. Virchaux, *Phys. Lett.* **B274** (1992) 221.
- 21) BCDMS collaboration, A.C. Benvenuti *et al.*, *Phys. Lett.* **B237** (1990) 592.
- 22) L.W. Whitlow, Ph.D. thesis, SLAC-Report -357 (1990).
- 23) D.J. Gross and C.H. Llewellyn Smith, *Nucl. Phys.* **B14** (1969) 337.
- 24) S.G. Gorishny and S.A. Larin, *Phys. Lett.* **B172** (1986) 109.
- 25) S.A. Larin and J.A.M. Vermaseren, *Phys. Lett.* **B259** (1991) 345.
- 26) CCFR-NUTEV collaboration, M.H. Shaevitz *et al.*, *Nucl. Phys. B (Proc. Suppl.)* **38** (1995) 188.
- 27) S.L. Adler, *Phys. Rev.* **143** (1963) 1144.
- 28) BEBC collaboration, D. Allasia *et al.*, *Phys. Lett.* **B135** (1984) 231; *Zeit. Phys.* **C28** (1985) 321.
- 29) K. Gottfried, *Phys. Rev. Lett.* **18** (1967) 1154
- 30) NMC collaboration, P. Amaudruz *et al.*, *Phys. Rev. Lett.* **66** (1991) 2712.
- 31) P.D.B. Collins, *Introduction to Regge Theory*, Cambridge University Press (1977).
- 32) A. Donnachie and P.V. Landshoff, *Zeit. Phys.* **C61** (1994) 139.
- 33) A.D. Martin, R.G. Roberts and W.J. Stirling, *Phys. Lett.* **B354** (1995) 155.
- 34) A. De Rujula, S.L. Glashow, H.D. Politzer, S.B. Treiman, F. Wilczek and A. Zee, *Phys. Rev.* **10** (1974) 1649.
- 35) R.D. Ball and S. Forte, *Phys. Lett.* **B335** (1994) 77; *ibid.* **B336** (1994) 77.
- 36) H1 collaboration, S. Aid *et al.*, *Phys. Lett.* **B354** (1995) 494.
- 37) E.A. Kuraev, L.N. Lipatov and V.S. Fadin, *Phys. Lett.* **B60** (1975) 50; *Sov. Phys. JETP* **44** (1976) 433; *ibid.* **45** (1977) 199;  
 Ya.Ya. Balitsky and L.N. Lipatov, *Sov. J. Nucl. Phys.* **28** (1978) 822.
- 38) S. Catani and F. Hautmann, *Nucl. Phys.* **B427** (1994) 475.
- 39) See for example:  
 R.K. Ellis, Z. Kunszt and E. Levin, *Nucl. Phys.* **B420** (1994) 517; *ibid.* **B433** (1995) 498(erratum);  
 R.K. Ellis, F. Hautmann and B.R. Webber, *Phys. Lett.* **B348** (1995) 582;  
 R.D. Ball and S. Forte, *Phys. Lett.* **B351** (1995) 513;  
 J.R. Forshaw, R.G. Roberts and R.S. Thorne, *Phys. Lett.* **B356** (1995) 79.
- 40) S. Catani, M. Ciafaloni and F. Hautmann, *Phys. Lett.* **B242** (1990) 97; *Nucl. Phys.* **B366** (1991) 657.
- 41) A.J. Askew, J. Kwiecinski, A.D. Martin and P.J. Sutton, *Phys. Rev.* **D47** (1993) 3775;  
*ibid.* **D49** (1994) 4402; *Mod. Phys. Lett.* **A8** (1993) 3813.
- 42) M. Ciafaloni, *Nucl. Phys.* **B296** (1988) 49;  
 S. Catani, F. Fiorani and G. Marchesini, *Phys. Lett.* **B234** (1990) 339; *Nucl. Phys.* **B336** (1990) 18.
- 43) J. Kwiecinski, A.D. Martin and P.J. Sutton, *Phys. Rev.* **D52** (1995) 1445.
- 44) A.H. Mueller, *Nucl. Phys.* **B415** (1994) 373;  
 A.H. Mueller and B. Patel, *Nucl. Phys.* **B425** (1994) 471;  
 See also: N.N. Nikolaev, B.G. Zakharov and V.R. Zoller, *Phys. Lett.* **B328** (1994) 486.
- 45) G. 't Hooft, *Nucl. Phys.* **B72** (1974) 461.
- 46) L.V. Gribov, E.M. Levin and M.G. Ryskin, *Phys. Rep.* **100** (1983) 1.

- 47) A.H. Mueller and J. Qiu, *Nucl. Phys.* **B268** (1986) 427
- 48) J. Kwiecinski, A.D. Martin, R.G. Roberts and W.J. Stirling, *Phys. Rev.* **D42** (1990) 3645.
- 49) R.G. Roberts, *The Structure of the Proton*, Cambridge University Press (1990).
- 50) J.D. Bjorken, *Phys. Rev.* **148** (1966) 1467; *Phys. Rev.* **D1** (1970) 1376.
- 51) F.E. Close and R.G. Roberts, *Phys. Lett.* **B316** (1993) 165.
- 52) J. Ellis and R.L. Jaffe, *Phys. Rev.* **D9** (1974) 1444; *ibid.* **D10** (1974) 1669.
- 53) SMC collaboration, D. Adams *et al.*, *Phys. Lett.* **B329** (1994) 399.
- 54) J. Ellis and M. Karliner, *Phys. Lett.* **B341** (1995) 397.
- 55) M. Gourdin, *Nucl. Phys.* **B38** (1972) 418.
- 56) R. Mertig and W.L. van Neerven, *Zeit. Phys.* **C70** (1996) 637; W. Vogelsang, *Phys. Rev.* **D54** (1996) 2023.
- 57) T. Gehrmann and W.J. Stirling, *Phys. Rev.* **D53** (1996) 6100.
- 58) G. Altarelli and G.G. Ross, *Phys. Lett.* **B212** (1988) 391.
- 59) A.V. Efremov and O.V. Teryaev, Proc. Int. Hadron Symposium, Bechnye, Czechoslovakia, 1988, eds. X. Fischer *et al.*, Czech Academy of Sciences, 1989, p. 302.
- 60) SLAC-E130 collaboration, M.J. Alguard *et al.*, *Phys. Rev. Lett.* **37** (1976) 1261; G. Baum *et al.*, *Phys. Rev. Lett.* **45** (1980) 2000; *ibid.* **51** (1983) 1135; SLAC-E143 collaboration, K. Abe *et al.*, *Phys. Rev. Lett.* **74** (1995) 346; *ibid.* **75** (1995) 25; EMC collaboration, J. Ashman *et al.*, *Nucl. Phys.* **B328** (1989) 1; SMC collaboration, B. Adeva *et al.*, *Phys. Lett.* **B302** (1993) 533; D. Adams *et al.*, *Phys. Lett.* **B329** (1994) 399; *ibid.* **B357** (1995) 248.

## 5

## Parton branching and jet simulation

Complete perturbative calculations in QCD have been performed only to next-to-leading order in most cases, or to one further order in  $\alpha_s$  for a few observables. The work involved increases roughly factorially with the order, so we cannot expect many more higher-order terms to be calculated soon. Nevertheless there are regions of phase space in which higher-order terms are enhanced and cannot be neglected. An example is the region of collinear parton emission from the struck parton in deep inelastic scattering. We saw in Section 4.3 that this region gives rise to logarithmic scaling violation in the structure functions. Another example is the high-thrust ( $T \rightarrow 1$ ) region in  $e^+e^-$  annihilation, discussed in Section 3.4. Here the contribution of order  $\alpha_s^n$  has a coefficient which is proportional to  $\ln^{2n-1}(1-T)/(1-T)$  at large  $T$ . The extra factor of  $\ln^2(1-T)$  for each power of  $\alpha_s$  makes fixed-order predictions unreliable at high thrust.

In the present chapter we shall adopt a somewhat different approach from that of earlier chapters. Instead of aiming for a precise prediction to some fixed order in perturbation theory, we shall seek an approximate result in which such enhanced terms are taken into account to all orders. We shall see that this leads to a physically appealing ‘parton shower’ picture which can readily be implemented in computer simulations, often called QCD Monte Carlo programs. The parton shower represents an approximate perturbative treatment of QCD dynamics at scales of momentum transfer-squared  $t$  greater than some infra-red cut-off value  $t_0$ , typically taken to be of the order of  $1 \text{ GeV}^2$ . The Monte Carlo method is particularly convenient because the perturbative treatment at  $t > t_0$  can be combined with a non-perturbative model of the hadronization process, assumed to take place at scales  $t < t_0$ . In this way one obtains a *QCD event generator*, *i.e.* a program which provides a complete model for a

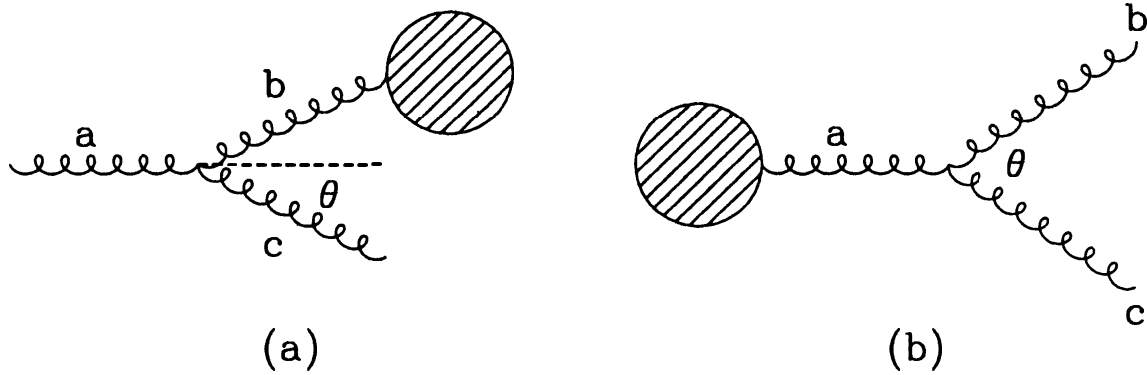


Fig. 5.1. Parton branching of (a) incoming and (b) outgoing partons.

given class of processes involving the interaction and/or production of hadrons.

Enhanced higher-order terms are associated with kinematic configurations for which the relevant QCD matrix elements are large. In particular, we have seen that there are enhancements when a soft gluon is emitted, or when a gluon or light quark splits into two almost collinear partons. The leading contributions of these soft and collinear configurations (and the corresponding enhanced virtual corrections) can be identified and summed to all orders, improving the convergence of the perturbation series.

We shall concentrate first on collinear enhancements, like those encountered in deep inelastic scattering. These are associated with *parton branching* on an incoming or outgoing line of a QCD Feynman diagram, as illustrated in Fig. 5.1. The shaded blobs represent the rest of the diagram, apart from the branching line, in this case a gluon. We shall calculate the contributions of such processes in some detail, because they form the basis not only for many tests of QCD but also for the QCD Monte Carlo programs mentioned above.

## 5.1 Parton branching

Fig. 5.2 shows the kinematics and notation for the branching of parton  $a$  into  $b + c$ . We assume that

$$p_b^2, p_c^2 \ll p_a^2 \equiv t \quad (5.1)$$

and for the moment we consider the case that  $a$  is an outgoing parton, which is called *timelike branching* since  $t > 0$ . The opening angle is  $\theta = \theta_b + \theta_c$ . Defining the energy fraction as

$$z = E_b/E_a = 1 - E_c/E_a , \quad (5.2)$$

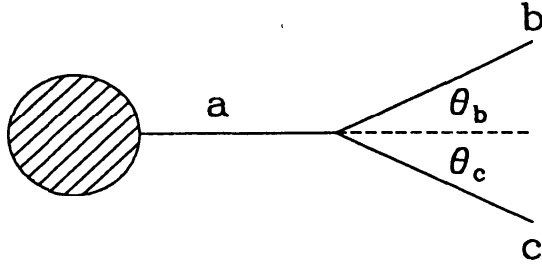


Fig. 5.2. Kinematics of timelike parton branching.

we have for small angles, where the matrix element is enhanced,

$$t = 2E_b E_c (1 - \cos \theta) = z(1 - z) E_a^2 \theta^2 , \quad (5.3)$$

and hence, using transverse momentum conservation,

$$\theta = \frac{1}{E_a} \sqrt{\frac{t}{z(1 - z)}} = \frac{\theta_b}{1 - z} = \frac{\theta_c}{z} . \quad (5.4)$$

We consider first the case that all the partons  $a, b$  and  $c$  are gluons. There will be a factor in the amplitude proportional to  $1/t$  from the propagator for gluon  $a$ , and a triple-gluon vertex factor

$$V_{ggg} = ig f^{ABC} \varepsilon_a^\alpha \varepsilon_b^\beta \varepsilon_c^\gamma [g_{\alpha\beta}(p_a - p_b)_\gamma + g_{\beta\gamma}(p_b - p_c)_\alpha + g_{\gamma\alpha}(p_c - p_a)_\beta] \quad (5.5)$$

where  $\varepsilon_i^\mu$  represents the polarization vector for gluon  $i$ . Note that here all momenta are defined as outgoing, so that  $p_a = -p_b - p_c$ . Using this and the conditions  $\varepsilon_i \cdot p_i = 0$ , we can write

$$V_{ggg} = -2ig f^{ABC} [(\varepsilon_a \cdot \varepsilon_b)(\varepsilon_c \cdot p_b) - (\varepsilon_b \cdot \varepsilon_c)(\varepsilon_a \cdot p_b) - (\varepsilon_c \cdot \varepsilon_a)(\varepsilon_b \cdot p_c)] . \quad (5.6)$$

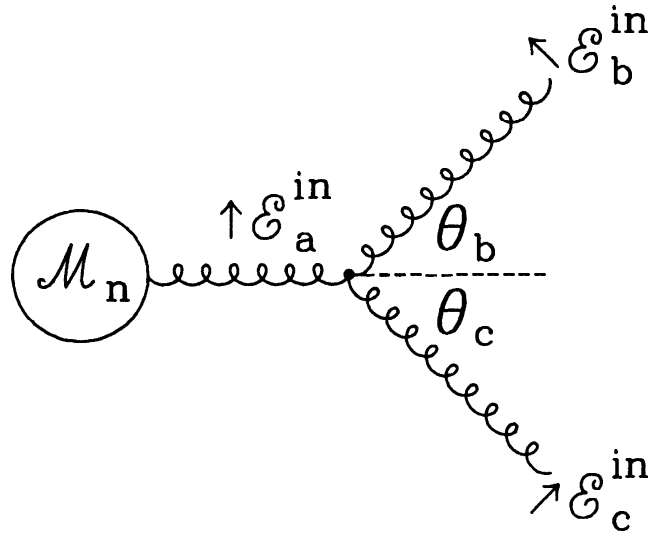
Since the three gluons are almost on mass-shell, we can take their polarization vectors to be purely transverse. We shall resolve them into plane polarization states,  $\varepsilon_i^{\text{in}}$  in the plane of branching and  $\varepsilon_i^{\text{out}}$  normal to the plane, as shown in Fig. 5.3, so that

$$\begin{aligned} \varepsilon_i^{\text{in}} \cdot \varepsilon_j^{\text{in}} &= \varepsilon_i^{\text{out}} \cdot \varepsilon_j^{\text{out}} = -1 \\ \varepsilon_i^{\text{in}} \cdot \varepsilon_j^{\text{out}} &= \varepsilon_i^{\text{out}} \cdot p_j = 0 . \end{aligned} \quad (5.7)$$

For small  $\theta$ , neglecting terms of order  $\theta^2$ , we have

$$\begin{aligned} \varepsilon_a^{\text{in}} \cdot p_b &= -E_b \theta_b = -z(1 - z) E_a \theta \\ \varepsilon_b^{\text{in}} \cdot p_c &= +E_c \theta = (1 - z) E_a \theta \\ \varepsilon_c^{\text{in}} \cdot p_b &= -E_b \theta = -z E_a \theta . \end{aligned} \quad (5.8)$$

Note that every vertex factor is proportional to  $\theta$ , which, together with the  $1/t \propto 1/\theta^2$  from the propagator, gives a  $1/\theta$  singularity in the amplitude. Putting everything together using Eq. (5.4), we can write the matrix

Fig. 5.3. Notation for  $g \rightarrow gg$  branching.

$\epsilon_a$	$\epsilon_b$	$\epsilon_c$	$F(z; \epsilon_a, \epsilon_b, \epsilon_c)$
in	in	in	$(1-z)/z + z/(1-z) + z(1-z)$
in	out	out	$z(1-z)$
out	in	out	$(1-z)/z$
out	out	in	$z/(1-z)$

Table 5.1. Polarization dependence of the branching  $g \rightarrow gg$ .

element squared for  $n+1$  partons in this small-angle region in terms of that for  $n$  partons,

$$|\mathcal{M}_{n+1}|^2 \sim \frac{4g^2}{t} C_A F(z; \epsilon_a, \epsilon_b, \epsilon_c) |\mathcal{M}_n|^2 \quad (5.9)$$

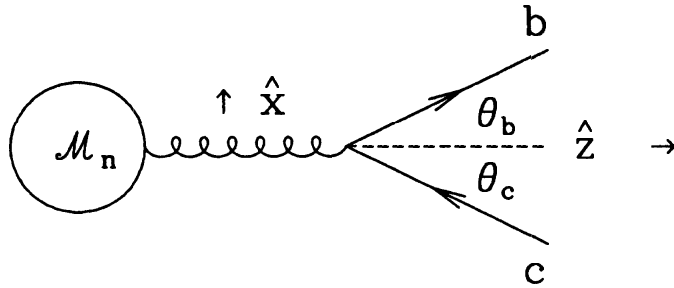
where the colour factor  $C_A = 3$  comes from  $f^{ABC} f^{ABC}$  and the functions  $F(z; \epsilon_a, \epsilon_b, \epsilon_c)$  are given in Table 5.1.

All polarization combinations not given in Table 5.1 are forbidden. Defining  $\langle F \rangle$  by averaging  $F(z; \epsilon_a, \epsilon_b, \epsilon_c)$  with respect to the polarization of  $a$  and summing over those of  $b$  and  $c$ , we find that

$$C_A \langle F \rangle \equiv \hat{P}_{gg}(z) = C_A \left[ \frac{1-z}{z} + \frac{z}{1-z} + z(1-z) \right] \quad (5.10)$$

where  $\hat{P}_{gg}(z)$  is called the unregularized *gluon splitting function* related to the corresponding Altarelli-Parisi kernel already encountered in Chapter 4.

We see from Table 5.1 that the enhancements in the matrix elements at  $z \rightarrow 0$  ( $b$  soft) and  $z \rightarrow 1$  ( $c$  soft) are associated with the emission of

Fig. 5.4. Notation for  $g \rightarrow q\bar{q}$  branching.

a soft gluon polarized in the plane of branching. Another important polarization effect is the correlation between the plane of branching and the polarization of the branching gluon. If we suppose that the polarization of gluon  $a$  is at an angle  $\phi$  to the plane then the function  $F$  becomes

$$\begin{aligned} F_\phi &\propto \sum_{\epsilon_{b,c}} |\cos \phi \mathcal{M}(\epsilon_a^{\text{in}}, \epsilon_b, \epsilon_c) + \sin \phi \mathcal{M}(\epsilon_a^{\text{out}}, \epsilon_b, \epsilon_c)|^2 \\ &= \cos^2 \phi \left[ \frac{1-z}{z} + \frac{z}{1-z} + 2z(1-z) \right] + \sin^2 \phi \left[ \frac{1-z}{z} + \frac{z}{1-z} \right] \\ &= \frac{1-z}{z} + \frac{z}{1-z} + z(1-z) + z(1-z) \cos 2\phi. \end{aligned} \quad (5.11)$$

The first three terms give the unpolarized result and the last gives the correlation, which favours an orientation in which the polarization of the branching gluon lies in the plane of branching. The correlation is quite weak, however: its coefficient  $z(1-z)$  vanishes in the enhanced regions  $z \rightarrow 0, 1$  and reaches its maximum at  $z = \frac{1}{2}$ , where it is still only  $1/9$  of the unpolarized contribution.

Consider next the branching of a gluon into a quark-antiquark pair, Fig. 5.4. Once again we have a factor of  $1/t$  in the amplitude from the gluon propagator, but the vertex factor is now

$$V_{gq\bar{q}} = -ig t_{bc}^A \bar{u}^b \gamma_\mu \epsilon_a^\mu v^c \quad (5.12)$$

where  $u^b$  and  $v^c$  are the quark and antiquark spinors. For this process we shall continue to use the plane polarization states defined above for the gluon, but will adopt helicity states for quarks and antiquarks. We follow the conventions of Bjorken and Drell [1] for spinors and Dirac algebra, in which

$$\gamma^0 = \begin{pmatrix} 1 & 0 \\ 0 & -1 \end{pmatrix}, \quad \gamma^i = \begin{pmatrix} 0 & \sigma_i \\ -\sigma_i & 0 \end{pmatrix} \quad (5.13)$$

where the matrix elements are themselves  $2 \times 2$  matrices and  $\sigma_i$  are the Pauli spin matrices. Then to first order in small angles the helicity spinors

$\varepsilon_a$	$\lambda_b$	$\lambda_c$	$F(z; \varepsilon_a, \lambda_b, \lambda_c)$
in	$\pm$	$\mp$	$(1 - 2z)^2$
out	$\pm$	$\mp$	1

Table 5.2. Polarization dependence of the branching  $g \rightarrow q\bar{q}$ .

are [1]

$$\begin{aligned} u_+^b &= \sqrt{E_b} \begin{pmatrix} 1 \\ \frac{1}{2}\theta_b \\ 1 \\ \frac{1}{2}\theta_b \end{pmatrix}, \quad u_-^b = \sqrt{E_b} \begin{pmatrix} -\frac{1}{2}\theta_b \\ 1 \\ \frac{1}{2}\theta_b \\ -1 \end{pmatrix}, \\ v_+^c &= i\sqrt{E_c} \begin{pmatrix} -\frac{1}{2}\theta_c \\ -1 \\ \frac{1}{2}\theta_c \\ 1 \end{pmatrix}, \quad v_-^c = i\sqrt{E_c} \begin{pmatrix} -1 \\ \frac{1}{2}\theta_c \\ -1 \\ \frac{1}{2}\theta_c \end{pmatrix}. \end{aligned} \quad (5.14)$$

Thus we find, for example,

$$-ig\bar{u}_+^b \gamma_\mu \varepsilon_a^{\text{in}\mu} v_-^c = \sqrt{E_b E_c} (\theta_b - \theta_c) = \sqrt{z(1-z)} (1 - 2z) E_a \theta, \quad (5.15)$$

and the matrix element relation analogous to Eq. (5.9) is

$$|\mathcal{M}_{n+1}|^2 \sim \frac{4g^2}{t} T_R F(z; \varepsilon_a, \lambda_b, \lambda_c) |\mathcal{M}_n|^2 \quad (5.16)$$

where the colour factor is now  $\text{Tr}(t^A t^A)/8 = T_R = 1/2$ . The non-vanishing functions  $F(z; \varepsilon_a, \lambda_b, \lambda_c)$  for quark and antiquark helicities  $\lambda_b$  and  $\lambda_c$  are given in Table 5.2.

In this case we see that the quark and antiquark helicities are always opposite, which is a consequence of the helicity conservation implied (for quarks of negligible mass) by the vector nature of the quark-gluon coupling. There are no soft ( $z \rightarrow 0$  or 1) singularities since these are associated only with gluon emission. The spin-averaged splitting function is

$$T_R \langle F \rangle \equiv \hat{P}_{qg}(z) = T_R [z^2 + (1 - z)^2]. \quad (5.17)$$

Note that in this case the amplitude vanishes at  $z = \frac{1}{2}$  when the gluon  $a$  is polarized in the plane of branching, indicating a strong anticorrelation between the polarization and the plane. The angular correlation is now given by

$$\begin{aligned} F_\phi &\propto \cos^2 \phi (1 - 2z)^2 + \sin^2 \phi \\ &= z^2 + (1 - z)^2 - 2z(1 - z) \cos 2\phi. \end{aligned} \quad (5.18)$$

$\lambda_a$	$\lambda_b$	$\varepsilon_c$	$F(z; \lambda_a, \lambda_b, \varepsilon_c)$
$\pm$	$\pm$	in	$(1+z)^2/(1-z)$
$\pm$	$\pm$	out	$1-z$

Table 5.3. Polarization dependence of the branching  $q \rightarrow qg$ .

Finally, for the branching in which a light quark (or antiquark) emits a gluon, the small-angle matrix element relation takes the form

$$|\mathcal{M}_{n+1}|^2 \sim \frac{4g^2}{t} C_F F(z; \lambda_a, \lambda_b, \varepsilon_c) |\mathcal{M}_n|^2 \quad (5.19)$$

with colour factor  $C_F = \text{Tr}(t^A t^A)/3 = 4/3$ . All the necessary ingredients have been given in the previous two cases, and we leave it as an exercise for the reader to derive the results in Table 5.3 for the polarization dependent function  $F(z; \lambda_a, \lambda_b, \varepsilon_c)$ . The spin-averaged splitting function becomes

$$C_F \langle F \rangle \equiv \hat{P}_{qq}(z) = C_F \frac{1+z^2}{1-z}. \quad (5.20)$$

Notice that helicity conservation ensures that the quark does not change its helicity in this branching. Only the amplitude for gluon polarization in the plane of branching has the soft gluon ( $z \rightarrow 1$ ) singularity: the ‘out’ amplitude actually vanishes at  $z = 1$ . Thus there is a preference for the gluon to be polarized in the plane, the angular correlation being given by

$$F_\phi \propto \frac{1+z^2}{1-z} + \frac{2z}{1-z} \cos 2\phi. \quad (5.21)$$

This angular correlation and those derived for the other branching processes are well illustrated by the angular distribution of four-jet events in  $e^+e^-$  annihilation, discussed in Chapter 3 and shown in Fig 3.11. Recall that the Bengtsson-Zerwas angle is the angle between the planes of the two hardest and two softest jets. The lowest-order Feynman diagrams contributing to four-jet production were given in Fig. 3.10. The two hardest jets tend to follow the directions of the quarks coming from the primary vertex, while the softer jets usually come from the produced quarks or gluons.

The three double bremsstrahlung diagrams in Fig. 3.10 give negligible correlations. The diagrams in which an emitted gluon splits into a quark-antiquark pair give a strong anti-correlation, as seen in the curve labelled ‘Abelian’ in Fig 3.11. This is because, as we have just seen, the gluon tends to be polarized in the plane of the primary jets and then prefers to split perpendicular to its polarization. On the other hand the splitting

into two gluons occurs more often parallel to the polarization. Although the correlation is much weaker than that in  $g \rightarrow q\bar{q}$ , the two-gluon splitting is dominant in QCD, due to its larger colour factor and soft gluon enhancements. Thus the Bengtsson-Zerwas angular distribution is flatter than would be expected in an Abelian theory with no triple-boson vertex, in agreement with experiment.

In order to compute cross sections from the matrix elements for the various branching processes we have to consider also the initial-state flux factor  $\mathcal{F}$  and the final-state  $n$ -parton phase space  $d\Phi_n$ :

$$d\sigma_n = \mathcal{F} |\mathcal{M}_n|^2 d\Phi_n . \quad (5.22)$$

For the timelike branching shown in Fig. 5.2, to go from the process with  $a$  outgoing to that in which it is replaced by  $b + c$ , we should replace

$$d\Phi_n = \dots \frac{d^3 p_a}{2(2\pi)^3 E_a} \quad (5.23)$$

by

$$d\Phi_{n+1} = \dots \frac{d^3 p_b}{2(2\pi)^3 E_b} \frac{d^3 p_c}{2(2\pi)^3 E_c} . \quad (5.24)$$

Now  $p_c = p_a - p_b$  and hence  $d^3 p_c = d^3 p_a$  at fixed  $p_b$ . Thus we find, in the usual small-angle approximation,

$$\begin{aligned} d\Phi_{n+1} &= d\Phi_n \frac{1}{2(2\pi)^3} \int E_b dE_b \theta_b d\theta_b d\phi dt \frac{dz}{1-z} \delta(t - E_b E_c \theta^2) \\ &\quad \delta(z - E_b/E_a) \\ &= d\Phi_n \frac{1}{4(2\pi)^3} dt dz d\phi , \end{aligned} \quad (5.25)$$

which gives

$$d\sigma_{n+1} = d\sigma_n \frac{dt}{t} dz \frac{d\phi}{2\pi} \frac{\alpha_s}{2\pi} CF \quad (5.26)$$

where  $C$  and  $F$  are respectively the colour factor and polarization dependent  $z$ -distribution introduced earlier. If we are not interested in the dependence on the azimuthal angle  $\phi$ , we can make the replacement

$$\int \frac{d\phi}{2\pi} CF = \hat{P}_{ba}(z) \quad (5.27)$$

where  $\hat{P}_{ba}(z)$  is the appropriate splitting function, to give

$$d\sigma_{n+1} = d\sigma_n \frac{dt}{t} dz \frac{\alpha_s}{2\pi} \hat{P}_{ba}(z) . \quad (5.28)$$

Finally let us consider the case of branching on an incoming line, as illustrated in Fig. 5.5, which is relevant to deep inelastic scattering. This

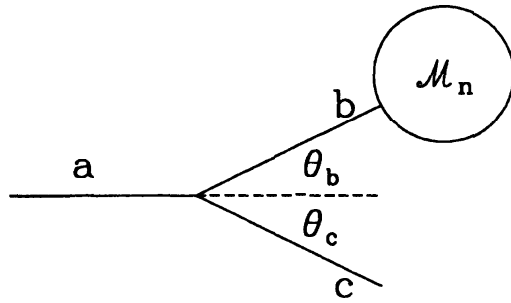


Fig. 5.5. Kinematics of spacelike parton branching.

branching will relate the process with  $b$  incoming to that with  $a$  incoming and  $c$  emitted. We can assume that

$$|p_a^2|, p_c^2 \ll |p_b^2| \equiv t \quad (5.29)$$

while as before  $z = E_b/E_a = 1 - E_c/E_a$ . Since the internal line has negative virtual mass-squared  $-t$ , this is called spacelike branching.

In the above treatment of the matrix elements for the various branching processes, we evaluated the vertex factors in the approximation that all lines were on mass-shell. Therefore the only changes we need to make in going from the timelike to the spacelike case are to the kinematics. For small angles we now have

$$t = E_a E_c \theta_c^2. \quad (5.30)$$

Including the phase space for the emitted parton  $c$  at fixed  $E_b$ , we find

$$\begin{aligned} d\Phi_{n+1} &= d\Phi_n \frac{1}{2(2\pi)^3} \int E_c dE_c \theta_c d\theta_c d\phi dt dz \delta(t - E_a E_c \theta_c^2) \\ &\quad \delta(z - E_b/E_a) \\ &= d\Phi_n \frac{1}{4(2\pi)^3} dt \frac{dz}{z} d\phi. \end{aligned} \quad (5.31)$$

However, in this case we must remember that the initial-state flux factor  $\mathcal{F}$  in Eq. (5.22) changes by a factor of  $z$  because of the change in energy of the incoming parton from  $E_b$  to  $E_a$ . Thus we find that Eqs. (5.26) and (5.28) also hold for spacelike branching.

## 5.2 Evolution equations

Next we consider the effect of multiple branching, that is, the enhancement of higher-order contributions associated with multiple small-angle parton emission. For the present we consider only a single type of branching, for example multiple gluon emission from a spacelike quark, as illustrated in Fig. 5.6. An incoming quark from the hadron  $A$ , initially with

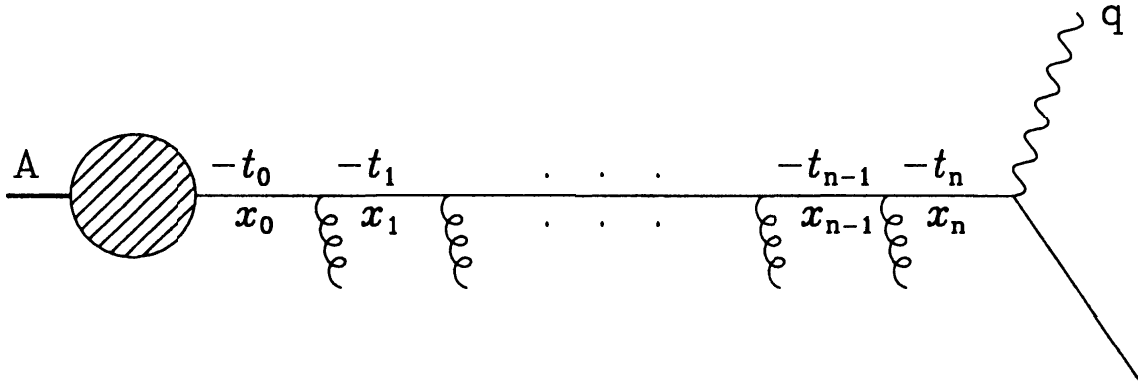


Fig. 5.6. Initial-state branching in deep inelastic lepton scattering.

a low virtual mass-squared  $-t_0$  and carrying a fraction  $x_0$  of the hadron's momentum, moves to more virtual masses and lower momentum fractions by successive small-angle emissions. Eventually it participates in a hard scattering process at a scale  $Q^2$ , for example deep inelastic lepton scattering, which involves the exchange of a photon of virtual mass-squared  $q^2 = -Q^2$ .

The cross section for the hard scattering process will depend on the scale  $Q^2$  and on the momentum fraction distribution of the partons seen by the virtual photon at this scale,  $f(x, Q^2)$ . We can derive an evolution equation for the scale-dependence of this distribution, as follows. First we introduce a pictorial representation of the evolution, which will also prove useful later for discussing the Monte Carlo simulation of the process. We represent every sequence of branchings by a path in  $(t, x)$ -space. Two such paths are shown in Fig. 5.7. Each branching corresponds to a step downwards, from a higher to a lower value of the momentum fraction  $x$ , at a value of  $t$  equal to (minus) the virtual mass-squared after the branching. At  $t = t_0$ , the paths have some distribution of starting points  $f(x_0, t_0)$  characteristic of the hadron  $A$  at that scale. Since the hard scattering sets an upper limit on the virtual mass scale of the struck parton, the distribution  $f(x, t)$  of partons that would be seen at any scale  $t$  is just the  $x$ -distribution of paths at that scale.

Consider now the change in the parton distribution  $f(x, t)$  when  $t$  is increased to  $t + \delta t$ . This is just the number of paths arriving in the element  $(\delta t, \delta x)$  minus the number leaving that element, divided by  $\delta x$ . In the case illustrated in Fig. 5.7, there is one path arriving and one leaving. To find the total number arriving, we must integrate the branching probability times the parton density over all higher momentum fractions  $x' = x/z$ , to obtain

$$\delta f_{\text{in}}(x, t) = \frac{\delta t}{t} \int_x^1 dx' dz \frac{\alpha_s}{2\pi} \hat{P}(z) f(x', t) \delta(x - zx')$$

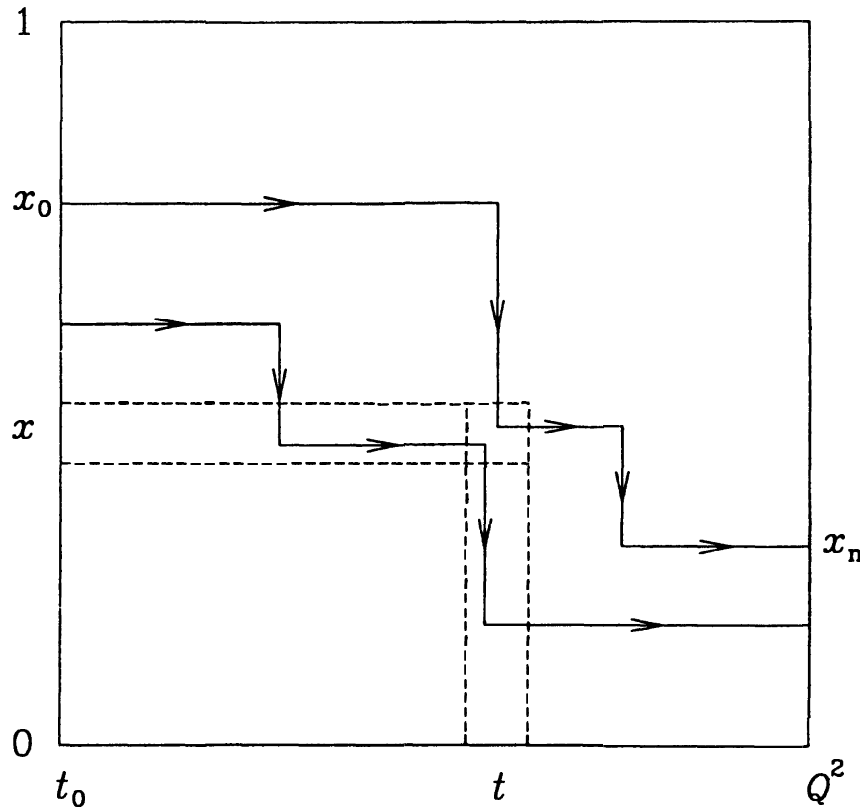


Fig. 5.7. Representation of parton branching by paths in  $(t, x)$ -space.

$$= \frac{\delta t}{t} \int_0^1 \frac{dz}{z} \frac{\alpha_s}{2\pi} \hat{P}(z) f(x/z, t) \quad (5.32)$$

where  $\hat{P}(z)$  is the relevant unregularized splitting function. For quark splitting as in Fig. 5.6,  $\hat{P}(z) = \hat{P}_{qq}(z)$ , given by Eq. (5.20). The lower limit of the  $z$ -integration can be written as either zero or  $x$  because the integrand vanishes for  $z < x$  ( $x' > 1$ ). For the number leaving the element, we integrate instead over all lower momentum fractions  $x' = zx$ :

$$\begin{aligned} \delta f_{\text{out}}(x, t) &= \frac{\delta t}{t} f(x, t) \int_0^x dx' dz \frac{\alpha_s}{2\pi} \hat{P}(z) \delta(x' - zx) \\ &= \frac{\delta t}{t} f(x, t) \int_0^1 dz \frac{\alpha_s}{2\pi} \hat{P}(z) . \end{aligned} \quad (5.33)$$

The net change in the population of the element is thus

$$\delta f(x, t) = \delta f_{\text{in}} - \delta f_{\text{out}} = \frac{\delta t}{t} \int_0^1 dz \frac{\alpha_s}{2\pi} \hat{P}(z) \left[ \frac{1}{z} f(x/z, t) - f(x, t) \right] . \quad (5.34)$$

Using the plus prescription defined in Eq. (4.72), we can define the regularized splitting function

$$P(z) = \hat{P}(z)_+ , \quad (5.35)$$

in terms of which the evolution equation for the parton density may be

written as

$$t \frac{\partial}{\partial t} f(x, t) = \int_x^1 \frac{dz}{z} \frac{\alpha_s}{2\pi} P(z) f(x/z, t). \quad (5.36)$$

We recognize Eq. (5.36) as the GLAP equation introduced in Chapter 4. The quantity  $f(x, t)$  represents the distribution of parton momentum fractions inside the incoming hadron  $A$  probed at scale  $t$ . In the timelike branching of an outgoing parton, it can be used to represent instead the momentum fraction distribution of produced partons. The boundary conditions and direction of evolution are different, but the form of the evolution equation remains the same.

When there are several different types of partons in the branching process, we have to generalize the evolution equation to take into account the different processes by which a parton of type  $i$  can enter or leave the element  $(\delta t, \delta x)$ . This leads to a coupled set of evolution equations of the form

$$t \frac{\partial}{\partial t} f_i(x, t) = \sum_j \int_x^1 \frac{dz}{z} \frac{\alpha_s}{2\pi} P_{ij}(z) f_j(x/z, t). \quad (5.37)$$

The regularized parton splitting functions  $P_{ij}(z)$  can be derived as follows. A quark ( $i = q$ ) can enter the element either from the branching of a quark of the same flavour into quark-gluon, or from the splitting of a gluon into quark-antiquark. On the other hand, it can only leave the element via the process  $q \rightarrow qg$ . Thus the plus prescription applies only to that part, giving

$$\begin{aligned} P_{qq}(z) &= \hat{P}_{qq}(z)_+ = C_F \left( \frac{1+z^2}{1-z} \right)_+ \\ P_{qg}(z) &= \hat{P}_{qg}(z) = T_R [z^2 + (1-z)^2]. \end{aligned} \quad (5.38)$$

For gluons ( $i = g$ ), things are a little more complicated. A gluon can arrive in the element either from  $g \rightarrow gg$  or from  $q \rightarrow qg$  (or  $\bar{q} \rightarrow \bar{q}g$ ). In the first of these, either of the produced gluons can contribute. Thus Eq. (5.32) for the number arriving in the element becomes

$$\begin{aligned} \delta f_{g,\text{in}}(x, t) &= \frac{\delta t}{t} \int_0^1 \frac{dz}{z} \frac{\alpha_s}{2\pi} \left\{ \hat{P}_{gg}(z) \left[ f_g \left( \frac{x}{z}, t \right) + f_g \left( \frac{x}{1-z}, t \right) \right] \right. \\ &\quad \left. + \hat{P}_{qq}(z) \left[ f_q \left( \frac{x}{1-z}, t \right) + f_{\bar{q}} \left( \frac{x}{1-z}, t \right) \right] \right\} \\ &= \frac{\delta t}{t} \int_0^1 \frac{dz}{z} \frac{\alpha_s}{2\pi} \left\{ 2\hat{P}_{gg}(z) f_g \left( \frac{x}{z}, t \right) \right. \\ &\quad \left. + \hat{P}_{qq}(1-z) \left[ f_q \left( \frac{x}{z}, t \right) + f_{\bar{q}} \left( \frac{x}{z}, t \right) \right] \right\}, \end{aligned} \quad (5.39)$$

where we have used the symmetry of  $\hat{P}_{gg}(z)$ , given by Eq. (5.10), under  $z \rightarrow 1 - z$ . A gluon can leave the element by splitting into either  $gg$  or  $q\bar{q}$  (with  $n_f$  possible flavours). The number leaving the element is thus

$$\delta f_{g,\text{out}}(x, t) = \frac{\delta t}{t} f_g(x, t) \int_0^1 dz \frac{\alpha_s}{2\pi} [\hat{P}_{gg}(z) + n_f \hat{P}_{qg}(z) dz] . \quad (5.40)$$

We can use the symmetry of  $\hat{P}_{gg}(z)$  again to write

$$\int_0^1 \hat{P}_{gg}(z) dz = 2C_A \int_0^1 \left[ \frac{z}{1-z} + \frac{1}{2}z(1-z) \right] dz , \quad (5.41)$$

while from Eq. (5.17)

$$\int_0^1 \hat{P}_{qg}(z) dz = \frac{2}{3}T_R . \quad (5.42)$$

We therefore find

$$\begin{aligned} P_{gg}(z) &= 2C_A \left[ \left( \frac{z}{1-z} + \frac{1}{2}z(1-z) \right)_+ + \frac{1-z}{z} + \frac{1}{2}z(1-z) \right] \\ &\quad - \frac{2}{3}n_f T_R \delta(1-z) , \\ P_{qg}(z) &= P_{g\bar{q}}(z) = \hat{P}_{qg}(1-z) = C_F \frac{1+(1-z)^2}{z} . \end{aligned} \quad (5.43)$$

Using the definition (4.72) of the plus prescription, one can easily check that

$$\begin{aligned} \left( \frac{z}{1-z} + \frac{1}{2}z(1-z) \right)_+ &= \frac{z}{(1-z)_+} + \frac{1}{2}z(1-z) + \frac{11}{12}\delta(1-z) \\ \left( \frac{1+z^2}{1-z} \right)_+ &= \frac{1+z^2}{(1-z)_+} + \frac{3}{2}\delta(1-z) , \end{aligned} \quad (5.44)$$

and so the regularized splitting functions  $P_{qg}$  and  $P_{gg}$  can be written in the alternative forms

$$\begin{aligned} P_{qg}(z) &= C_F \left[ \frac{1+z^2}{(1-z)_+} + \frac{3}{2}\delta(1-z) \right] \\ P_{gg}(z) &= 2C_A \left[ \frac{z}{(1-z)_+} + \frac{1-z}{z} + z(1-z) \right] \\ &\quad + \frac{1}{6}(11C_A - 4n_f T_R)\delta(1-z) , \end{aligned} \quad (5.45)$$

which coincide with the leading-order kernels given in Eq. (4.94). Notice that in both cases the singularity in the integrand of the evolution equations (5.37) at  $z = 1$ , corresponding to emission of a soft gluon, is removed by the plus prescription. The remaining singularity of  $P_{gg}$  at

$z = 0$  is outside the region of integration ( $x < z < 1$ ) and therefore all the integrals are finite.

The above formulation of the GLAP equations is convenient for obtaining analytical solutions for the evolution of parton distributions, as we have already seen in Chapter 4. To study more detailed features of the branching process, and in particular to say anything about the structure of the corresponding final states, a numerical approach based on the Monte Carlo simulation technique is useful. In this approach it is preferable to eliminate the plus prescription from the evolution equations, in the following way. For the moment we go back to the simplified treatment in which there is only one type of branching. We introduce the function

$$\Delta(t) \equiv \exp \left[ - \int_{t_0}^t \frac{dt'}{t'} \int dz \frac{\alpha_s}{2\pi} \hat{P}(z) \right], \quad (5.46)$$

which is called the *Sudakov form factor*. We shall see shortly that this function has a simple physical interpretation. Now we can write Eq. (5.34) as

$$t \frac{\partial}{\partial t} f(x, t) = \int \frac{dz}{z} \frac{\alpha_s}{2\pi} \hat{P}(z) f(x/z, t) + \frac{f(x, t)}{\Delta(t)} t \frac{\partial}{\partial t} \Delta(t) \quad (5.47)$$

and hence

$$t \frac{\partial}{\partial t} \left( \frac{f}{\Delta} \right) = \frac{1}{\Delta} \int \frac{dz}{z} \frac{\alpha_s}{2\pi} \hat{P}(z) f(x/z, t). \quad (5.48)$$

Notice that this is similar in form to the Altarelli-Parisi equation (5.36), except that  $f$  is replaced by  $f/\Delta$  and the regularized splitting function  $P$  is replaced by the unregularized one  $\hat{P}$ . This equation can be integrated to give an integral equation for  $f(x, t)$  in terms of the initial parton distribution  $f(x, t_0)$ :

$$f(x, t) = \Delta(t) f(x, t_0) + \int_{t_0}^t \frac{dt'}{t'} \frac{\Delta(t)}{\Delta(t')} \int \frac{dz}{z} \frac{\alpha_s}{2\pi} \hat{P}(z) f(x/z, t'). \quad (5.49)$$

Equation (5.49) can be given a simple interpretation using the  $(t, x)$ -space paths depicted in Fig. 5.7. The first term on the right-hand side is the contribution from paths that do not branch between scales  $t_0$  and  $t$ . Thus the Sudakov form factor  $\Delta(t)$  is simply the probability of evolving from  $t_0$  to  $t$  without branching. The second term is the contribution from all paths which have their last branching at scale  $t'$ . The factor of  $\Delta(t)/\Delta(t')$  represents the probability of evolving from  $t'$  to  $t$  without branching. This is consistent with the above interpretation of  $\Delta(t)$  because we see from Eq. (5.46) that  $\Delta(t_0) = 1$ .

The generalization of Eq. (5.46) to take account of several types of parton is straightforward. Each parton species  $i$  has its own form factor  $\Delta_i(t)$ , which describes its probability of evolving from  $t_0$  to  $t$  without

branching. Since the branching probability has to be summed over all possible processes  $i \rightarrow j$ , we have

$$\Delta_i(t) \equiv \exp \left[ - \sum_j \int_{t_0}^t \frac{dt'}{t'} \int dz \frac{\alpha_s}{2\pi} \hat{P}_{ji}(z) \right], \quad (5.50)$$

where  $\hat{P}_{ji}(z)$  is the unregularized  $i \rightarrow j$  splitting function. Correspondingly, Eq. (5.48) becomes

$$t \frac{\partial}{\partial t} \left( \frac{f_i}{\Delta_i} \right) = \frac{1}{\Delta_i} \sum_j \int \frac{dz}{z} \frac{\alpha_s}{2\pi} \hat{P}_{ij}(z) f_j(x/z, t). \quad (5.51)$$

Our discussion of the Sudakov form factor up to this point has been somewhat schematic. We have ignored the infra-red singularity of the unregularized splitting functions at  $z = 1$ , which needs to be removed in order for the form factors to be defined.<sup>1</sup> In the form (5.37) of the evolution equations, the singularity is regularized by the plus prescription, but in the form (5.51) we must introduce an explicit infra-red cut-off,  $z < 1 - \epsilon(t)$ . Branchings with  $z$  above this range are classified as *unresolvable*: they involve the emission of an undetectably soft parton. The Sudakov form factor with this cut-off then gives the probability of evolving from  $t_0$  to  $t$  without any *resolvable* branching.

Although we have not mentioned virtual corrections explicitly, the Sudakov form factor in fact sums enhanced virtual (parton loop) as well as real (parton emission) contributions to all orders. The virtual corrections affect the no-branching probability, and are included via unitarity, which is just the fact that the sum of the branching and no-branching probabilities must be unity. The resolvable branching probability tells us via unitarity the sum of the virtual and unresolvable real contributions: the latter two are both divergent but their sum is finite, and is included consistently in Eq. (5.51).

The definition of the infra-red cut-off  $\epsilon(t)$  is to some extent a matter of choice about what we classify as a resolvable emission. For timelike branching, a natural resolution limit is provided by the cut-off on the parton virtual mass-squared,  $t > t_0$ . Working in a frame in which all the parton energies are much larger than their virtual masses, or equivalently defining  $z$  as the fraction of  $p_+ = E + p_z$  with the  $z$ -axis along the momentum of parton  $a$ , the transverse momentum in the timelike branching  $a \rightarrow bc$  is

$$p_T^2 = z(1-z)p_a^2 - (1-z)p_b^2 - zp_c^2 > 0. \quad (5.52)$$

---

<sup>1</sup> The integrand  $\hat{P}_{gg}(z)$  in the gluon form factor also has a singularity at  $z = 0$  but this can be mapped to  $z = 1$  using the symmetry property (5.41).

Hence for  $p_a^2 = t$  and  $p_b^2, p_c^2 > t_0$  we require

$$z(1-z) > t_0/t , \quad (5.53)$$

that is,

$$z, 1-z > \epsilon(t) = \frac{1}{2} - \frac{1}{2}\sqrt{1 - 4t_0/t} \simeq t_0/t . \quad (5.54)$$

With such a cut-off, the Sudakov form factor of the quark, for example, becomes

$$\Delta_q(t) \simeq \exp \left[ - \int_{2t_0}^t \frac{dt'}{t'} \int_{t_0/t'}^{1-t_0/t'} dz \frac{\alpha_s}{2\pi} \hat{P}_{qq}(z) \right] . \quad (5.55)$$

If we assume that the argument of the running coupling  $\alpha_s$  is simply the virtual mass-squared scale  $t'$ , this behaves at large  $t$  like

$$\left( \frac{t_0}{t} \right)^{p_1} \left( \frac{\alpha_s(t)}{\alpha_s(t_0)} \right)^{p_2} \quad (5.56)$$

where  $p_1$  and  $p_2$  are fixed powers. Thus, according to this assumption, the form factor vanishes roughly like a negative power of  $t$  at large  $t$ .

A more careful treatment of the running coupling suggests [2] that we should use as its argument  $z(1-z)t'$ , which from Eq. (5.52) is essentially the transverse momentum-squared. Expanding to next-to-leading order, we have

$$\alpha_s(z(1-z)t) = \alpha_s(t) + \beta_0 \ln[z(1-z)] \alpha_s^2(t)/4\pi + \dots , \quad (5.57)$$

which, combined with a  $1/(1-z)$  singularity in the splitting function  $\hat{P}(z)$ , produces a next-to-leading behaviour of the form  $\ln(1-z)/(1-z)$  as  $z \rightarrow 1$ . This behaviour is indeed found in explicit higher-order calculations of the splitting functions  $P_{qq}$  and  $P_{gg}$ . The more singular behaviour near the cut-off in Eq. (5.55) then leads to a form factor that vanishes more rapidly at large  $t$ . Instead of (5.56) one finds

$$\Delta_q(t) \sim \left( \frac{\alpha_s(t)}{\alpha_s(t_0)} \right)^{p_3 \ln t} , \quad (5.58)$$

which tends to zero faster than any negative power of  $t$ .

In the spacelike branching  $a \rightarrow bc$  it is the produced spacelike parton  $b$  that sets the largest scale  $|p_b^2| = t > 0$ . The kinematics again require that  $1-z$ , the momentum fraction carried by the emitted parton  $c$  with  $p_c^2 > t_0$ , should be greater than  $\epsilon(t) \sim t_0/t$  at large  $t$ . A cut-off at small values of the momentum fraction  $z$  carried by parton  $b$  is not obligatory, since the value of  $z$  is in any case greater than  $x$ , the momentum fraction of the parton which participates in the hard subprocess (see Fig. 5.6). For simplicity one may take  $z > t_0/t$ , as in the timelike case.

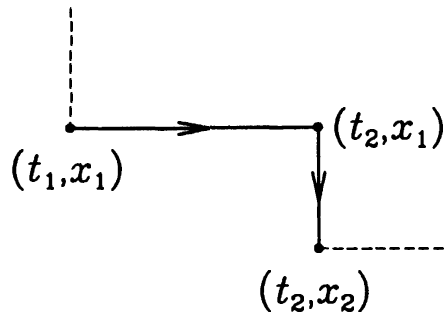


Fig. 5.8. Fundamental step in  $(t, x)$ -space.

The infra-red cut-offs that we have discussed in this section follow from kinematics and the constraint that each outgoing parton should have virtual mass-squared greater than  $t_0$ . In fact, however, the QCD branching picture that we have been using so far takes into account only amplitudes which have collinear enhancements. In the infra-red region there are also non-collinear amplitudes with enhancements due to soft gluon emission. We shall see in Section 5.5 that these interfere destructively in a way that effectively reduces the available phase space for parton branching, leading to more restrictive effective cut-offs than those defined above.

### 5.3 Monte Carlo method

The formulation of parton branching in terms of the Sudakov form factor is well suited to computer implementation, and is the basis of the ‘parton shower’ Monte Carlo programs for simulating QCD jets. We describe here the basic Monte Carlo branching algorithm in its simplest form, neglecting the complications of different possible branchings and QCD coherence effects. The former can be included straightforwardly using the formulae in the previous subsection. The latter will be the topic of the next subsection.

The basic problem that the Monte Carlo branching algorithm has to solve is as follows: given the virtual mass scale and momentum fraction  $(t_1, x_1)$  after some step of the evolution, or as initial conditions, generate the values  $(t_2, x_2)$  after the next step.

As shown in Fig. 5.8, the first quantity to be generated by the algorithm is the value of  $t_2$ . We saw above that the probability of evolving from  $t_1$  to  $t_2$  without (resolvable) branching is  $\Delta(t_2)/\Delta(t_1)$  where  $\Delta(t)$  is the Sudakov form factor. Thus  $t_2$  can be generated with the correct probability distribution by solving the equation

$$\frac{\Delta(t_2)}{\Delta(t_1)} = \mathcal{R} \quad (5.59)$$

where  $\mathcal{R}$  is a random number distributed uniformly in the interval  $[0, 1]$ .<sup>2</sup>

If the value of  $t_2$  is higher than the hard subprocess scale  $Q^2$ , this means that no further branching occurs (see Fig. 5.7). Otherwise, we have to generate the value of the momentum fraction  $z = x_2/x_1$  for the next branching, with a probability distribution proportional to  $(\alpha_s/2\pi)P(z)$ , where  $P(z)$  is the appropriate splitting function. We can do this by solving the equation

$$\int_{\epsilon}^{x_2/x_1} dz \frac{\alpha_s}{2\pi} P(z) = \mathcal{R}' \int_{\epsilon}^{1-\epsilon} dz \frac{\alpha_s}{2\pi} P(z) \quad (5.60)$$

where  $\mathcal{R}'$  represents another random number in the interval  $[0, 1]$  and  $\epsilon$  is the infra-red cut-off for resolvable branching.

The above discussion applies to spacelike parton branching, as depicted in Fig. 5.6. The values of  $(t_i, x_i)$  generated by successive applications of the algorithm define the virtual masses and momentum fractions of the exchanged quark, from which the momenta of the emitted gluons can be computed. The azimuthal angles of their emission need to be specified by a further Monte Carlo algorithm, which in this case should generate the angles uniformly in the range  $[0, 2\pi]$ . More generally, for example when the exchanged spacelike parton is a gluon, the azimuths must be generated taking into account the polarization correlations discussed in Section 5.1.

Each emitted gluon in Fig. 5.6, and in general each parton with timelike momentum in a parton shower, can itself undergo further branching, which can be dealt with by a similar algorithm. The main difference in the timelike case is that  $t$  evolves *downwards* towards the cut-off value  $t_0$  rather than upwards towards the hard process scale  $Q^2$ . The probability of evolving downwards without branching between  $t_1$  and  $t_2$  is  $\Delta(t_1)/\Delta(t_2)$  and hence the equation corresponding to (5.59) in the timelike case is

$$\frac{\Delta(t_1)}{\Delta(t_2)} = \mathcal{R}. \quad (5.61)$$

Note that since  $\Delta(t_0) = 1$  this equation has no solution for  $t_2 > t_0$  if  $\mathcal{R} < \Delta(t_1)$ . This correctly generates the probability for no (resolvable) branching. If timelike branching does occur, the procedure for generating the momentum fraction  $z$  is the same as that described above for the spacelike case.

As a consequence of successive timelike branching, a *parton cascade* develops, as illustrated for  $e^+e^-$  annihilation in Fig. 5.9. Each outgoing

---

<sup>2</sup> If the form factor is known in closed form, Eq. (5.59) can be solved numerically, for example using Newton's method. Otherwise the values of the form factor can be tabulated and the solution obtained by interpolation.

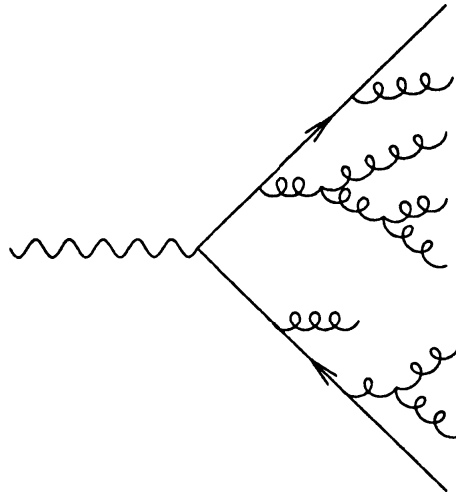


Fig. 5.9. Parton shower in  $e^+e^-$  annihilation.

line becomes the source of a new cascade, until the Monte Carlo algorithm generates a ‘no branching’ step in the evolution of its virtual mass. Those that do branch produce partons of lower virtual masses, which become more likely to generate no branching. Eventually all outgoing lines have stopped branching and the cascade ceases. At this stage, which depends on the cut-off scale  $t_0$ , the outgoing partons have to be converted into hadrons via a *hadronization model* if the Monte Carlo program is to be used for the simulation of real events. We shall discuss the different available models in Section 5.6.

#### 5.4 Backward evolution

The branching algorithm described above generates what is known as *forward* evolution. At each step, a parton with timelike momentum is emitted and the emitting parton moves to a lower (more negative, in the spacelike case) virtual mass-squared. In Fig. 5.7, the initial momentum fraction  $x_0$  of the emitting parton is known, but the final value  $x_n$  depends on the values of  $z = x_{i+1}/x_i$  selected in the intervening steps. This is convenient in timelike evolution, such as that in  $e^+e^-$  annihilation, where we start with a quark and antiquark with  $x_0 \simeq 1$  and generate a shower of partons with a range of momentum fractions. However, in spacelike cascades it is more convenient and efficient to start by specifying the momentum fraction  $x_n$  of the final parton, and then to generate  $x_{n-1}, \dots, x_0$  by *backward* evolution. This is because in this case it is the final partons, with the most negative virtual masses-squared, that participate in the hard subprocess.

In deep inelastic lepton scattering, for example, it is preferable to start by generating the hard lepton-quark scattering, which fixes the momen-

tum fraction of the struck quark (neglecting its virtuality for the moment) at the Bjorken value  $Q^2/2\nu$ , as discussed in Chapter 4. Another important case is the Drell-Yan process for vector boson production in hadron-hadron collisions, to be considered in Chapter 9. In this process a quark from one incoming hadron and an antiquark from the other, with momentum fractions  $x_q$  and  $x_{\bar{q}}$ , collide to make a boson of mass  $M$  where  $M^2 \simeq x_q x_{\bar{q}} s$ ,  $\sqrt{s}$  being the hadron-hadron centre-of-mass energy. Thus we want the product of the final  $x_n$ s of the two spacelike partons to have just the right value in order to form a particular boson. If the cascades are generated forwards, then most of the time the product will not have the right value and the contribution to the cross section will be negligible, leading to a very low efficiency. If, on the other hand, we generate the initial-state cascades backwards, then we can choose an appropriate combination of momenta (and flavours) every time.

Efficient backward evolution cannot be achieved simply by running the forward evolution algorithm in reverse. For example, if one solves Eq. (5.60) for  $x_1$  given  $x_2$ , then a fraction of the time one obtains  $x_1 > 1$ , which is unphysical. Thus naive backward evolution, like forward evolution, generates many configurations that have to be rejected, leading to low efficiency.

The correct prescription for backward evolution [3,4] involves the use of a modified form factor, which takes the local parton density  $f(x, t)$  into account in choosing the next value of the evolution variable  $t$ . The probability of evolving backwards from  $(t_2, x)$  to  $(t_1, x)$  without branching is given by the function

$$\Pi(t_1, t_2; x) = \frac{f(x, t_1) \Delta(t_2)}{f(x, t_2) \Delta(t_1)}. \quad (5.62)$$

In other words, in place of the Sudakov form factor  $\Delta(t_i)$  we should now use  $\Delta(t_i)/f(x, t_i)$ . The correct distribution of  $t_1$  in the elementary backward step shown in Fig. 5.10 is then obtained by solving the equation

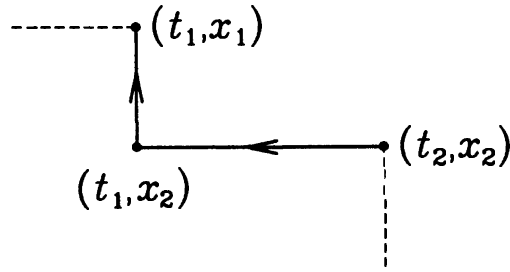
$$\Pi(t_1, t_2; x_2) = \mathcal{R} \quad (5.63)$$

where  $\mathcal{R}$  is a random number distributed uniformly in the interval  $[0, 1]$ .

When generating the corresponding value of the momentum fraction  $x_1$ , we have to multiply by the extra factor of  $f(x_1, t_1)$  that will be divided out in the next backward step in  $t$ . Thus we have to generate  $z = x_2/x_1$  with a probability distribution proportional to

$$\frac{\alpha_s}{2\pi} \frac{P(z)}{z} f(x_2/z, t_1) \quad (5.64)$$

where  $P(z)$  is the appropriate splitting function. This can be done using a method similar to that used for the forward evolution, Eq. (5.60).

Fig. 5.10. Backward step in  $(t, x)$ -space.

To derive Eq. (5.62), let us define  $dF$  as the fraction of partons at  $(t_2, x)$  that came from branching between  $t$  and  $t + dt$ . Then the fraction that did not branch between  $t_1$  and  $t_2$  is

$$\Pi(t_1, t_2; x) = 1 - \int_{t_1}^{t_2} dF. \quad (5.65)$$

Now it follows from the evolution equation (5.49) that

$$\begin{aligned} f(x, t_2) dF &= \frac{dt}{t} \frac{\Delta(t_2)}{\Delta(t)} \int \frac{dz}{z} \frac{\alpha_s}{2\pi} \hat{P}(z) f(x/z, t) \\ &= dt \frac{\partial}{\partial t} \left[ \frac{\Delta(t_2)}{\Delta(t)} f(x, t) \right]. \end{aligned} \quad (5.66)$$

Performing the integration in Eq. (5.65), we obtain the result (5.62).

In the original paper on this subject [3], the backward evolution form factor (5.62) was given in the apparently different form

$$\Pi(t_1, t_2; x) = \exp \left\{ - \int_{t_1}^{t_2} \frac{dt}{t} \int \frac{dz}{z} \frac{\alpha_s}{2\pi} \hat{P}(z) \frac{f(x/z, t)}{f(x, t)} \right\}. \quad (5.67)$$

It is left as an exercise for the reader to show from the original form of the evolution equation, Eq. (5.34), that this is equivalent to Eq. (5.62).

The effect of the ratio of parton distributions in Eq. (5.62) is to suppress branching at large  $x$ , where  $f(x, t)$  is a decreasing function of  $t$ , and to enhance it at low  $x$ , where  $f(x, t)$  is increasing. This is correct because partons at higher  $x$  are less likely to have undergone branching, which always reduces the value of  $x$ . Similarly, the factor of  $f(x_2/z, t_1)$  in the distribution of  $z$  suppresses branching from regions in which the parton density at  $x_1 = x_2/z$  is low. In particular, it ensures that the selected value of  $x_1$  is always less than unity.

We have presented the backward evolution algorithm for a single type of branching, *e.g.*  $q \rightarrow qg$ . As was the case for the evolution equations (5.37), it is straightforward to generalize the above treatment by attaching the appropriate labels to the splitting functions, form factors and parton distributions.

One difference between forward and backward evolution is that the former may be used as a way of solving the GLAP equations (5.37), to obtain the  $t$ -dependence of the parton distributions. In backward evolution, the parton distributions are part of the input: they are used to ‘guide’ the evolution paths towards the most populated regions of  $(t, x)$ -space. The primary aim is to generate the correct distribution of the partons emitted in the initial-state cascade.

### 5.5 Coherent branching

So far in this Chapter we have been developing a parton branching formalism which takes account of collinear enhancements to all orders in perturbation theory. In addition, there are enhancements associated with soft gluon emission. We have seen evidence of these in the singularities of the small-angle parton splitting functions for soft gluon emission, but they are more general. Whenever an external line of a QCD Feynman graph with momentum  $p$  and mass  $m$  (not necessarily small) emits a gluon of momentum  $q$ , there is a propagator factor of

$$\frac{1}{(p \pm q)^2 - m^2} = \frac{\pm 1}{2p \cdot q} = \frac{\pm 1}{2\omega E(1 - v \cos \theta)} \quad (5.68)$$

where  $\omega$  is the energy of the gluon,  $E$  and  $v$  the energy and velocity of the parton emitting it, and  $\theta$  the angle of emission. For light partons  $v \rightarrow 1$  and we have a collinear enhancement as  $\theta \rightarrow 0$ . However, there is also an enhancement as  $\omega \rightarrow 0$  for any velocity and emission angle.

The soft enhancement corresponds to a colour factor times a universal, spin-independent factor of

$$F_{\text{soft}} = \frac{p \cdot \epsilon}{p \cdot q} \quad (5.69)$$

in the amplitude, where  $\epsilon$  is the polarization vector of the emitted gluon. In the case of emission from a quark, for example, apart from the factor of  $1/2p \cdot q$  there is a numerator factor of the form  $N \cdot \epsilon$ , where, as  $\omega \rightarrow 0$ ,

$$\begin{aligned} N^\mu &= (\not{p} + \not{q} + m)\gamma^\mu u(p) \\ &\rightarrow (\gamma^\nu \gamma^\mu p_\nu + \gamma^\mu m)u(p) \\ &= (2p^\mu - \gamma^\mu \not{p} + \gamma^\mu m)u(p) \\ &= 2p^\mu u(p). \end{aligned} \quad (5.70)$$

In the last step we have used the Dirac equation for the on-mass-shell spinor  $u(p)$ . The universal factor  $F_{\text{soft}}$  corresponds to the classical *eikonal formula* for the radiation from a current  $p^\mu$ , which is valid in the long-wavelength limit.

Notice that there is no soft enhancement of radiation from an off-mass-shell internal line of a Feynman graph, since the associated denominator factor  $(p + q)^2 - m^2 \rightarrow p^2 - m^2 \neq 0$  as  $\omega \rightarrow 0$ .

An enhancement factor in the amplitude for each external line implies that the cross section has a factor which is a sum over all pairs of external lines  $\{i, j\}$ :

$$d\sigma_{n+1} = d\sigma_n \frac{d\omega}{\omega} \frac{d\Omega}{2\pi} \frac{\alpha_s}{2\pi} \sum_{i,j} C_{ij} W_{ij} \quad (5.71)$$

where  $d\Omega$  is the element of solid angle for the emitted gluon,  $C_{ij}$  is a colour factor to be computed, and the *radiation function*  $W_{ij}$  is given by

$$W_{ij} = \frac{\omega^2 p_i \cdot p_j}{p_i \cdot q \, p_j \cdot q} = \frac{1 - v_i v_j \cos \theta_{ij}}{(1 - v_i \cos \theta_{iq})(1 - v_j \cos \theta_{jq})}. \quad (5.72)$$

The colour-weighted sum of radiation functions in Eq. (5.71) is sometimes called the *antenna pattern* of the process.

Although the radiation function (5.72) represents an interference contribution from lines  $i$  and  $j$ , it can be separated into two parts containing the leading collinear singularities. For simplicity we consider here the case of massless emitting particles,  $v_i = v_j = 1$ . Then we can write

$$W_{ij} = W_{ij}^{[i]} + W_{ij}^{[j]} \quad (5.73)$$

where

$$W_{ij}^{[i]} = \frac{1}{2} \left( W_{ij} + \frac{1}{1 - \cos \theta_{iq}} - \frac{1}{1 - \cos \theta_{jq}} \right). \quad (5.74)$$

The function (5.74) has a remarkable property known as *angular ordering*. Suppose we write the angular integration in Eq. (5.71) in terms of polar and azimuthal angles with respect to the direction of line  $i$ ,

$$d\Omega = d\cos \theta_{iq} d\phi_{iq}, \quad (5.75)$$

and then carry out the azimuthal integration. We find that

$$\begin{aligned} \int_0^{2\pi} \frac{d\phi_{iq}}{2\pi} W_{ij}^{[i]} &= \frac{1}{1 - \cos \theta_{iq}} \quad \text{if } \theta_{iq} < \theta_{ij} \\ &= 0 \quad \text{otherwise.} \end{aligned} \quad (5.76)$$

In other words, after azimuthal averaging, the contribution from this term is confined to a cone, centred on the direction of line  $i$ , extending in angle as far as the direction of line  $j$ . Similarly, the contribution  $W_{ij}^{[j]}$ , after averaging over  $\phi_{jq}$ , is confined to a cone centred on line  $j$  extending as far as line  $i$ .

To prove the angular ordering property of  $W_{ij}^{[i]}$ , we note that

$$1 - \cos \theta_{jq} = a - b \cos \phi_{iq} \quad (5.77)$$

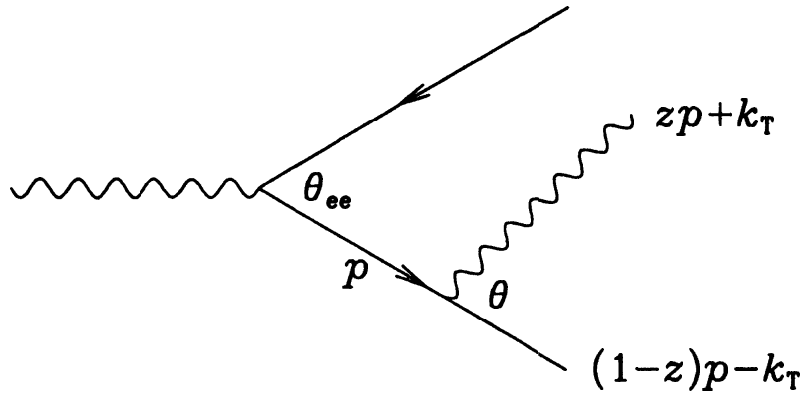


Fig. 5.11. Soft photon emission from an electron-positron pair.

where

$$a = 1 - \cos \theta_{ij} \cos \theta_{iq}, \quad b = \sin \theta_{ij} \sin \theta_{iq}. \quad (5.78)$$

Defining  $z = \exp(i\phi_{iq})$ , we have

$$I_{ij}^{[i]} \equiv \int_0^{2\pi} \frac{d\phi_{iq}}{2\pi} \frac{1}{1 - \cos \theta_{jq}} = \frac{1}{i\pi b} \oint \frac{dz}{(z - z_+)(z - z_-)} \quad (5.79)$$

where the  $z$ -integration contour is the unit circle and

$$z_{\pm} = \frac{a}{b} \pm \sqrt{\frac{a^2}{b^2} - 1}. \quad (5.80)$$

Now only the pole at  $z = z_-$  can lie inside the unit circle and therefore

$$I_{ij}^{[i]} = \sqrt{\frac{1}{a^2 - b^2}} = \frac{1}{|\cos \theta_{iq} - \cos \theta_{ij}|}. \quad (5.81)$$

Hence

$$\int_0^{2\pi} \frac{d\phi_{iq}}{2\pi} W_{ij}^{[i]} = \frac{1}{2(1 - \cos \theta_{iq})} [1 + (\cos \theta_{iq} - \cos \theta_{ij}) I_{ij}^{[i]}], \quad (5.82)$$

which gives Eq. (5.76).

The angular ordering property of soft emission is an example of a coherence effect common to all gauge theories. In electrodynamics it accounts for the suppression of soft bremsstrahlung from electron-positron pairs (called the *Chudakov effect*), which has a simple heuristic explanation in terms of old-fashioned time-ordered perturbation theory. Consider the emission of a soft photon at angle  $\theta$  from an electron in a pair with opening angle  $\theta_{ee} < \theta$ , as shown in Fig. 5.11.

For simplicity we shall assume  $\theta_{ee}, \theta \ll 1$ . Then the transverse momentum of the photon is  $k_T \sim zp\theta$  and the energy imbalance at the  $e \rightarrow e\gamma$  vertex is

$$\Delta E \sim k_T^2/zp \sim zp\theta^2. \quad (5.83)$$

According to the uncertainty principle the time available for the photon emission is  $\Delta t \sim 1/\Delta E$ . In this time interval the transverse separation of the pair will become  $\Delta b \sim \theta_{ee}\Delta t$ . In order for there to be a non-negligible probability of photon emission, the photon must be able to resolve this transverse separation. This will be the case if

$$\Delta b > \lambda/\theta \sim (zp\theta)^{-1} \quad (5.84)$$

where  $\lambda$  is the photon wavelength. However, this implies that

$$\theta_{ee}(zp\theta^2)^{-1} > (zp\theta)^{-1}, \quad (5.85)$$

and hence that  $\theta_{ee} > \theta$ . Thus soft photon emission is suppressed at angles larger than the opening angle of the pair. Photons at larger angles cannot resolve the individual electron and positron charges and see only the net charge of the system, which in this case is zero, implying no emission.

The only complication in going from electro- to chromodynamics is that the electric charges are replaced by colour charges. In a suitable representation of the colour algebra, we can represent the colour charge of particle  $i$  by a vector  $\mathbf{Q}_i$  such that  $\mathbf{Q}_i^2 = C_F = 4/3$  for a quark,  $\mathbf{Q}_i^2 = C_A = 3$  for a gluon and  $\mathbf{Q}_i^2 = 0$  for a colour singlet. In this notation, the colour factor in Eq. (5.71) is

$$C_{ij} = -\mathbf{Q}_i \cdot \mathbf{Q}_j. \quad (5.86)$$

For two external lines forming a colour singlet, as in  $e^+e^- \rightarrow q\bar{q}$  for example, we have  $\mathbf{Q}_i + \mathbf{Q}_j = 0$  and hence  $C_{ij} = \mathbf{Q}_i^2 = \mathbf{Q}_j^2$ . In this case the angular ordering operates as in electrodynamics, suppressing radiation outside the cones extending from  $i$  to  $j$  and vice-versa.

A more interesting case is that of three partons ( $i, j, k$ ) forming a colour singlet, as in  $e^+e^- \rightarrow q\bar{q}g$ . The soft gluon radiation pattern will be determined by the expression

$$\begin{aligned} W &= -\mathbf{Q}_i \cdot \mathbf{Q}_j W_{ij} - \mathbf{Q}_j \cdot \mathbf{Q}_k W_{jk} - \mathbf{Q}_i \cdot \mathbf{Q}_k W_{ik} \\ &= \frac{1}{2} \left[ \mathbf{Q}_i^2 (W_{ij} + W_{ik} - W_{jk}) + \mathbf{Q}_j^2 (W_{ij} + W_{jk} - W_{ik}) \right. \\ &\quad \left. + \mathbf{Q}_k^2 (W_{ik} + W_{jk} - W_{ij}) \right]. \end{aligned} \quad (5.87)$$

Let us study in detail the configuration in which  $i$  and  $j$  are close in angle, forming a system  $l$  with colour charge  $\mathbf{Q}_l = \mathbf{Q}_i + \mathbf{Q}_j = -\mathbf{Q}_k$ , as depicted in Fig. 5.12. Using the decomposition (5.73), we can write Eq. (5.87) in the form

$$\begin{aligned} W &= \mathbf{Q}_i^2 (W_{ij}^{[i]} + \tilde{W}_{jk}^{[i]} - \tilde{W}_{ik}^{[i]}) + \mathbf{Q}_j^2 (W_{ij}^{[j]} + \tilde{W}_{ik}^{[j]} - \tilde{W}_{jk}^{[j]}) \\ &\quad + \mathbf{Q}_k^2 (\tilde{W}_{jk}^{[i]} + \tilde{W}_{ik}^{[j]} + \frac{1}{2}W_{ik}^{[k]} + \frac{1}{2}W_{jk}^{[k]}) \end{aligned} \quad (5.88)$$

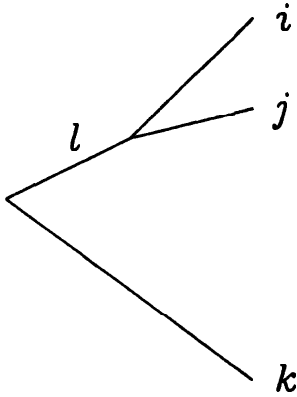


Fig. 5.12. Soft gluon emission from a three-parton system.

where

$$\tilde{W}_{jk}^{[i]} = \frac{1}{2}(W_{ik}^{[i]} - W_{ij}^{[i]}) , \quad \tilde{W}_{ik}^{[j]} = \frac{1}{2}(W_{jk}^{[j]} - W_{ij}^{[j]}) . \quad (5.89)$$

Note that the collinear singularities along the directions of  $i$  and  $j$  are cancelled in the expressions (5.89). Since the angle between  $i$  and  $j$  is small, we can approximate the direction of  $i$  or  $j$  by that of  $l$  in all functions that are not singular in the directions of  $i$  or  $j$ . Thus we can write

$$\begin{aligned} W_{ik}^{[k]} &\simeq W_{jk}^{[k]} \simeq W_{lk}^{[k]} \\ \tilde{W}_{jk}^{[i]} &\simeq \tilde{W}_{ik}^{[j]} \simeq \frac{1}{2}\tilde{W}_{lk}^{[ij]} , \end{aligned} \quad (5.90)$$

where  $\tilde{W}_{lk}^{[ij]}$  has the following meaning after averaging over the azimuthal angle with respect to  $l$ :

$$\begin{aligned} \tilde{W}_{lk}^{[ij]} &= W_{lk}^{[i]} \quad \text{for } \theta_{iq} > \theta_{ij} \\ &= 0 \quad \text{for } \theta_{iq} < \theta_{ij} . \end{aligned} \quad (5.91)$$

Putting everything together, we can write Eq. (5.88) in this approximation as

$$W \simeq Q_i^2 W_{ij}^{[i]} + Q_j^2 W_{ij}^{[j]} + Q_k^2 W_{lk}^{[k]} + Q_l^2 \tilde{W}_{lk}^{[ij]} . \quad (5.92)$$

Eq. (5.92) has a simple interpretation: each of the partons  $i$ ,  $j$  and  $k$  radiates in proportion to its colour charge squared. When  $i$  and  $j$  are close in angle, their incoherent contributions are limited (after azimuthal averaging) to cones of half-angle  $\theta_{ij}$ . At larger angles, out to the direction of  $k$ , they give a coherent contribution in proportion to their combined colour charge squared,  $Q_l^2$ . This contribution can be computed as if it came from an internal line of momentum  $p_l = p_i + p_j$ , but in reality it comes coherently from the two external lines.

The above treatment can be extended to higher orders, leading to a *coherent parton branching* formalism that can be used to compute soft gluon

enhancements to all orders. The rules for coherent branching involve a simple modification of those for the collinear branching process considered earlier: in place of the virtual mass-squared variable  $t$ , we should use as evolution variable the opening angle  $\theta$ , or more precisely the variable

$$\zeta = \frac{p_b \cdot p_c}{E_b E_c} \simeq 1 - \cos \theta \quad (5.93)$$

for the branching  $a \rightarrow bc$ , and impose angular ordering  $\zeta' < \zeta$  where  $\zeta$  and  $\zeta'$  refer to successive branchings. The propagator factor  $dt/t$  in Eq. (5.28) is replaced by  $d\zeta/\zeta$ . Each parton radiates in proportion to its colour charge squared. In fact, if we use the appropriate splitting function  $\hat{P}(z)dz$  in place of the soft approximation  $Q_a^2 d\omega/\omega$ , the same formalism treats correctly both soft and collinear enhancements. Thus the basic formula for coherent branching becomes

$$d\sigma_{n+1} = d\sigma_n \frac{d\zeta}{\zeta} dz \frac{\alpha_s}{2\pi} \hat{P}_{ba}(z) . \quad (5.94)$$

In place of the virtual mass-squared cut-off used to terminate the collinear branching process and to regulate its infra-red divergences, we need to introduce an angular cut-off  $\zeta_0$  for the coherent branching. Again, this is to some extent a matter of choice, depending on how we classify a parton emission as unresolvable. The simplest choice is of the form

$$\zeta_0 = t_0/E^2 \quad (5.95)$$

for a parton of energy  $E$ . Then  $t_0$  can once again be taken to be the minimum mass-squared. For radiation from a particle  $i$  of finite mass-squared  $t_0$ , the radiation function (5.72) receives a diagonal contribution,

$$\begin{aligned} \frac{\omega^2 p_i \cdot p_j}{p_i \cdot q p_j \cdot q} &\rightarrow \omega^2 \left( \frac{p_i \cdot p_j}{p_i \cdot q p_j \cdot q} - \frac{p_i^2}{(p_i \cdot q)^2} \right) \\ &\simeq \frac{1}{\zeta} \left( 1 - \frac{t_0}{E^2 \zeta} \right) , \end{aligned} \quad (5.96)$$

and so the angular distribution of radiation is indeed cut off at  $\zeta_0 = t_0/E^2$ .

With the cut-off prescription (5.95), the most convenient definition of the evolution variable is not  $\zeta$  itself but rather

$$\tilde{t} = E^2 \zeta \geq t_0 . \quad (5.97)$$

When using this variable, we have to remember that the angular ordering condition  $\zeta_b, \zeta_c < \zeta_a$  for the branching  $a \rightarrow bc$  translates into

$$\tilde{t}_b < z^2 \tilde{t}, \quad \tilde{t}_c < (1-z)^2 \tilde{t} \quad (5.98)$$

where  $\tilde{t} = \tilde{t}_a$  and  $z = E_b/E_a$ . Thus the cut-off condition on  $z$  becomes

$$\sqrt{t_0/\tilde{t}} < z < 1 - \sqrt{t_0/\tilde{t}} . \quad (5.99)$$

Neglecting the masses of  $b$  and  $c$ , the virtual mass-squared of  $a$  and the transverse momentum of the branching are given by

$$t = z(1-z)\tilde{t}, \quad p_t^2 = z^2(1-z)^2\tilde{t}. \quad (5.100)$$

Thus for the coherent branching process, the Sudakov form factor of the quark, for example, takes the form

$$\tilde{\Delta}_q(\tilde{t}) = \exp \left\{ - \int_{4t_0}^{\tilde{t}} \frac{dt'}{t'} \int_{\sqrt{t_0/t'}}^{1-\sqrt{t_0/t'}} \frac{dz}{2\pi} \alpha_s(z^2(1-z)^2 t') \hat{P}_{qq}(z) \right\}. \quad (5.101)$$

At large  $\tilde{t}$  this falls more slowly than the function (5.58), but still faster than any negative power of  $\tilde{t}$ . The slower fall implies less branching, which is due to the suppression of soft gluon emission by angular ordering.

## 5.6 Hadronization models

After the parton shower described in the previous sections has terminated, we are left with a set of partons with virtualities (virtual masses-squared) of the order of the cut-off scale  $t_0$ . From this point we enter the low momentum-transfer, long-distance regime in which non-perturbative effects become important. The most important of these effects is hadronization, which converts the partons into the observed hadrons. At present we only have models for the hadronization process. These models are discussed briefly in the present section.

In principle the shower cut-off  $t_0$  is an arbitrary parameter, unconnected with hadronization, for which the intrinsic energy scale is presumably of order  $\Lambda$ . On the other hand, when  $t_0$  is increased the parton shower is terminated earlier and there are less partons to hadronize, with higher virtualities. These more virtual partons should be capable of producing more hadrons. Thus the hadronization model should ideally have a parameter  $t_0$  whose effect cancels when the parton shower and hadronization phases of jet fragmentation are combined. In practice, cancellation will be imperfect owing to deficiencies of the model, and  $t_0$  becomes a parameter to be varied in optimizing agreement with experiment. The favoured values tend to be rather small (a few times  $\Lambda$ ) when the parton shower is handled carefully, implying that an extrapolation of perturbation theory is a more reliable guide to physics at such scales than the existing hadronization models.

One general approach to hadronization, based on the observation that perturbation theory seems to work well down to rather low scales, is the hypothesis of *local parton-hadron duality* [5]. Here one supposes only that the flow of momentum and quantum numbers at the hadron level tends to follow the flow established at the parton level. Thus, for example, the

flavour of the quark initiating a jet should be found in a hadron near the jet axis. The extent to which the hadron flow deviates from the parton flow reflects the irreducible smearing of order  $\Lambda$  due to hadron formation.

The simplest more explicit hadronization model [6] is the longitudinal phase space or ‘tube’ model,<sup>3</sup> in which a parton (or, more realistically, a colour-connected pair of partons) produces a jet of light hadrons which occupy a tube in  $(y, p_t)$ -space, where  $y = \frac{1}{2} \ln[(E + p_z)/(E - p_z)]$  is rapidity and  $p_t$  is transverse momentum, both measured with respect to the direction of the initial parton. If the hadron density in this space is  $\rho(p_t)$ , the energy and momentum of a tube of rapidity length  $Y$  are

$$\begin{aligned} E &= \int_0^Y dy d^2 p_t \rho(p_t) p_t \cosh y = \lambda \sinh Y \\ P &= \int_0^Y dy d^2 p_t \rho(p_t) p_t \sinh y = \lambda(\cosh Y - 1) \sim E - \lambda, \end{aligned} \quad (5.102)$$

where  $\lambda = \int d^2 p_t \rho(p_t) p_t$  sets the hadronization scale. Notice that the jet momentum  $P$  receives a negative hadronization correction of relative order  $\lambda/E = 2\lambda/Q$  for a two-jet configuration of total energy  $Q$ . Thus one generally expects hadronization effects to scale with energy like  $1/Q$ .

From Eqs. (5.102) we expect a mean-square hadronization contribution to jet masses of

$$\langle M^2 \rangle_{\text{had}} = E^2 - P^2 \sim \lambda Q. \quad (5.103)$$

Comparing the perturbative predictions for jet masses with experiment, one finds that a hadronization correction corresponding to

$$\lambda \sim 0.5 \text{ GeV} \quad (5.104)$$

is required. Note that this implies a fairly large jet mass, about 7 GeV at  $Q \sim M_Z$ , in addition to the perturbative contribution.

Consider for example the thrust distribution, discussed in Chapter 3. The thrust of a two-jet event is precisely the jet momentum divided by the jet energy, and therefore we expect a hadronization correction of  $-2\lambda/Q$ . The purely perturbative prediction for the mean value of the thrust is [7]

$$\langle T \rangle = 1 - 0.334 \alpha_S - 1.02 \alpha_S^2 + \mathcal{O}(\alpha_S^3), \quad (5.105)$$

which implies that  $\langle 1 - T \rangle \sim 0.055$  at  $Q = M_Z$ , assuming  $\alpha_S(M_Z^2) \sim 0.12$ . The value measured at LEP is  $\langle 1 - T \rangle = 0.068 \pm 0.003$ , the discrepancy of  $0.013 \pm 0.003$  being in agreement with the expected non-perturbative contribution of  $2\lambda/Q \sim 0.011$ . Fig. 5.13 shows that the same formula, *viz.*

---

<sup>3</sup> This model is essentially the simplest version of the string model; we call it a tube to avoid confusion with the more sophisticated Lund string model discussed below.

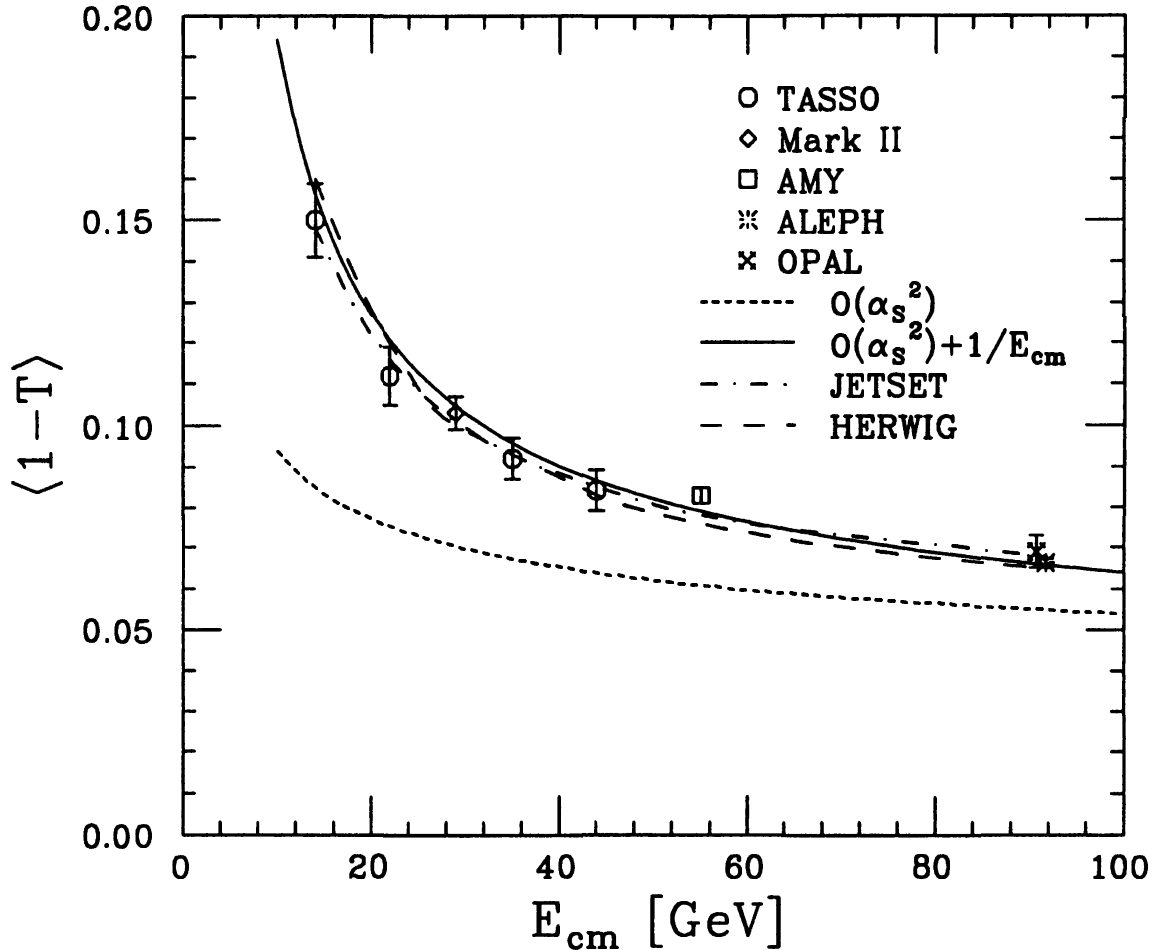


Fig. 5.13.  $\langle 1 - T \rangle$ , where  $T$  is the thrust, in  $e^+e^-$  annihilation.

the  $\mathcal{O}(\alpha_s^2)$  perturbative prediction plus  $2\lambda/Q = 1 \text{ GeV}/E_{\text{cm}}$ , describes the energy dependence of  $\langle 1 - T \rangle$  well down to  $E_{\text{cm}} \sim 15 \text{ GeV}$ .

Also shown in Fig. 5.13 are the predictions of the QCD event generators HERWIG and JETSET, to be discussed in Section 5.7. It can be seen that the hadronization models built into these event generators also give rise to non-perturbative contributions of the required size and energy-dependence.

In order to make more detailed predictions, we need a specific model for the mechanism of hadronization. Over the years, three classes of models have been developed, which we outline briefly in the following subsections.

### 5.6.1 Independent fragmentation

The simplest scheme for generating hadron distributions from those of partons is to suppose that each parton fragments independently. The original approach of Field and Feynman [8] was designed to reproduce the limited transverse momenta and approximate scaling of energy frac-

tion distributions observed in quark jets produced in  $e^+e^-$  annihilation at moderate energies. The fragmenting quark is combined with an anti-quark from a  $q\bar{q}$  pair created out of the vacuum, to give a ‘first-generation’ meson with energy fraction  $z$ . The leftover quark, with energy fraction  $(1 - z)$ , is fragmented in the same way, and so on until the leftover energy falls below some cut-off. Scaling follows from the energy independence of the distribution assumed for  $z$ , which is known as the *fragmentation function*. The limited transverse momenta come from the relative transverse momenta of the created  $q\bar{q}$  pairs, which are given a Gaussian distribution.

For gluon fragmentation, the gluon is first split into a  $q\bar{q}$  pair, either assigning all the gluon’s momentum to one or the other ( $z = 0$  or  $1$ ) with equal probability [9], so that the gluon behaves as a quark of random flavour, or using the  $g \rightarrow q\bar{q}$  Altarelli-Parisi splitting function [10].

With about four parameters to describe the fragmentation function, the width of the transverse momentum distribution, the ratio of strange to nonstrange pair creation, and the ratio of vector to pseudoscalar meson production, the model proved quite successful in describing the broad features of two-jet and three-jet final states in  $e^+e^-$  annihilation at moderate energies [9-11].

A weakness of the independent fragmentation scheme, as formulated above, is that the fragmentation of a parton is supposed to depend on its energy rather than its virtuality. Indeed, the fragmenting parton is usually assumed to remain on mass-shell, leading to violations of momentum conservation that have to be corrected by rescaling momenta after hadronization is completed. The residual colour and flavour of the leftover parton in each jet also have to be neutralized at this stage. There are further problems when jets become close together in angle. Instead of merging smoothly together into a single jet, as would happen if their fragmentation depended on their combined effective mass, even two precisely collinear jets remain distinguishable from a single jet.

### 5.6.2 String model

The string model of hadronization [12-14] is most easily described for  $e^+e^-$  annihilation. Neglecting for the moment the possibility of gluon bremsstrahlung, the produced quark and antiquark move out in opposite directions, losing energy to the colour field, which is supposed to collapse into a stringlike configuration between them. The string has a uniform energy per unit length, corresponding to a linear quark confining potential, which is consistent with quarkonium spectroscopy. The string breaks up into hadron-sized pieces through spontaneous  $q\bar{q}$  pair production in its intense colour field.

In practice, the string fragmentation approach does not look very dif-

ferent from independent fragmentation for the simple quark-antiquark system. The string may be broken up starting at either the quark or the antiquark end, or both simultaneously (the breaking points have space-like separations, so their temporal sequence is frame dependent), and it proceeds iteratively by  $q\bar{q}$  pair creation, as in independent fragmentation. What one gains is a more consistent and covariant picture, together with some constraints on the fragmentation function [14], to ensure independence of whether one starts at the quark or the antiquark, and on the transverse momentum distribution [15], which is now related to the tunnelling mechanism by which  $q\bar{q}$  pairs are created in the colour field of the string.

The string model becomes more distinct from independent fragmentation when gluons are present [16]. These are supposed to produce kinks on the string, each initially carrying localized energy and momentum equal to that of its parent gluon. The fragmentation of the kinked string leads to an angular distribution of hadrons in  $e^+e^-$  three-jet final states that is different from that predicted by independent fragmentation and in better agreement with experiment [17].

For multiparton states, such as those produced by the parton branching process at high  $Q^2$ , or for low values of the shower cut-off  $t_0$ , there is ambiguity about how strings should be connected between the various endpoints (quarks and antiquarks) and kinks (gluons). However, to leading order in  $N^{-2}$  where  $N = 3$  is the number of colours, it is always possible to arrange the produced partons in a *planar* configuration, as discussed in Section 4.6.5. Then each has an equal and opposite colour to that of a neighbour (both neighbours, in the case of a gluon), like the quark and antiquark in the simplest  $e^+e^-$  final state. It seems most reasonable to stretch the string between these colour-connected neighbours. The reformulation of parton showers in terms of sequential splitting of colour dipoles [18] leads to the same prescription for string connection.

A schematic picture of the production of a multihadronic final state in  $e^+e^-$  annihilation according to the string model is shown in Fig. 5.14. Notice that whenever a gluon splits perturbatively into a quark-antiquark pair during the evolution of the parton shower, an additional string segment is produced. On the other hand, gluons which remain at the end of the shower (*i.e.* at the cut-off scale  $t_0$ ) lead to kinks in the string segment which connects them. Each string segment then breaks up into hadrons as described above.

### 5.6.3 Cluster model

An important property of the parton branching process is the *preconfinement* of colour [19]. Preconfinement implies that the pairs of colour-

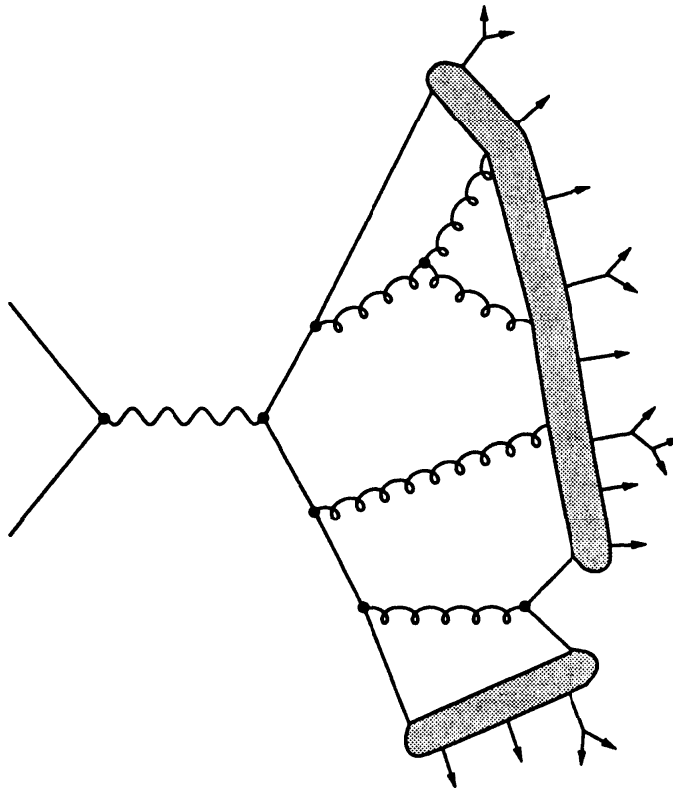


Fig. 5.14. Parton shower with string hadronization model for  $e^+e^- \rightarrow \text{hadrons}$ .

connected neighbouring partons discussed above have an asymptotic mass distribution that falls rapidly at high masses and is asymptotically  $Q^2$ -independent and universal. This suggests a class of *cluster hadronization* models, in which colour-singlet *clusters* of partons form after the perturbative phase of jet development and then decay into the observed hadrons.

The simplest way for colour-singlet clusters to form after parton branching is through non-perturbative splitting of gluons into  $q\bar{q}$  pairs [20]. Neighbouring quarks and antiquarks can then combine into singlets. The resulting cluster mass spectrum is again universal and steeply falling at high masses. Its precise form is determined by the QCD scale  $\Lambda$ , the cut-off scale  $t_0$ , and to a lesser extent the gluon-splitting mechanism. Typical cluster masses are normally two or three times  $\sqrt{t_0}$ .

If a low value of  $t_0$  is used, of the order of 1 GeV $^2$  or less, most clusters have masses of up to a few GeV/c $^2$  and it is reasonable to treat them as superpositions of meson resonances. In a popular model [20,21], each such cluster is assumed to decay isotropically in its rest frame into a pair of hadrons, with branching ratios determined simply by density of states. The reduced phase space for cluster decay into heavy mesons and baryons is then sufficient to account for the multiplicities of the various kinds of hadrons observed in  $e^+e^-$  final states. Furthermore, the hadronic energy and transverse momentum distributions agree quite well with experiment,

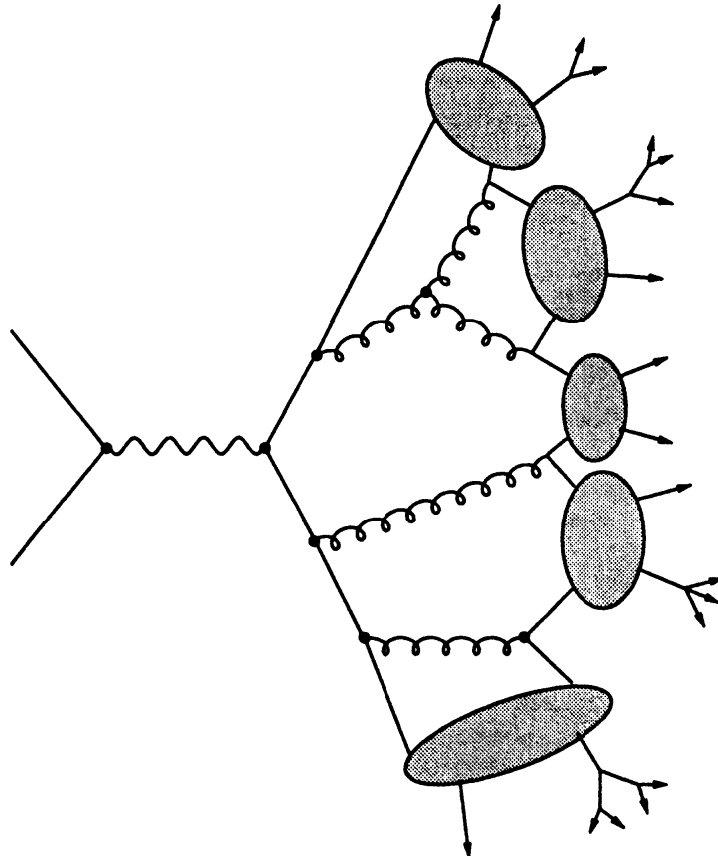


Fig. 5.15. Parton shower with cluster hadronization model for  $e^+e^- \rightarrow \text{hadrons}$ .

without the introduction of any adjustable fragmentation functions. Also, the angular distribution in  $e^+e^-$  three-jet events is successfully described, as in the string model, provided soft gluon coherence is taken into account (see Section 5.5).

Fig. 5.15 shows the cluster hadronization of the same parton shower as in Fig. 5.14. The gluons that remain after the parton shower are split non-perturbatively into quark-antiquark pairs. The planar configuration of the shower determines that neighbouring pairs (not from the same gluon) can form colour-singlet mesonic clusters, which then undergo isotropic quasi-two-body decay into the observed hadrons.

An alternative approach to cluster formation and decay is to use a higher value of the cut-off  $t_0$  and an anisotropic, multihadron decay scheme for the resulting heavy clusters [22]. Clearly, this approach lies somewhere between the low-mass cluster and string models. In practice, even with a low value of  $t_0$  one needs to invoke a more complicated decay scheme for the small fraction of clusters that have masses of more than a few  $\text{GeV}/c^2$ , for which isotropic two-body decay is an implausible hypothesis.

## 5.7 QCD event generators

There are three classes of programs for generating full events from parton showers, using each of the three above-mentioned hadronization models.

Because of the difficulties discussed in connection with the independent fragmentation model, one would expect it to work best for the higher-momentum hadrons in final states consisting of a few well-separated jets. Probably on account of its simplicity, it was initially the model used most widely in conjunction with initial- and final-state parton branching for the simulation of hard hadron-hadron collisions, in the programs ISAJET [23], COJETS [24] and FIELDAJET [25].

The string hadronization model outlined above, with many further refinements, is the basis of the JETSET simulation program [26], which also includes final-state parton branching with optional angular ordering. This program gives a very good detailed description of hadronic final states in  $e^+e^-$  annihilation up to the highest energies studied so far.

The JETSET hadronization scheme is also used, in combination with initial- and final-state parton branching, in the other very successful Lund simulation programs PYTHIA [27] for hadron-hadron and LEPTO [28] for lepton-hadron collisions. The alternative formulation of parton showers in terms of colour dipole splitting mentioned above is implemented in the program ARIADNE [29], which also uses JETSET for hadronization.

The program HERWIG [4,30] uses a low-mass cluster hadronization model [21] in conjunction with initial- and final-state parton branching to simulate a wide variety of hard scattering processes. The branching algorithm includes angular ordering and azimuthal correlations due to coherence and gluon polarization. This approach gives a good account of diverse data with relatively few adjustable parameters.

Results from JETSET and HERWIG on the mean value of the thrust parameter are shown in Fig. 5.13. Both the string and cluster hadronization models lead a  $1/E_{\text{cm}}$  dependence of the non-perturbative contribution to this quantity, as seen in the data and in the simple ‘tube’ model discussed earlier.

## References

- 1) J.D. Bjorken and S.D. Drell, *Relativistic Quantum Mechanics*, McGraw Hill, New York (1964).
- 2) D. Amati, A. Bassutto, M. Ciafaloni, G. Marchesini and G. Veneziano, *Nucl. Phys.* **B173** (1980) 429.
- 3) T. Sjöstrand, *Phys. Lett.* **B157** (1985) 321.
- 4) G. Marchesini and B.R. Webber, *Nucl. Phys.* **B310** (1988) 461.
- 5) Ya.I. Azimov, Yu.L. Dokshitzer, V.A. Khoze and S.I. Troyan, *Phys. Lett.* **B165** (1985) 147; *Zeit. Phys.* **C27** (1985) 65.

- 6) R.P. Feynman, *Photon Hadron Interactions*, W.A. Benjamin, New York (1972).
- 7) Z. Kunszt, P. Nason, G. Marchesini and B.R. Webber, in 'Z Physics at LEP 1', CERN 89-08, vol. 1, p. 373.
- 8) R.D. Field and R.P. Feynman, *Phys. Rev. D* **15** (1977) 2590; *Nucl. Phys. B* **138** (1978) 1.
- 9) P. Hoyer *et al.*, *Nucl. Phys. B* **161** (1979) 349.
- 10) A. Ali *et al.*, *Phys. Lett. B* **93** (1980) 155.
- 11) A. Ali *et al.*, *Nucl. Phys. B* **168** (1980) 409.
- 12) X. Artru and G. Mennessier, *Nucl. Phys. B* **70** (1974) 93.
- 13) M.G. Bowler, *Zeit. Phys. C* **11** (1981) 169.
- 14) B. Andersson, G. Gustafson and B. Söderberg, *Zeit. Phys. C* **20** (1983) 317; *Nucl. Phys. B* **264** (1986) 29.
- 15) B. Andersson, G. Gustafson, G. Ingelman and T. Sjöstrand, *Phys. Rep.* **97** (1983) 33.
- 16) T. Sjöstrand, *Nucl. Phys. B* **248** (1984) 469.
- 17) JADE collaboration, W. Bartel *et al.*, *Phys. Lett. B* **157** (1985) 340; TPC collaboration, H. Aihara *et al.*, *Zeit. Phys. C* **28** (1985) 31; TASSO collaboration, M. Althoff *et al.*, *Zeit. Phys. C* **29** (1985) 29.
- 18) G. Gustafson, *Phys. Lett. B* **175** (1986) 453; G. Gustafson and U. Pettersson, *Nucl. Phys. B* **306** (1988) 746.
- 19) D. Amati and G. Veneziano, *Phys. Lett. B* **83** (1979) 87; A. Bassutto, M. Ciafaloni and G. Marchesini, *Phys. Lett. B* **83** (1979) 207; G. Marchesini, L. Trentadue and G. Veneziano, *Nucl. Phys. B* **181** (1980) 335.
- 20) R.D. Field and S. Wolfram, *Nucl. Phys. B* **213** (1983) 65.
- 21) B.R. Webber, *Nucl. Phys. B* **238** (1984) 492.
- 22) T.D. Gottschalk, *Nucl. Phys. B* **214** (1983) 201.
- 23) F.E. Paige and S.D. Protopopescu, in Proc. UCLA Workshop, eds. H.-U. Bengtsson *et al.*, World Scientific, Singapore (1986).
- 24) R. Odorico, *Comp. Phys. Comm.* **32** (1984) 139; *ibid.* **59** (1990) 527.
- 25) R.D. Field, *Nucl. Phys. B* **264** (1986) 687.
- 26) T. Sjöstrand, *Comp. Phys. Comm.* **39** (1986) 347; M. Bengtsson and T. Sjöstrand, *Comp. Phys. Comm.* **43** (1987) 367.
- 27) H.-U. Bengtsson and T. Sjöstrand, *Comp. Phys. Comm.* **46** (1987) 43; T. Sjöstrand, *Comp. Phys. Comm.* **82** (1994) 74.
- 28) G. Ingelman, in Proc. Workshop on Physics at HERA, eds. W. Buchmüller and G. Ingelman, DESY, Hamburg (1991).
- 29) L. Lönnblad, *Comp. Phys. Comm.* **71** (1992) 15.
- 30) G. Marchesini, B.R. Webber, G. Abbiendi, I.G. Knowles, M.H. Seymour and L. Stanco, *Comp. Phys. Comm.* **67** (1992) 465.

# 6

## Jet properties beyond fixed order

We illustrated in Chapter 3 the use of perturbation theory to calculate ‘infra-red safe’ quantities such as the  $e^+e^-$  total cross section and thrust distribution. There are in addition predictions that can be made concerning some quantities that are ‘infra-red sensitive’, *i.e.* that have infra-red and collinear singularities in perturbation theory. Such quantities can still be handled provided the singularities can be collected into an overall factor which describes the sensitivity of the quantity to long-distance physics. The divergence of this factor corresponds to the fact that long-distance phenomena are not reliably predicted by perturbation theory. For example, quarks and gluons are free to propagate over macroscopic distances in perturbation theory, whereas in reality they are confined inside hadrons. Therefore the divergent factor should be replaced by a finite factor determined experimentally by measurements at a relatively short distance scale. Once this is done, perturbation theory can be used to predict the scale dependence of the quantity.

The best known example of a perturbative prediction of a factorizable infra-red-sensitive quantity is the phenomenon of scaling violation, discussed in Chapter 4. There we studied the parton distributions inside a hadron, probed by deep inelastic lepton scattering. Here we consider the related phenomenon for the fragmentation of a jet, produced for example in  $e^+e^-$  annihilation, into hadrons of a given type  $h$ .

### 6.1 Jet fragmentation

We start by defining *fragmentation functions*, which are dimensionless functions that describe single particle distributions in the final state. The total fragmentation function for hadrons of type  $h$  in  $e^+e^-$  annihilation

at c.m. energy  $\sqrt{s}$  is defined as

$$F^h(x, s) = \frac{1}{\sigma_{\text{tot}}} \frac{d\sigma}{dx} (e^+ e^- \rightarrow hX) \quad (6.1)$$

where  $x = 2E_h/\sqrt{s} \leq 1$  is the scaled hadron energy (in practice, the approximation  $x = x_p = 2p_h/\sqrt{s}$  is often used). Since each hadron of type  $h$  contributes to the fragmentation function (6.1), its integral with respect to  $x$  gives the average multiplicity of those hadrons:

$$\langle n_h(s) \rangle = \int_0^1 dx F^h(x, s) . \quad (6.2)$$

Similarly, the integral of  $x F^h(x, s)$  gives the total scaled energy carried by hadrons of that type, which implies the sum rule

$$\sum_h \int_0^1 dx x F^h(x, s) = 2 . \quad (6.3)$$

The fragmentation function (6.1) can be represented as a sum of contributions from the different primary partons  $i = u, d, \dots, g$ :

$$F^h(x, s) = \sum_i \int_x^1 \frac{dz}{z} C_i(s; z, \alpha_s) D_i^h(x/z, s) . \quad (6.4)$$

In lowest order the coefficient function  $C_g$  for gluons is zero, while for quarks  $C_i = g_i(s)\delta(1-z)$  where  $g_i(s)$  is the appropriate electroweak coupling. In particular,  $g_i(s)$  is proportional to the charge-squared of parton  $i$  at  $s \ll M_Z^2$ , when weak effects can be neglected.

We cannot compute the fragmentation functions  $D_i^h$  from perturbation theory, since the production of hadrons is not a perturbative process. We might consider trying to compute functions  $D_i^j$  that would describe the fragmentation of partons of type  $i$  into partons of type  $j$ . However, they would be infinite, since the probability of emitting a collinear gluon or light quark is divergent. Nevertheless, as for the parton distribution functions  $f_i(x, t)$  in deep inelastic scattering, one can show [1] that at high values of the energy-squared scale  $t$  all such divergences are factorizable, in the sense that we can write

$$D_i^j(x, t) = \sum_k \int_x^1 dz K_i^k(z, t, t_0) D_k^j(x/z, t_0) , \quad (6.5)$$

where the kernel function  $K_i^k$  is perturbatively calculable and at  $t_0 = t$  we have  $K_i^k(z, t, t) = \delta_{ik} \delta(1-z)$ .

In the real world, hadrons are formed and fragmentation functions are not divergent. As long as the scales  $t$  and  $t_0$  are large, we would not expect the form of Eq. (6.5) to be affected by such long-distance phenomena. Therefore we replace  $j$  by  $h$  and apply the equation to hadronic

fragmentation functions. After measuring these functions at some scale  $t_0$ , we can use the equation to predict their form at any other scale  $t$ , as long as both  $t$  and  $t_0$  are large enough for perturbation theory to be applicable in the calculation of the kernel  $K_i^k$ .

### 6.1.1 Scaling violation

The approach outlined above is very close to that adopted for the analysis of the scale dependence of parton distribution functions in Chapter 4. In a fragmentation function  $x$  represents the fraction of a parton's momentum carried by a produced hadron, whereas in a parton distribution it represents the fraction of a hadron's momentum carried by a constituent parton. In both cases, the simplest parton-model approach, represented by the independent fragmentation model (Section 5.6.1) in the case of fragmentation, would predict a scale-independent  $x$  distribution. Furthermore we obtain similar violations of this scaling behaviour when QCD corrections are taken into account.

Consider the change in a fragmentation function  $D_i(x, t)$  or a parton distribution function  $f_i(x, t)$  when the scale is increased from  $t$  to  $t + dt$ . As discussed in Section 5.2, such a change can only occur via the splitting of a parton of type  $i$  in this scale interval. Hence the fragmentation functions satisfy evolution equations like those for parton distributions:

$$t \frac{\partial}{\partial t} D_i(x, t) = \sum_j \int_x^1 \frac{dz}{z} \frac{\alpha_s}{2\pi} P_{ji}(z, \alpha_s) D_j(x/z, t). \quad (6.6)$$

Notice that the splitting function is now  $P_{ji}$  rather than  $P_{ij}$  since here  $D_j$  represents the fragmentation of the final parton, whereas  $f_j$  in Eq. (5.37) represented the distribution of the initial parton. The splitting functions again have perturbative expansions of the form

$$P_{ji}(z, \alpha_s) = P_{ji}^{(0)}(z) + \frac{\alpha_s}{2\pi} P_{ji}^{(1)}(z) + \dots \quad (6.7)$$

where the lowest-order functions  $P_{ji}^{(0)}(z)$  are the same as those in deep inelastic scattering but the higher-order terms are different. The effect of splitting is, however, the same in both cases: as the scale increases, one observes a scaling violation in which the  $x$  distribution is shifted towards lower values.

As in the case of the parton distribution functions, the most common strategy for solving the evolution equations (6.6) is to take moments (Mellin transforms) with respect to  $x$ :

$$\tilde{D}(j, t) = \int_0^1 dx x^{j-1} D(x, t), \quad (6.8)$$

the inverse Mellin transformation being

$$D(x, t) = \frac{1}{2\pi i} \int_C dj x^{-j} \tilde{D}(j, t), \quad (6.9)$$

where the integration contour  $C$  in the complex  $j$  plane is parallel to the imaginary axis and to the right of all singularities of the integrand. Again we can consider fragmentation function combinations which are non-singlet (in flavour space) such as  $D_V = D_{q_i} - D_{\bar{q}_i}$  or  $D_{q_i} - D_{q_j}$ . In these combinations the mixing with the flavour singlet gluons drops out and for a fixed value of  $\alpha_s$  the solution is simply

$$\tilde{D}_V(j, t) = \tilde{D}_V(j, t_0) \left( \frac{t}{t_0} \right)^{\gamma_{qq}(j, \alpha_s)}, \quad (6.10)$$

where the quantity  $\gamma_{qq}$  is the Mellin transform of  $\alpha_s P_{qq}/2\pi$ . The resulting dependence on  $t$  violates scaling rules based on naive dimensional analysis, and therefore the power  $\gamma_{qq}$  is called an *anomalous dimension*. For a running coupling  $\alpha_s(t)$ , however, the scaling violation is no longer power-behaved. Inserting the lowest-order form (2.42) for the running coupling, we find the solution

$$\tilde{D}_V(j, t) = \tilde{D}_V(j, t_0) \left( \frac{\alpha_s(t_0)}{\alpha_s(t)} \right)^{d_{qq}(j)}, \quad d_{qq}(j) = \frac{\gamma_{qq}^{(0)}(j)}{2\pi b}, \quad (6.11)$$

which varies like a power of  $\ln t$ .

For the singlet fragmentation function

$$D_S = \sum_i (D_{q_i} + D_{\bar{q}_i}) \quad (6.12)$$

we have mixing with the fragmentation of the gluon and the evolution equation becomes a matrix relation as in the deep inelastic scattering case:

$$t \frac{\partial}{\partial t} \begin{pmatrix} \tilde{D}_S \\ \tilde{D}_g \end{pmatrix} = \begin{pmatrix} \gamma_{qq} & 2n_f \gamma_{gg} \\ \gamma_{gg} & \gamma_{gg} \end{pmatrix} \begin{pmatrix} \tilde{D}_S \\ \tilde{D}_g \end{pmatrix}. \quad (6.13)$$

The anomalous dimension matrix in this equation has two real eigenvalues given by Eq. (4.140). Expressing  $D_S$  and  $D_g$  as linear combinations of the corresponding eigenvectors  $D_+$  and  $D_-$ , we find that they evolve as superpositions of terms of the form (6.11) with  $\gamma_+$  and  $\gamma_-$  in the place of  $\gamma_{qq}$ .

At small  $x$ , corresponding to  $j \rightarrow 1$ , the  $g \rightarrow g$  anomalous dimension becomes dominant and we find  $\gamma_+ \rightarrow \gamma_{gg} \rightarrow \infty$ ,  $\gamma_- \rightarrow \gamma_{qq} \rightarrow 0$ . This region requires special treatment, which will be presented in the next subsection.

As mentioned earlier, the splitting functions and anomalous dimensions for fragmentation (timelike branching) are the same as those for

deep inelastic scattering (spacelike branching) in lowest order, as given by Eq. (4.129), but they differ in higher orders. Corresponding to Eqs. (4.107) - (4.112), in the  $\overline{\text{MS}}$  factorization/renormalization scheme the non-singlet timelike splitting functions (for  $x \neq 1$ ) are [2]

$$\begin{aligned} P_{qq}^{V(1)} &= C_F^2 \left\{ \left[ 2 \ln x \ln(1-x) + \frac{3}{2} \ln x - 2 \ln^2 x \right] p_{qq}(x) \right. \\ &\quad - \left( \frac{7}{2} + \frac{3}{2}x \right) \ln x + \frac{1}{2}(1+x) \ln^2 x - 5(1-x) \Big\} \\ &\quad + C_F C_A \left\{ \left[ \frac{1}{2} \ln^2 x + \frac{11}{6} \ln x + \frac{67}{18} - \frac{\pi^2}{6} \right] p_{qq}(x) \right. \\ &\quad \left. + (1+x) \ln x + \frac{20}{3}(1-x) \right\} \\ &\quad + C_F T_f \left\{ - \left[ \frac{2}{3} \ln x + \frac{10}{9} \right] p_{qq}(x) - \frac{4}{3}(1-x) \right\} \quad (6.14) \end{aligned}$$

$$\begin{aligned} P_{q\bar{q}}^{V(1)} &= C_F \left( C_F - \frac{C_A}{2} \right) \left\{ 2p_{qq}(-x) S_2(x) \right. \\ &\quad \left. + 2(1+x) \ln x + 4(1-x) \right\}. \quad (6.15) \end{aligned}$$

Note that  $P_{q\bar{q}}^{V(1)}$  is the same as in the spacelike case. The singlet functions are [3]<sup>1</sup>

$$\begin{aligned} P_{qq}^{(1)} &= C_F^2 \left\{ -1 + x + \left( \frac{1}{2}x - \frac{3}{2} \right) \ln x + \frac{1}{2}(1+x) \ln^2 x \right. \\ &\quad + \left[ \frac{3}{2} \ln x - 2 \ln^2 x + 2 \ln x \ln(1-x) \right] p_{qq}(x) \\ &\quad \left. + 2p_{qq}(-x) S_2(x) \right\} \\ &\quad + C_F C_A \left\{ \frac{14}{3}(1-x) + \left[ \frac{11}{6} \ln x + \frac{1}{2} \ln^2 x + \frac{67}{18} - \frac{\pi^2}{6} \right] p_{qq}(x) \right. \\ &\quad \left. - p_{qq}(-x) S_2(x) \right\} \\ &\quad + C_F T_f \left\{ -\frac{52}{3} + \frac{28}{3}x - \left( 10 + 18x + \frac{16}{3}x^2 \right) \ln x + \frac{112}{9}x^2 \right. \\ &\quad \left. - \frac{40}{9x} + 2(1+x) \ln^2 x - \left[ \frac{10}{9} + \frac{2}{3} \ln x \right] p_{qq}(x) \right\} \quad (6.16) \end{aligned}$$

$$P_{qg}^{(1)} = T_f^2 \left\{ -\frac{8}{3} - \left[ \frac{16}{9} + \frac{8}{3} \ln x + \frac{8}{3} \ln(1-x) \right] p_{qg}(x) \right\}$$

---

<sup>1</sup> Note that the published version of ref. [3] contains some misprints.

$$\begin{aligned}
& + C_F T_f \left\{ -2 + 3x + (-7 + 8x) \ln x - 4 \ln(1-x) \right. \\
& + (1-2x) \ln^2 x + \left[ -2 \ln^2(x(1-x)) - 2 \ln \left( \frac{1-x}{x} \right) \right. \\
& \left. \left. + 16S_1(x) + 2\pi^2 - 10 \right] p_{qg}(x) \right\} \\
& + C_A T_f \left\{ -\frac{152}{9} + \frac{166}{9}x - \frac{40}{9x} + \left( -\frac{4}{3} - \frac{76}{3}x \right) \ln x \right. \\
& + 4 \ln(1-x) + (2+8x) \ln^2 x + \left[ 8 \ln x \ln(1-x) - \ln^2 x \right. \\
& \left. - \frac{4}{3} \ln x + \frac{10}{3} \ln(1-x) \right. \\
& \left. + 2 \ln^2(1-x) - 16S_1(x) - \frac{7\pi^2}{3} + \frac{178}{9} \right] p_{qg}(x) \\
& \left. + 2p_{qg}(-x) S_2(x) \right\} \tag{6.17}
\end{aligned}$$

$$\begin{aligned}
P_{gq}^{(1)} = & C_F^2 \left\{ -\frac{1}{2} + \frac{9}{2}x + \left( -8 + \frac{1}{2}x \right) \ln x + 2x \ln(1-x) \right. \\
& + \left( 1 - \frac{1}{2}x \right) \ln^2 x + \left[ \ln^2(1-x) + 4 \ln x \ln(1-x) \right. \\
& \left. - 8S_1(x) - \frac{4}{3}\pi^2 \right] p_{gq}(x) \Big\} \\
& + C_F C_A \left\{ \frac{62}{9} - \frac{35}{18}x - \frac{44}{9}x^2 + \left( 2 + 12x + \frac{8}{3}x^2 \right) \ln x \right. \\
& - 2x \ln(1-x) - (4+x) \ln^2 x + p_{gq}(-x) S_2(x) \\
& + \left[ -2 \ln x \ln(1-x) - 3 \ln x - \frac{3}{2} \ln^2 x - \ln^2(1-x) \right. \\
& \left. + 8S_1(x) + \frac{7\pi^2}{6} + \frac{17}{18} \right] p_{gq}(x) \Big\} \tag{6.18}
\end{aligned}$$

$$\begin{aligned}
P_{gg}^{(1)} = & C_F T_f \left\{ -4 + 12x - \frac{164}{9}x^2 + \left( 10 + 14x + \frac{16}{3}x^2 + \frac{16}{3x} \right) \ln x \right. \\
& + \frac{92}{9x} + 2(1+x) \ln^2 x \Big\}
\end{aligned}$$

$$\begin{aligned}
& + C_A T_f \left\{ 2 - 2x + \frac{26}{9} \left( x^2 - \frac{1}{x} \right) - \frac{4}{3} (1+x) \ln x \right. \\
& - \left( \frac{20}{9} + \frac{8}{3} \ln x \right) p_{gg}(x) \Big\} \\
& + C_A^2 \left\{ \frac{27}{2} (1-x) + \frac{67}{9} \left( x^2 - \frac{1}{x} \right) + \left( \frac{11}{3} - \frac{25}{3}x - \frac{44}{3x} \right) \ln x \right. \\
& - 4(1+x) \ln^2 x + 2p_{gg}(-x) S_2(x) + \left[ 4 \ln x \ln(1-x) \right. \\
& \left. \left. - 3 \ln^2 x + \frac{22}{3} \ln x - \frac{\pi^2}{3} + \frac{67}{9} \right] p_{gg}(x) \right\} \tag{6.19}
\end{aligned}$$

where  $S_2(x)$  is given in Eq. (4.113) and

$$S_1(x) = \int_0^{1-x} \frac{dz}{z} \ln(1-z). \tag{6.20}$$

In terms of the dilogarithm function defined in Eq. (3.36),  $S_2(x)$  is given by Eq. (4.114) and

$$S_1(x) = -\text{Li}_2(1-x) = \text{Li}_2(x) + \ln x \ln(1-x) - \frac{\pi^2}{6}. \tag{6.21}$$

Endpoint contributions at  $x = 1$  may again be evaluated using the sum rules (4.115) and (4.116). They are found to be the same as those in Eqs. (4.118)–(4.120).

The small- $x$  limits of the splitting functions are now

$$\begin{aligned}
P_{qq} &\rightarrow -\frac{\alpha_s}{2\pi} \frac{40C_F T_f}{9x} \\
P_{qg} &\rightarrow -\frac{\alpha_s}{2\pi} \frac{40C_A T_f}{9x} \\
P_{gq} &\rightarrow \frac{2C_F}{x} - \frac{\alpha_s}{2\pi} \frac{4C_F C_A}{x} \ln^2 x \\
P_{gg} &\rightarrow \frac{2C_A}{x} - \frac{\alpha_s}{2\pi} \frac{4C_A^2}{x} \ln^2 x. \tag{6.22}
\end{aligned}$$

Note that the higher-order terms in  $P_{gq}$  and  $P_{gg}$  are more singular as  $x \rightarrow 0$  than those for deep inelastic scattering, Eq. (4.122). As a result, the resummation of enhanced terms in the fragmentation functions at small  $x$  yields a completely different behaviour from that of the small- $x$  structure functions discussed in Section 4.6. This will be studied in detail in the following two subsections.

There are several complications in the experimental study of scaling violation in jet fragmentation functions [4]. First, the energy dependence of the electroweak couplings  $g_i(s)$  that enter into Eq. (6.4) is especially

strong in the energy region presently under study ( $\sqrt{s} = 20 - 90$  GeV). In particular, the  $b$ -quark contribution more than doubles in this range. The fragmentation of the  $b$  quark into charged hadrons, including the weak decay products of the  $b$ -flavoured hadron, is expected to be substantially softer than that of the other quarks, so its increased contribution can give rise to a ‘fake’ scaling violation. A smaller, partially compensating effect is expected in charm fragmentation. These effects can be eliminated by extracting the  $b$  and  $c$  fragmentation functions at  $\sqrt{s} = M_Z$  from tagged heavy quark events, and evolving them separately to other energies.

Secondly, one requires the gluon fragmentation function  $D_g(x, s)$  in addition to those of the quarks. Although the gluon does not couple directly to the electroweak current, it contributes in higher order, and mixes with the quarks through evolution. Its fragmentation can be studied in tagged heavy-quark three-jet ( $Q\bar{Q}g$ ) events, or via the longitudinal fragmentation function (to be discussed below).

A final complication is that power corrections to fragmentation functions, of the form  $f(x)/Q^p$ , are not well understood. As in the case of event shapes, Monte Carlo studies [4] suggest that hadronization can lead to  $1/Q$  corrections. Therefore, possible contributions of this form should be included in the parametrization when fitting the scaling violation.

The results of an analysis of scaling violation in the charged hadron spectrum by the ALEPH collaboration [5], based on a comparison of LEP data with those from lower-energy experiments, are shown in Fig. 6.1. An overall fit in the range  $22 \leq \sqrt{s} \leq 91.2$  GeV,  $0.1 < x < 0.8$ , incorporating full next-to-leading-order evolution and a simple parametrization of  $1/Q$  power corrections, gives a good description of the data in the fitted region, as shown by the curves.<sup>2</sup> The fitted power corrections are small and the value obtained for  $\alpha_s(M_Z^2)$  ( $0.126 \pm 0.009$ ) is not highly sensitive to the form assumed for them. Indeed, a leading  $1/Q^2$  dependence is not ruled out, and it may be that in this case the Monte Carlo models are misleading and  $1/Q$  corrections are in fact absent. An operator-product approach to fragmentation, developed in ref. [6], does indeed suggest that  $1/Q$  corrections are absent.

### 6.1.2 Average multiplicity

The average number of hadrons of type  $h$  in a jet initiated by a parton  $i$  at scale  $t$ ,  $\langle n_h(t) \rangle_i$ , is just the integral of the fragmentation function,

---

<sup>2</sup> The fitted curves do not extrapolate well into the small- $x$  region, but a next-to-leading-order treatment would not be expected to be reliable there: see the next section.

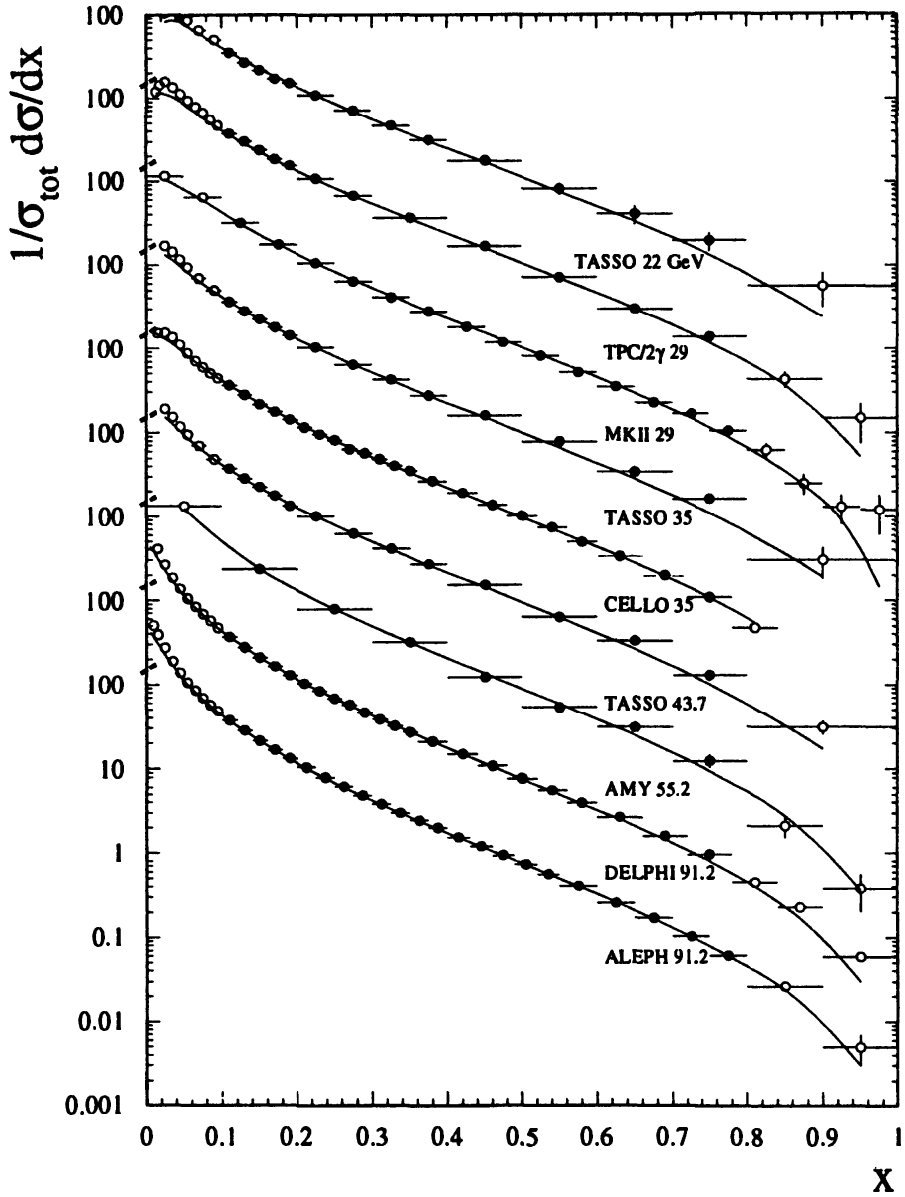


Fig. 6.1. Scaling violation in  $e^+e^-$  fragmentation functions. Figure from ref. [5].

which is the  $j = 1$  moment in the notation of Eq. (6.8):

$$\langle n_h(t) \rangle_i = \int_0^1 dx D_i^h(x, t) = \tilde{D}_i^h(1, t). \quad (6.23)$$

If we try to compute the  $t$  dependence of this quantity, we immediately encounter the problem that the lowest-order expressions for the anomalous dimensions  $\gamma_{gq}$  and  $\gamma_{gg}$  in Eq. (4.129) are divergent at  $j = 1$ . The reason is that for  $j \leq 1$  the moments of the splitting functions in Eq. (4.94) are dominated by the region of small  $z$ , where  $P_{gi}(z)$  has a divergence associated with soft gluon emission.

In fact, however, we can still solve the evolution equation for the average multiplicity provided we take into account the suppression of soft gluon

emission due to coherence, as discussed in Chapter 5. We saw there that the leading effect of coherence is obtained simply by changing the evolution variable from virtual mass-squared to the quantity  $\tilde{t} = E^2(1 - \cos \theta)$ , for which the ordering condition is (5.98). Thus, after redefining  $t$  as  $\tilde{t}$ , Eq. (6.6) may be written in integrated form as

$$D_i(x, t) = D_i(x, t_0) + \sum_j \int_x^1 \frac{dz}{z} \int_{t_0}^{z^2 t} \frac{dt'}{t'} \frac{\alpha_s}{2\pi} P_{ji}(z, \alpha_s) D_j(x/z, t') , \quad (6.24)$$

or in differential form

$$t \frac{\partial}{\partial t} D_i(x, t) = \sum_j \int_x^1 \frac{dz}{z} \frac{\alpha_s}{2\pi} P_{ji}(z, \alpha_s) D_j(x/z, z^2 t) . \quad (6.25)$$

Notice that this differs from the conventional evolution equation (6.6) only in the  $z$ -dependent change of scale on the right-hand side. This change is not important for most values of  $x$  but we shall see that it is crucial at small  $x$ .

For simplicity, consider first the solution of Eq. (6.25) taking  $\alpha_s$  fixed and neglecting the sum over different branchings. Then taking moments as usual we have

$$t \frac{\partial}{\partial t} \tilde{D}(j, t) = \frac{\alpha_s}{2\pi} \int_x^1 dz z^{j-1} P(z) \tilde{D}(j, z^2 t) . \quad (6.26)$$

Now if we try a solution of the form

$$D(j, t) \propto t^{\gamma(j, \alpha_s)} \quad (6.27)$$

we find that the anomalous dimension  $\gamma(j, \alpha_s)$  must satisfy the implicit equation

$$\gamma(j, \alpha_s) = \frac{\alpha_s}{2\pi} \int_0^1 dz z^{j-1+2\gamma(j, \alpha_s)} P(z) . \quad (6.28)$$

When  $j - 1$  is not small, we may neglect the  $2\gamma(j, \alpha_s)$  in the exponent of Eq. (6.28) and then we obtain the usual explicit formula for the anomalous dimension. For  $j \simeq 1$ , the region we are interested in, the  $z \rightarrow 0$  behaviour of  $P(z)$  dominates and we may as a first approximation keep only those terms that are singular at  $z = 0$ . The most important such term appears in the gluon-gluon splitting function:  $P_{gg}(z) \rightarrow 2C_A/z$  as  $z \rightarrow 0$ , which implies that near  $j = 1$

$$\gamma_{gg}(j, \alpha_s) = \frac{C_A \alpha_s}{\pi} \frac{1}{j - 1 + 2\gamma_{gg}(j, \alpha_s)} \quad (6.29)$$

and hence

$$\gamma_{gg}(j, \alpha_s) = \frac{1}{4} \left[ \sqrt{(j - 1)^2 + \frac{8C_A \alpha_s}{\pi}} - (j - 1) \right]$$

$$= \sqrt{\frac{C_A \alpha_s}{2\pi}} - \frac{1}{4}(j-1) + \frac{1}{32}\sqrt{\frac{2\pi}{C_A \alpha_s}}(j-1)^2 + \dots \quad (6.30)$$

Thus for  $j \rightarrow 1$  the gluon-gluon anomalous dimension is proportional to the square root of  $\alpha_s$ . How can this behaviour emerge from perturbation theory, which deals only in integer powers of  $\alpha_s$ ? The answer is that at any fixed  $j \neq 1$  we can expand Eq. (6.30) in a different way for sufficiently small  $\alpha_s$ :

$$\gamma_{gg}(j, \alpha_s) = \frac{C_A \alpha_s}{\pi} \frac{1}{(j-1)} - 2 \left( \frac{C_A \alpha_s}{\pi} \right)^2 \frac{1}{(j-1)^3} + \dots \quad (6.31)$$

This series displays the terms that are most singular as  $j \rightarrow 1$  in each order. The first term, for example, corresponds to the fact that

$$\gamma_{gg}(j, \alpha_s) = \frac{\alpha_s}{2\pi} \gamma_{gg}^{(0)}(j) + O(\alpha_s^2), \quad (6.32)$$

where we see from Eq. (4.129) that

$$\gamma_{gg}^{(0)}(j) = \frac{2C_A}{j-1} + \dots, \quad (6.33)$$

the dots representing terms that are not singular as  $j \rightarrow 1$ . The terms displayed in Eq. (6.31) just correspond to the Mellin transform of the small- $x$  behaviour of the gluon splitting function  $P_{gg}(x)$  given in Eq. (6.22). The most singular terms as  $j \rightarrow 1$  ( $x \rightarrow 0$ ) have been *resummed* in the expression (6.30), allowing the perturbation series to be analytically continued outside its circle of convergence  $|\alpha_s| < (\pi/8C_A)|j-1|^2$ . By definition, the behaviour outside this circle (in particular, at  $j=1$ ) cannot be represented by the series Eq. (6.31) any more, even though it is fully implied by it.

At sufficiently small  $x$ , the  $j \rightarrow 1$  singularity of the gluon-gluon anomalous dimension dominates in all fragmentation functions, and this in turn determines the asymptotic behaviour of their first moments, *i.e.* of average multiplicities. To predict this behaviour quantitatively we need to take account of the running of  $\alpha_s$ , which can be done in the same way as for the other moments. Writing Eq. (6.27) in the form

$$\tilde{D}(j, t) \sim \exp \left[ \int^t \gamma_{gg}(j, \alpha_s) \frac{dt'}{t'} \right], \quad (6.34)$$

we have only to replace  $\gamma_{gg}(j, \alpha_s)$  in the integrand by  $\gamma_{gg}(j, \alpha_s(t'))$ . We then use Eq. (2.5)

$$\int^t \gamma_{gg}(j, \alpha_s(t')) \frac{dt'}{t'} = \int^{\alpha_s(t)} \frac{\gamma_{gg}(j, \alpha_s)}{\beta(\alpha_s)} d\alpha_s, \quad (6.35)$$

where  $\beta(\alpha_s) = -b\alpha_s^2 + \dots$ , to find

$$\begin{aligned}\tilde{D}(j, t) &\sim \exp \left[ \frac{1}{b} \sqrt{\frac{2C_A}{\pi\alpha_s}} - \frac{1}{4b\alpha_s}(j-1) \right. \\ &+ \left. \frac{1}{48b} \sqrt{\frac{2\pi}{C_A\alpha_s^3}} (j-1)^2 + \dots \right]_{\alpha_s=\alpha_s(t)}.\end{aligned}\quad (6.36)$$

In  $e^+e^-$  annihilation the scale  $t$  (the upper limit on  $E^2(1 - \cos\theta)$  for any branching) is of the order of the centre-of-mass energy-squared  $s$ , and so the average multiplicity of any hadron species has the asymptotic behaviour

$$\langle n(s) \rangle = D(1, s) \propto \exp \frac{1}{b} \sqrt{\frac{6}{\pi\alpha_s(s)}} \sim \exp \sqrt{\frac{6}{\pi b} \ln \left( \frac{s}{\Lambda^2} \right)}. \quad (6.37)$$

If the next-to-leading singularities of the anomalous dimensions, *i.e.* the terms with one less power of  $1/(j-1)$ , are also resummed, the expression (6.37) is multiplied by a power of  $\alpha_s(s)$  [7]:

$$\langle n(s) \rangle \propto \exp \left[ \frac{1}{b} \sqrt{\frac{6}{\pi\alpha_s(s)}} + \left( \frac{1}{4} + \frac{5n_f}{54\pi b} \right) \ln \alpha_s(s) \right]. \quad (6.38)$$

The resulting prediction, shown by the curve in the upper part of Fig. 6.2, is in very good agreement with experiment. In this comparison there are two free parameters: the constant of proportionality in Eq. (6.38) and the scale parameter  $\Lambda_{\text{mult}}$  in  $\alpha_s(s)$ .  $\Lambda_{\text{mult}}$  is not necessarily equal to  $\Lambda_{\overline{\text{MS}}}$ , because the renormalization scheme dependence of  $\langle n(s) \rangle$  only appears at next-to-next-to-leading order, and corrections to Eq. (6.38) of this order have not yet been calculated. In fact, however, the value used in Fig. 6.2,  $\Lambda_{\text{mult}} = 226$  MeV, corresponding to  $\alpha_s(M_Z^2) = 0.118$ , is rather close to  $\Lambda_{\overline{\text{MS}}}$ , indicating that further higher-order corrections should be small.

We postpone discussion of the second multiplicity moment, shown in the lower part of Fig. 6.2, until Section 6.3.

### 6.1.3 Small- $x$ fragmentation

The behaviour of  $\tilde{D}(j, s)$  away from  $j = 1$  determines the form of small- $x$  fragmentation functions via the inverse Mellin transformation (6.9). Keeping the first three terms in the Taylor expansion of the exponent, as displayed in Eq. (6.36), gives a simple Gaussian function of  $j$  which transforms into a Gaussian in the variable  $\xi \equiv \ln(1/x)$ :

$$xD(x, s) \propto \exp \left[ -\frac{1}{2\sigma^2} (\xi - \xi_p)^2 \right], \quad (6.39)$$

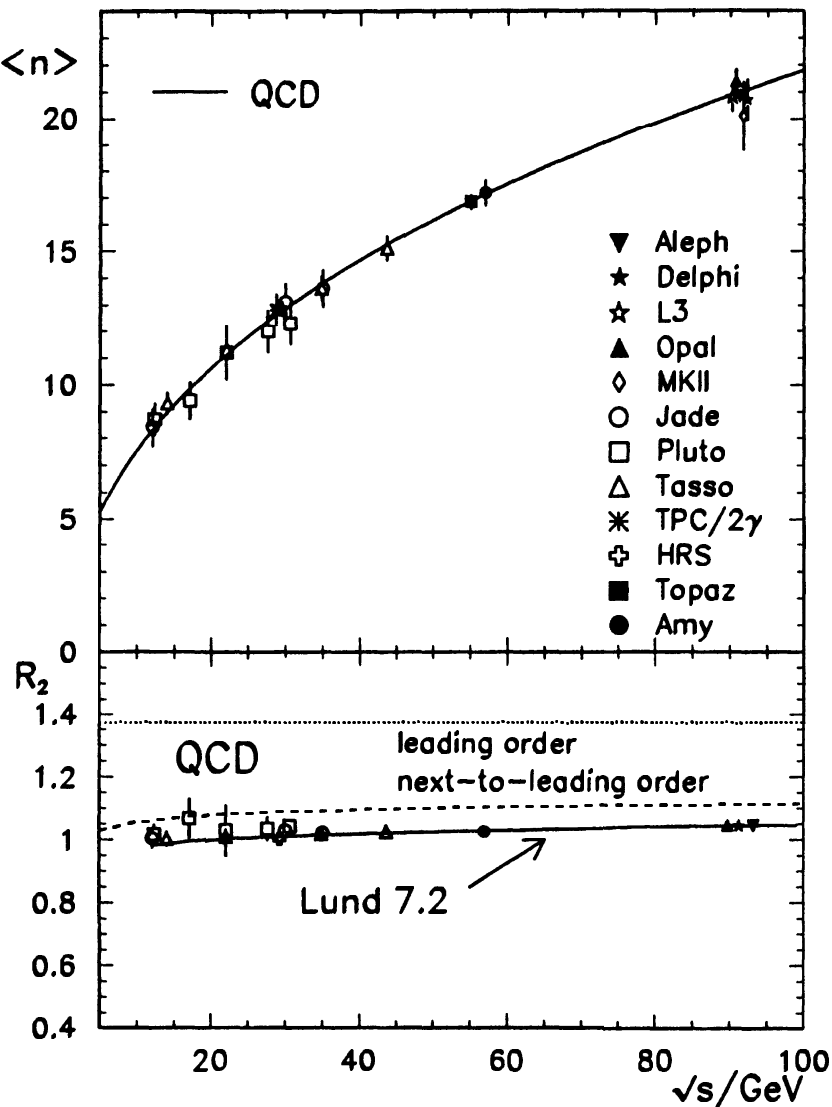


Fig. 6.2. Mean and second moment of charged hadron multiplicity in  $e^+e^-$  annihilation. Figure from ref. [8].

where the peak position is

$$\xi_p = \frac{1}{4b\alpha_S(s)} \simeq \frac{1}{4} \ln \left( \frac{s}{\Lambda^2} \right) \quad (6.40)$$

and the width of the distribution of  $\xi$  is

$$\sigma = \left( \frac{1}{24b} \sqrt{\frac{2\pi}{C_A \alpha_S^3(s)}} \right)^{\frac{1}{2}} \propto \left[ \ln \left( \frac{s}{\Lambda^2} \right) \right]^{\frac{3}{4}}. \quad (6.41)$$

Again, one can compute next-to-leading corrections to these predictions. In the method of ref. [9], the corrections are included in an analytical form known as the ‘modified leading logarithmic approximation’ (MLLA), while in ref. [10] they are used to compute the higher moment corrections to the Gaussian form (6.39). The results of the two calculations are

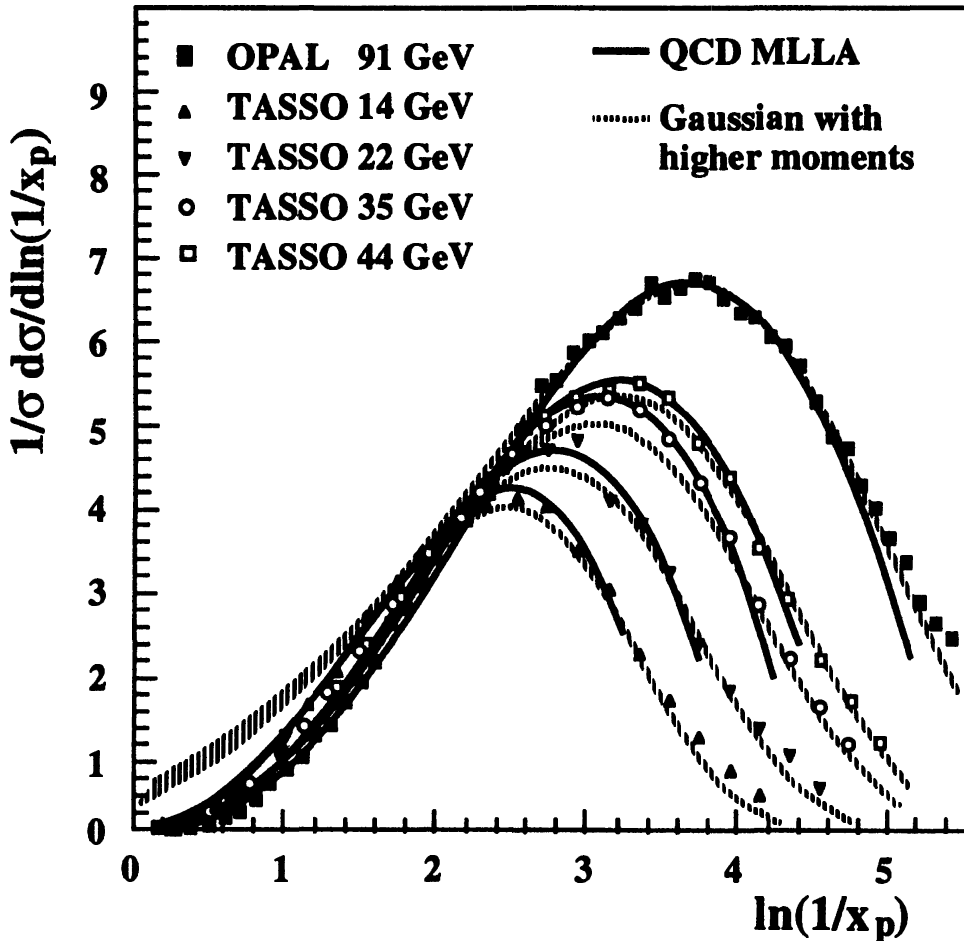


Fig. 6.3. Distribution of  $\xi = \ln(1/x)$  in  $e^+e^-$  annihilation, with data from refs. [11,12]. Figure from ref. [12].

shown by the solid and broken sets of curves, respectively, in Fig. 6.3. At small  $x$  (large  $\xi$ ), where they should be valid, both calculations agree well with the form and energy dependence of the measured fragmentation functions. The MLLA calculation includes some terms that become important at large  $x$  (small  $\xi$ ) and therefore agrees with the data in that region as well. As in the case of the average multiplicity, the parameter  $\Lambda$  in Eqs. (6.40) and (6.41) should be treated as a free parameter, because the renormalization scheme sensitivity is beyond the accuracy of the present calculations. In the fits shown in Fig. 6.3, the values of  $\Lambda$  are  $253 \pm 30$  MeV for the MLLA and  $255 \pm 26$  MeV for the modified Gaussian parametrization respectively.

The predicted energy dependence (6.40) of the peak in the  $\xi$  distribution is a striking illustration of soft gluon coherence, which is the origin of the suppression of hadron production at small  $x$ . Of course, a decrease at very small  $x$  is expected on purely kinematical grounds, but this would occur at particle energies proportional to their masses, *i.e.* at  $x \propto m/\sqrt{s}$

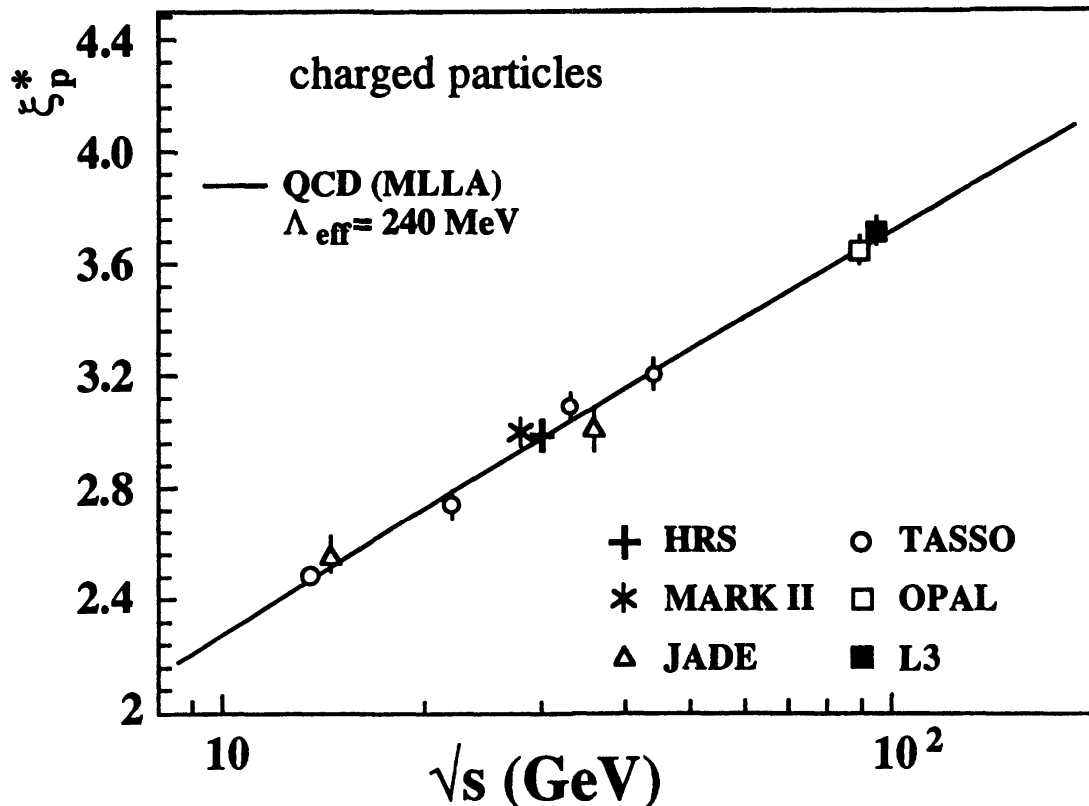


Fig. 6.4. Position of the peak in the  $\xi$ -distribution. Figure from ref. [13].

and hence  $\xi \sim \frac{1}{2} \ln s$ . Thus if the suppression were purely kinematic the peak position  $\xi_p$  would vary twice as rapidly with energy, which is ruled out by the data (see Fig. 6.4).

#### 6.1.4 Longitudinal fragmentation

The ALEPH [5] and OPAL [14] collaborations at LEP have presented results of analyses of the longitudinal fragmentation function in  $e^+e^-$  annihilation. This is defined in terms of the joint distribution in the energy fraction  $x$  and the angle  $\theta$  between the observed hadron and the incoming electron beam [4]:

$$\frac{1}{\sigma_{\text{tot}}} \frac{d^2\sigma}{dx d\cos\theta} = \frac{3}{8} (1 + \cos^2\theta) F_T(x) + \frac{3}{4} \sin^2\theta F_L(x) + \frac{3}{4} \cos\theta F_A(x), \quad (6.42)$$

where  $F_T$ ,  $F_L$  and  $F_A$  are respectively the transverse, longitudinal and asymmetric fragmentation functions.<sup>3</sup> As their names imply,  $F_T$  and  $F_L$  represent the contributions from virtual bosons polarized transversely or longitudinally with respect to the direction of motion of the hadron  $h$ .

<sup>3</sup> All these functions also depend on the c.m. energy  $\sqrt{s}$ , which we take to be fixed here.

$F_A$  is a parity-violating contribution which comes from the interference between the  $Z^0$  and photon contributions. Integrating over all angles, we obtain the total fragmentation function,  $F = F_T + F_L$ . Each of these functions can be represented as a convolution of the parton fragmentation functions  $D_i$  with appropriate coefficient functions  $C_i^{T,L,A}$  as in Eq. (6.4). The transverse and longitudinal coefficient functions are [2,15]

$$\begin{aligned} C_q^T(z) &= \delta(1-z) + O(\alpha_s) \\ C_g^T(z) &= O(\alpha_s) \\ C_q^L(z) &= C_F \frac{\alpha_s}{2\pi} + O(\alpha_s^2) \\ C_g^L(z) &= 4C_F \frac{\alpha_s}{2\pi} \left( \frac{1}{z} - 1 \right) + O(\alpha_s^2), \end{aligned} \quad (6.43)$$

which implies that

$$F_L(x) = C_F \frac{\alpha_s}{2\pi} \int_x^1 \frac{dz}{z} \left[ F_T(z) + 4 \left( \frac{z}{x} - 1 \right) D_g(z) \right] + O(\alpha_s^2). \quad (6.44)$$

Thus the gluon fragmentation function  $D_g$  can be extracted to leading order from measurements of  $F_T$  and  $F_L$ .

Fig. 6.5 shows the OPAL data [14] on the transverse and longitudinal fragmentation functions for charged particles. Note from Eq. (6.44) that  $F_L$  is  $O(\alpha_s)$  relative to  $F_T$ ; it also falls more steeply with  $x$ . Therefore even with LEP statistics the errors are large for  $x > 0.3$ . However, one still obtains useful information on the gluon fragmentation function over the full range of  $x$ , as shown in Fig. 6.6. Because the relation (6.44) is known only to leading order, there is an ambiguity about the energy scale at which  $D_g$  is measured. Since the gluon contribution comes from three-jet events, one might expect the appropriate scale to be about one third of the centre-of-mass energy. Comparisons with JETSET Monte Carlo predictions at scales straddling this value are shown. In Section 6.4 we shall discuss data on gluon jet fragmentation obtained more directly from three-jet events.

Similar results on the longitudinal fragmentation function have been obtained by the ALEPH collaboration [5], who include this information as a constraint on the gluon fragmentation function in their fit to scaling violation shown in Fig. 6.1.

Summed over all particle types, the total fragmentation function satisfies the energy sum rule (6.3), which we may write as

$$\frac{1}{2} \int_0^1 dx x F(x) = 1. \quad (6.45)$$

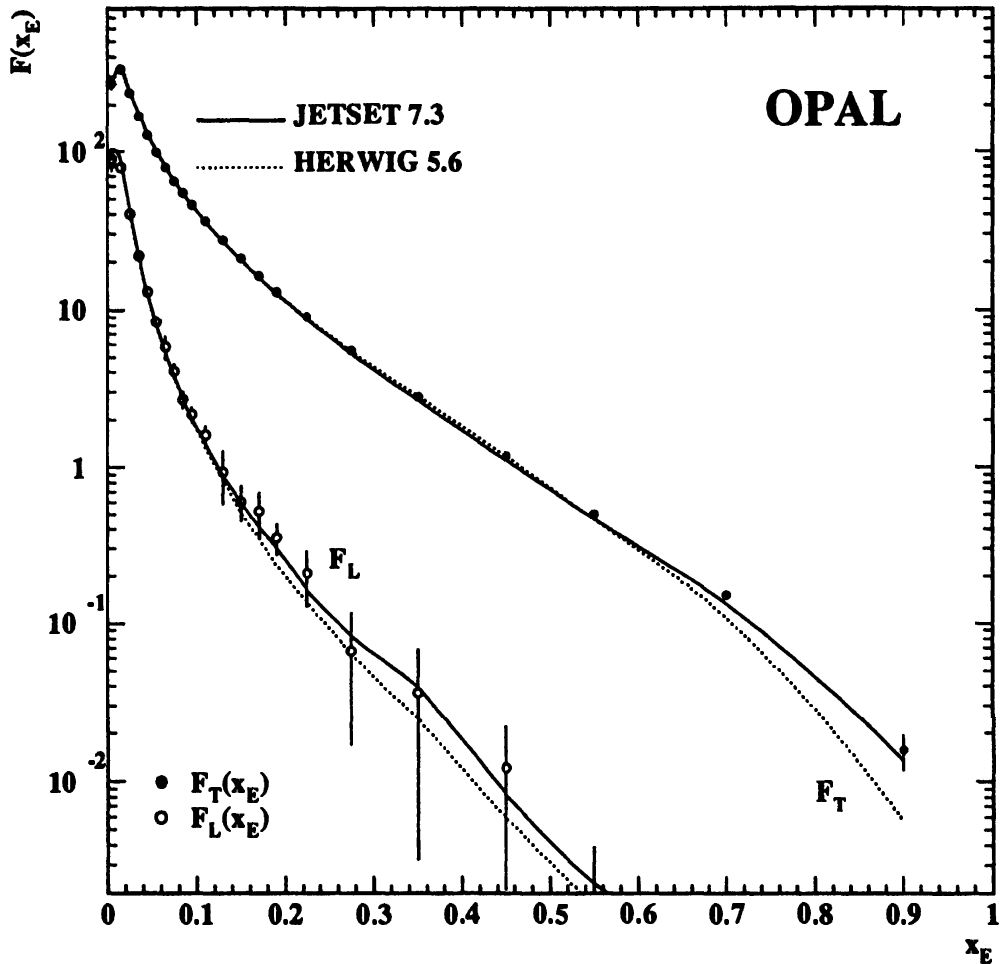


Fig. 6.5. Transverse and longitudinal fragmentation functions in  $Z^0 \rightarrow \text{hadrons}$ . Figure from ref. [14].

Similarly the integrals

$$\frac{1}{2} \int_0^1 dx x F_{T,L}(x) \equiv \frac{\sigma_{T,L}}{\sigma_{\text{tot}}} \quad (6.46)$$

give the transverse and longitudinal fractions of the total cross section. The perturbative prediction is [16]

$$\begin{aligned} \frac{\sigma_L}{\sigma_{\text{tot}}} &= \frac{\alpha_s}{\pi} + \left( \frac{601}{40} - \frac{6}{5}\zeta(3) - \frac{37}{36}n_f \right) \left( \frac{\alpha_s}{\pi} \right)^2 + O(\alpha_s^3) \\ &\simeq \frac{\alpha_s}{\pi} + (13.583 - 1.028n_f) \left( \frac{\alpha_s}{\pi} \right)^2 \end{aligned} \quad (6.47)$$

where the  $\zeta$  function is given in Eq. (3.19). Comparing with Eq. (3.17), we see that the whole of the  $O(\alpha_s)$  correction to  $\sigma_{\text{tot}}$  comes from the longitudinal part, while the  $O(\alpha_s^2)$  correction receives both longitudinal and transverse contributions.

The OPAL data point for  $\sigma_L/\sigma_{\text{tot}}$  is shown, together with the per-

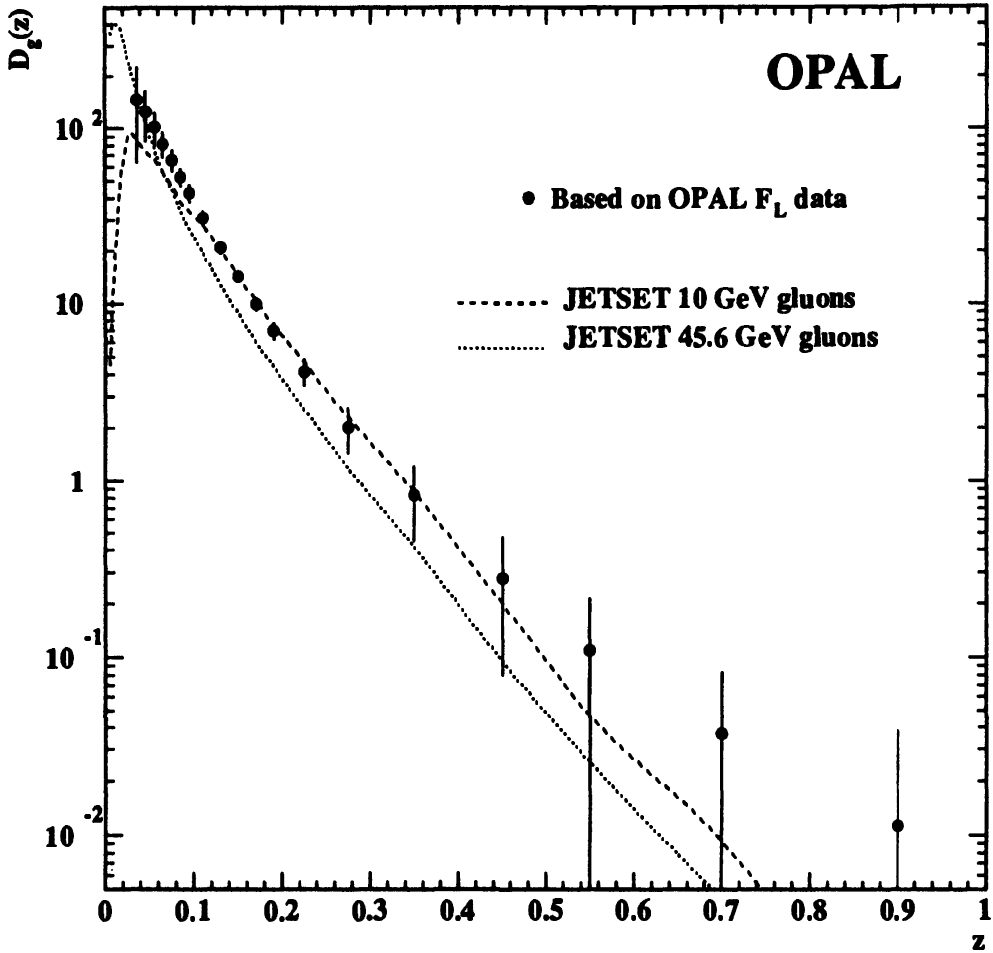


Fig. 6.6. Gluon fragmentation function extracted from  $F_{T,L}$ . Figure from ref. [14].

turbative predictions, in Fig. 6.7. The data lie somewhat above the next-to-leading-order prediction (dashed), which suggests that higher-order and/or non-perturbative corrections are significant. An estimate of the latter is provided by the difference between the JETSET Monte Carlo hadron-level prediction (dot-dashed) and the perturbative result. This difference shows a clear  $1/Q$  behaviour, with a coefficient of about 1 GeV, illustrating once again the characteristic energy dependence of hadronization effects.

In fact, using the simple ‘tube’ model of hadronization discussed in Section 5.6, the correction to the longitudinal cross is found to be

$$\left\langle \frac{\delta\sigma_L}{\sigma_{\text{tot}}} \right\rangle_{\text{had}} = \frac{\pi\lambda}{2Q} \simeq \frac{0.8 \text{ GeV}}{Q}, \quad (6.48)$$

Adding this to the next-to-leading-order prediction gives the solid curve in Fig. 6.7, which agrees well with the JETSET prediction. The correction arises from mixing between the transverse and longitudinal angular dependences in Eq. (6.42) due to hadronization. The transverse cross

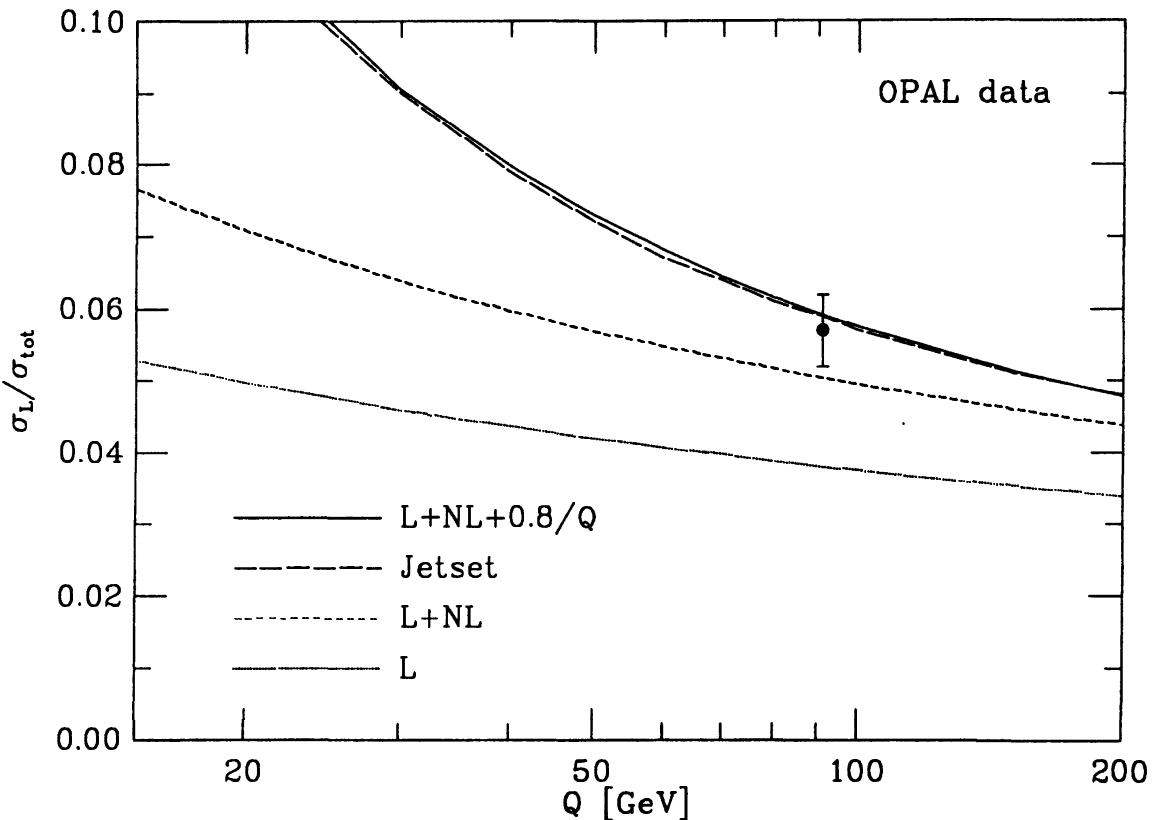


Fig. 6.7. Longitudinal fraction of the  $e^+e^-$  hadronic cross section.

section receives an equal and opposite correction, and so there is no  $1/Q$  term in the total cross section.

### 6.1.5 Fragmentation in deep inelastic scattering

Jet physics in  $ep$  collisions promises to be a rich field of study for the new HERA collider at DESY. One can, for example, compare the properties of jets in  $e^+e^-$  and  $ep$  collisions, which is a good test of the factorizability of jet fragmentation functions discussed above.

The most direct comparison is between one hemisphere of an  $e^+e^-$  event, defined with respect to the thrust axis, and the ‘current jet hemisphere’ of deep inelastic scattering in the Breit frame [17,18]. The Breit frame is the one in which the momentum transfer from the lepton,  $q^\mu$ , has only a  $z$ -component:  $q^\mu = (0, 0, 0, Q)$ . In the parton model, in this frame the struck quark enters from the right with  $z$ -momentum  $p_z = -\frac{1}{2}Q$  and sees the exchanged virtual boson as a ‘brick wall’, from which it simply rebounds with  $p_z = +\frac{1}{2}Q$ . Thus the right-hand hemisphere of the final state should look like one hemisphere of an  $e^+e^-$  annihilation event at  $E_{cm} = Q$ . The left-hand (‘beam jet’) hemisphere, on the other hand, is different from  $e^+e^-$  because it contains the proton remnant, moving with momentum  $p_z = -(1-x)Q/2x$  in this frame.

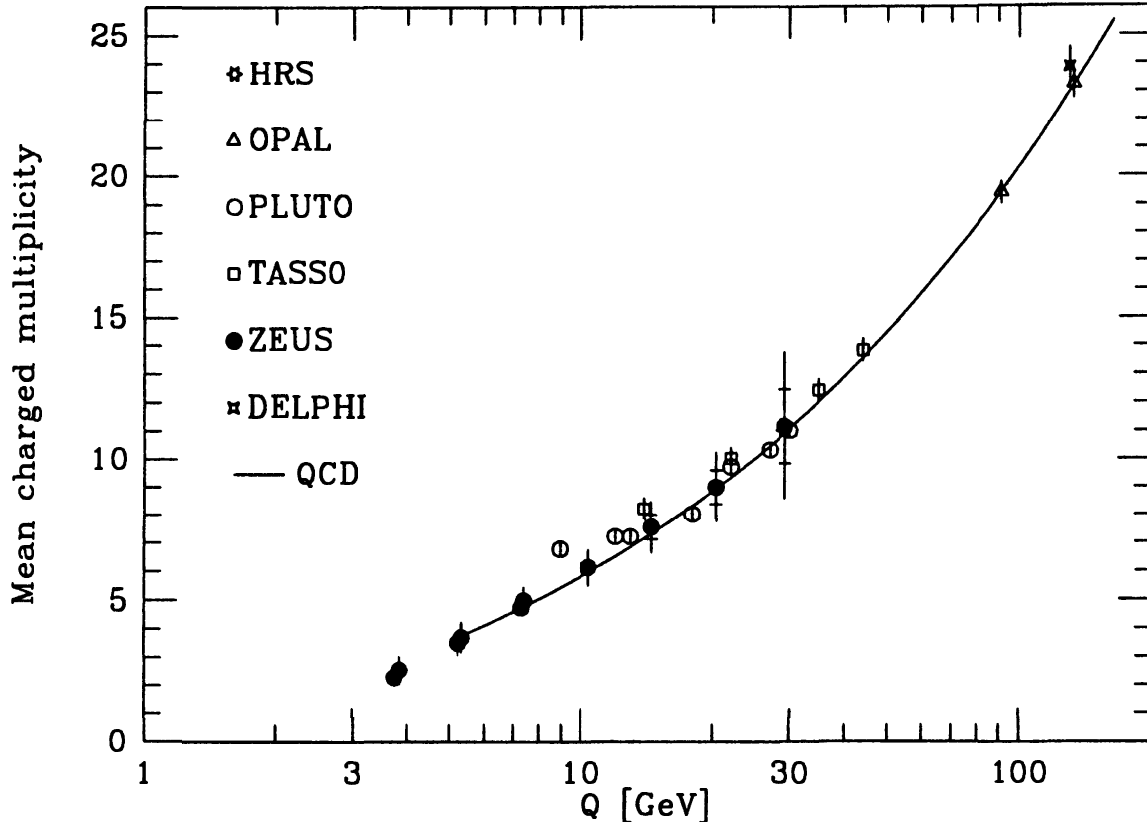


Fig. 6.8. Mean charged multiplicity in  $e^+e^-$  and  $ep$  current jet fragmentation. Adapted from ref. [19].

Fig. 6.8 shows the results of such a comparison by the ZEUS collaboration [19], in this case comparing twice the charged multiplicity in the Breit frame current hemisphere with that observed in  $e^+e^-$  annihilation (corrected for  $K_S$  and  $\Lambda^0$  decays and therefore differing slightly from Fig. 6.2). The  $e^+e^-$  results are shown by the open symbols. We see that the  $e^+e^-$  and  $ep$  data are consistent. On a more detailed level, one would expect small differences, due to the different mixtures of quark flavours and higher-order corrections in the two processes. The curve shows Eq. (6.38), this time with scale parameter  $\Lambda_{\text{mult}} = 1 \text{ GeV}$ , corresponding to the slightly more rapid increase in the  $ep$  data at low scales.

A more elaborate comparison is shown in Fig. 6.9. Here the position of the peak in the distribution of  $\ln(1/x_p)$ , where  $x_p = 2p/Q$  in the Breit frame, is compared with that found in  $e^+e^-$  annihilation (Fig. 6.4). We see again that the HERA data exhibit the same  $Q$ -dependence as the  $e^+e^-$  data, in remarkable agreement with the theoretical predictions.

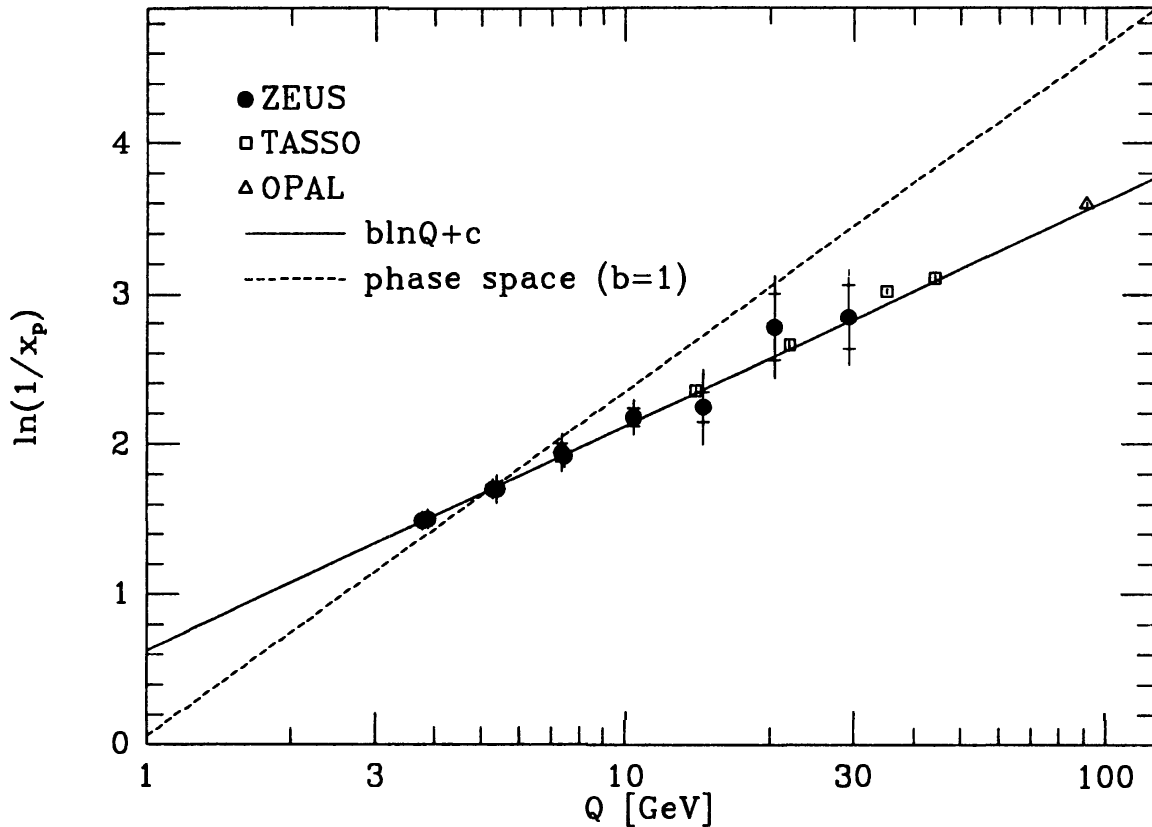


Fig. 6.9. Position of the peak in  $\ln(1/x_p)$  in  $e^+e^-$  and  $ep$  current jet fragmentation. Adapted from ref. [19].

## 6.2 Generating function method

A useful calculational technique based on the parton branching formalism involves the use of *generating functions* or, more powerfully, *generating functionals* [9,18]. We concentrate here on the former, which are mathematically simpler. Let  $P_p(n)$  represent the probability of finding  $n$  objects of a particular type in the final state of a given process  $p$ , where for example the objects could be charged hadrons and the process could be  $e^+e^-$  annihilation at a given centre-of-mass energy. Alternatively, the objects could be jets, defined by a given jet algorithm with a certain resolution  $y_{\text{cut}}$ , see Section 3.3. The corresponding generating function is defined as

$$\phi_p(u) = \sum_{n=0}^{\infty} u^n P_p(n) . \quad (6.49)$$

We can recover the probability distribution  $P_p(n)$  itself by successive differentiation at  $u = 0$ :

$$P_p(n) = \frac{1}{n!} \left. \frac{d^n \phi_p}{du^n} \right|_{u=0} . \quad (6.50)$$

On the other hand the *binomial moments* of the distribution are obtained by differentiating at  $u = 1$

$$\begin{aligned}\langle n \rangle_p &= \sum_{n=0}^{\infty} n P_p(n) = \left. \frac{d\phi_p}{du} \right|_{u=1} \\ \langle n(n-1)\dots(n-k+1) \rangle_p &= \left. \frac{d^k \phi_p}{du^k} \right|_{u=1}.\end{aligned}\quad (6.51)$$

Consider specifically the case of  $e^+e^-$  annihilation. To leading order the final state is quark-antiquark and therefore the generating function is simply

$$\phi_{e^+e^-}(u) = \phi_q(u)\phi_{\bar{q}}(u) \quad (6.52)$$

where  $\phi_q$  ( $\phi_{\bar{q}}$ ) represents the generating function for the fragmentation of a quark (antiquark) into objects of the required type. In general there should be a sum over flavours on the right-hand side, with appropriate relative probabilities, but we shall assume flavour independence, which is a reasonable first approximation when the detected objects are charged particles or jets. In these cases the objects also form a charge-conjugation invariant set, and so  $\phi_q = \phi_{\bar{q}}$ . Then Eq. (6.52) becomes simply

$$\phi_{e^+e^-}(u) = [\phi_q(u)]^2. \quad (6.53)$$

Now we derive an equation for  $\phi_q$ , the generating function for quark fragmentation. This will depend on the scale of the hard process in which the jet is produced, which in  $e^+e^-$  annihilation is the centre-of-mass energy squared,  $s$ . As discussed in Section 5.5, to take account of coherence in jet evolution we use the scale variable  $\tilde{t}$  defined by Eqs. (5.93) and (5.97), which we denote in what follows by  $t$ . Thus we write Eq. (6.53) as

$$\phi_{e^+e^-}(u, s) = [\phi_q(u, t)]_{t=s}^2. \quad (6.54)$$

The scale dependence of the generating function may be found using the parton branching formalism of Chapter 5. When a parton of type  $a$  branches into  $b$  and  $c$ , the generating function  $\phi_a$  is replaced by  $\phi_b\phi_c$ . Following the steps that led to Eq. (5.49) for the parton distribution, and taking coherence into account according to Eqs. (5.98) and (5.100), we obtain

$$\begin{aligned}\phi_q(u, t) &= \phi_q(u, t_0)\Delta_q(t) + \int_{t_0}^t \frac{dt'}{t'} \frac{\Delta_q(t)}{\Delta_q(t')} \int dz \frac{\alpha_s(z^2(1-z)^2t')}{2\pi} \\ &\quad \times \hat{P}_{qq}(z)\phi_q(u, z^2t')\phi_q(u, (1-z)^2t').\end{aligned}\quad (6.55)$$

This equation is valid in the next-to-leading logarithmic approximation, that is, it takes account of the double logarithmic singularities generated by collinear soft gluon emission to all orders, and also the terms with

one less logarithm due to emission that is collinear but not soft. In this approximation we can simplify the integrand considerably. The  $q \rightarrow q$  splitting function is

$$\hat{P}_{qq}(z) = C_F \frac{1+z^2}{1-z} = C_F \left( \frac{2}{1-z} - 1 - z \right) \simeq C_F \left( \frac{2}{1-z} - \frac{3}{2} \right), \quad (6.56)$$

where in the last expression we have replaced the non-singular part by its average with respect to  $z$ , since all the other terms in the integrand depend on  $z$  only logarithmically. For the same reason we may replace  $z$  by 1 in all the argument factors except for  $(1-z)$  in the singular part. Writing  $(1-z)^2 t' = t''$ , Eq. (6.55) becomes

$$\begin{aligned} \phi_q(u, t) &= \phi_q(u, t_0) \Delta_q(t) + \frac{C_F}{2\pi} \int_{t_0}^t \frac{dt'}{t'} \frac{\Delta_q(t)}{\Delta_q(t')} \phi_q(u, t') \\ &\quad \times \left[ \int_{t_0}^{t'} \frac{dt''}{t''} \alpha_s(t'') \phi_q(u, t'') - \frac{3}{4} \alpha_s(t') \phi_q(u, t') \right], \end{aligned} \quad (6.57)$$

which has the solution

$$\phi_q(u, t) = \phi_q(u, t_0) \Delta_q(t) \exp \left[ \int_{t_0}^t dt' \Gamma_q(t, t') \phi_g(u, t') \right] \quad (6.58)$$

where

$$\Gamma_q(t, t') = \frac{C_F}{2\pi} \frac{\alpha_s(t')}{t'} \left( \ln \frac{t}{t'} - \frac{3}{2} \right). \quad (6.59)$$

Note that the Sudakov form factor (5.101) may be written in terms of the branching function (6.59) as

$$\Delta_q(t) = \exp \left[ - \int_{t_0}^t dt' \Gamma_q(t, t') \right]. \quad (6.60)$$

Thus Eq. (6.58) satisfies the unitarity constraint  $\phi_q(1, t) = \phi_g(1, t) = 1$ , which follows from the definition (6.49).

The solution (6.58) is expressed in terms of the gluon jet generating function  $\phi_g$ , which satisfies a branching equation analogous to (6.55). Making the same next-to-leading logarithmic approximations that led to Eq. (6.57), we obtain

$$\begin{aligned} \phi_g(u, t) &= \phi_g(u, t_0) \Delta_g(t) + \int_{t_0}^t \frac{dt'}{t'} \frac{\Delta_g(t)}{\Delta_g(t')} \left\{ \phi_g(u, t') \right. \\ &\quad \times \frac{C_A}{2\pi} \left[ \int_{t_0}^{t'} \frac{dt''}{t''} \alpha_s(t'') \phi_g(u, t'') - \frac{11}{6} \alpha_s(t') \phi_g(u, t') \right] \\ &\quad \left. + \frac{n_f}{6\pi} \alpha_s(t') [\phi_g(u, t')]^2 \right\}, \end{aligned} \quad (6.61)$$

where the last term on the right-hand side comes from the splitting  $g \rightarrow q\bar{q}$ . Introducing the functions

$$\begin{aligned}\Gamma_g(t, t') &= \frac{C_A}{2\pi} \frac{\alpha_s(t')}{t'} \left( \ln \frac{t}{t'} - \frac{11}{6} \right) \\ \Gamma_f(t') &= \frac{n_f}{6\pi} \frac{\alpha_s(t')}{t'} ,\end{aligned}\quad (6.62)$$

we may write this in a form similar to Eq. (6.58):

$$\begin{aligned}\phi_g(u, t) &= \phi_g(u, t_0) \Delta_g(t) \exp \left[ \int_{t_0}^t dt' \{ \Gamma_g(t, t') \phi_g(u, t') \right. \\ &\quad \left. + \Gamma_f(t') [\phi_q(u, t')]^2 / \phi_g(u, t') \} \right] \quad (6.63)\end{aligned}$$

where

$$\Delta_g(t) = \exp \left[ - \int_{t_0}^t dt' \{ \Gamma_g(t, t') + \Gamma_f(t') \} \right]. \quad (6.64)$$

In the following sections we shall use these results to calculate properties of the multiplicity distributions of hadrons and sub-jets within jets.

### 6.3 Multiplicity distributions

In principle we can compute the energy scale dependence of the cross section for any fixed multiplicity  $n$  from the generating function equations (6.58) and (6.63). Consider, for example, the probability of producing no objects of the prescribed type (for example, no charged particles, only neutrals) in  $e^+e^-$  annihilation at c.m. energy  $\sqrt{s}$ . This is given by

$$\begin{aligned}P_{e^+e^-}(0, s) &= \phi_{e^+e^-}(0, s) = [\phi_q(0, s)]^2 \\ &= P_{e^+e^-}(0, t_0) [\Delta_q(s)]^2 \exp \left[ 2 \int_{t_0}^s dt \Gamma_q(s, t) \phi_g(0, t) \right], \quad (6.65)\end{aligned}$$

where  $\phi_g(0, t)$  is to be obtained by solving the implicit equation (6.63). We can see that it must behave roughly like  $\Delta_g(t)$ , which vanishes faster than any inverse power at large  $t$ . Therefore the exponent in Eq. (6.65) is asymptotically negligible and we find at high energy

$$P_{e^+e^-}(0, s) \sim P_{e^+e^-}(0, t_0) [\Delta_q(s)]^2 \quad (6.66)$$

which again vanishes faster than any power of  $s$ . In general the cross section for any fixed multiplicity may rise at low energy but must eventually become dominated by the Sudakov factor and decrease rapidly.

Another application of the generating function method is the calculation of multiplicity moments according to Eq. (6.51). For brevity, we

introduce the following notation for the mean and first binomial moment in process  $p$ :

$$\begin{aligned}\langle n \rangle_p &\equiv N_p \\ \langle n(n-1) \rangle_p &\equiv M_p.\end{aligned}\quad (6.67)$$

Eq. (6.53) is valid to next-to-leading logarithmic accuracy, and so to this precision the  $e^+e^-$  moments are related to those of a quark jet as follows:

$$\begin{aligned}N_{e^+e^-} &= 2N_q \\ M_{e^+e^-} &= 2(M_q + N_q^2).\end{aligned}\quad (6.68)$$

We check first that the average multiplicity is consistent with that obtained in Section 6.1.2. From Eqs. (6.58) and (6.63) we obtain the coupled integral equations

$$\begin{aligned}N_q(t) &= N_q(t_0) + \int_{t_0}^t dt' \Gamma_q(t, t') N_g(t') \\ N_g(t) &= N_g(t_0) + \int_{t_0}^t dt' \left\{ \Gamma_g(t, t') N_g(t') \right. \\ &\quad \left. + \Gamma_f(t')[2N_q(t') - N_g(t')] \right\}.\end{aligned}\quad (6.69)$$

By successive differentiation with respect to  $t$  we find

$$\begin{aligned}t \frac{d}{dt} \left( t \frac{dN_q}{dt} \right) &= \frac{C_F}{2\pi} \alpha_s(t) \left( N_g - \frac{3}{2} t \frac{dN_g}{dt} \right) \\ t \frac{d}{dt} \left( t \frac{dN_g}{dt} \right) &= \frac{C_A}{2\pi} \alpha_s(t) \left( N_g - \frac{11}{6} t \frac{dN_g}{dt} \right) \\ &\quad + \frac{n_f}{6\pi} \alpha_s(t) t \frac{d}{dt} (2N_q - N_g).\end{aligned}\quad (6.70)$$

The asymptotic behaviour is dominated by the first term on the right-hand side in each of these equations, which gives

$$N_q(t) \sim \frac{C_F}{C_A} N_g(t) \propto \exp \frac{1}{b} \sqrt{\frac{2C_A}{\pi \alpha_s(t)}}, \quad (6.71)$$

in agreement with Eq. (6.37).

Now we turn to the calculation of the second moment. By differentiating Eqs. (6.58) and (6.63) twice at  $u = 1$  we obtain

$$\begin{aligned}M_q(t) &= M_q(t_0) - [N_q(t_0)]^2 + [N_q(t)]^2 + \int_{t_0}^t dt' \Gamma_q(t, t') M_g(t') \\ M_g(t) &= M_g(t_0) - [N_g(t_0)]^2 + [N_g(t)]^2 + \int_{t_0}^t dt' \left\{ \Gamma_g(t, t') M_g(t') \right. \\ &\quad \left. + \Gamma_f(t')[2M_q(t') - M_g(t') + 2\{N_g(t') - N_q(t')\}^2] \right\}.\end{aligned}\quad (6.72)$$

Again retaining only the dominant term on the right-hand side, we see that  $M_{q,g}$  should be asymptotically proportional to  $N_g^2$ . Substituting this form and using Eq. (6.71), we find

$$M_q \sim \left(1 + \frac{C_F}{3C_A}\right) N_q^2, \quad M_g \sim \frac{4}{3} N_g^2. \quad (6.73)$$

A quantity that is convenient experimentally is the relative size of the second multiplicity moment, measured by the ratio

$$R_{2,p} \equiv \frac{\langle n(n-1) \rangle_p}{\langle n \rangle_p^2} = \frac{M_p}{N_p^2}. \quad (6.74)$$

From Eqs. (6.68) and (6.73), we obtain the prediction

$$R_{2,e^+e^-} = \frac{M_q + N_q^2}{2N_q^2} \sim 1 + \frac{C_A}{6C_F} = \frac{11}{8}. \quad (6.75)$$

Eq. (6.75) implies that asymptotically the width of the multiplicity distribution should grow in proportion to its mean value, which is qualitatively in agreement with experiment. Similarly, the higher moments  $\langle n^k \rangle$  are predicted to grow like  $\langle n \rangle^k$ . This means that the asymptotic multiplicity distribution can be represented by a scale-invariant function of  $n/\langle n \rangle$ ,

$$P(n) \sim \frac{1}{\langle n \rangle} \Psi\left(\frac{n}{\langle n \rangle}\right), \quad (6.76)$$

a property known as Koba-Nielsen-Olesen (KNO) scaling [20].

In quantitative terms, the asymptotic QCD prediction of the form of the KNO function  $\Psi$  is rather different from that observed experimentally. For example, the measured value of  $R_2$  for charged particles in  $e^+e^-$  annihilation is about 1 instead of 11/8. The next-to-leading correction to Eq. (6.75) is in fact of order  $\sqrt{\alpha_s}$  with a negative coefficient [21]

$$\begin{aligned} R_{2,e^+e^-} &\sim 1 + \frac{C_A}{6C_F} - \left[ \frac{55}{108} \frac{C_A}{C_F} + \left(1 - 6 \frac{C_F}{C_A}\right) \frac{n_f}{54C_A} \right] \sqrt{\frac{C_A \alpha_s}{2\pi}} \\ &= \frac{11}{8} (1 - 0.55\sqrt{\alpha_s}). \end{aligned} \quad (6.77)$$

As shown in the lower plot of Fig. 6.2, the effect of the next-to-leading correction (6.77) is to bring the prediction for  $R_{2,e^+e^-}$  much closer to the measured value. The good agreement of the Lund (JETSET) prediction with the data suggests that hadronization and higher-order perturbative corrections can account for the remaining difference. The higher moments ratios  $R_k$ , defined by

$$R_k \equiv \langle n(n-1)\dots(n-k+1) \rangle / \langle n \rangle^k, \quad (6.78)$$

have similar corrections with coefficients that grow with  $k$ , making the next-to-leading-order predictions progressively less reliable for higher moments [21].

## 6.4 Quark and gluon jet differences

The results of the previous section suggest that there should be characteristic differences between jets initiated by quarks and gluons. For example, Eq. (6.71) predicts that the average multiplicity of *any* type of object in a gluon jet should become  $C_A/C_F = 9/4$  times greater than that in a quark jet asymptotically, while Eq. (6.73) predicts that the asymptotic multiplicity distribution should also become wider for a gluon jet, by the square root of  $C_A/C_F$ .

These differences arise from the greater effective colour charge-squared of the gluon, which is proportional to  $C_A$  as opposed to  $C_F$  for the quark. The dominant asymptotic contribution to the multiplicity from a quark jet comes from the emission by the initial quark of a highly virtual gluon, which then generates a gluon jet. Thus one factor of  $C_A$  in the cascade is replaced by  $C_F$ , leading to a reduction in the average multiplicity by a factor of  $C_F/C_A$ . The second moment is reduced by the same factor, and so the width of the multiplicity distribution is also decreased.

As a consequence of the higher multiplicity, the fragmentation function of a gluon jet would be expected to be softer, *i.e.* more concentrated at low values of the momentum fraction  $x$ , than that of a quark jet. Actually, the treatment in Section 6.1.3 shows that the shape of the low- $x$  fragmentation function – the Gaussian peak in  $\ln(1/x)$  – is the same for quark and gluon jets in leading (and in fact also next-to-leading) logarithmic approximation. What *is* different is the height of the peak, which should again be in the ratio  $C_F : C_A$  for quarks versus gluons asymptotically. To conserve momentum, this implies a relative reduction in the gluon fragmentation function at higher  $x$ .

Another characteristic difference is that gluon jets should be broader than quark jets. We saw in Section 3.3 that the Sterman-Weinberg two-jet fraction for  $e^+e^-$  annihilation takes the form (3.32) in lowest order, which means that the angular size  $\delta_q$  of the quark jets for a given small energy fraction  $\epsilon$  is

$$\delta_q \sim \exp \left[ \frac{\pi(1-f_2)}{4C_F\alpha_S(s)\ln\epsilon} \right]. \quad (6.79)$$

Since  $1/\alpha_S(s)$  increases logarithmically with energy, this means that the angular jet width, for a fixed Sterman-Weinberg fraction  $f_2$ , decreases like a negative power of  $s$ . For a final state consisting of two gluon jets, as

would be seen in the decay of a  ${}^1S_0$  heavy quark-antiquark bound state, for example, the analogous calculation gives a factor of  $C_A$  in place of  $C_F$  and therefore

$$\delta_g \sim \delta_q^{C_F/C_A}. \quad (6.80)$$

Thus the power decrease of the angular width is less rapid for gluon jets.

The experimental data on gluon jet properties show the predicted qualitative differences from quark jets, although at present energy scales the differences are less marked than those expected asymptotically [22,23]. For example, Fig. 6.10 shows the data of the OPAL collaboration on the fragmentation function for gluon jets produced in three-jet decays of  $Z^0$  bosons into  $b$  quarks,  $Z^0 \rightarrow b\bar{b}g$ . The label ‘ $k_\perp$  definition:  $y_{\text{cut}} = 0.02$ ’ indicates that the  $k_T$  or Durham jet algorithm (3.33), with  $y = 0.02$ , was used to obtain the three-jet sample. The gluon jets were selected in the following way. The most energetic jet was assumed to be a quark jet, which is true in about 97% of events. Of the two remaining jets, one was ‘tagged’ as a  $b$ - or  $\bar{b}$ -quark jet by the presence of a secondary vertex due to the decay of a  $b$ -flavoured hadron. With about 93% probability, the remaining jet is then a gluon jet. The comparative points for light ( $uds$ ) quark jets were obtained by a combination of anti-tagging secondary vertices and selecting jets that have a charged track with  $x > 0.45$ . In heavy-quark jets, this is less likely because of the weak decay of the heavy hadron. The data are corrected for the selection and detector effects; the correction factors are shown in the upper plot.

We see that the gluon fragmentation function is indeed softer than that for light quarks, with a higher peak at small  $x$ . A direct comparison with the  $b$  quark jets does not show such clear differences, because the  $b$  jets contain the products of the weak decay of the  $b$ -flavoured hadron, which also tend to be soft.

Notice that the gluon fragmentation function obtained from this analysis is consistent with that deduced from the longitudinal fragmentation function, Fig. 6.6.

## 6.5 Resummation of event shapes

As we discussed in Section 3.4, event shape variable distributions in  $e^+e^-$  annihilation provide some of the cleanest tests of QCD and a powerful way of determining the strong coupling  $\alpha_s$ . The perturbative prediction of the thrust distribution, for example, has the form

$$\begin{aligned} \frac{1}{\sigma} \frac{d\sigma}{dT} = & \alpha_s(\mu^2) A_1(T) + [\alpha_s(\mu^2)]^2 A_2(T, s/\mu^2) \\ & + [\alpha_s(\mu^2)]^3 A_3(T, s/\mu^2) + \dots \end{aligned} \quad (6.81)$$

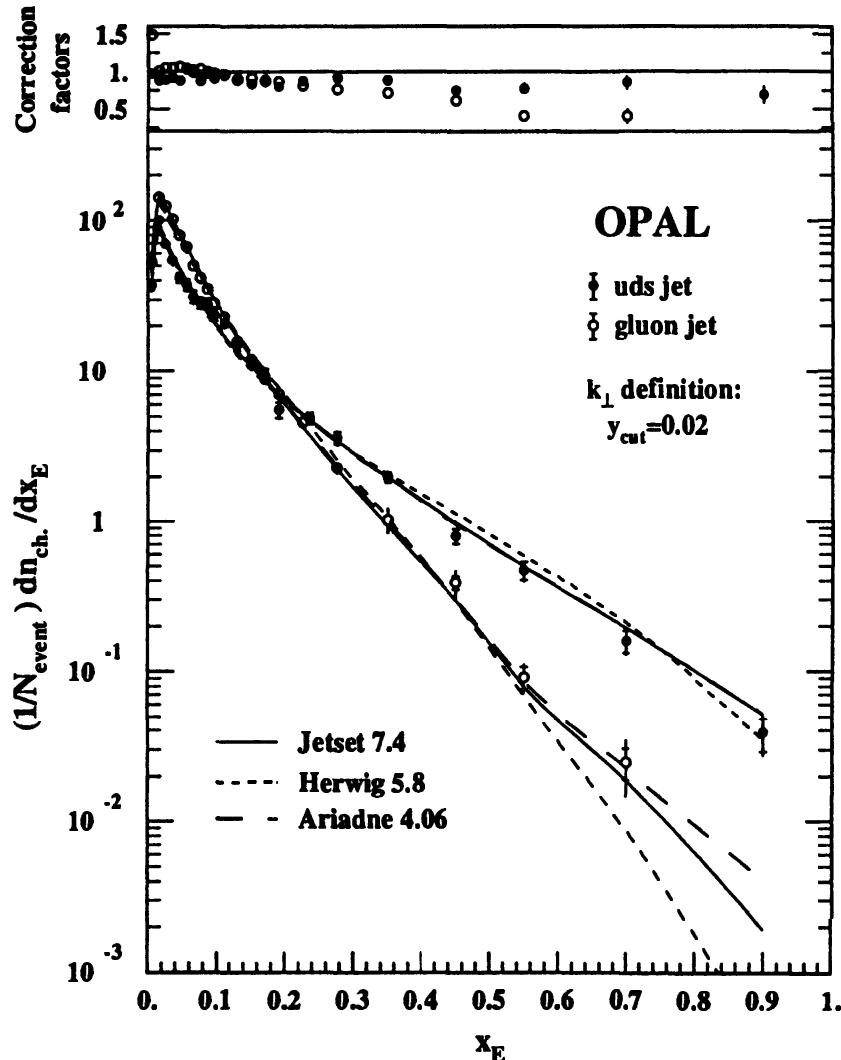


Fig. 6.10. Comparison between light (*uds*) quark and gluon jet fragmentation functions, and the predictions of various event generators. Figure from ref. [23].

where we know  $A_1(T)$  and  $A_2(T, s/\mu^2)$  in full. Thus a fit to the data neglecting the unknown higher-order terms yields a measured value of  $\alpha_S(\mu^2)$ . Assuming that  $A_3$  is of order unity, we would expect a relative precision of the order of  $\alpha_S^2$  ( $\sim 2\%$  at  $Z^0$  energies).

In addition to the fact that we do not yet know the full form of  $A_3$ , a number of factors limit the reliability of the perturbative prediction.

1. *Large logarithms.* These enhance higher-order terms and limit the range of thrust that can be used for determining  $\alpha_S$ . Near the two-jet configuration (*i.e.* at high thrust) the perturbative coefficients become very large:

$$A_n(T) \underset{T \rightarrow 1}{\sim} \frac{\ln^{2n-1}(1-T)}{1-T}. \quad (6.82)$$

Thus for the higher orders to be negligible it is not sufficient to have

$\alpha_s \ll 1$ ; we need in fact  $\alpha_s \ln^2(1 - T) \ll 1$ . This is a significant limitation, since most of the data are at high  $T$ , where  $\alpha_s \ln^2(1 - T) \sim 1$  even at the highest available energies.

2. *Renormalization scale dependence.* The coefficients beyond the first depend on the arbitrary renormalization scale  $\mu^2$  used in calculating them. For the second term we have explicitly

$$A_2(T, s/\mu^2) = A_2(T, 1) - b A_1(T) \ln(s/\mu^2), \quad (6.83)$$

where  $b$  is the first coefficient of the QCD  $\beta$  function, defined in Eq. (2.8). The scale dependence of  $A_2$  is necessary in order to cancel that of the running coupling to the same order, see Eq. (3.21):

$$\alpha_s(\mu^2) = \alpha_s(s) + b \alpha_s^2 \ln(s/\mu^2) + \dots, \quad (6.84)$$

but a residual scale dependence is left in order  $\alpha_s^3$ . It is particularly worrying that the data are fitted best by using a small scale [24],  $\mu^2 \ll s$ , which generates large higher-order terms when expressed in terms of  $\alpha_s(s)$ . It might be argued that this corresponds to the fact that a physical scale much smaller than  $s$ , for example the typical transverse momentum of an emitted gluon  $\mu^2 \sim (1 - T)s$ , is controlling the dynamics. However, physics should be independent of  $\mu$ , which is just an artifact of our method of calculation. In any case, a change of scale cannot be the whole story, because this produces only one logarithmic factor for each power of  $\alpha_s$ , whereas the coefficients (6.82) contain two such factors.

3. *Hadronization corrections.* As discussed in Section 5.6, hadronization is outside the domain of perturbation theory and its effects can only be estimated at present through the use of models, of which the most successful are those built into parton shower simulation programs [25,26]. In the programs, one can easily turn off the hadronization phase of the simulation and compare the distributions generated at the parton and hadron levels. However, modern shower simulations operate not by performing an exact perturbative calculation up to a fixed order, but rather by treating enhanced terms, such as the explicit logarithms described above, to all orders. They therefore generate parton configurations of arbitrarily high multiplicity, typically much larger than the maximum of four partons generated at order  $\alpha_s^2$ , and are not well suited to estimating the hadronization corrections for fixed-order calculations.

The above difficulties can be alleviated by identifying the explicit large logarithms in each order of perturbation theory and resumming them to all orders. The resummation is most effective when the logarithmic terms

*exponentiate*, i.e. when they combine in such a way that the logarithm of the cross section is less divergent in the two-jet limit. This is made more precise in the following subsection.

### 6.5.1 Exponentiation and resummation

Instead of working with the event shape distribution directly, it is convenient to introduce the event shape fraction, which for the thrust distribution is

$$f(\tau) = \int_{1-\tau}^1 dT \frac{1}{\sigma} \frac{d\sigma}{dT}. \quad (6.85)$$

This quantity is somewhat analogous to the two-jet fraction  $f_2$ , with  $\tau = 1 - T$  playing the role of the jet resolution  $y$ . By exponentiation of such a quantity, we mean more precisely that at small  $\tau$  (high thrust)

$$f(\tau) = C(\alpha_s) \exp G[\alpha_s, \ln(1/\tau)] + D(\alpha_s, \tau) \quad (6.86)$$

where, writing the large logarithm as  $L = \ln(1/\tau)$ ,

$$\begin{aligned} C(\alpha_s) &= 1 + \sum_{n=1}^{\infty} C_n a^n, \\ G(\alpha_s, L) &= \sum_{n=1}^{\infty} \sum_{m=1}^{n+1} G_{nm} a^n L^m \\ &\equiv L g_1(\alpha_s L) + g_2(\alpha_s L) + \alpha_s g_3(\alpha_s L) + \dots, \end{aligned} \quad (6.87)$$

and the remainder  $D(\alpha_s, \tau)$  vanishes as  $\tau \rightarrow 0$ . For later convenience we have defined  $a = \alpha_s/2\pi$  in the expansions, and have suppressed the dependence on the renormalization scale  $\mu^2$  for the moment. The function  $g_1$  resums all the *leading logarithms*  $\alpha_s^n L^{n+1}$ , while  $g_2$  contains the *next-to-leading logarithmic* (NLL) terms  $\alpha_s^n L^n$ , and  $g_3$  etc. represent the remaining *subdominant* logarithmic corrections  $\alpha_s^n L^m$  with  $0 < m < n$ . The important point is that, whereas the event fraction itself has up to two factors of  $L$  for each power of  $\alpha_s$ , its logarithm has only one extra  $L$  for each  $\alpha_s$ . The double logarithms come purely from the expansion of the exponential function.

If exponentiation takes place and we know the leading and next-to-leading functions  $g_1(u)$  and  $g_2(u)$  of Eq. (6.87) in the region  $u \lesssim 1$ , then, provided the subdominant contributions  $g_3(u)$  etc. behave reasonably in this region, we can predict  $\ln f$  reliably for  $\alpha_s L \lesssim 1$ . This is a much larger region than the one  $\alpha_s L^2 \ll 1$  in which the original perturbative expansion was applicable.

A knowledge of both  $g_1(u)$  and  $g_2(u)$  is necessary not only to extend the region of validity consistently to  $\alpha_s L \lesssim 1$  but also to gain some control of

the renormalization scale dependence of the prediction. This is because the scale dependence of the leading function  $g_1(u)$  has to be cancelled order-by-order by contributions from  $g_2(u)$ . Thus  $g_2(u)$  has a dependence on the renormalization scale  $\mu^2$ , of the form

$$g_2(u, \mu^2) = g_2(u, s) - bu^2 \frac{dg_1}{du} \ln \left( \frac{s}{\mu^2} \right), \quad (6.88)$$

which is the analogue of Eq. (6.83) for exponentiated quantities. As in the case of a fixed-order prediction, if the resulting resummed expression still shows a strong residual scale dependence, this can be taken as a warning that neglected higher-order terms may be anomalously large, since they have to cancel this dependence. Furthermore, since  $\alpha_s$  itself is not defined until the scale is specified, the calculation of  $g_2(u)$  is essential if one wishes to use resummation to improve the determination of  $\alpha_s$ .

The exponentiation of event shapes follows primarily from the corresponding property of QCD matrix elements in the soft and collinear regions [27]. In addition, however, one must establish that the phase space defining the event fraction for a particular shape variable does not spoil this property near the two-jet limit. Schematically we have

$$f(\tau) = \frac{1}{\sigma} \sum_n \int |\mathcal{M}_n|^2 d\Phi_n(\tau) \quad (6.89)$$

where  $\Phi_n(\tau)$  defines the  $n$ -parton phase space for shape values bounded by  $\tau$ . One has to show essentially that each term in the sum factorizes at small  $\tau$ , possibly after some suitable integral transformation of Eq. (6.89), in such a way that successive terms form an exponential series. The coherent branching formalism developed in the previous chapter is very useful for this purpose [28]. Usually the problem can be recast in the form of an integral equation, whose solution gives the exponent function  $G(\alpha_s, L)$  directly. It should be emphasized that the exponentiation of the event fraction has only been established for a limited number of event shape variables, and for some variables it is known that exponentiation does *not* occur.

In the case of the thrust and some related event shapes, exponentiation may be established through a connection with the jet mass distribution. Each event can be divided into two jet hemispheres by the plane orthogonal to the thrust axis. Suppose that the invariant masses-squared of the multiparticle systems in the two hemispheres are  $k^2$  and  $\bar{k}^2$ . Then since the thrust is simply proportional to the resultant three-momentum in each hemisphere, it is related to  $k^2$  and  $\bar{k}^2$  by elementary two-body kinematics. At high thrust we have explicitly

$$T = 1 - k^2/s - \bar{k}^2/s - 2k^2\bar{k}^2/s^2 + \dots . \quad (6.90)$$

The last term shown is of order  $\tau^2$  and so it and higher terms contribute only to the remainder function  $D(\alpha_s, \tau)$  in Eq. (6.86). Hence to logarithmic accuracy we can write schematically

$$\Phi_n(\tau) = \Phi_n(k^2 + \bar{k}^2 < s) . \quad (6.91)$$

Thus to the required accuracy the event fraction can be written in terms of  $J(\bar{k}^2, s)$ , the jet mass distribution measured at scale  $s$ , as

$$f(\tau) = \int_0^{\tau s} dk^2 \int_0^{\tau s - k^2} d\bar{k}^2 J(k^2, s) J(\bar{k}^2, s) . \quad (6.92)$$

This expression can be factorized in terms of the Laplace transform

$$\tilde{J}_\nu(s) = \int_0^\infty dk^2 e^{-\nu k^2} J(k^2, s) . \quad (6.93)$$

One finds that

$$f(\tau) = \frac{1}{2\pi i} \int_C \frac{d\nu}{\nu} e^{\nu \tau s} [\tilde{J}_\nu(s)]^2 \quad (6.94)$$

where the inverse transform contour  $C$  lies to the right of all singularities of the integrand. A derivation of the Laplace-transformed jet mass distribution  $\tilde{J}_\nu(s)$  to NLL accuracy may be found in ref. [29].

In this way one finds that the function  $g_1(u = \alpha_s L)$  which resums the leading logarithms is [30,31]

$$g_1(u) = -\frac{C_F}{\pi b^2 u} [(1 - 2bu) \ln(1 - 2bu) - 2(1 - bu) \ln(1 - bu)] . \quad (6.95)$$

At small  $u$ ,  $g_1(u) \sim -C_F u / \pi$ , giving

$$f(\tau) \sim \exp(-2aC_F L^2) \quad (6.96)$$

in the limit  $\alpha_s L \ll 1$ . We see that the dominant effect of resummation is to suppress the event fraction at small  $\tau$ , leading to a turn-over instead of a divergence in the distribution at high thrust. This is a Sudakov form factor effect: in order for an event to have very high thrust, the produced quark and antiquark must have emitted very little gluon bremsstrahlung, which is very improbable. Note however that the double logarithmic approximation (6.96) is not reliable in the vicinity of the turn-over, since it predicts that the latter occurs at  $\alpha_s L = \pi/2C_F = 1.2$ , which is inconsistent with the assumption that  $\alpha_s L \ll 1$ . Using the full leading-logarithmic result (6.95) gives a turn-over at lower thrust,  $\alpha_s L \sim 0.5$ .

The next-to-leading function  $g_2$  is found to be [28]

$$g_2(u) = -\frac{C_F \kappa}{2\pi^2 b^2} [2 \ln(1 - bu) - \ln(1 - 2bu)]$$

$$\begin{aligned}
& - \frac{3C_F}{2\pi b} \ln(1 - bu) - \frac{2\gamma_E C_F}{\pi b} [\ln(1 - bu) - \ln(1 - 2bu)] \\
& - \frac{C_F b'}{\pi b^2} [\ln(1 - 2bu) - 2 \ln(1 - bu) \\
& + \frac{1}{2} \ln^2(1 - 2bu) - \ln^2(1 - bu)] \\
& - \ln \Gamma(1 - g_1(u) - ug'_1(u)) ,
\end{aligned} \tag{6.97}$$

where  $\kappa = (201 - 9\pi^2 - 10n_f)/18$ ,  $\gamma_E = 0.5772\dots$  is the Euler constant, and  $b'$  is the second  $\beta$  function coefficient defined in Eq. (2.8). If we renormalize at a scale  $\mu^2 \neq s$ ,  $g_2$  receives an extra contribution as specified in Eq. (6.88).

The same approach yields a very similar formula [32] for the distribution of the ‘heavy jet mass’  $\rho = \text{Max}\{k^2, \bar{k}^2\}/s$ . Other quantities that have been fully resummed to NLL accuracy after being shown to exponentiate include the energy-energy correlation [33] and an shape variable called the ‘jet broadening’, which measures the transverse energy relative to the thrust axis [34].

### 6.5.2 Combining with fixed-order predictions

To obtain an improved prediction throughout the whole of phase space we should combine the resummed expression, valid at small  $\tau$ , with the full second-order result, valid elsewhere. This is equivalent to evaluating the remainder function  $D(\alpha_s, \tau)$  in Eq. (6.86).

The simplest procedure is the so-called ‘log matching’ scheme, in which one recasts Eq. (6.86) in the form

$$\ln f(\tau) = K(\alpha_s) + G(\alpha_s, L) + H(\alpha_s, \tau) \tag{6.98}$$

where again  $K(\alpha_s)$  represents a power series in  $\alpha_s$  and  $H(\alpha_s, \tau)$  is a remainder that vanishes as  $\tau \rightarrow 0$ . Writing the full second-order prediction as

$$f(\tau) = 1 + aA(\tau) + a^2B(\tau) + O(\alpha_s^3), \tag{6.99}$$

we have

$$\ln f(\tau) = aA(\tau) + a^2\{B(\tau) - \frac{1}{2}[A(\tau)]^2\} + O(\alpha_s^3). \tag{6.100}$$

The functions  $A(\tau)$  and  $B(\tau)$  are conveniently tabulated in ref. [35].

To resum logarithmic terms of order  $\alpha_s^3$  and beyond, we should add  $G(\alpha_s, L)$  to this expression after subtracting its first- and second-order parts, which are already included in  $A(\tau)$  and  $B(\tau)$ . Hence the resummed prediction with  $K(\alpha_s)$  and  $H(\alpha_s, \tau)$  evaluated to second order is

$$\begin{aligned}
\ln f(\tau) &= Lg_1(\alpha_s L) + g_2(\alpha_s L) + a(A(\tau) - G_{11}L - G_{12}L^2) \\
&+ a^2(B(\tau) - \frac{1}{2}[A(\tau)]^2 - G_{22}L^2 - G_{23}L^3),
\end{aligned} \tag{6.101}$$

where the functions  $g_1$  and  $g_2$  are given in Eqs. (6.95) and (6.97) respectively, and the coefficients  $G_{nm}$  are obtained by expanding them to second order:

$$\begin{aligned} G_{11} &= +3C_F \\ G_{12} &= -2C_F \\ G_{22} &= -\frac{4}{3}\pi^2 C_F^2 + \left(\frac{1}{3}\pi^2 - \frac{169}{36}\right) C_F C_A + \frac{11}{18} C_F n_f \\ G_{23} &= -\frac{11}{3} C_F C_A + \frac{2}{3} C_F n_f . \end{aligned} \quad (6.102)$$

Notice that in this matching scheme the subdominant term  $a^2 G_{21} L$ , representing the first contribution from  $\alpha_S g_3(\alpha_S L)$  in Eq. (6.87), is implicitly included and exponentiated as a part of  $B(\tau)$ . Thus the largest missing subdominant contribution is of order  $\alpha_S^3 L^2$ , which is suppressed by four large logarithms relative to the leading term in  $f(\tau)$  of this order. Other matching procedures can be defined, which differ by subdominant terms of the same order and thus are equally valid, but in general they require more care to ensure the exponentiation of subdominant logarithms [28].

The resummation and matching procedure described above yields the results shown in Fig. 6.11. The effects of resummation become large for  $T > 0.9$ . At lower thrust the effect is still appreciable but can be compensated by a change of renormalization scale. In fact, the resummed curve is fortuitously reproduced quite well by the fixed-order formula if one uses a very low scale ( $\mu^2 \sim 0.001s$ ), combined with a smaller value of  $\alpha_S(M_Z^2)$ . This explains the empirical preference for low scales remarked on earlier.

Several experimental studies have been performed comparing resummed event shape predictions with data [36-40]. An example is shown in Fig. 6.12. We see that after hadronization corrections the prediction compares well with the data over a wide range of thrust, although the corrections become large and rapidly-varying outside the fitted region. The label  $f = 1$  indicates the scale choice  $\mu^2 = s$ . The error shown for  $\alpha_S$  is the statistical error of the fitting procedure only. The total experimental error of  $\pm 0.002$  is small compared to the theoretical uncertainties coming from scale dependence and hadronization, estimated at around  $\pm 0.005$ .

The results of resummed determinations of  $\alpha_S$  will be summarized in Chapter 12. The most important general feature of these analyses is that they no longer show a preference for small values of the renormalization scale  $\mu^2$ : indeed a fit usually cannot be obtained for  $\mu^2 \ll s$ . Since the principal large logarithms have been explicitly resummed, there is no dynamical argument for using a scale much different from  $s$ , and most resummed analyses quote a theoretical uncertainty corresponding to a rather small range of scales around  $\mu^2 \sim s$ . This, combined with a somewhat reduced scale dependence in the region  $\mu^2 \sim s$ , leads to a reduction

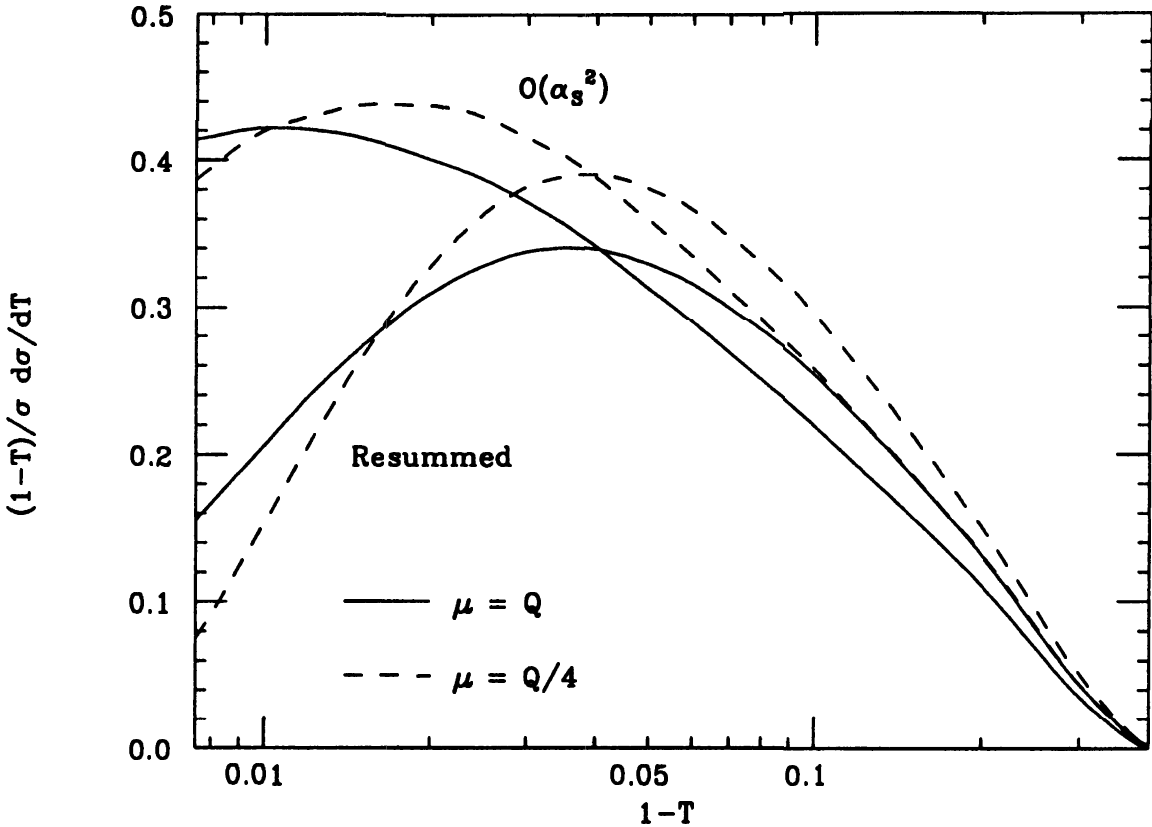


Fig. 6.11. Fixed-order and resummed predictions for the thrust distribution in  $Z^0 \rightarrow \text{hadrons}$ , for five-flavour  $\Lambda_{\overline{\text{MS}}} = 250 \text{ MeV}$  [ $\alpha_s(M_Z^2) = 0.120$ ], without hadronization corrections. Adapted from ref. [28].

in the quoted uncertainties in  $\alpha_s$  due to scale dependence. The central values of  $\alpha_s$  are slightly larger than those obtained from fixed-order analyses, since the small scales preferred by the latter tend to be correlated with smaller values of  $\alpha_s$ .

## 6.6 Resummation of jet rates

The large logarithms that occur in the  $e^+e^- n$ -jet fractions  $f_n$  at small values of the jet resolution parameter  $y$  ( $y_{\text{cut}}$ ) can also be resummed using the coherent branching formalism [41], provided the jets are defined using the  $k_T$  (Durham) jet clustering algorithm described in Section 3.3. By comparing the definition Eq. (3.38) of the jet resolution with Eq. (5.97) for the coherent evolution variable (called  $t$  in this chapter), we see that in order for the two final-state jets from a branching to be resolvable we require that

$$\min[z^2, (1-z)^2]t > sy , \quad (6.103)$$

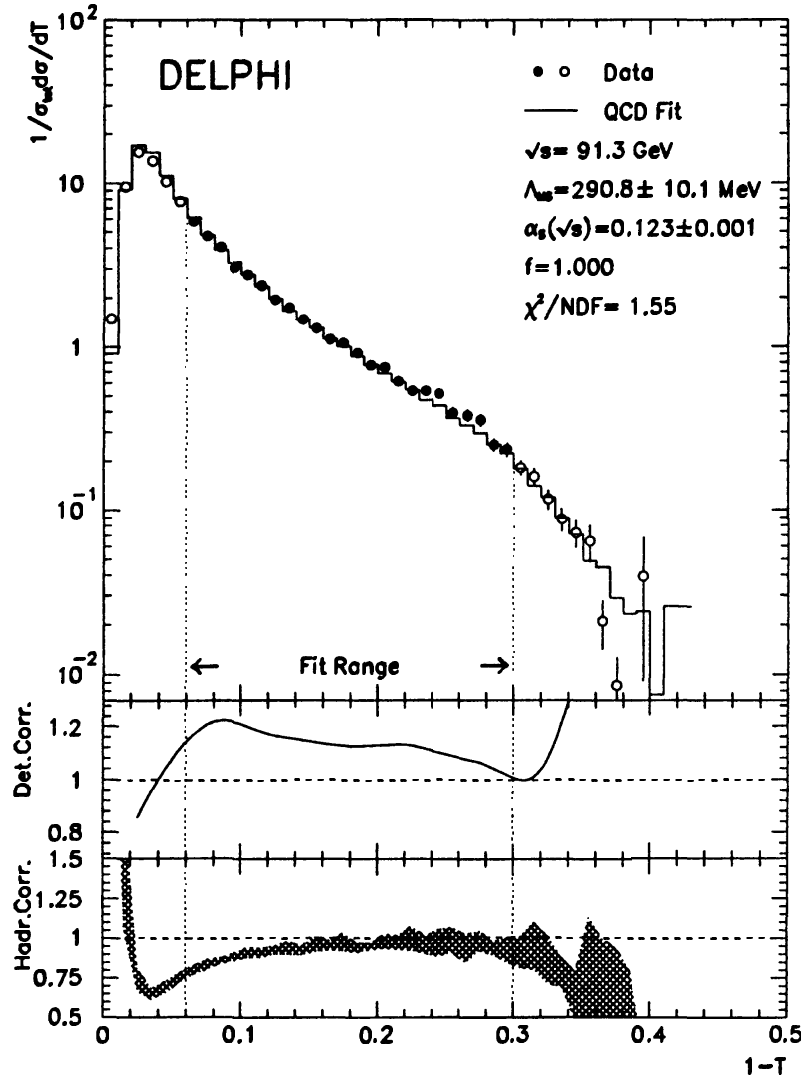


Fig. 6.12. Resummed prediction for the thrust distribution in  $Z^0 \rightarrow$  hadrons, corrected for hadronization, fitted to data of the DELPHI collaboration. The lower curves show the detector and hadronization correction factors. Figure from ref. [39].

i.e. that

$$\sqrt{t_0/t} < z < 1 - \sqrt{t_0/t} \quad (6.104)$$

where

$$t_0 \equiv sy . \quad (6.105)$$

The boundary condition (6.104) is precisely equivalent to the infra-red cut-off condition (5.99), with the reinterpretation (6.105) of the cut-off in terms of the jet resolution. It means that exactly one jet can be resolved in a quark or gluon jet at scale  $t = t_0$ , and hence that

$$\phi_{q,g}(u, t_0) = u \quad (6.106)$$

in the generating function formalism of Section 6.2.

Inserting the boundary values (6.106) in Eqs. (6.58) and (6.63), we obtain equations for the absolutely normalized jet generating functions in next-to-leading logarithmic approximation, which can be used to predict the jet rates at small values of  $y$  by repeated differentiation at  $u = 0$ . In terms of the Sudakov form factors (6.60,6.64), defining

$$\Delta_f(t) = [\Delta_q(t)]^2 / \Delta_g(t) , \quad (6.107)$$

one finds

$$\begin{aligned} f_2(s, y) &= [\Delta_q(s)]^2 , \\ f_3(s, y) &= 2 [\Delta_q(s)]^2 \int_{t_0}^s dt \Gamma_q(s, t) \Delta_g(t) , \\ f_4(s, y) &= 2 [\Delta_q(s)]^2 \left\{ \left[ \int_{t_0}^s dt \Gamma_q(s, t) \Delta_g(t) \right]^2 \right. \\ &\quad + \int_{t_0}^s dt \Gamma_q(s, t) \Delta_g(t) \int_{t_0}^t dt' \left[ \Gamma_g(t, t') \Delta_g(t') \right. \\ &\quad \left. \left. + \Gamma_f(t') \Delta_f(t') \right] \right\} . \end{aligned} \quad (6.108)$$

We see that a simple exponentiation of  $\ln y$  terms is valid for the two-jet fraction  $f_2$ , whereas the higher multijet rates satisfy a form of exponentiation only in the pseudo-Abelian limit  $\Gamma_g, \Gamma_f \rightarrow 0$ :

$$f_{k+2}(s, y) = \frac{1}{k!} \left[ 2 \int_{t_0}^s dt \Gamma_q(s, t) \right]^k \cdot [\Delta_q(s)]^2 + (\Gamma_g \text{ and } \Gamma_f \text{ terms}) . \quad (6.109)$$

Data on the  $y$  ( $y_{\text{cut}}$ ) dependence of the jet fractions at LEP are shown in Fig. 6.13. The curves are from the JETSET event generator, which includes the above physics in its parton shower simulation, together with a string hadronization model, as discussed in Section 5.7. All the multijet fractions have the same qualitative behaviour: they rise rapidly with decreasing  $y$  reach a maximum and then fall off again at very small  $y$ . The fall-off comes from the Sudakov form factor, which appears as an overall factor expressing the fact that it becomes increasingly difficult to keep the jet multiplicity fixed as the  $k_T$  resolution becomes very fine. Notice that the effect of hadronization, shown by the difference between the dashed and solid curves, is to increase the number of jets resolved at the smallest values of  $y$ .

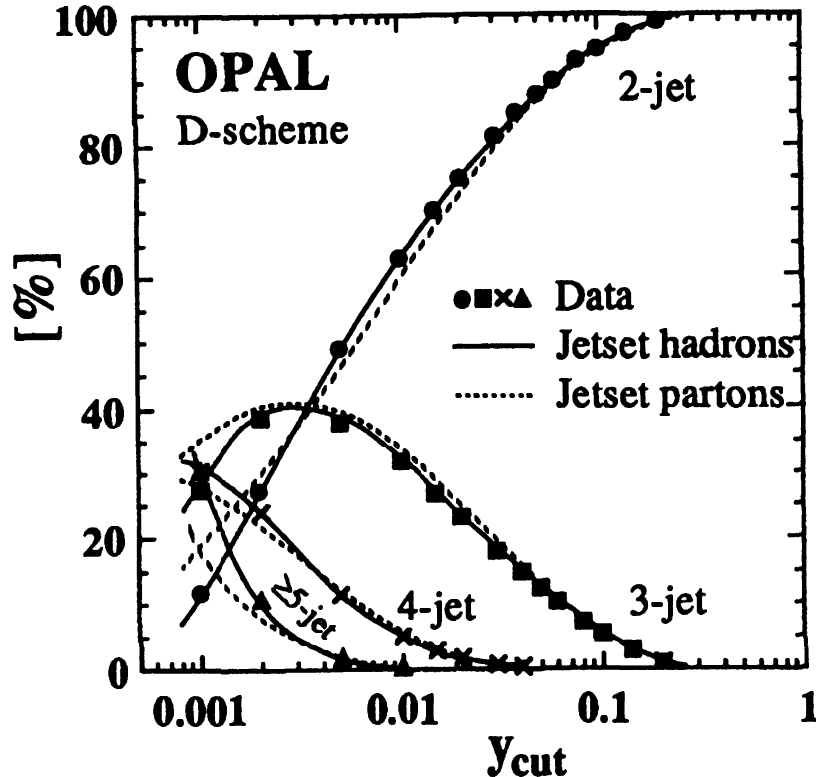


Fig. 6.13. OPAL data and JETSET predictions for multijet rates in  $e^+e^-$  annihilation at 91 GeV. Figure from ref. [42].

## 6.7 Average jet multiplicity

A study of the mean multiplicity of jets rather than hadrons in  $e^+e^-$  annihilation offers many experimental and theoretical advantages [43]. On the experimental side, the dependence of this quantity on jet resolution tests the same kind of physics as the energy dependence and can be studied in a single experiment at fixed energy. Furthermore, every hadronic event contributes at every value of the resolution, so the statistical and systematic errors are greatly reduced.

From the theoretical viewpoint, the jet multiplicity has the advantage of being fully computable in perturbation theory. There is no arbitrary normalization parameter, and the specified  $k_T$ -resolution scale  $t_0 = s y$  ( $y \equiv y_{\text{cut}}$ ) takes the place of the infra-red cut-off parameter in the hadron multiplicity calculation. At large values of  $y$  the jet multiplicity is reliably predicted by fixed-order perturbation theory, while at small values, for the  $k_T$  algorithm, large logarithms can be resummed using the generating function formalism. Finally at very small  $y$ , where  $t_0$  is of the order of the hadronization scale, we can hope to learn about the hadronization process

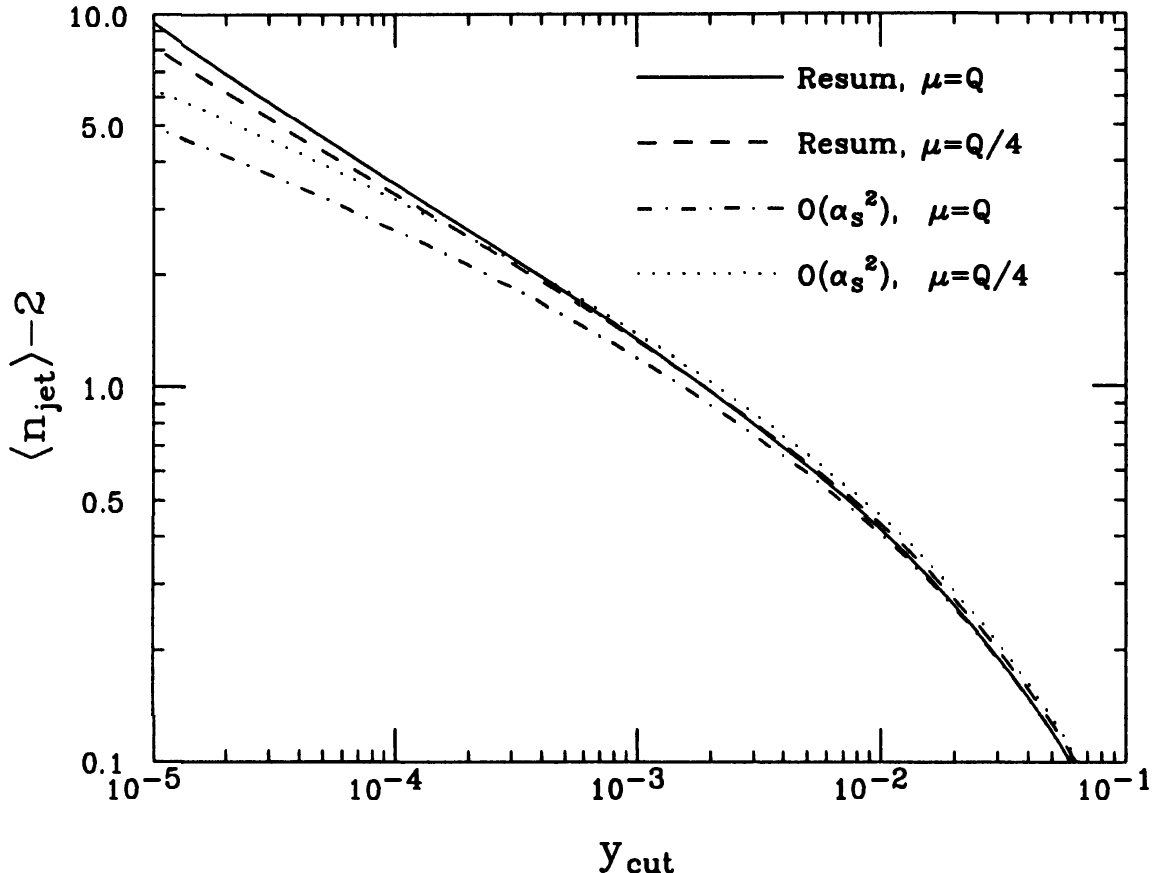


Fig. 6.14. Fixed-order and resummed predictions for the mean jet multiplicity in  $Z^0 \rightarrow \text{hadrons}$ , for  $\Lambda_{\overline{\text{MS}}} = 250$  MeV, without hadronization corrections.

by comparing the extrapolated perturbative prediction with experimental data.

To any fixed order  $\alpha_s^n$ , the mean jet multiplicity  $\langle n_{\text{jet}} \rangle$  is given by the multijet fractions computed to the same order. The  $O(\alpha_s^2)$  predictions at  $s = M_Z^2$  for different values of the renormalization scale  $\mu^2$  are shown in Fig. 6.14. The dependence on the renormalization scale is seen to be fairly weak, making the mean jet multiplicity a good quantity for the determination of  $\alpha_s$ .

Like the multijet rates, the mean jet multiplicity contains double logarithms that dominate at small values of  $y$ . But whereas in the exclusive rates these logarithms sum up mainly to provide a universal Sudakov suppression, in the inclusive multiplicity they generate a rapidly rising behaviour, with a rate of increase greater than any power of  $L = \ln(1/y)$ . Keeping only the double-logarithmic terms, one finds explicitly that

$$\begin{aligned} \langle n_{\text{jet}} \rangle &= 2 + a C_F L^2 + \frac{1}{12} a^2 C_F C_A L^4 + \frac{1}{360} a^3 C_F C_A^2 L^6 + \dots \\ &= 2 + 2 \frac{C_F}{C_A} (\cosh \sqrt{a C_A L^2} - 1) \end{aligned} \quad (6.110)$$

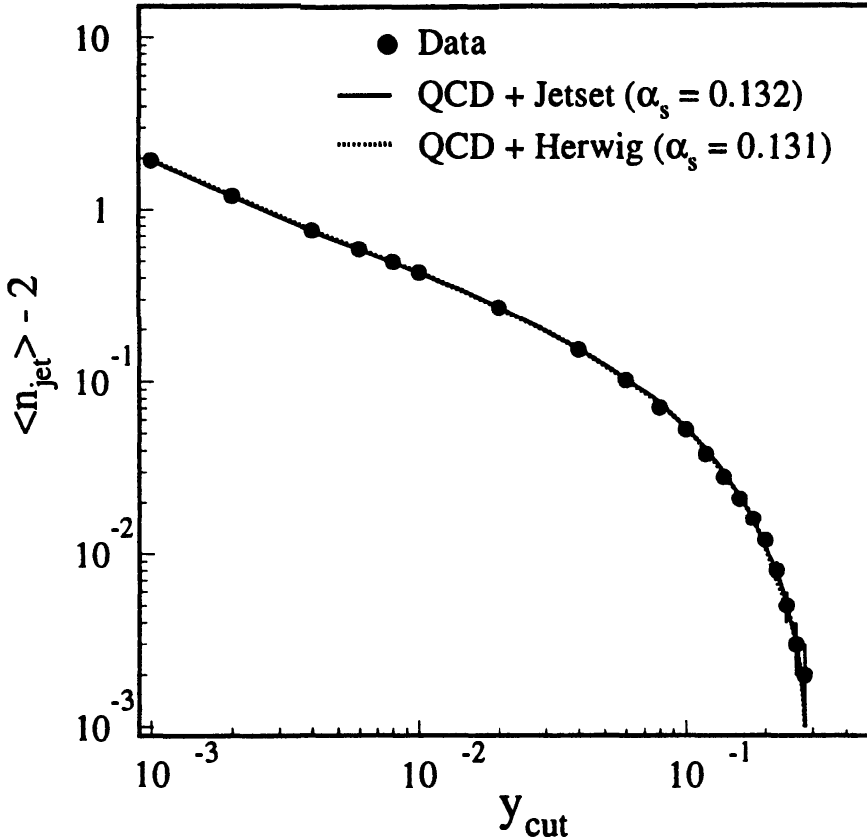


Fig. 6.15. Resummed prediction for the mean jet multiplicity in  $Z^0 \rightarrow \text{hadrons}$ , corrected for hadronization, fitted to data of the L3 collaboration. Figure from ref. [37].

$$\sim \frac{C_F}{C_A} \exp \sqrt{a C_A L^2} .$$

This is the analogue of the  $\exp \sqrt{\ln s}$  behaviour of the hadron multiplicity, Eq. (6.37). In fact, recalling that  $a = \alpha_s(s)/2\pi = 1/2\pi b \ln(s/\Lambda)$  and  $y = t_0/s$ , we have

$$\sqrt{a C_A L^2} \simeq \sqrt{\frac{2C_A}{\pi b}} \left[ \sqrt{\ln \left( \frac{s}{\Lambda^2} \right)} - \sqrt{\ln \left( \frac{t_0}{\Lambda^2} \right)} \right] , \quad (6.111)$$

as long as  $\alpha_s L \ll 1$  (even if  $\alpha_s L^2 \gg 1$ ).

Notice that in the double-logarithmic approximation the  $n$ th order term in Eq. (6.110) has colour factor  $C_F C_A^{n-1}$ . This means that the dominant contribution comes from emission of a single gluon from the quark or antiquark, followed by multiple branching within the gluon jet. We also see how an asymptotic dependence on  $\sqrt{\alpha_s}$  is obtained from a power series in  $\alpha_s$  when one drops the exponentially decreasing part of the sum.

The prediction can again be extended to next-to-leading logarithmic accuracy by means of the coherent branching formalism. The jet multi-

plicities satisfy the coupled integral equations (6.69) with the inhomogeneous terms  $N_{q,g}(t_0) = 1$ . Solutions to these equations can be obtained in closed form in terms of modified Bessel functions [9,43].

As in the case of event shape distributions, the NLL prediction can be improved further by matching with the exact two-loop result, after subtraction of the logarithmic terms that have been resummed. The resulting prediction for  $e^+e^-$  annihilation is shown in Fig. 6.14.

We should note that, since  $\langle n_{\text{jet}} \rangle$  does not have the simple exponentiating form (6.86), the resummation of leading ( $\alpha_s^n L^{2n}$ ) and next-to-leading ( $\alpha_s^n L^{2n-1}$ ) logarithms does not fully include the renormalization scale dependence of even the leading terms, which is of order  $\alpha_s^{n+1} L^{2n} = \alpha_s^{n+1} L^{2(n+1)-2}$ , *i.e.* next-to-next-to-leading. Therefore the determination of  $\alpha_s$  from jet multiplicity is only strictly reliable at larger  $y$ . As illustrated in Fig. 6.15, the prediction is in very good agreement with experiment for a value of  $\alpha_s(M_Z^2)$  consistent with that found from event shape analyses.

Although we have considered here the mean jet multiplicity in  $e^+e^-$  annihilation, similar arguments can be applied to other hard processes, such as deep inelastic scattering (DIS) [44]. In such cases we also have to deal with ‘initial-state’ jets, *i.e.* those associated with incoming coloured partons. The multiplicity of initial-state jets depends not only on the momentum transfer-squared of the hard process ( $Q^2$  in DIS) but also on the momentum fraction carried by the incoming struck parton (Bjorken  $x$  in DIS). If the struck parton has high  $x$ , it is less likely to have emitted initial-state jets, and so the jet multiplicity is reduced. Conversely an incoming parton at small  $x$  is more likely to have emitted jets, and so the multiplicity is enhanced at small  $x$ . The momentum not carried by emitted jets is carried by the ‘beam jet(s)’, which consists of unresolvable collinear and/or soft initial-state emission, together with the remnant partons of the incoming hadron(s) and any further hadrons produced in soft interactions of the remnants.

## References

- 1) J.C. Collins and D.E. Soper, *Ann. Rev. Nucl. Part. Sci.* **37** (1987) 383.
- 2) G. Curci, W. Furmanski and R. Petronzio, *Nucl. Phys.* **B175** (1980) 27; E.G. Floratos, C. Kounnas and R. Lacaze, *Nucl. Phys.* **B192** (1981) 417.
- 3) W. Furmanski and R. Petronzio, preprint TH.2933–CERN (1980); *Phys. Lett.* **B97** (1980) 437.
- 4) P. Nason and B.R. Webber, *Nucl. Phys.* **B421** (1994) 473.
- 5) ALEPH collaboration, D. Buskulic *et al.*, *Phys. Lett.* **B357** (1995) 487; *ibid.* **B364** (1995) 247 (erratum).
- 6) I.I. Balitsky and V.M. Braun, *Nucl. Phys.* **B361** (1991) 93.

- 7) A.H. Mueller, *Nucl. Phys.* **B213** (1983) 85; erratum quoted in *ibid.* **B241** (1984) 141; *ibid.* **B228** (1983) 351.
- 8) M. Schmelling, *Physica Scripta* **51** (1995) 683.
- 9) Yu.L. Dokshitzer, V.A. Khoze, A.H. Mueller and S.I. Troyan, *Basics of Perturbative QCD*, Editions Frontières, Paris (1991).
- 10) C.P. Fong and B.R. Webber, *Nucl. Phys.* **B355** (1992) 54.
- 11) TASSO collaboration, W. Braunschweig *et al.*, *Zeit. Phys.* **C47** (1990) 187.
- 12) OPAL collaboration, D. Akrawy *et al.*, *Phys. Lett.* **B247** (1990) 617.
- 13) L3 collaboration, B. Adeva *et al.*, *Phys. Lett.* **B259** (1991) 199.
- 14) OPAL collaboration, R. Akers *et al.*, *Zeit. Phys.* **C68** (1995) 203.
- 15) G. Altarelli, R.K. Ellis, G. Martinelli and S-Y. Pi, *Nucl. Phys.* **B160** (1979) 301.
- 16) P.J. Rijken and W.L. van Neerven, Leiden preprint INLO-PUB-4/96.
- 17) R.P. Feynman, *Photon Hadron Interactions*, W.A. Benjamin, New York (1972).
- 18) Yu.L. Dokshitzer, V.A. Khoze and S.I. Troyan, in *Perturbative Quantum Chromodynamics*, ed. A.H. Mueller, World Scientific, Singapore (1989).
- 19) ZEUS collaboration, M. Derrick *et al.*, *Zeit. Phys.* **C67** (1995) 93.
- 20) Z. Koba, H.B. Nielsen and P. Olesen, *Nucl. Phys.* **B40** (1972) 317.
- 21) E.D. Malaza and B.R. Webber, *Nucl. Phys.* **B267** (1986) 702.
- 22) TASSO collaboration, W. Braunschweig *et al.*, *Zeit. Phys.* **C45** (1989) 1; AMY collaboration, Y.K. Kim *et al.*, *Phys. Rev. Lett.* **63** (1989) 1772; OPAL collaboration, G. Alexander *et al.*, *Phys. Lett.* **B265** (1991) 462; P.D. Acton *et al.*, *Zeit. Phys.* **C58** (1993) 387; R. Akers *et al.*, *Zeit. Phys.* **C68** (1995) 179.
- 23) OPAL collaboration, G. Alexander *et al.*, *Zeit. Phys.* **C69** (1996) 543.
- 24) ALEPH collaboration, D. Decamp *et al.*, *Phys. Lett.* **B234** (1990) 399; *ibid.* **B255** (1991) 623; *ibid.* **B257** (1991) 479; DELPHI collaboration, P. Aarne *et al.*, *Phys. Lett.* **B240** (1990) 271; *ibid.* **B247** (1990) 167; L3 collaboration, B. Adeva *et al.*, *Phys. Lett.* **B237** (1990) 136; *ibid.* **B248** (1990) 464; OPAL collaboration, M.Z. Akrawy *et al.*, *Phys. Lett.* **B252** (1990) 159, *Zeit. Phys.* **C47** (1990) 505; *ibid.* **C49** (1991) 375.
- 25) T. Sjöstrand, *Comp. Phys. Comm.* **39** (1984) 347; M. Bengtsson and T. Sjöstrand, *Comp. Phys. Comm.* **43** (1987) 367.
- 26) G. Marchesini and B.R. Webber, *Nucl. Phys.* **B310** (1988) 461; G. Marchesini, B.R. Webber, G. Abbiendi, I.G. Knowles, M.H. Seymour and L. Stanco, *Comp. Phys. Comm.* **67** (1992) 465.
- 27) Yu.L. Dokshitzer, and D.I. Dyakonov, *Phys. Lett.* **B84** (1979) 234; G. Parisi and R. Petronzio, *Nucl. Phys.* **B154** (1979) 427; A. Bassutto, M. Ciafaloni and G. Marchesini, *Nucl. Phys.* **B163** (1980) 477; G. Curci and M. Greco, *Phys. Lett.* **B92** (1980) 175; J.C. Collins and D.E. Soper, *Ann. Rev. Nucl. Part. Sci.* **37** (1987) 383.
- 28) S. Catani, L. Trentadue, G. Turnock and B.R. Webber, *Nucl. Phys.* **B407** (1993) 3.
- 29) S. Catani and L. Trentadue, *Phys. Lett.* **B217** (1989) 539, *Nucl. Phys.* **B327** (1989) 353; *ibid.* **B353** (1991) 183.
- 30) M. Greco, *Phys. Rev.* **D23** (1981) 2791.
- 31) K. Tesima and M.F. Wade, *Zeit. Phys.* **C52** (1991) 43.
- 32) S. Catani, G. Turnock and B.R. Webber, *Phys. Lett.* **B272** (1991) 368.
- 33) J. Kodaira and L. Trentadue, *Phys. Lett.* **B123** (1982) 335; J.C. Collins and D.E. Soper, *Nucl. Phys.* **B284** (1987) 253; G. Turnock, Cambridge preprint Cavendish-HEP-91/3, unpublished.
- 34) S. Catani, G. Turnock and B.R. Webber, *Phys. Lett.* **B295** (1992) 269.

- 35) Z. Kunszt, P. Nason, G. Marchesini and B.R. Webber, in *Z Physics at LEP 1*, CERN Yellow Book 89-08, vol. 1, p. 373 (1989).
- 36) ALEPH collaboration, D. Decamp *et al.*, *Phys. Lett.* **B284** (1992) 163.
- 37) L3 collaboration, O. Adriani *et al.*, *Phys. Lett.* **B284** (1992) 471.
- 38) OPAL collaboration, P.D. Acton *et al.*, *Zeit. Phys.* **C59** (1993) 1.
- 39) DELPHI collaboration, P. Abreu *et al.*, *Zeit. Phys.* **C59** (1993) 21.
- 40) SLD collaboration, K. Abe *et al.*, *Phys. Rev.* **D51** (1995) 962.
- 41) S. Catani, Yu.L. Dokshitzer, M. Olsson, G. Turnock and B.R. Webber, *Phys. Lett.* **B269** (1991) 432.
- 42) OPAL collaboration, P.D. Acton *et al.*, *Zeit. Phys.* **C55** (1992) 1.
- 43) S. Catani, Yu.L. Dokshitzer, F. Fiorani and B.R. Webber, *Nucl. Phys.* **B377** (1992) 445.
- 44) S. Catani, Yu.L. Dokshitzer and B.R. Webber, *Phys. Lett.* **B322** (1994) 263.

# Hadroproduction of jets and photons

In this chapter we shall consider the application of the parton model to processes involving two hadrons in the initial state. We will first discuss whether parton distribution functions measured in lepton-hadron scattering (and defined in Chapter 4) can be used in hadron-hadron scattering. This adds a new feature to the issue of factorization. In Chapter 4 we saw that different processes involving one incoming hadron (such as  $F_2$  and  $F_L$ ) could be described in terms of universal parton distributions. Remarkably this result continues to hold in processes with two incoming hadrons.

Having established the validity of the QCD parton model in this new context we will go on to discuss the production of jets and direct photons. The scattering processes  $e^+e^- \rightarrow e^+e^-$ ,  $e^+e^- \rightarrow \gamma\gamma$ , ... provide fundamental tests of QED. The analogous processes for QCD,  $q\bar{q} \rightarrow q\bar{q}$ ,  $q\bar{q} \rightarrow gg$ , ... can be studied in the production of large transverse momentum jets in hadron-hadron collisions. After defining some kinematics, we show how the jet inclusive cross section is calculated in the QCD improved parton model. We study the  $p_T$  and angular distributions, and compare the theoretical predictions with the experimental data. We extend the discussion to include multijet cross sections and the energy flow profiles of jets. Finally we describe the related process of direct photon production. The production of lepton pairs in hadron-hadron collisions will be described in Chapter 9.

## 7.1 The QCD improved parton model

The high-energy interactions of hadrons are described by the QCD improved parton model. In this model a hard scattering process between

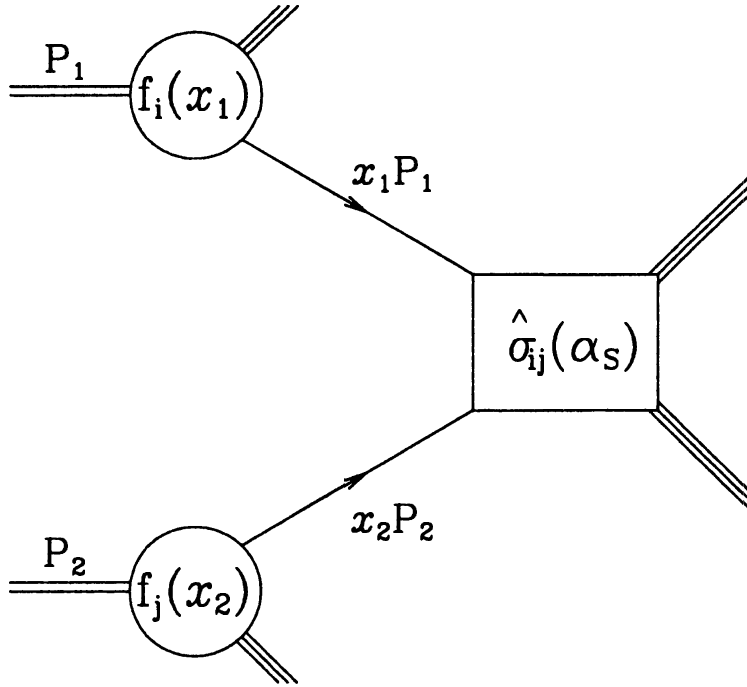


Fig. 7.1. The parton model description of a hard scattering process.

two hadrons is the result of an interaction between the quarks and gluons which are the constituents of the incoming hadrons. The incoming hadrons provide ‘broad-band’ beams of partons which possess varying fractions of the momenta of their parent hadrons, as described in Chapter 4.

The cross section for a hard scattering process initiated by two hadrons with four-momenta \$P\_1\$ and \$P\_2\$ can be written as

$$\sigma(P_1, P_2) = \sum_{i,j} \int dx_1 dx_2 f_i(x_1, \mu^2) f_j(x_2, \mu^2) \hat{\sigma}_{ij}(p_1, p_2, \alpha_s(\mu^2), Q^2/\mu^2). \quad (7.1)$$

corresponding to the structure illustrated in Fig. 7.1. The momenta of the partons which participate in the hard interaction are \$p\_1 = x\_1 P\_1\$ and \$p\_2 = x\_2 P\_2\$. The characteristic scale of the hard scattering is denoted by \$Q\$. This could be, for example, the mass of a weak boson or heavy quark, or the transverse momentum of a jet. The functions \$f\_i(x, \mu^2)\$ are the usual QCD quark or gluon distributions, defined at a factorization scale \$\mu\$. The short-distance cross section for the scattering of partons of types \$i\$ and \$j\$ is denoted by \$\hat{\sigma}\_{ij}\$. Since the coupling is small at high energy, the short-distance cross section can be calculated as a perturbation series in the running coupling \$\alpha\_s\$. Therefore the \$(n+k)\$th-order approximation to

the short-distance cross section is given by

$$\hat{\sigma} = \alpha_S^k \sum_{m=0}^n c^{(m)} \alpha_S^m, \quad (7.2)$$

where the  $c^{(m)}$  are functions of the kinematic variables and the factorization scale. Different hard processes will contribute with different leading powers  $k$ . Thus  $W$  production will contribute at  $k = 0$ , whereas jet production at large  $p_T$  has  $k = 2$ .

In the leading approximation ( $n = 0$ ) the short-distance cross section is identical to the normal parton scattering cross section calculated in exactly the same way as the cross section for a QED process. In higher orders, the short-distance cross section is derived from the parton scattering cross section by removing long-distance pieces and factoring them into the parton distribution functions. This is necessary because the perturbatively calculated cross section contains contributions from interactions which occur long before the hard scattering. These pieces can be factored out and absorbed into the description of the incoming hadrons. The remaining cross section involves only high momentum transfers (and therefore short times and distances) and is insensitive to the physics of low momentum scales. In particular, the short-distance cross section does not depend on the details of the hadron wave function or the type of the incoming hadron. It is a purely short-distance construct and is calculable in perturbation theory because of asymptotic freedom. This factorization property of the cross section can be proved to all orders in perturbation theory. For more details, see ref. [1]. A heuristic argument for the validity of factorization is given in the next section. Factorization is a fundamental property of the theory which turns QCD into a reliable calculational tool with controllable approximations, distinguishing it from the ‘naive’ parton model of Feynman [2].

The *factorization scale*  $\mu$  in Eq. (7.1) is an arbitrary parameter. It can be thought of as the scale which separates the long- and short-distance physics. Thus a parton emitted with a small transverse momentum, less than the scale  $\mu$ , is considered part of the hadron structure and is absorbed into the parton distribution. A parton emitted at large transverse momentum is part of the short-distance cross section. The scale  $\mu$  should be chosen to be of the order of the hard scale  $Q$  which characterizes the parton-parton interaction. The more terms included in the perturbative expansion, the weaker the dependence on  $\mu$  will be. This is exactly as discussed in Section 3.1 for the renormalization scale. In fact, in Eq. (7.1) the renormalization and factorization scales have been set equal. More

generally, one has

$$\begin{aligned}\sigma &= \sum_{i,j} \int dx_1 dx_2 f_i(x_1, \mu_F^2) f_j(x_2, \mu_F^2) \\ &\times \sum_{m=0}^n (\alpha_s(\mu_R^2))^{(m+k)} \hat{\sigma}_{ij}^{(m)} \left( p_1, p_2, \frac{Q^2}{\mu_F^2}, \frac{Q^2}{\mu_R^2} \right). \quad (7.3)\end{aligned}$$

As the scales are varied, the perturbative coefficients at higher order change in such a way that the cross section to all orders is independent of the scales:

$$\frac{\partial \sigma}{\partial \mu_F} = \frac{\partial \sigma}{\partial \mu_R} = 0. \quad (7.4)$$

The simplifying assumption of a single scale  $\mu = \mu_R = \mu_F$  is often made, and the standard choice is  $\mu = Q$ , the hard scattering scale.

Finally, it should be emphasized that Eq. (7.1) is not a description of the majority of the events which occur at a hadron-hadron collider. Most collisions yield only soft particles in the final state. However, as we shall see, the QCD parton model can be used to describe the most interesting classes of events which do involve a hard interaction.

## 7.2 Factorization of the cross section

The property of factorization allows us to use the QCD parton model to describe inelastic processes. In this section we shall present a simple classical model that illustrates why the factorization property holds and when it should fail. As an example of a hard process we consider the production of a massive vector boson  $V$  (in practice, an off-shell photon or a  $W$ - or  $Z$ -boson) in the collision of two hadrons,

$$H_1(P_1) + H_2(P_2) \rightarrow V + X. \quad (7.5)$$

This is in many respects the simplest hard process involving two hadrons, since the observed vector boson in the final state carries no colour and its leptonic decay products are observed directly. It is therefore the easiest to analyse theoretically. A full discussion of vector boson production will be given in Chapter 9.

A very important theoretical issue is whether the partons in hadron  $H_1$ , through the influence of their colour fields, change the distribution of partons in hadron  $H_2$  before the vector boson is produced, thus spoiling the simple parton picture. Soft gluons which are emitted long before the collision are potentially troublesome in this respect. This is the new feature which was not present in our discussion of processes involving one incoming hadron.

We shall argue that soft gluons do not in fact spoil the parton picture, using a simple model [3] from classical electrodynamics. The vector potential due to an electromagnetic current density  $J$  is given by [4]

$$A^\mu(t, \vec{x}) = \int dt' d\vec{x}' \frac{J^\mu(t', \vec{x}')} {|\vec{x} - \vec{x}'|} \delta(t' + |\vec{x} - \vec{x}'| - t), \quad (7.6)$$

where the delta function provides the retarded behaviour required by causality. Consider a particle with charge  $e$  travelling in the positive  $z$  direction with constant velocity  $\beta$ . The non-zero components of the current density are

$$\begin{aligned} J^t(t, \vec{x}) &= e\delta(\vec{x} - \vec{r}(t)), \\ J^z(t, \vec{x}) &= e\beta\delta(\vec{x} - \vec{r}(t)), \quad \vec{r}(t) = \beta t \hat{z}, \end{aligned} \quad (7.7)$$

where  $\hat{z}$  is a unit vector in the  $z$  direction. The charge passes through the origin at time  $t = 0$ . At an observation point (the position of hadron  $H_2$ ) described by coordinates  $x, y$  and  $z$ , the vector potential at time  $t$  due to the passage of the fast-moving charge is obtained by performing the integrations in Eq. (7.6) using the current density of Eq. (7.7). The result is

$$\begin{aligned} A^t(t, \vec{x}) &= \frac{e\gamma}{\sqrt{[x^2 + y^2 + \gamma^2(\beta t - z)^2]}}, \\ A^x(t, \vec{x}) &= 0 \\ A^y(t, \vec{x}) &= 0 \\ A^z(t, \vec{x}) &= \frac{e\gamma\beta}{\sqrt{[x^2 + y^2 + \gamma^2(\beta t - z)^2]}}, \end{aligned} \quad (7.8)$$

where  $\gamma^2 = 1/(1-\beta^2)$ . The observation point can be taken to be the target hadron  $H_2$  which is at rest near the origin, so that  $\gamma \approx s/m^2$ . Note that for large  $\gamma$  and fixed non-zero  $(\beta t - z)$  some components of the potential tend to a constant independent of  $\gamma$ , suggesting that there will be non-zero fields which are not in coincidence with the arrival of the particle, even at high energy. However at large  $\gamma$  the potential is a pure gauge piece, *i.e.*  $A^\mu = \partial^\mu \chi$  where  $\chi$  is a scalar function, and hence does not lead to electric or magnetic fields. This indicates that a covariant formulation which uses the vector potential  $A$  will not be the most efficient method to handle this problem, since we will have large fields which asymptotically will have no effect.

We now show that the vector potential (7.8) leads to field strengths which vanish at high energy. For example, the electric field along the  $z$  direction is

$$E^z(t, \vec{x}) = F^{tz} \equiv \frac{\partial A^z}{\partial t} + \frac{\partial A^t}{\partial z} = \frac{e\gamma(\beta t - z)}{[x^2 + y^2 + \gamma^2(\beta t - z)^2]^{\frac{3}{2}}}. \quad (7.9)$$

The leading terms in  $\gamma$  cancel and the field strengths are of order  $1/\gamma^2$  and hence of order  $m^4/s^2$ . Thus the force experienced by a charge in the hadron  $H_2$ , at any fixed time before the arrival of the quark, decreases as  $m^4/s^2$ . There are residual interactions which distort the distribution of quarks in hadron  $H_2$ , before the arrival of hadron  $H_1$ , but their effects vanish at high energies. A breakdown of factorization at order  $1/s^2$  is therefore to be expected in perturbation theory, and has been demonstrated explicitly in ref. [5]. Note that these effects are due to the long-range nature of the massless vector field. In the realistic case of an incoming colour-neutral hadron there are no long-range colour fields. It is therefore possible that power corrections to factorization, *i.e.* terms of order  $(m^2/s)^n$ , will occur only at a higher power of  $n$  than suggested by the above argument. In Chapter 9 we will consider vector boson production, dropping all terms suppressed by powers of  $s$ . The rest of this chapter considers jet production in the same approximation. The QCD-improved parton model will provide a valid description of these processes.

### 7.3 Luminosities

At a particle collider the rate  $N$  at which events of a given type occur is determined by the *luminosity* of the machine,  $L$ , multiplied by the cross section for the relevant scattering process,  $\sigma$ :

$$N = L\sigma . \quad (7.10)$$

The machine luminosity  $L$  is controlled by the parameters of the collider. For example, for a  $p\bar{p}$  collider we have

$$L = \frac{f}{\pi} \frac{N_p N_{\bar{p}}}{n_b} \frac{\gamma}{\sqrt{\beta_x^* \beta_y^* E_x^* E_y^*}} , \quad (7.11)$$

where  $f$  is the revolution frequency,  $n_b$  is the number of bunches and  $\gamma = E/m$  is the normal relativistic factor. The luminosity of a collider can be increased by increasing the number of protons (antiprotons),  $N_p$ , ( $N_{\bar{p}}$ ), or by decreasing the transverse emittance of the beams,  $E_x^*$ ,  $E_y^*$  or by decreasing the wavelength of the betatron oscillations of the beams,  $\beta_x^*$ ,  $\beta_y^*$ . An introduction to the physics of high-energy colliders can be found in ref. [6].

The process cross section  $\sigma$  is, of course, independent of the machine parameters. Nevertheless, for hard scattering processes at a hadron collider it is helpful to consider it as a product of a *parton luminosity* factor, for the relevant partons  $i$  and  $j$  inside the colliding hadrons, and a subprocess cross section  $\hat{\sigma}_{ij}$  for the parton-parton collision. We see from Eq. (7.1) that the parton luminosity is determined by the parton distri-

bution functions,  $f_i(x_1, \mu^2)$  and  $f_j(x_2, \mu^2)$ . Since the partons only carry a fraction of their parent hadron's momentum, the available centre-of-mass energy-squared of the parton-parton collision,  $\hat{s}$ , is less than the overall hadron-hadron collision energy,  $s$ , by a factor of  $x_1 x_2 \equiv \tau$ . A convenient way to quantify this is to define differential parton luminosities  $dL_{ij}/d\tau$  as follows:

$$\begin{aligned} \tau \frac{dL_{ij}}{d\tau} &= \frac{1}{1 + \delta_{ij}} \int_0^1 dx_1 dx_2 \\ &\times [(x_1 f_i(x_1, \mu^2) x_2 f_j(x_2, \mu^2)) + (1 \leftrightarrow 2)] \delta(\tau - x_1 x_2). \end{aligned} \quad (7.12)$$

The prefactor with the Kronecker delta avoids double counting for the case of identical partons. We now assume that  $\hat{\sigma}$  depends only on  $\hat{s}$ . This property is true for many processes, such as the total cross section for the production of a lepton pair, described in Chapter 9. In this case the cross section can be written as

$$\sigma(s) = \sum_{\{ij\}} \int_{\tau_0}^1 \frac{d\tau}{\tau} \left[ \frac{1}{s} \frac{dL_{ij}}{d\tau} \right] \left[ \hat{s} \hat{\sigma}_{ij} \right], \quad (7.13)$$

where the sum runs over all relevant pairs of partons  $\{ij\}$ . The minimum centre-of-mass energy-squared at which the hard subprocess can occur, denoted by  $\tau_0 s$ , provides a lower cut-off on the  $x$ -range of the participating partons. The first object in square brackets in Eq. (7.13) has the dimensions of a cross section. The second object in square brackets is dimensionless and is approximately determined by couplings. Hence knowing the luminosities we can estimate cross sections.

Figs. 7.2-7.5 show parton luminosities for hadron colliders of present and future interest calculated using the MRS(A) set of parton distributions [7]. As an example, we estimate the cross section for the production of two gluon jets with  $p_T > 0.5$  TeV at  $\sqrt{s} = 14$  TeV. We assume that  $\sqrt{\hat{s}} = 1$  TeV and from Fig. 7.2 we find

$$\left[ \frac{1}{s} \frac{dL_{ij}}{d\tau} \right] \approx 10^3 \text{ pb}. \quad (7.14)$$

The gluon-gluon scattering cross section first occurs at order  $\alpha_s^2$  and hence  $\hat{s} \hat{\sigma}_{gg}$  can be estimated to be about  $10^{-2}$  if we take  $\alpha_s \approx 0.1$ . Assuming that the logarithmic integral in Eq. (7.13) gives a factor of order unity, the estimate for the gluon jet cross section is 10 pb. Thus at the LHC collider operating at a luminosity of  $L = 10^{34} \text{ cm}^{-2}\text{s}^{-1}$ , we expect an event with a pair of 500 GeV jets every ten seconds.

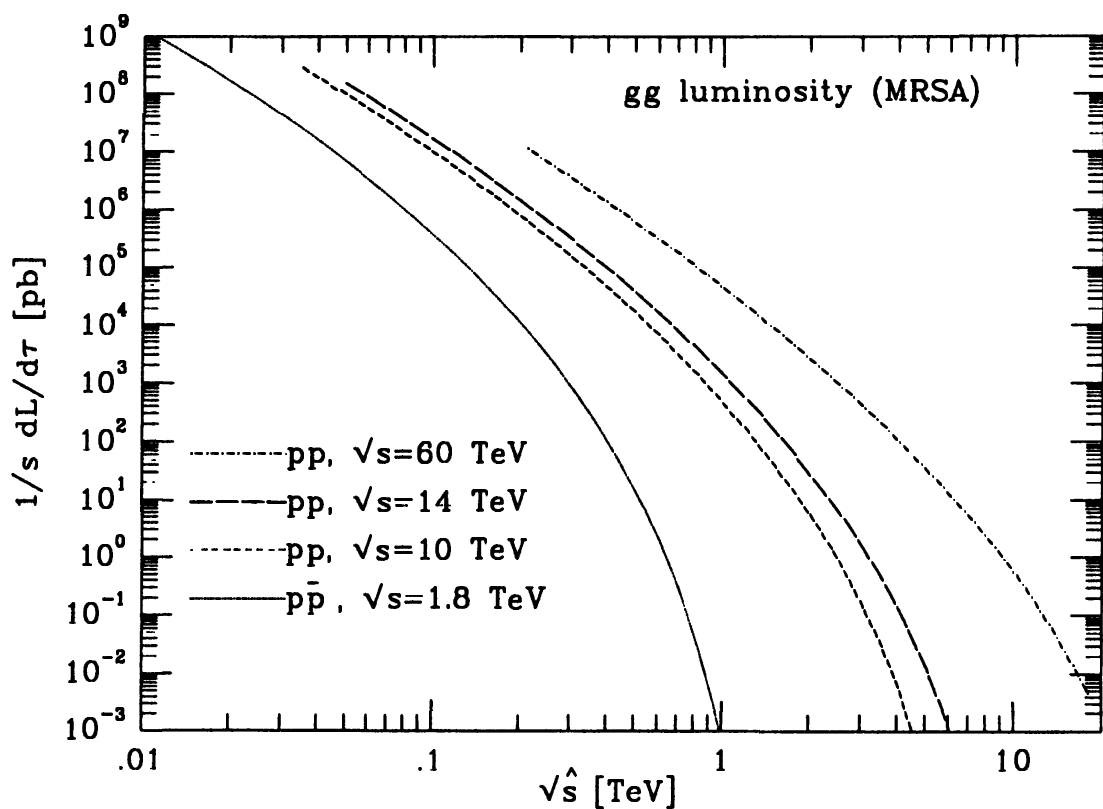


Fig. 7.2. Luminosity plot for gluon-gluon induced processes.

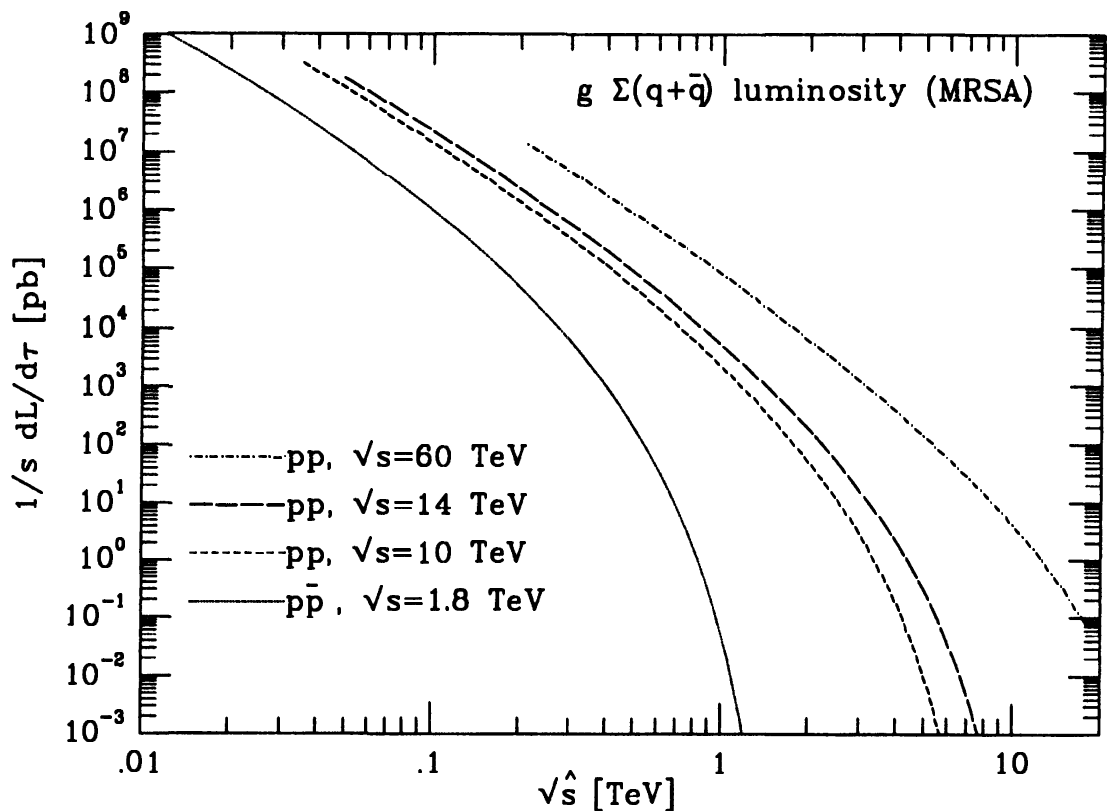


Fig. 7.3. Luminosity plot for gluon-quark induced processes.

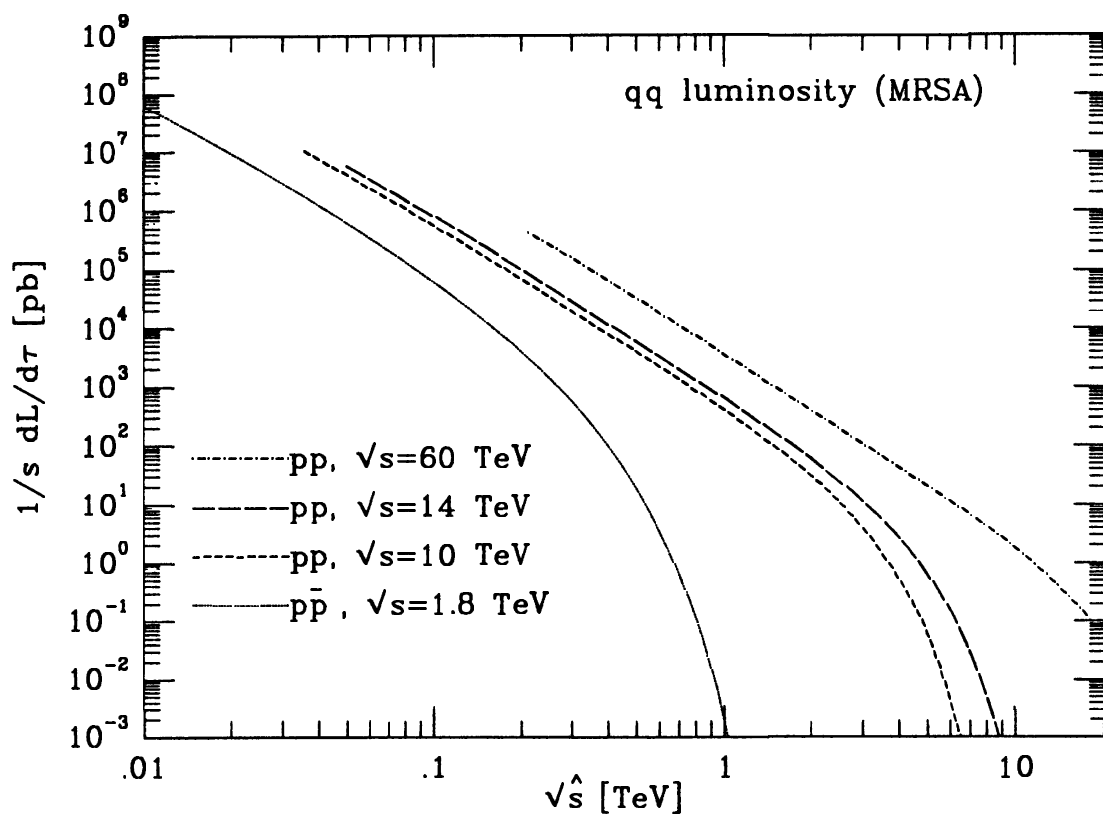


Fig. 7.4. Luminosity plot for quark-quark induced processes.

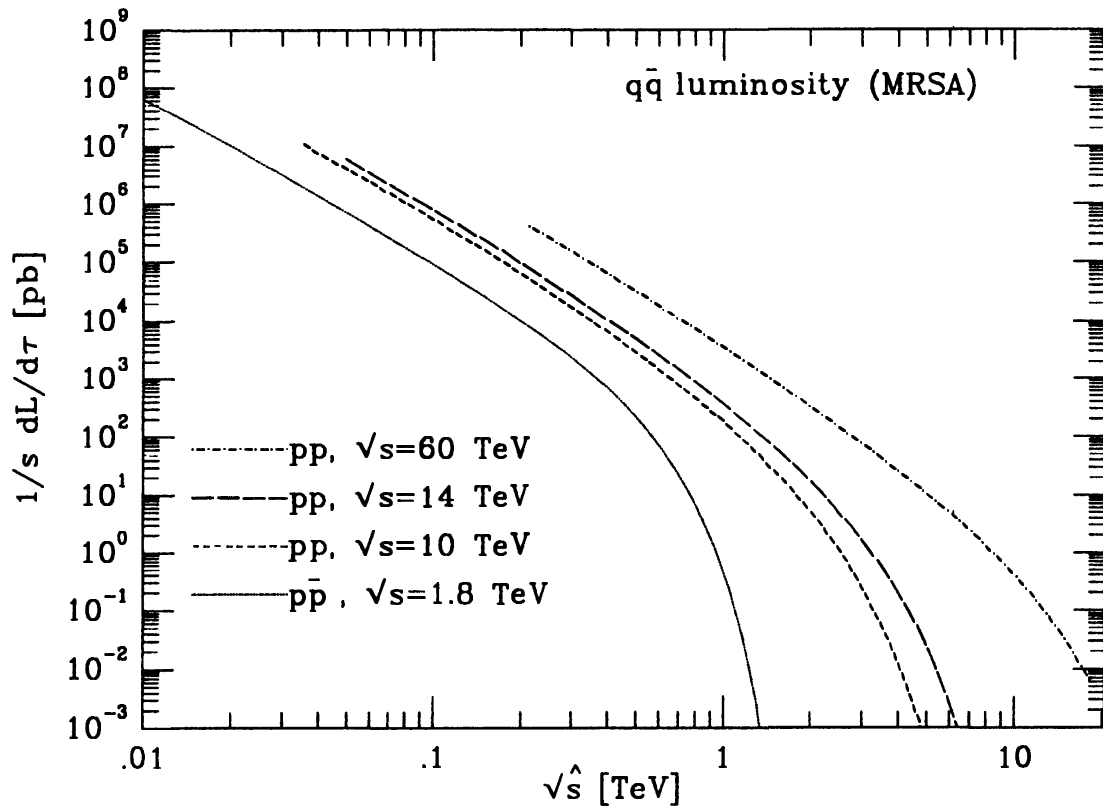


Fig. 7.5. Luminosity plot for quark-antiquark induced processes.

## 7.4 Kinematics and jet definition

As described above, the scattering of two hadrons provides two broadband beams of incoming partons. These incoming beams have a spectrum of longitudinal momenta determined by the parton distribution functions. The centre of mass of the parton-parton scattering is normally boosted with respect to that of the two incoming hadrons. It is therefore useful to classify the final state in terms of variables which transform simply under longitudinal boosts. For this purpose we introduce the rapidity  $y$ , the transverse momentum  $p_T$  and the azimuthal angle  $\phi$ . In terms of these variables, the four-momentum of a particle of mass  $m$  may be written as

$$\begin{aligned} p^\mu &= (E, p_x, p_y, p_z) \\ &= (m_T \cosh y, p_T \sin \phi, p_T \cos \phi, m_T \sinh y), \end{aligned} \quad (7.15)$$

where the transverse mass is defined as  $m_T = \sqrt{p_T^2 + m^2}$ . The rapidity  $y$  is defined by

$$y = \frac{1}{2} \ln \left( \frac{E + p_z}{E - p_z} \right), \quad (7.16)$$

and is additive under the restricted class of Lorentz transformations corresponding to a boost along the  $z$  direction. Rapidity differences are boost invariant.

In practice the rapidity is often replaced by the pseudorapidity variable  $\eta$ ,

$$\eta = -\ln \tan(\theta/2), \quad (7.17)$$

which coincides with the rapidity in the  $m \rightarrow 0$  limit. It is a more convenient variable experimentally, since the angle  $\theta$  from the beam direction is measured directly in the detector. It is also standard to use the transverse energy

$$E_T = E \sin \theta, \quad (7.18)$$

rather than the transverse momentum  $p_T$ , because it is the former quantity which is measured in a hadron calorimeter.

Many methods can be used to define what is meant by a jet of hadrons. There is no ‘best’ definition, but in order to make a proper comparison one must be sure that both theoretical and experimental analyses use the same definition. As we discussed in Chapter 3, one can use a *cone algorithm* based on the energy deposition in an angular region (e.g. the Sterman-Weinberg definition), or a *clustering algorithm* based on combining particle momenta (e.g. the JADE algorithm). For hadron-hadron collisions, the most commonly used definition is of the cone type: a jet is

a concentration of transverse energy  $E_T$  in a ‘cone’ of radius  $R$ , where

$$R = \sqrt{(\Delta\eta)^2 + (\Delta\phi)^2}. \quad (7.19)$$

By defining  $R$  in terms of  $\Delta\eta$  (rather than, say  $\Delta\theta$ ) we obtain a jet measure invariant under longitudinal boosts. In the two-dimensional  $\eta, \phi$  plane, curves of constant  $R$  are circles around the axis of the jet. The cone size  $R$  can be varied and the measured jet cross section will depend on the value chosen. The dependence of the cross section on the value of  $R$  will be discussed in Section 7.8.

## 7.5 Two-jet cross sections

In QCD, two-jet events result when an incoming parton from one hadron scatters off an incoming parton from the other hadron to produce two high-transverse-momentum partons which are observed as jets. From momentum conservation, the two final-state partons are produced with equal and opposite momenta in the subprocess centre-of-mass frame. If only two partons are produced, and the relatively small intrinsic transverse momentum of the incoming partons is neglected, then the two jets will be back-to-back in azimuth and balanced in transverse momentum in the laboratory frame<sup>1</sup>.

For a  $2 \rightarrow 2$  parton scattering process

$$\text{parton}_i(p_1) + \text{parton}_j(p_2) \rightarrow \text{parton}_k(p_3) + \text{parton}_l(p_4), \quad (7.20)$$

described by a matrix element  $\mathcal{M}$ , the parton cross section is

$$\frac{E_3 E_4 d^6 \hat{\sigma}}{d^3 p_3 d^3 p_4} = \frac{1}{2\hat{s}} \frac{1}{16\pi^2} \overline{\sum} |\mathcal{M}|^2 \delta^4(p_1 + p_2 - p_3 - p_4), \quad (7.21)$$

where  $\overline{\sum}$  denotes the average and sum over the initial- and final-state spins and colours respectively. All parton processes which contribute in lowest order can be derived from the diagrams shown in Fig. 7.6 by including other diagrams which are related by crossing. Expressions for the leading-order matrix elements squared  $\overline{\sum} |\mathcal{M}|^2$  are given in Table 7.1, using the notation  $\hat{s} = (p_1 + p_2)^2$ ,  $\hat{t} = (p_1 - p_3)^2$  and  $\hat{u} = (p_2 - p_3)^2$ . To give an idea of the relative importance of these processes (at equal parton luminosities) we also show the values of the invariant matrix elements squared at  $90^\circ$  in the centre of mass ( $\theta^* = \pi/2$ ,  $\hat{t} = \hat{u} = -\hat{s}/2$ ). Processes with initial gluons are more important because of the larger colour charge of the gluons.

---

<sup>1</sup> The intrinsic transverse momentum of the partons will be discussed in Chapter 9.

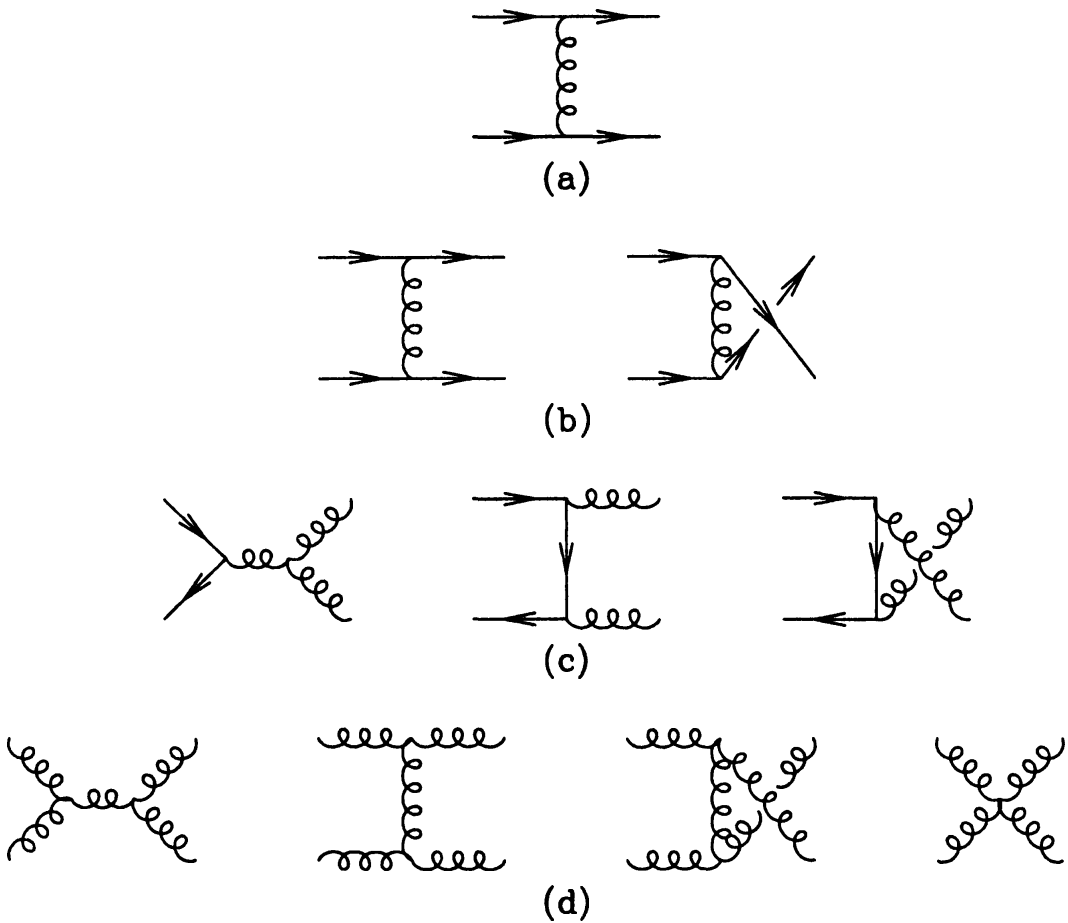


Fig. 7.6. Diagrams for jet production.

The two-jet cross section may be written as a sum of terms each representing the contribution to the cross section from a particular combination of incoming ( $i, j$ ) and outgoing ( $k, l$ ) partons. Using Eq. (7.21), the result for the two-jet inclusive cross section is

$$\frac{d^3\sigma}{dy_3 dy_4 dp_T^2} = \frac{1}{16\pi s^2} \sum_{i,j,k,l=q,\bar{q},g} \frac{f_i(x_1, \mu^2)}{x_1} \frac{f_j(x_2, \mu^2)}{x_2} \times \overline{\sum} |\mathcal{M}(ij \rightarrow kl)|^2 \frac{1}{1 + \delta_{kl}} \quad (7.22)$$

where the  $f_i(x, \mu^2)$  represent the distributions for partons of type  $i$  ( $i = u, \bar{u}, d, \bar{d}, g, \dots$  etc.), evaluated at momentum scale  $\mu$ , and  $y_3$  and  $y_4$  represent the laboratory rapidities of the outgoing partons. The momentum fractions  $x_1, x_2$  are determined by momentum conservation to be

$$x_1 = \frac{1}{2} x_T (e^{y_3} + e^{y_4}), \quad x_2 = \frac{1}{2} x_T (e^{-y_3} + e^{-y_4}) \quad (7.23)$$

where  $x_T = 2p_T/\sqrt{s}$ . For massless partons the rapidity  $y_i$  and pseudorapidity  $\eta_i$  may be used interchangeably, as may the transverse momentum  $p_T$  and transverse energy  $E_T$ . The Kronecker delta symbol introduces the

Process	$\sum  \mathcal{M} ^2/g^4$	$\theta^* = \pi/2$
$q q' \rightarrow q q'$	$\frac{4}{9} \frac{\hat{s}^2 + \hat{u}^2}{\hat{t}^2}$	2.22
$q \bar{q}' \rightarrow q \bar{q}'$	$\frac{4}{9} \frac{\hat{s}^2 + \hat{u}^2}{\hat{t}^2}$	2.22
$q q \rightarrow q q$	$\frac{4}{9} \left( \frac{\hat{s}^2 + \hat{u}^2}{\hat{t}^2} + \frac{\hat{s}^2 + \hat{t}^2}{\hat{u}^2} \right) - \frac{8}{27} \frac{\hat{s}^2}{\hat{u}\hat{t}}$	3.26
$q \bar{q} \rightarrow q' \bar{q}'$	$\frac{4}{9} \frac{\hat{t}^2 + \hat{u}^2}{\hat{s}^2}$	0.22
$q \bar{q} \rightarrow q \bar{q}$	$\frac{4}{9} \left( \frac{\hat{s}^2 + \hat{u}^2}{\hat{t}^2} + \frac{\hat{t}^2 + \hat{u}^2}{\hat{s}^2} \right) - \frac{8}{27} \frac{\hat{u}^2}{\hat{s}\hat{t}}$	2.59
$q \bar{q} \rightarrow g g$	$\frac{32}{27} \frac{\hat{t}^2 + \hat{u}^2}{\hat{t}\hat{u}} - \frac{8}{3} \frac{\hat{t}^2 + \hat{u}^2}{\hat{s}^2}$	1.04
$g g \rightarrow q \bar{q}$	$\frac{1}{6} \frac{\hat{t}^2 + \hat{u}^2}{\hat{t}\hat{u}} - \frac{3}{8} \frac{\hat{t}^2 + \hat{u}^2}{\hat{s}^2}$	0.15
$g q \rightarrow g q$	$-\frac{4}{9} \frac{\hat{s}^2 + \hat{u}^2}{\hat{s}\hat{u}} + \frac{\hat{u}^2 + \hat{s}^2}{\hat{t}^2}$	6.11
$g g \rightarrow g g$	$\frac{9}{2} \left( 3 - \frac{\hat{t}\hat{u}}{\hat{s}^2} - \frac{\hat{s}\hat{u}}{\hat{t}^2} - \frac{\hat{s}\hat{t}}{\hat{u}^2} \right)$	30.4

Table 7.1. The invariant matrix elements squared  $\sum |\mathcal{M}|^2$  for two-to-two parton subprocesses with massless partons [8]. The colour and spin indices are averaged (summed) over initial (final) states.

statistical factor necessary for identical final-state partons. If we assume that the detector and jet algorithm are 100% efficient, the pseudorapidities and transverse energies of the outgoing jets may be identified with those of the outgoing partons at lowest order.

We now consider the kinematics of the two produced jets in detail. The laboratory rapidity ( $\bar{y}$ ) of the two-parton system and the equal and opposite rapidities ( $\pm y^*$ ) of the two jets in the parton-parton centre-of-

mass system are given in terms of the observed rapidities by

$$\bar{y} = (y_3 + y_4)/2, \quad y^* = (y_3 - y_4)/2. \quad (7.24)$$

For a massless parton the centre-of-mass scattering angle  $\theta^*$  is given by

$$\cos \theta^* = \frac{p_z^*}{E^*} = \frac{\sinh y^*}{\cosh y^*} = \tanh \left( \frac{y_3 - y_4}{2} \right). \quad (7.25)$$

Thus a measurement of the difference in rapidity of the two jets in the laboratory frame determines the subprocess centre-of-mass scattering angle.

The longitudinal momentum fractions of the incoming partons  $x_1$  and  $x_2$  in Eq. (7.23) are given in terms of  $p_T$ ,  $y_3$  and  $y_4$ :

$$x_1 = x_T e^{\bar{y}} \cosh y^*, \quad x_2 = x_T e^{-\bar{y}} \cosh y^*, \quad \bar{y} = \frac{1}{2} \ln(x_1/x_2). \quad (7.26)$$

Finally, the invariant mass of the jet-jet system can be written as

$$M_{JJ}^2 = \hat{s} = 4p_T^2 \cosh^2 y^*. \quad (7.27)$$

Given a knowledge of the parton distributions from deep inelastic scattering experiments, Eq. (7.22) may be used to make leading-order QCD predictions for jet production in hadron-hadron collisions. For example, the inclusive jet cross section at the parton level may be obtained by integrating Eq. (7.21) over the momentum of one of the jets:

$$\frac{Ed^3\hat{\sigma}}{d^3p} \equiv \frac{d^3\hat{\sigma}}{dyd^2p_T} = \frac{1}{2\hat{s}} \frac{1}{8\pi^2} \sum |M|^2 \delta(\hat{s} + \hat{t} + \hat{u}), \quad (7.28)$$

where  $\hat{t}$  and  $\hat{u}$  are fixed by  $\hat{s}$  and the centre-of-mass scattering angle,

$$\hat{t} = -\frac{1}{2}\hat{s}(1 - \cos \theta^*), \quad \hat{u} = -\frac{1}{2}\hat{s}(1 + \cos \theta^*). \quad (7.29)$$

Again assuming that the detector and jet algorithm are 100% efficient, so that  $p_J^\mu = p_{\text{parton}}^\mu$ , the single-jet inclusive cross section is obtained from Eq. (7.28) by folding in the parton distribution functions:

$$\begin{aligned} \frac{E_J d^3\sigma}{d^3p_J} &= \frac{1}{16\pi^2 s} \sum_{i,j,k,l=q,g} \int_0^1 \frac{dx_1}{x_1} \frac{dx_2}{x_2} f_i(x_1, \mu^2) f_j(x_2, \mu^2) \\ &\times \overline{\sum} |M(ij \rightarrow kl)|^2 \frac{1}{1 + \delta_{kl}} \delta(\hat{s} + \hat{t} + \hat{u}). \end{aligned} \quad (7.30)$$

We emphasize that this result corresponds to massless quarks and gluons and that no distinction is made between quark and gluon jets.

## 7.6 Comparison with experiment

Although large- $p_T$  jet production has been studied at different particle accelerators over a period of many years, the definitive data are from the

high-energy  $p\bar{p}$  colliders, *i.e.* from the UA1 and UA2 collaborations at the CERN  $Spp\bar{S}$  collider ( $\sqrt{s} = 546$  GeV and 630 GeV) and from the CDF and D0 collaborations at the FNAL Tevatron collider ( $\sqrt{s} = 1.8$  TeV). It appears that only at these very high collision energies does the identification and measurement of large- $p_T$  jets become relatively unambiguous. At lower energies it is difficult to separate the jets from the other ‘underlying’ hadrons in the event. Early searches for jets also suffered from what is called ‘trigger bias’. In order to look for jets one selects experimentally events with high-momentum tracks. Momentum balance then dictates that there will be tracks elsewhere in the event which display a jet-like structure. The solution is to implement a trigger which does not bias one to a particular shape of event. One possibility, which does not bias one to a particular shape of event, is to require a minimum value for the total transverse energy.

Two quantities are particularly useful for comparing theory with experiment. The first is the jet  $p_T$  distribution, obtained from the inclusive cross section by

$$\frac{Ed^3\sigma}{d^3p} \equiv \frac{d^3\sigma}{d^2p_T dy} \rightarrow \frac{1}{2\pi E_T} \frac{d^2\sigma}{dE_T d\eta}, \quad (7.31)$$

where the third expression follows if we assume that the jets are approximately massless.

Fig. 7.7 shows the jet  $E_T$  distribution averaged over the rapidity range  $0.1 < |\eta| < 0.7$ , measured in  $p\bar{p}$  collisions at  $\sqrt{s} = 1.8$  TeV. The points are taken from a data sample corresponding to an integrated luminosity of  $19.5 \text{ pb}^{-1}$ . The curve is the QCD prediction, calculated in next-to-leading order (*i.e.*  $O(\alpha_S^3)$ ) [10,11] and using the MRS(D0) parton distributions from ref. [12]. The next-to-leading-order contributions considerably reduce the dependence on the scale parameter  $\mu$ , and allow a more precise treatment of effects due to the finite width of the jet.

Below  $E_T = 200$  GeV the agreement in Fig. 7.7 is excellent, especially considering that there are essentially no free parameters in the theoretical prediction. The data and the theory agree over six orders of magnitude. However for  $E_T > 200$  GeV the CDF data lie slightly above the theoretical prediction. A similar discrepancy is found when other parton distributions are used, reflecting the fact that the high  $E_T$  jets are predominantly produced using the well-measured quark distributions. The fraction of the cross section coming from the various sub-processes is illustrated in Fig. 7.8. Gluon-gluon scattering is important at low  $E_T$ . Quark-(anti)quark scattering is important at the high  $E_T$  end, but it does not overwhelm the gluon-quark scattering contribution, which is important in all regions.

Since Fig. 7.7 shows the statistical errors only, we must first discuss the

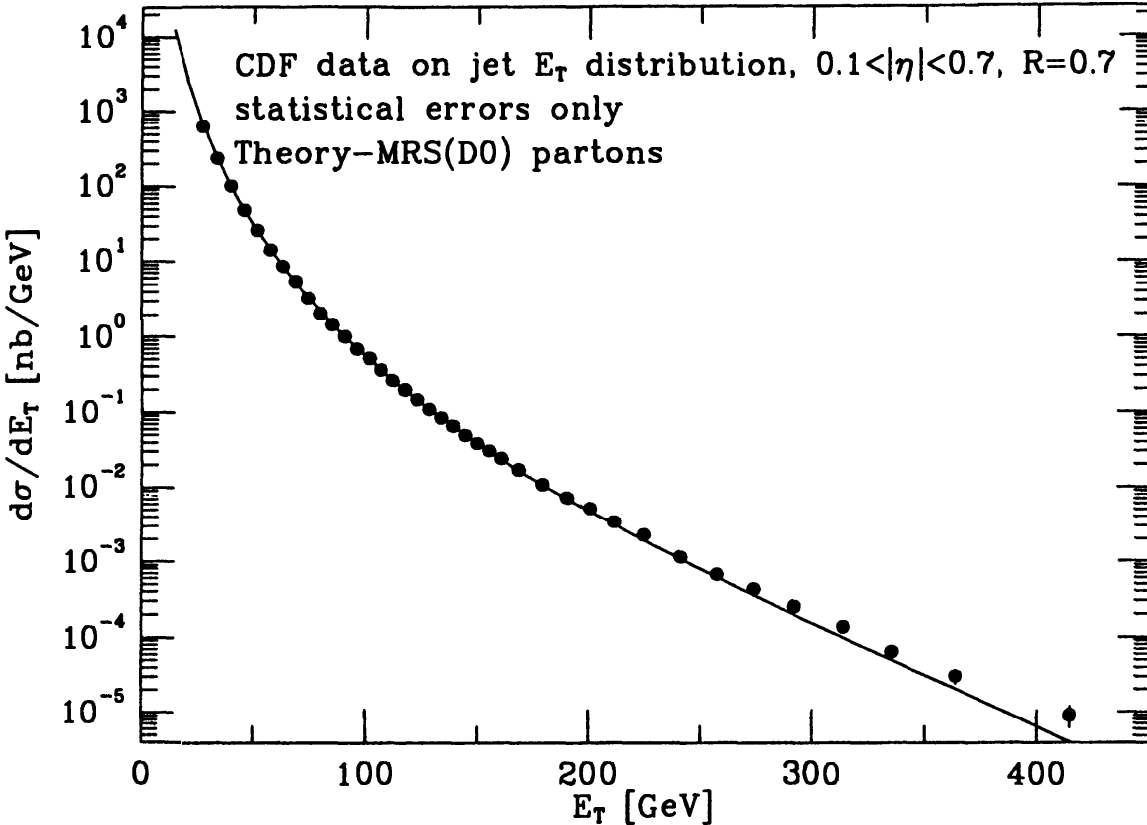


Fig. 7.7. Jet  $E_T$  distribution from the CDF collaboration [9], compared with a next-to-leading order QCD prediction from ref. [11].

systematic errors before concluding that this discrepancy is significant. The systematic errors are large (between 50% and 75%) [9]. Notice that with a steeply falling distribution a small change in the energy scale can produce a large change in the cross section. However the systematic errors are correlated, and therefore it is hard to envisage a systematic error which will correct the discrepancy at large  $E_T$  without destroying the agreement at smaller  $E_T$ . A similar measurement by the D0 collaboration [13] does not show an excess at large  $E_T$ , although the size of the systematic errors does not allow one to conclude that there is a discrepancy between the two data sets.

Events at large  $E_T$  correspond to scattering at the shortest distance scale ever probed in the laboratory ( $d \sim 10^{-18}$ m). An excess of events would be very exciting and could be an indication of quark substructure or other non-Standard Model physics. At the time of writing it is too early to say.

The second quantity of interest is the jet angular distribution. In the parton-parton centre of mass, the angular distribution is sensitive to the form of the  $2 \rightarrow 2$  matrix elements. The differential cross section for a jet pair of mass  $M_{JJ}$  produced at an angle  $\theta^*$  to the beam direction in the

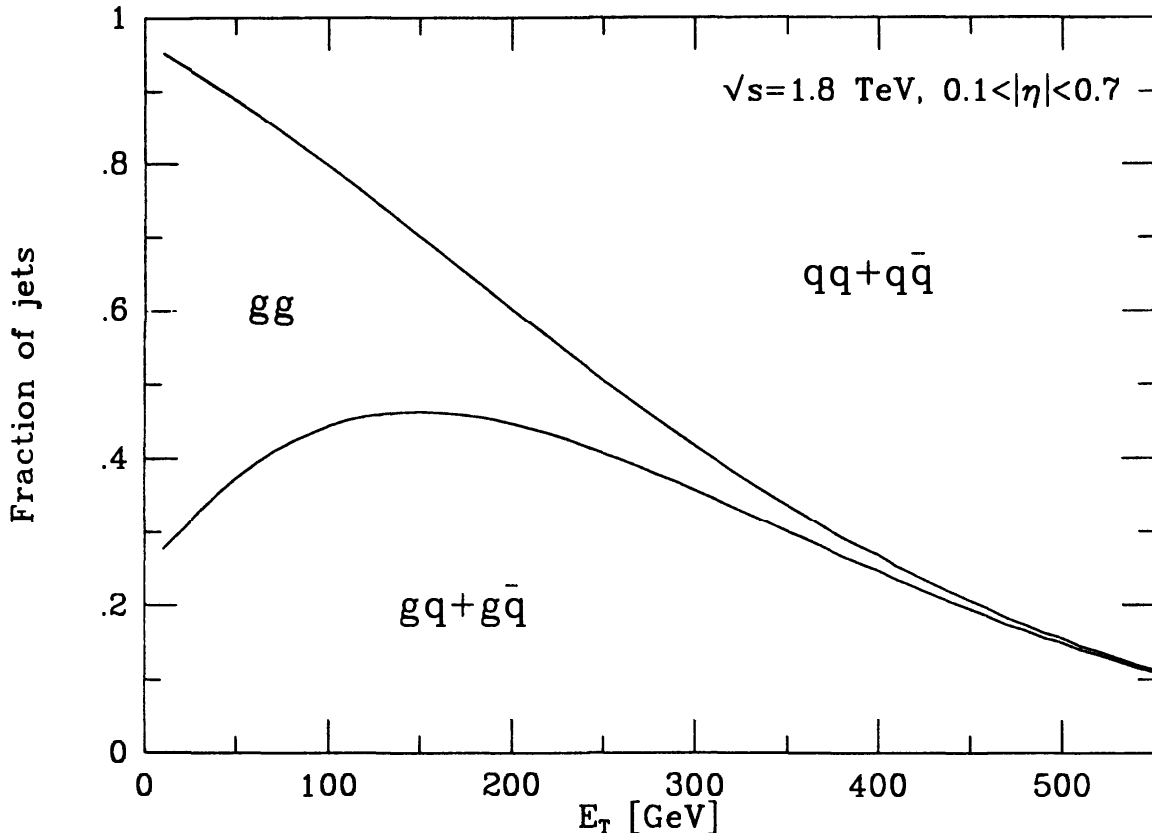


Fig. 7.8. Plot showing the fraction of the jet  $E_T$  distribution initiated by different parton combinations.

jet-jet centre of mass can readily be obtained from Eq. (7.22) using the transformation

$$dp_T^2 dy_3 dy_4 \equiv \frac{1}{2} s dx_1 dx_2 d \cos \theta^* \quad (7.32)$$

to give

$$\begin{aligned} & \frac{d^2\sigma}{dM_{JJ}^2 d \cos \theta^*} \\ &= \sum_{i,j=q,\bar{q},g} \int_0^1 dx_1 dx_2 f_i(x_1, \mu^2) f_j(x_2, \mu^2) \delta(x_1 x_2 s - M_{JJ}^2) \frac{d\hat{\sigma}^{ij}}{d \cos \theta^*} \\ &= \sum_{\{ij\}} \frac{\tau_J}{s} \frac{dL_{ij}(\tau_J, \mu^2)}{d\tau_J} \frac{d\hat{\sigma}^{ij}}{d \cos \theta^*}, \end{aligned} \quad (7.33)$$

with  $\tau_J = M_{JJ}^2/s$  and

$$\frac{d\hat{\sigma}^{ij}}{d \cos \theta^*} = \sum_{k,l} \frac{1}{32\pi M_{JJ}^2} \overline{\sum} |\mathcal{M}(ij \rightarrow kl)|^2 \frac{1}{1 + \delta_{kl}}. \quad (7.34)$$

Note that for each subprocess  $d\hat{\sigma}/d \cos \theta^*$  is symmetrized in  $\hat{t}$  and  $\hat{u}$  (unless

$k \equiv l$ ). Thus, for example, from Table 7.1 we have

$$\frac{d\hat{\sigma}^{ud}}{d\cos\theta^*} = \frac{\pi\alpha_s^2}{2M_{JJ}^2} \frac{4}{9} \left[ \frac{4 + (1 + \cos\theta^*)^2}{(1 - \cos\theta^*)^2} + \frac{4 + (1 - \cos\theta^*)^2}{(1 + \cos\theta^*)^2} \right]. \quad (7.35)$$

Numerically, the most important subprocesses for a  $p\bar{p}$  collider are  $gg \rightarrow gg$ ,  $gq \rightarrow gq$  and  $q\bar{q} \rightarrow q\bar{q}$ . For each of these, the  $\theta^*$  distributions have the familiar Rutherford scattering behaviour at small angle, characteristic of the exchange of a massless vector boson in the  $t$ -channel:

$$\frac{d\hat{\sigma}}{d\cos\theta^*} \sim \frac{1}{\sin^4(\theta^*/2)}. \quad (7.36)$$

To study deviations from this behaviour it is convenient to plot the data in terms of the variable  $\chi$ , which removes the Rutherford singularity [16],

$$\chi = \frac{1 + \cos\theta^*}{1 - \cos\theta^*}. \quad (7.37)$$

In the small angle limit ( $\chi \rightarrow \infty$ ) the cross section differential in  $\chi$  is then

$$\frac{d\hat{\sigma}}{d\chi} \sim \text{constant}, \quad (7.38)$$

if we ignore the angular dependence in the coupling constant and the parton distributions. Data on the jet-jet angular distribution are shown in Fig. 7.9 together with theoretical predictions. The full prediction in the absence of scaling violation, indicated by a dotted curve in Fig. 7.9, is unable to explain the data. The data are even more peaked in the forward direction than Eq. (7.36). The next-to-leading QCD prediction [15] which includes scaling violation in the coupling constant and the parton distributions, provides an adequate description of the data.

Note that these data automatically rule out certain other quark scattering mechanisms. For example, a model in which quarks scatter by exchanging a *scalar* gluon would give

$$\frac{d\hat{\sigma}}{d\cos\theta^*} \sim \text{constant}, \quad \frac{d\hat{\sigma}}{d\chi} \sim \frac{1}{(1 + \chi)^2}. \quad (7.39)$$

It is also interesting to note that the angular dependences of the dominant subprocesses are very similar. Fig. 7.10 shows the  $\cos\theta^*$  dependence of the  $qg \rightarrow qg$  and  $q\bar{q} \rightarrow q\bar{q}$  subprocesses normalized to  $gg \rightarrow gg$ . These ratios are evidently almost constant at the numerical values  $4/9$  and  $(4/9)^2$  respectively. This can be understood in terms of the colour structure of the Feynman diagrams and by looking at Table 7.1. Thus to a good approximation the  $gg \rightarrow gg$  subprocess can be used as the ‘universal’ subprocess in the result given in Eq. (7.33), *i.e.* the angular dependence effectively factors out leaving a convolution of parton distributions. This

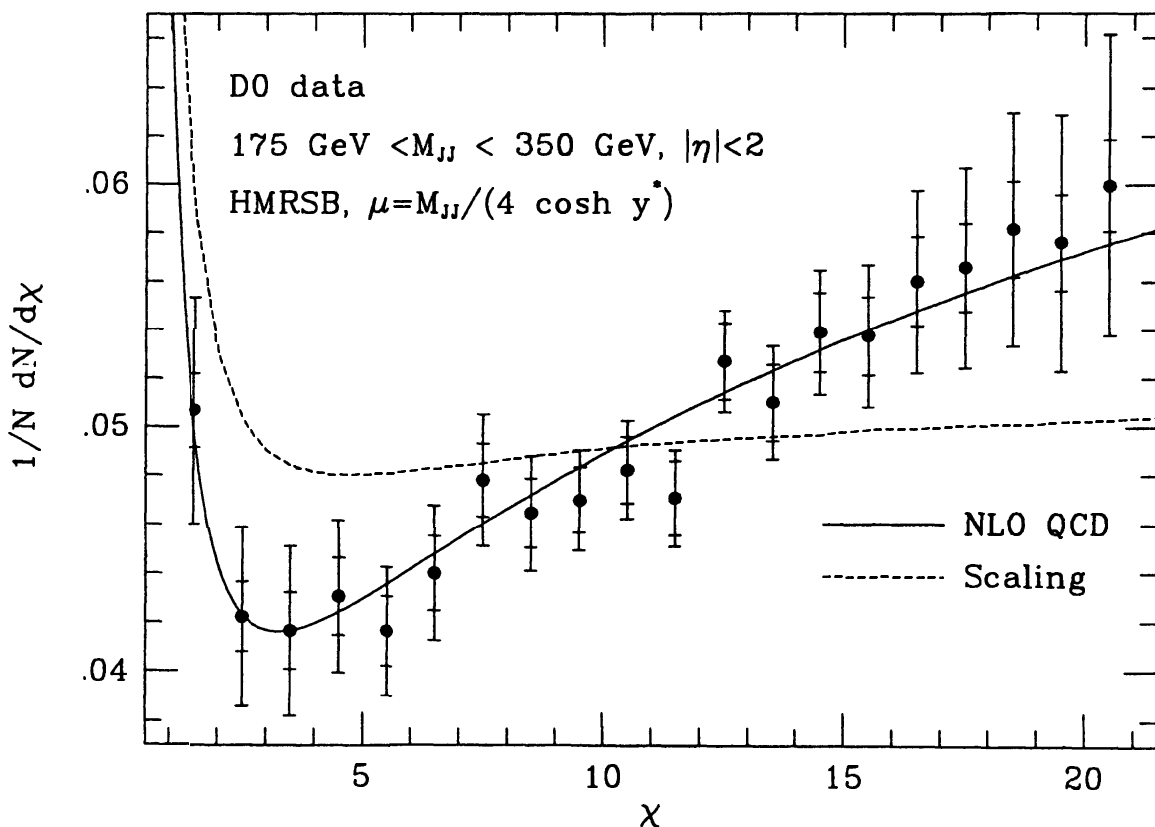


Fig. 7.9. Distribution of  $\chi$  from the D0 collaboration [14] compared with QCD predictions [15].

is called the *single effective subprocess approximation* [16]. In terms of the single effective structure function

$$S(x, \mu^2) = g(x, \mu^2) + \frac{4}{9} [q(x, \mu^2) + \bar{q}(x, \mu^2)], \quad (7.40)$$

the jet cross section is given by

$$\begin{aligned} \frac{d^2\sigma}{dM_{JJ}^2 d\cos\theta^*} &\approx \int_0^1 dx_1 dx_2 S(x_1, \mu^2) S(x_2, \mu^2) \\ &\times \delta(x_1 x_2 s - M_{JJ}^2) \frac{d\hat{\sigma}^{gg}}{d\cos\theta^*}. \end{aligned} \quad (7.41)$$

## 7.7 Multijet production

As long as the jets are required to be well separated in phase space, multijet cross sections can be calculated from scattering processes involving many quarks and gluons in the final state. This is a straightforward generalization of the procedure for  $e^+e^-$  annihilation explained in Chapter 3. In this way one defines an  $n$ -jet cross section  $\sigma^n$  for producing  $n$  jets which satisfy, say,  $p_T^i > p_{T\min}$ ,  $|\eta^i| < \eta_{\max}$  and  $R_{ij} > R_{\min}$  for  $i, j = 1, \dots, n$ . In

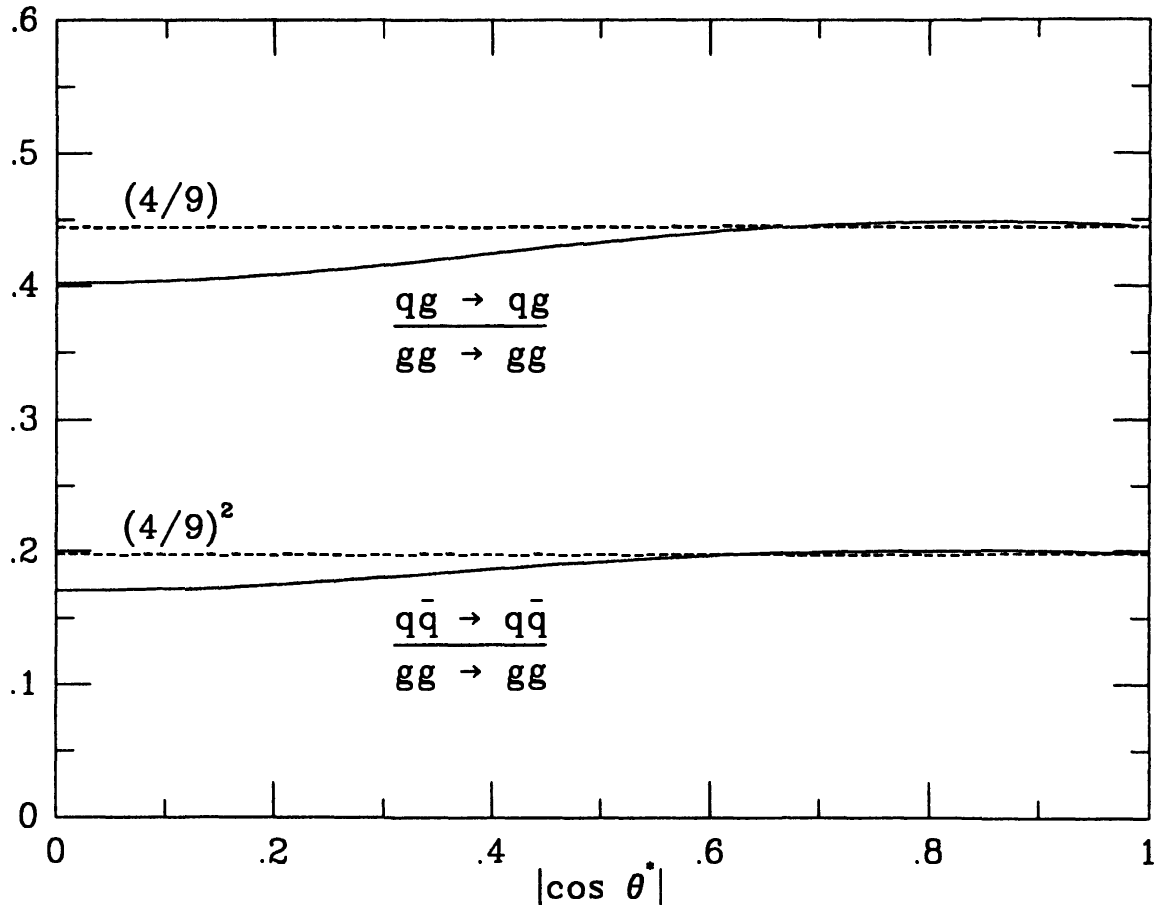


Fig. 7.10. Quark-antiquark and quark-gluon angular distributions, normalized to that for  $gg \rightarrow gg$ .

leading-order QCD, these cross sections are calculated at the parton level from ‘tree-level’ Feynman diagrams, *i.e.* diagrams without any internal loops. The general expression is again obtained from Eq. (7.1):

$$\sigma^n = \sum_{i,j,k_1,\dots,k_n=q,\bar{q},g} \int_0^1 dx_1 dx_2 f_i(x_1, \mu^2) f_j(x_2, \mu^2) \hat{\sigma}^{ij \rightarrow k_1, \dots, k_n}. \quad (7.42)$$

The leading-order matrix elements for all the  $2 \rightarrow 2, 3, 4, 5$  processes are known [17]. Since each  $n$ -jet cross section is proportional to  $\alpha_S^n$ , the cross sections fall roughly geometrically with increasing  $n$ .

Events with three jets at large transverse energy are described in QCD by amplitudes with two incoming partons and three outgoing partons. Compact expressions for all the two-to-three parton scattering processes have been given by Berends *et al.* [18]. For a complete description it is sufficient to consider the following four processes:

- (A)  $q(p_1) + q'(p_2) \rightarrow q(p_3) + q'(p_4) + g(k)$
- (B)  $q(p_1) + q(p_2) \rightarrow q(p_3) + q(p_4) + g(k)$

$$(C) \quad q(p_a) + \bar{q}(p_b) \rightarrow g(p_1) + g(p_2) + g(p_3) \\ (D) \quad g(p_1) + g(p_2) \rightarrow g(p_3) + g(p_4) + g(p_5). \quad (7.43)$$

The momentum assignments for the partons are given in brackets. All other matrix elements for two-to-three parton amplitudes may be obtained by crossing from the above four processes.

The matrix elements squared for the processes (*A* – *D*), after averaging (summing) over the initial (final) colours and spins are given below. We have set the masses of the quarks equal to zero. With the momentum assignments of Eq. (7.43) the matrix element for process (*A*) is [19]

$$\overline{\sum} |\mathcal{M}^{(A)}|^2 = \frac{g^6 C_F}{N} \left( \frac{s^2 + s'^2 + u^2 + u'^2}{2tt'} \right) \left( 2C_F ([14] + [23]) + \frac{1}{N} [12; 34] \right). \quad (7.44)$$

Throughout this section, the dependence on the SU(*N*) colour group is shown explicitly ( $C_A = N = 3$ ,  $C_F = 4/3$ ). The kinematic variables are defined as follows:

$$s = (p_1 + p_2)^2, \quad t = (p_1 - p_3)^2, \quad u = (p_1 - p_4)^2, \\ s' = (p_3 + p_4)^2, \quad t' = (p_2 - p_4)^2, \quad u' = (p_2 - p_3)^2. \quad (7.45)$$

For compactness of notation we have introduced the eikonal factor  $[ij]$ , which is defined as

$$[ij] = \frac{\mathbf{p}_i \cdot \mathbf{p}_j}{\mathbf{p}_i \cdot \mathbf{k} \mathbf{k} \cdot \mathbf{p}_j}. \quad (7.46)$$

The origin of these factors has been described in Section 5.5. We have also defined the following sum of eikonal terms:

$$[12; 34] = 2[12] + 2[34] - [13] - [14] - [23] - [24]. \quad (7.47)$$

Note that, in the limit that the four-vector  $\mathbf{k}$  is parallel to  $\mathbf{p}_i$ , the coefficient of the denominator  $\mathbf{p}_i \cdot \mathbf{k}$  is equal to zero for all  $i$  in the sum of terms given in Eq. (7.47). This combination is therefore free from collinear singularities. In addition, it appears in Eq. (7.44) suppressed by a colour factor  $1/N$  relative to the other terms, making it numerically small throughout phase space. For this reason such terms can usually be neglected in phenomenological applications, such as Monte Carlo programs.

In the same notation, the result for process (*B*) with four identical quarks may be written [19]

$$\overline{\sum} |\mathcal{M}^{(B)}|^2 = \frac{g^6 C_F}{N} \left[ \left( \frac{s^2 + s'^2 + u^2 + u'^2}{2tt'} \right) \left( 2C_F ([14] + [23]) + \frac{1}{N} [12; 34] \right) \right]$$

$$\begin{aligned}
& + \left( \frac{s^2 + s'^2 + t^2 + t'^2}{2uu'} \right) \left( 2C_F ([13] + [24]) + \frac{1}{N} [12; 34] \right) \\
& - \frac{2}{N} \frac{(s^2 + s'^2)(ss' - tt' - uu')}{4tt'u'u'} \left( 2C_F ([12] + [34]) + \frac{1}{N} [12; 34] \right) .
\end{aligned} \tag{7.48}$$

To write the results for the remaining two processes, we introduce a compact notation for the dot product of two four-momenta,

$$\{ij\} \equiv p_i \cdot p_j . \tag{7.49}$$

Using the momentum assignments of Eq. (7.43) the result for process (C) may be written as [18]

$$\begin{aligned}
\overline{\sum} |\mathcal{M}^{(C)}|^2 = & \frac{g^6(N^2 - 1)}{4N^4} \sum_{i=1}^3 \frac{\{ai\}\{bi\}(\{ai\}^2 + \{bi\}^2)}{\{a1\}\{a2\}\{a3\}\{b1\}\{b2\}\{b3\}} \\
& \times \left[ (N^2 + 1)\{ab\} - N^2 \sum_P \frac{\{a1\}\{b2\} + \{a2\}\{b1\}}{\{12\}} \right. \\
& \left. + \frac{N^4}{\{ab\}} \sum_P \frac{\{a3\}\{b3\}(\{a1\}\{b2\} + \{a2\}\{b1\})}{\{23\}\{31\}} \right] .
\end{aligned} \tag{7.50}$$

The sums run over the three cyclic permutations  $P$  of the momentum labels of the final-state gluons.

Using the momentum labels of Eq. (7.43) the result for process (D) is [18]

$$\begin{aligned}
\overline{\sum} |\mathcal{M}^{(D)}|^2 = & \frac{g^6 N^3}{240(N^2 - 1)} \left[ \sum_P \{12\}^4 \right] \left[ \sum_P \{12\}\{23\}\{34\}\{45\}\{51\} \right] \\
& \times \left( \prod_{i < j} \{ij\} \right)^{-1} .
\end{aligned} \tag{7.51}$$

The sums run over the 120 permutations of the momentum labels.

These matrix elements display the typical bremsstrahlung structure with the emission of soft and collinear gluons predominating. This is particularly clear from the form of the result given in Eqs. (7.44) and (7.48) where the dominant contributions come from the region in which the eikonal factors are large. From the tree-level Feynman diagrams one can also show that the same effective structure function which is relevant for two-jet production, Eq. (7.40), is also valid to a very good approximation for three-jet production [20].

We now turn to the comparison of these results with experimental data. For three final-state (massless) partons the final-state parton configuration, at fixed centre-of-mass energy, is specified by five independent variables. Two variables are required to specify how the available energy is

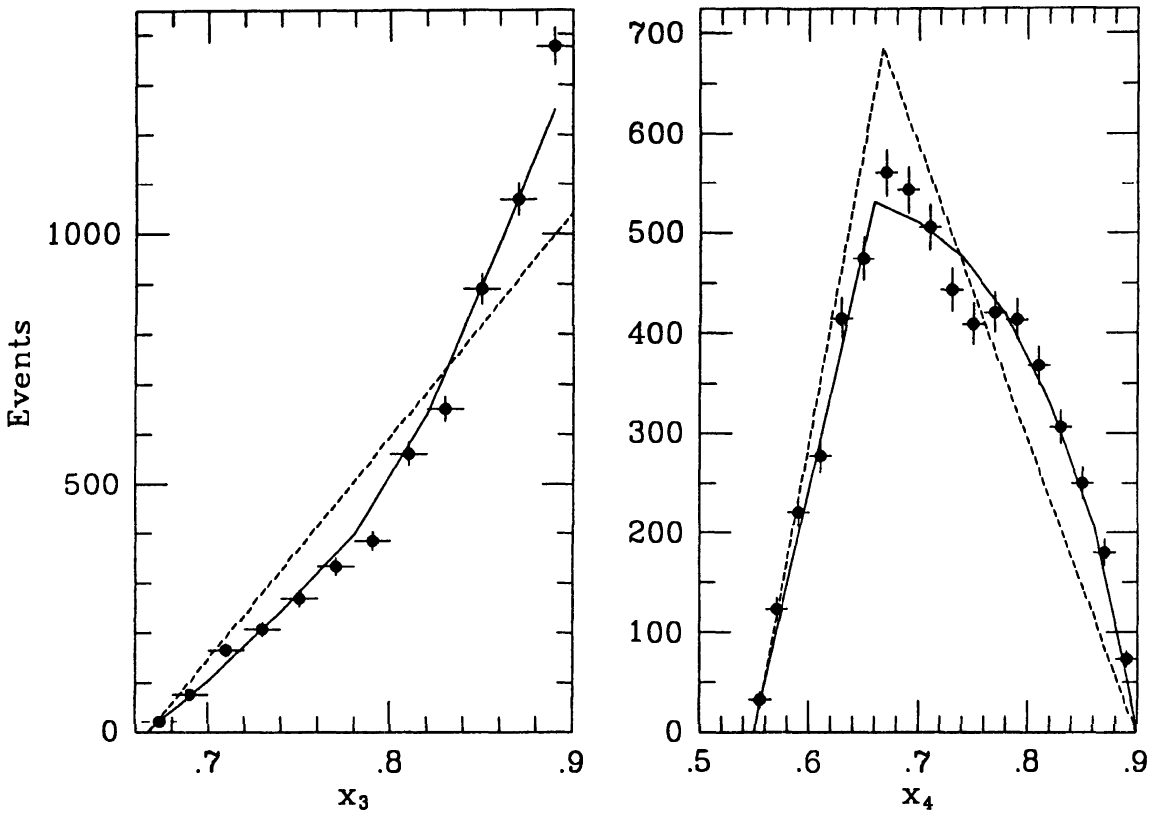


Fig. 7.11. Distribution in the variable  $x_3$  and  $x_4$  in a sample of three jet events, as measured by the CDF collaboration [21]. The solid and dashed lines are the predictions from QCD and phase space respectively.

shared between the three final-state partons, and two variables serve to fix the orientation of the three-jet system with respect to the axis defined by the colliding partons. The last variable is an overall azimuthal angle. If  $x_3$ ,  $x_4$ , and  $x_5$  are the energies of the outgoing partons, scaled such that  $x_3 + x_4 + x_5 = 2$  and ordered such that  $x_3 > x_4 > x_5$ , and  $\theta_i$  is the angle between parton  $i$  and the beam direction, then the subprocess differential cross section can be written using the three-particle massless phase space of Eq. (3.9):

$$\frac{d^4\hat{\sigma}}{dx_3 dx_4 d \cos \theta_1 d\psi} = \frac{1}{1024\pi^4} \overline{\sum} |\mathcal{M}|^2. \quad (7.52)$$

In Eq. (7.52) the variable  $\psi$  is the angle between the plane containing jet-2 and jet-3 and the plane containing jet-1 and the axis defined by the incoming partons.

There is again excellent agreement between the above theoretical predictions and the experimental data. As an example, Fig. 7.11 shows the distribution in the variable  $x_3$  measured by the CDF collaboration. The solid line is the prediction from QCD, based on the tree-level  $2 \rightarrow 3$  parton scattering amplitudes, and the dashed line is the prediction from

phase space alone. The data clearly favour the former. Next-to-leading (*i.e.*  $O(\alpha_S^4)$ ) corrections to the  $2 \rightarrow 3$  parton scattering amplitudes have also been calculated [22]. Since the  $2 \rightarrow 4$  parton scattering amplitudes are also known [17] it is now possible to make predictions for three jet cross sections at next-to-leading order.

Multijet cross sections with 2, 3, 4, 5 and 6 jets have been measured and compared to QCD predictions [23]. These processes are also important because they provide backgrounds to many of the signals for new particle production. For example, QCD four-jet production is a background to one of the decays of the Higgs boson,  $H \rightarrow W^+W^- \rightarrow 4$  jets (see Chapter 11).

### 7.8 Jet profiles

As emphasized earlier, the precise value of a jet cross section depends on the jet definition: in particular it depends on the cone size  $R$  defined in Eq. (7.19). The use of slightly different cone algorithms hinders the comparison of jet cross sections from different experiments and the comparison of experiment with theory. For this reason a standard cone algorithm<sup>2</sup> has been proposed in ref. [24]. In this algorithm the transverse energy, pseudorapidity and azimuth of the jet are calculated by performing energy weighted sums over the particles or calorimeter towers contained within a cone of radius  $R$ ,

$$\begin{aligned} E_T &= \sum_{i \in R} E_{Ti}, \\ \eta_{\text{jet}} &= \frac{1}{E_T} \sum_{i \in R} E_{Ti} \eta_i, \\ \phi_{\text{jet}} &= \frac{1}{E_T} \sum_{i \in R} E_{Ti} \phi_i. \end{aligned} \quad (7.53)$$

The choice  $R = 0.7$  is recommended in this standard algorithm.

The CDF data on the cone size dependence are shown, together with various theoretical predictions, in Fig. 7.12. The cross section increases as the cone is enlarged. This feature is first present in the theory at next-to-leading order. At lowest order a parton is identified with a jet; it is only when one has additional radiation which can fall either inside or outside the cone that the theoretical cross section depends on the cone size. In the small- $R$  limit and in next-to-leading order the theoretical cross section depends logarithmically on  $R$  as  $R \rightarrow 0$  (similar to the behaviour of the  $e^+e^-$  Sterman-Weinberg jet cross section, Eq. (3.32), in

---

<sup>2</sup> This proposal, known as the ‘Snowmass accord’, is more honoured in the breach than the observance.

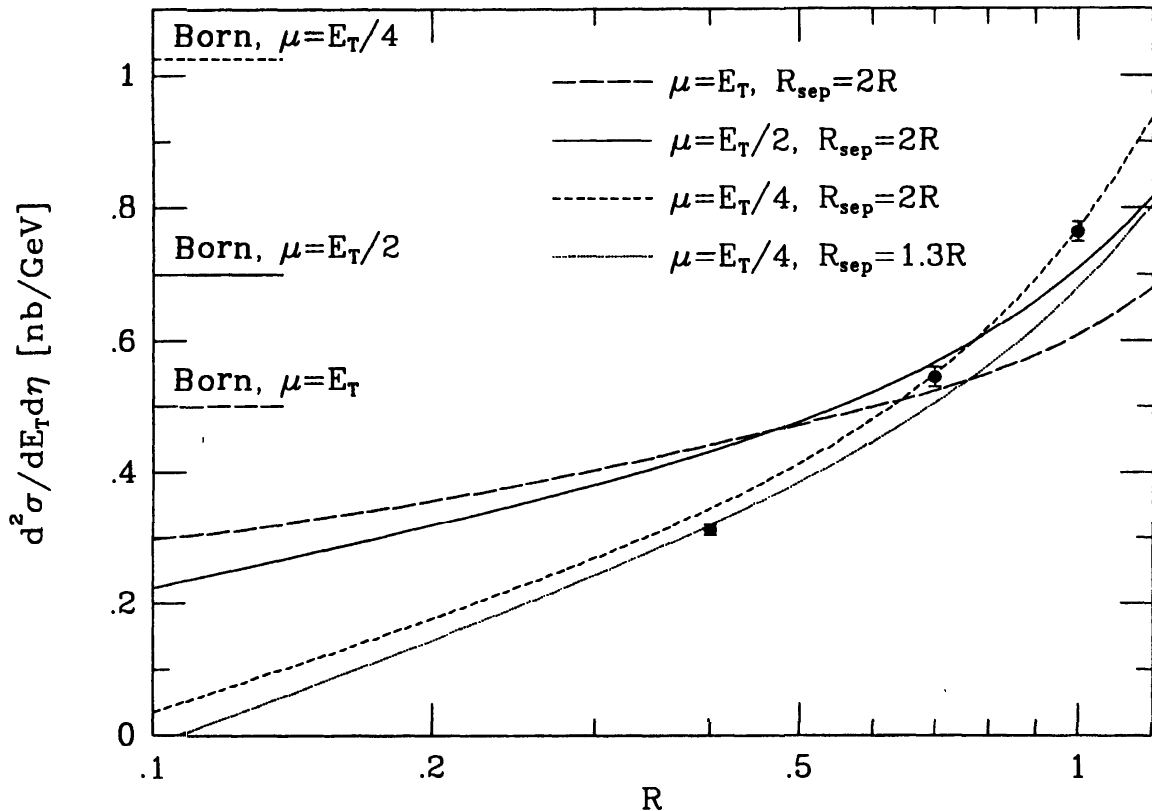


Fig. 7.12. Jet cross section at  $\sqrt{s} = 1800$  GeV,  $E_T = 100$  GeV and  $0.1 < |\eta| < 0.7$  versus cone size  $R$ : data from the CDF collaboration [25], compared with QCD predictions [15]. The cross section in the Born approximation for the three choices of scale is shown on the left of the plot. Adapted from ref. [15].

the limit  $\delta \rightarrow 0$ ). The curves show the Born and next-to-leading-order predictions for different choices of the renormalization and factorization scale  $\mu$ . Note that the scale dependence of the higher-order prediction is weak for  $R = 0.7$ , the value used for the comparison of  $E_T$  dependence in Fig. 7.7. The additional parameter  $R_{\text{sep}}$  in Fig. 7.12 is related to the criterion for jet merging in the particular jet algorithm used by the CDF collaboration. If two jets have a large enough angular separation, there is a dip in the  $E_T$  distribution between them and they are resolved by the CDF algorithm as distinct jets, even though they may have separation less than  $2R$  and would therefore fit within a single cone. This is simulated in the theoretical calculation by merging partons only if they have separation  $R_{ij} < R_{\text{sep}}$ . Then  $R_{\text{sep}} = 2R$  corresponds to the basic cone algorithm, with no special criterion for merging. From Fig. 7.12 we see that the theoretical cross section is not very sensitive to  $R_{\text{sep}}$ . A value less than  $2R$  is favoured for small cone sizes.

In addition to the cone size dependence, one can study the jet profile as measured by the transverse energy flow within the cone. At next-to-leading order the energy profile of a jet is modelled by a pair of partons.

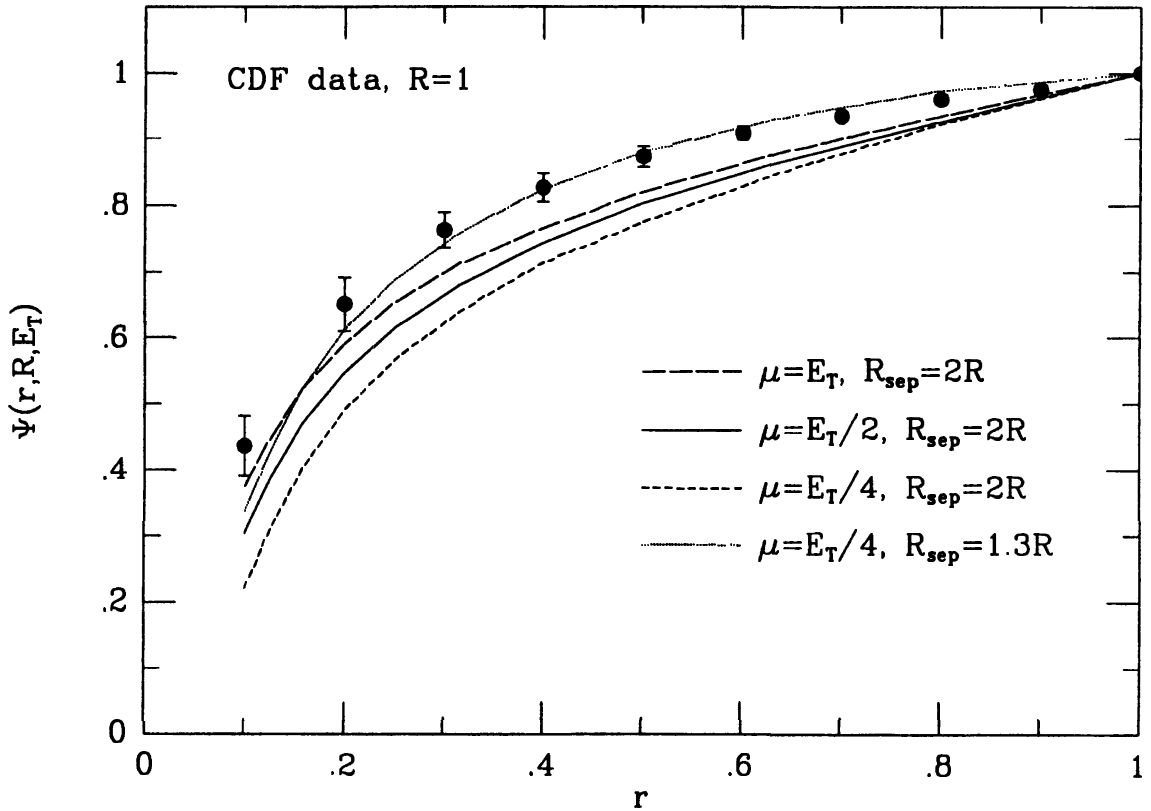


Fig. 7.13. Jet profile  $\Psi(r, R, E_T)$  versus inner cone size  $r$  at  $R = 1$  and  $E_T = 100$  GeV: data from the CDF collaboration [26] compared with QCD predictions [15].

Since the dependence on the cone size appears first at this order it is a leading-order prediction for the energy profile. Consequently the theoretical prediction has a strong dependence on the renormalization scale. In addition because in  $O(\alpha_s^3)$  the theoretical jet is made of at most two partons, there is a strong dependence of the prediction for the jet profile on the details of the jet algorithm. Because of these limitations, there is not yet a fully satisfactory quantitative description of the profiles of jets in next-to-leading-order QCD.

Fig. 7.13 shows the fractional  $E_T$  profile  $\Psi(r, R, E_T)$ , defined as the average fraction of the jet transverse energy that lies inside a coaxial inner cone of radius  $r < R$ . Not surprisingly, since we are asking a more detailed question, the theoretical result is more sensitive to the details of the cone algorithm. Here a smaller value of  $R_{\text{sep}}$  is definitely preferred: the data points are systematically above the predictions obtained with an unmodified cone algorithm, corresponding to a greater concentration of energy near the jet core, but agree well with  $R_{\text{sep}} = 1.3$ .

Fig. 7.14 shows the jet profile for jets in two different  $E_T$  ranges. At fixed value of  $r$ , the function  $\Psi$  grows as a function of  $E_T$ , indicating that a greater fraction of the energy of the jet lies in the sub-cone of radius  $r$ .

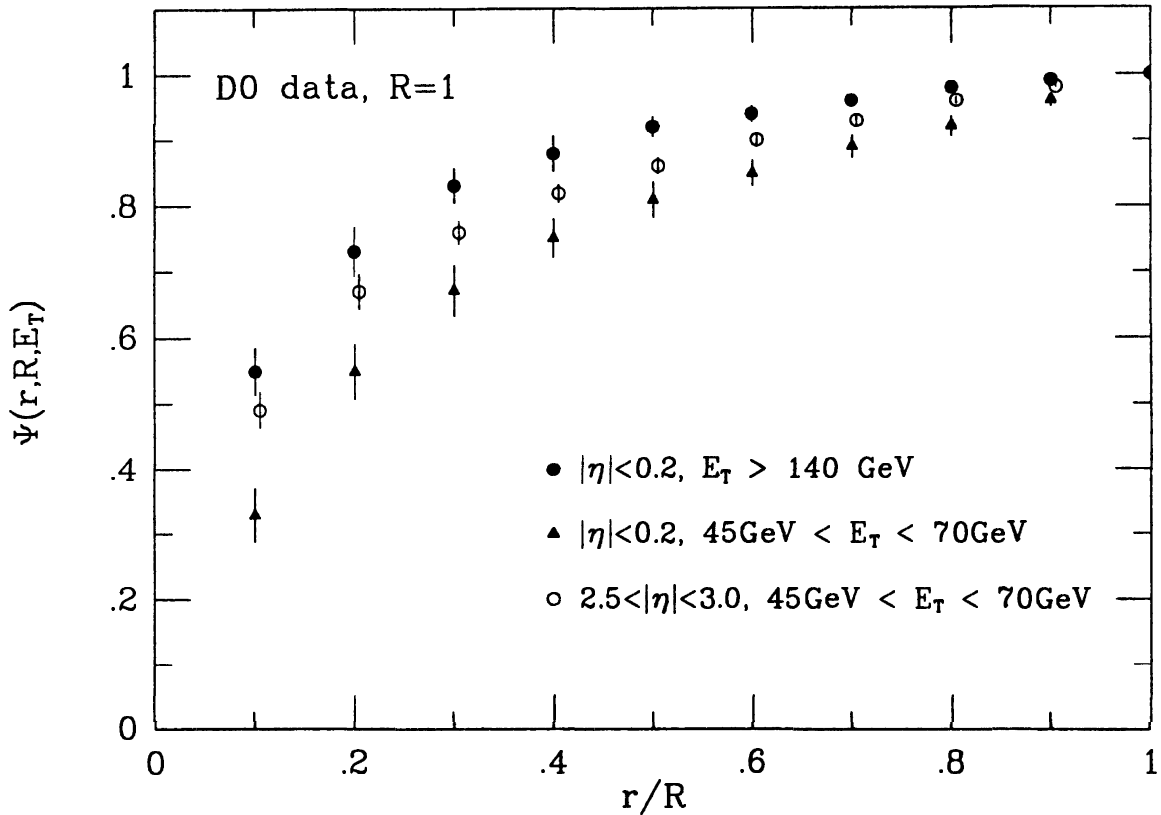


Fig. 7.14. Energy flow profiles of central and forward jets, as measured by the D0 collaboration [28].

Jets therefore become narrower with increasing  $E_T$ .

Interesting results have been obtained from comparisons of jet profiles in  $e^+e^-$  and  $p\bar{p}$  collisions. For this purpose the OPAL collaboration [27] have applied a cone algorithm, essentially identical to that used by the Tevatron  $p\bar{p}$  collider experiments [26,28], to their  $e^+e^-$  data. The results are shown in Fig. 7.15. Here  $\Psi(r)$  is the transverse energy fraction lying in a sub-cone of size  $r < R$ ,  $\Psi(r, R, E_T)$ , averaged over  $E_T > 35$  GeV at  $R = 1$ . We see that the  $e^+e^-$  jet profile falls less steeply than the  $p\bar{p}$  one: the  $e^+e^-$  jets are narrower. This is qualitatively as expected, since the  $p\bar{p}$  jets at these relatively low  $E_T$  values are mostly gluon jets, which, as discussed in Section 6.4, should be broader than the  $e^+e^-$  quark jets.

Some support for this interpretation of Fig. 7.15 is provided by data from the D0 collaboration [28] on the comparative profiles of forward and central jets (Fig. 7.14). In the forward directions, hard collisions involving high- $x$  constituents of the incoming hadrons are selected, and these tend to be quarks more often than the lower- $x$  constituents involved in central collisions (see Eq. (7.26)). Thus a narrower profile would be expected for forward jets, as seen in the data.

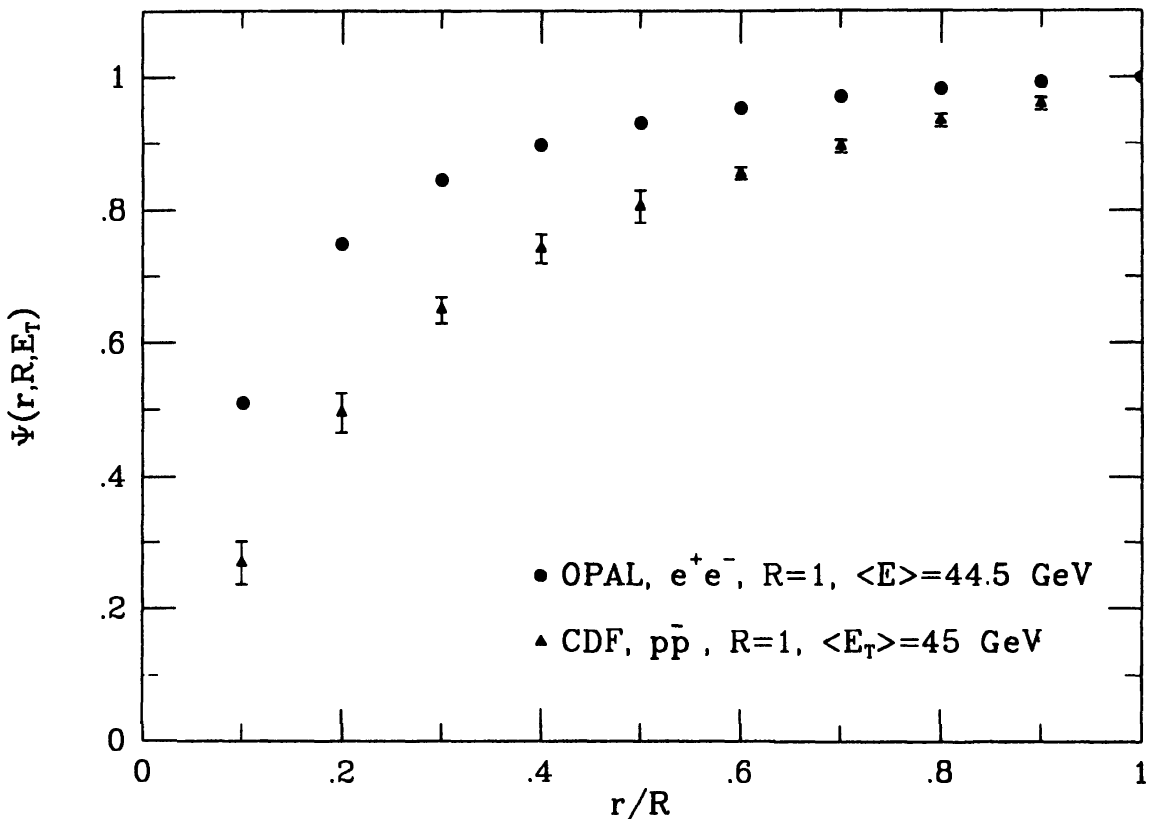


Fig. 7.15. Energy flow profiles of jets, measured with identical cone algorithms in  $e^+e^-$  [27] and  $p\bar{p}$  collisions [26].

## 7.9 Direct photon production

High transverse momentum direct (or ‘prompt’) photon production and high transverse momentum jet production are two closely related phenomena. From an experimental point of view, the study of direct photon production has several advantages with respect to the study of jets: the energy resolution of electromagnetic calorimeters is generally better than the resolution of hadronic calorimeters, and systematic uncertainties in the photon energy scale are smaller. Furthermore, since photons do not fragment, the direction and energy of photons is straightforwardly measured in the calorimeter without the need for a jet algorithm to reconstruct a jet. Only the relatively low rate for the production of direct photons ( $O(\alpha\alpha_S)$  compared to  $O(\alpha_S^2)$  for jets) and the non-negligible background from jet production processes (where direct photons are mimicked by  $\pi^0$ s decaying to  $\gamma\gamma$  for example) have limited the usefulness of direct photon production for making quantitative QCD tests.

At leading order in perturbation theory there are two subprocesses: (a) the annihilation process  $q\bar{q} \rightarrow \gamma g$ , and (b) the Compton process  $qg \rightarrow \gamma q$ , shown in Fig. 7.16. The corresponding invariant matrix elements squared

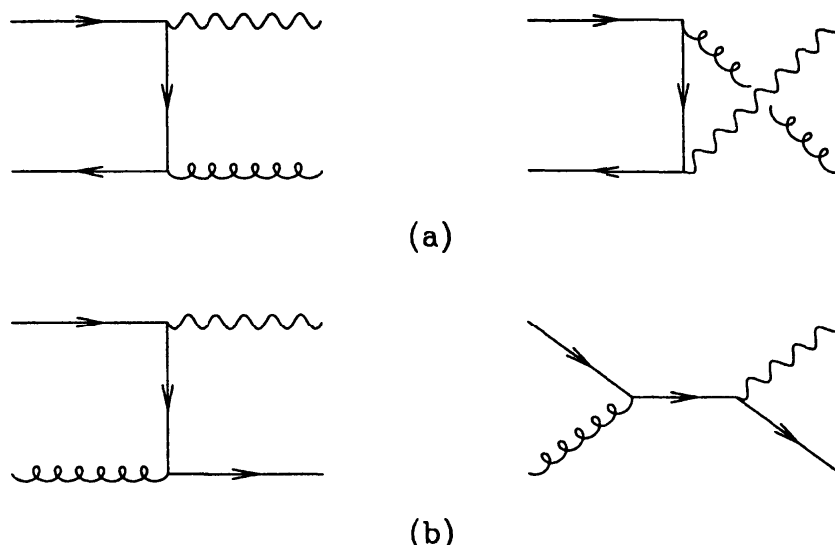


Fig. 7.16. Leading-order diagrams for the production of direct photons (or vector bosons) with large transverse momentum.

Process	$\sum  \mathcal{M} ^2 / (g^2 e_q^2)$
$q \bar{q} \rightarrow \gamma^* g$	$\frac{(N^2 - 1)}{N^2} \frac{t^2 + u^2 + 2s(s+t+u)}{tu}$
$g q \rightarrow \gamma^* q$	$- \frac{1}{N} \frac{s^2 + u^2 + 2t(s+t+u)}{su}$

Table 7.2. Lowest order processes for virtual photon production. The colour and spin indices are averaged (summed) over initial (final) states. For a real photon ( $s + t + u = 0$ ) and for SU(3) we have  $N = 3$ .

are given in Table 7.2. Depending on the nature of the colliding hadrons and on the values of  $\sqrt{s}$  and  $p_T (\equiv p_T^\gamma)$ , either of these two subprocesses can dominate. For photons produced centrally, *i.e.* with  $y \approx 0$  in the colliding hadrons' centre-of-mass frame, the initial-state partons are probed at  $x \sim x_T = 2p_T/\sqrt{s}$ , see Eq. (7.26). At medium and large  $x$  there is a natural hierarchy of parton distributions in the proton,  $q \gg g \gg \bar{q}$ , while at small  $x$ ,  $g \gg q, \bar{q}$  (Fig. 4.3). Thus, for example, in proton-proton or proton-nucleus collisions the  $qg$  Compton process dominates over essentially all the  $p_T$  range, while in proton-antiproton collisions the Compton process dominates at low  $p_T$  and the (valence-valence)  $q\bar{q}$  annihilation process dominates at high  $p_T$ . This makes direct photon production particularly useful for constraining the gluon distribution – recall that in deep inelastic structure functions the gluon contributes only at next-to-leading order.

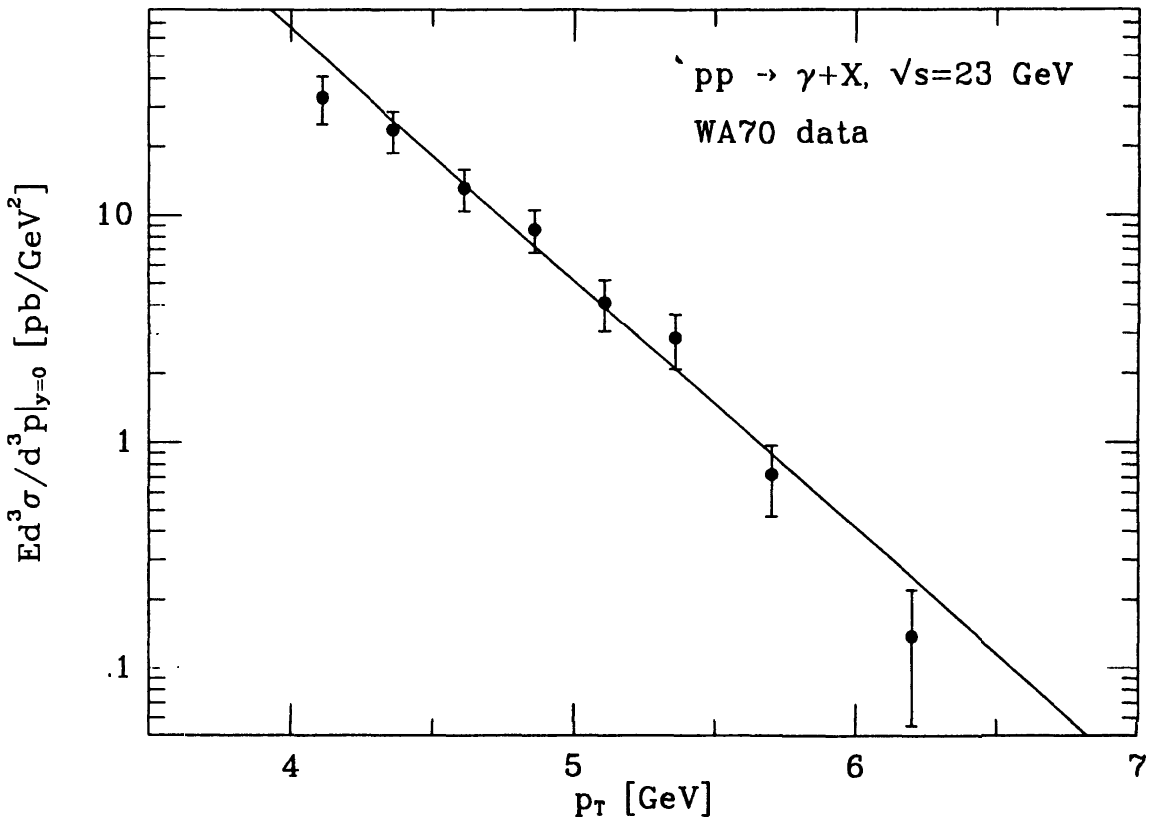


Fig. 7.17. Direct photon  $p_T$  distribution measured by the WA70 collaboration [29]. The curve is a next-to-leading order QCD calculation, as described in the text.

All direct photon data show good agreement with QCD over a large energy range. As an example, Fig. 7.17 shows WA70 data [29] on the photon  $p_T$  distribution for  $pp \rightarrow \gamma X$  at  $\sqrt{s} = 23$  GeV. The curves include the next-to-leading order ( $O(\alpha\alpha_s^2)$ ) contributions [30], and use the MRS(A') parton distributions of ref. [31]. In fact the gluon distribution in this set is partially constrained by these data in the global fit.

The higher-order perturbative corrections exhibit several interesting features. Examples of two diagrams which contribute at next-to-leading order are shown in Fig. 7.18. In Fig. 7.18(a) there is a collinear singularity when the momenta of the final-state quark and gluon are parallel. This is the same type of singularity that occurs in the process  $e^+e^- \rightarrow q\bar{q}(g)$  discussed in Chapter 3, and once again the divergence cancels when real and virtual gluon contributions are summed. The net effect is a finite  $O(\alpha_s)$  correction to the leading-order process. The contribution from Fig. 7.18(b) is more interesting. Again there is a collinear singularity, this time when the photon and quark momenta are parallel. This singularity does not cancel, but instead has to be absorbed into a photon ‘fragmentation function’  $D_q^\gamma(z, \mu^2)$  representing the probability of finding a photon carrying longitudinal momentum fraction  $z$  in a quark jet

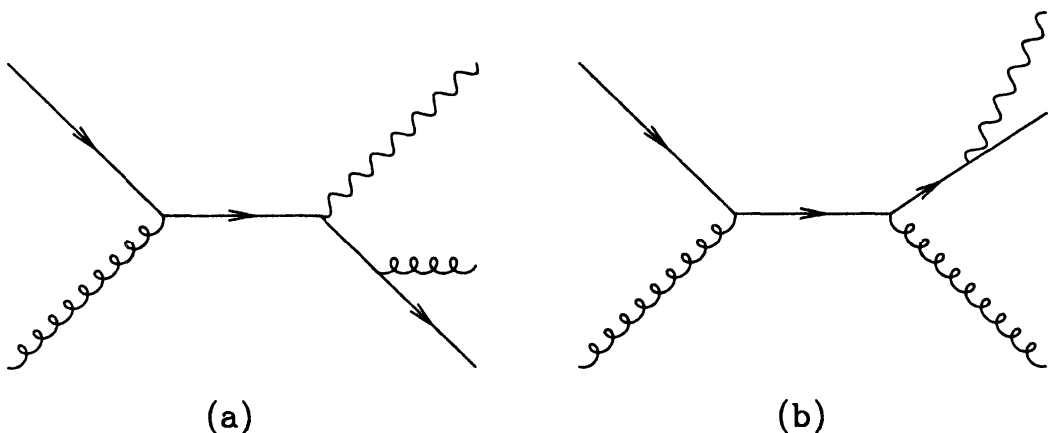


Fig. 7.18. Diagrams which contribute to the direct photon cross section at next-to-leading order.

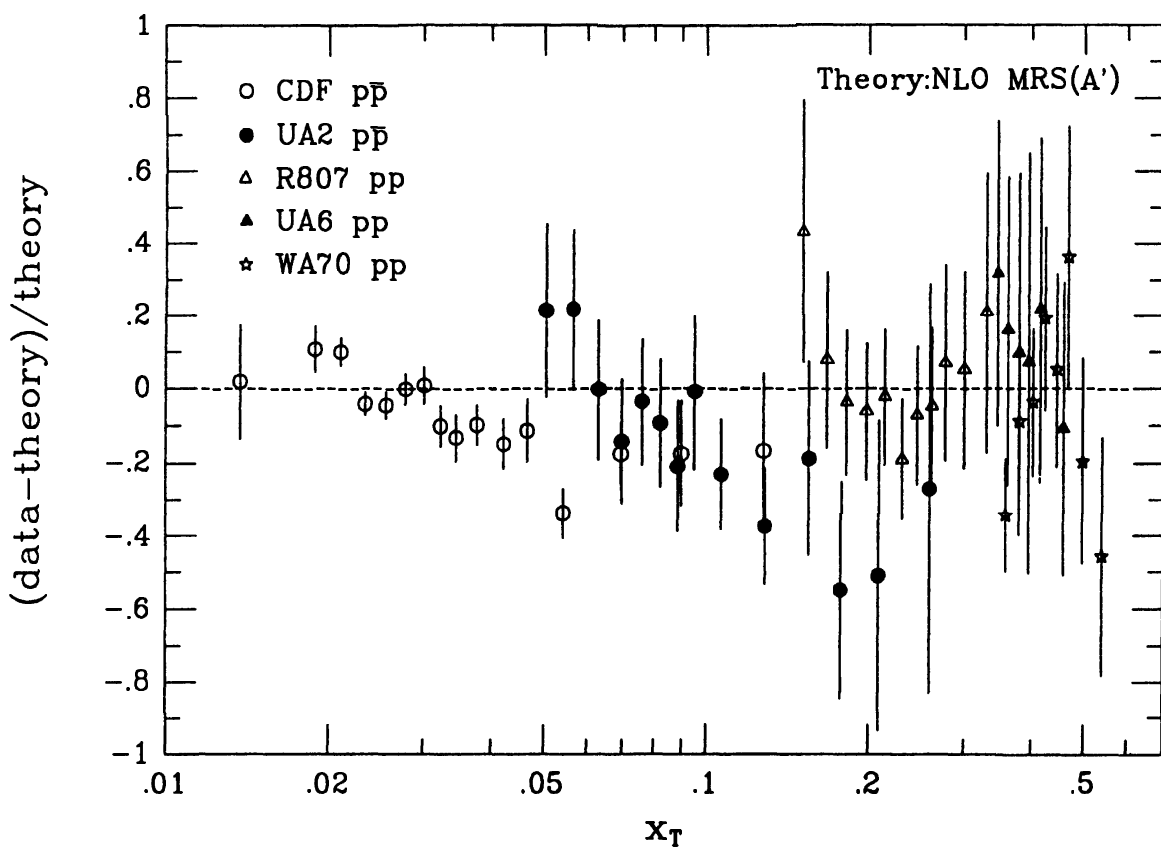


Fig. 7.19. Comparison of fixed-target and collider direct photon data [35] with a next-to-leading order QCD calculation. Adapted from ref. [31].

at scale  $\mu$ . This fragmentation function is not calculable in perturbation theory, but obeys a GLAP evolution equation similar to that for the hadron fragmentation functions  $D_q^h$  shown in Eq. (6.6). The contribution to the cross section from Fig. 7.18(b) therefore contains a ‘fragmentation contribution’ piece of the form

$$\hat{\sigma}(qg \rightarrow qg) \otimes D_q^\gamma(z, p_T^2), \quad (7.54)$$

where the hard scattering process is one of the  $O(\alpha_s^2)$  leading-order contributions to the inclusive jet cross section, and the fragmentation function is  $O(\alpha)$  [32]. Although formally of  $O(\alpha_s)$  compared to the leading-order contribution, the fragmentation contribution is numerically important.

The reason is that the photon fragmentation function has a very different scale dependence from hadron fragmentation functions. As  $\mu^2$  increases, the latter shrink to small  $z$ , as shown in Fig. 6.1. In contrast, the photon fragmentation function increases uniformly with the scale over the whole  $z$  range, *i.e.*  $D_q^\gamma(z, \mu^2) \sim d^\gamma(z) \ln \mu^2$  as  $\mu^2 \rightarrow \infty$ . Therefore when  $p_T$  is large, the  $\ln p_T^2$  growth of the fragmentation function in Eq. (7.54) compensates one of the  $\alpha_s(p_T^2)$  couplings in the subprocess cross section, and the contribution is effectively of order  $\alpha_s(p_T^2)\alpha$ , *i.e.* the same as the leading-order contribution. A more detailed discussion can be found, for example, in ref. [33].

The additional fragmentation contributions are particularly important at small  $p_T/\sqrt{s}$ , for direct photon production at the Tevatron  $p\bar{p}$  collider [34]. Fig. 7.19 shows a comparison [31] of a range of  $pp$  and  $p\bar{p}$  prompt photon data [35] with the predictions of next-to-leading order QCD, including fragmentation contributions. The relative difference between data and theory is shown as a function of the variable  $x_T = 2p_T/\sqrt{s}$ . The agreement is satisfactory. Note that the theoretical predictions do not include non-perturbative contributions (*e.g.* from ‘intrinsic’ transverse momentum of the initial-state partons), which may be non-negligible at small  $p_T$ .

## References

- 1) J.C. Collins and D.E. Soper, *Ann. Rev. Nucl. Part. Sci.* **37** (1987) 383.
- 2) R.P. Feynman, *Photon Hadron Interactions*, W.A. Benjamin, New York (1972).
- 3) R. Basu *et al.*, *Nucl. Phys.* **B244** (1984) 221.
- 4) J.D. Jackson, *Classical Electrodynamics*, John Wiley (1962).
- 5) R. Doria, J. Frenkel and J.C. Taylor, *Nucl. Phys.* **B168** (1980) 93.
- 6) D.A. Edwards and M.J. Syphers, *An introduction to the physics of high energy accelerators*, Wiley, New York (1993);  
P. Bryant and K. Johnsen, *Circular accelerators and storage rings*, Cambridge University Press (1983);  
H. Wiedemann, *Particle Accelerator Physics*, Springer (1993).

- 7) A.D. Martin, R.G. Roberts and W.J. Stirling, *Phys. Rev.* **D50** (1994) 6734.
- 8) B.L. Combridge, J. Kripfganz and J. Ranft, *Phys. Lett.* **B70** (1977) 234.
- 9) CDF collaboration, F. Abe *et al.*, *Phys. Rev. Lett.* **77** (1996) 438.
- 10) R.K. Ellis and J.C. Sexton *Nucl. Phys.* **B269** (1986) 445.
- 11) S.D. Ellis, Z. Kunszt and D.E. Soper, *Phys. Rev. Lett.* **64** (1990) 2121.
- 12) A.D. Martin, R.G. Roberts and W.J. Stirling, *Phys. Rev. D47* (1993) 867; *Phys. Lett.* **B306** (1993) 145.
- 13) D0 collaboration, G. C. Blazey, Proceedings of the 31st Rencontres de Moriond: QCD and High-energy Hadronic Interactions, Les Arcs, France, Fermilab-Conf-96-132-E (1996).
- 14) D0 collaboration, H. Weerts, Proceedings of the 9th Topical Workshop on Proton-Antiproton Collider Physics, eds. K. Kondo and S. Kim, Universal Academy Press, Inc, Tokyo, Japan (1994).
- 15) S.D. Ellis, Z. Kunszt and D.E. Soper, *Phys. Rev. Lett.* **69** (1992) 3615.
- 16) B. Combridge and C.J. Maxwell, *Nucl. Phys.* **B239** (1984) 429.
- 17) M. Mangano and S. Parke, *Phys. Rep.* **200** (1991) 301 and references therein.
- 18) F.A. Berends *et al.*, *Phys. Lett.* **B103** (1981) 124.
- 19) R.K. Ellis, G. Marchesini and B.R. Webber, *Nucl. Phys.* **B286** (1987) 643.
- 20) B. Combridge and C.J. Maxwell, *Phys. Lett.* **B151** (1985) 299; F. Halzen and P. Hoyer, *Phys. Lett.* **B130** (1983) 326.
- 21) CDF collaboration, F. Abe *et al.*, *Phys. Rev. D45* (1992) 1448.
- 22) Z. Bern, L. Dixon and D.A. Kosower, *Phys. Rev. Lett.* **70** (1993) 2677; *Nucl. Phys.* **B437** (1995) 259; Z. Kunszt, A. Signer and Z. Trócsányi, *Phys. Lett.* **B336** (1994) 529.
- 23) CDF collaboration, F. Abe *et al.*, *Phys. Rev. Lett.* **75** (1995) 605.
- 24) J. Huth *et al.*, *Research directions for the decade*, Proceedings of the 1990 DPF summer study on High Energy Physics, Snowmass, Colorado, World Scientific (1990).
- 25) CDF collaboration, F. Abe *et al.*, *Phys. Rev. Lett.* **68** (1992) 1104.
- 26) CDF collaboration, F. Abe *et al.*, *Phys. Rev. Lett.* **70** (1993) 713.
- 27) OPAL collaboration, R. Akers *et al.*, *Zeit. Phys.* **C63** (1994) 197.
- 28) S. Abachi *et al.*, *Phys. Lett.* **B357** (1995) 500.
- 29) WA70 collaboration, M. Bonesini *et al.*, *Zeit. Phys.* **C38** (1988) 371.
- 30) P. Aurenche, R. Baier, M. Fontannaz and D. Schiff, *Nucl. Phys.* **B286** (1987) 553; *ibid.* **B297** (1988) 661.
- 31) A.D. Martin, R.G. Roberts and W.J. Stirling, *Phys. Lett.* **B354** (1995) 155.
- 32) P. Aurenche, P. Chiappetta, M. Fontannaz, J.Ph. Guillet and E. Pilon, *Nucl. Phys.* **B399** (1993) 34; L.E. Gordon and W. Vogelsang, *Phys. Rev. D48* (1993) 3136.
- 33) J.F. Owens, *Rev. Mod. Phys.* **59** (1987) 465.
- 34) M. Glück, L.E. Gordon, E. Reya and W. Vogelsang, *Phys. Rev. Lett.* **73** (1994) 388.
- 35) WA70 collaboration, M. Bonesini *et al.*, ref. [29]; UA6 collaboration, G. Sozzi *et al.*, *Phys. Lett.* **B317** (1993) 243; AFS collaboration (R807), T. Akesson *et al.*, *Sov. J. Nucl. Phys.* **51** (1990) 836; UA2 collaboration, J. Alitti *et al.*, *Phys. Lett.* **B299** (1993) 174; CDF collaboration, F. Abe *et al.*, *Phys. Rev. Lett.* **73** (1994) 2662.

# 8

## Electroweak interactions

Although the main topic of this book is the study of QCD, it is in practice impossible to ignore the electroweak interactions. From an experimental point of view they are inextricably linked with QCD. The success of the present day  $e^+e^-$  colliders in the study of QCD is due to the large event rates which occur at the  $Z$  boson resonance. In addition, many of the event signatures at hadronic colliders involve either the production of vector bosons or leptons coming from the weak decays of heavy quarks. This chapter describes the Standard Electroweak Model [1], which, together with the discovery of QCD, was the triumph of the 1960s and 1970s. The model provides a unified description of the weak and electromagnetic interactions in terms of a renormalizable, gauge invariant field theory. We shall present the Lagrangian of the model and the Feynman rules which follow from it, together with some consequences of the standard model couplings. A more complete treatment of the electroweak sector of the Standard Model can be found, for example, in ref. [2].

### 8.1 Gauge boson interactions

In QED the Lagrangian density has the property of local gauge invariance. The analogous property for QCD was explained in Section 1.3. The Lagrangian for the photon field  $A^\mu$  coupled to an electron field  $\psi$  is given by

$$\mathcal{L} = -\frac{1}{4}F^{\mu\nu}F_{\mu\nu} + \bar{\psi}(iD - m_e)\psi, \quad F^{\mu\nu} = \partial^\mu A^\nu - \partial^\nu A^\mu. \quad (8.1)$$

$D$  is the covariant derivative, which in QED takes the form

$$D_\alpha = \partial_\alpha + ieA^\alpha. \quad (8.2)$$

The Lagrangian (8.1) is invariant under independent redefinitions of the phase of the field  $\psi$  at each space-time point,

$$\psi'(x) = \exp i\theta(x) \psi(x), \quad (8.3)$$

provided that the gauge field  $A^\mu$  transforms as

$$A'_\mu(x) = A_\mu(x) - \frac{1}{e} \partial_\mu \theta(x). \quad (8.4)$$

The Lagrangian thus possesses a local gauge invariance under transformations of the field belonging to the U(1) gauge group, Eq. (8.3). There is a single gauge coupling  $e$  corresponding to this gauge group.

The Standard Electroweak Model is based on the more complicated group  $SU(2) \otimes U(1)$ . Initially the Lagrangian of this model contains three massless bosons,  $W^i$  ( $i = 1, 2, 3$ ), associated with the gauge group  $SU(2)$  and one massless boson,  $B$ , associated with the U(1) gauge group. The Lagrangian of the gauge bosons is written as

$$\mathcal{L} = -\frac{1}{4} W^{i\mu\nu} W_{\mu\nu}^i - \frac{1}{4} B^{\mu\nu} B_{\mu\nu}, \quad (8.5)$$

where the field strength tensors of the U(1) gauge field  $B$  and the  $SU(2)$  gauge fields  $W^i$  are

$$W_{\mu\nu}^i = \partial_\mu W_\nu^i - \partial_\nu W_\mu^i - g_W \epsilon^{ijk} W_\mu^j W_\nu^k \quad (8.6)$$

$$B_{\mu\nu} = \partial_\mu B_\nu - \partial_\nu B_\mu, \quad (8.7)$$

$g_W$  being the  $SU(2)$  gauge coupling. Note that the vector bosons  $W^i$  already have interactions because of the non-Abelian nature of their symmetry group,  $SU(2)$ . This is entirely analogous to the fact that gluons carry colour charge in QCD.

The coupling of the gauge fields to fermionic matter fields is implemented using the covariant derivative, which is

$$D^\mu = \delta_{ij} \partial^\mu + ig_W (T \cdot W^\mu)_{ij} + iY \delta_{ij} g'_W B^\mu \quad (8.8)$$

where  $g'_W$  is the U(1) gauge coupling. The matrices  $T$  are a representation of the  $SU(2)$  *weak isospin* algebra and the U(1) charge  $Y$  is called the *weak hypercharge*. In order to specify the coupling to matter we therefore have to choose the  $SU(2)$  representation,  $T$ , and the U(1) gauge charge,  $Y$ , for the matter fields.

The tensor  $\epsilon^{ijk}$  appears in Eq. (8.6) because its components are the structure constants of  $SU(2)$ :

$$[T^i, T^j] = i\epsilon^{ijk} T^k, \quad \epsilon^{123} = 1. \quad (8.9)$$

Defining  $W_\mu^\pm = (W_\mu^1 \mp iW_\mu^2)/\sqrt{2}$  and  $T^\pm = T^1 \pm iT^2$  we have

$$W_\mu \cdot T = W_\mu^3 T_3 + \frac{1}{\sqrt{2}} W_\mu^+ T^+ + \frac{1}{\sqrt{2}} W_\mu^- T^- \quad (8.10)$$

where the matrices  $T^\pm$  and  $T^3$  satisfy the relations

$$\begin{aligned}[T^+, T^-] &= 2T^3 \\ [T^3, T^\pm] &= \pm T^\pm.\end{aligned}\quad (8.11)$$

$T^+$  and  $T^-$  are the weak isospin raising and lowering operators. For example, in the doublet representation of  $SU(2)$  we have

$$T^3 = \begin{pmatrix} \frac{1}{2} & 0 \\ 0 & -\frac{1}{2} \end{pmatrix}, \quad T^+ = \begin{pmatrix} 0 & 1 \\ 0 & 0 \end{pmatrix}, \quad T^- = \begin{pmatrix} 0 & 0 \\ 1 & 0 \end{pmatrix}. \quad (8.12)$$

The Lagrangian of Eq. (8.5) evidently describes four massless vector bosons forming a singlet ( $B$ ) and a triplet ( $W^\pm, W^3$ ) under weak isospin. The model cannot yet describe the real world because there is only one massless vector boson observed in nature, the photon. The addition of explicit mass terms for three of the bosons would violate local gauge invariance and spoil the renormalizability of the theory. It is necessary to introduce a mechanism of symmetry breaking which gives mass to all but one of the vector bosons and retains only one conserved charge, the electric charge. This can be achieved by spontaneous symmetry breaking similar to that described in Chapter 1 for the case of chiral symmetry breaking in QCD. In that case, we saw that the breaking gave rise to a massless Goldstone boson (pion) for each broken symmetry generator. In the electroweak theory, the Goldstone degrees of freedom are not manifest as massless particles but instead combine with the corresponding gauge bosons to give them mass, as will be explained below.

## 8.2 The Higgs mechanism

In the Standard Electroweak Model, the fundamental  $SU(2) \otimes U(1)$  electroweak symmetry is broken by the *Higgs mechanism* [3]. A single complex doublet of scalar Higgs fields is introduced

$$\phi = \begin{pmatrix} \phi^+ \\ \phi^0 \end{pmatrix}. \quad (8.13)$$

The upper and lower components will be identified *a posteriori* as having electric charge one and zero respectively, but for the moment the superscripts only serve to distinguish the two fields. These fields transform as a doublet under  $SU(2)$ . By assigning them a weak hypercharge of one half we fix their transformation properties under  $U(1)$ . A Lagrangian invariant under local  $SU(2) \otimes U(1)$  transformations is obtained by coupling the field  $\phi$  to the vector bosons using the covariant derivative defined in Eq. (8.8),

$$\mathcal{L} = (\partial^\mu \phi^\dagger + ig_W W^\mu \cdot T \phi^\dagger + \frac{1}{2} ig'_W B^\mu \phi^\dagger)$$

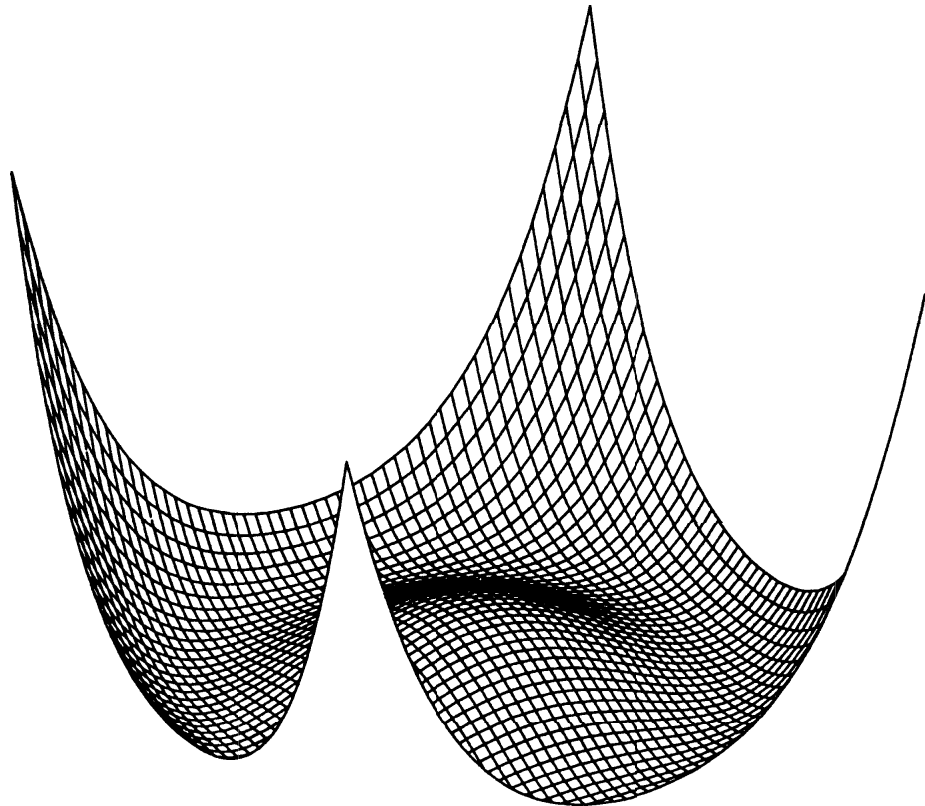


Fig. 8.1. The scalar potential which gives rise to spontaneous symmetry breaking in the Standard Model.

$$\times (\partial_\mu \phi - ig_W W_\mu \cdot T\phi - \frac{1}{2}ig'_W B_\mu \phi) - \mathcal{V}(\phi^\dagger \phi) . \quad (8.14)$$

The Higgs potential  $\mathcal{V}$  is chosen to be of the form

$$\mathcal{V}(\phi^\dagger \phi) = \lambda (\phi^\dagger \phi)^2 - \mu^2 \phi^\dagger \phi . \quad (8.15)$$

Note that this potential has a different sign for the mass term from that usually chosen. As a result, with the parameters  $\lambda, \mu^2 > 0$ , this potential has a classical minimum which is not at  $\phi = 0$ .

To illustrate this phenomenon it is helpful to replace the complex fields in Eq. (8.13) by four real components

$$\begin{pmatrix} \phi^+ \\ \phi^0 \end{pmatrix} = \begin{pmatrix} \phi_1 + i\phi_3 \\ \phi_2 + i\phi_4 \end{pmatrix} . \quad (8.16)$$

Since the potential  $\mathcal{V}$  is a function of

$$\phi^\dagger \phi = \phi_1^2 + \phi_2^2 + \phi_3^2 + \phi_4^2 , \quad (8.17)$$

it is clearly invariant under four-dimensional rotations. The situation is illustrated in Fig. 8.1 where, in order to represent a four-dimensional rotation in a two-dimensional plot, we arbitrarily set  $\phi_3$  and  $\phi_4$  equal to zero. Fig. 8.1 then shows the potential  $\mathcal{V}(\phi^\dagger \phi)$  in the  $\phi_1, \phi_2$  plane. There

is evidently a circle of degenerate minima, corresponding to

$$|\phi| = \sqrt{\frac{\mu^2}{2\lambda}} \equiv \frac{v}{\sqrt{2}} . \quad (8.18)$$

Transitions between field configurations on this circle cost no energy and correspond to massless excitations.

We next choose a particular direction in the internal SU(2) space for the minimum of  $\phi$ ,

$$\langle \phi \rangle = \frac{1}{\sqrt{2}} \begin{pmatrix} 0 \\ v \end{pmatrix} . \quad (8.19)$$

The direction chosen is of no consequence; the important feature is the residual U(1) invariance. Transformations generated by  $T^3 + Y$  leave the vacuum expectation value invariant, *i.e.*

$$(T^3 + Y) \langle \phi \rangle = 0 . \quad (8.20)$$

This combination is the single unbroken generator which is identified with the electric charge,

$$Q \equiv T^3 + Y = \begin{pmatrix} 1 & 0 \\ 0 & 0 \end{pmatrix} . \quad (8.21)$$

The choice of the vacuum expectation value in Eq. (8.19) breaks the SU(2)  $\otimes$  U(1) symmetry, since it identifies a particular direction in the internal group space. We shall need to consider the fluctuations around this new minimum, so we introduce a reparametrization of the Higgs field,

$$\phi = U^{-1}(\xi) \begin{pmatrix} 0 \\ (H + v)/\sqrt{2} \end{pmatrix} \quad (8.22)$$

$$U(\xi) = \exp(-iT \cdot \xi/v) . \quad (8.23)$$

Note that we still have four real degrees of freedom, (three  $\xi$ s and one  $H$ ), equivalent to the two complex fields. We now make a gauge transformation of the form

$$\phi \rightarrow U(\xi)\phi \quad (8.24)$$

$$T \cdot W^\mu \rightarrow UT \cdot W^\mu U^{-1} + \frac{i}{g_W} (\partial^\mu U) U^{-1} . \quad (8.25)$$

The  $\xi$  degrees of freedom no longer appear in the Higgs Lagrangian, Eq. (8.14). As we shall see below, they will reappear as the longitudinal modes of the massive gauge bosons. This gauge, in which there are no unphysical degrees of freedom, is called the *unitary gauge*. The Higgs boson  $H$  is the only remaining dynamical field. The Higgs Lagrangian

now becomes

$$\begin{aligned}\mathcal{L} = & \frac{1}{2}\partial_\mu H\partial^\mu H - \mathcal{V}\left(\frac{(v+H)^2}{2}\right) \\ & + \frac{(v+H)^2}{8}\chi^\dagger(2g_W T \cdot W_\mu + g'_W B_\mu)(2g_W T \cdot W^\mu + g'_W B^\mu)\chi,\end{aligned}\quad (8.26)$$

where  $\chi$  is a unit vector along the direction of the vacuum expectation value (8.19)

$$\chi = \begin{pmatrix} 0 \\ 1 \end{pmatrix}. \quad (8.27)$$

We therefore have three generators of the  $SU(2) \otimes U(1)$  symmetry which are spontaneously broken. As described in Chapter 1, Goldstone's theorem would lead us to expect three massless bosons. However, this theorem does not apply if the theory contains long-range vector fields with the same quantum numbers as the would-be Goldstone bosons. When such fields are present, the massless Goldstone modes provide the extra longitudinal degrees of freedom necessary to change the quanta of the vector fields from massless to massive bosons.

To see how this works in practice, we examine the terms quadratic in the vector boson fields:

$$\mathcal{L}_M = \frac{v^2}{8} \left[ (g_W W_\mu^3 - g'_W B_\mu)(g_W W^{3\mu} - g'_W B^\mu) + 2g_W^2 W_\mu^- W^{+\mu} \right]. \quad (8.28)$$

The propagator for the  $B$  and  $W^3$  fields is not diagonal. We therefore redefine the electrically neutral fields by introducing new fields  $A_\mu$  and  $Z_\mu$  which propagate independently,

$$\begin{pmatrix} W_\mu^3 \\ B_\mu \end{pmatrix} = \begin{pmatrix} \cos \theta_W & \sin \theta_W \\ -\sin \theta_W & \cos \theta_W \end{pmatrix} \begin{pmatrix} Z_\mu \\ A_\mu \end{pmatrix}, \quad (8.29)$$

where the angle  $\theta_W$  (the Weinberg or electroweak mixing angle) is fixed by the relative strengths of the coupling constants:

$$\sin^2 \theta_W = \frac{g'_W^2}{g_W^2 + g'_W^2} \simeq 0.23. \quad (8.30)$$

After this rotation the quadratic terms in the vector boson fields become

$$\mathcal{L}_M = \frac{g_W^2 v^2}{4} W_\mu^+ W^{-\mu} + \frac{(g_W^2 + g'_W^2)v^2}{8} Z_\mu Z^\mu. \quad (8.31)$$

We therefore find that the  $W$  and  $Z$  bosons have acquired masses, given by

$$M_W = \frac{1}{2}v g_W, \quad (8.32)$$

$$M_Z = \frac{1}{2}v\sqrt{g_W^2 + g'_W{}^2} \equiv \frac{M_W}{\cos \theta_W}. \quad (8.33)$$

The photon remains massless because there are no terms quadratic in the field  $A$  in Eq. (8.31). As we shall see below, low-energy weak interactions allow us to make the identification

$$\frac{g_W^2}{8M_W^2} \equiv \frac{1}{2v^2} = \frac{G_F}{\sqrt{2}} \quad (8.34)$$

where  $G_F$  is the Fermi constant. The measured value,  $G_F = 1.166 \times 10^{-5}$  GeV $^{-2}$ , therefore implies that the vacuum expectation value of the Higgs field,  $v$ , is 246 GeV.

In summary, the Higgs field  $\phi$  acquires a non-zero vacuum expectation value at a particular point on the circle of minima away from  $\phi = 0$  and the symmetry is spontaneously broken. However, this does not give rise to Goldstone bosons: instead, three of the four scalar field components get ‘eaten’ by the gauge particles to form massive vector bosons ( $W^\pm, Z^0$ ), and there remains a single physical neutral scalar particle — the Higgs boson ( $H$ ).

The self-couplings of the Higgs boson are

$$\mathcal{L}_{\text{Higgs}} = \frac{1}{2}\partial_\mu H\partial^\mu H - \mu^2 H^2 - \lambda v H^3 - \frac{1}{4}\lambda H^4, \quad (8.35)$$

and its mass  $M_H$  is therefore

$$M_H = \sqrt{2}\mu \equiv \sqrt{2\lambda}v. \quad (8.36)$$

One combination of the parameters in the Higgs potential, Eq. (8.15),  $\mu^2/\lambda = v^2$  is fixed by the measured parameters of the electroweak theory. The other parameter, which is related to the physical Higgs mass, is essentially arbitrary.

This is the ‘minimal model’. Many extensions of the Standard Model (supersymmetry, grand unification, ...) retain the Higgs mechanism as the primary method for mass generation for gauge bosons, but with more complicated Higgs sectors and more Higgs bosons.

### 8.2.1 Boson couplings

The fundamental couplings between the bosons are shown in Fig. 8.2. Note that the Higgs boson couples to weak gauge bosons with the normal weak interaction strength.

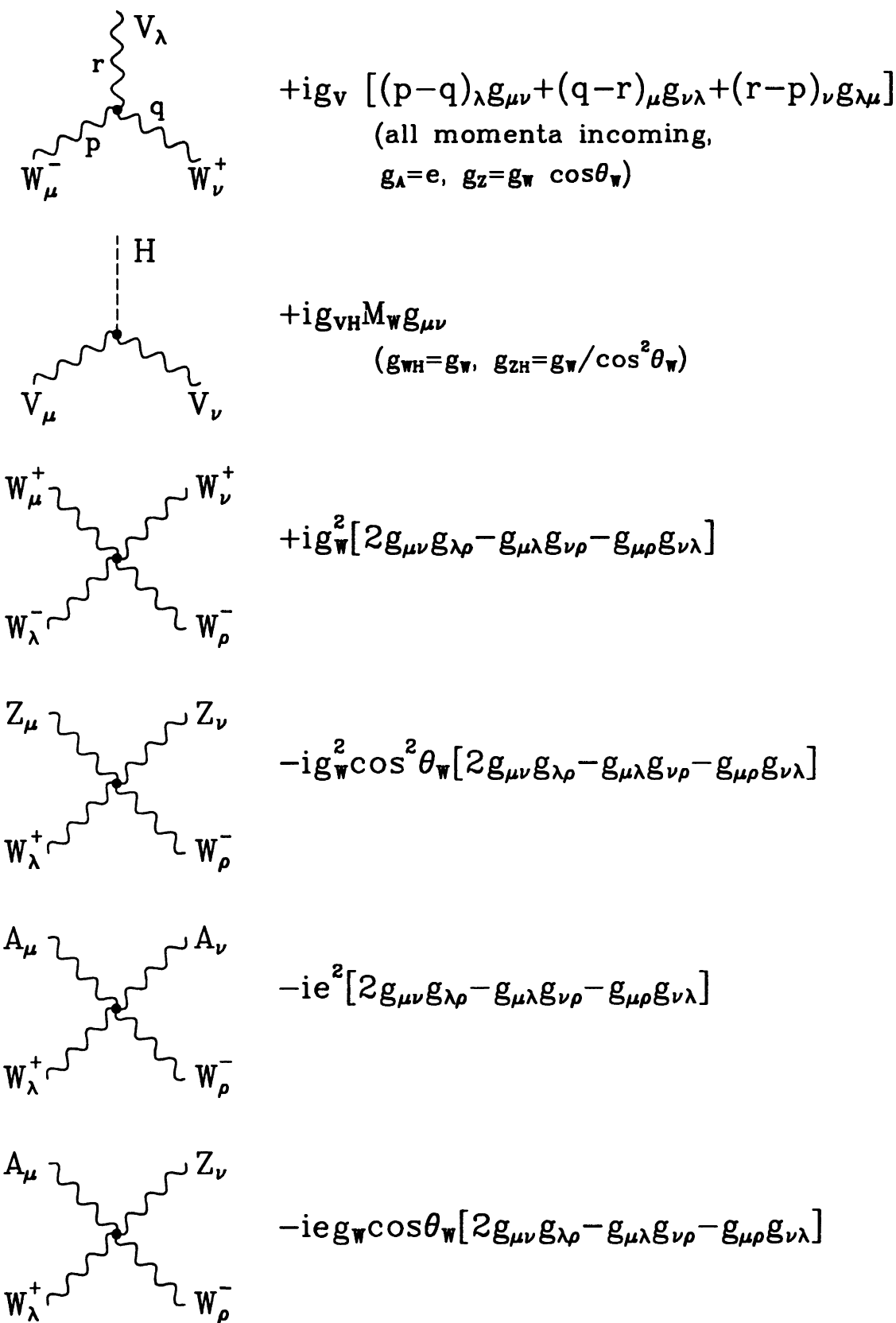


Fig. 8.2. Feynman rules for boson interactions.

As an example of the use of these Feynman rules, we calculate the partial width of the Standard Model Higgs boson into  $W$  pairs, which will be needed in Chapter 11. We find that the tree-level invariant matrix element squared for the process

$$H \rightarrow W^+ W^- , \quad (8.37)$$

summed over final-state polarizations, is given by

$$\sum |\mathcal{M}|^2 = \frac{g_W^2 M_H^4}{4 M_W^2} \left( 1 - 4 \frac{M_W^2}{M_H^2} + 12 \frac{M_W^4}{M_H^4} \right) . \quad (8.38)$$

The Lorentz-invariant phase space for decay into two particles is

$$d\Phi_2(P, p_1, p_2) = \frac{1}{8\pi} \frac{2|p_1|}{M_P} \frac{d\Omega}{4\pi} , \quad (8.39)$$

where  $p_1$  is the three-momentum of the decay products in the rest frame of the decaying particle, which has mass  $M_P$ , and  $d\Omega$  is the element of solid angle. Including the initial-state normalization factor of  $1/(2M_H)$ , we obtain the final result for the Higgs partial width into  $W$  bosons:

$$\Gamma(H \rightarrow W^+ W^-) = \frac{g_W^2 M_H^3}{64\pi M_W^2} \left( 1 - \frac{4M_W^2}{M_H^2} \right)^{\frac{1}{2}} \left( 1 - \frac{4M_W^2}{M_H^2} + \frac{12M_W^4}{M_H^4} \right) . \quad (8.40)$$

Note that for  $M_H \gg M_W$  the tree-level Higgs width grows and eventually becomes larger than its mass,

$$\Gamma(H \rightarrow W^+ W^-) = \left( \frac{M_H^3}{M_U^2} \right) , \quad M_U = 1.74 \text{ TeV} . \quad (8.41)$$

The scale at which  $\Gamma_H > M_H$  is set by  $M_U$ . This growth arises from the decay into longitudinally polarized  $W$ s, as will be discussed in more detail later.

### 8.2.2 The $\rho$ parameter

From the masses of the vector bosons and the value of the weak mixing angle one can define the parameter  $\rho$  [4],

$$\rho = \frac{M_W^2}{M_Z^2 \cos^2 \theta_W} . \quad (8.42)$$

This parameter is equal to unity in the Standard Electroweak Model at the tree-graph level, see Eq. (8.33). Using the measured values  $M_W = 80.22 \pm 0.26$  GeV [5],  $M_Z = 91.1884 \pm 0.0022$  GeV [6] and  $\sin^2 \theta_W = 0.2325 \pm 0.0013$  obtained from the measured couplings of the  $Z$  [6], we find that the measured value of  $\rho$  is indeed equal to unity to an accuracy of better than 1 percent ( $\rho = 1.008 \pm 0.007$ ). This is an impressive verification of a Standard Model prediction. However this relationship is

not a consequence of spontaneous symmetry breaking *per se* but rather of the particular form of the Higgs potential. For example, the  $\rho$  parameter would not be equal to unity in a model with an isospin triplet of Higgs fields [4].

In order to investigate this point further, it is useful to construct an alternative form for the Higgs Lagrangian in which its extra global symmetries are apparent [7]. As noted in Eq. (8.17), the potential is a function of

$$\phi^\dagger \phi = \phi_1^2 + \phi_2^2 + \phi_3^2 + \phi_4^2, \quad (8.43)$$

and hence we have an SO(4) symmetry. However, it is more convenient to express this SO(4) symmetry as the product SU(2)  $\otimes$  SU(2), the group SO(4) being isomorphic to SU(2)  $\otimes$  SU(2).

Let us construct a  $2 \times 2$  matrix out of the doublet Higgs field and its complex conjugate

$$\Phi = \begin{pmatrix} \phi^0 & \phi^+ \\ -\phi^+ & \phi^0 \end{pmatrix}. \quad (8.44)$$

After the removal of a normalization factor, the matrix  $\Phi$  is a special unitary matrix. It is made up of the columns  $i\tau_2 \phi^*$  and  $\phi$ , where  $\tau_j$  is the  $j$ -th Pauli matrix. It is easy to show that if  $\phi$  transforms as a doublet,

$$\phi \rightarrow \exp(i\theta \tau \cdot n) \phi = (\cos \theta + i\tau \cdot n \sin \theta) \phi \quad (8.45)$$

then so does  $i\tau_2 \phi^*$ , using the identity  $\tau_2 \tau_j^* \tau_2 = \tau_j$ .

The potential  $\mathcal{V}$  is a function of  $\text{Tr}(\Phi^\dagger \Phi)$  and is therefore invariant under the transformation

$$\Phi \rightarrow U_L \Phi U_R^\dagger \quad (8.46)$$

where  $U_L$  and  $U_R$  are special unitary  $2 \times 2$  matrices. The left one,  $U_L$ , is the familiar gauged SU(2) invariance. The Higgs Lagrangian becomes

$$\mathcal{L} = \frac{1}{2} \{ \text{Tr} [(D_\mu \Phi)^\dagger D^\mu \Phi] + \mu^2 \text{Tr} [\Phi^\dagger \Phi] - \lambda \text{Tr} [\Phi^\dagger \Phi \Phi^\dagger \Phi] \}, \quad (8.47)$$

where the covariant derivative in the present notation is

$$D_\mu \Phi = \partial_\mu \Phi + \frac{1}{2} i g_W W_\mu \cdot \tau \Phi - \frac{1}{2} i g'_W B_\mu \Phi \tau_3. \quad (8.48)$$

The last term breaks the  $SU(2)_R$  symmetry, so we consider first the limit  $g'_W = 0$ . Then the Lagrangian including the gauge fields has the full  $SU(2)_L \otimes SU(2)_R$  symmetry if the  $W$  field transforms as a triplet under the gauged  $SU(2)_L$  and as a singlet under the global  $SU(2)_R$ . The vacuum expectation value of the Higgs field is

$$\langle \Phi \rangle = \frac{v}{\sqrt{2}} \begin{pmatrix} 1 & 0 \\ 0 & 1 \end{pmatrix}. \quad (8.49)$$

After symmetry breaking, the group is broken down to a single SU(2) (or equivalently O(3)):

$$\langle \Phi \rangle \rightarrow U \langle \Phi \rangle U^\dagger = \langle \Phi \rangle, \quad (8.50)$$

where the left and right transformations are now the same. The residual O(3) symmetry means that the quadratic terms in the  $W$  field in Eq. (8.31) must take the form

$$W_\mu^1 W^{1\ \mu} + W_\mu^2 W^{2\ \mu} + W_\mu^3 W^{3\ \mu} = 2W_\mu^- W^{+\ \mu} + W_\mu^3 W^{3\ \mu}, \quad (8.51)$$

from which it follows that  $M_W = M_Z$ , i.e.  $\rho = 1$  in the limit we are considering,  $g'_W = 0$ . Now suppose that  $g'_W \neq 0$ . The SU(2) symmetry of the Higgs field ensures that the mass difference between the  $W$  and the  $Z$  arises only from the symmetry-breaking term in Eq. (8.48). The net effect is to replace the  $W^3$  field in (8.51) by  $W^3 - (g'_W/g_W)B$ , and therefore the relation between the couplings and the boson masses in Eqs. (8.32,8.33), corresponding to  $\rho = 1$ , is preserved. As a consequence  $\rho$  is constrained to be unity before the inclusion of symmetry-breaking effects from other sectors of the Standard Model. For this reason the residual symmetry is referred to as ‘custodial SU(2)’ [7].

The fermion mass sector of the Standard Model, to be discussed in the next section, does not respect the custodial SU(2) symmetry. Higher-order radiative corrections involving fermions will thus cause calculable corrections to the value of the  $\rho$  parameter. In fact, the largest effect comes from the top quark mass [4]:

$$\rho - 1 \approx \frac{3G_F}{8\sqrt{2}\pi^2} m_t^2 = 0.01 \left( \frac{m_t}{175 \text{ GeV}} \right)^2. \quad (8.52)$$

### 8.3 Fermion multiplets and interactions

The coupling of the gauge bosons to fermions which preserves gauge symmetry is specified by the covariant derivative, Eq. (8.8). Before symmetry breaking, the coupling of the fermions to the vector bosons is given by

$$\mathcal{L} = \bar{\psi}_R i(\partial + ig'_W Y_R B) \psi_R + \bar{\psi}_L i(\partial + ig_W \cdot T W + ig'_W Y_L B) \psi_L. \quad (8.53)$$

The U(1) charges of the left- and right-handed fermions,  $Y_L$  and  $Y_R$ , are chosen to satisfy the relation  $Q = T^3 + Y$ , so that after symmetry breaking we obtain the correct values of the electric charges,  $Q$ . For the case of leptons the left-handed fields are put into doublets

$$\psi_L = \gamma_L \begin{pmatrix} \nu_e \\ e^- \end{pmatrix}, \quad \gamma_L \begin{pmatrix} \nu_\mu \\ \mu^- \end{pmatrix}, \quad \gamma_L \begin{pmatrix} \nu_\tau \\ \tau^- \end{pmatrix} \quad (8.54)$$

Fermion			$T_L^3$	$Y_L$	$T_R^3$	$Y_R$	$Q_f$
$u$	$c$	$t$	$+\frac{1}{2}$	$+\frac{1}{6}$	0	$+\frac{2}{3}$	$+\frac{2}{3}$
$d$	$s$	$b$	$-\frac{1}{2}$	$+\frac{1}{6}$	0	$-\frac{1}{3}$	$-\frac{1}{3}$
$\nu_e$	$\nu_\mu$	$\nu_\tau$	$+\frac{1}{2}$	$-\frac{1}{2}$	-	-	0
$e^-$	$\mu^-$	$\tau^-$	$-\frac{1}{2}$	$-\frac{1}{2}$	0	-1	-1

Table 8.1. Weak isospin and hypercharge assignments.

where as before

$$\gamma_R = \frac{1}{2}(1 + \gamma_5), \quad \gamma_L = \frac{1}{2}(1 - \gamma_5). \quad (8.55)$$

The right-handed fields are all SU(2) singlets:

$$\psi_R = \gamma_R e^-, \quad \gamma_R \mu^-, \quad \gamma_R \tau^-. \quad (8.56)$$

Similarly the quarks form three left-handed doublets

$$\psi_L = \gamma_L \begin{pmatrix} u \\ d' \end{pmatrix}, \quad \gamma_L \begin{pmatrix} c \\ s' \end{pmatrix}, \quad \gamma_L \begin{pmatrix} t \\ b' \end{pmatrix}, \quad (8.57)$$

and the right-handed quarks are again singlets. The primes on the down-type quarks in Eq. (8.57) will be explained in Section 8.3.3. The hypercharges are assigned so that the quarks and leptons have the charges given in Table 8.1.

We see that the fermions fall naturally into three families (sometimes called *generations*). Each family is made up of a left-handed doublet of quark fields (in each of three colours), a left-handed doublet of leptons and all the corresponding right-handed fields.

### 8.3.1 Anomaly cancellation

The theoretical motivation for grouping the quarks and leptons as shown in Table 8.1 is that complete families are required for the cancellation of anomalies in the currents which couple to gauge fields. Hence, for example, the top quark must exist as the partner of the  $b, \tau$  and  $\nu_\tau$ , completing the third family.

Anomalies occur in a theory if symmetries present at the classical level are destroyed by quantum effects [8]. They typically involve contributions to the divergence of a current which is conserved at the classical level. If the gauge currents are anomalous, the Ward identities, which are vital for the proof that the gauge theory is renormalizable, are invalidated.

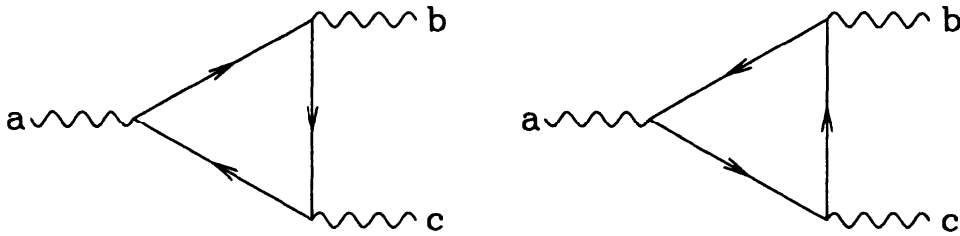


Fig. 8.3. Diagrams responsible for the simplest anomalies.

An important class of anomalies arises from the simple triangle diagram with two vector currents and one axial vector current, as shown in Fig. 8.3. Elimination of the anomalies for a particular current in the lowest-order triangle diagram is sufficient to ensure that the current remains anomaly free, even after the inclusion of more complicated diagrams [9].

If the gauge currents  $a$ ,  $b$  and  $c$  which interact at the three corners of the triangle couple to the matrices  $L^a$ ,  $L^b$  and  $L^c$  for the left-handed fields, and to the matrices  $R^a$ ,  $R^b$  and  $R^c$  for the right-handed fields, the vector-vector-axial vector triangle anomaly is proportional to

$$A = \text{Tr} (R^a \{R^b, R^c\}) - \text{Tr} (L^a \{L^b, L^c\}) \quad (8.58)$$

where the trace means a sum over all possible fermion triangles. We are imagining here that all the families of left- and right-handed fermions are assembled in a single column vector, on which the matrices  $L^a$  and  $R^a$  act.

In order to show that the combination given in Eq. (8.58) vanishes in the Standard Model, we shall first demonstrate a pair of useful results:

$$i) \quad \text{Tr} (T^a \{T^b, T^c\}) = 0, \quad (8.59)$$

$$ii) \quad \text{Tr} (Y_L^3 - Y_R^3) = 3 \text{Tr} (Y_L [T^3]^2). \quad (8.60)$$

In these equations  $T$  is a matrix which operates on all left-handed fields. Because all such fields are in doublets, the matrices  $T$  are block diagonal and each block is made up of a doublet representation of SU(2). The matrices  $T$  therefore obey the same SU(2) algebra as the individual blocks. Eq. (8.59) follows because there is no SU(2) tensor to which the trace could be proportional: the only available tensor is  $\epsilon^{abc}$ , which is antisymmetric. The second result follows from the two facts that all left-handed fields are in doublets and that there are no massless charged fields, *i.e.* each left-handed charged field has a corresponding right-handed field, so that

$$\text{Tr} (Q_L^3 - Q_R^3) \equiv \text{Tr} ([T^3 + Y_L]^3 - Y_R^3) = 0. \quad (8.61)$$

Expanding the second of these equations, we have  $\text{Tr} ([T^3]^3) = 0$  by Eq. (8.59), and  $\text{Tr} (T^3 Y_L^2) = 0$  since the trace of each block of  $T^a$  with a common value of  $Y_L$  is zero. Hence we obtain Eq. (8.60).

Having established these identities we now proceed to demonstrate the cancellation of anomalies in the Standard Electroweak Model. Substituting the Standard Model couplings into Eq. (8.58), with all combinations of the SU(2) matrices  $T^a$  or the U(1) matrices  $Y$ , we obtain the form of the anomaly for the various gauge currents of the theory. Two of the resulting traces of the couplings vanish for each fermion doublet (*i.e.* separately for leptons and quarks):

$$\text{Tr} (T^a \{T^b, T^c\}) = 0, \quad \text{Tr} (T^a Y_L^2) = 0. \quad (8.62)$$

The other two traces vanish only for a complete family [10]

$$\text{Tr} (Y_R^3 - Y_L^3) = 0, \quad \text{Tr} (Y_L \{T^a, T^b\}) = 0. \quad (8.63)$$

Note that because of Eq. (8.60) the two conditions in Eq. (8.63) are equivalent to a single constraint. To show the anomaly cancellation it is therefore sufficient to demonstrate that

$$\text{Tr} (Y_L \{T^a, T^b\}) = \text{Tr} (Q_L \{T^a, T^b\}) = 0. \quad (8.64)$$

The first form of this equation shows that a non-zero contribution can only occur for  $a = b$ , otherwise there are cancellations within a single doublet. The second form makes it clear that for  $a = b$  the condition reduces to the single condition that the charge matrix for the left-handed fields must be traceless,

$$\text{Tr } Q_L = 0. \quad (8.65)$$

This condition is satisfied in the Standard Model for each complete family. This remarkable equation implies a relation between the fact that quarks occur in three colours and that they have fractional charges, that is,

$$3(Q_u + Q_d) + Q_e = 0. \quad (8.66)$$

The Standard Model by itself provides no explanation of this fact.

It should be noted that there are still anomalies in global (non-gauged) currents in the Standard Model. Such anomalies are harmless since they do not destroy renormalizability. For example, the strong isospin current corresponds to a global symmetry (in the approximation  $m_u = m_d$ ) and is anomalous. It is this anomaly which is responsible for  $\pi^0$  decay, as discussed in Chapter 1.

### 8.3.2 Fermion masses and couplings

The Higgs field  $\phi$  gives masses to the fermions via Yukawa interactions with the fermion fields. After spontaneous symmetry breaking, a Yukawa interaction of the form  $g_f \bar{\psi}_f \psi_f \phi$  leads to a fermion mass,  $m_f = g_f v / \sqrt{2}$ , and residual  $\bar{\psi}_f \psi_f H$  interactions of strength  $g_f = \sqrt{2}m_f/v$ . The values

$g_u$	$2 \times 10^{-5}$	$g_c$	$9 \times 10^{-3}$	$g_t$	1
$g_d$	$4 \times 10^{-5}$	$g_s$	$8 \times 10^{-4}$	$g_b$	$3 \times 10^{-2}$
$g_e$	$3 \times 10^{-6}$	$g_\mu$	$6 \times 10^{-4}$	$g_\tau$	$1 \times 10^{-2}$

Table 8.2. Yukawa couplings.

Fermions			$Q_f$	$V_f$	$A_f$
$u$	$c$	$t$	$+\frac{2}{3}$	$(+\frac{1}{2} - \frac{4}{3} \sin^2 \theta_W) \sim +0.191$	$+\frac{1}{2}$
$d$	$s$	$b$	$-\frac{1}{3}$	$(-\frac{1}{2} + \frac{2}{3} \sin^2 \theta_W) \sim -0.345$	$-\frac{1}{2}$
$\nu_e$	$\nu_\mu$	$\nu_\tau$	0	$\frac{1}{2}$	$+\frac{1}{2}$
$e$	$\mu$	$\tau$	-1	$(-\frac{1}{2} + 2 \sin^2 \theta_W) \sim -0.036$	$-\frac{1}{2}$

Table 8.3. Couplings of fermions to the  $Z$  boson. The numerical values of  $V_f$  are for  $\sin^2 \theta_W = 0.232$ .

of the Yukawa couplings required to reproduce the observed pattern of masses are shown in Table 8.2. The Standard Model offers no explanation for the wide range of Yukawa couplings required.

The interaction Lagrangian can be expressed in terms of physical fields by substituting for  $B$  and  $W^3$  using Eq. (8.29):

$$\begin{aligned} \mathcal{L} = & \sum_f \bar{\psi}_f \left( i\partial^\mu - m_f - g_W \frac{m_f H}{2M_W} \right) \psi_f \\ & - \frac{g_W}{2\sqrt{2}} \sum_f \bar{\psi}_f (\gamma^\mu (1 - \gamma_5) T^+ W_\mu^+ + \gamma^\mu (1 - \gamma_5) T^- W_\mu^-) \psi_f \\ & - e \sum_f q_f \bar{\psi}_f A \psi_f - \frac{g_W}{2 \cos \theta_W} \sum_f \bar{\psi}_f \gamma^\mu (V_f - A_f \gamma_5) \psi_f Z_\mu . \end{aligned} \quad (8.67)$$

The couplings of the fermions to the  $Z$  boson are

$$\begin{aligned} V_f &= T_f^3 - 2Q_f \sin^2 \theta_W , \\ A_f &= T_f^3 , \end{aligned} \quad (8.68)$$

where  $Q_f$  is the charge of the fermion in units of the positron electric charge  $e$ . The values of  $e$  and the weak SU(2) charge  $g_W$  are related by

$$e = g_W \sin \theta_W . \quad (8.69)$$

These couplings are summarized in Table 8.3. They have been measured experimentally; Fig. 8.4 shows the constraints on the couplings from the

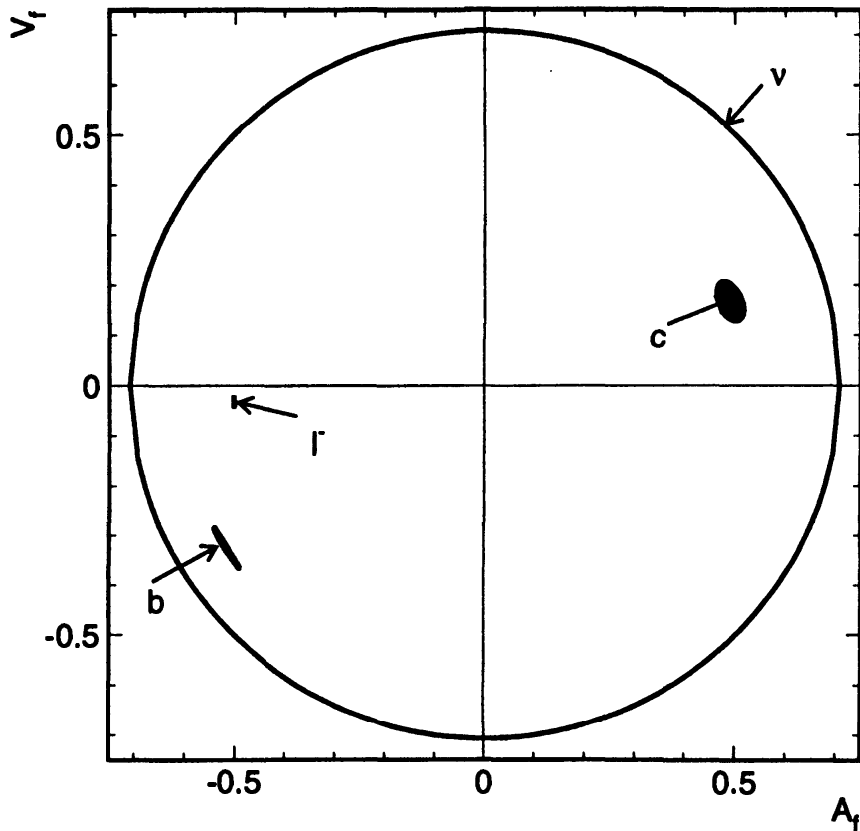


Fig. 8.4. Fermion couplings to the  $Z$  boson as measured at LEP. Figure from ref. [11].

LEP data. The charged lepton couplings all lie within the small rectangle indicated, and are consistent with lepton universality. The width of the  $Z$  boson into neutrinos, obtained by subtracting the observed channels from the total width, measures the quantity,  $V_\nu^2 + A_\nu^2$ . These measurements constrain it to lie on the circle in Fig. 8.4. Small deviations from the values given in Table 8.3 are due to electroweak radiative corrections.

Fig. 8.5 shows the Feynman rules derived from Eq. (8.67). Also shown are the propagators of the vector boson fields in the unitary gauge defined by Eq. (8.24). In this gauge only real physical particles propagate. To relate the electroweak parameters to those of low-energy weak interactions we consider the amplitude for the decay  $\mu^- \rightarrow e^- \bar{\nu}_e \nu_\mu$ , which according to the Feynman rules given in Fig. 8.5 is

$$\frac{-ig_W^2}{2} \bar{u}(\nu_\mu) \gamma^\alpha \gamma_L u(\mu) \bar{u}(e) \gamma^\beta \gamma_L v(\bar{\nu}_e) \left( -g_{\alpha\beta} + \frac{k_\alpha k_\beta}{M_W^2} \right) \frac{1}{k^2 - M_W^2}. \quad (8.70)$$

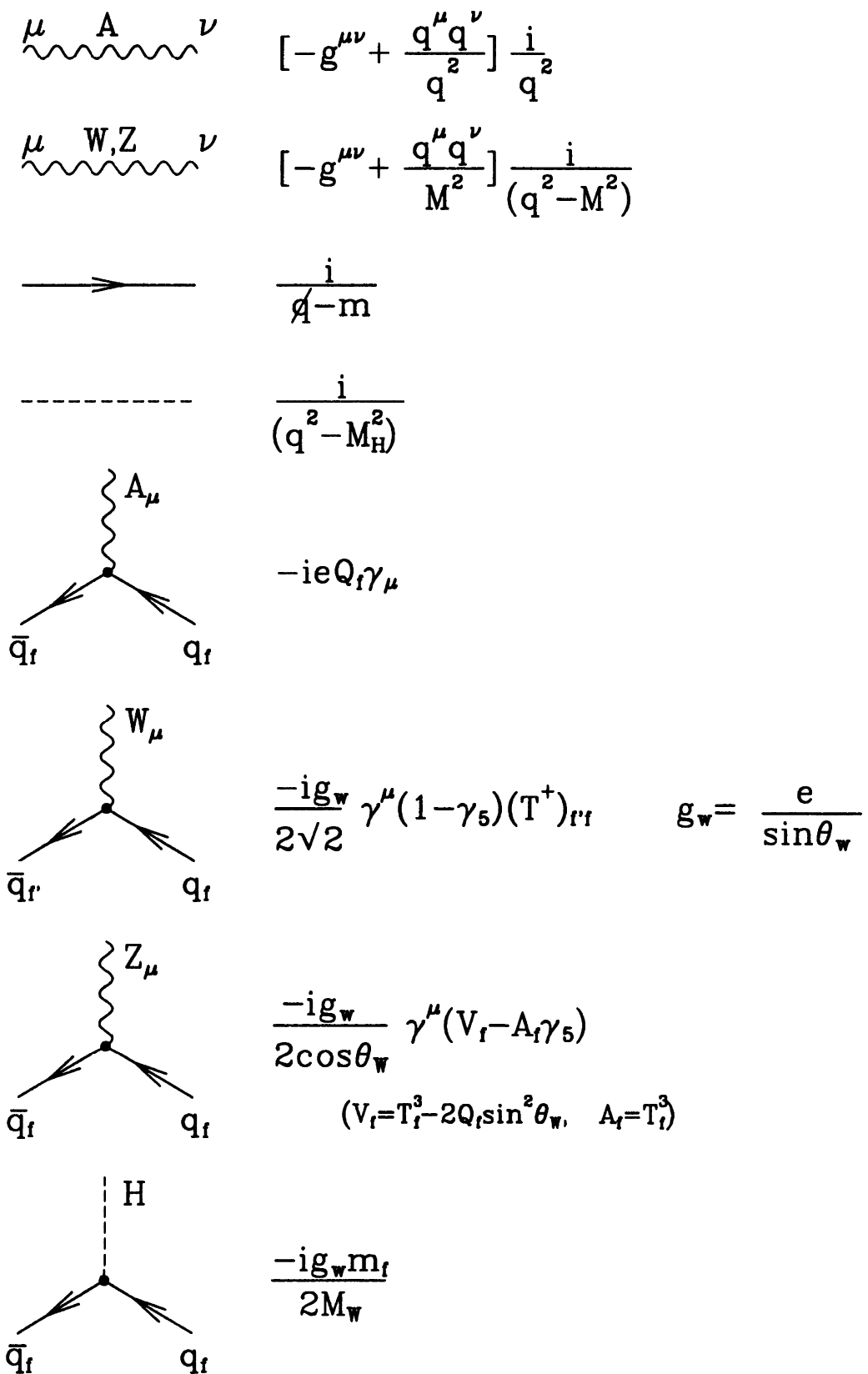


Fig. 8.5. Propagators and Feynman rules for fermion interactions.

At low energies this reproduces the Fermi model,

$$\frac{iG_F}{\sqrt{2}} \bar{u}(\nu_\mu) \gamma^\alpha (1 - \gamma_5) u(\mu) \bar{u}(e) \gamma_\alpha (1 - \gamma_5) v(\bar{\nu}_e), \quad (8.71)$$

provided that the weak charge  $g_W$  is related to the Fermi constant  $G_F$  as follows:

$$\frac{G_F}{\sqrt{2}} = \frac{g_W^2}{8M_W^2}. \quad (8.72)$$

Note that whereas the Higgs boson couples to the  $W$  and  $Z$  with a standard weak coupling strength, the coupling to the fermions is proportional to the fermion mass. In other words, the Higgs boson prefers to couple to the heaviest available fermions. This is manifest in the partial decay widths (see Chapter 11), which are readily obtained from the diagrams of Figs. 8.2 and 8.5.

The Standard Model thus contains a large number of arbitrary Yukawa couplings to fix the quark and charged lepton masses (plus the quark mixing matrix, discussed below), together with four more basic parameters: the two couplings  $g_W, g'_W$ , the Higgs vacuum expectation value  $v$  and the Higgs mass  $M_H$ . The influence of the Higgs mass on low-energy observables is rather mild. Thus at low energy, neglecting fermion masses, we have to supply the values of three physical observables to make predictions with the Standard Model. These are normally taken to be the value of the low-energy fine structure constant,  $\alpha$ , the value of the Fermi constant as measured in muon decay, and the mass of the  $Z$  boson, measured with great accuracy at LEP. Their values are [5,6]

$$\alpha^{-1} = 137.035\,989\,5(61) \quad (8.73)$$

$$G_F = 1.166\,39(2) \times 10^{-5} \text{ GeV}^{-2} \quad (8.74)$$

$$M_Z = 91.188\,5(22) \text{ GeV} \quad (8.75)$$

At tree level their relationships to the fundamental parameters of the Standard Electroweak Model are

$$\begin{aligned} \alpha &= \frac{g_W^2 \sin^2 \theta_W}{4\pi}, \\ G_F &= \frac{1}{\sqrt{2}v^2}, \\ M_Z &= \frac{\frac{1}{2}g_W v}{\cos \theta_W}. \end{aligned} \quad (8.76)$$

### 8.3.3 The CKM matrix

The primed down-type quarks  $q'$  in Eq. (8.57) differ from the mass eigenstate combinations  $q$  by a unitary transformation,  $V$ :

$$\begin{pmatrix} d' \\ s' \\ b' \end{pmatrix} = V \begin{pmatrix} d \\ s \\ b \end{pmatrix}. \quad (8.77)$$

The matrix  $V$  is known as the Cabibbo-Kobayashi-Maskawa (CKM) matrix [12]

$$V = \begin{pmatrix} V_{ud} & V_{us} & V_{ub} \\ V_{cd} & V_{cs} & V_{cb} \\ V_{td} & V_{ts} & V_{tb} \end{pmatrix}. \quad (8.78)$$

The constraint of unitarity is  $V^\dagger V = 1$ . Written out explicitly, this imposes nine conditions

$$\sum_{j=1}^3 |V_{ij}|^2 = \sum_{i=1}^3 |V_{ij}|^2 = 1, \quad (8.79)$$

$$\sum_{k=1}^3 V_{ki}^* V_{kj} = 0 \quad (i \neq j). \quad (8.80)$$

It is important to establish how many independent parameters the CKM matrix contains. In general, an  $n \times n$  unitary matrix depends on  $n^2$  real parameters. Since a real unitary matrix is an orthogonal matrix, with  $\frac{1}{2}n(n - 1)$  independent elements, it follows that there are  $\frac{1}{2}n(n - 1)$  parameters that can be represented by real mixing angles. The remaining  $\frac{1}{2}n(n + 1)$  parameters are phases. However,  $2n - 1$  of these can be absorbed into arbitrary phase rotations of the quark fields  $q$  and  $q'$ , leaving  $\frac{1}{2}(n - 1)(n - 2)$  phases. This means that for  $n = 3$  we have three independent mixing angles and one phase.

The standard parametrization of the CKM matrix is

$$V = \begin{pmatrix} c_{12}c_{13} & s_{12}c_{13} & s_{13}e^{-i\delta} \\ -s_{12}c_{23} - c_{12}s_{23}s_{13}e^{i\delta} & c_{12}c_{23} - s_{12}s_{23}s_{13}e^{i\delta} & s_{23}c_{13} \\ s_{12}s_{23} - c_{12}c_{23}s_{13}e^{i\delta} & -c_{12}s_{23} - s_{12}c_{23}s_{13}e^{i\delta} & c_{23}c_{13} \end{pmatrix} \quad (8.81)$$

with  $s_{ij} = \sin \theta_{ij}$ ,  $c_{ij} = \cos \theta_{ij}$ . In the Standard Model the phase  $\delta$  is responsible for CP violation. Note that if we had only two generations there would be one mixing angle (the Cabibbo angle) and no phases, and hence no possibility for CP violation arising from the mixing matrix.

The experimental limits on the magnitudes of individual matrix ele-

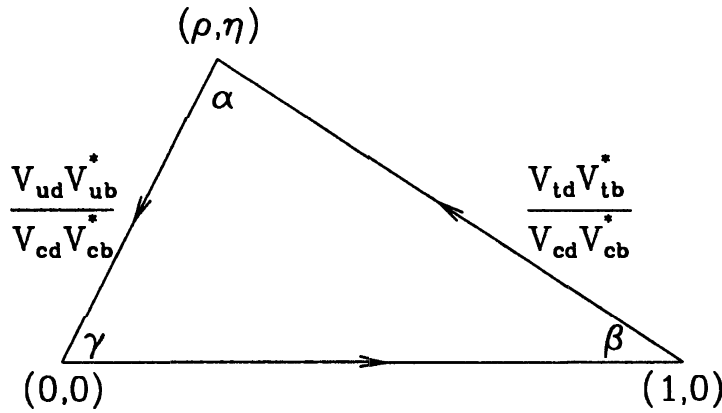


Fig. 8.6. Unitarity triangle.

ments, taking into account constraints derived from unitarity, are [5]

$$V = \begin{pmatrix} 0.9745 - 0.9757 & 0.219 - 0.224 & 0.002 - 0.005 \\ 0.218 - 0.224 & 0.9736 - 0.9750 & 0.036 - 0.046 \\ 0.004 - 0.014 & 0.034 - 0.046 & 0.9989 - 0.9993 \end{pmatrix}. \quad (8.82)$$

It can be seen that the mixing angles are small, and satisfy a hierarchy

$$1 \gg \theta_{12} \gg \theta_{23} \gg \theta_{13}. \quad (8.83)$$

Thus it makes sense to use a small-angle approximation to the general mixing matrix, Eq. (8.81). This leads to a representation due to Wolfenstein [13]. Identifying  $s_{12} = \lambda$  we may write  $V_{cb} \simeq s_{23} = A\lambda^2$  and  $V_{ub} = s_{13}e^{-i\delta} = A\lambda^3(\rho - i\eta)$  with  $A \simeq 1$  and  $|\rho - i\eta| < 1$ . Then, retaining terms up to  $O(\lambda^3)$ ,

$$V \simeq \begin{pmatrix} 1 - \lambda^2/2 & \lambda & A\lambda^3(\rho - i\eta) \\ -\lambda & 1 - \lambda^2/2 & A\lambda^2 \\ A\lambda^3(1 - \rho - i\eta) & -A\lambda^2 & 1 \end{pmatrix}. \quad (8.84)$$

From Eq. (8.82) we see that the poorly determined elements are  $V_{td}$  and  $V_{ub}$ . Therefore the most interesting relationship that can be derived from unitarity is an equation relating these two elements. In fact choosing the values  $d_b$  for  $ij$  in Eq.(8.80) we obtain

$$V_{ub}^*V_{ud} + V_{cb}^*V_{cd} + V_{tb}^*V_{td} = 0. \quad (8.85)$$

This relation between complex numbers defines a triangle in the complex plane, known as a unitarity triangle, shown in Fig. 8.6. Since  $V_{ud}$  and  $V_{tb}$  are both close to one we may approximate Eq. (8.85) by

$$V_{ub}^* + V_{cb}^*V_{cd} + V_{td} = 0. \quad (8.86)$$

The accurate determination of the angles and lengths of the sides of this unitarity triangle remains a challenge for experiment.

### 8.4 $W$ and $Z$ decay properties

The Standard Model predictions for the partial decay widths of the  $W$  and  $Z$  bosons into the various fermion-antifermion final states can be tested with great precision at present-day high-energy  $e^+e^-$  and  $p\bar{p}$  colliders. In this section we derive some simple results for the decay widths. At leading order in electroweak perturbation theory, the partial width for the decay of the  $Z$  boson into a fermion-antifermion pair,

$$Z(q) \rightarrow f(p)\bar{f}(p') , \quad (8.87)$$

is given (in the Standard Model) by

$$\frac{-ig_W}{2\cos\theta_W} \bar{u}(p)\gamma^\mu(V_f - A_f\gamma_5)v(p')\epsilon_\mu(q). \quad (8.88)$$

The invariant matrix element squared for this process summed (averaged) over final (initial) polarizations is given by

$$\overline{\sum}|\mathcal{M}|^2 = \frac{8}{3}\frac{G_F M_Z^4}{\sqrt{2}}(|V_f|^2 + |A_f|^2) . \quad (8.89)$$

The sum over the three polarizations of the  $Z$  boson is performed using

$$\sum_i \epsilon_\mu^{(i)}(q)\epsilon_\nu^{(i)*}(q) = -g_{\mu\nu} + \frac{q_\mu q_\nu}{M_Z^2} . \quad (8.90)$$

The two-particle phase space is given by Eq. (8.39). The final result for the partial width is

$$\begin{aligned} \Gamma(Z^0 \rightarrow f\bar{f}) &= C \frac{G_F M_Z^3}{6\sqrt{2}\pi} (|V_f|^2 + |A_f|^2) \\ &= 332 C(|V_f|^2 + |A_f|^2) \text{ MeV} , \end{aligned} \quad (8.91)$$

where  $C$  is a colour normalization factor which is 1 for leptons and 3 for quarks. The corresponding result for the  $W$  boson is

$$\Gamma(W^+ \rightarrow f\bar{f}') = C \frac{G_F M_W^3}{6\sqrt{2}\pi} . \quad (8.92)$$

The  $W^+$  decay rate refers to the sum of the decays to a given quark of charge  $\frac{2}{3}$  and all antiquarks of charge  $\frac{1}{3}$ , e.g.  $W^+ \rightarrow u\bar{d} + u\bar{s} + u\bar{b}$ . For any individual mode  $W \rightarrow f_i\bar{f}_j$  there is an additional factor  $|V_{ij}|^2$  from the CKM mixing matrix.

Using these results for the partial widths of the  $W$  and the  $Z$  we can calculate the branching ratios for the various fermion-antifermion decay modes shown in Table 8.4. Note the sizeable branching fraction for decay into  $b$  quarks.

There is also a large branching fraction of the  $Z$  boson into neutrinos, which are not detectable. The measurement of the width for decay of

Process	Relative coupling	Branching Ratio
$W^+ \rightarrow e^+ \bar{\nu}, \mu^+ \bar{\nu}, \tau^+ \bar{\nu}$	1	$3 \times 11.1\%$
$W^+ \rightarrow u\bar{d} + u\bar{s} + u\bar{b}$	3	33.3%
$W^+ \rightarrow c\bar{d} + c\bar{s} + c\bar{b}$	3	33.3%
$Z \rightarrow \nu_e \bar{\nu}_e, \nu_\mu \bar{\nu}_\mu, \nu_\tau \bar{\nu}_\tau$	$\frac{1}{2}$	$3 \times 6.8\%$
$Z \rightarrow e^+ e^-, \mu^+ \mu^-, \tau^+ \tau^-$	$\frac{1}{4} + (\frac{1}{2} - 2 \sin^2 \theta_W)^2$	$3 \times 3.4\%$
$Z \rightarrow u\bar{u}, c\bar{c}$	$3 [\frac{1}{4} + (\frac{1}{2} - \frac{4}{3} \sin^2 \theta_W)^2]$	$2 \times 11.8\%$
$Z \rightarrow d\bar{d}, s\bar{s}, b\bar{b}$	$3 [\frac{1}{4} + (\frac{1}{2} - \frac{2}{3} \sin^2 \theta_W)^2]$	$3 \times 15.2\%$

Table 8.4. Vector boson decay into fermion-antifermion.

the  $Z$  boson into invisible particles counts the number of light neutrino species. The theoretical result for the ratio of the width into one species of neutrino, divided by the width into one species of lepton is

$$\frac{\Gamma(Z \rightarrow \nu\bar{\nu})}{\Gamma(Z \rightarrow l^+l^-)} = \frac{2}{1 + (1 - 4 \sin^2 \theta_W)^2} \approx 1.99. \quad (8.93)$$

The experimental result [6] for the ratio of ‘invisible’ width to the width into one type of lepton pair is

$$\frac{\Gamma(Z \rightarrow \text{inv})}{\Gamma(Z \rightarrow l^+l^-)} = 5.956 \pm 0.031, \quad (8.94)$$

This measurement fixes the number of light neutrino species to be  $2.991 \pm 0.016$  [6].

At hadron colliders one can normally only detect the decays of the vector bosons into charged leptons. Although the hadronic decay modes are enhanced relative to the leptonic modes, at a hadron collider there is a very serious background to the former from normal QCD two-jet production<sup>1</sup>.

## 8.5 Vector boson scattering

The underlying gauge theory structure of the Standard Electroweak Model leads to strong cancellations in the high-energy behaviour of amplitudes for the scattering of gauge bosons [15]. In this section we illustrate these

<sup>1</sup> A statistically significant signal for the hadronic decay of the  $W$  and  $Z$ , at the expected level, has been found by the UA2 collaboration [14].

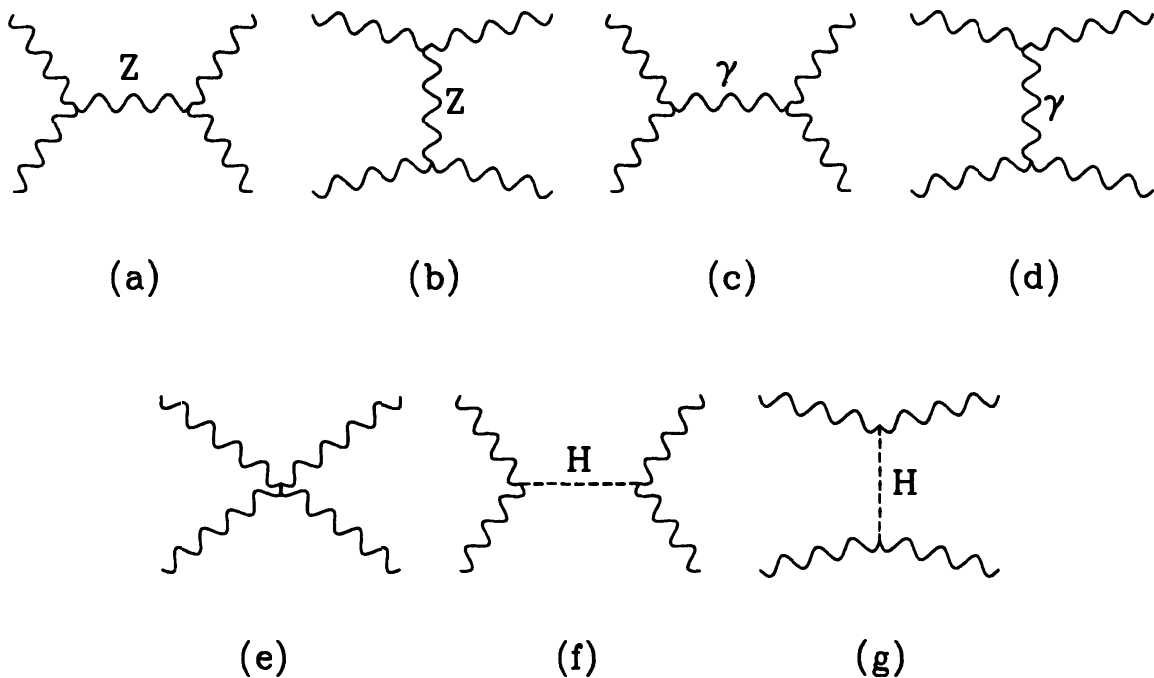


Fig. 8.7. Tree diagrams for  $W^+ + W^- \rightarrow W^+ + W^-$  scattering.

cancellations by considering the scattering of  $W$ -bosons. The relevant diagrams, shown in Fig. 8.7, can be calculated using the Feynman rules of Fig. 8.2. The calculation will also allow us to display the role of the physical Higgs boson in  $WW$  scattering.

## Consider the process

$$W^+(p_+) + W^-(p_-) \rightarrow W^+(q_+) + W^-(q_-) \quad (8.95)$$

in the centre-of-mass frame in which the incoming  $W$  bosons travel along the  $z$  axis. In this frame the kinematics of the reaction may be written as

$$\begin{aligned} p_{\pm} &= (E, 0, 0, \pm p), \\ q_{+} &= (E, 0, \pm p \sin \theta, \pm p \cos \theta), \end{aligned} \quad (8.96)$$

where  $E^2 - p^2 = M_W^2$  and  $\theta$  is the centre-of-mass scattering angle. The vector bosons can have longitudinal or transverse polarizations. Here we consider only the scattering of longitudinal bosons, which is responsible for the leading behaviour at high energy. The longitudinal polarization vectors for the  $W$  bosons are

$$\begin{aligned}\varepsilon_L(p_{\pm}) &= \left( \frac{p}{M_W}, 0, 0, \pm \frac{E}{M_W} \right), \\ \varepsilon_L(q_{\pm}) &= \left( \frac{p}{M_W}, 0, \pm \frac{E}{M_W} \sin \theta, \pm \frac{E}{M_W} \cos \theta \right). \quad (8.97)\end{aligned}$$

The polarizations satisfy the Lorentz condition  $\epsilon(k) \cdot k = 0$  and are normalized so that  $\epsilon^2 = -1$ . In the high-energy limit we find that the result

for the diagrams in Fig. 8.7 involving the three-boson vertex is

$$T^{a-d} = g_W^2 \left\{ \frac{p^4}{M_W^4} [3 - 6 \cos \theta - \cos^2 \theta] + \frac{p^2}{M_W^2} \left[ \frac{9}{2} - \frac{11}{2} \cos \theta - 2 \cos^2 \theta \right] \right\}, \quad (8.98)$$

neglecting terms not enhanced by factors of  $p^2/M_W^2$ . The corresponding result for the diagram with the four-boson vertex is

$$T^e = g_W^2 \left\{ \frac{p^4}{M_W^4} [-3 + 6 \cos \theta + \cos^2 \theta] + \frac{p^2}{M_W^2} [-4 + 6 \cos \theta + 2 \cos^2 \theta] \right\}. \quad (8.99)$$

Finally, the graphs involving Higgs exchange give

$$T^{f-g} = g_W^2 \left\{ \frac{p^2}{M_W^2} \left[ -\frac{1}{2} - \frac{1}{2} \cos \theta \right] - \frac{M_H^2}{4M_W^2} \left[ \frac{s}{s - M_H^2} + \frac{t}{t - M_H^2} \right] \right\}. \quad (8.100)$$

Because of the longitudinal polarizations, the high-energy behaviour of individual graphs in Fig. 8.7 grows with the centre-of-mass momentum like

$$T(s, t) = A \left( \frac{p}{M_W} \right)^4 + B \left( \frac{p}{M_W} \right)^2 + C. \quad (8.101)$$

On summing over graphs, the term  $A$  cancels without including the Higgs graphs, ( $f$ ) and ( $g$ ). The full cancellation of the  $B$  term involves the Higgs boson in an essential way. On summing all graphs the result is

$$T(s, t) = -g_W^2 \frac{M_H^2}{4M_W^2} \left[ \frac{s}{s - M_H^2} + \frac{t}{t - M_H^2} \right] \quad (8.102)$$

$$\equiv -4 \left[ \lambda + \frac{(\lambda v)^2}{s - 2\lambda v^2} + \frac{(\lambda v)^2}{t - 2\lambda v^2} \right]. \quad (8.103)$$

Eq. (8.103) results from substituting for  $M_W$  and  $M_H$  using Eqs. (8.32) and (8.36). It is no accident that this expression looks like the amplitude for the scattering of charged scalar particles. The longitudinal components of the  $W$  are derived from the charged components of the Higgs doublet  $\phi$ . The result of Eq. (8.103) can be simply calculated from the theory without gauge couplings in which there are three Goldstone bosons interacting with one massive scalar:

$$\begin{aligned} \mathcal{L}_{\text{Goldstone}} = & \frac{1}{2} \partial_\mu H \partial^\mu H + \frac{1}{2} \partial_\mu z \partial^\mu z + \partial_\mu w^+ \partial^\mu w^- - \lambda v H^2 \\ & - \lambda v H (2w^+ w^- + z^2 + H^2) - \frac{1}{4} \lambda (2w^+ w^- + z^2 + H^2)^2. \end{aligned} \quad (8.104)$$

The two charged massless Goldstone bosons are denoted by  $w^\pm$  and the diagrams are shown in Fig. 8.8.

Although the leading-order  $WW$  scattering amplitude does not diverge at high energy, it might still be too large to be consistent with the fundamental physical limitation due to unitarity of the scattering matrix. To

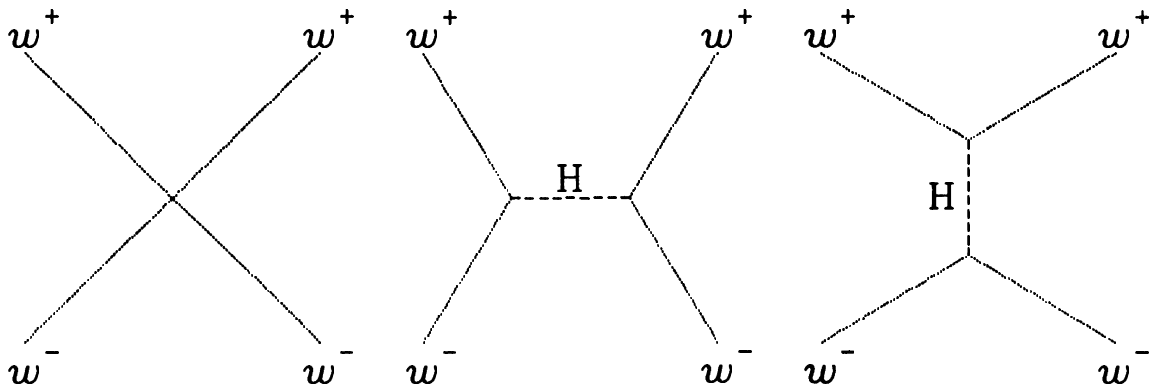


Fig. 8.8. Tree diagrams for  $w^+ + w^- \rightarrow w^+ + w^-$  scattering.

derive the unitarity limit on the high-energy behaviour it is convenient to perform a partial wave expansion,

$$T(s, t) = 16\pi \sum_J (2J + 1) a_J(s) P_J(\cos \theta), \quad (8.105)$$

where  $P_J$  are the Legendre polynomials,  $P_0(x) = 1$ ,  $P_1(x) = x$  and  $P_2(x) = \frac{1}{2}(3x^2 - 1)$  etc., and  $\cos \theta = 1 + 2t/s$  at high energy. The partial wave expansion decomposes the amplitudes into the contributions from various total angular momenta  $J$ . The differential cross section, neglecting particles masses, is given by

$$\frac{d\sigma}{d\Omega} = \frac{1}{64\pi^2 s} |T(s, t)|^2. \quad (8.106)$$

Inserting Eq. (8.105) and using the orthogonality property of the Legendre polynomials,

$$\int_{-1}^1 dx P_J(x) P_K(x) = \delta_{JK} \frac{2}{2J + 1}, \quad (8.107)$$

we find that the total cross section is given by

$$\sigma = 16\pi \sum_J (2J + 1) |a_J(s)|^2. \quad (8.108)$$

Using the optical theorem

$$\sigma = \frac{1}{s} \text{Im } T(s, 0), \quad (8.109)$$

we find that

$$|a_J|^2 = \text{Im } a_J \quad (8.110)$$

and hence the modulus of  $a_J$  cannot exceed one. Since  $J$  is conserved, the modulus of each partial wave amplitude cannot exceed its initial value, which for a plane-wave incoming state is one.

From Eq. (8.102), we find that the result for the  $J = 0$  partial wave amplitude is

$$\begin{aligned} a_0(s) &= -\frac{G_F M_H^2}{8\pi\sqrt{2}} \left[ 2 + \frac{M_H^2}{s - M_H^2} - \frac{M_H^2}{s} \ln \left( 1 + \frac{s}{M_H^2} \right) \right] \\ &\rightarrow -\frac{G_F M_H^2}{4\pi\sqrt{2}}. \end{aligned} \quad (8.111)$$

In the second line of this equation we have taken the limit  $s \gg M_H^2$ . Since unitarity will be violated if  $|a_0| > 1$ , this implies that  $M_H^2 < 4\sqrt{2}\pi/G_F$ . A slightly more sophisticated analysis [16], involving consideration of all elastic boson-boson scattering channels, gives the limit

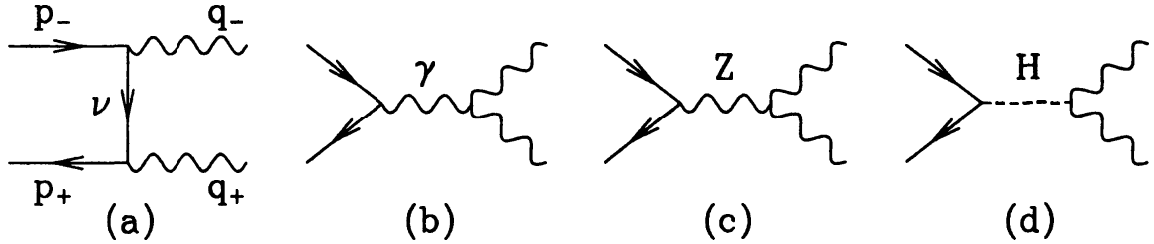
$$M_H < \left( \frac{8\sqrt{2}\pi}{3G_F} \right)^{\frac{1}{2}} \approx 1 \text{ TeV}. \quad (8.112)$$

We therefore find that if the limit in Eq. (8.112) is exceeded then weak interactions will become strong, *i.e.* the high-energy scattering of weak bosons will not be adequately described by perturbation theory. It is important to stress the nature of the limit that we have derived. If Eq. (8.112) is violated the perturbative methods which we have used to derive the bound cannot be trusted. The Higgs mass can exceed the value given by the bound, but in that case its properties cannot be analysed using perturbation theory. Therefore if we can investigate the scattering of longitudinal vector bosons at a high-energy hadron collider, we will either discover the Higgs boson or see strong interactions of the electroweak bosons, or both. This provides a compelling motivation for the construction of such a machine.

## 8.6 Vector boson pair production

We have seen that the Standard Model makes specific predictions for the couplings of vector bosons, which follow from the non-Abelian symmetry and the local gauge invariance of the Lagrangian. It is important to test these predictions as precisely as possible. As described above, gauge cancellations amongst the couplings have an enormous effect on the high-energy behaviour of  $WW$  scattering. A process which will be subjected to experimental scrutiny in the more immediate future is the production of  $W$  pairs in  $e^+e^-$  annihilation.

We consider the process  $e^-e^+ \rightarrow W^-W^+$  with Feynman diagrams shown in Fig. 8.9. For simplicity we set the electron mass to zero in which case Fig. 8.9(d) makes no contribution. The outgoing vector bosons can have longitudinal or transverse polarizations. Here we consider only

Fig. 8.9. Diagrams for  $e^- e^+ \rightarrow W^- W^+$ .

the longitudinal polarization, which is responsible diagram-by-diagram for the leading behaviour at high energy. We choose a frame in which the outgoing momenta are directed along the  $z$  axis. Then the polarization vectors are

$$\begin{aligned}\epsilon_L(q_{\pm}) &= \left( \frac{\mathbf{q}}{M_W}, 0, 0, \pm \frac{E}{M_W} \right) \\ &\sim \frac{1}{M_W} \left( q_{\pm} - \frac{M_W^2}{2E^2} q_{\mp} \right).\end{aligned}\quad (8.113)$$

Because of these terms, the individual diagrams shown in Fig. 8.9 will lead to amplitudes which grow like  $E^2$ . If we are only interested in the leading terms we may contract each vector boson with the leading term in Eq. (8.113). The contribution of diagram (a) is given by

$$M = \frac{(-ig_W)^2}{8} \bar{v}(-p_+) \not{q}(q_+) (1 - \gamma_5) \frac{i}{\not{p}_- - \not{q}_-} \not{q}(q_-) (1 - \gamma_5) u(p_-). \quad (8.114)$$

Inserting the leading term for the polarizations from Eq. (8.113) and dropping non-leading terms, we obtain

$$M = -i \frac{(-ig_W)^2}{8M_W^2} \bar{v}(-p_+) (\not{q}_+ - \not{q}_-) (1 - \gamma_5) u(p_-). \quad (8.115)$$

The contribution of the photon exchange diagram (b), using the Feynman rules of Figs. 8.2 and 8.5, is

$$\begin{aligned}M &= (-ig_W)(ig_W) Q_e \sin^2 \theta_W \bar{v}(-p_+) \gamma^\rho u(p_-) \frac{-ig_{\rho\alpha}}{(q_+ + q_-)^2} \\ &\times V^{\alpha\beta\delta}(q_+ + q_-, -q_-, -q_+, \epsilon_\beta(q_-) \epsilon_\delta(q_+) ).\end{aligned}\quad (8.116)$$

The contribution of the  $Z$  exchange diagram (c) is

$$\begin{aligned}M &= \frac{(-ig_W)(ig_W)}{2} \bar{v}(-p_+) \gamma^\rho (V_e - A_e \gamma_5) u(p_-) \frac{-ig_{\rho\alpha}}{(q_+ + q_-)^2 - M_Z^2} \\ &\times V^{\alpha\beta\delta}(q_+ + q_-, -q_-, -q_+, \epsilon_\beta(q_-) \epsilon_\delta(q_+) )\end{aligned}\quad (8.117)$$

where

$$V^{\alpha\beta\delta}(p, q, r) = g^{\alpha\beta}(p^\delta - q^\delta) + g^{\beta\delta}(q^\alpha - r^\alpha) + g^{\delta\alpha}(r^\beta - p^\beta). \quad (8.118)$$

Hence we find, using the approximate longitudinal polarization vector of Eq. (8.113),

$$\begin{aligned} V^{\alpha\beta\delta}(q_+ + q_-, -q_-, -q_+) \epsilon_\beta(q_-) \epsilon_\delta(q_+) \\ = -\frac{(q_+ + q_-)^2}{2M_W^2} [q_+^\alpha - q_-^\alpha] + O(1). \end{aligned} \quad (8.119)$$

The result for the sum of the  $Z$  and  $\gamma$  exchange contributions, after inserting the values for  $V_e$  and  $A_e$ , is

$$M = i \frac{(-ig_W)^2}{8M_W^2} \bar{v}(-p_+) (q_+ - q_-)(1 - \gamma_5) u(p_-), \quad (8.120)$$

which cancels exactly with Eq. (8.115). So we see that the leading high-energy behaviour is cancelled, as a result of the relationship between the three-boson couplings and the couplings to fermions imposed by the gauge structure.

The total cross section for  $W^+W^-$  production by a massless fermion-antifermion pair is given by [17]

$$\begin{aligned} \sigma = & \frac{2\pi\alpha^2}{s} \left\{ \left[ \left( Q_i + \frac{V_i}{2x_W} \frac{s}{s - M_Z^2} \right)^2 + \left( \frac{A_i}{2x_W} \frac{s}{s - M_Z^2} \right)^2 \right] A(y_W, \beta_W) \right. \\ & - \frac{\text{sign}(Q_i)}{2x_W} \left( Q_i + \frac{V_i + A_i}{2x_W} \frac{s}{s - M_Z^2} \right) \sum_j |V_{ij}|^2 I(y_W, \beta_W) \\ & \left. + \frac{1}{8x_W^2} \left( \sum_j |V_{ij}|^2 \right)^2 E(y_W, \beta_W) \right\}, \end{aligned} \quad (8.121)$$

where  $x_W = \sin^2 \theta_W$ ,  $y_W = M_W^2/s$  and  $\beta_W = \sqrt{1 - 4y_W}$ . The matrix  $V_{ij}$  here refers to the CKM matrix, necessary in the case of initial quarks. The three terms in Eq. (8.121) correspond to the square of the  $s$ -channel exchange diagram, the interference between  $s$ - and  $t$ -channel exchange diagrams and the square of the  $t$ -channel exchange diagram, respectively. The functions  $A$ ,  $I$  and  $E$  are given by

$$\begin{aligned} A(y, \beta) &= \frac{\beta^3}{y^2} \left[ \frac{1}{24} + \frac{5}{6}y + \frac{1}{2}y^2 \right] \\ I(y, \beta) &= \frac{\beta}{y^2} \left[ \frac{1}{24} + \frac{3}{4}y - \frac{7}{6}y^2 - y^3 \right] - 4y(1 + \frac{1}{2}y) \ln \left( \frac{1+\beta}{1-\beta} \right) \\ E(y, \beta) &= \frac{\beta}{y^2} \left[ \frac{1}{24} + \frac{5}{6}y - 2y^2 \right] + 2(1 - 2y) \ln \left( \frac{1+\beta}{1-\beta} \right). \end{aligned} \quad (8.122)$$

Because of the singular nature of these functions at small  $y$ , individual terms lead to contributions to the cross section which grow like  $s$ , due

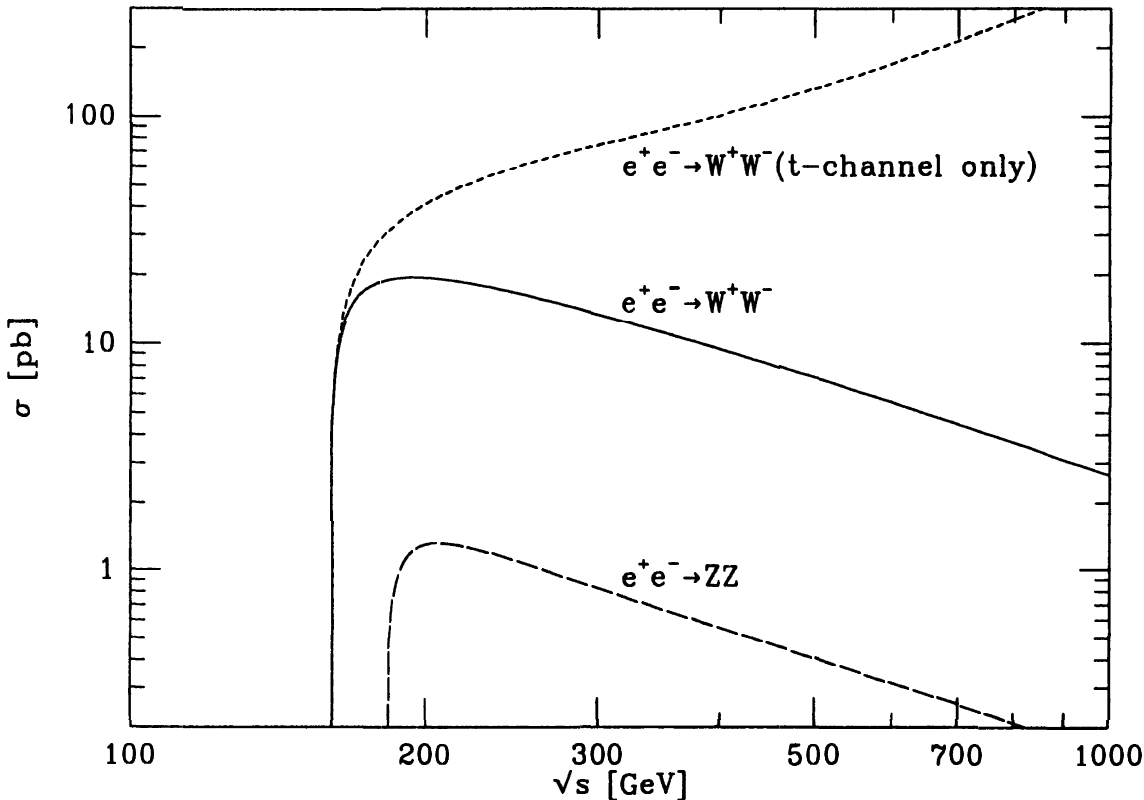


Fig. 8.10.  $W$  and  $Z$  pair cross sections in  $e^+e^-$  annihilation.

to the production of longitudinal gauge bosons. This behaviour is cancelled on summing over all diagrams because of the gauge structure of the underlying Lagrangian. Fig. 8.10 shows the  $W$  pair production cross section. To illustrate the strength of the cancellation we also show the contribution from the  $t$ -channel exchange diagram, *i.e.* the third line of Eq. (8.121) calculated using Fig. 8.9(a) alone.

The corresponding formula for  $Z$  pair production is

$$\sigma = \frac{\pi\alpha^2}{4sx_W^2(1-x_W)^2} (V_i^4 + A_i^4 + 6V_i^2A_i^2) \left[ \frac{1+4y_Z^2}{1-2y_Z} \ln \left( \frac{1+\beta_Z}{1-\beta_Z} \right) - \beta_Z \right] \quad (8.123)$$

where  $y_Z = M_Z^2/s$  and  $\beta_Z = \sqrt{1-4y_Z}$ . Fig. 8.10 also shows the  $Z$  pair production cross section as a function of energy.

Vector boson pair production can also be studied at hadronic colliders. The techniques for calculating single vector boson production in hadron-hadron reactions will be described in the next chapter. Fig. 8.11 shows the cross sections for the production of pairs of vector bosons calculated at lowest order in perturbation theory<sup>2</sup>. Higher-order QCD corrections have

<sup>2</sup> In this figure we assume that the weak bosons have zero width. In practice the non-zero widths will allow the production of off-shell bosons and modify the threshold region.

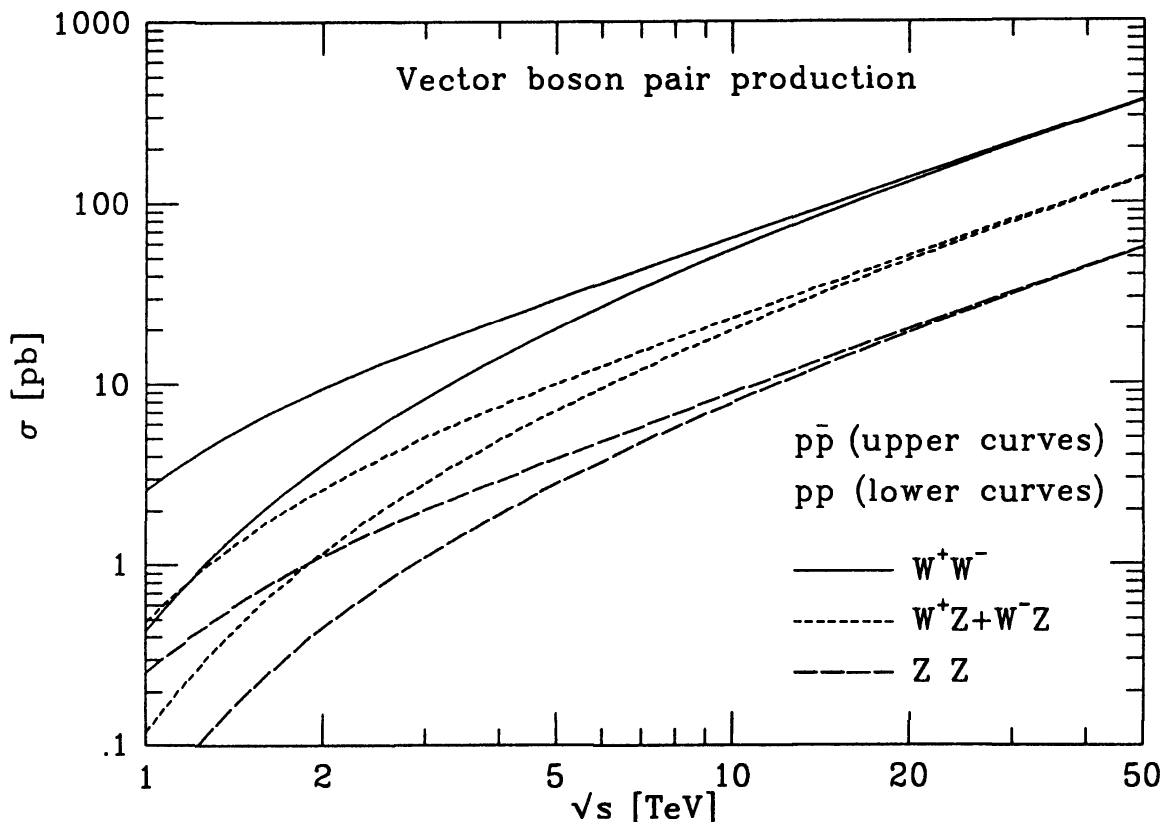


Fig. 8.11. Vector boson pair production cross sections in  $p\bar{p}$  and  $pp$  collisions.

been calculated to all of these processes and tend to increase the cross sections. For details we refer the reader to refs. [18-20].

## References

- 1) S. Glashow, *Nucl. Phys.* **B22** (1961) 579;  
A. Salam, in *Elementary Particle Theory*, ed. N. Svartholm, Almqvist and Forlag, Stockholm (1968);  
S. Weinberg, *Phys. Rev. Lett.* **19** (1967) 1264.
- 2) T-P. Cheng and L-F. Li, *Gauge theory of elementary particle physics*, Oxford University Press (1984);  
H. Georgi, *Weak interactions and modern particle theory*, Addison-Wesley (1984);  
E.S. Abers and B.W. Lee, *Phys. Rep.* **9C** (1973) 1.
- 3) P.W. Higgs, *Phys. Lett.* **12** (1964) 132; *Phys. Rev. Lett.* **13** (1964) 508; *Phys. Rev.* **145** (1966) 1156;  
R. Brout and F. Englert, *Phys. Rev. Lett.* **13** (1964) 321.
- 4) D.A. Ross and M. Veltman, *Nucl. Phys.* **B95** (1975) 135;  
M. Veltman, *Nucl. Phys.* **B123** (1977) 89.
- 5) Particle Data Group, L. Montanet *et al.*, *Review of Particle Properties*, *Phys. Rev.* **D50** (1994) 1173.
- 6) LEP electroweak working group, preprint CERN-PPE/95-172 (1995).
- 7) S. Weinberg, *Phys. Rev.* **D19** (1979) 1277;  
L. Susskind, *Phys. Rev.* **D20** (1979) 2619;  
P. Sikivie *et al.*, *Nucl. Phys.* **B173** (1980) 189.

- 8) S.L. Adler, *Phys. Rev.* **177** (1969) 2426;  
J.S. Bell and R. Jackiw, *Nuovo Cimento* **60A** (1969) 47.
- 9) S.L. Adler and W.A. Bardeen, *Phys. Rev.* **182** (1969) 1517;  
W.A. Bardeen, *Phys. Rev.* **184** (1969) 1848.
- 10) C. Bouchiat, J. Iliopoulos and P. Meyer, *Phys. Lett.* **B38** (1972) 519;  
D.J. Gross and R. Jackiw, *Phys. Rev.* **D6** (1972) 477.
- 11) D. Schaile, Proc. XXVII Int. Conf. on High Energy Physics, Glasgow, July 1994, eds.  
P.J. Bussey and I.G. Knowles, Institute of Physics Publishing, Bristol (1995), Vol. I,  
p. 27.
- 12) N. Cabibbo, *Phys. Rev. Lett.* **10** (1961) 531;  
M. Kobayashi and T. Maskawa, *Prog. Theor. Phys.* **49** (1973) 652.
- 13) L. Wolfenstein, *Phys. Rev. Lett.* **51** (1983) 1945.
- 14) UA2 collaboration, R. Ansari *et al.*, *Phys. Lett.* **B168** (1987) 452.
- 15) C.H. Llewellyn Smith, *Phys. Lett.* **B46** (1973) 233;  
J.M. Cornwall, D.M. Levin and G. Tiktopoulos, *Phys. Rev.* **D10** (1974) 1145.
- 16) B.W. Lee, C. Quigg and H.B. Thacker, *Phys. Rev. Lett.* **38** (1977) 883; *Phys. Rev.* **D16** (1977) 1519.
- 17) R.W. Brown and K.O. Mikaelian, *Phys. Rev.* **D19** (1979) 922;  
R.W. Brown *et al.*, *Phys. Rev.* **D20** (1979) 1164.
- 18) S. Frixione, *Nucl. Phys.* **B410** (1993) 280;  
J. Ohnemus, *Phys. Rev.* **D44** (1991) 1403.
- 19) S. Frixione, P. Nason and G. Ridolfi, *Nucl. Phys.* **B383** (1992) 3;  
J. Ohnemus, *Phys. Rev.* **D44** (1991) 3477.
- 20) B. Mele, P. Nason and G. Ridolfi, *Nucl. Phys.* **B357** (1991) 409;  
J. Ohnemus and J.F. Owens, *Phys. Rev.* **D43** (1991) 3626.

## 9

# The production of vector bosons

It was first pointed out by Drell and Yan [1] that parton model ideas developed for deep inelastic scattering could be extended to certain processes in hadron-hadron collisions. The paradigm process is the production of a lepton pair  $l^+l^-$  with a large invariant mass-squared,  $M^2 = (p_{l+} + p_{l-})^2 \gg 1 \text{ GeV}^2$ , by quark-antiquark annihilation — the Drell-Yan process. In the naive parton model, the cross section  $\sigma_{AB}$  for producing such a pair in the collision of beam  $A$  and target  $B$  is obtained by simply weighting the subprocess cross section  $\hat{\sigma}$  for  $q\bar{q} \rightarrow l^+l^-$  with the parton distribution functions  $f_q(x)$  and  $f_{\bar{q}}(x)$  extracted from deep inelastic scattering, and summing over all quark-antiquark combinations in the beam and target:

$$\sigma_{AB} = \sum_q \int dx_1 dx_2 f_q(x_1) f_{\bar{q}}(x_2) \hat{\sigma}_{q\bar{q} \rightarrow l^+l^-} . \quad (9.1)$$

At lowest order in perturbation theory, and assuming  $M \ll M_Z$ , the subprocess cross section is given by the annihilation process,  $q\bar{q} \rightarrow \gamma^* \rightarrow l^+l^-$ . The formal domain of validity of Eq. (9.1) is the asymptotic ‘scaling’ limit  $M^2, s \rightarrow \infty, \tau = M^2/s$  fixed, analogous to the Bjorken limit,  $Q^2, \nu \rightarrow \infty, x = Q^2/2\nu$  fixed, of deep inelastic scattering. The general structure is illustrated in Fig. 9.1.

The good agreement between theoretical predictions based on (9.1) and measured Drell-Yan cross sections provided confirmation of the validity of this parton model approach. It was the first time that a hadron-hadron cross section could be calculated from first principles. The parton model formalism also survived the inclusion of perturbative QCD corrections. Even though collinear singularities occur in the calculation of real and virtual gluon corrections to the lowest-order process, these turn out to be the *same* as those which arise in deep inelastic scattering structure function calculations, described in Section 4.3. They can therefore be

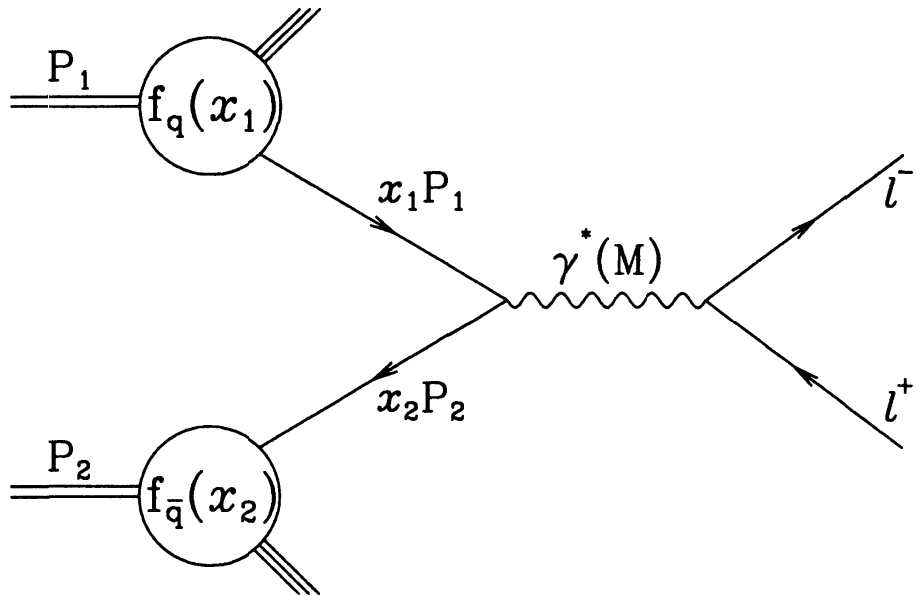


Fig. 9.1. Lepton pair production in the Drell-Yan model.

absorbed into ‘renormalized’, scale-dependent parton distributions.<sup>1</sup> The key point is that *all* collinear divergences appearing in the Drell-Yan corrections can be factored into renormalized parton distributions in this way. Factorization theorems show that this is a general feature of inclusive ‘hard-scattering’ processes in hadron-hadron collisions [2]. We will see explicitly how this happens at  $O(\alpha_s)$  in the following section. Taking into account the leading corrections, Eq. (9.1) then becomes

$$\sigma_{AB} = \sum_q \int dx_1 dx_2 f_q(x_1, M^2) f_{\bar{q}}(x_2, M^2) \hat{\sigma}_{q\bar{q} \rightarrow l^+ l^-}. \quad (9.2)$$

A final step is to take into account the finite contributions left behind after the singularities have been factored into the parton distributions. These constitute a genuine  $O(\alpha_s)$  perturbative correction to the cross section, sometimes called the ‘K-factor’:

$$\begin{aligned} \sigma_{AB} &= \sum_q \int dx_1 dx_2 f_q(x_1, M^2) f_{\bar{q}}(x_2, M^2) \\ &\times [\hat{\sigma}_0 + a \hat{\sigma}_1 + a^2 \hat{\sigma}_2 + \dots]_{q\bar{q} \rightarrow l^+ l^-}, \end{aligned} \quad (9.3)$$

with  $a = \alpha_s(M^2)/2\pi$ . The structure displayed in Eq. (9.3) is completely general, applicable to a wide variety of hard-scattering processes, including jet and heavy flavour production described in Chapters 7 and 10 respectively. Most of the important hard-scattering processes have been

<sup>1</sup> We use ‘renormalized’ here in the sense of Chapter 4, i.e. having combined collinear divergences with an unphysical bare distribution to produce a finite, physical parton distribution.

calculated to next-to-leading order in perturbation theory, *i.e.* up to and including the  $\hat{\sigma}_1$  terms. The Drell-Yan process itself has been calculated to next-to-next-to-leading order.

In the following section we discuss the Drell-Yan cross section in detail, first in the parton model and then with perturbative corrections, illustrating the factorization property described above. We then extend the discussion to include  $Z$  and  $W$  production in high-energy  $p\bar{p}$  collisions. These are also Drell-Yan cross sections, with the subprocess  $q\bar{q} \rightarrow \gamma^* \rightarrow l^+l^-$  replaced by  $q\bar{q} \rightarrow Z \rightarrow l^+l^-$  and  $q\bar{q}' \rightarrow W \rightarrow l\nu$  respectively.

## 9.1 The Drell-Yan mechanism

The lowest-order cross section for quark-antiquark annihilation into a lepton pair via an intermediate off-mass-shell photon is easily obtained from the  $e^+e^- \rightarrow q\bar{q}$  cross section presented in Chapter 3, Eq. (3.5):

$$\hat{\sigma}(q(p_1)\bar{q}(p_2) \rightarrow l^+l^-) = \frac{4\pi\alpha^2}{3\hat{s}} \frac{1}{N} Q_q^2, \quad (9.4)$$

where  $\hat{s} = (p_1 + p_2)^2$ . Note that  $\hat{\sigma}(q\bar{q} \rightarrow l^+l^-)$  is smaller than  $\hat{\sigma}(l^+l^- \rightarrow q\bar{q})$  by a colour factor of  $1/N^2 = 1/9$  because of the average over the colours of the initial-state quarks. In other words, only when the colour of the quark matches the colour of the antiquark can the annihilation into a colour singlet final state take place. In general the incoming quark and antiquark have a spectrum of collision energies  $\sqrt{\hat{s}}$ , and so it is more appropriate to consider the differential lepton pair mass distribution. Thus the subprocess cross section for producing a lepton pair of mass  $M$  is

$$\frac{d\hat{\sigma}}{dM^2} = \frac{\sigma_0}{N} Q_q^2 \delta(\hat{s} - M^2), \quad \sigma_0 = \frac{4\pi\alpha^2}{3M^2}. \quad (9.5)$$

In the centre-of-mass frame of the two hadrons, the four-momenta of the incoming partons are

$$\begin{aligned} p_1 &= \frac{\sqrt{\hat{s}}}{2}(x_1, 0, 0, x_1), \\ p_2 &= \frac{\sqrt{\hat{s}}}{2}(x_2, 0, 0, -x_2). \end{aligned} \quad (9.6)$$

The square of the  $q\bar{q}$  collision energy  $\hat{s}$  is related to the overall hadron-hadron collision energy by  $\hat{s} = (p_1 + p_2)^2 = x_1 x_2 s$ . Substituting Eq. (9.5) into Eq. (9.1) gives the parton-model cross section for this process:

$$\begin{aligned} \frac{d\sigma}{dM^2} &= \int_0^1 dx_1 dx_2 \sum_q \{f_q(x_1)f_{\bar{q}}(x_2) + (q \leftrightarrow \bar{q})\} \\ &\times \frac{d\hat{\sigma}}{dM^2}(q\bar{q} \rightarrow l^+l^-) \end{aligned}$$

$$\begin{aligned}
&= \frac{\sigma_0}{N} \int_0^1 dx_1 dx_2 \delta(x_1 x_2 s - M^2) \\
&\quad \times \left[ \sum_q Q_q^2 \{ f_q(x_1) f_{\bar{q}}(x_2) + (q \leftrightarrow \bar{q}) \} \right]. \tag{9.7}
\end{aligned}$$

Following the usual convention, the sum here is over quarks only and the additional  $\bar{q}q$  contributions are indicated explicitly.

In the parton model, the distribution functions  $f_i(x)$  are independent of  $M^2$  (*cf.* Eq. (9.2)), and so the lepton pair cross section (9.7) multiplied by  $M^4$  exhibits scaling in the variable  $\tau = M^2/s$ :

$$\begin{aligned}
M^4 \frac{d\sigma}{dM^2} &= \frac{4\pi\alpha^2}{3N} \tau \int_0^1 dx_1 dx_2 \delta(x_1 x_2 - \tau) \\
&\quad \times \left[ \sum_q Q_q^2 \{ f_q(x_1) f_{\bar{q}}(x_2) + (q \leftrightarrow \bar{q}) \} \right] \\
&= \frac{4\pi\alpha^2}{3N} \tau \mathcal{F}(\tau). \tag{9.8}
\end{aligned}$$

Note that this is exactly analogous to the approximate Bjorken scaling of the deep inelastic structure functions  $F_i(x, Q^2)$ , or equivalently of the scattering cross section  $Q^4 d^2\sigma^{IN}/dx dQ^2$ . The Drell-Yan cross section data do indeed exhibit scaling behaviour to a good approximation, see for example the review in ref. [3], thus confirming the parton model picture.

From Eq. (9.6), the rapidity of the lepton pair (Eq. (7.16)) is given in terms of the parton momentum fractions by

$$y = \frac{1}{2} \ln \left( \frac{x_1}{x_2} \right), \tag{9.9}$$

and hence

$$x_1 = \sqrt{\tau} \exp(y), \quad x_2 = \sqrt{\tau} \exp(-y). \tag{9.10}$$

The double-differential cross section is therefore

$$\frac{d^2\sigma}{dM^2 dy} = \frac{\sigma_0}{Ns} \left[ \sum_q Q_q^2 \{ f_q(x_1) f_{\bar{q}}(x_2) + (q \leftrightarrow \bar{q}) \} \right] \tag{9.11}$$

with  $x_1$  and  $x_2$  given by Eq. (9.10). By measuring the distribution in rapidity and mass of the lepton pair one can in principle directly measure the quark and antiquark distribution functions of the colliding hadrons.

The crucial assumption in the derivation of Bjorken scaling in the covariant parton model, described in Section 4.2, is that the hadronic amplitude  $B(k, p)$  of Fig. 4.4 is strongly damped when the virtuality  $k^2$  of the emitted parton becomes ‘large’, where ‘large’ means much greater than a typical hadronic mass scale. An equivalent statement is that the parton

can have only limited transverse momentum  $k_T$  relative to the direction of the parent hadron in the infinite momentum frame. We can generalize the idea of a parton probability distribution to take this ‘intrinsic’ transverse momentum into account:

$$d\xi f(\xi) \longrightarrow d^2k_T d\xi P(\vec{k}_T, \xi), \quad (9.12)$$

with  $\int d^2k_T P(\vec{k}_T, \xi) = f(\xi)$ .

When the hard scattering scale in an inclusive process is very large, it may be a reasonable approximation to neglect the intrinsic  $k_T$  altogether, which corresponds to  $P(\vec{k}_T, \xi) = \delta(\vec{k}_T) f(\xi)$ . Note that this approximation is implicit in the representations (9.6) of the momenta of the annihilating  $q$  and  $\bar{q}$  in the derivation of the Drell-Yan cross section given above. This automatically implies that the lepton pair has zero transverse momentum. In fact experiments show that Drell-Yan lepton pairs have a distribution in transverse momentum, and this can be used to infer the distribution in the partons’ intrinsic  $k_T$ . To see how this works, consider a simple model in which  $P(\vec{k}_T, \xi) = h(\vec{k}_T) f(\xi)$ . In this case, the distribution in the transverse momentum  $\vec{p}_T$  of the lepton pair is given simply by

$$\frac{1}{\sigma} \frac{d^2\sigma}{d^2p_T} = \int d^2k_{T1} d^2k_{T2} \delta^{(2)}(\vec{k}_{T1} + \vec{k}_{T2} - \vec{p}_T) h(\vec{k}_{T1}) h(\vec{k}_{T2}), \quad (9.13)$$

where  $\sigma \equiv d^2\sigma/dM^2dy$  as defined above.

Data on the lepton pair transverse momentum from the CFS collaboration [4] (from fixed-target  $pN$  collisions with  $p_{lab} = 400$  GeV,  $\sqrt{s} = 27.4$  GeV) are shown in Fig. 9.2. The curve corresponds to a Gaussian intrinsic  $k_T$  distribution

$$h(\vec{k}_T) = \frac{b}{\pi} \exp(-bk_T^2), \quad (9.14)$$

with  $\langle k_T \rangle = (\pi/4b)^{\frac{1}{2}} = 760$  MeV. Note that substituting this into (9.13) gives

$$\frac{1}{\sigma} \frac{d^2\sigma}{d^2p_T} = \frac{b}{2\pi} \exp(-bp_T^2/2). \quad (9.15)$$

The data at small  $p_T$  are evidently very well described by such a distribution, and the magnitude of the corresponding intrinsic transverse momentum is indeed of the order of a typical hadronic mass scale. Notice, however, that there is an excess of events at large transverse momentum. This is evidence for a new *perturbative* mechanism for generating large  $p_T$ : the  $2 \rightarrow 2$  scattering processes  $q\bar{q} \rightarrow \gamma^*g$  and  $qg \rightarrow \gamma^*q$ . Historically, the relative abundance of Drell-Yan lepton pairs with large transverse momentum was one of the first pieces of evidence that the parton model was

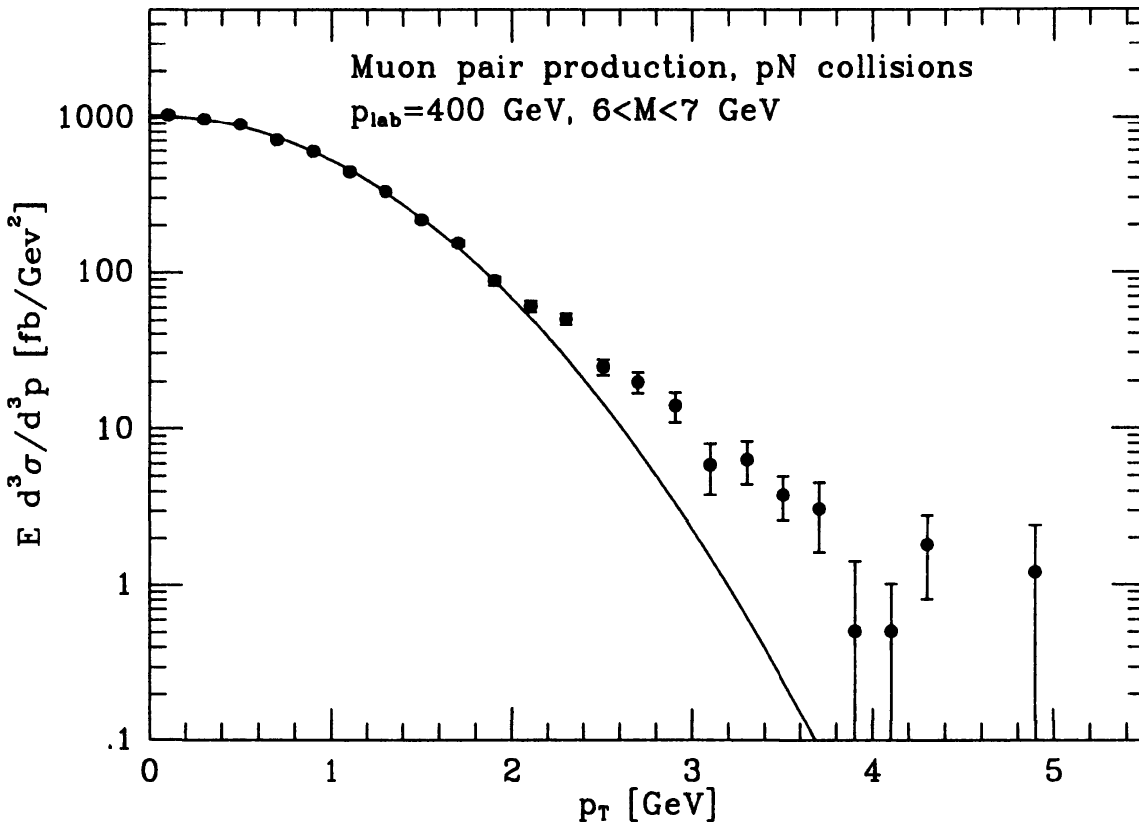


Fig. 9.2. The lepton pair transverse momentum from the CFS collaboration [4]. The curve corresponds to a Gaussian intrinsic  $k_T$  distribution for the annihilating partons.

incomplete. It indicated that quarks could ‘hard-scatter’ strongly, generating the transverse momentum of the lepton pair by emitting a gluon with large transverse momentum. For very large  $p_T$  ( $\gg M$ ) we would expect a transverse momentum distribution similar to that of a *real* photon (see Chapter 7), *i.e.*

$$\frac{d^2\sigma}{d^2p_T} \sim \frac{\alpha_s(p_T^2)}{p_T^4}, \quad (9.16)$$

which gives a much harder distribution at large  $p_T$  than the Gaussian  $\exp(-bp_T^2/2)$  distribution which describes the behaviour at small  $p_T$ . The transition between the two behaviours is clearly visible in the data. Quantitative estimates of the perturbative large- $p_T$  tail measured in fixed-target Drell-Yan experiments give reasonable agreement with the data, although theoretical and experimental uncertainties preclude any precise test of the theory. The situation is somewhat improved for the analogous processes of large-transverse-momentum  $W$  and  $Z$  production at high-energy  $p\bar{p}$  colliders (see Section 9.4.4 below).

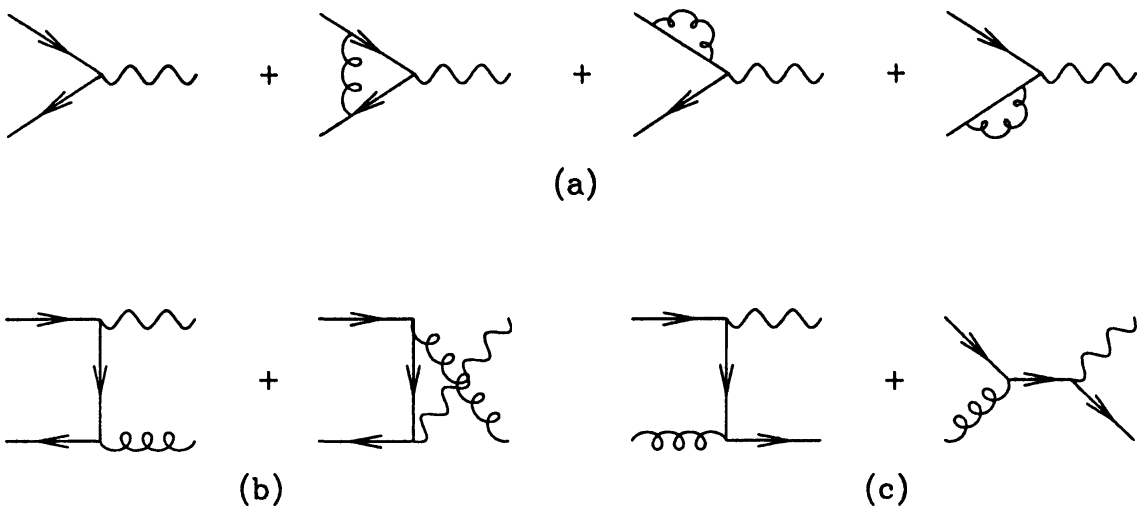


Fig. 9.3. The leading- and next-to-leading-order diagrams for the Drell-Yan process.

## 9.2 Perturbative QCD corrections

In this section we calculate the  $O(\alpha_s)$  corrections to the parton model Drell-Yan cross section. The calculation is similar in many respects to that for the corresponding correction to the deep inelastic structure function  $F_2$ , described in Chapter 4. We begin by considering the parton-level Drell-Yan cross section for the leading-order process  $q(p_1) + \bar{q}(p_2) \rightarrow l^+l^-$ :

$$M^4 \frac{d\hat{\sigma}}{dM^2} = \frac{4\pi\alpha^2}{3N} \tau \hat{\mathcal{F}}(\tau), \quad (9.17)$$

where, from Eq. (9.5),

$$\hat{\mathcal{F}}(\tau) = Q_q^2 \delta(1 - \tau) \quad (9.18)$$

for a single flavour of quark with charge  $Q_q$ . In general,  $\hat{\mathcal{F}}$  will have a perturbative expansion in powers of the strong coupling:

$$\hat{\mathcal{F}}(\tau) = \hat{\mathcal{F}}_0(\tau) + \frac{\alpha_s}{2\pi} \hat{\mathcal{F}}_1(\tau) + \dots \quad (9.19)$$

The diagrams which contribute at  $O(\alpha_s)$  are shown in Fig. 9.3. There are evidently three classes of contributions: (a) virtual gluon corrections to the leading-order contribution ( $\hat{\mathcal{F}}_1^{q\bar{q},V}$ ), (b) real gluon corrections from  $q(p_1) + \bar{q}(p_2) \rightarrow \gamma^* + g(k)$  ( $\hat{\mathcal{F}}_1^{q\bar{q},R}$ ), and (c) the quark-gluon scattering process  $q(p_1) + g(p_2) \rightarrow \gamma^* + q(k)$  ( $\hat{\mathcal{F}}_1^{qg}$ ) together with the corresponding  $\bar{q}g$  contribution. The calculation of each of these proceeds just as for the  $O(\alpha_s)$  corrections to  $\hat{F}_2$ . Diagram by diagram, three types of divergence are encountered:  $\hat{\sigma}(q\bar{q} \rightarrow l^+l^-)$  ultraviolet divergences from the loop

integrals, infra-red divergences from the contribution (both real and virtual) of soft ( $k^\mu \rightarrow 0$ ) gluons, and collinear divergences from the  $q \rightarrow qg$  and  $g \rightarrow q\bar{q}$  splitting of the initial-state partons. The same regularization schemes discussed in Chapters 3 and 4 can be used here. The results which follow correspond to the dimensional regularization scheme, in which the number of space-time dimensions is changed from 4 to  $4 - 2\epsilon$  and a scale  $\mu^2$  is introduced to preserve the dimensions of physical quantities.

In fact only the collinear divergences fail to cancel when all diagrams are added together. The result is (ignoring terms  $O(\epsilon)$  or higher)

$$\begin{aligned}\hat{\mathcal{F}}_1^{q\bar{q}} &= \hat{\mathcal{F}}_1^{q\bar{q},R} + \hat{\mathcal{F}}_1^{q\bar{q},V} \\ &= Q_q^2 \frac{\alpha_s(\mu^2)}{2\pi} \left[ 2 \left( -\frac{1}{\epsilon} - \ln(4\pi) + \gamma_E + \ln \frac{M^2}{\mu^2} \right) P_{q\bar{q}}^{(0)}(\tau) + D_q(\tau) \right] \\ \hat{\mathcal{F}}_1^{qg} &= Q_q^2 \frac{\alpha_s(\mu^2)}{2\pi} \left[ \left( -\frac{1}{\epsilon} - \ln(4\pi) + \gamma_E + \ln \frac{M^2}{\mu^2} \right) P_{qg}^{(0)}(\tau) + D_g(\tau) \right].\end{aligned}\tag{9.20}$$

The functions  $D_q$  and  $D_g$  are [5,6]

$$\begin{aligned}D_q(z) &= C_F \left[ 4(1+z^2) \left( \frac{\ln(1-z)}{1-z} \right)_+ - 2 \frac{1+z^2}{1-z} \ln z \right. \\ &\quad \left. + \delta(1-z) \left( \frac{2\pi^2}{3} - 8 \right) \right], \\ D_g(z) &= T_R \left[ (z^2 + (1-z)^2) \ln \frac{(1-z)^2}{z} + \frac{1}{2} + 3z - \frac{7}{2}z^2 \right],\end{aligned}\tag{9.21}$$

and the plus distribution is defined in Eq. (4.72). The important point to notice is that the coefficients of the  $1/\epsilon$  singularity are exactly the same as those encountered in the deep inelastic processes  $\gamma^* q \rightarrow qg$  and  $\gamma^* g \rightarrow q\bar{q}$ . They are just the leading-order splitting functions defined in Eq. (4.94). Thus when the bare parton distributions, which must be convoluted with the  $\hat{\mathcal{F}}_1^{q\bar{q}}$  and  $\hat{\mathcal{F}}_1^{qg}$  functions, are replaced by scale-dependent ‘renormalized’ distributions (see Section 4.3), the singularities exactly cancel. In the  $\overline{\text{MS}}$  factorization scheme, this is achieved by the replacement  $q_0(x) \rightarrow q(x, \mu^2)$ , where (cf. Eq. (4.83))

$$\begin{aligned}q(x, \mu^2) &= q_0(x) + \frac{\alpha_s(\mu^2)}{2\pi} \left( -\frac{1}{\epsilon} - \ln(4\pi) + \gamma_E \right) \\ &\quad \times \int_x^1 \frac{d\xi}{\xi} \left[ P_{q\bar{q}}^{(0)}(x/\xi) q_0(\xi) + P_{qg}^{(0)}(x/\xi) g_0(\xi) \right] + O(\alpha_s^2).\end{aligned}\tag{9.22}$$

The above calculation is an explicit verification at  $O(\alpha_s)$  of a factor-

ization theorem [2] (see also Section 7.2) which states that for a general class of inclusive ‘hard-scattering’ processes in hadron-hadron collisions all collinear singularities at every order in perturbation theory can be absorbed into universal parton distributions, whose scale dependence is determined by the GLAP evolution equations. The remaining finite perturbative corrections modify the leading-order parton-model cross section, just as for the  $e^+e^- \rightarrow \text{hadrons}$  total cross section of Chapter 3, for example.

As discussed in Chapter 4, other choices of factorization scheme are possible. For example in the DIS scheme [5] all the finite corrections are absorbed into the renormalized distributions in the calculation of  $F_2$ . The Drell-Yan cross section can equally well be expressed in terms of DIS parton distributions, but then the finite perturbative correction must be modified to take into account the extra finite pieces absorbed into the distributions. Explicitly,

$$\begin{aligned} D_q^{\text{DIS}}(z) &= D_q(z) - 2C_q^{\overline{\text{MS}}}(z), \\ D_g^{\text{DIS}}(z) &= D_g(z) - C_g^{\overline{\text{MS}}}(z), \end{aligned} \quad (9.23)$$

where the coefficient functions  $C_q^{\overline{\text{MS}}}$  and  $C_g^{\overline{\text{MS}}}$  are defined in Eq. (4.85). Substitution then gives

$$\begin{aligned} D_q^{\text{DIS}}(z) &= C_F \left[ \frac{3}{(1-z)_+} - 6 - 4z + 2(1+z^2) \left( \frac{\ln(1-z)}{1-z} \right)_+ \right. \\ &\quad \left. + \delta(1-z) \left( 1 + \frac{4\pi^2}{3} \right) \right], \\ D_g^{\text{DIS}}(z) &= T_R \left[ (z^2 + (1-z)^2) \ln(1-z) + \frac{3}{2} - 5z + \frac{9}{2}z^2 \right]. \end{aligned} \quad (9.24)$$

The full result to  $\mathcal{O}(\alpha_s)$ , in the  $\overline{\text{MS}}$  scheme with  $\mu^2 = M^2$ , is

$$\begin{aligned} M^4 \frac{d\sigma}{dM^2} &= \frac{4\pi\alpha^2}{3N} \tau \int_0^1 dx_1 dx_2 dz \delta(x_1 x_2 z - \tau) \\ &\quad \times \left[ \sum_q Q_q^2 \{ f_q(x_1, M^2) f_{\bar{q}}(x_2, M^2) + (q \leftrightarrow \bar{q}) \} \right. \\ &\quad \times \left( \delta(1-z) + \frac{\alpha_s(M^2)}{2\pi} D_q(z) \right) \\ &\quad + \sum_q Q_q^2 \{ f_g(x_1, M^2) (f_q(x_2, M^2) + f_{\bar{q}}(x_2, M^2)) \right. \\ &\quad \left. + (q, \bar{q} \leftrightarrow g) \} \times \frac{\alpha_s(M^2)}{2\pi} D_g(z) \right]. \end{aligned} \quad (9.25)$$

The magnitude of the  $O(\alpha_s)$  correction depends on the lepton pair mass and on the overall collision energy. At fixed-target energies and masses the correction is large and positive, of the order of 50% or more. In this regime of relatively large  $\tau$ , the (negative) contribution from the quark-gluon scattering term is quite small. However, in high-energy  $p\bar{p}$  and  $pp$  collisions, where  $\tau$  is much smaller, the  $D_g$  term is more important and the overall correction is smaller. For  $W$  and  $Z$  production (in  $p\bar{p}$  collisions at  $\sqrt{s} = 630$  GeV, 1.8 TeV) the  $O(\alpha_s)$  correction increases the lowest-order cross section by about 20 – 30%.

The  $O(\alpha_s^2)$  corrections to the Drell-Yan cross section have also been calculated [7]. The expressions are too lengthy to present here. In addition to the  $q\bar{q}$  and  $qg$  processes, which contribute at next-to-leading order, there are also contributions from the higher-order processes  $qq \rightarrow qql^+l^-$  and  $gg \rightarrow q\bar{q}l^+l^-$ . The  $O(\alpha_s^2)$  corrections are generally smaller than the  $O(\alpha_s)$  corrections, the exact values depending on the lepton pair mass, the collision energy, and the type of beam and target.

The majority of the Drell-Yan data is for the double differential cross section,  $d^2\sigma/dMdy$ , in a restricted range of  $y$ , or for the related quantity  $d^2\sigma/dMdxF$ , where  $x_F$  is the longitudinal momentum fraction of the lepton pair,

$$x_F = \frac{2}{\sqrt{s}} (p_{l+} + p_{l-})_L \approx x_1 - x_2 . \quad (9.26)$$

The variable  $x_F$  is known as ‘Feynman  $x$ ’. For these cross sections, the QCD corrections are only known to  $O(\alpha_s)$  at present [5,6].

### 9.3 Comparison with experiment

The Drell-Yan cross section has been measured by many experiments, with a wide variety of beams, targets and energies. A compilation of these data, together with comparisons with theoretical predictions, can be found in ref. [3]. As an example of such a comparison, Fig. 9.4 shows data from the E605 collaboration [8] on the cross section  $s d^2\sigma/d\tau dy$  for  $pCu \rightarrow \mu^+\mu^-$  at  $p_{lab} = 800$  GeV ( $\sqrt{s} = 38.8$  GeV). The curve is the theoretical prediction calculated at next-to-leading order, using the MRS(A) parton distributions [9]. The agreement is excellent, and suggests that the (unknown) higher-order corrections in this case are small.

Several important pieces of information can be obtained from Drell-Yan cross section data. Low-mass lepton pair production in high-energy hadron-hadron collisions is sensitive to the small  $x$  behaviour of the parton distributions. In  $pp$  or  $pN$  collisions the cross section is proportional to the sea quark distribution,  $\bar{q}(x, \mu^2)$ . This provides complementary

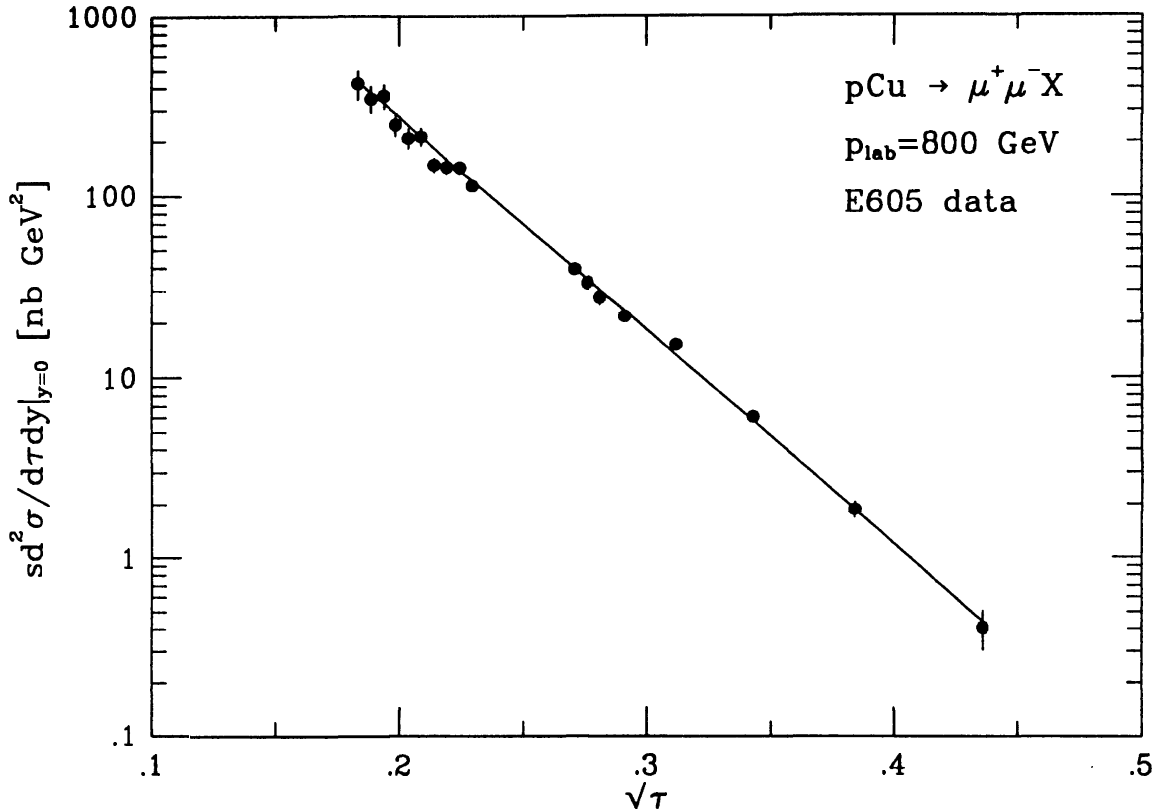


Fig. 9.4. The Drell-Yan cross section measured by the E605 collaboration [8] compared with the next-to-leading-order theoretical prediction.

information to deep inelastic structure function data, and in fact Drell-Yan data such as those shown in Fig. 9.4 can be used to constrain the antiquark distributions in global fits, see for example refs. [9,10]. Equally important is the fact that the distributions of quarks in *pions* (for which no deep inelastic scattering data are available) can be extracted from Drell-Yan data in  $\pi p$  and  $\pi N$  collisions [11].

Finally, Fig. 9.5 shows the next-to-leading-order prediction for lepton pair production in  $p\bar{p}$  collisions at  $\sqrt{s} = 1.8$  TeV, together with data from the CDF collaboration [12,13]. The most striking feature here is the appearance of the  $Z$  resonance at  $M \sim M_Z$ . At such high energies, the  $q\bar{q} \rightarrow \gamma^* \rightarrow l^+l^-$  contribution in Fig. 9.1 must be supplemented by the additional contribution from  $s$ -channel  $Z$  exchange, so that Eq. (9.4) becomes

$$\hat{\sigma}(q(p_1)\bar{q}(p_2) \rightarrow l^+l^-) = \frac{4\pi\alpha^2}{3\hat{s}} \frac{1}{N} \left( Q_q^2 - 2Q_q V_l V_q \chi_1(\hat{s}) + (A_l^2 + V_l^2)(A_q^2 + V_q^2) \chi_2(\hat{s}) \right), \quad (9.27)$$

in the notation of Eq. (3.1). Apart from an overall colour-averaging factor, this is identical to the  $e^+e^- \rightarrow q\bar{q}$  cross section discussed in Chapter 3 and

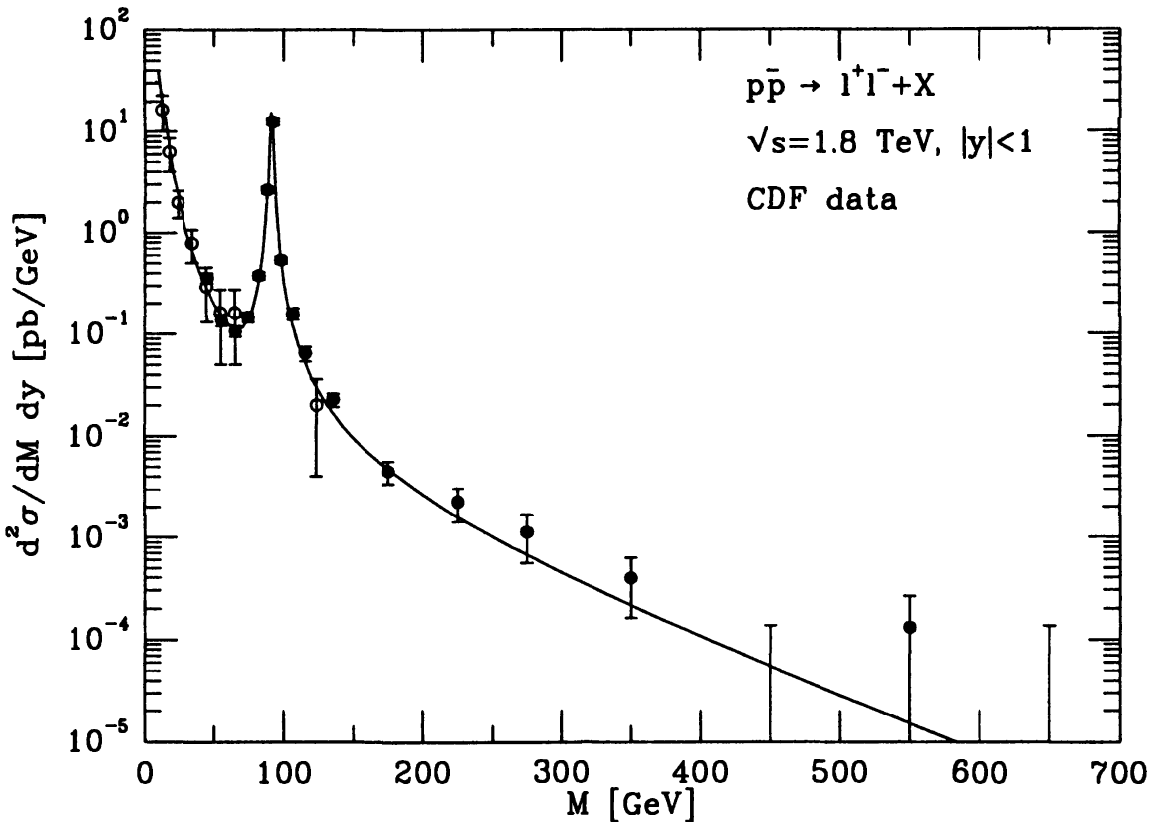


Fig. 9.5. The lepton pair cross section in  $p\bar{p}$  collisions at  $\sqrt{s} = 1.8 \text{ TeV}$ , with CDF data from ref. [12] (open circles) and ref. [13] (solid circles). The curve is the next-to-leading-order QCD prediction using the parton distributions from ref. [9].

shown in Fig. 3.13. In practice, lepton pair production with  $M \sim M_Z$  is analysed in terms of the production cross section for  $Z$  bosons ( $q\bar{q} \rightarrow Z$ ), multiplied by the branching ratio for decay into the leptonic final state ( $Z \rightarrow l^+l^-$ ). To see how this decomposition arises, we note that when  $\hat{s} \approx M_Z^2$ , the right-hand side of Eq. (9.27) is dominated by the term proportional to  $\chi_2$ , given in Eq. (3.2). In the limit of very narrow width we may replace the Breit-Wigner distribution in  $\chi_2$  by a delta function

$$\frac{1}{(\hat{s} - M_Z^2)^2 + M_Z^2 \Gamma_Z^2} \approx \frac{\pi}{M_Z \Gamma_Z} \delta(\hat{s} - M_Z^2). \quad (9.28)$$

The normalization is fixed by the condition that the two distributions have the same integral:

$$\int_{-\infty}^{\infty} ds \frac{1}{(s - M^2)^2 + M^2 \Gamma^2} = \frac{1}{M\Gamma} \left[ \tan^{-1} \left( \frac{s - M^2}{M\Gamma} \right) \right] \Big|_{-\infty}^{\infty} = \frac{\pi}{M\Gamma}. \quad (9.29)$$

Eq. (9.28) is called the narrow width approximation.

Integrating the subprocess cross section (9.27) over lepton pair masses

in the vicinity of  $M_Z$  (*i.e.*  $|M - M_Z| < \Delta$  with  $\Gamma_Z \ll \Delta \ll M_Z$ ) we obtain, using Eq. (9.28),

$$\begin{aligned} \int_{(M_Z - \Delta)^2}^{(M_Z + \Delta)^2} dM^2 \frac{d\hat{\sigma}}{dM^2} &\approx \frac{\pi}{N} \sqrt{2} G_F M_Z^2 (A_q^2 + V_q^2) \frac{\Gamma(Z \rightarrow l^+ l^-)}{\Gamma_Z} \delta(\hat{s} - M_Z^2) \\ &= BR(Z \rightarrow l^+ l^-) \hat{\sigma}(q\bar{q} \rightarrow Z), \end{aligned} \quad (9.30)$$

where

$$\hat{\sigma}(q\bar{q} \rightarrow Z) = \frac{\pi}{3} \sqrt{2} G_F M_Z^2 (A_q^2 + V_q^2) \delta(\hat{s} - M_Z^2). \quad (9.31)$$

In deriving the result in Eq. (9.30) we have used the expression for the leptonic decay width of the  $Z$  boson calculated in Section 8.4.

## 9.4 *W* and *Z* boson production

The discovery in 1983 of the  $W$  and  $Z$  gauge bosons at the CERN  $p\bar{p}$  collider [14] provided dramatic confirmation of the Standard Electroweak Model described in Chapter 8. In this section we discuss the physics of  $W$  and  $Z$  production in  $p\bar{p}$  collisions, with particular reference to measurements at the CERN and Fermilab colliders with  $\sqrt{s} = 0.63$  TeV and 1.8 TeV respectively. We first describe the total production cross sections, and then some kinematic distributions of the  $W$  and  $Z$  and their decay products.

### 9.4.1 Production cross sections

The  $W$  and  $Z$  decay widths are small ( $\Gamma_W = 2.08$  GeV and  $\Gamma_Z = 2.50$  GeV in the Standard Model) compared to their masses, and so it is sufficient to consider the production of effectively stable particles, multiplying the cross sections by the appropriate final-state branching ratios. At leading order, the  $q\bar{q} \rightarrow W, Z$  subprocess cross sections are readily obtained from the couplings of the gauge bosons to fermions derived in Chapter 8:

$$\begin{aligned} \hat{\sigma}^{q\bar{q} \rightarrow W} &= \frac{\pi}{3} \sqrt{2} G_F M_W^2 |V_{qq'}|^2 \delta(\hat{s} - M_W^2) \\ \hat{\sigma}^{q\bar{q} \rightarrow Z} &= \frac{\pi}{3} \sqrt{2} G_F M_Z^2 (V_q^2 + A_q^2) \delta(\hat{s} - M_Z^2), \end{aligned} \quad (9.32)$$

where  $V_{qq'}$  is the appropriate CKM matrix element.

The  $O(\alpha_s)$  perturbative QCD corrections to the  $W$  and  $Z$  cross sections are the same as the Drell-Yan corrections (for a virtual photon of the same mass) presented in Section 9.2 — the gluon is ‘flavour blind’ and couples in the same way to the annihilating quark and antiquark. The  $O(\alpha_s^2)$  corrections are also the same, apart from an internal quark-triangle graph

contribution to  $Z$  production only which is, however, numerically small [15].

Fig. 9.6 shows the  $O(\alpha_s^2)$  theoretical predictions for the  $W$  and  $Z$  cross sections (multiplied by the Standard Model leptonic branching ratios  $\text{BR}(W \rightarrow l\nu) = 0.1084$  and  $\text{BR}(Z \rightarrow l^+l^-) = 0.0336$ ) compared with measurements from the  $p\bar{p}$  collider experiments [16].<sup>2</sup> The parton distributions are the MRS(A') set [17], with the factorization and renormalization scales  $\mu_F = \mu_R = M_{W,Z}$ . A  $\pm 5\%$  theoretical error band on the predictions is included to allow for the uncertainties arising from the parton distributions, electroweak parameters, scale variation and unknown higher-order corrections.

The agreement between theory and experiment is very good. This is a non-trivial test of the  $\mu^2$  evolution of the parton distributions, since in this calculation they are evaluated at much higher  $\mu^2$  values ( $\sim 10^4 \text{ GeV}^2$ ) than those typical of the fixed-target deep inelastic scattering data ( $\sim 10^{1-2} \text{ GeV}^2$ ) which determine the  $x$  dependence. The QCD perturbation series also appears to be well under control: the next-to-leading- and next-to-next-to-leading-order contributions constitute 16% and 2% respectively of the total  $W$  cross section at 1.8 TeV.

In the calculation of the branching ratio for  $W \rightarrow l\nu$  used in the theoretical predictions shown in Fig. 9.6, the Standard Model prediction for the total  $W$  decay width is used. However the comparison between theory and data in Fig. 9.6 can also be used to obtain a *measurement* of  $\Gamma_W$ . Indeed before the top quark was discovered, this method was used to set limits on a possible  $\Gamma(W \rightarrow tb)$  contribution to  $\Gamma_W$ , and hence on  $m_t$  [18]. It is advantageous to consider the ratio  $R$  of the cross sections times branching ratios shown in Fig. 9.6. Several uncertainties, for example the uncertainty in the collider luminosity, cancel in the ratio. Thus,

$$\begin{aligned} R &= \frac{N(W \rightarrow l\nu_l)}{N(Z \rightarrow l^+l^-)} = \frac{\sigma_W}{\sigma_Z} \cdot \frac{\text{BR}(W \rightarrow l\nu_l)}{\text{BR}(Z \rightarrow l^+l^-)} = R_\sigma \cdot R_{BR} \\ R_{BR} &= \frac{B(W \rightarrow l\nu)}{B(Z \rightarrow l^+l^-)} = \frac{\Gamma(W \rightarrow l\nu)}{\Gamma_W} \frac{\Gamma_Z}{\Gamma(Z \rightarrow l^+l^-)}. \end{aligned} \quad (9.33)$$

The cross section ratio  $R_\sigma$  is calculable theoretically. The dependence on parton distributions and on the renormalization and factorization scales is somewhat smaller than for the individual cross sections. The  $Z$  leptonic and total widths are measured accurately at LEP and SLC, see for example [19]. The partial  $\Gamma(W \rightarrow l\nu_l)$  width can be calculated precisely in the Standard Model, see Chapter 8. Hence, using Eq. (9.33), a measurement of  $R$  gives information on  $\Gamma_W$ .

---

<sup>2</sup> The dominant  $W, Z \rightarrow q\bar{q}$  decay channels are swamped by the large QCD two-jet background, see Chapter 7.

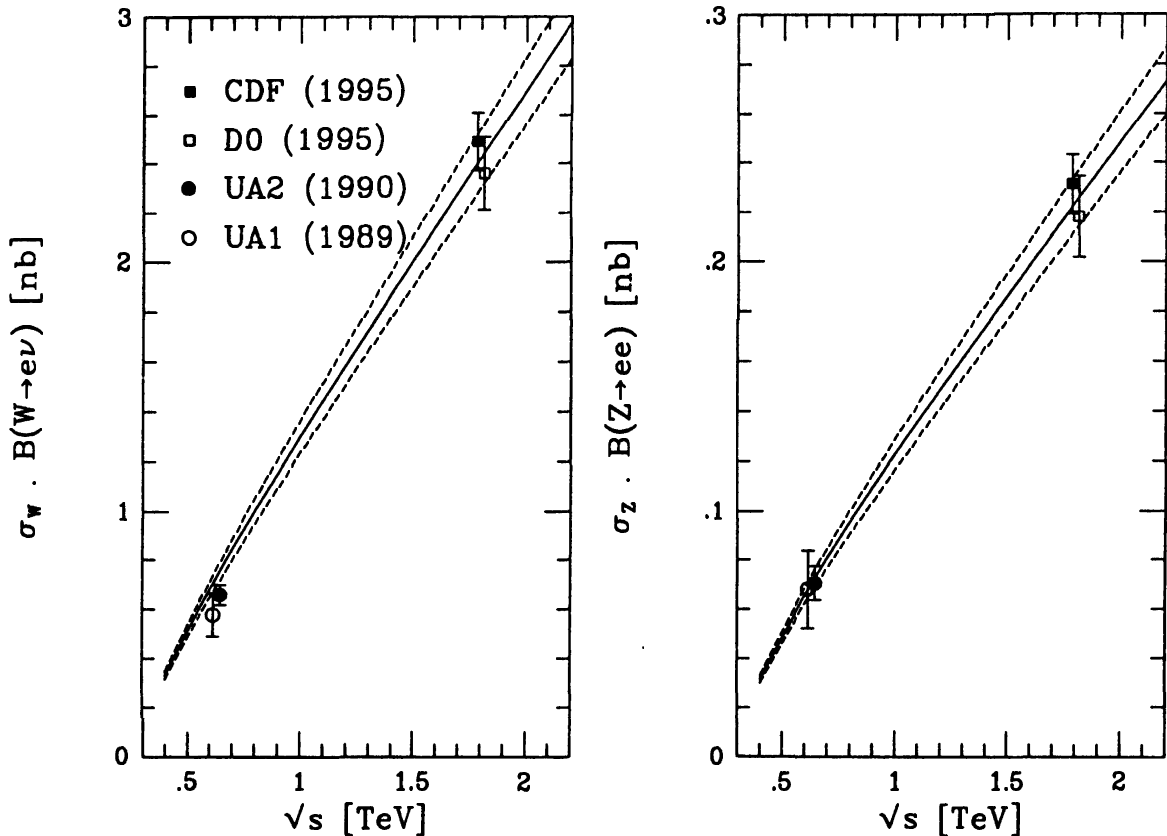


Fig. 9.6. Comparison of  $W$  and  $Z$  cross section measurements in  $p\bar{p}$  collisions with theoretical predictions. The systematic and statistical errors on the measurements have been combined in quadrature.

The measured values of  $R$  from the Tevatron  $p\bar{p}$  collider are [20]:

$$\begin{aligned} R &= 10.90 \pm 0.49(\text{stat.} \oplus \text{sys.}) & (\text{D0}), \\ R &= 10.9 \pm 0.32(\text{stat.}) \pm 0.29(\text{sys.}) & (\text{CDF}), \end{aligned} \quad (9.34)$$

which correspond to

$$\begin{aligned} \Gamma_W &= 2.044 \pm 0.092 \text{ GeV} & (\text{D0}), \\ \Gamma_W &= 2.064 \pm 0.085 \text{ GeV} & (\text{CDF}). \end{aligned} \quad (9.35)$$

The theoretical prediction — assuming no ‘anomalous’ decay channels and no  $W \rightarrow tb$  contribution — is a function of the  $W$  mass. For  $M_W = 80.33 \pm 0.15$  GeV (see Eq. (9.51)) the prediction is

$$\Gamma_W = 2.085 \pm 0.012 \text{ GeV}, \quad (9.36)$$

in good agreement with the measured values.

#### 9.4.2 *W* rapidity asymmetry

The  $W$  and  $Z$  rapidity distributions are calculated in exactly the same way as for Drell-Yan lepton pair production, Eq. (9.11). The predicted

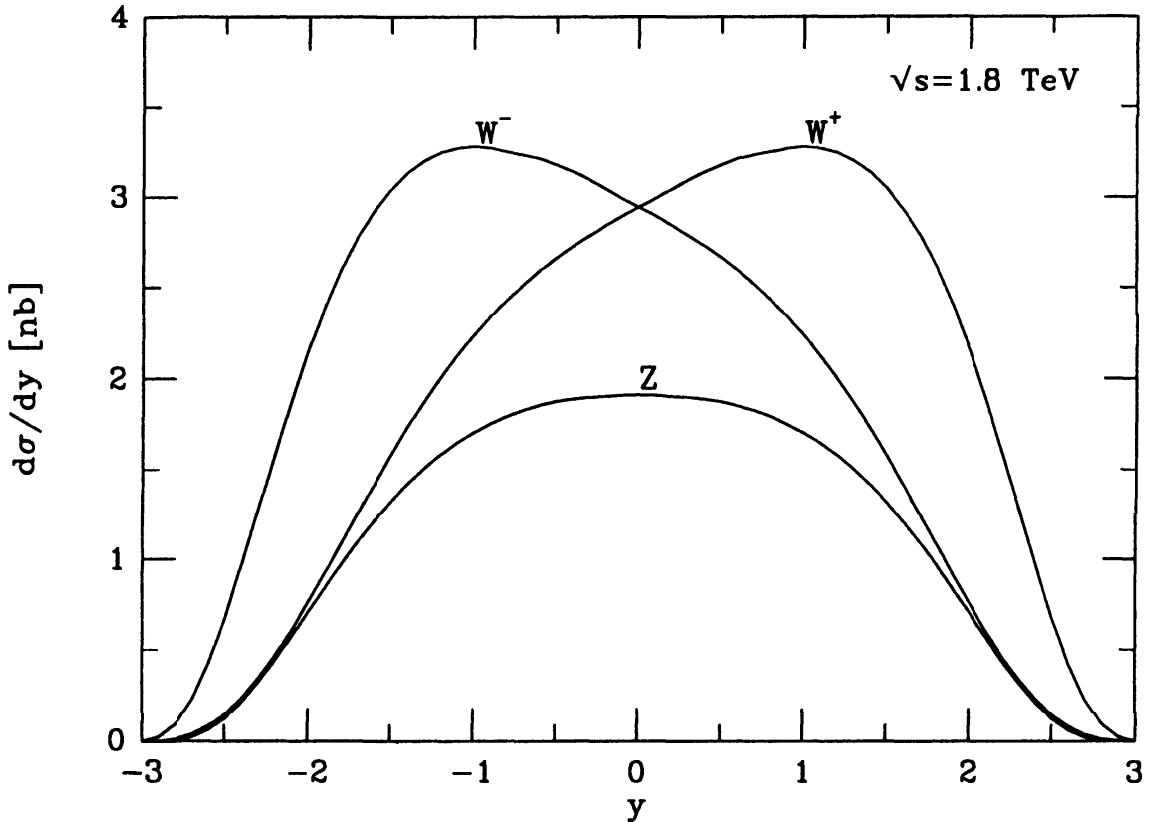


Fig. 9.7.  $W^+$ ,  $W^-$  and  $Z$  rapidity distributions in  $p\bar{p}$  collisions at  $\sqrt{s} = 1.8$  TeV.

distributions for  $W^\pm$ ,  $Z$  production in  $p\bar{p}$  collisions at  $\sqrt{s} = 1.8$  TeV are shown in Fig. 9.7. Here we have defined  $y > 0$  to be the direction of the incoming proton. While CP invariance requires that the  $Z$  distribution is symmetric about  $y = 0$ , the same is *not* true for  $W$  production. Neglecting sea quark contributions to the cross section, a  $W^+$  is obtained from the annihilation of a (valence)  $u$  quark from the proton and a (valence)  $d$  quark from the antiproton. Since  $u$  quarks in a proton are in general moving faster than  $d$  quarks (see Fig. 4.3), the  $W^+$  bosons are produced preferentially in the proton direction, as shown in Fig. 9.7. Likewise,  $W^-$  bosons are produced preferentially in the antiproton direction. In fact the  *$W$  rapidity asymmetry*,

$$A_W(y) = \frac{d\sigma(W^+)/dy - d\sigma(W^-)/dy}{d\sigma(W^+)/dy + d\sigma(W^-)/dy}, \quad (9.37)$$

provides a very sensitive measure of the relative shape of the  $u$  and  $d$  quark distributions [21]. In particular,  $A_W$  is strongly correlated with the *slope* of  $d(x)/u(x)$ . We can see this from a simple model calculation in which only valence quarks contribute to the production cross section. Then, following Eq. (9.11), we have (adopting the notation  $u(x) = f_u(x)$ ,

using the fact that  $u_p(x) = \bar{u}_{\bar{p}}(x)$  etc., and suppressing scale dependence)

$$A_W(y) \approx \frac{u(x_1)d(x_2) - d(x_1)u(x_2)}{u(x_1)d(x_2) + d(x_1)u(x_2)} = \frac{R(x_2) - R(x_1)}{R(x_2) + R(x_1)}, \quad (9.38)$$

where  $R(x) = d(x)/u(x)$  and

$$x_1 = x_0 \exp(+y), \quad x_2 = x_0 \exp(-y), \quad x_0 = M_W/\sqrt{s}. \quad (9.39)$$

For small  $y$  we can write  $x_{1,2} = x_0 \pm yx_0 + \dots$  and  $R(x_{1,2}) = R(x_0) \pm yx_0 R'(x_0) + \dots$ , so that

$$A_W(y) \approx -yx_0 \frac{R'(x_0)}{R(x_0)}. \quad (9.40)$$

The asymmetry is therefore predicted to be linear in  $y$  for small  $y$ , with a coefficient proportional to the slope of  $d(x)/u(x)$  evaluated at  $x = M_W/\sqrt{s}$  (and  $\mu^2 \sim M_W^2$ ). The asymmetry is slightly reduced by the inclusion of the non-valence contributions and by  $O(\alpha_s)$  perturbative corrections, but a strong sensitivity to the  $d/u$  ratio remains.

Unfortunately the  $W$  rapidity is difficult to measure accurately because of the undetected neutrino in the final state. What *can* be measured with high precision is the closely related charged lepton asymmetry  $A_l(y)$ . However the inclusion of the leptonic decay in the measurement provides an additional complication: because of the  $V - A$  structure of the weak charged current, the charged lepton is not produced isotropically in the  $W$  rest frame. In particular, for the process

$$d(p_d) + \bar{u}(p_u) \rightarrow e^-(p_e) + \bar{\nu}(p_\nu), \quad (9.41)$$

where the momentum labels are indicated in brackets, we obtain (using the couplings derived from the electroweak Lagrangian — see Chapter 8),

$$\begin{aligned} \sum |\mathcal{M}(d\bar{u} \rightarrow e^-\bar{\nu})|^2 &= 16 \left( \sqrt{2}G_F M_W^2 \right)^2 |V_{ud}|^2 \\ &\times \frac{(p_u \cdot p_e)^2}{((p_u + p_d)^2 - M_W^2)^2 + M_W^2 \Gamma_W^2}. \end{aligned} \quad (9.42)$$

Likewise, for the charge-conjugate process  $u\bar{d} \rightarrow e^+\nu$  we have exactly the same expression, where now  $p_u$  is the momentum of the incoming  $u$  quark etc. If we define  $\theta^*$  to be the  $e^+(e^-)$  polar angle of emission in the  $W^+(W^-)$  rest frame, measured with respect to the direction of the incident  $\bar{p}(p)$ , and if we assume that all incoming quarks (antiquarks) are constituents of the proton (antiproton), then for the above matrix elements we have

$$(p_u \cdot p_e)^2 = \frac{M_W^4}{16} (1 + \cos \theta^*)^2. \quad (9.43)$$

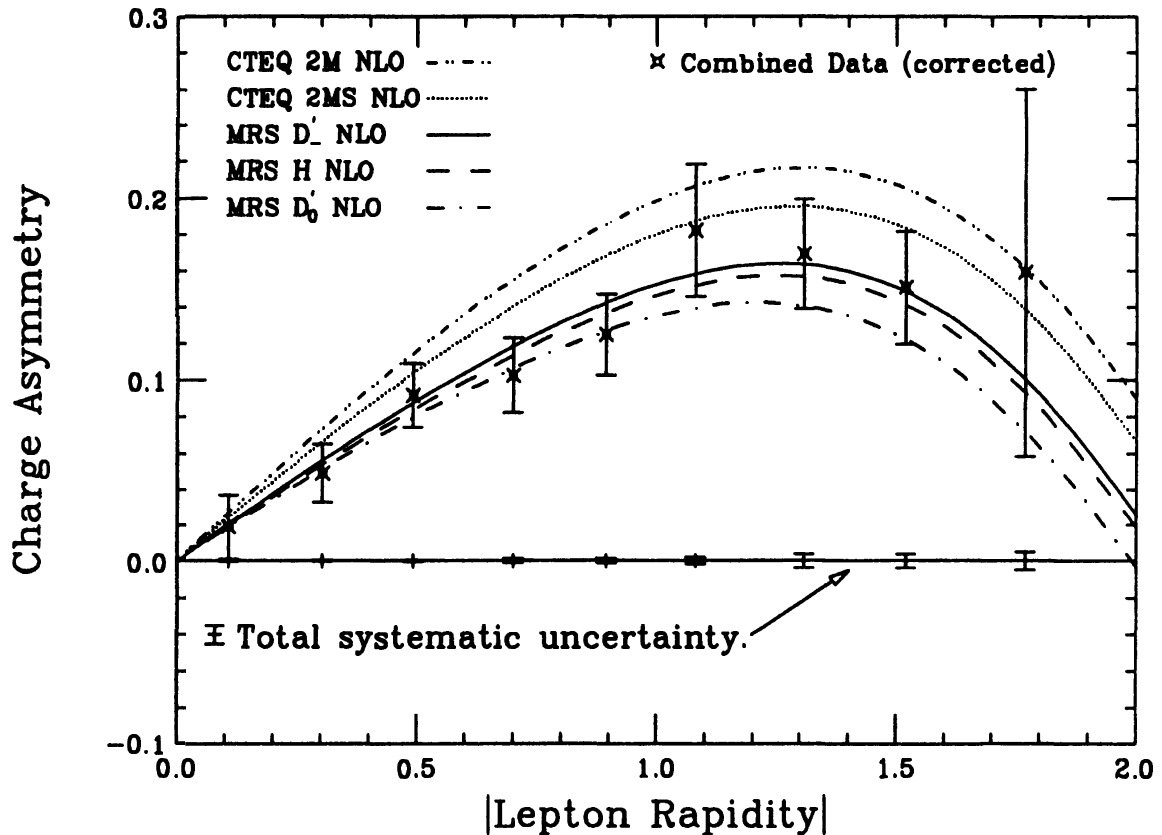


Fig. 9.8. Charged lepton rapidity asymmetry measured by the CDF collaboration compared with the predictions using various parton distributions. Figure from ref. [22].

The cross section is therefore maximal when the outgoing electron (positron) moves in the direction of the incoming proton (antiproton). In fact there is a simple angular momentum argument for this. In the Standard Model, the  $W$  couples to negative helicity fermions and positive helicity antifermions. Angular momentum conservation therefore requires the outgoing fermion (electron) to preferentially follow the direction of the incoming fermion (quark), which is usually the direction of the incoming proton. This is in the *opposite* sense to the  $W^\pm$  production asymmetry (Fig. 9.7), and so the charged lepton asymmetry is smaller than that of the  $W$  boson itself.

As an example of how well the lepton asymmetry can discriminate between parton distributions, Fig. 9.8 shows data from the CDF collaboration [22] compared to the predictions using various sets of parton distributions. In principle, all of these describe deep inelastic structure function data equally well, and so the lepton asymmetry measurement provides an important additional constraint on the distributions in global fits (see, for example, refs. [9,10]).

We have already seen in Fig. 9.7 that the  $Z$  rapidity distribution should

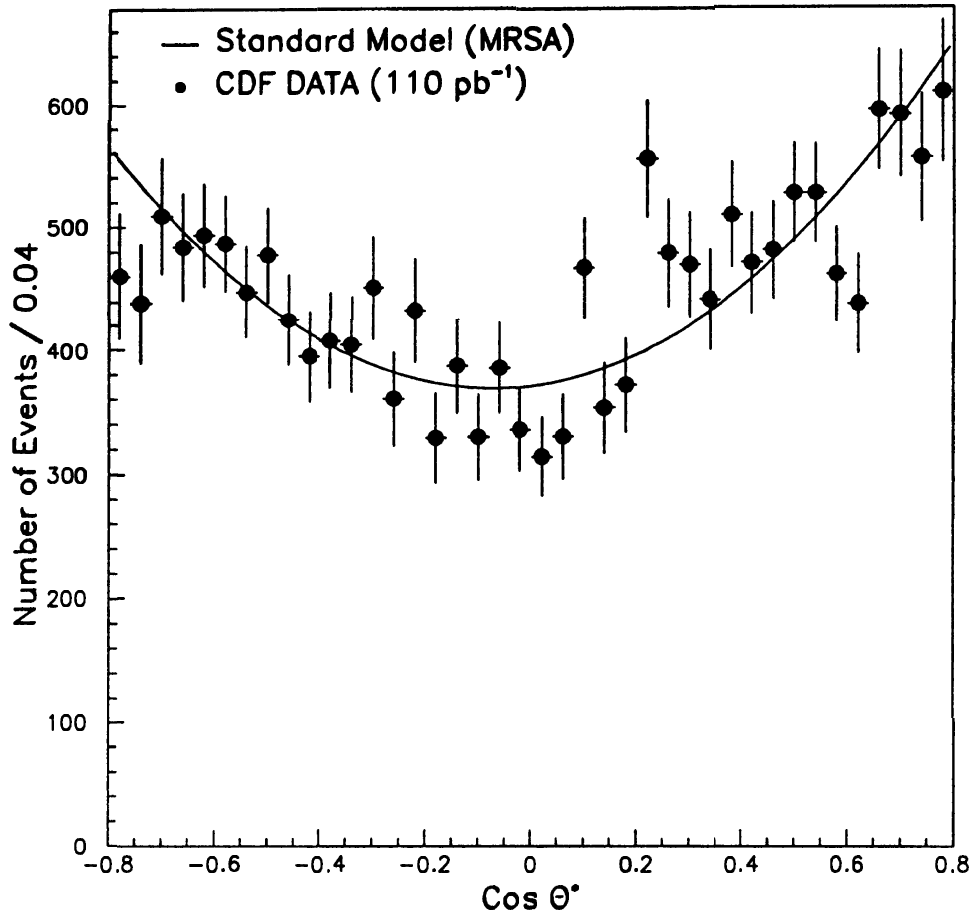


Fig. 9.9. Angular distribution of leptons from  $Z$ -boson decay measured by the CDF collaboration. Figure from ref. [23].

be symmetric about  $y = 0$ . However, because the coupling of the  $Z$  to fermions is a combination of left- and right-handed pieces, the lepton angular distribution is an admixture of  $(1 \pm \cos \theta^*)^2$  terms, the relative amounts being determined by the weak mixing parameter  $\sin^2 \theta_W$ . Fig. 9.9 shows the angular distribution of electron pairs with  $75 \text{ GeV} < M_{e^+e^-} < 105 \text{ GeV}$ , *i.e.* around the  $Z$  peak, measured by the CDF collaboration [23]. The curve is the Standard Model prediction with  $\sin^2 \theta_W = 0.232$ . The agreement between theory and experiment is good. Note, however, that the precision on  $\sin^2 \theta_W$  obtained from fitting these data falls far short of that obtained from the analogous distributions in  $e^+e^-$  annihilation at LEP and SLC, see for example ref. [19].

#### 9.4.3 $W$ transverse mass

In the rest frame of the decaying  $W$ , the energy of the charged lepton (which we shall assume for definiteness to be an electron) is simply  $M_W/2$ , and this can be utilized to make a precision measurement of the  $W$  mass. Because the neutrino is not directly detected in the experiments, it is

difficult to reconstruct the  $W$  rest frame precisely. However the *transverse* momentum of the electron, which is invariant under longitudinal boosts, also carries information on  $M_W$ .

We have seen (Eq. (9.43)) that in the  $W$  rest frame the angular distribution of the electron is

$$\frac{1}{\sigma} \frac{d\sigma}{d \cos \theta^*} = \frac{3}{8} (1 + \cos^2 \theta^*) , \quad (9.44)$$

where we have averaged over  $W^+$  and  $W^-$  production. If we assume that the  $W$  has zero transverse momentum, then  $\cos \theta^*$  is given in terms of the transverse momentum ( $p_{Te}$ ) of the electron by

$$\cos \theta^* = \left( 1 - \frac{4p_{Te}^2}{M_W^2} \right)^{\frac{1}{2}} , \quad (9.45)$$

so that

$$\frac{1}{\sigma} \frac{d\sigma}{dp_{Te}^2} = \frac{3}{M_W^2} \left( 1 - \frac{4p_{Te}^2}{M_W^2} \right)^{-\frac{1}{2}} \left( 1 - \frac{2p_{Te}^2}{M_W^2} \right) . \quad (9.46)$$

The distribution (9.46) is strongly peaked at  $p_{Te} = M_W/2$  (the *Jacobian peak*) and can therefore provide an accurate measurement of  $M_W$ . In reality, the square-root singularity of the distribution is somewhat smeared out by the finite width and non-zero transverse momentum of the  $W$  bosons. Information from the missing (*i.e.* neutrino) transverse momentum can also be taken into account, thus further sharpening the dependence of the distribution on  $M_W$ . Identifying the magnitude and azimuthal angle of the missing transverse energy with the neutrino transverse momentum, one can define the *transverse mass*,

$$M_T^2 = 2|p_{Te}| |p_{T\nu}| (1 - \cos \Delta\phi_{e\nu}) . \quad (9.47)$$

At leading order (*i.e.*  $q\bar{q}' \rightarrow W \rightarrow e\nu$ ) and in the absence of any quark transverse momentum, we have  $|p_{Te}| = |p_{T\nu}| = p^*$ ,  $\Delta\phi_{e\nu} = \pi$ , and so  $M_T = 2|p_{Te}|$ . The transverse mass distribution therefore also has a Jacobian peak, at  $M_T = M_W$ . In terms of measuring  $M_W$ , the advantage of using the transverse mass distribution is that it is less sensitive to the transverse momentum ( $p_T^W$ ) of the  $W$  boson. If  $p_T^W$  is small, the transverse momenta of the leptons in the laboratory and  $W$  centre-of-mass frames are related by a simple Galilean transformation:

$$\begin{aligned} p_{Te} &= p^* + \frac{1}{2} p_T^W \\ p_{T\nu} &= -p^* + \frac{1}{2} p_T^W . \end{aligned} \quad (9.48)$$

It is straightforward to show that, to leading order in  $p_T^W$ , Eq. (9.47) is unchanged by such a transformation.

Fig. 9.10 shows the transverse mass distribution for  $W \rightarrow e\nu$  production measured by the CDF collaboration at the Tevatron  $p\bar{p}$  collider [24]. A similar distribution is obtained for  $W \rightarrow \mu\nu$ , and combining the results of a fit to both gives

$$\text{CDF} : M_W = 80.41 \pm 0.18 \text{ GeV}. \quad (9.49)$$

The corresponding (preliminary) result from the D0 collaboration (for  $W \rightarrow e\nu$  only) is [25]

$$\text{D0} : M_W = 80.331 \pm 0.270 \text{ GeV}. \quad (9.50)$$

Combining these results with earlier measurements by CDF [26] and UA2 [27] gives the *world average* value [25]

$$M_W = 80.33 \pm 0.15 \text{ GeV}. \quad (9.51)$$

One of the largest contributions to the error on  $M_W$  has an interesting origin. Charged leptons with large rapidity are not detected, and so in practice what is relevant is the transverse mass distribution in the presence of a cut,  $|y_e| < y_0$ . However in the presence of such a cut, the transverse mass distribution is no longer independent of the longitudinal momentum of the  $W$ . This introduces a non-negligible dependence of the measured  $M_W$  value on the parton distributions used in the fit in Fig. 9.10, and any uncertainty in the parton distributions translates directly into an uncertainty on  $M_W$ . We can see how this dependence arises by writing the electron rapidity in terms of the rapidity of the  $W$  and the rapidity of the electron in the  $W$  rest frame:

$$\begin{aligned} y_e &= y_W + y^* \\ &\simeq \frac{1}{2} \ln \left( \frac{x_1}{x_2} \right) + \frac{1}{2} \ln \left( \frac{1 + \cos \theta^*}{1 - \cos \theta^*} \right), \end{aligned} \quad (9.52)$$

where we have used Eq. (9.9). For a given  $\cos \theta^*$  (equivalently  $p_{T e}$ ), therefore, the integration over the parton momentum fractions is restricted by the allowed range of  $y_e$ . In fact the resulting transverse mass distribution is correlated with the  $u/d$  parton ratio [28], and therefore with the lepton rapidity asymmetry discussed in Section 9.4.2. This allows the lepton asymmetry to discriminate between parton distributions used in fitting the measured  $M_T$  distribution [24,25].

#### 9.4.4 *W* and *Z* transverse momentum distributions

Like Drell-Yan lepton pairs, most  $W$  and  $Z$  bosons (collectively denoted by  $V$ ) are produced with relatively little transverse momentum, *i.e.*  $p_T \ll M_V$ . However, part of the total cross section corresponds to the production of large transverse momentum bosons. The relevant mechanisms are

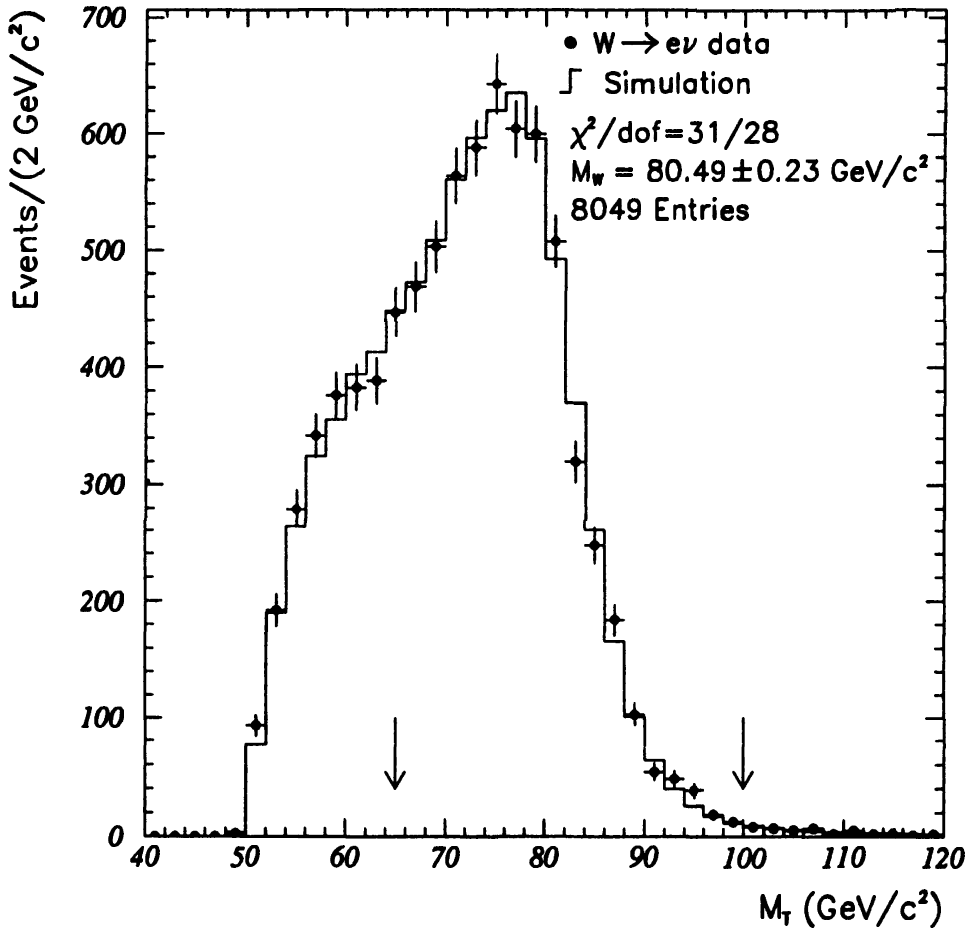


Fig. 9.10.  $W \rightarrow e\nu$  transverse mass distribution measured by the CDF collaboration. Figure from ref. [24].

the  $2 \rightarrow 2$  processes  $q\bar{q} \rightarrow Vg$  and  $qg \rightarrow Vq$ . The diagrams are identical to those for large  $p_T$  direct photon production, Fig. 7.16, and the annihilation and Compton matrix elements are, from Table 7.2 with an appropriate change in the overall coupling,

$$\begin{aligned} \sum |M_{q\bar{q} \rightarrow Wg}|^2 &= \pi \alpha_s \sqrt{2} G_F M_W^2 |V_{q\bar{q}}|^2 \frac{8}{9} \frac{t^2 + u^2 + 2M_W^2 s}{tu}, \\ \sum |M_{qg \rightarrow Wq}|^2 &= \pi \alpha_s \sqrt{2} G_F M_W^2 |V_{q\bar{q}}|^2 \frac{1}{3} \frac{s^2 + u^2 + 2tM_W^2}{-su}, \end{aligned} \quad (9.53)$$

with similar results for the  $Z$  boson. The transverse momentum distributions  $d\sigma/dp_T^2$  are obtained by convoluting these matrix elements with parton distributions in the usual way. The next-to-leading-order ( $O(\alpha_s^2)$ ) perturbative corrections, obtained from real emission processes like  $q\bar{q} \rightarrow Vgg$  and virtual (loop) corrections to the leading-order processes, have also been calculated [29].

Data on the  $p_T$  distribution of the  $W$  boson from the CDF collaboration

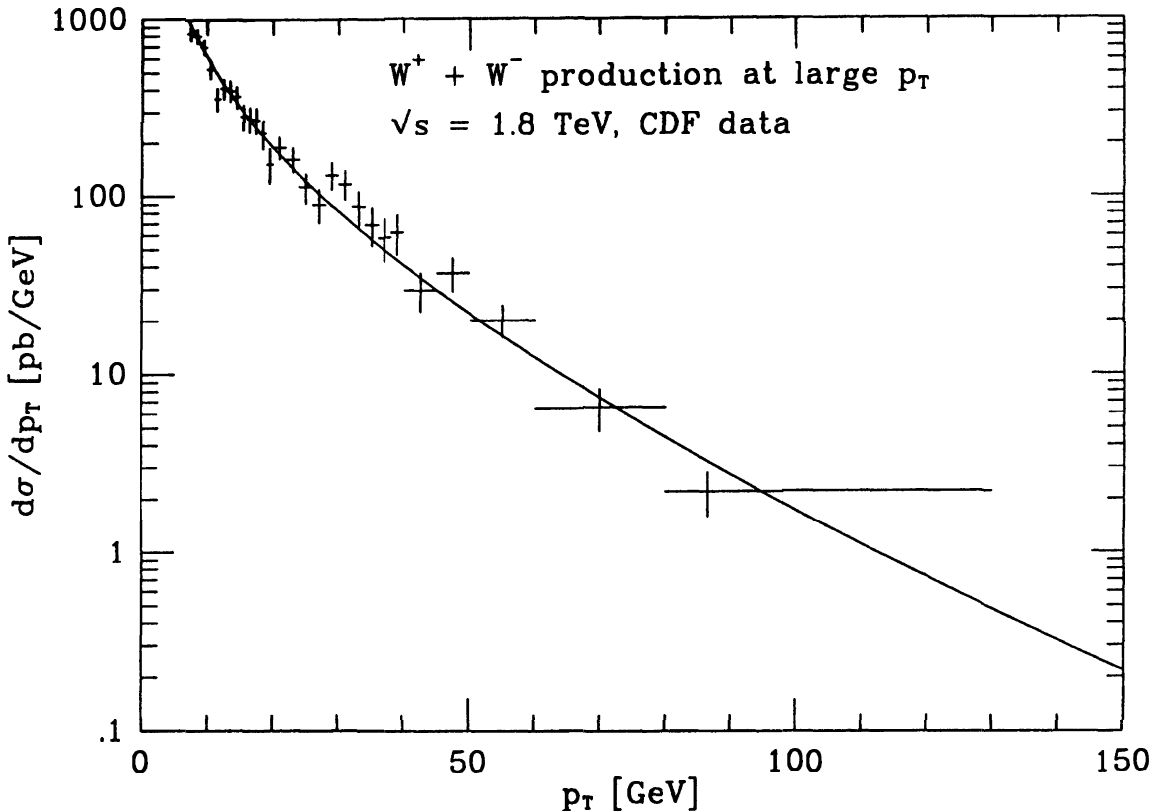


Fig. 9.11. *W* transverse momentum distribution measured by the CDF collaboration [30], with the next-to-leading-order QCD prediction.

[30] are shown in Fig. 9.11, together with the next-to-leading-order QCD prediction. The agreement is very satisfactory over the  $p_T$  range shown.

The poles at  $t = 0$  and  $u = 0$  in the matrix elements of Eq. (9.53) cause the leading-order theoretical cross section to diverge as  $p_T \rightarrow 0$ . The leading behaviour at small  $p_T$  comes from the emission of a soft ( $k^\mu \rightarrow 0$ ) gluon in the process  $q\bar{q} \rightarrow Vg$ . Schematically (with  $M = M_W$  or  $M_Z$ )

$$\frac{d\sigma^R}{dp_T^2} = \alpha_s \left( A \frac{\ln(M^2/p_T^2)}{p_T^2} + B \frac{1}{p_T^2} + C(p_T^2) \right), \quad (9.54)$$

where  $A$  and  $B$  are calculable coefficients and  $C$  is an integrable function. We have already seen, however, that the complete  $O(\alpha_s)$  (real plus virtual) correction to the total cross section is finite. Virtual corrections to  $q\bar{q} \rightarrow V$  only contribute at  $p_T = 0$ , i.e.  $d\sigma^V/dp_T^2 \propto \delta(p_T^2)$ , and their contribution to the differential distribution essentially introduces a ‘plus prescription’ on the singular parts of the gluon emission cross section:

$$\frac{d\sigma^{R+V}}{dp_T^2} = \alpha_s \left( A \left[ \frac{\ln(M^2/p_T^2)}{p_T^2} \right]_+ + B \left[ \frac{1}{p_T^2} \right]_+ + \overline{C}(p_T^2) \right), \quad (9.55)$$

such that the integrated contribution is finite,<sup>3</sup>

$$\int dp_T^2 \frac{d\sigma^{R+V}}{dp_T^2} = \alpha_s \int dp_T^2 \bar{C}(p_T^2). \quad (9.56)$$

An important ingredient missing from the above derivation is the *non-perturbative* contribution to the  $p_T$  distribution. At very small  $p_T$ , the intrinsic transverse motion of the quarks and gluons inside the colliding hadrons cannot be neglected. We have already seen how the intrinsic  $k_T$  is well parametrized by a Gaussian distribution with  $\langle k_T \rangle = 760$  MeV. This non-perturbative contribution has to be combined with the perturbative large  $p_T$  tail given by Eq. (9.55). A simple convolution in transverse-momentum space of the perturbative distribution in Eq. (9.55) with non-perturbative intrinsic  $k_T$  distributions as in Eq. (9.13) is one method of doing this.

For  $p_T \gg \langle k_T \rangle$  a purely perturbative approach should be adequate. However, if at the same time  $p_T \ll M$  then higher-order terms in the perturbation series cannot be neglected. In particular, the emission of multiple soft gluons becomes important and the leading contributions at each order have the form

$$\begin{aligned} \frac{1}{\sigma} \frac{d\sigma}{dp_T^2} \simeq & \frac{1}{p_T^2} \left[ A_1 \alpha_s \ln \frac{M^2}{p_T^2} + A_2 \alpha_s^2 \ln^3 \frac{M^2}{p_T^2} + \dots \right. \\ & \left. + A_n \alpha_s^n \ln^{2n-1} \frac{M^2}{p_T^2} + \dots \right], \end{aligned} \quad (9.57)$$

where the  $A_i$  are calculable coefficients of order unity. The higher-order terms in the series are evidently important when

$$\alpha_s \ln^2 \frac{M^2}{p_T^2} \gtrsim 1. \quad (9.58)$$

Taking into account the relative magnitude of the  $A_n$  coefficients, this corresponds to  $p_T$  values less than 10 – 15 GeV.

Fortunately, the leading logarithms in Eq. (9.57) can be *resummed* to all orders in perturbation theory. In fact the distribution at small  $p_T$  appears at first sight to be exactly analogous to the thrust distribution near  $T = 1$  in  $e^+e^- \rightarrow$  hadrons discussed in Chapter 3 — compare (9.57) and (6.81, 6.82). The coefficients  $A_n$  are in fact the same in both cases, and therefore we might expect a similar Sudakov form factor suppression at small  $p_T$ . Indeed the resummed double leading logarithms give (*cf.*

---

<sup>3</sup> Recall that  $\int_0^1 dx [f(x)]_+ = 0$ .

Eq. (6.96))

$$\frac{1}{\sigma} \frac{d\sigma}{dp_T^2} \simeq \frac{d}{dp_T^2} \exp \left( -\frac{\alpha_S}{2\pi} C_F \ln^2 \frac{M^2}{p_T^2} \right) , \quad (9.59)$$

which vanishes at  $p_T = 0$ . However, this result is misleading. The Sudakov suppression of the thrust distribution near  $T = 1$  is due to the suppression of gluon bremsstrahlung in that region. In contrast, the production of a  $W$  or  $Z$  boson with  $p_T \approx 0$  does *not* require that all emitted gluons are soft, merely that their *vector* transverse momentum sum is small. In particular, the double-leading-logarithm result (9.59) omits contributions from the multiple emission of soft gluons with  $k_{Ti} \sim p_T$  and  $\sum_i \vec{k}_{Ti} = \vec{p}_T$ . Such additional contributions ‘fill in’ the dip at  $p_T \approx 0$  predicted by (9.59).

A more complete analysis of the small  $p_T$  distribution therefore requires proper treatment of transverse momentum conservation in multiple gluon emission [31]. This is achieved by introducing the two-dimensional impact parameter vector  $\vec{b}$ , which is the Fourier conjugate of  $\vec{p}_T$ , and writing

$$\delta^{(2)} \left( \sum_{i=1}^n \vec{k}_{Ti} - \vec{p}_T \right) = \frac{1}{(2\pi)^2} \int d^2 b e^{-i\vec{b} \cdot \vec{p}_T} \prod_{i=1}^n e^{i\vec{b} \cdot \vec{k}_{Ti}} , \quad (9.60)$$

for the emission of  $n$  soft gluons. The Sudakov form factor then appears in  $b$ -space after resumming large  $\ln(b^2 M^2)$  logarithms.

As for  $e^+e^-$  event shapes, a complete formalism has been developed for taking account of all large  $\ln(M^2/p_T^2)$  logarithms in the perturbation series at small  $p_T$  [32,33,34]. In particular, the result for the small  $p_T(Z)$  distribution is

$$\begin{aligned} \frac{d\sigma}{dp_T^2} \simeq & \sum_q \sigma_0^{qq} \frac{1}{2} \int_0^\infty db b J_0(bp_T) \exp(-S(b, M_Z)) \\ & \int_0^1 dx_1 dx_2 \delta(x_1 x_2 - \frac{M_Z^2}{s}) [q(x_1, (b_0/b)^2) \bar{q}(x_2, (b_0/b)^2) + (q \leftrightarrow \bar{q})] , \end{aligned} \quad (9.61)$$

where

$$\sigma_0^{q\bar{q}} = \pi \sqrt{2} G_F M_Z^2 (V_q^2 + A_q^2) / (3s) \quad (9.62)$$

and  $b_0 = 2 \exp(-\gamma_E)$  ( $\gamma_E = 0.5772 \dots$  is the Euler constant). The Sudakov form factor in  $b$ -space is  $\exp(-S)$  where [32]

$$\begin{aligned} S(b, Q) &= \int_{(b_0/b)^2}^{Q^2} \frac{dq^2}{q^2} \left[ \ln \frac{Q^2}{q^2} A(\alpha_S(q^2)) + B(\alpha_S(q^2)) \right] , \\ A(\alpha_S) &= \sum_{n=1}^{\infty} \left( \frac{\alpha_S}{2\pi} \right)^n A^{(n)} , \end{aligned}$$

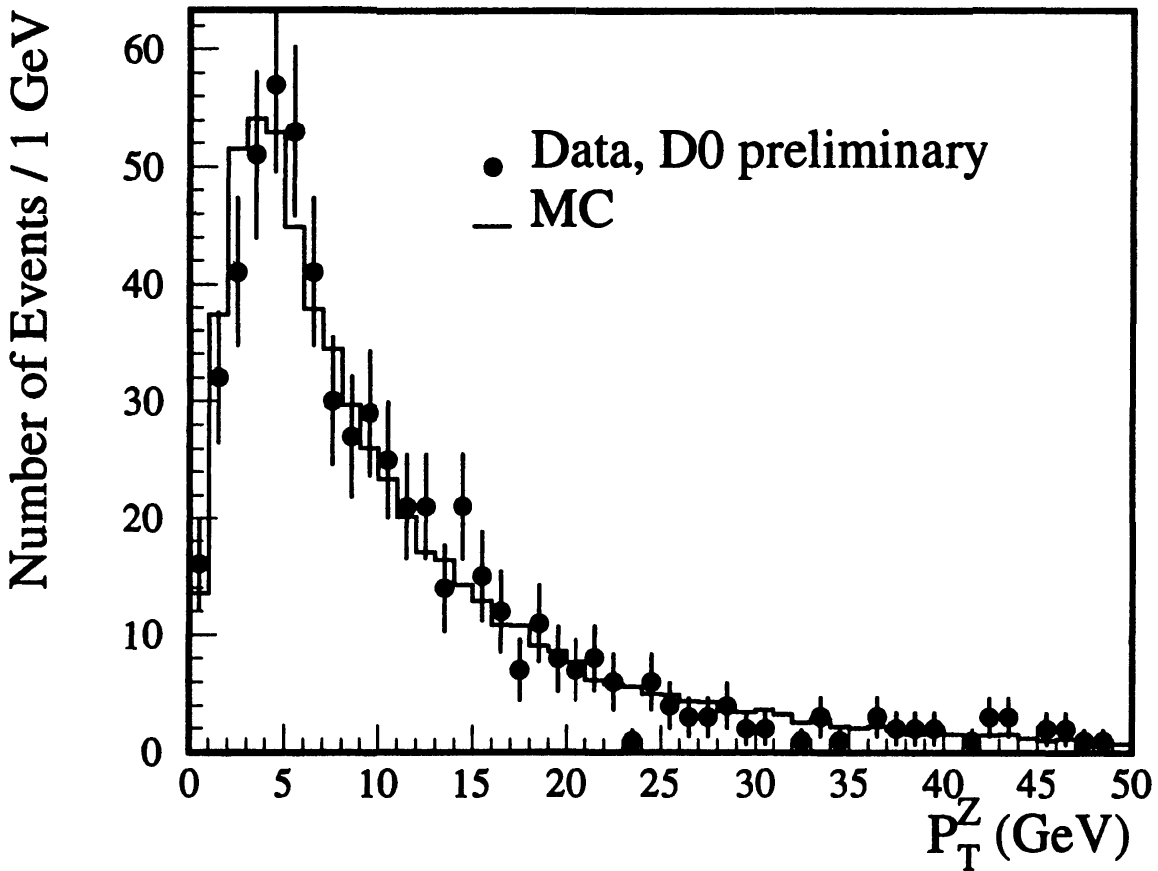


Fig. 9.12.  $Z$  transverse momentum distribution measured by the D0 collaboration [37], with the resummed theoretical prediction (labelled MC) from ref. [36].

$$B(\alpha_s) = \sum_{n=1}^{\infty} \left( \frac{\alpha_s}{2\pi} \right)^n B^{(n)}. \quad (9.63)$$

The  $A^{(n)}$  and  $B^{(n)}$  coefficients for  $n = 1, 2$  have been calculated, see refs. [33,35].

The small- $p_T$  distribution can, in principle, be used as a test of the resummed QCD perturbation series. In practice, however, there are some difficulties — for example, some non-perturbative cut-off or smearing must be included to make the  $b$  integral in Eq. (9.61) converge at large  $b$  and to avoid infra-red problems from evaluating  $\alpha_s$  and the parton distributions at low scales. This introduces a significant theoretical uncertainty; see, for example, ref. [36]. Fig. 9.12 shows an example of a comparison of theory and experiment for the  $Z$   $p_T$  distribution measured by the D0 collaboration [37]. The theoretical prediction incorporates both the resummed higher-order contributions at small  $p_T$ , and the exact next-to-leading-order correction at large  $p_T$ . Considering the uncertainties in both, experiment and theory evidently agree well.

#### 9.4.5 Multijet production with *W* and *Z*

One of the most important Standard Model processes in high-energy hadron-hadron collisions is the production of a *W* or *Z* with accompanying hadronic (*i.e.* quark or gluon) jets. Most ‘new physics’ processes, for example the production of heavy quarks, Higgs bosons and supersymmetric particles, can be mimicked by the production of vector bosons in association with jets. It is therefore important to be able to estimate these backgrounds accurately. In addition, quantitative tests of QCD are possible: the rate of multijet production is dependent on the strong coupling constant and the kinematic distributions of the jets probe the underlying scattering matrix elements.

By introducing the same ‘infra-red safe’ techniques for defining perturbative jet cross sections as were described in the context of multijet production in Chapters 3 and 7, we can decompose the total *W* cross section into its multijet components:

$$\sigma_W = \sigma_{W+0j} + \sigma_{W+1j} + \sigma_{W+2j} + \sigma_{W+3j} + \dots \quad (9.64)$$

where, schematically,

$$\begin{aligned} \sigma_{W+0j} &= a_0 + \alpha_S a_1 + \alpha_S^2 a_2 + \dots \\ \sigma_{W+1j} &= \alpha_S b_1 + \alpha_S^2 b_2 + \dots \\ \sigma_{W+2j} &= \alpha_S^2 c_2 + \dots \\ &\dots \end{aligned} \quad (9.65)$$

The  $a_i, b_i, c_i, \dots$  coefficients in these expansions are in general functions of the jet-definition parameters, in particular the cone size used to cluster the partons into jets, and the transverse momentum, rapidity and separation cuts imposed on the jets/clusters. For example, as the cone size is decreased the cross sections for the production of a large number of jets increase, in exact analogy with the dependence of the jet fractions in  $e^+e^- \rightarrow \text{hadrons}$  on  $y_{\text{cut}}$  in Fig. 3.7. At the same time, the *sum* at each order in perturbation theory, *i.e.*

$$\begin{aligned} a_0 &= \hat{\sigma}_0 \\ a_1 + b_1 &= \hat{\sigma}_1 \\ a_2 + b_2 + c_2 &= \hat{\sigma}_2 \\ &\dots \end{aligned}, \quad (9.66)$$

is independent of the jet parameters and corresponds simply to the perturbative expansion of the total cross section discussed in Section 9.4.1.

The leading contributions to the cross sections,  $a_0, b_1, c_2, \dots$ , can be calculated from the matrix elements for the ‘tree-level’ parton processes:  $ij \rightarrow V + k_1 \dots k_n$ , where  $V = W, Z$  and  $i, j, k_r = q, g$ . Provided that the

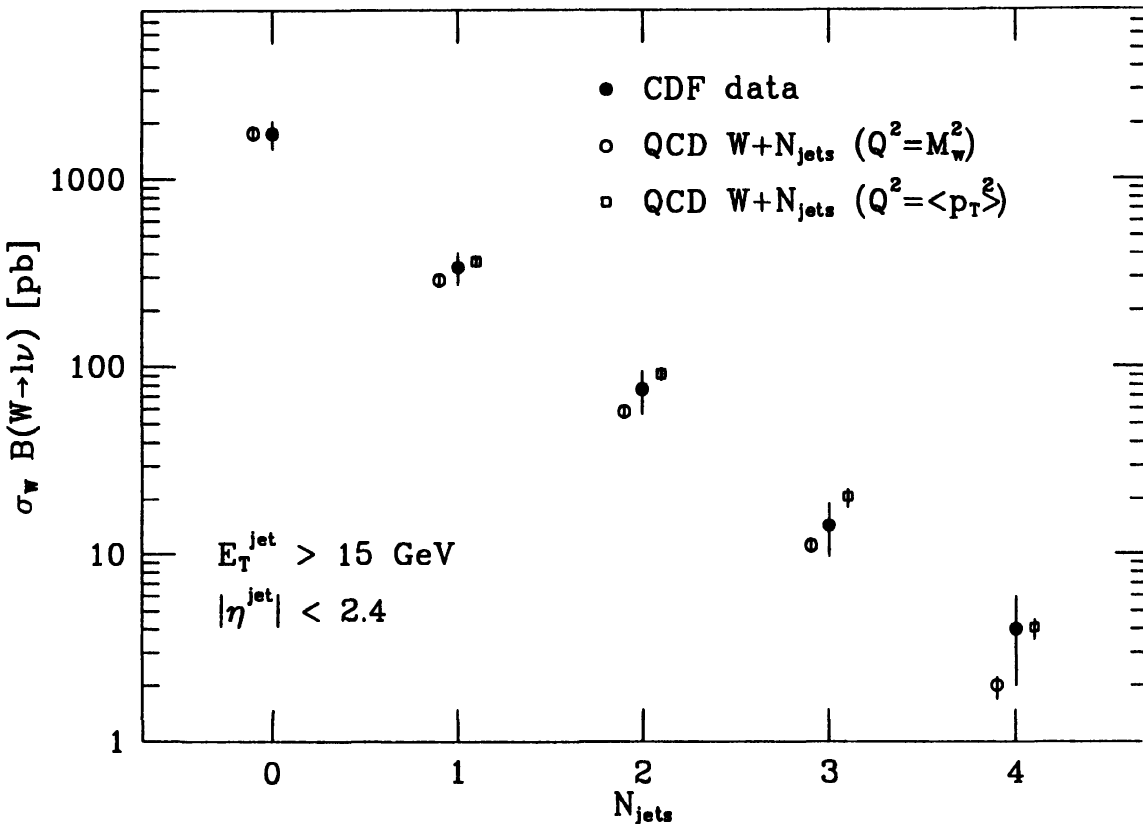


Fig. 9.13.  $W$  cross section as a function of jet multiplicity measured by the CDF collaboration and compared with theoretical predictions.

jets are required to be energetic and well-separated, these leading contributions provide a reasonable approximation to the multijet cross sections. As an illustration, Fig. 9.13 shows the tree-level predictions [38] for the jet cross sections  $\sigma_{W+nj}$ ,  $n \leq 4$  compared with measurements from the CDF collaboration in  $p\bar{p}$  collisions at  $\sqrt{s} = 1.8$  TeV [39]. As with all leading-order calculations, there is a non-negligible factorization/renormalization scale dependence which becomes stronger as the number of jets increases. In Fig. 9.13 predictions are shown for two scale choices,  $Q^2 = \langle p_T^{jet} \rangle^2$  and  $Q^2 = M_W^2$ . It is interesting to note the almost exact geometric relation between the jet fractions: *i.e.* with this choice of cuts the measured  $0, \dots, 4$  jet cross sections are well-parametrized by  $\sigma_n = \sigma_0(0.20)^n$ . Given the complexity of the multiparton matrix elements, it is perhaps surprising that the predictions are related in this simple way.

Next-to-leading-order corrections are at present known only for the  $W + 0$  and 1 jet production cross sections [40,41]. An interesting test of the theory is provided by the angular distribution of the  $W$  in  $W + 1$  jet production. At leading order, the cross section is obtained from the  $q\bar{q}' \rightarrow Wg$  and  $qg \rightarrow Wq$  scattering processes whose matrix elements are given in (9.53). The spin- $\frac{1}{2}$  quark propagator in both these processes

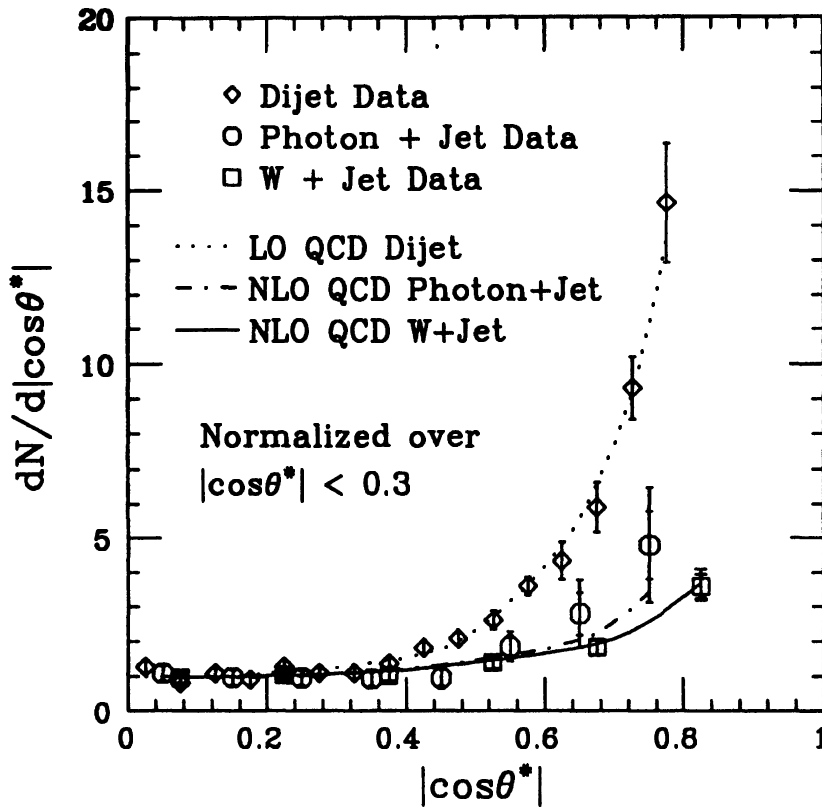


Fig. 9.14. Distribution in the polar angle  $\theta^*$  for  $W + \text{jet}$ , jet + jet and photon + jet production measured by the CDF collaboration compared with theoretical predictions. Figure from ref. [42].

produces a characteristic behaviour

$$\frac{d\sigma}{d \cos \theta^*} \sim \frac{1}{1 - |\cos \theta^*|} \quad (9.67)$$

for the distribution in the polar angle  $\theta^*$  of the  $W$  in the  $W$ -jet centre-of-mass frame. This is in contrast to the jet  $\theta^*$  distribution in jet-jet production (see Eq. (7.36)),

$$\frac{d\sigma}{d \cos \theta^*} \sim \frac{1}{(1 - |\cos \theta^*|)^2}, \quad (9.68)$$

which arises from the t-channel exchange of a spin-1 gluon in  $gg \rightarrow gg$ ,  $qg \rightarrow qg$  and  $qq \rightarrow qq$  scattering. The predicted difference in the forward/backward peaking behaviour of  $W$ -jet and jet-jet production is clearly seen in the data. Fig. 9.14 shows the  $\theta^*$  distribution for the two processes measured by the CDF collaboration [42] in  $p\bar{p}$  collisions at  $\sqrt{s} = 1.8$  TeV. The figure also shows the  $\theta^*$  distribution of the photon in photon-jet production which, for the leading-order  $qg \rightarrow \gamma q$  and  $q\bar{q} \rightarrow \gamma q$  processes, is also expected to show a  $1/(1 - |\cos \theta^*|)$  behaviour (see Table 7.2). Notice that the photon distribution appears to be slightly more

peaked than the  $W$  distribution, presumably because of the additional contributions to the former from higher-order ‘fragmentation’ processes such as  $qg \rightarrow q(\rightarrow \gamma)g$  (see Section 7.9).

## References

- 1) S.D. Drell and T.M. Yan, *Ann. Phys.* **66** (1971) 578.
- 2) See for example: J.C. Collins and D.E. Soper, *Ann. Rev. Nucl. Part. Sci.* **37** (1987) 383, and references therein.
- 3) W.J. Stirling and M.R. Whalley, *J. Phys. G: Nucl. Part. Phys.* **19** (1993) D1.
- 4) CFS collaboration, A.S. Ito *et al.*, *Phys. Rev.* **D23** (1981) 604.
- 5) G. Altarelli, R.K. Ellis and G. Martinelli, *Nucl. Phys.* **B143** (1978) 521; *ibid.* **B146** (1978) 544(erratum); *ibid.* **B157** (1979) 461.
- 6) J. Kubar-Andre and F.E. Paige, *Phys. Rev.* **D19** (1979) 221;  
J. Kubar-Andre, M. Le Bellac, J.L. Meunier and G. Plaut, *Nucl. Phys.* **B175** (1980) 251.
- 7) R. Hamberg, T. Matsuura and W.L. van Neerven, *Nucl. Phys.* **B345** (1990) 331; *ibid.* **B359** (1991) 343;  
W.L. van Neerven and E.B. Zijlstra, *Nucl. Phys.* **B382** (1992) 11.
- 8) E605 collaboration, G. Moreno *et al.*, *Phys. Rev.* **D43** (1991) 2815.
- 9) A.D. Martin, R.G. Roberts and W.J. Stirling, *Phys. Rev.* **D50** (1994) 6734.
- 10) CTEQ collaboration, H.L. Lai *et al.*, *Phys. Rev.* **D51** (1995) 4763.
- 11) J.F. Owens, *Phys. Rev.* **D30** (1984) 943;  
A.D. Martin, R.G. Roberts, W.J. Stirling and P.J. Sutton, *Phys. Rev.* **D45** (1992) 2349.
- 12) CDF collaboration, F. Abe *et al.*, *Phys. Rev.* **D49** (1994) 1.
- 13) CDF collaboration, A. Bodek, Proc. Int. Workshop on Deep Inelastic Scattering and Related Phenomena, Rome, April 1996.
- 14) UA1 collaboration, G. Arnison *et al.*, *Phys. Lett.* **B122** (1983) 103;  
UA2 collaboration, G. Banner *et al.*, *Phys. Lett.* **B122** (1983) 476.
- 15) K. Hikasa, *Phys. Rev.* **D29** (1984) 1939;  
D.A. Dicus and S.S.D. Willenbrock, *Phys. Rev.* **D34** (1986) 148.
- 16) UA1 collaboration, C. Albajar *et al.*, *Zeit. Phys.* **C44** (1989) 15;  
UA2 collaboration, J. Alitti *et al.*, *Phys. Lett.* **B267** (1992) 365;  
CDF collaboration, F. Abe *et al.*, *Phys. Rev. Lett.* **76** (1996) 3070;  
D0 collaboration, S. Abachi *et al.*, *Phys. Rev. Lett.* **75** (1995) 1456.
- 17) A.D. Martin, R.G. Roberts and W.J. Stirling, *Phys. Lett.* **B354** (1995) 155.
- 18) F. Halzen and K. Mursula, *Phys. Rev. Lett.* **51** (1983) 857;  
K. Hikasa, *Phys. Rev.* **D29** (1984) 1939.
- 19) D. Schaile, Proc. XXVII Int. Conf. on High Energy Physics, Glasgow, July 1994, eds. P.J. Bussey and I.G. Knowles, Institute of Physics Publishing, Bristol (1995), Vol. I, p. 27.
- 20) CDF collaboration, F. Abe *et al.*, *Phys. Rev. Lett.* **73** (1994) 220;  
D0 collaboration, S. Abachi *et al.*, *Phys. Rev. Lett.* **75** (1995) 1456.
- 21) E.L. Berger, F. Halzen, C.S. Kim and S. Willenbrock, *Phys. Rev.* **D40** (1989) 83; *ibid.* **D40** (1989) 3789(erratum).
- 22) CDF collaboration, F. Abe *et al.*, *Phys. Rev. Lett.* **74** (1995) 850.
- 23) CDF collaboration, F. Abe *et al.*, preprint Fermilab-Pub-96/071-E (1996).
- 24) CDF collaboration, F. Abe *et al.*, *Phys. Rev. Lett.* **75** (1995) 11; *Phys. Rev.* **D52** (1995) 4784.

- 25) D0 collaboration, U. Heintz, presented at *Les Rencontres de Physique de la Vallée d'Aoste, La Thuile*, 1996, preprint Fermilab-Conf-96/143-E (1996).
- 26) CDF collaboration, F. Abe *et al.*, *Phys. Rev. Lett.* **65** (1990) 2243; *Phys. Rev. D* **43** (1991) 2070.
- 27) UA2 collaboration, J. Alitti *et al.*, *Phys. Lett.* **B276** (1992) 354.
- 28) A.D. Martin and W.J. Stirling, *Phys. Lett.* **B237** (1990) 551.
- 29) P. Arnold and M.H. Reno, *Nucl. Phys.* **B319** (1989) 37; *ibid.* **B330** (1990) 284(*erratum*);  
R. Gonsalves, J. Pawłowski and C.-F. Wai, *Phys. Rev. D* **40** (1989) 2245.
- 30) CDF collaboration, F. Abe *et al.*, *Phys. Rev. Lett.* **66** (1991) 2951.
- 31) G. Parisi and R. Petronzio, *Nucl. Phys.* **B154** (1979) 427.
- 32) J.C. Collins and D.E. Soper, *Nucl. Phys.* **B193** (1981) 381; *ibid.* **B197** (1982) 446;  
*ibid.* **B213** (1983) 545(*erratum*).
- 33) J. Kodaira and L. Trentadue, *Phys. Lett.* **B112** (1982) 66; *ibid.* **B123** (1983) 335.
- 34) J.C. Collins, D.E. Soper and G. Sterman, *Nucl. Phys.* **B250** (1985) 199.
- 35) C.T.H. Davies and W.J. Stirling, *Nucl. Phys.* **B244** (1984) 337.
- 36) G.A. Ladinsky and C.P. Yuan, *Phys. Rev. D* **50** (1994) 4239.
- 37) D0 collaboration, D.L. Pušeljić, presented at the  $\bar{p}p$  Workshop, Fermilab, 1995.
- 38) F.A. Berends, W.T. Giele, H. Kuijf and B. Tausk, *Nucl. Phys.* **B357** (1991) 32.
- 39) CDF collaboration, F. Abe *et al.*, *Phys. Rev. Lett.* **70** (1993) 4043.
- 40) H. Baer and M.H. Reno, *Phys. Rev. D* **44** (1991) 3375.
- 41) W.T. Giele, E.W.N. Glover and D.A. Kosower, *Nucl. Phys.* **B403** (1993) 633.
- 42) CDF collaboration, F. Abe *et al.*, *Phys. Rev. Lett.* **73** (1994) 2296.

# 10

## Heavy quarks

One of the motivations for collider experiments is to discover new heavy objects. It is therefore important to test our understanding of such processes by predicting the production rates for the known heavy objects, such as the top, bottom and charm quarks, and to compare the predictions with experimental measurements.

Aspects of the production of heavy quarks in  $e^+e^-$  annihilation have already been considered in Chapter 3. We shall concentrate here on the hadronic production of heavy quarks. An idea of the relative cross sections and signal-to-background ratios for  $c$ ,  $b$  and  $t$  quark production at various present and future accelerators can be obtained from Table 10.1. As we shall see, the description of hadronic production is possible in perturbative QCD when the mass of the produced quark is large compared to 1 GeV, the typical scale of the strong interactions. Because the cross sections are generally large, hadronic interactions offer the potential to produce the large number of heavy quarks necessary to study their decays in detail. However, at present, much of the information on states containing  $c$  and  $b$  quarks comes from  $e^+e^-$  annihilation, because of the better signal-to-background ratios at  $e^+e^-$  colliders.

As an illustration of the power of hadron colliders we consider the case of  $b$  production. For example, at the Fermilab Tevatron running at a luminosity of  $2 \times 10^{31} \text{ cm}^{-2}\text{s}^{-1}$ ,  $b$  quarks are produced at 400 Hz. This should be contrasted with an  $e^+e^-$  machine such as CESR operating at a luminosity of  $2 \times 10^{32} \text{ cm}^{-2}\text{s}^{-1}$ , where the rate of  $b$  production is  $\sim 0.1 \text{ Hz}$ <sup>1</sup>. A large sample of  $bs$  is necessary to observe CP violation in the decays of

---

<sup>1</sup> A large effort is put into upgrading the luminosities of colliding beam machines. These numbers will soon be out of date.

Process	$\sqrt{s}$ [GeV]	Cross section	$\sigma_{QQ}/\sigma_{tot}$
$\pi N \rightarrow c\bar{c}$	25	$20 \mu b$	0.1%
$pN \rightarrow c\bar{c}$	38	$40 \mu b$	0.1%
$\gamma N \rightarrow c\bar{c}$	19	$0.7 \mu b$	0.4%
$pp \rightarrow b\bar{b}$	40	20 nb	$10^{-6}$
$p\bar{p} \rightarrow b\bar{b}$	1800	$20 \mu b$	0.03%
$pp \rightarrow b\bar{b}$	14000	$300 \mu b$	0.5%
$e^+e^- \rightarrow b\bar{b}$	10.48	1 nb	25%
$e^+e^- \rightarrow b\bar{b}$	91	7 nb	15%
$p\bar{p} \rightarrow t\bar{t}$	1800	5 pb	$10^{-10}$
$pp \rightarrow t\bar{t}$	14000	800 pb	$10^{-8}$
$e^+e^- \rightarrow t\bar{t}$	500	500 fb	5%

Table 10.1. Approximate rates for heavy quark production.

hadrons containing  $b$  quarks and to measure  $B, -\overline{B}$ , mixing. In addition, hadronic production of  $b$  quarks gives access to a wide spectrum of states, including mesons containing both bottom and charm ( $b\bar{c}$ ) and baryonic states containing  $b$  quarks. This is in contrast to  $e^+e^-$  machines operating at the  $T(4S)$  resonance where only the lowest-lying  $B^0$  and  $B^+$  states are produced.

The disadvantage of hadronically produced heavy quarks is that they have to be distinguished from a large background of other hadrons. Table 10.1 shows the discrimination against background which is necessary. This is achieved by using the special properties of the decay products to trigger on the interesting events.

## 10.1 Charm and bottom quark decays

The existence of hadrons containing heavy quarks is deduced by observation of their decays. Therefore any experiment which measures the cross section for the production of hadrons containing heavy quarks must make assumptions concerning the branching fraction to the observed mode. Since leptons play an important role in the identification of heavy quarks we will begin by discussing semi-leptonic decays.

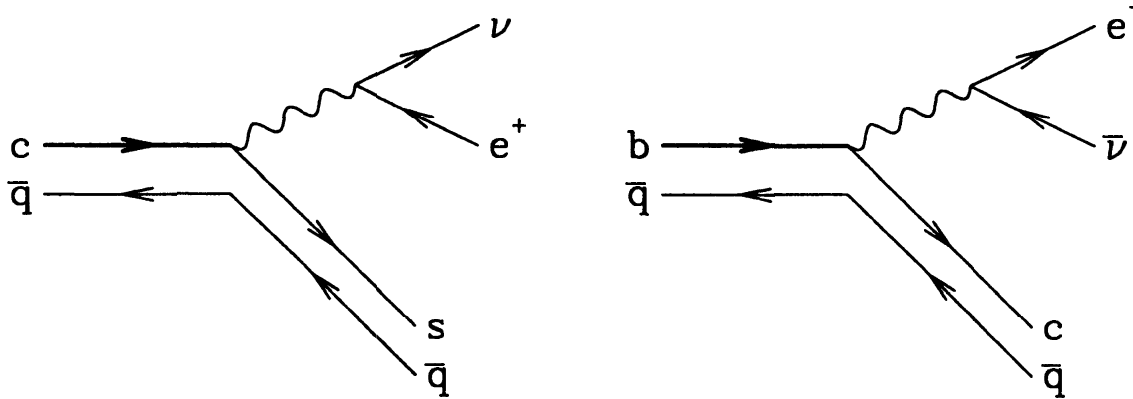


Fig. 10.1. CKM-favoured spectator diagrams for  $c$  and  $b$  meson decay.

### 10.1.1 Semi-leptonic decays

The simplest approach is to treat the semi-leptonic decays of hadrons containing  $c$  and  $b$  quarks in analogy with the decay of a free muon. This is called the *spectator model*, since the quarks which accompany the heavy quark  $Q$  in the hadron are assumed to play no role in the decay.

The Lagrangian responsible for the semi-leptonic decay of a  $c$  or  $b$  quark has the normal  $V - A$  structure familiar from muon decay, apart from the factor  $V_{qQ}$  coming from the Cabibbo-Kobayashi-Maskawa (CKM) matrix defined in Section 8.3.3. For the moment we consider only the CKM-favoured decays, for which the Lagrangians are

$$\mathcal{L}^{(c)} = -\frac{G_F}{\sqrt{2}} V_{cs} \bar{s} \gamma^\mu (1 - \gamma_5) c \bar{\nu} \gamma_\mu (1 - \gamma_5) e , \quad (10.1)$$

$$\mathcal{L}^{(b)} = -\frac{G_F}{\sqrt{2}} V_{cb} \bar{c} \gamma^\mu (1 - \gamma_5) b \bar{\nu} \gamma_\mu (1 - \gamma_5) \nu . \quad (10.2)$$

The generalization to CKM-disfavoured decays is straightforward. The diagrams responsible for these decays are shown in Fig. 10.1. The matrix elements for  $c$  and  $b$  decay, taking into account the finite masses of the quarks, are

$$\begin{aligned} \overline{\sum} |\mathcal{M}^{(c)}|^2 &= 64 G_F^2 |V_{cs}|^2 c \cdot e^+ s \cdot \nu , \\ \overline{\sum} |\mathcal{M}^{(b)}|^2 &= 64 G_F^2 |V_{cb}|^2 b \cdot \bar{\nu} c \cdot e^- , \end{aligned} \quad (10.3)$$

where  $b, c, s, \nu, \bar{\nu}, e^+$  and  $e^-$  now stand for the four-momenta of the particles in the decay. The structure of the matrix elements given in Eq. (10.3) has already been commented on in our discussion of the angular distribution in  $W$  decay in Chapter 9. In the standard model, the  $V - A$  form of the charged weak current determines that fermions participating in weak decay are predominantly left-handed and antifermions predominantly right-handed. Consequently angular momentum conservation dic-

tates that the  $s$  and  $\nu$  momenta prefer to be anti-parallel in  $c$  quark decay. The endpoint configuration in which the  $e^+$  recoils against the parallel  $s$  and  $\nu$  is thus disfavoured. We therefore expect a soft spectrum for the positron coming from the decay of a charm meson. Conversely we expect a hard spectrum for the neutrino (or for the electron coming from the decay of a  $b$  quark). These features are apparent in the matrix elements, Eq. (10.3).

The semi-leptonic decay rate is obtained by including the three-particle phase space and flux factor as follows:

$$\Gamma_{\text{sl}}^{(Q)} = \frac{m_Q}{2^8 \pi^3} \int dx dy \theta(x+y-x_m) \theta(x_m-x-y+xy) \overline{\sum} |\mathcal{M}^{(Q)}|^2 \quad (10.4)$$

where  $x$  and  $y$  are the rescaled energies of the charged and neutral leptons,  $x = 2E_e/m_Q$ ,  $y = 2E_\nu/m_Q$  in the frame in which the heavy quark  $Q$  is at rest. The kinematic endpoint of the spectrum is denoted by  $x_m$  and is given by  $x_m = 1 - \epsilon^2$  where  $\epsilon = m_q/m_Q$ . The parameter  $\epsilon$  is equal to  $m_s/m_c$  for  $c$  decay and equal to  $m_c/m_b$  for  $b$  decay. The result for the semi-leptonic widths of the  $c$  and the  $b$  is

$$\begin{aligned} \frac{d\Gamma_{\text{sl}}^{(c)}}{dxdy} &= |V_{cs}|^2 \Gamma_0(m_c) [12x(x_m - x)] \\ \frac{d\Gamma_{\text{sl}}^{(b)}}{dxdy} &= |V_{cb}|^2 \Gamma_0(m_b) [12y(x_m - y)] \end{aligned} \quad (10.5)$$

where  $\Gamma_0$  is the rescaled muon decay rate,

$$\Gamma_0(m_Q) = \frac{G_F^2 m_Q^5}{192\pi^3}. \quad (10.6)$$

The lepton spectra calculated from Eq. (10.5) are

$$\frac{d\Gamma_{\text{sl}}^{(c)}}{dx} = |V_{cs}|^2 \Gamma_0(m_c) \left[ \frac{12x^2(x_m - x)^2}{(1-x)} \right] \quad (10.7)$$

$$\frac{d\Gamma_{\text{sl}}^{(b)}}{dx} = |V_{cb}|^2 \Gamma_0(m_b) \left[ \frac{2x^2(x_m - x)^2}{(1-x)^3} \right] (6 - 6x + xx_m + 2x^2 - 3x_m). \quad (10.8)$$

These spectra are plotted in Fig. 10.2. Note that, as expected, the  $e^+$  from charm decay has a soft spectrum. The form of the lepton spectrum from  $b$  decay is of great interest. The electron spectrum for the CKM-disfavoured mode  $b \rightarrow u$  is hard. The measurement of leptons with energies beyond the kinematic limit for  $b \rightarrow c$  [1] is the primary method by which information about  $V_{ub}$  is obtained. The value derived for  $V_{ub}$  depends in detail on the form of the lepton spectrum in the endpoint region, which may

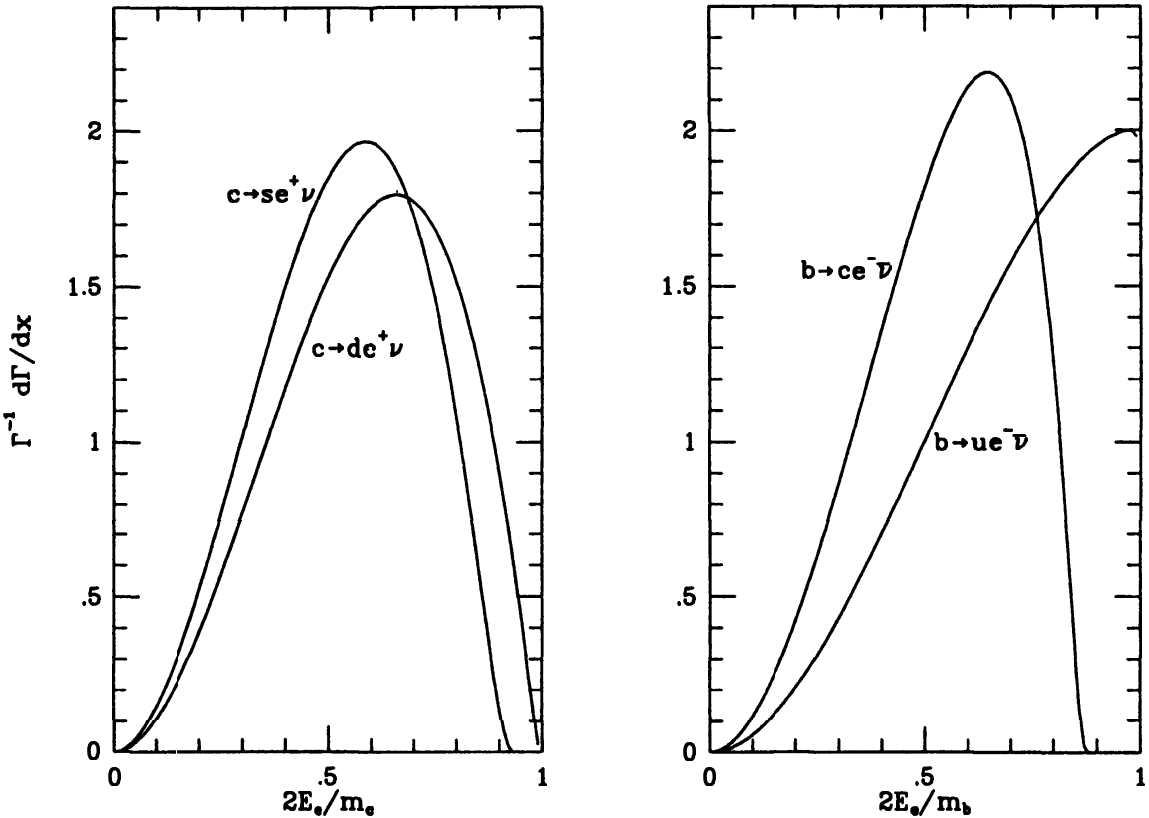


Fig. 10.2. Shapes of the lepton spectra in  $c$  and  $b$  decay.

not be well predicted by the simple spectator model [2]. Allowing for this theoretical uncertainty, the measured value is  $|V_{ub}/V_{cb}| = 0.08 \pm 0.02$  [3].

After integration of either Eq. (10.7) or Eq. (10.8), the semi-leptonic width including mass effects is found to be

$$\Gamma_{sl}^{(Q)} = |V_{Qq}|^2 \Gamma_0(m_Q) f\left(\frac{m_q}{m_Q}\right) \quad (10.9)$$

where the function  $f$  is given by

$$f(\epsilon) = (1 - \epsilon^4)(1 - 8\epsilon^2 + \epsilon^4) - 24\epsilon^4 \ln \epsilon. \quad (10.10)$$

Including the CKM-disfavoured mode  $c \rightarrow d$  the result for the semi-leptonic decay of the  $c$  quark is

$$\Gamma_{sl}^{(c)} = \Gamma_0(m_c) \left[ f(m_s/m_c) |V_{cs}|^2 + f(m_d/m_c) |V_{cd}|^2 \right]. \quad (10.11)$$

This expression has a large numerical uncertainty dependent on the value chosen for the charm quark mass. The result is also subject to strong interaction corrections; since we are interested here in a rough check of the model, we ignore these for the case of charm. If we take a value of  $m_c = 1.4$  GeV, the theoretical estimate for the semi-leptonic width is

$$\Gamma_{sl} = 1.1 \times 10^{-10} \text{ MeV}. \quad (10.12)$$

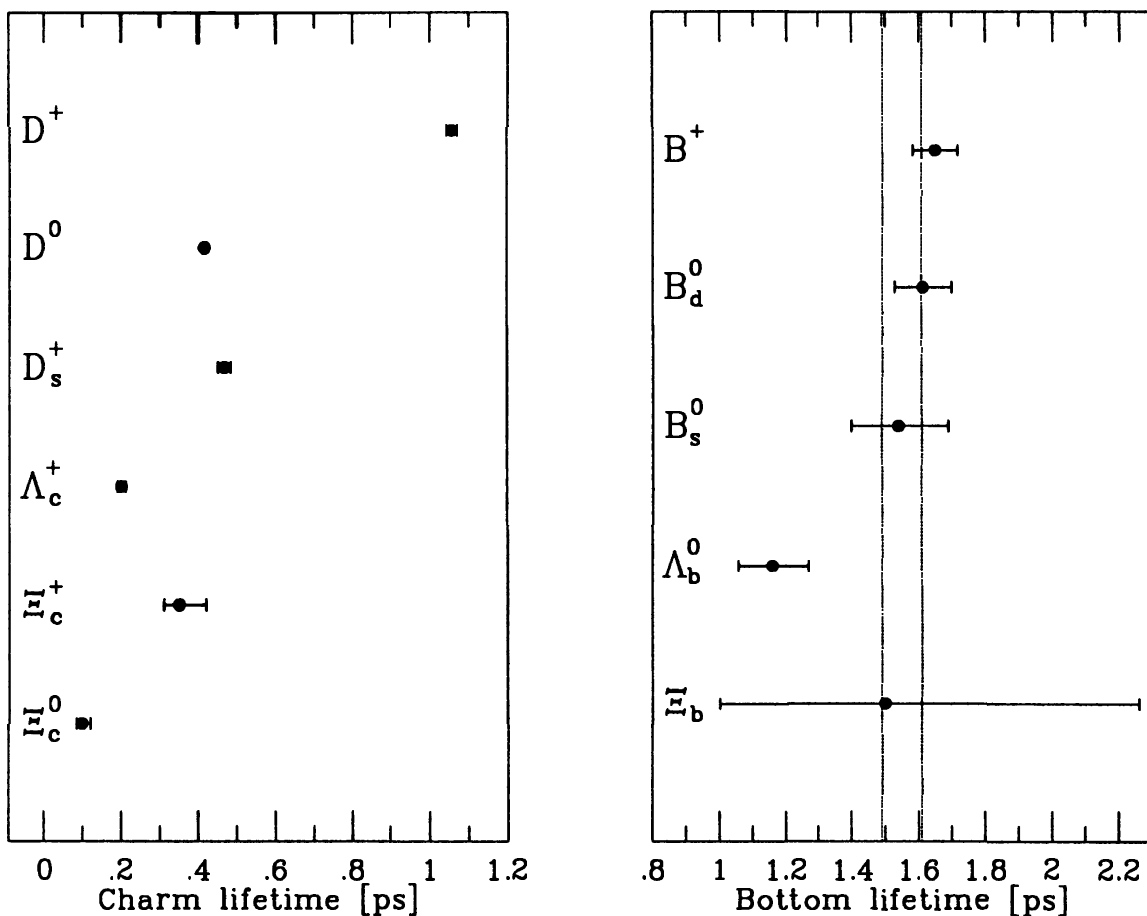


Fig. 10.3. The measured lifetimes of hadrons containing  $c$  and  $b$  quarks [3,4].

Using the measured semi-leptonic branching ratios of the  $D^+$  and  $D^0$ , which are  $17.2 \pm 1.9\%$  and  $7.7 \pm 1.2\%$  respectively [3], and the measured lifetimes shown in Fig. 10.3, we can calculate the semi-leptonic widths

$$\begin{aligned}\Gamma_{sl}(D^0) &= (1.22 \pm 0.20) \times 10^{-10} \text{ MeV} \\ \Gamma_{sl}(D^+) &= (1.07 \pm 0.13) \times 10^{-10} \text{ MeV.}\end{aligned}\quad (10.13)$$

Comparing Eqs. (10.12) and (10.13) we see that the spectator model gives a fair description of the semi-leptonic decays of  $D$  mesons.

We may repeat the same exercise for the semi-leptonic decays of  $B$  mesons. The theoretical decay width is,

$$\Gamma_{sl}^{(b)} = \Gamma_0(m_b) f\left(\frac{m_c}{m_b}\right) |V_{cb}|^2 \eta_0, \quad (10.14)$$

The CKM-disfavoured mode makes a negligible contribution to the total rate. Strong interaction corrections, which can be appreciable because  $\alpha_S(m_b^2)$  is large, are summarized by the factor  $\eta_0 \approx 0.87$  [5]. The experimental values can be obtained using the measured semi-leptonic branching ratios of the  $B^\pm$  and  $B^0$ , which are  $10.1 \pm 1.8 \pm 1.5\%$  and  $10.9 \pm 0.7 \pm 1.1\%$  respectively [6]. When combined with the lifetimes in Fig. 10.3, the semi-

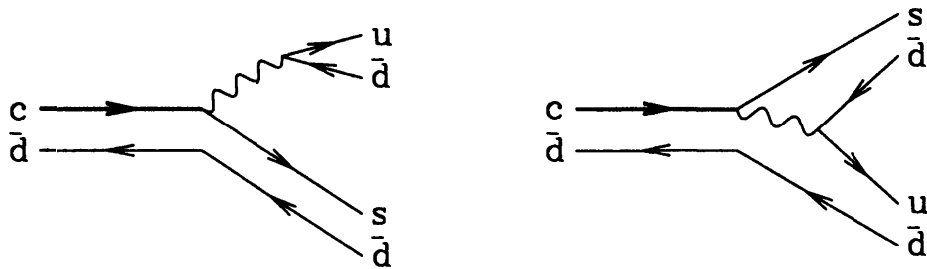


Fig. 10.4. Amplitudes contributing to  $D^+$  decay.

leptonic widths of the  $B$  mesons are found to be

$$\begin{aligned}\Gamma_{\text{sl}}(B^0) &= (0.48 \pm 0.12) \times 10^{-10} \text{ MeV} \\ \Gamma_{\text{sl}}(B^+) &= (0.43 \pm 0.18) \times 10^{-10} \text{ MeV.}\end{aligned}\quad (10.15)$$

Eq. (10.14) can be used to determine  $V_{cb}$ . For example, choosing the values  $m_b = 4.8 \text{ GeV}$ ,  $m_c = 1.4 \text{ GeV}$  and  $V_{cb} = 0.04$  one obtains

$$\Gamma_{\text{sl}} = 2.7 \times 10^{-8} |V_{cb}|^2 \text{ MeV} = 0.44 \times 10^{-10} \text{ MeV.} \quad (10.16)$$

For further details and references to the original papers see ref. [7].

### 10.1.2 Hadronic decays

The simplest estimate for the total width and hence the lifetime is obtained using the spectator model. Thus, for example, in the decay of a  $D^+$  meson, a non-spectator diagram would result from the annihilation of the charm quark with the anti-strange quark. This type of diagram is not considered in the spectator model. Diagrams involving spectators are suppressed by powers of the heavy quark mass, because of the small probability of overlap of the light and heavy quarks. The width in the spectator model is given simply by the weak decay of the heavy quark followed by the subsequent decay of the resulting virtual  $W$  boson.

Because of the three colours of quarks, the hadronic decay of the  $W$  to  $u\bar{d}$  is three times as likely as the decay to  $e\nu_e$  or  $\mu\nu_\mu$ , so that

$$BR(c \rightarrow eX) = \frac{1}{1 + 1 + 3}, \quad (10.17)$$

ignoring strong interaction effects. Therefore the prediction of the simplest spectator model for the total width of a charmed hadron is given by multiplying the semi-leptonic width (10.12) by five. This leads to an expected lifetime for charmed hadrons of the order of 1.2 ps. The spectator model also predicts that the lifetimes of all charmed hadrons should be the same. This prediction is not borne out by the data, as can be seen from Fig. 10.3. For example, the lifetimes of the  $D^+$  and the  $D^0$  mesons are very different.

Since the semi-leptonic widths (10.13) are approximately equal, we can conclude that the failure of the spectator model is due to differences in the hadronic widths of the charmed hadrons. Many reasons can be put forward for the departures from the simple spectator model, such as non-spectator diagrams and strong radiative corrections. Fig. 10.4 shows that in the case of CKM-favoured  $D^+$  decay there are two contributing diagrams which can interfere destructively and hence lead to a longer  $D^+$  lifetime. However, such interference effects should be suppressed by powers of  $m_c$ , because of the small overlap of the  $\bar{d}$  coming from the charm decay with the spectator  $\bar{d}$ . The former is initially localized in a volume of order  $1/m_c^3$ , whereas the latter is distributed throughout the  $D$  meson state. Since these interference effects appear to be important, we conclude that the charm quark is too light to be treated as a heavy quark in this context. Although there is a qualitative understanding of  $D$  meson decay, there is as yet no reliable quantitative description of all data on non-leptonic charm quark decays.

We obtain more encouraging results when we apply the spectator model to hadronic  $B$  hadron decays. *A priori*, one might expect the  $B$  lifetime to be a factor of  $(m_c/m_b)^5$  shorter than the estimate for the charm quark lifetime given above. However this mass effect is almost entirely cancelled by the factor of  $|V_{cb}|^2$  which occurs in the expression for the width. The calculation of the semi-leptonic branching ratio for  $B$  decays is complicated even in the spectator model, because of the many channels which are kinematically allowed for the decay. A detailed calculation [8] gives  $BR(b \rightarrow eX) > 12.5\%$ , which is compatible with the measured value.

As shown in Fig. 10.3, the ground-state hadrons containing  $b$  quarks have roughly equal lifetimes, in accordance with the spectator model<sup>2</sup>. Calculating the total width from the theoretical semi-leptonic width in Eq. (10.16) and the measured semi-leptonic branching ratio, we obtain a lifetime of about 1.6 ps. The measured average  $b$  lifetime [4], shown by the band in Fig. 10.3, is  $1.55 \pm 0.06$  ps, corresponding to a proper lifetime expressed in units of length of  $c\tau = 463 \pm 18$   $\mu\text{m}$ . A  $b$  quark with momentum 20 GeV has a relativistic  $\gamma$  factor of about 4. A  $B$  meson of this momentum decaying after one lifetime will travel about 1.9 mm, which is a decay distance large enough to be measured with a particle detector. Thus the fact that  $V_{cb}$  is so small (*cf.* Eq. (10.16)) allows the measurement of separated vertices in the decays of fast moving  $B$  hadrons.

---

<sup>2</sup> Note however that the  $\Lambda_b$  lifetime is shorter than expected in the spectator model.

## 10.2 Top quark decays

### 10.2.1 Conventional decays

At the Fermilab Tevatron operating at  $\sqrt{s} = 1.8$  TeV about 500  $t\bar{t}$  pairs will be produced per 100 pb $^{-1}$  of integrated luminosity. This estimate assumes that the total production cross section for a top quark of mass  $m_t = 175$  GeV is about 5 pb. A more refined estimate will be given later in this chapter.

In order to identify these top quarks we must know their decay modes. We shall start by considering the decays of a free top quark in the Standard Model. Since  $m_t > M_W + m_b$  a top quark decays predominantly into a  $b$  quark and an on-shell  $W$  boson

$$t \rightarrow W^+ + b \quad \begin{matrix} \\ \downarrow \\ l^+ + \nu \end{matrix} \quad (10.18)$$

$$t \rightarrow W^+ + b \quad \begin{matrix} \\ \downarrow \\ q + \bar{q} \end{matrix} \quad (10.19)$$

where the charged lepton,  $l$ , coming from the decay of the  $W$  can be an electron, a muon or a tau. If both top quarks decay to jets via the hadronic ( $q\bar{q}$ ) decays of the  $Ws$ , the top quark event will be hard to identify. It is therefore usual to look for the top in channels in which one or both of the  $W$  bosons decays leptonically. The interesting final states therefore contain either a single charged lepton and jets, or two charged leptons and jets. For the latter case the background is smallest when one of the charged leptons is a muon and the other is an electron. The presence of  $b$  quarks in the final state is of great help in identifying top quark events. A  $b$  quark is tagged either by the lepton coming from its semi-leptonic decay, or by the fact that its decay products point back to a vertex displaced from the primary interaction point.

In the simplest approximation the branching ratio to leptons is given by counting the decay modes of the  $W$ , (viz.  $e\bar{\nu}_e$ ,  $\mu\bar{\nu}_\mu$ ,  $\tau\bar{\nu}_\tau$  and three colours of  $u\bar{d}$  and  $c\bar{s}$ , cf. Table. (8.4))

$$BR(W^+ \rightarrow e^+ \bar{\nu}) = \frac{1}{3+3+3} \approx 11\%. \quad (10.20)$$

With a perfect detector the numbers of events expected at  $\sqrt{s} = 1.8$  TeV per 100 pb $^{-1}$  are

$$\begin{aligned} N(e\mu + \text{jets}) &= 2 \times .11 \times .11 \times 500 \approx 12 \\ N(e + \text{jets}) &= 2 \times .11 \times .66 \times 500 \approx 72. \end{aligned} \quad (10.21)$$

The existence of both of these decay modes with the correct ratio is a first test of the decay modes of the top.

The  $W$  boson coming from top decay can be either left-handed ( $L$ ) or longitudinally ( $0$ ) polarized. The invariant matrix elements squared for the two processes are

$$\begin{aligned}\overline{\sum}|\mathcal{M}_L|^2 &= \frac{2G_F m_t^4}{\sqrt{2}} |V_{tb}|^2 \left[ 2x^2(1-x^2+y^2) \right] \\ \overline{\sum}|\mathcal{M}_0|^2 &= \frac{2G_F m_t^4}{\sqrt{2}} |V_{tb}|^2 \left[ 1 - x^2 - y^2(2+x^2-y^2) \right],\end{aligned}\quad (10.22)$$

where  $x = M_W/m_t$ ,  $y = m_b/m_t$ . The result for the total width is therefore

$$\Gamma(t \rightarrow bW) = \frac{G_F m_t^3}{8\pi\sqrt{2}} |V_{tb}|^2 I(x, y), \quad (10.23)$$

where

$$I(x, y) = \left[ (1-x^2)(1+2x^2) - y^2(2-x^2-y^2) \right] \lambda^{\frac{1}{2}}(1, x, y) \quad (10.24)$$

and  $\lambda(a, b, c) = (a^2 - (b+c)^2)(a^2 - (b-c)^2)$ . Keeping a non-zero  $b$  mass in the calculation of the total width leads to a correction of about 0.3%. We shall therefore neglect the  $b$  mass throughout the following discussion. In the limit  $m_t \gg M_W$ , we can also neglect the  $W$  mass and the total  $t$  width is given simply by

$$\Gamma(t \rightarrow bW) = \frac{G_F m_t^3}{8\pi\sqrt{2}} |V_{tb}|^2 \approx 1.76 \text{ GeV} \left( \frac{m_t}{175 \text{ GeV}} \right)^3. \quad (10.25)$$

From Eq. (10.24) the corrections to this result are of order  $(M_W/m_t)^4$ . In the numerical evaluation we have set  $V_{tb} \approx 1$  as suggested by the unitarity relation (cf. Eq. (8.79))

$$|V_{tb}|^2 + |V_{cb}|^2 + |V_{ub}|^2 = 1. \quad (10.26)$$

This unitarity relation can be tested by measuring the branching fraction

$$B = \frac{\Gamma(t \rightarrow Wb)}{\Gamma(t \rightarrow Wq)}. \quad (10.27)$$

The ratio of the number of top events containing one and two tagged  $b$  jets is sensitive to this branching ratio. The first  $b$  jet signals the presence of a top event. If the tagging efficiency is known, the fraction of events which contain second  $b$  jet is a measure of the branching fraction in Eq. (10.27) and hence to  $V_{tb}$ .

The CKM-disfavoured process  $t \rightarrow s$  requires knowledge of  $V_{ts}$ , which can be estimated using another unitarity relation (cf. Eq. (8.80))

$$V_{us}^* V_{ub} + V_{cs}^* V_{cb} + V_{ts}^* V_{tb} = 0, \quad (10.28)$$

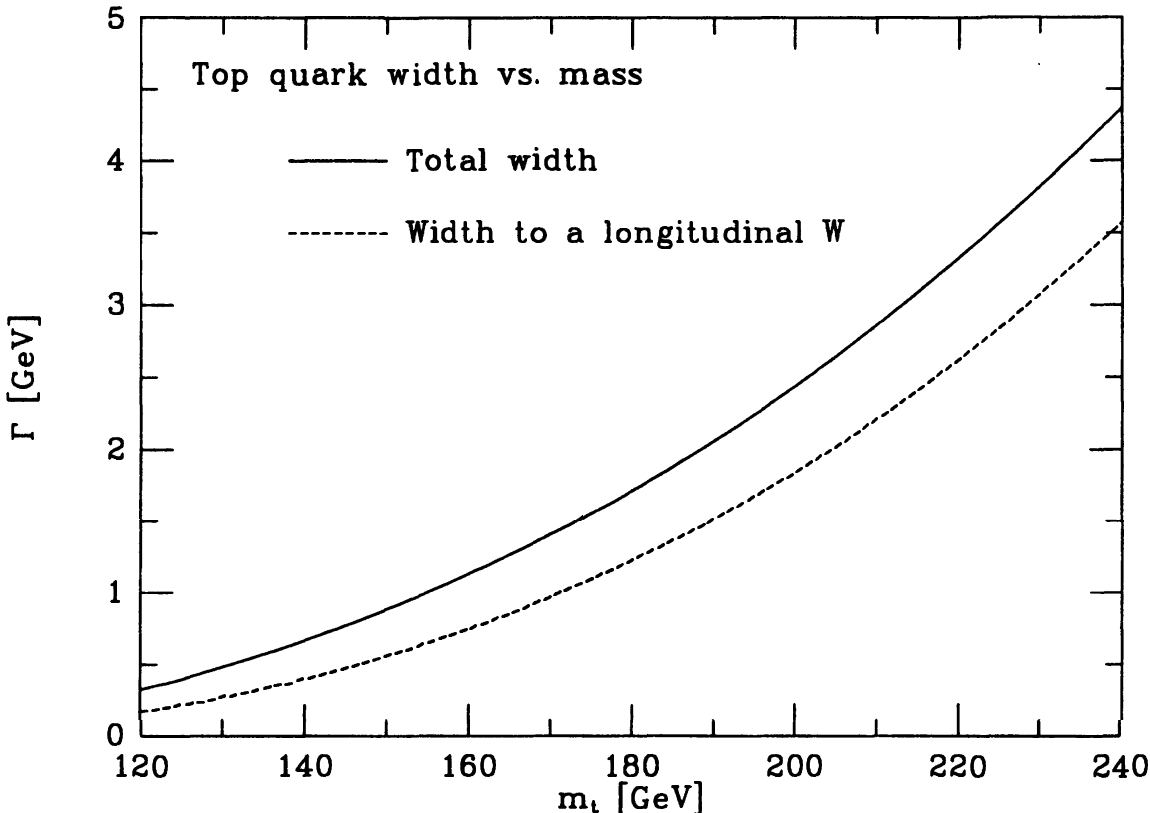


Fig. 10.5. Top quark total width and the width to a longitudinal  $W$ .

leading to  $|V_{ts}| \approx |V_{cb}|$ . The branching ratio into strange quarks is therefore expected to be  $\sim 0.2\%$ . The total width is almost identical with the width into  $b$  quarks.

Fig. 10.5 shows the width of the top quark as a function its mass. The top quark has a ‘semi-weak’ decay rate, *i.e.* a rate involving only one power of the Fermi constant. We therefore have a novel situation. Because of its large mass and semi-weak decay rate, the total decay width of the top quark is bigger than the typical hadronic scale. The lifetime of the top quark is only of order  $10^{-25}$  seconds and it therefore decays before it has time to hadronize. Strong interaction effects may alter the details of final states containing top quarks but hadrons containing the top quark are not formed.

Note that the contribution of longitudinal vector bosons to the total width is a significant fraction, as shown in Fig. 10.5. Information about the longitudinal components of the vector bosons is especially significant. These components are supplied by the symmetry breaking mechanism which gives the  $W$  bosons their mass as described in Chapter 8. In the standard model the branching fraction of the top quark to longitudinal

Ws can be calculated from Eq. (10.22). Neglecting  $m_b$  we obtain

$$\frac{\Gamma(t \rightarrow bW_0)}{\Gamma(t \rightarrow bW)} = \frac{m_t^2}{m_t^2 + 2M_W^2}. \quad (10.29)$$

It is important to check this prediction. The polarization state of the  $W$  controls the angular distribution of the leptons into which it decays. We may define the lepton helicity angle  $\theta_e^*$ , which is the angle of the charged lepton in the rest frame of the  $W$ , with respect to the original direction of travel of the  $W$  (*i.e.* anti-parallel to the recoiling  $b$  quark). If the  $b$  quark jet is identified, this angle can be defined experimentally as

$$\cos \theta_e^* \approx \frac{b \cdot (e^+ - \nu)}{b \cdot (e^+ + \nu)} \approx \frac{4b \cdot e^+}{m_t^2 - M_W^2} - 1, \quad (10.30)$$

in an obvious notation where  $t, b, e^+$  and  $\nu$  represent four-momenta.

The angular distribution can be obtained by writing down the full matrix element squared for both the decay of the top and the decay of the  $W$ . This can be obtained by analogy with Eq. (10.3) after re-instating the momentum dependence and width in the  $W$  boson propagator:

$$\overline{\sum} |\mathcal{M}^{(t)}|^2 = 64G_F^2 |V_{tb}|^2 t \cdot e^+ b \cdot \nu \frac{M_W^4}{(w^2 - M_W^2)^2 + M_W^2 \Gamma_W^2}. \quad (10.31)$$

The four-momentum of the  $W$  boson line is denoted by  $w = e^+ + \nu$ . The factor coming from the  $W$  propagator is largest when the value of the invariant mass  $w^2 = (e^+ + \nu)^2$  is equal to the mass of the  $W$ ; the distribution becomes narrower as the total width  $\Gamma_W$  becomes smaller. In the narrow width approximation, Eq. (9.28), we may replace the Breit-Wigner distribution by a delta function

$$\frac{1}{(w^2 - M_W^2)^2 + M_W^2 \Gamma_W^2} \approx \frac{\pi}{M_W \Gamma_W} \delta(w^2 - M_W^2). \quad (10.32)$$

The phase space volume element for decay into  $j$  particles,

$$d\Phi_j(P, p_1, \dots, p_j) = (2\pi)^4 \delta(P - \sum_{i=1,j} p_i) \prod_{i=1,j} \frac{d^3 p_i}{2E_i (2\pi)^3}, \quad (10.33)$$

can be expressed recursively as the product of two-body decays. For the specific case of a three-body final state, which is of interest here, we have

$$d\Phi_3(P, p_1, p_2, p_3) = \frac{1}{2\pi} \int dp_{23}^2 d\Phi_2(P, p_1, p_{23}) d\Phi_2(p_{23}, p_2, p_3), \quad (10.34)$$

where  $p_{23} = p_2 + p_3$ . Therefore the decay width is given by

$$\Gamma = \frac{1}{4\pi m_t} \int dw^2 d\Phi_2(t, b, w) d\Phi_2(w, e, \nu) \overline{\sum} |\mathcal{M}^{(t)}|^2. \quad (10.35)$$

In the narrow width approximation we find that Eq.(10.31) may be written using Eq. (10.30) as

$$\begin{aligned} \overline{\sum} |\mathcal{M}^{(t)}|^2 &= \left[ \overline{\sum} |\mathcal{M}_0|^2 \times |D_0|^2 + \overline{\sum} |\mathcal{M}_L|^2 \times |D_L|^2 \right] \\ &\times \frac{\pi}{M_W \Gamma_W} \delta(w^2 - M_W^2). \end{aligned} \quad (10.36)$$

Here  $M_0, M_L$  are given in Eq. (10.22) with  $y = 0$  and  $D_0, D_L$  are the helicity amplitudes for the decay of a longitudinal and left-handed  $W$  boson respectively:

$$\begin{aligned} |D_0|^2 &= \frac{G_F M_W^4}{\sqrt{2}} \frac{1}{2} \sin^2 \theta_e^* \\ |D_L|^2 &= \frac{G_F M_W^4}{\sqrt{2}} \frac{1}{4} (1 - \cos \theta_e^*)^2. \end{aligned} \quad (10.37)$$

We can perform the phase space integration in Eq. (10.35) using

$$d\Phi_2(P, p_1, p_2) = \frac{1}{8\pi} \frac{2|p_1|}{M_P} \frac{d\Omega}{4\pi}, \quad (10.38)$$

where  $p_1$  is the three-momentum of the decay products in the rest-frame of the decaying particle, which has mass  $M_P$ , and  $d\Omega$  is the element of solid angle. In the narrow width approximation for the  $W$ , the top width into  $b\bar{e}\nu$  is given by the product of the width into  $bW$  and the  $W$  branching ratio into  $e\nu$ :

$$\Gamma(t \rightarrow b\bar{e}\nu) = \Gamma(t \rightarrow bW) \frac{\Gamma(W \rightarrow e\nu)}{\Gamma_W}, \quad (10.39)$$

where (cf. Eq. (8.92))

$$\Gamma(W \rightarrow e\nu) = \frac{G_F M_W^3}{6\sqrt{2}\pi}. \quad (10.40)$$

The normalized angular distribution of the charged leptons is therefore given by,

$$\frac{1}{N} \frac{dN(W \rightarrow e\nu)}{d\cos \theta_e^*} = \frac{3}{4(m_t^2 + 2M_W^2)} \left[ m_t^2 \sin^2 \theta_e^* + M_W^2 (1 - \cos \theta_e^*)^2 \right], \quad (10.41)$$

as shown in Fig. 10.6. A sample of 1000 tagged top events will allow a measurement of the branching fraction into longitudinal  $Ws$  with a statistical precision of 3% [9].

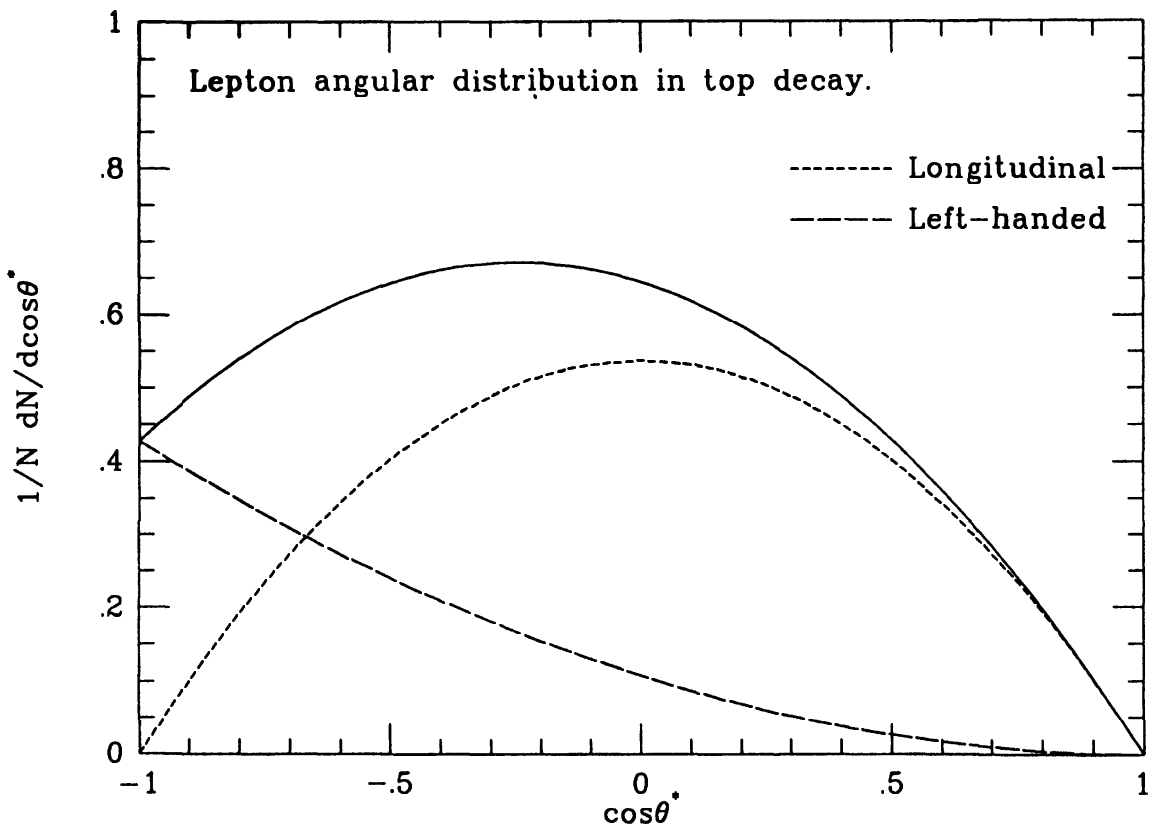


Fig. 10.6. Lepton angular distributions in top decay.

### 10.2.2 Unconventional decays

The experimental ratio

$$R = \frac{t\bar{t} \rightarrow e\mu + \text{jets}}{t\bar{t} \rightarrow \mu + \text{jets}} = \frac{\Gamma(t \rightarrow e + \text{jets})}{\Gamma(t \rightarrow \mu + \text{jets})} \quad (10.42)$$

gives information about the ratio of the semi-leptonic and non-leptonic widths of the top quark. In the Standard Model  $R$  is approximately one sixth. The exact value depends on the treatment of tau leptons (e.g. whether the leptonic decays of the  $\tau$  produce a lepton which is energetic enough to be classified in the lepton sample along with the  $e$  and the  $\mu$ ).

It is important to look for unconventional decays of the top quark, which, if they were large enough, would give rise to a different value for the ratio  $R$ , Eq. (10.42). As an example, we consider a simple extension of the Standard Model which involves the introduction of a second Higgs doublet. Top quark decay in this model has been investigated in refs. [10,11]. In order to avoid strangeness-changing neutral currents [12] one must couple all quarks of a given charge to only one Higgs doublet. After spontaneous symmetry breaking we are left with two charged Higgs bosons  $H^\pm$  and three neutral ones. The Lagrangian responsible for the

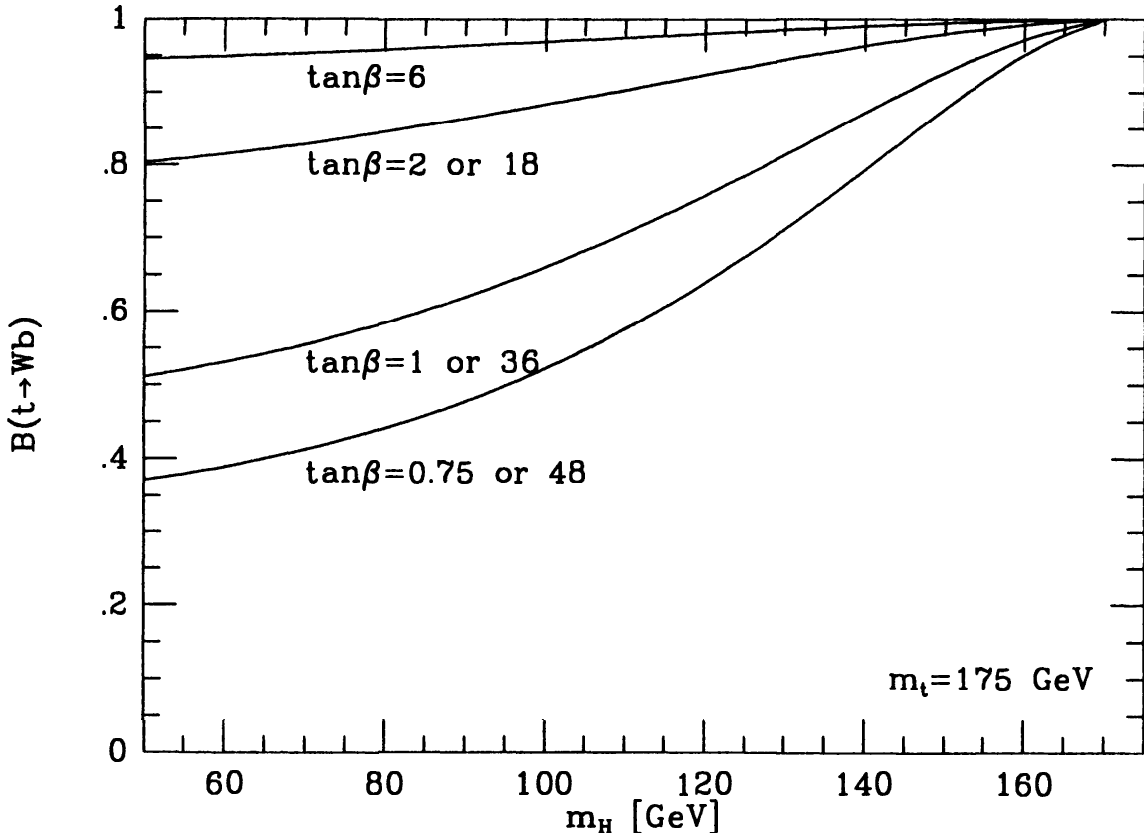


Fig. 10.7. Branching fraction to  $W$  with charged Higgs decay.

decay of the top quark contains an extra contribution given by

$$\mathcal{L} = \frac{g_W}{\sqrt{2}M_W} V_{tb} H^+ \left[ m_t \cot \beta \bar{t}_R b_L + m_b \tan \beta \bar{t}_L b_R \right], \quad (10.43)$$

where  $q_{R/L} = \frac{1}{2}(1 \pm \gamma_5)q$  and  $\tan \beta$  is the ratio of the vacuum expectation values of the two Higgs fields. If  $M_H < m_t - m_b$ , the top quark can decay to the charged Higgs boson with partial width

$$\Gamma(t \rightarrow bH^+) = \frac{G_F m_t^3}{8\pi\sqrt{2}} |V_{tb}|^2 J\left(\frac{M_H}{m_t} \frac{m_b}{m_t}, \tan \beta\right), \quad (10.44)$$

where

$$J(x, y, t) = \left[ \left( \frac{1}{t^2} + y^2 t^2 \right) (1 + y^2 - x^2) + 4y^2 \right] \lambda^{\frac{1}{2}}(1, x, y). \quad (10.45)$$

The width has a minimum for  $\tan \beta = \sqrt{m_t/m_b} \sim 6$ . The branching fraction  $t \rightarrow Wb$  is reduced from unity by the availability of the decay to the charged Higgs boson:

$$B(t \rightarrow Wb) = \frac{\Gamma(t \rightarrow Wb)}{\Gamma(t \rightarrow Wb) + \Gamma(t \rightarrow Hb)}. \quad (10.46)$$

Fig. 10.7 shows the branching fraction into  $W$  bosons (10.46) as a func-

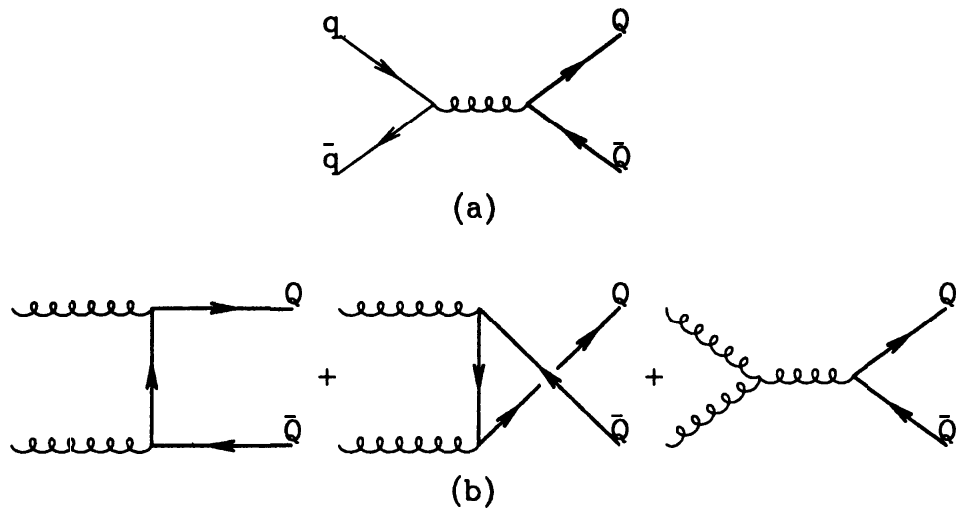


Fig. 10.8. Lowest-order Feynman diagrams for heavy quark production.

tion of the charged Higgs boson mass, for various choices of the unknown angle  $\beta$ .

The decay modes of the  $H^+$  determine the signature for its detection: it should decay predominantly to  $c\bar{s}$  and  $\tau\nu_\tau$ , with a predominance of the former at small  $\tan\beta$ . If the vacuum expectation values of the two Higgs fields are taken to be equal ( $\tan\beta = 1$ ), the branching fraction into  $c\bar{s}$  is 64% and into  $\tau\nu_\tau$  is 31%.

## 10.3 Heavy quark production

### 10.3.1 Leading order

We now turn to the mechanisms by which hadrons containing heavy quarks are produced in hadronic reactions. The leading-order processes for the production of a heavy quark  $Q$  of mass  $m$  in hadron-hadron collisions are

$$(a) \quad q(p_1) + \bar{q}(p_2) \rightarrow Q(p_3) + \bar{Q}(p_4) \\ (b) \quad g(p_1) + g(p_2) \rightarrow Q(p_3) + \bar{Q}(p_4), \quad (10.47)$$

where the four-momenta of the partons are given in brackets. The Feynman diagrams which contribute to the matrix elements in  $O(g^2)$  are shown in Fig. 10.8<sup>3</sup>. The corresponding invariant matrix elements squared [13,14] which result from the diagrams in Fig. 10.8 are given in Table 10.2. The matrix elements squared have been averaged (summed) over initial (final) colours and spins, as indicated by  $\sum$ . We have introduced the following

<sup>3</sup> We remind the reader that  $g^2 = 4\pi\alpha_s$ .

Process	$\overline{\sum} \mathcal{M} ^2/g^4$
$q \bar{q} \rightarrow Q \bar{Q}$	$\frac{4}{9}(\tau_1^2 + \tau_2^2 + \frac{\rho}{2})$
$g g \rightarrow Q \bar{Q}$	$(\frac{1}{6\tau_1\tau_2} - \frac{3}{8})(\tau_1^2 + \tau_2^2 + \rho - \frac{\rho^2}{4\tau_1\tau_2})$

Table 10.2. Lowest-order processes for heavy quark production.  $\overline{\sum}|\mathcal{M}|^2$  is the invariant matrix element squared. The colour and spin indices are averaged (summed) over initial (final) states.

notation for the ratios of scalar products:

$$\tau_1 = \frac{2p_1 \cdot p_3}{\hat{s}}, \quad \tau_2 = \frac{2p_2 \cdot p_3}{\hat{s}}, \quad \rho = \frac{4m^2}{\hat{s}}, \quad \hat{s} = (p_1 + p_2)^2. \quad (10.48)$$

In leading order, the short-distance cross section is obtained from the invariant matrix element in the usual way:

$$d\hat{\sigma}_{ij} = \frac{1}{2\hat{s}} \frac{d^3 p_3}{(2\pi)^3 2E_3} \frac{d^3 p_4}{(2\pi)^3 2E_4} (2\pi)^4 \delta^4(p_1 + p_2 - p_3 - p_4) \overline{\sum} |\mathcal{M}_{ij}|^2. \quad (10.49)$$

The first factor is the flux factor for massless incoming particles. The other terms come from the phase space for  $2 \rightarrow 2$  scattering.

Consider first the hadronic differential cross section. In terms of the rapidity,  $y$ , (Eq. (7.16)) and transverse momentum,  $p_T$ , the relativistically invariant phase space volume element of the final-state heavy quarks is

$$\frac{d^3 p}{E} = dy \, d^2 p_T. \quad (10.50)$$

Using Eqs. (7.1) and (10.49) the result for the invariant cross section may be written as

$$\frac{d\sigma}{dy_3 dy_4 d^2 p_T} = \frac{1}{16\pi^2 \hat{s}^2} \sum_{ij} x_1 f_i(x_1, \mu^2) x_2 f_j(x_2, \mu^2) \overline{\sum} |\mathcal{M}_{ij}|^2. \quad (10.51)$$

The energy-momentum delta function in Eq. (10.49) fixes the values of  $x_1$  and  $x_2$  if we know the transverse momenta and rapidity of the outgoing heavy quarks. In the centre-of-mass system of the incoming hadrons we may write the components of the parton four-momenta as

$$\begin{aligned} p_1 &= \frac{1}{2}\sqrt{s}(x_1, 0, 0, x_1) \\ p_2 &= \frac{1}{2}\sqrt{s}(x_2, 0, 0, -x_2) \\ p_3 &= (m_T \cosh y_3, p_T, 0, m_T \sinh y_3) \end{aligned}$$

$$p_4 = (m_T \cosh y_4, -p_T, 0, m_T \sinh y_4). \quad (10.52)$$

Applying energy and momentum conservation, we obtain

$$x_1 = \frac{m_T}{\sqrt{s}}(e^{y_3} + e^{y_4}), \quad x_2 = \frac{m_T}{\sqrt{s}}(e^{-y_3} + e^{-y_4}), \quad \hat{s} = 2m_T^2(1 + \cosh \Delta y). \quad (10.53)$$

The quantity  $m_T = \sqrt{(m^2 + p_T^2)}$  is the transverse mass of the heavy quarks and  $\Delta y = y_3 - y_4$  is the rapidity difference between them.

Using Eqs.(10.51) and (10.53), we may write the cross section for the production of a heavy quark-antiquark pair, calculated in lowest-order perturbation theory, as

$$\begin{aligned} \frac{d\sigma}{dy_3 dy_4 d^2 p_T} &= \frac{1}{64\pi^2 m_T^4 (1 + \cosh(\Delta y))^2} \\ &\times \sum_{ij} x_1 f_i(x_1, \mu^2) x_2 f_j(x_2, \mu^2) \overline{\sum} |\mathcal{M}_{ij}|^2. \end{aligned} \quad (10.54)$$

Expressed in terms of  $m, m_T$  and  $\Delta y$ , the matrix elements for the two processes in Table 10.2 are

$$\overline{\sum} |\mathcal{M}_{q\bar{q}}|^2 = \frac{4g^4}{9} \left( \frac{1}{1 + \cosh(\Delta y)} \right) \left( \cosh(\Delta y) + \frac{m^2}{m_T^2} \right), \quad (10.55)$$

$$\overline{\sum} |\mathcal{M}_{gg}|^2 = \frac{g^4}{24} \left( \frac{8 \cosh(\Delta y) - 1}{1 + \cosh(\Delta y)} \right) \left( \cosh(\Delta y) + 2 \frac{m^2}{m_T^2} - 2 \frac{m^4}{m_T^4} \right). \quad (10.56)$$

Note the form of the matrix elements squared as the rapidity separation  $\Delta y$  between the two heavy quarks becomes large

$$\overline{\sum} |\mathcal{M}_{q\bar{q}}|^2 \sim \text{constant}, \quad \overline{\sum} |\mathcal{M}_{gg}|^2 \sim \exp \Delta y. \quad (10.57)$$

The cross section in Eq. (10.54) is therefore damped at large  $\Delta y$  and the dominant contribution to the total cross section comes from the region  $\Delta y \leq 1$ . From Eq. (10.57) we see that heavy quarks produced by light quark annihilation are more closely correlated in rapidity than those produced by gluon-gluon fusion.

We shall now illustrate why it is plausible that heavy quark production should be described by perturbation theory [15]. We consider the propagators in the diagrams shown in Fig. 10.8. In terms of the above variables they can be written as

$$\begin{aligned} (p_1 + p_2)^2 &= 2p_1 \cdot p_2 = 2m_T^2(1 + \cosh \Delta y), \\ (p_1 - p_3)^2 - m^2 &= -2p_1 \cdot p_3 = -m_T^2(1 + e^{-\Delta y}), \\ (p_2 - p_3)^2 - m^2 &= -2p_2 \cdot p_3 = -m_T^2(1 + e^{\Delta y}). \end{aligned} \quad (10.58)$$

Note that the propagators are all off-shell by a quantity of least of order  $m^2$ . It is this fact which distinguishes the production of a light quark

from the production of a heavy quark. When a light quark is produced by these diagrams the lower cut-off on the virtuality of the propagators is provided by the light quark mass, which is less than the QCD scale  $\Lambda$ . Since propagators with small virtualities give the dominant contribution, the production of a light quark will not be calculable in perturbative QCD. In the production of a heavy quark, the lower cut-off is provided by the mass  $m$ . Heavy quark production is therefore controlled by  $\alpha_s$  evaluated at the heavy quark scale.

Note also that the contribution to the cross section from values of  $p_T$  which are much greater than the quark mass is also suppressed. The differential cross section falls like  $1/m_T^4$  and as  $m_T$  increases, the incoming parton flux decreases because of the increase of  $x_1$  and  $x_2$  according to Eq. (10.53). Since all dependence on the transverse momentum appears in the transverse mass combination, the dominant contribution to the cross section comes from transverse momenta of the order of the mass of the heavy quark.

Thus for a sufficiently heavy quark we expect the methods of perturbation theory to be applicable. It is the mass  $m$  which provides the large scale in the production. The heavy quarks have transverse momenta of the order of  $m$  and are produced close in rapidity. The production is predominantly central, because of the rapidly falling parton fluxes. Final-state interactions which transform the heavy quarks into the observed hadrons will not change the size of the cross section. A possible mechanism which might spoil this simple picture would be the interaction of the produced heavy quark with the debris of the incoming hadrons. However these interactions with spectator partons are suppressed by powers of  $m$  [16]. For large enough  $m$  they can therefore be ignored.

The theoretical arguments summarized above do not address the issue of whether the charmed quark is sufficiently heavy that the hadroproduction of charmed hadrons in all regions of phase space is well described by only processes (a) and (b) and their perturbative corrections. The applicability of these calculations to charm production will be discussed in Section 10.4.

### 10.3.2 Higher-order corrections

The lowest-order terms presented above are the beginning of a systematic expansion in the running coupling. For simplicity we will only discuss the radiative corrections to the total cross section. Higher-order corrections to differential cross sections have been discussed in refs. [17,18]. The

hadronic cross section is determined as usual by

$$\sigma(P_1, P_2) = \sum_{i,j} \int dx_1 dx_2 f_i(x_1, \mu^2) f_j(x_2, \mu^2) \hat{\sigma}_{ij}(s, m^2 \mu^2) \quad (10.59)$$

where

$$\hat{\sigma}_{ij}(s, m^2, \mu^2) = \frac{\alpha_s^2(\mu^2)}{m^2} \mathcal{F}_{ij}\left(\rho, \frac{\mu^2}{m^2}\right). \quad (10.60)$$

Eq. (10.60) completely describes the short-distance cross section for the production of a heavy quark of mass  $m$  in terms of the functions  $\mathcal{F}_{ij}$ , where the indices  $i$  and  $j$  specify the types of the incoming partons. The variable  $\mu$  is the renormalization and factorization scale. Its role is described later in this section. The dimensionless functions  $\mathcal{F}_{ij}$  have the following perturbative expansion:

$$\mathcal{F}_{ij}\left(\rho, \frac{\mu^2}{m^2}\right) = \mathcal{F}_{ij}^{(0)}(\rho) + 4\pi\alpha_s(\mu^2) \left[ \mathcal{F}_{ij}^{(1)}(\rho) + \overline{\mathcal{F}}_{ij}^{(1)}(\rho) \ln\left(\frac{\mu^2}{m^2}\right) \right] + \mathcal{O}(\alpha_s^2) \quad (10.61)$$

where  $\rho$  is defined in Eq. (10.48).

The lowest-order functions  $\mathcal{F}_{ij}^{(0)}$  defined in Eq. (10.61) are obtained by integrating Eq. (10.49) using the results of Table 10.2. The results are

$$\begin{aligned} \mathcal{F}_{q\bar{q}}^{(0)}(\rho) &= \frac{\pi\beta\rho}{27} \left[ (2 + \rho) \right], \\ \mathcal{F}_{gg}^{(0)}(\rho) &= \frac{\pi\beta\rho}{192} \left[ \frac{1}{\beta} [\rho^2 + 16\rho + 16] \ln\left(\frac{1+\beta}{1-\beta}\right) - 28 - 31\rho \right], \\ \mathcal{F}_{gq}^{(0)}(\rho) &= \mathcal{F}_{g\bar{q}}^{(0)}(\rho) = 0, \end{aligned} \quad (10.62)$$

and  $\beta = \sqrt{1 - \rho}$ . The functions  $\mathcal{F}_{ij}^{(0)}$  vanish both at threshold ( $\beta \rightarrow 0$ ) and at high energy ( $\rho \rightarrow 0$ ). Note that the quark-gluon process is zero in lowest order, but is present in higher orders.

The functions  $\mathcal{F}_{ij}^{(1)}$  are known [19,20]. Examples of the types of diagrams which contribute are shown in Fig. 10.9. The full calculation involves both real and virtual corrections. For full details we refer the reader to ref. [19]. In order to calculate the  $\mathcal{F}_{ij}$  in perturbation theory we must perform both renormalization and factorization of mass singularities. The subtractions required for renormalization and factorization are done at mass scale  $\mu$ . The dependence on  $\mu$  of the next-to-leading-order term is displayed explicitly in Eq. (10.61).

As discussed in Section 7.1,  $\mu$  is an unphysical parameter. The physical predictions should be invariant under changes of  $\mu$  at the appropriate order in perturbation theory. If we have performed a calculation to  $\mathcal{O}(\alpha_s^3)$ ,

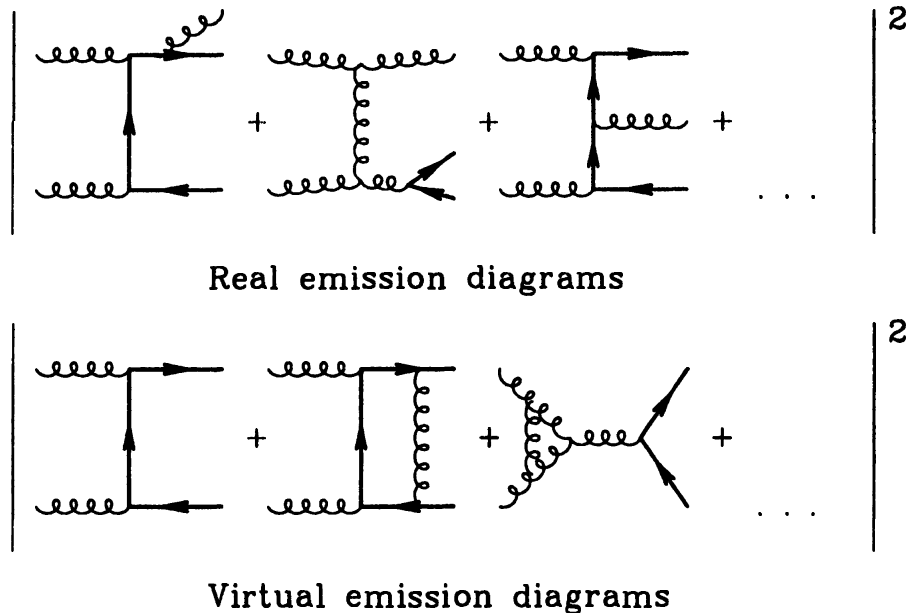


Fig. 10.9. Examples of higher-order corrections to heavy quark production.

varyations of the scale  $\mu$  will lead to corrections of  $O(\alpha_s^4)$ ,

$$\mu^2 \frac{d}{d\mu^2} \sigma = O(\alpha_s^4). \quad (10.63)$$

In this equation  $\sigma$  is the hadronic cross section as determined by Eq. (10.59). Using Eq. (10.63) we find that the term  $\bar{\mathcal{F}}^{(1)}$ , which controls the  $\mu$  dependence of the higher-order perturbative contributions, is fixed in terms of the lower-order result  $\mathcal{F}^{(0)}$ :

$$\begin{aligned} \bar{\mathcal{F}}_{ij}^{(1)}(\rho) &= \frac{1}{8\pi^2} \left[ 4\pi b \mathcal{F}_{ij}^{(0)}(\rho) - \int_\rho^1 dz_1 \sum_k \mathcal{F}_{kj}^{(0)}\left(\frac{\rho}{z_1}\right) P_{ki}^{(0)}(z_1) \right. \\ &\quad \left. - \int_\rho^1 dz_2 \sum_k \mathcal{F}_{ik}^{(0)}\left(\frac{\rho}{z_2}\right) P_{kj}^{(0)}(z_2) \right]. \end{aligned} \quad (10.64)$$

In obtaining this result we have used the renormalization group equation for the running coupling, Eq. (2.7)

$$\mu^2 \frac{d}{d\mu^2} \alpha_s(\mu^2) = -b \alpha_s^2 + \dots \quad (10.65)$$

and the lowest-order form of the GLAP equation, Eq. (4.90)

$$\mu^2 \frac{d}{d\mu^2} f_i(x, \mu^2) = \frac{\alpha_s(\mu^2)}{2\pi} \sum_k \int_x^1 \frac{dz}{z} P_{ik}^{(0)}(z) f_k\left(\frac{x}{z}, \mu^2\right) + \dots \quad (10.66)$$

This illustrates an important point which is a general feature of renormalization group improved perturbation series in QCD. The coefficient of the perturbative correction depends on the choice made for the scale

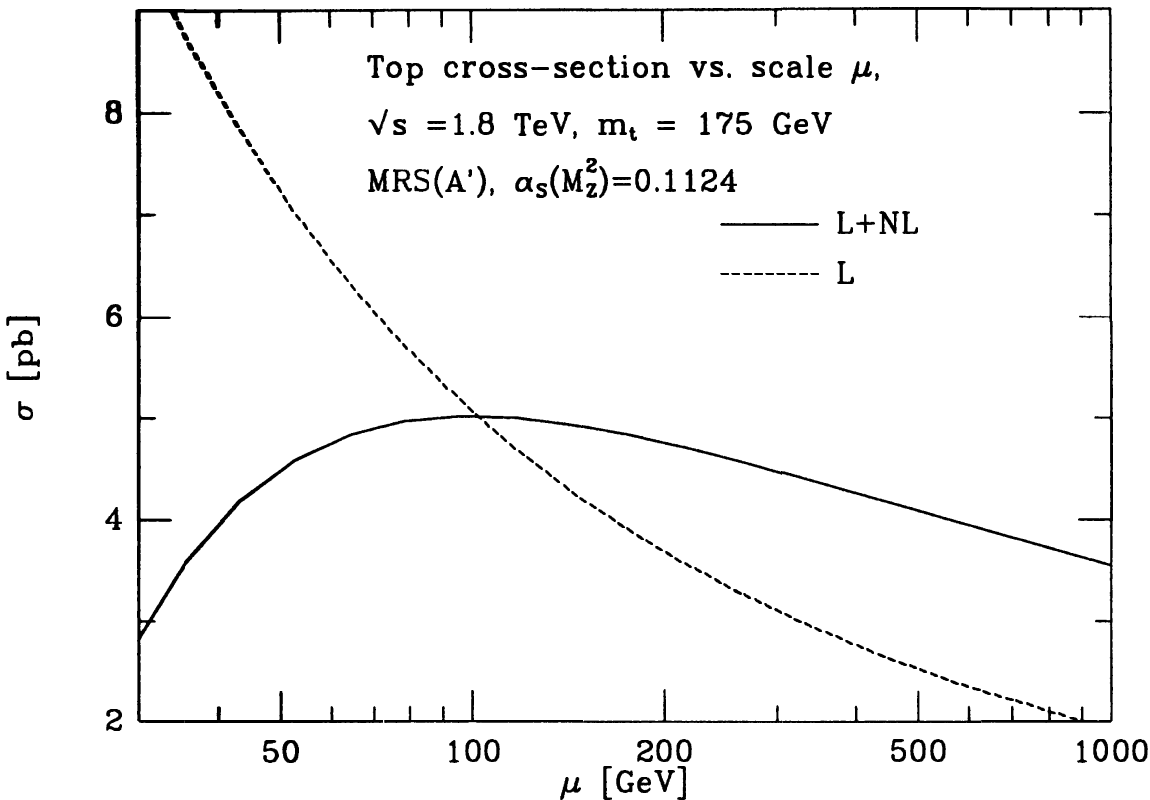


Fig. 10.10. Scale dependence of the top quark cross section in leading and next-to-leading order of perturbation theory.

$\mu$ , but the scale dependence changes the result in such a way that the physical result is independent of that choice. Thus the scale dependence is formally small because it is of higher order in  $\alpha_s$ . This does not assure us that the scale dependence is actually *numerically* small for all series. A pronounced dependence on the scale  $\mu$  is a signal of an untrustworthy perturbation series.

We elaborate on this point by showing the scale dependence found in two cases of current interest. First, in Fig. 10.10, we show the scale dependence found for the hadroproduction of a 175 GeV top quark in leading and next-to-leading order at  $\sqrt{s} = 1.8$  TeV in  $p\bar{p}$  collisions. The inclusion of the higher-order terms leads to a stabilization of the theoretical prediction with respect to changes in scale. The situation for the bottom quark is quite different. In Fig. 10.11 the scale dependence of the bottom quark cross section is shown. The cross section is approximately doubled by the inclusion of the higher-order corrections, which evidently do nothing to improve the stability of the prediction under changes of scale. It is apparent that the predictions for bottom production at collider energies are subject to considerable uncertainty.

We now turn to the question of flavour excitation. In the flavour excitation model the heavy quark is considered to be already present in

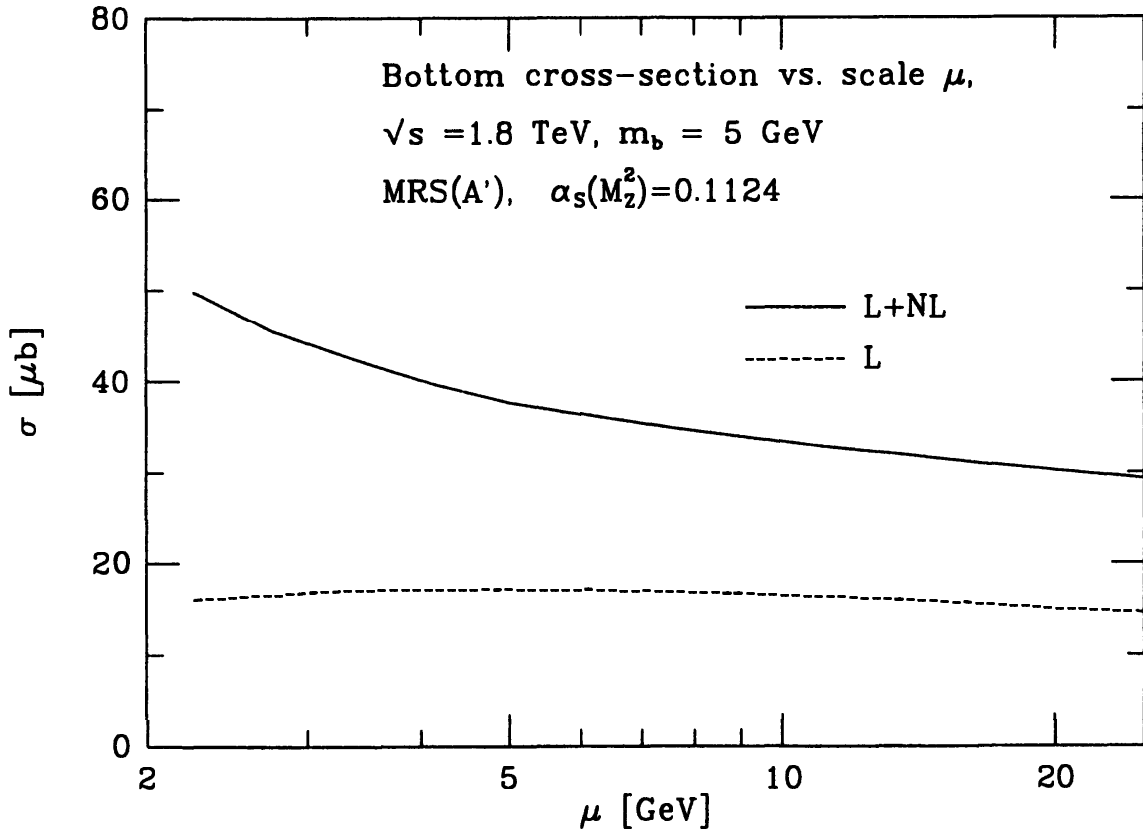


Fig. 10.11. Scale dependence of the bottom quark cross section in leading and next-to-leading order of perturbation theory.

the incoming hadron. It is excited by the exchange of a gluon with the other hadron and appears on mass-shell in the final state. An example of a flavour excitation diagram is shown in Fig. 10.12(a). Note that in calculating the flavour excitation contribution the incoming heavy quark is treated as if it were on its mass-shell. If we denote the momentum transfer between the two incoming partons as  $q$ , the parton cross section will contain a factor  $1/q^4$  coming from the square of the propagator of the exchanged gluon. Therefore this graph appears to be sensitive to momentum scales all the way down to the hadronic scale, (*i.e.* sensitive to low  $q$ ). This casts doubt on the applicability of perturbative QCD to these processes.

We now sketch an analysis [15] which leads an important conclusion: when considering the total cross section, flavour excitation contributions should not be included. The net contribution of these diagrams is already included as a higher-order correction to the gluon-gluon fusion process. The analysis begins from the observation that the flavour excitation graph is already present as a subgraph of the first two diagrams shown in Fig. 10.12(b). Does the flavour excitation approximation accurately represent the contributions of these diagrams? In particular is the  $1/q^4$  pole,

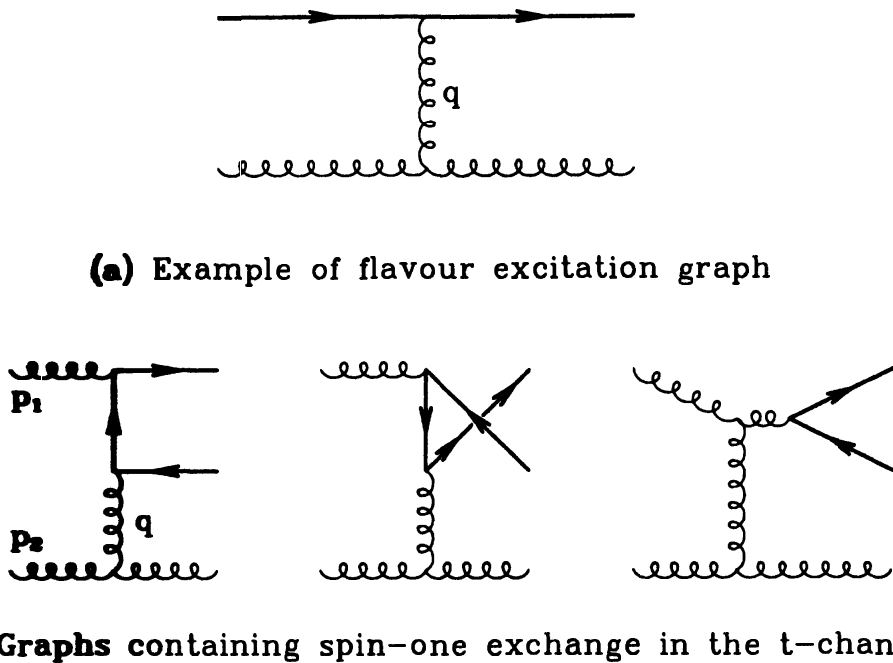


Fig. 10.12. Graphs relevant for discussion of flavour excitation.

which is the **signature** of the presence of the flavour excitation, present in these diagrams?

We shall now indicate why the  $1/q^4$  behaviour is *not* present in the sum of all three diagrams displayed in Fig. 10.12(b). In addition we shall demonstrate that the coefficient of the remaining  $1/q^2$  term has the simple structure expected from QCD factorization. The remaining sensitivity to low  $q^2$  can be factored out and absorbed in the parton distribution functions. Let us define the ‘plus’ and ‘minus’ components (also called ‘light-cone’ coordinates) of any vector  $q$  as follows:

$$q^+ = q^0 + q^z, \quad q^- = q^0 - q^z, \quad q^2 = q^+ q^- - q_T \cdot q_T. \quad (10.67)$$

We choose the upper incoming gluon in Fig. 10.12(b) to be directed along the ‘plus’ direction,  $p_1 = p_1^+$ , and the lower incoming gluon to be directed along the ‘minus’ direction,  $p_2 = p_2^-$ . We are interested in the production of heavy quarks in the ‘fragmentation region’ of the incoming upper gluon, far above the threshold  $s \gg 4m^2$ . In this region the rapidities of the produced heavy quarks are large and the  $q^2$  of the exchanged gluon can be small,  $|q^2| \ll m^2$ . If the virtuality of the exchanged gluon is large,  $|q^2| \geq m^2$ , all the propagators of the diagrams in Fig. 10.12(b) are hard and the diagrams give rise to finite higher-order corrections. We therefore consider only the region  $|q^2| \ll m^2$ .

In the small- $q^2$  region the ‘plus’ component of  $q$  is small, because the

lower final-state gluon is on-shell,

$$(p_2 - q)^2 = 0, \quad q^+ = \frac{q^2}{2p_2^-}, \quad (10.68)$$

since in the centre-of-mass system  $p_1^+ = p_2^- = \sqrt{s}$ . The ‘minus’ component of  $q$  is determined from the condition that the invariant mass of the  $Q\bar{Q}$  system must be close to threshold otherwise the heavy quark propagators will become large and suppress the cross section,

$$(p_1 + q)^2 \approx 4m^2, \quad q^- \approx \frac{m^2}{p_1^+}. \quad (10.69)$$

The variable  $q^-$  is therefore also small since  $p_1^+ = \sqrt{s}$ . We therefore find that in the fragmentation region of the upper incoming hadron,

$$q^2 = q^+q^- - q_T \cdot q_T \approx -q_T^2. \quad (10.70)$$

The current  $J$  to which the exchanged gluon of momentum  $q$  couples is determined by the upper parts of the three diagrams in Fig. 10.12(b). In the fragmentation region the ‘plus’ component of the current  $J$  is projected out by the lower part of the diagram which, in the soft approximation, gives a factor of  $p_2^-$ . Because of the current conservation relation,

$$q^\mu J_\mu = q^+ J^- + q^- J^+ - q_T \cdot J_T = 0, \quad (10.71)$$

which is a property of the sum of all three diagrams, we may write

$$J^+ \approx \frac{q_T \cdot J_T}{q^-}, \quad (10.72)$$

since  $q^+ \ll q^-$  and  $J^- \ll J^+$ . Ignoring overall factors, our result for the invariant matrix element squared is given by

$$|\mathcal{M}|^2 \sim \frac{1}{x^2} \frac{|q_T \cdot J_T|^2}{q_T^4}, \quad (10.73)$$

where  $x = q^-/p_2^-$ . Eq. (10.73) explicitly shows that the  $1/q_T^4$  behaviour is cancelled. In addition, after averaging over azimuthal directions in the transverse plane and including a flux factor  $1/(2s)$  the contribution of these diagrams to the cross section may be written as

$$\sigma \sim \frac{\alpha_s C_A}{\pi} \int \frac{dq_T^2}{q_T^2} \int \frac{dx}{x} \frac{1}{2x s} \sum |\varepsilon_T \cdot J_T|^2. \quad (10.74)$$

The coefficient of the  $1/q_T^2$  term takes the form of a low- $x$  splitting function  $\sim 1/x$ , times a cross section for the scattering of gluons with transverse polarization  $\varepsilon_T$  and longitudinal momentum fraction  $x$ . It can therefore be factorized in the standard way. For further details we refer the reader

to ref. [15]. The calculation of ref. [19] provides an explicit verification of this cancellation in the total cross section.

## 10.4 Charm and bottom quark production

In this section we will compare the next-to-leading theory outlined above to experimental data on bottom and charm production. For the purposes of this comparison it is important to assess the theoretical errors on the cross section prediction, which can be as large as the experimental errors. The value of the heavy quark mass  $m$  is the principal parameter controlling the size of the cross section. The  $m$  dependence is much more marked than the  $1/m^2$  dependence in the short-distance cross section expected from Eq. (10.60). As the mass decreases, the values of  $x$  at which the parton distributions are evaluated become smaller (*cf.* Eq. (10.53)) and the cross section rises because of the growth of the parton flux.

The approach which we shall take to the estimate of theoretical errors in heavy quark cross sections is taken from refs. [21,22]. We shall take the charm and bottom masses to lie in the ranges

$$\begin{aligned} 1.2 &< m_c < 1.8 \text{ GeV} \\ 4.5 &< m_b < 5.0 \text{ GeV}. \end{aligned} \quad (10.75)$$

A second important parameter is the value of the strong coupling. The value of  $\alpha_s$  is fixed by the fitting procedure which determines the parton distributions and is correlated with the form of the gluon distribution. However, to be conservative, it is customary to consider a slightly larger range of  $\Lambda$  than fixed by the parton distribution fits. An overall view of the uncertainty in  $\alpha_s$  is given in Chapter 12. In this chapter we just present the range of five flavour  $\Lambda$  used in the plots without comment. For fixed-target charm and bottom hadroproduction by pions the range is

$$60 \text{ MeV} < \Lambda_{\overline{\text{MS}}}(5) < 204 \text{ MeV}, \quad (10.76)$$

with corresponding variations of the nucleon structure functions [23]. The pion distributions functions are from ref. [24]. We shall arbitrarily choose to vary the scale parameter  $\mu$  in the range  $m/2 < \mu < 2m$  to test the sensitivity to  $\mu$ . We shall consider the extremum of all these variations to give an estimate of the theoretical error.

We immediately encounter a difficulty with this procedure in the case of charm. Variations of  $\mu$  down to  $m/2$  will carry us into the region  $\mu < 1 \text{ GeV}$  in which we certainly do not trust perturbation theory. A estimate of the theoretical error on charm production cross sections in this way is

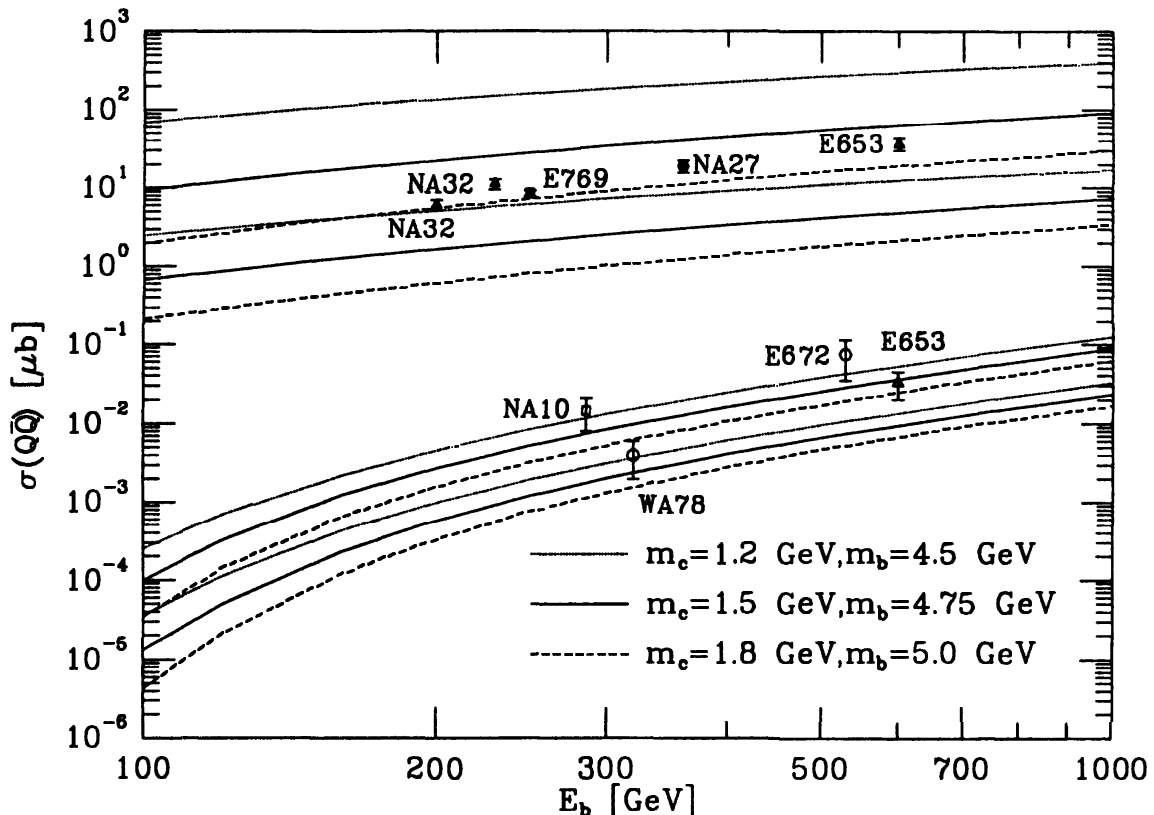


Fig. 10.13. Data on pion hadroproduction of  $c\bar{c}$  and  $b\bar{b}$  vs. beam energy compared with theory. Adapted from ref. [22].

therefore not possible. In calculating the curves for charm production the lower limit on the factorization scale is taken to be  $\mu_F = 2m_c$ .

The dependence on the value chosen for the heavy quark mass is particularly acute for the case of charm production. In fact, variations due to plausible changes in the quark mass, Eq. (10.75), are bigger than the uncertainties due to variations in the other parameters. We shall therefore take the aim of studies of the hadroproduction and photoproduction of charm to be the search for an answer to the following question: Is there a reasonable value for the charm quark mass which can accommodate the majority of the data?

In Fig. 10.13, adapted from ref. [22], we show the theoretical prediction for charm and bottom production using pion beams. Note the scale of the figure and the large spread in the theoretical predictions. Also plotted is a compilation of data. For the references to the original data we refer the reader to ref. [22]. We see that a value of  $m_c = 1.5$  GeV gives a fair description of the data on the hadroproduction of charm. After inclusion of the  $O(\alpha_s^3)$  corrections, the data can be explained without recourse to very small values of the charmed quark mass.

This conclusion is further reinforced by consideration of the data on

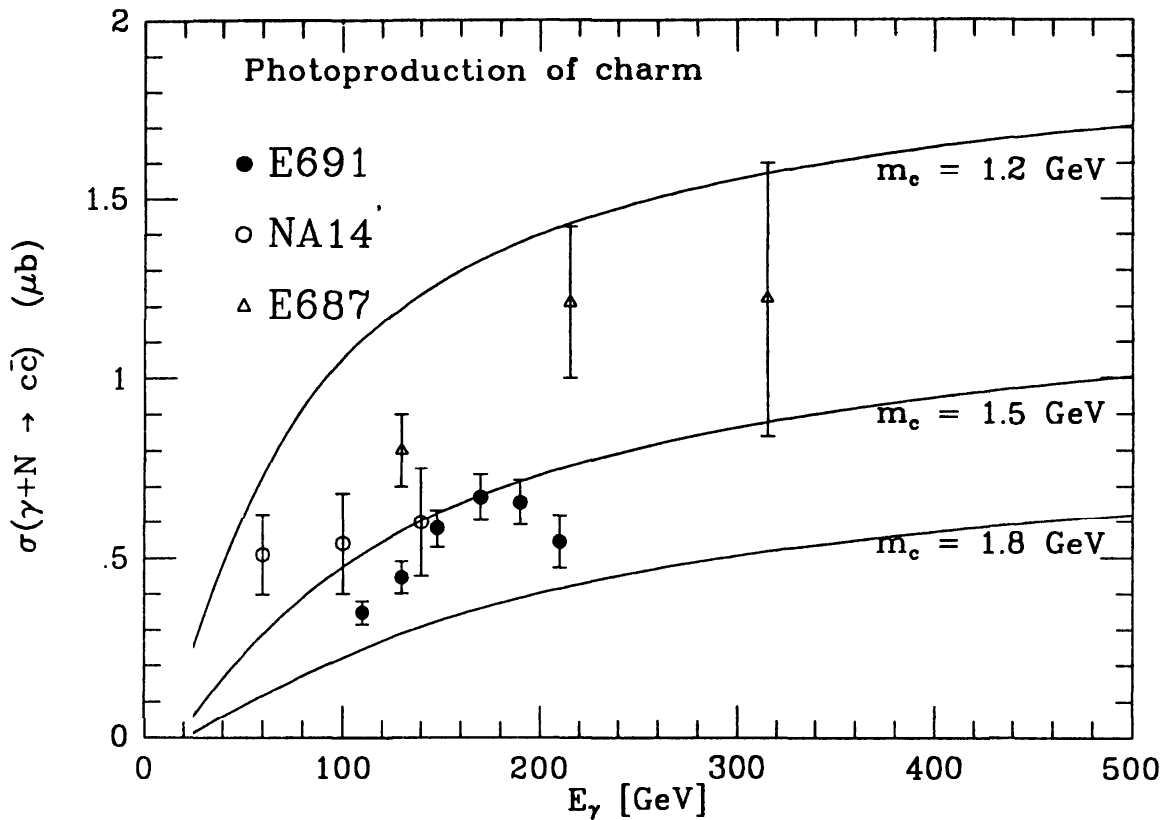


Fig. 10.14. Data on photoproduction of charm compared with theoretical lower limits [29].

photoproduction of charm. The higher-order  $O(\alpha\alpha_S^2)$  corrections to photoproduction have been considered in ref. [25]. After inclusion of these higher-order terms we obtain predictions for the total cross section as a function of the energy of the photon beam. The principal uncertainty comes from the value of the heavy quark mass, so we have plotted the minimum cross section which is obtained by varying  $\Lambda$  in the range

$$90 \text{ MeV} < \Lambda_{\overline{\text{MS}}}(5) < 250 \text{ MeV}, \quad (10.77)$$

and the scale  $\mu$  within the range  $1 \text{ GeV} < \mu < 2m$  for three values of the charm quark mass. The comparison with the data on the photoproduction of charm [26,27,28], shown in Fig. 10.14, indicates that charm quark masses smaller than 1.5 GeV are not needed to give an acceptable explanation of the data.

In conclusion, within the large uncertainties present in the theoretical estimates, modern data on the production of charm can be explained with a charm quark mass of the order of 1.5 GeV. This is not true of all data on the hadroproduction of charm, especially the older experiments. For a review of the older experimental situation we refer the reader to ref. [30]. Much information is also available on the  $x_F$  and  $p_T$  distributions of charmed hadrons, as well as data on the correlations between the

produced heavy quark and antiquark. For a comparison of these data with theoretical predictions we refer the reader to ref. [22].

At fixed-target energies the cross section for the production of bottom quarks is theoretically more reliable. The scale dependence plot has a characteristic form similar to Fig. 10.10 and it is possible to make estimates of the theoretical errors. The comparison with data on the production of bottom in pion beams at fixed-target energies is shown in Fig. 10.13.

As emphasized above, the theoretical prediction for bottom quark production at collider energies is very uncertain. The cause of this large uncertainty is principally the very small value of  $x$  at which the parton distributions are probed. In fact, at present collider energies, ( $\sqrt{s} = 1.8$  TeV), the bottom cross section is sensitive to the gluon distribution function at values of  $x < 10^{-2}$ . Measurements of the gluon distribution function [31] at such small values of  $x$  are not very precise and this leads to an uncertainty in the cross section. An associated problem is the form of the short-distance cross section in the large  $\hat{s}$  region. From Eq. (10.62) we see that lowest-order short-distance cross sections,  $\mathcal{F}^{(0)}$ , tend to zero in the large  $\hat{s}$  region. This is a consequence of the fact that they involve at most spin- $\frac{1}{2}$  exchange in the  $t$ -channel, as shown in Fig. 10.8. The higher-order corrections to the  $gg$  and  $gq$  processes have a different behaviour because they involve spin-1 exchange in the  $t$ -channel. The relevant diagrams for the  $gg$  process are shown in Fig. 10.12(b). In the high energy limit they yield a constant cross section, independent of energy [19]. Naturally these high- $\hat{s}$  contributions are damped by the small number of energetic gluons in the parton flux, but at collider energies the region  $\sqrt{\hat{s}} \gg m$  makes a sizeable contribution to the bottom cross section. The fact that this constant behaviour is present in both  $\mathcal{F}^{(1)}$  and  $\overline{\mathcal{F}}^{(1)}$  defined in Eq. (10.61) indicates the sensitivity of the size of this term to the value chosen for  $\mu$ . There is therefore an interplay between the size of this term and the small- $x$  behaviour of the gluon distribution function.

The calculations of ref. [19] also allow us to examine the  $p_T$  and rapidity distributions of the one heavy quark inclusive cross section,  $p\bar{p} \rightarrow b + X$ . Although the prediction of the total bottom cross section at collider energy is uncertain, it is plausible that the shape of the transverse momentum and rapidity distributions is well described by the form found in lowest-order perturbation theory. The supporting evidence for this conjecture is shown in Fig. 10.15, which demonstrates that the inclusion of the first non-leading correction does not significantly modify the shape of the transverse momentum and rapidity distributions. At a fixed value of  $\mu$ , the two curves lie on top of one another if the lowest order is multiplied by a constant factor. Similar results hold also for the shape of the top quark distribution [17].

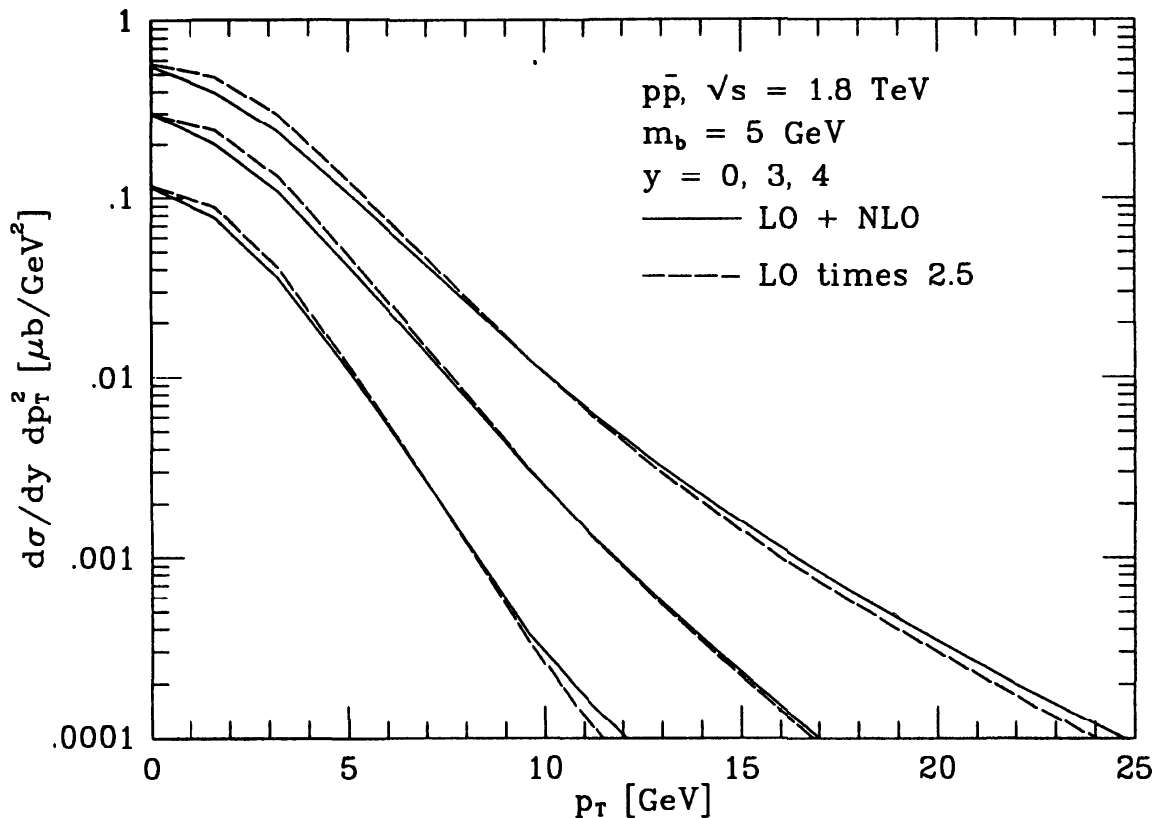


Fig. 10.15. The shape of the  $p_T$  distribution for bottom quark production. Figure from ref. [17].

The UA1 collaboration have investigated the transverse momentum distribution of the produced bottom quarks [32]. In Fig. 10.16 a comparison of UA1 data with the full  $\alpha_S^3$  prediction is made. The data are plotted as a function of the lower cut-off  $p_T^b(\min)$  on the transverse momentum of the  $b$  quark. The theoretical curves [22] are predictions for the production of  $b$  quarks. The data have been corrected for the fragmentation of a  $b$  quark into a  $B$  hadron and hence can be compared directly with the theoretical prediction. The cross section at the Born level is  $O(\alpha_S^2)$  so there is evidently a considerable sensitivity in the theoretical prediction to the value chosen  $\alpha_S$  (or for  $\Lambda$ ). The range of five-flavour  $\Lambda$  in the  $\overline{\text{MS}}$  scheme is chosen in order to cover both the preferred value of deep inelastic scattering, ( $\Lambda \approx 150$  MeV) and the value preferred by experiments at the  $Z$ -pole, ( $\Lambda \approx 300$  MeV). The match between experiment and these values of  $\Lambda$  can be checked by referring back to Fig. 2.5. The agreement between experiment and theory in Fig. 10.16 is satisfactory.

The corresponding prediction for the  $p_T$  dependence of the bottom production cross section at the Tevatron is shown in Fig. 10.17, compared with data from the CDF and D0 collaborations, obtained using various methods to detect the  $b$  quarks. The data tend to lie on the high side

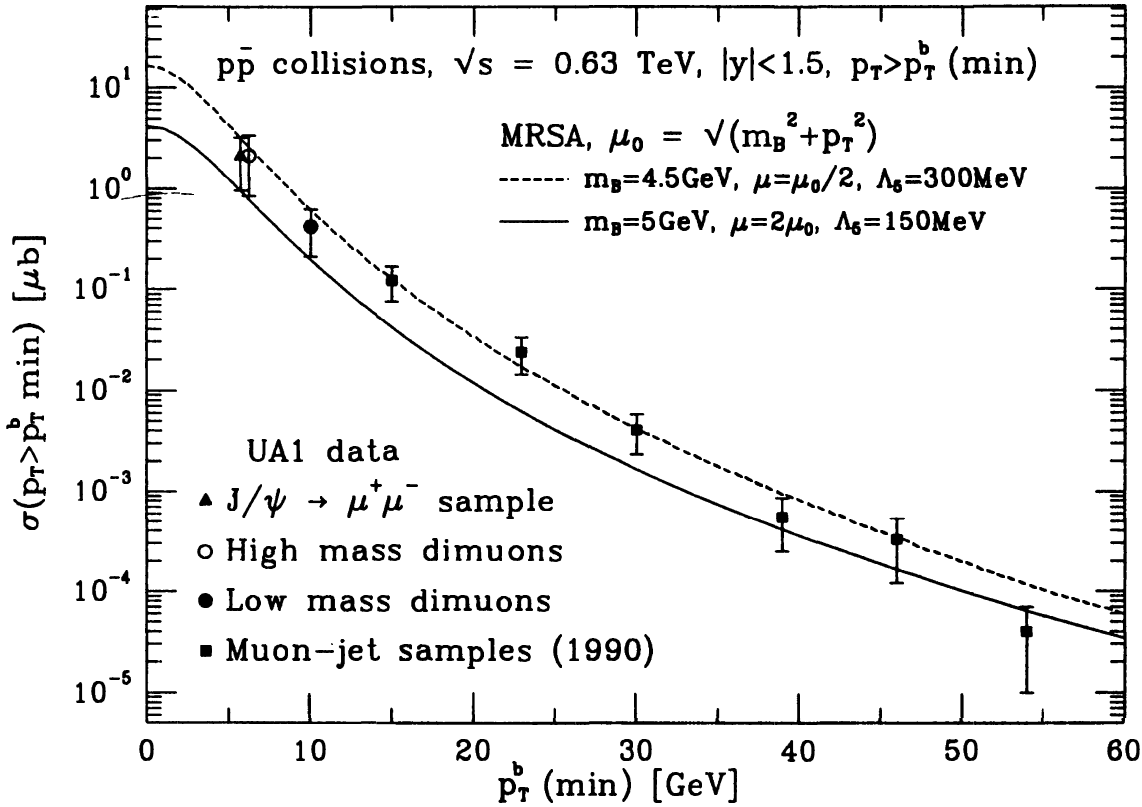


Fig. 10.16. The cross section for bottom quark production at CERN [32].

of the theoretical prediction. Resummation of small  $x$  effects [35] may lead to a further enhancement of the theoretical prediction, perhaps by about 30%. In view of the large theoretical uncertainties, the agreement between theory and experiment can be considered satisfactory.

## 10.5 Top quark production

The belief that the top quark had to exist was based both on theoretical and experimental evidence. The theoretical motivation is that complete families are required for the cancellation of anomalies in the currents which couple to gauge fields. Hence as explained in Section 8.3 the partner of the  $b, \tau$  and  $\nu_\tau$  was needed to complete the third family.

An experimental reason to believe in the existence of the top quark was the determination of the weak isospin of the bottom quark by  $e^+e^-$  annihilation experiments. The produced  $b$  and  $\bar{b}$  quarks are identified either by looking for displaced vertices or by looking for leptons which have a large  $p_T$  relative to the jet axis. As may be seen from Eq. (3.1), the forward-backward asymmetry of  $b$  jets in  $e^+e^-$  annihilation at the  $Z$

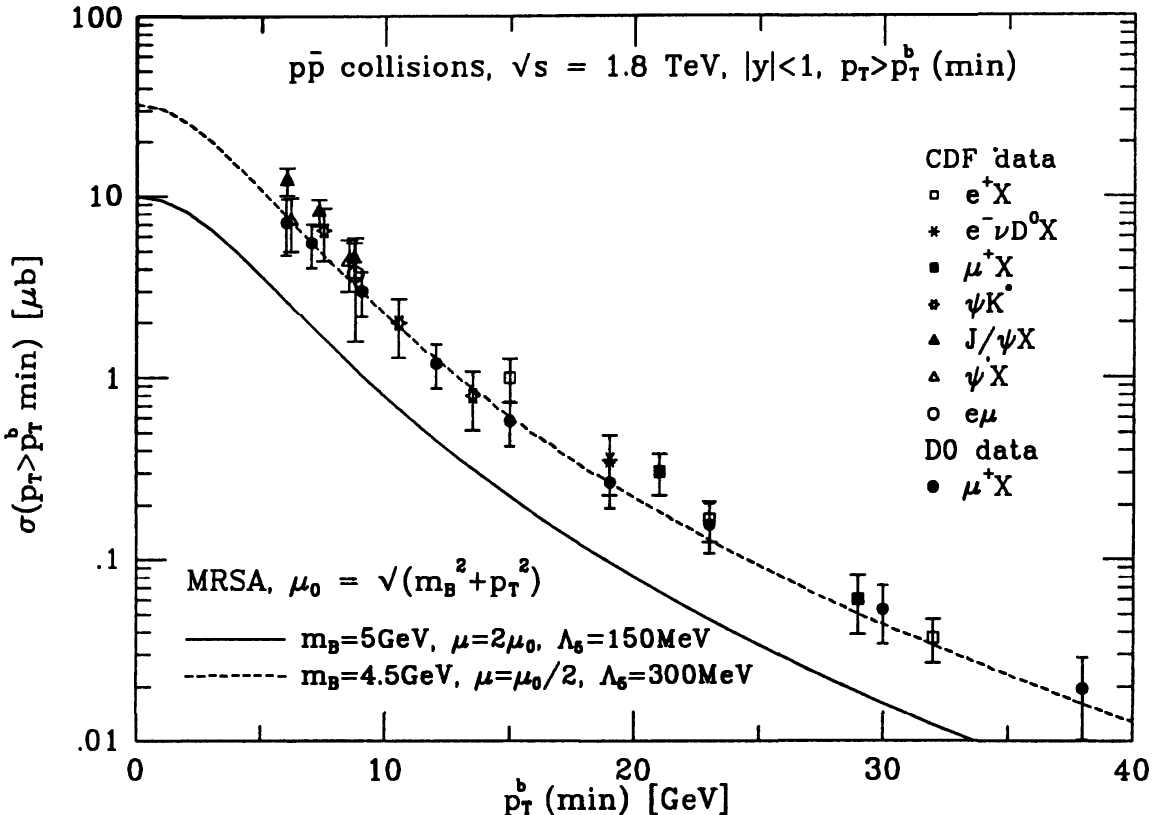


Fig. 10.17. The cross section for bottom quark production at Fermilab [33,34].

resonance is controlled by couplings to the electron and the  $b$  quark,

$$A_{FB}(b) = \frac{3}{4} \frac{2V_e A_e}{V_e^2 + A_e^2} \frac{2V_b A_b}{V_b^2 + A_b^2}. \quad (10.78)$$

On the other hand from Eq. (8.91) the total width of the  $Z$  into  $b$  quarks is given by

$$\Gamma(Z \rightarrow b\bar{b}) = \frac{G_F M_Z^3}{2\sqrt{2}\pi} (V_b^2 + A_b^2). \quad (10.79)$$

Taking the couplings to the electron to have their standard values, these two measurements are sufficient to measure the left- and right-handed weak isospin of the  $b$  quark. An early determination of the couplings of the  $b$  quark (before the discovery of the top) gave the values [36],

$$T^3(b_L) = -0.490^{+0.015}_{-0.012}, \quad T^3(b_R) = -0.028 \pm 0.056. \quad (10.80)$$

The simplest hypothesis is therefore that the left-handed bottom quark is in an SU(2) doublet with the top quark, although more complicated schemes are certainly possible. More precise values of the couplings of the  $b$  quark are now available [37,38]. It is less interesting to express them as constraints on the weak isospin of the  $b$  quark since the discovery of the  $t$  quark.

	$m_t$ [GeV]	$\sigma$ [pb]
CDF	$175.6 \pm 5.7(\text{stat}) \pm 7.4(\text{sys})$	$7.5^{+1.6}_{-1.6}$
D0	$170 \pm 15(\text{stat}) \pm 10(\text{sys})$	$5.2^{+1.8}_{-1.8}$

Table 10.3. Current results for top quark production from Fermilab [41,42].

Indirect constraints on the mass of the top quark are obtained from precision electroweak measurements, such as the  $W$  mass measurement. As described in Section 8.2.2 the top mass leads to observable effects on the  $\rho$  parameter. The current limits on the top quark mass from precision electroweak measurements are [38]

$$m_t = 178^{+8+17}_{-8-20} \text{ GeV}. \quad (10.81)$$

The value extracted for the top quark mass has a mild dependence on the mass of the Higgs boson. The central value is extracted for  $M_H = 300$  GeV. The second error corresponds to varying the Higgs boson mass in the range  $60 \text{ GeV} < M_H < 1 \text{ TeV}$ .

The first direct evidence for the top quark was the observation of its production in  $p\bar{p}$  collisions at Fermilab [39,40]. The current results from the two collaborations [41,42] based on about  $100 \text{ pb}^{-1}$  per experiment at  $\sqrt{s} = 1.8 \text{ TeV}$  are given in Table 10.3. Note that the measured cross sections are extremely small. Indeed with the measured cross sections one predicts that only about 1300  $t\bar{t}$  pairs have been produced at Fermilab. The actual number of events observed is further reduced by the branching ratios to observable modes and by experimental acceptances and efficiencies. It should be noted that the top quark mass is still quite uncertain. In the following sections we will discuss the comparison of the experimental results with theory, using a nominal value of 175 GeV.

### 10.5.1 Top cross section

The expected cross section for the process

$$p + \bar{p} \rightarrow t + \bar{t} + X \quad (10.82)$$

is shown in Fig. 10.18 as a function of the top mass at  $\sqrt{s} = 1.8$  and 2 TeV. The errors on the theoretical prediction will be discussed below. The cross section is calculated using next-to-leading-order QCD. Also plotted are the results at  $\sqrt{s} = 1.8 \text{ TeV}$  of the CDF and D0 collaborations at the time of writing. As discussed above, the top quark cross section is calculable in perturbation theory because  $m_t \gg \Lambda$ . This condition is certainly valid for the case of the top quark and suggests that its production cross

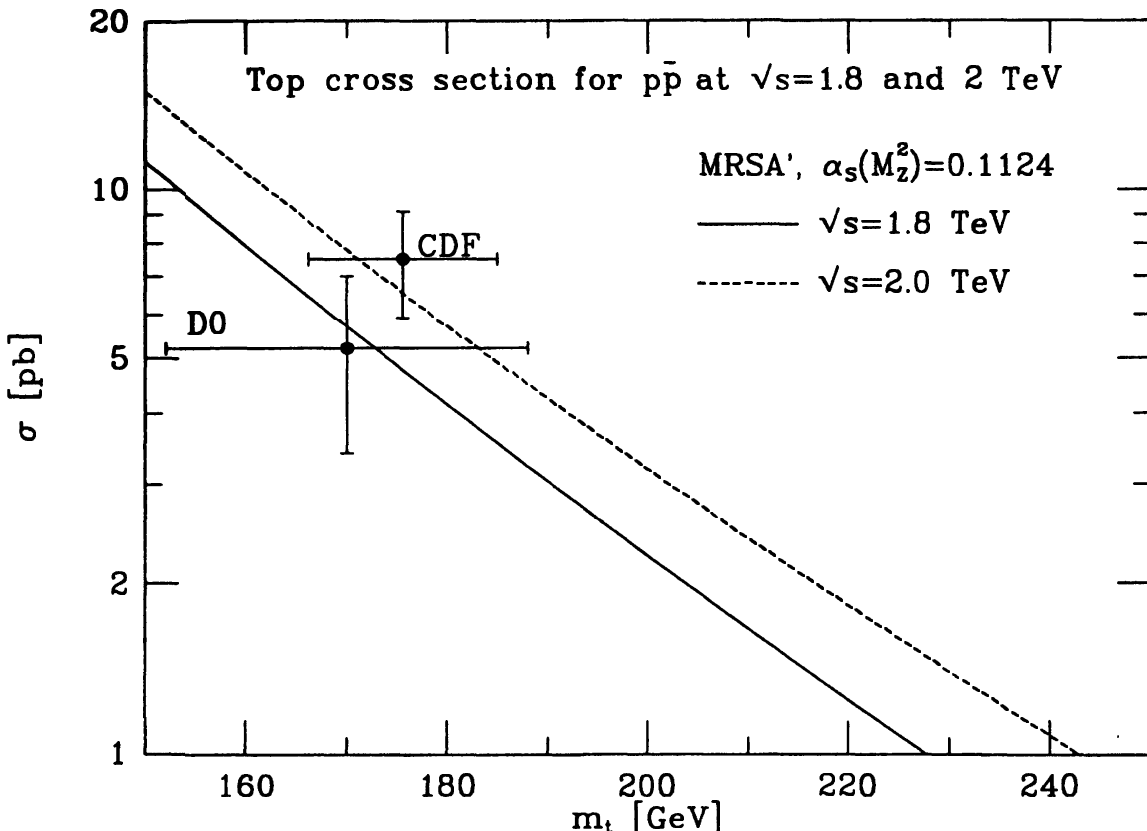


Fig. 10.18. The cross section for top quark production versus  $m_t$ .

section should be well determined. Next-to-leading order corrections to the  $q\bar{q}$  process are found to be moderate, with the bulk of the correction occurring near threshold. Corrections to the  $gg$  process are large, both at threshold and at high energy.

The relative importance of the various kinematic regions is determined by the parton luminosity defined in Eq. (7.12):

$$\frac{dL_{ij}}{d \ln \tau} = \frac{1}{1 + \delta_{ij}} \int_0^1 dx_1 dx_2 \\ \times [(x_1 f_i^A(x_1, \mu^2) x_2 f_j^B(x_2, \mu^2)) + (1 \leftrightarrow 2)] \delta(\tau - x_1 x_2) \quad (10.83)$$

where  $f_i^A$  is the density of partons of type  $i$  in hadron  $A$ . In terms of these parton fluxes the hadronic cross-section is given by

$$\frac{d\sigma(s)}{\ln \tau} = \frac{\alpha_s^2(\mu^2)}{2m^2} \sum_{i,j} \frac{dL_{ij}(\tau, \mu)}{d \ln \tau} \mathcal{F}_{ij}\left(\frac{\rho^H}{\tau}, \frac{\mu^2}{m^2}\right). \quad (10.84)$$

Fig. 10.19 shows that at  $\sqrt{s} = 1.8$  TeV, the top quark is produced predominantly by  $q\bar{q}$  annihilation, with large corrections near threshold. For  $m = 175$  GeV, about 90% of the cross section is due to  $q\bar{q}$  annihilation. This implies that calculations of the cross section should be quite reliable,

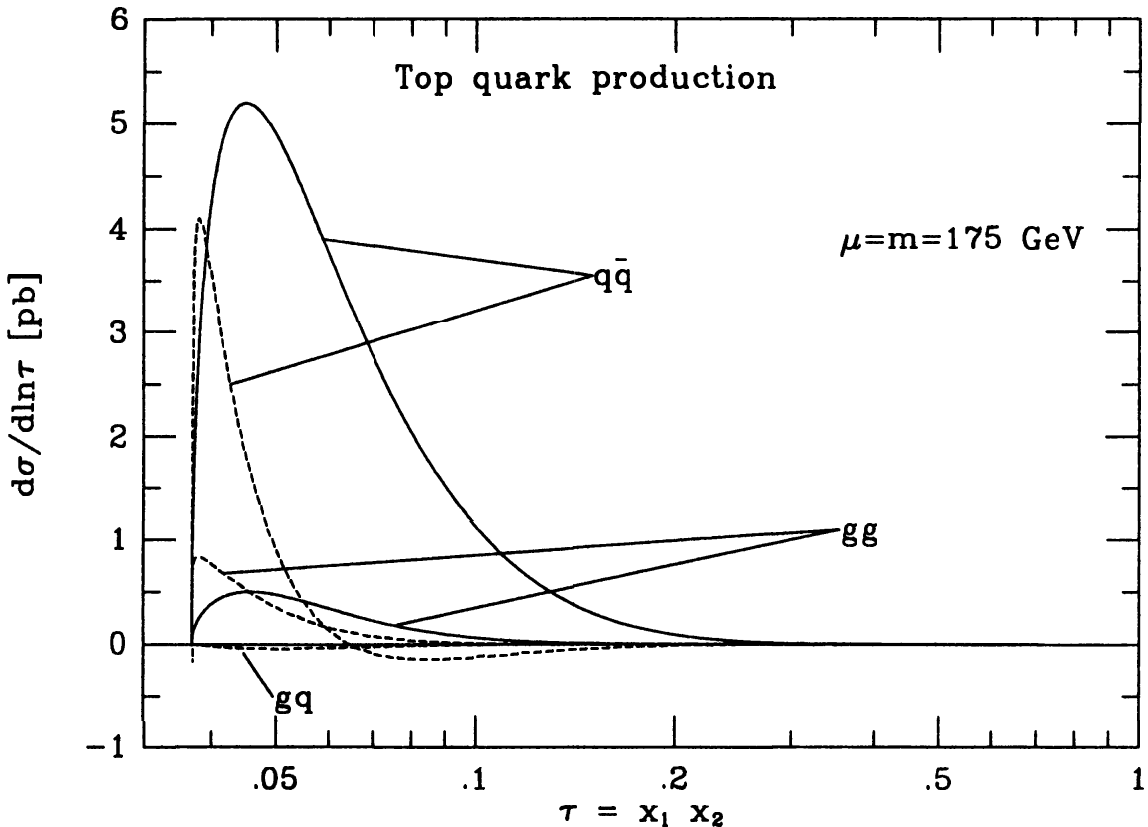


Fig. 10.19.  $O(\alpha_s^2)$  curves (solid) and  $O(\alpha_s^3)$  curves (dashed).

because they depend on well-measured quark distribution functions.

Near threshold ( $\beta \rightarrow 0$ ), the results for the functions  $\mathcal{F}_{ij}^{(0,1)}$  defined in Eq. (10.61) are

$$\begin{aligned}\mathcal{F}_{q\bar{q}}^{(1)} &\rightarrow \mathcal{N}_{q\bar{q}} \left[ -\frac{\pi^2}{6} + \beta \left( \frac{16}{3} \ln^2(8\beta^2) - \frac{82}{3} \ln(8\beta^2) \right) \right] \\ \mathcal{F}_{gg}^{(1)} &\rightarrow \mathcal{N}_{gg} \left[ \frac{11\pi^2}{42} + \beta \left( 12 \ln^2(8\beta^2) - \frac{366}{7} \ln(8\beta^2) \right) \right]\end{aligned}\quad (10.85)$$

and  $\mathcal{F}_{q\bar{q}}^{(0)}, \mathcal{F}_{gg}^{(0)} \rightarrow O(\beta)$ . The normalization constants are defined by

$$\mathcal{N}_{ij} = \frac{1}{8\pi^2} \frac{\mathcal{F}_{ij}^{(0)}}{\beta}, \quad \mathcal{N}_{q\bar{q}} = \frac{1}{72\pi}, \quad \mathcal{N}_{gg} = \frac{7}{1536\pi}. \quad (10.86)$$

The rapid rise of the cross section near threshold displayed in Fig. 10.19 is due to the logarithmic terms in Eq. (10.85). These corrections are larger for smaller top quark mass, when gluon-gluon processes are more important. The constant behaviour of the cross section near threshold is a consequence of the Coulomb singularity. This effect is repulsive in the dominant  $q\bar{q}$  octet channel. The correction due to this effect is small; after resumming the Coulomb terms it is found that additional correction

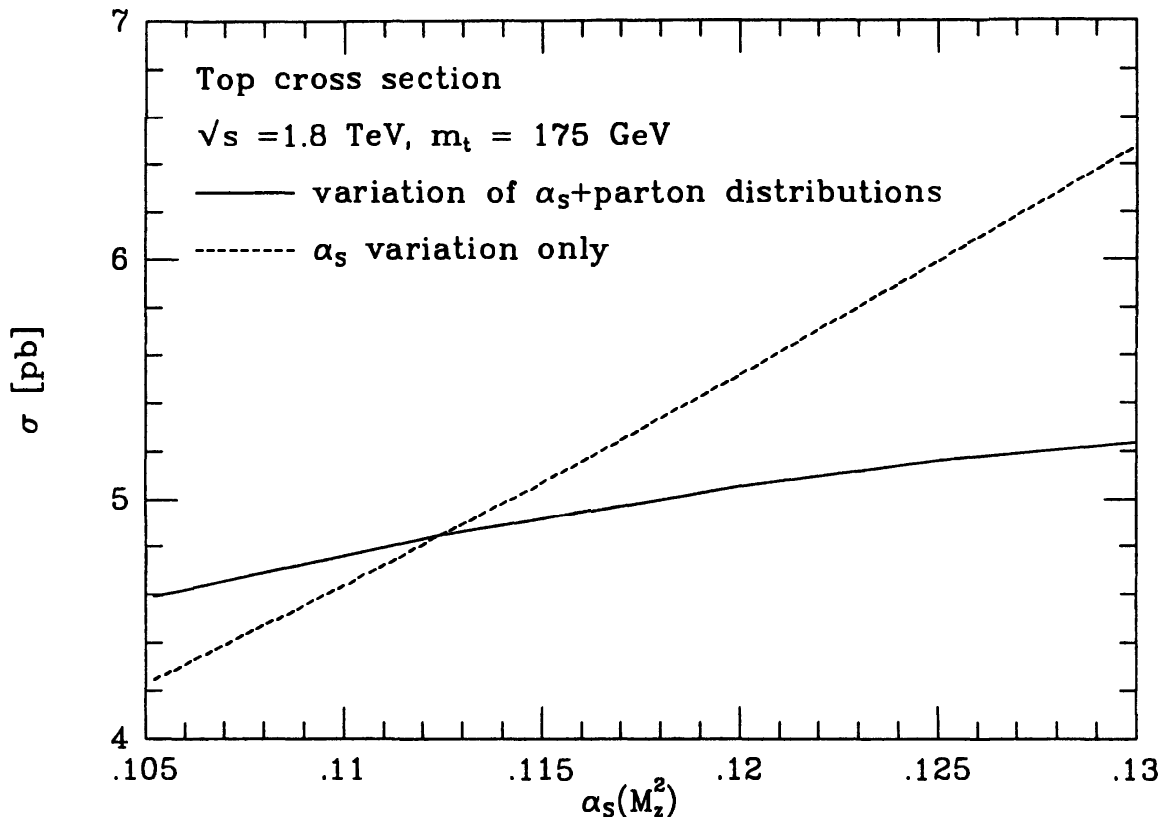


Fig. 10.20. The cross section for top quark production versus  $\alpha_s(M_z^2)$ . Adapted from ref. [44].

to the cross section not included in the next-to-leading order calculation is less than one percent, in part because of cancellation between  $gg$  and  $q\bar{q}$  channels [43,44].

We now turn to numerical estimates. Earlier estimates are given in [44-48]. The input parameters which we have to specify are the form of the parton distributions, the value of  $\alpha_s$  and the value of the renormalization and factorization scale,  $\mu$ . For the MRS(A') distribution,  $\alpha_s(M_z^2) = 0.1124$ , the result for  $m_t = 175 \text{ GeV}$  and  $\mu = m_t$  is  $\sigma = 4.84 \text{ pb}$ . The sensitivity to the form of the parton distribution functions is quite small mainly because the top quark is predominantly produced by the well-measured quark distributions. The effect of the  $\alpha_s$  uncertainty is more important. Increasing  $\alpha_s$  without changing the parton distributions gives the dashed curve in Fig. 10.20. This calculation of the dependence on  $\alpha_s$  is an overestimate since it does not take into account the increased shrinkage of the quark distribution functions for larger  $\alpha_s$  in the evolution from lower energy where they are measured [48]. Fig. 10.20 shows the predicted value of the top cross section using parton distribution functions [49] which have been fitted with different fixed values of  $\alpha_s$ . The overall dependence of the cross section on the value of  $\alpha_s$  is quite small. We

estimate the errors in the cross section by taking  $0.105 < \alpha_s(M_Z^2) < 0.130$  and  $m_t/2 < \mu < 2m_t$  and find that at a fixed top mass the cross section is unlikely to be uncertain by more than  $\pm 15\%$ . The final result for the top quark cross section is

$$\sigma(m_t = 175 \text{ GeV}) = 4.84^{+0.73}_{-0.69} \text{ pb.} \quad (10.87)$$

The cross sections quoted above are given in the narrow width approximation.

### 10.5.2 Prospects for top studies

As noted in the previous section, the cross section for  $t\bar{t}$  production at the Tevatron collider is extremely small. Therefore in order to study the top quark in more detail it is necessary to increase either the energy or the luminosity of the collider (or both).

The next collider run at the Fermilab Tevatron is scheduled for 1999 after completion of the Main Injector project. The energy will be increased to  $\sqrt{s} = 2 \text{ TeV}$  and the luminosity will increase to about  $40 \text{ pb}^{-1}$  per week from the present value of  $4 \text{ pb}^{-1}$  per week. For  $m_t = 175 \text{ GeV}$  the higher energy increases the  $t\bar{t}$  cross section by about 37% relative to its value at  $\sqrt{s} = 1.8 \text{ TeV}$ .

Therefore in the early years of the next century one will have data samples in  $p\bar{p}$  annihilation at  $\sqrt{s} = 2 \text{ TeV}$  measured in inverse femtobarns. The constraints on the Standard Electroweak Model from the top quark and  $W$  mass measurements which will be possible with these data can be seen in Fig. 10.21, calculated using ref. [50]. The band of values at each value of the Higgs boson mass corresponds to the uncertainty on the value of the electromagnetic fine structure constant at the  $Z$  mass [51]

$$[\alpha(M_Z^2)]^{-1} = 128.89 \pm 0.09. \quad (10.88)$$

With  $2 \text{ fb}^{-1}$  of data, CDF estimate measurement errors of  $\delta M_W = 40 \text{ MeV}$  and  $\delta m_t = 4 \text{ GeV}$  [52].

As shown in Fig. 10.22, the expected cross section in  $pp$  interactions at 14 TeV is

$$\sigma = 785^{+300}_{-130} \text{ pb.} \quad (10.89)$$

This is more than a factor of one hundred larger than the cross section at the Tevatron, primarily due to the large flux of incoming gluons. More 90% of the cross section at the LHC is due to processes with incoming gluons. Therefore at a luminosity of  $10^{34} \text{ cm}^{-2} \text{ s}^{-1}$  we expect about seven top quark pairs produced per second. The large cross section and luminosity will make the LHC a powerful machine to study the top quark.

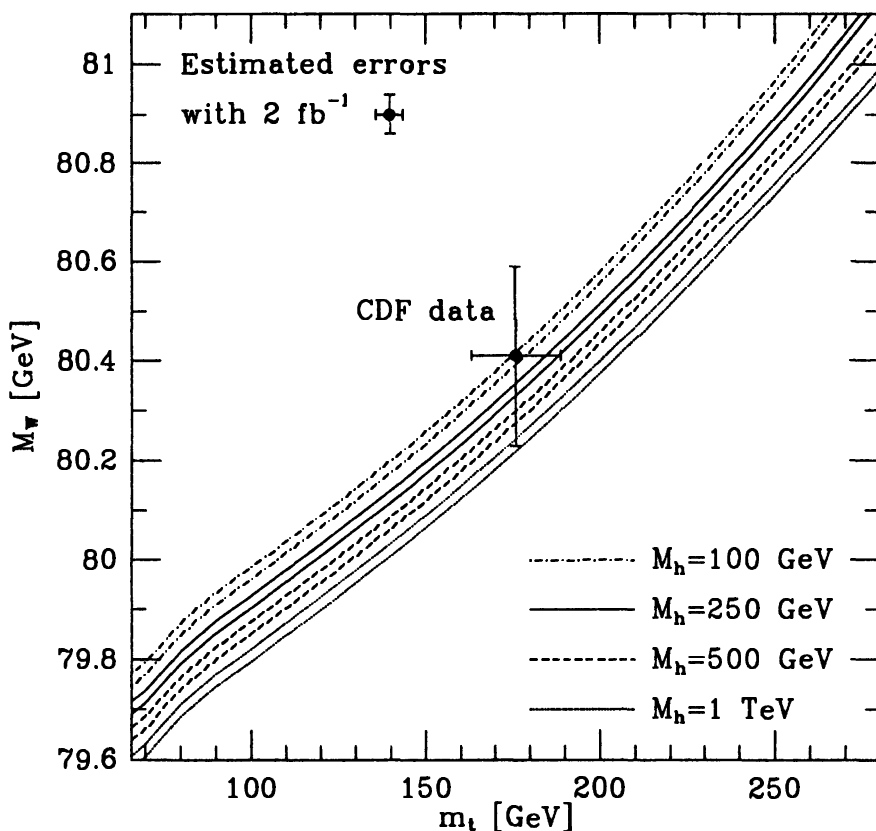


Fig. 10.21. Testing the Standard Electroweak Model.

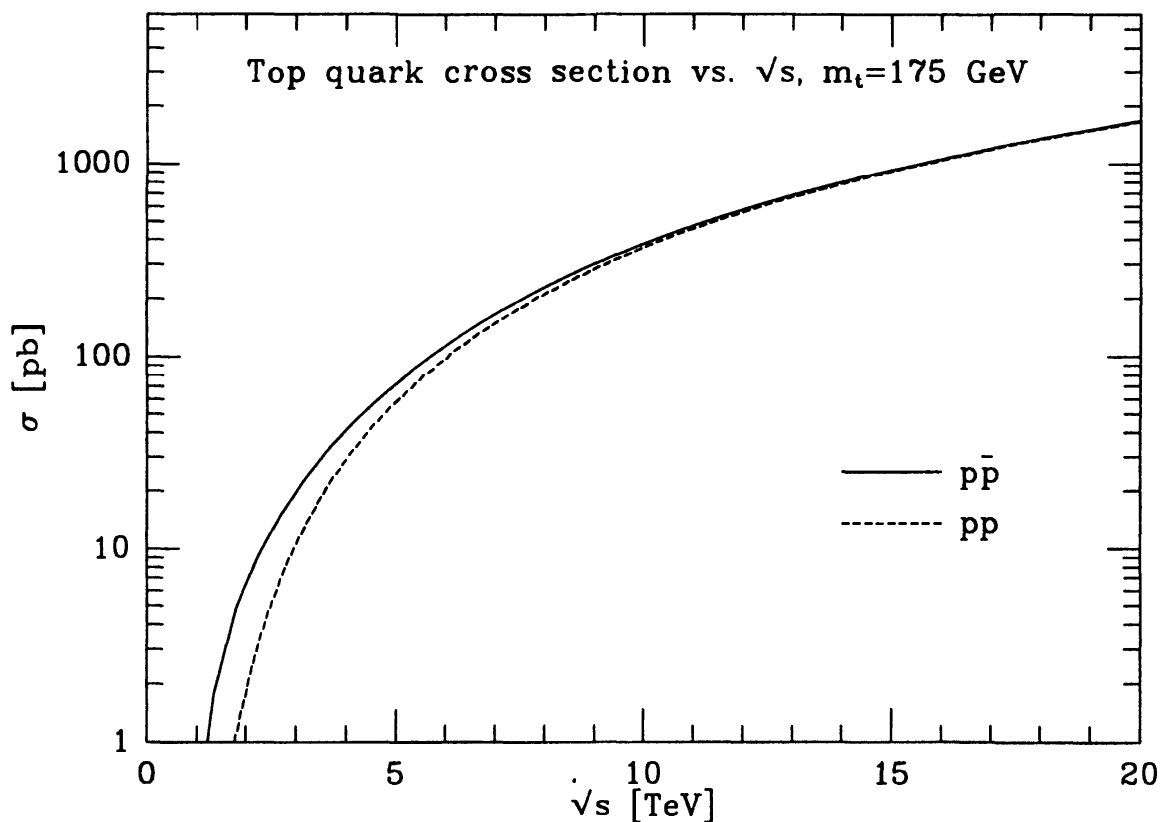


Fig. 10.22. The cross section for top quark production versus energy.

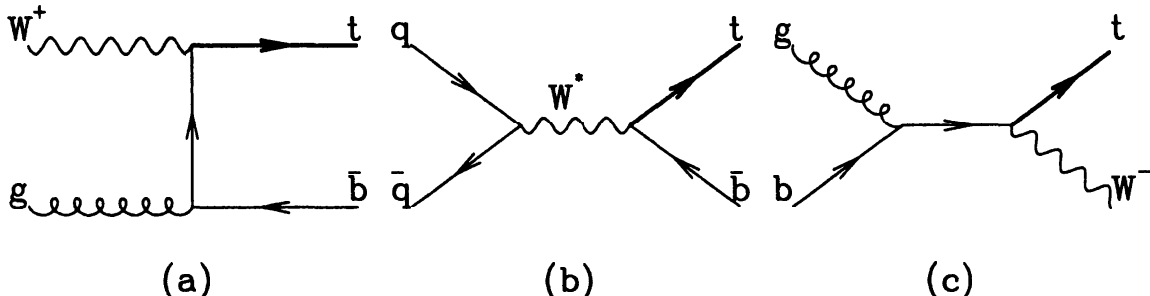


Fig. 10.23. Diagrams for single top production.

Because the top quark is so heavy, we can think of paying the price of a weak interaction in order to have the advantage of producing only a single top [53]. Three possible single-top quark production mechanisms are

$$(a) \quad Wg \rightarrow t\bar{b}, \quad (10.90)$$

$$(b) \quad q\bar{q} \rightarrow t\bar{b}, \quad (10.91)$$

$$(c) \quad gb \rightarrow tW^- . \quad (10.92)$$

Representative diagrams are shown in Fig. 10.23. It is found that the raw rate for these processes as observed in the lepton + jets channel is at least a factor of ten below the standard production mechanism at  $\sqrt{s} = 1.8$  TeV, as shown in Fig. 10.24. A measurement of the single top cross section will place a constraint on  $V_{tb}$  [9].

## 10.6 Heavy quarks in jets

### 10.6.1 Fragmentation functions for heavy quarks

Parton model calculations predict the rates for heavy quark production. It is, however, the decay products of a heavy hadron that are actually observed. The process of fragmentation, *viz.* the attachment of a light antiquark  $\bar{q}$  to a heavy quark  $Q$  leads to only a slight deceleration of the latter. Following [54] we can model the amplitude for a rapidly moving heavy quark  $Q$  of momentum  $P$  to fragment into a hadron  $H = Q\bar{q}$  of momentum  $zP$  and a light quark  $q$  (Fig. 10.25) by calculating the energy difference before and after fragmentation,

$$\begin{aligned}\Delta E &= E_Q - E_H - E_q \\ &= \sqrt{m_Q^2 + P^2} - \sqrt{m_H^2 + z^2 P^2} - \sqrt{m_q^2 + (1-z)^2 P^2} \\ &\approx \frac{m_Q^2}{2P} \left[ 1 - \frac{1}{z} - \frac{\epsilon_Q}{1-z} \right]\end{aligned}\quad (10.93)$$

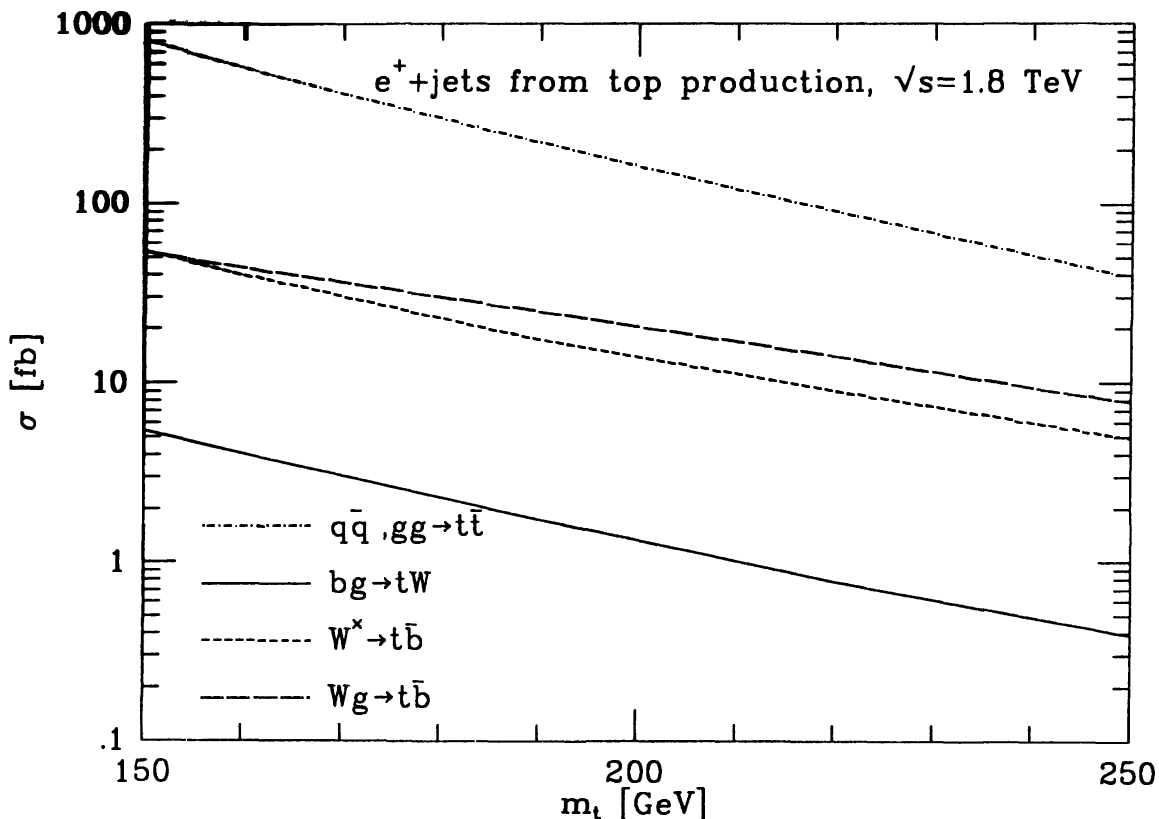


Fig. 10.24. The cross section for positron + jets versus top quark mass.

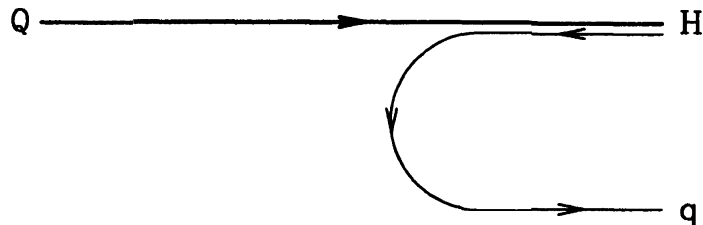


Fig. 10.25. Model for heavy quark fragmentation.

where  $\epsilon_Q = m_q^2/m_Q^2$  and we have taken  $m_H = m_Q$  for simplicity. The transition amplitude is modelled by the energy denominator,  $T \simeq 1/\Delta E$ . Squaring the amplitude and including a factor of  $1/z$  for longitudinal phase space, we obtain the *Peterson function* for the fragmentation of a heavy quark  $Q$  into a heavy hadron  $H$ :

$$D_Q^H(z) = \frac{N_H}{z} \left[ 1 - \frac{1}{z} - \frac{\epsilon_Q}{1-z} \right]^{-2}. \quad (10.94)$$

The normalization factors  $N_H$  are constrained by the sum over all hadrons containing the heavy quark:

$$\sum_H \int dz D_Q^H(z) = 1. \quad (10.95)$$

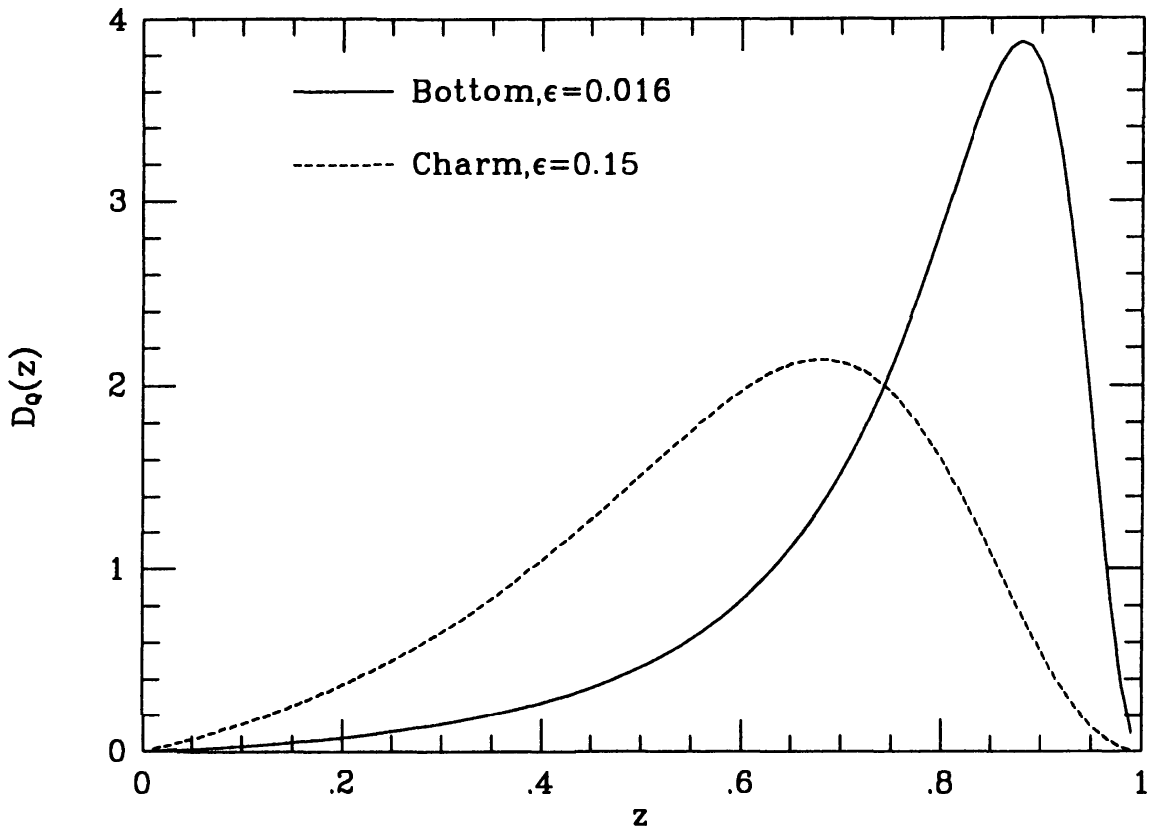


Fig. 10.26. The Peterson model for  $b$  and  $c$  fragmentation functions.

The Peterson function is plotted in Fig. 10.26 for  $\epsilon_c = 0.15$  and  $\epsilon_b = 0.016$ . In principle,  $\epsilon_Q$  is fixed by the heavy and light quark masses, but in practice it is treated as a free parameter.

#### 10.6.2 Heavy quarks in gluon jets

Another question of experimental interest is the frequency with which heavy quarks are found amongst the fragmentation products of a light quark or gluon jet. Since hadrons containing heavy quarks have appreciable semi-leptonic branching ratios, such events will often lead to final states with leptons in jets. If we wish to use lepton plus jet events as a signature for new physics we must understand the background due to heavy quark production and decay.

This issue is logically unrelated to the total heavy quark cross section. As discussed above, the total cross section is dominated by events with a small transverse energy, of the order of the quark mass  $m$ . Jet events inhabit a different region of phase space, since they contain a cluster of transverse energy  $E_T \gg m$ . This kinematic region gives a small contribution to the total heavy quark cross section.

A gluon fragmenting into a heavy quark pair must have a virtuality  $k^2 >$

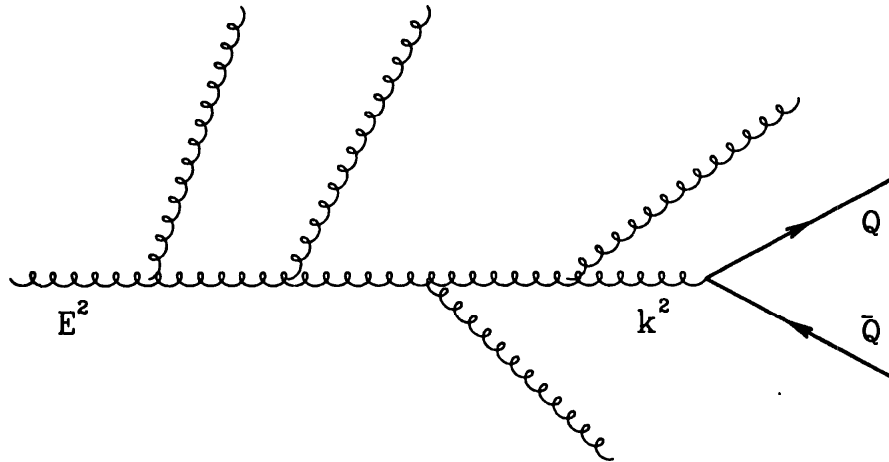


Fig. 10.27. Heavy quark production in jets.

$4m^2$  and so perturbative methods should be applicable for a sufficiently heavy quark. The number of  $Q\bar{Q}$  pairs per gluon jet is calculable [55] from diagrams such as the one shown in Fig. 10.27. The calculation has two parts. First one has to calculate  $n_g(E^2, k^2)$ , the number of gluons of off-shellness  $k^2$  inside a jet produced in a hard process at scale  $E^2$ . Secondly, one needs the transition probability for a gluon with off-shellness  $k^2$  to split into a pair of heavy quarks.

The number of gluons of virtual mass-squared  $k^2$  inside a gluon jet produced at scale  $E^2$  is given by [55]

$$n_g(E^2, k^2) \simeq \left[ \frac{\ln(E^2/\Lambda^2)}{\ln(k^2/\Lambda^2)} \right]^a \cosh \left\{ \sqrt{\frac{2C_A}{\pi b}} \left[ \sqrt{\ln \left( \frac{E^2}{\Lambda^2} \right)} - \sqrt{\ln \left( \frac{k^2}{\Lambda^2} \right)} \right] \right\} \quad (10.96)$$

where

$$a = -\frac{1}{4} - \frac{5n_f}{54\pi b} \quad (10.97)$$

(cf. Eq. (6.38)),  $b$  being the first coefficient in the expansion of the  $\beta$  function, Eq. (10.65). The calculation of the gluon multiplicity (10.96) requires the imposition of the angular ordering constraint which takes into account the coherence of the emitted soft gluons [56], as discussed in Chapter 5. In fact Eq. (10.96) is closely related to the average jet multiplicity (6.110). See refs. [57,58] for more detailed discussion, and for the extension to light quark jets.

Defining  $R_{Q\bar{Q}}$  as the mean number of  $Q\bar{Q}$  pairs per gluon jet, and ignoring for the moment the gluon branching calculated above, one finds

$$R_{Q\bar{Q}} = \int_{4m^2}^{E^2} \frac{dk^2}{k^2} \frac{\alpha_s(k^2)}{2\pi} \int_{z_-}^{z_+} \frac{1}{2} \left[ z^2 + (1-z)^2 + \frac{2m^2}{k^2} \right] dz \quad (10.98)$$

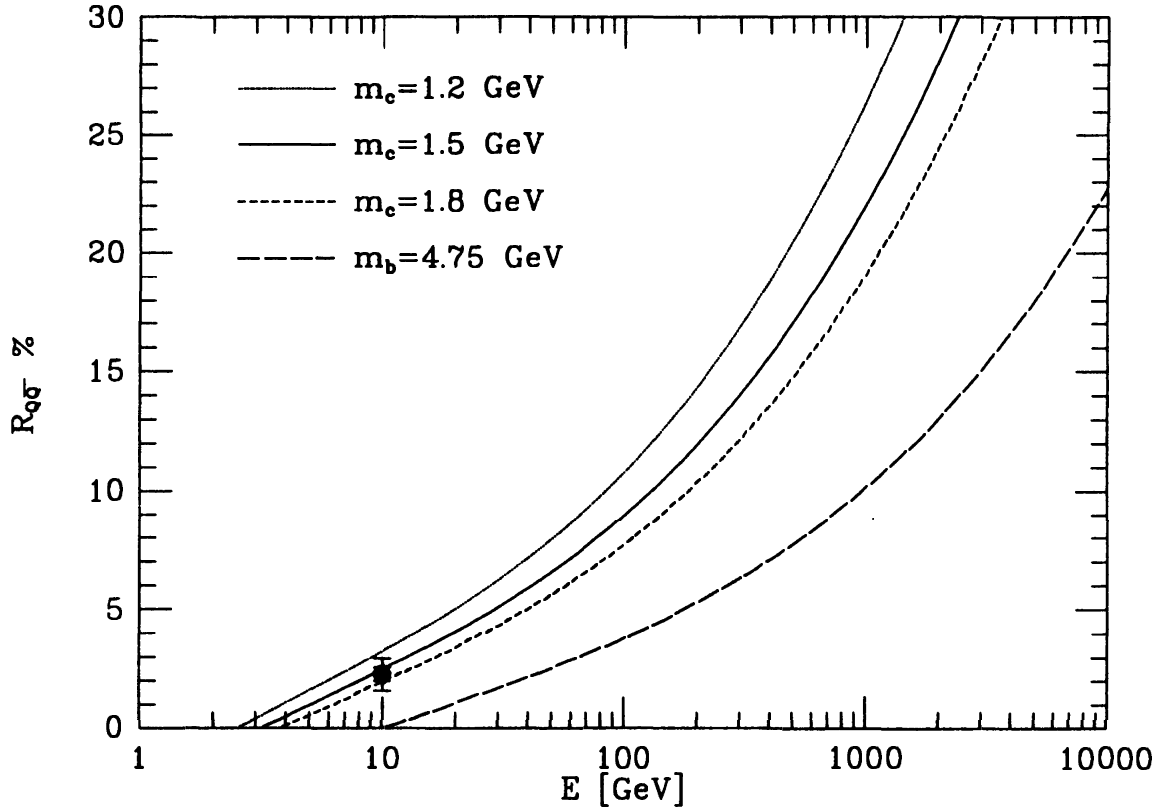


Fig. 10.28. Heavy quarks in gluon jets compared with OPAL data on charm [59].

where the longitudinal momentum fraction of the heavy quark, is denoted by  $z$ , for which the integration limits are  $z_{\pm} = (1 \pm \beta)/2$  with  $\beta = \sqrt{(1 - 4m^2/k^2)}$ . The  $z$ -integrand is the Altarelli-Parisi splitting function for  $g \rightarrow q\bar{q}$ , generalized to massive quarks. To take gluon branching into account one should include the multiplicity factor  $n_g(E^2, k^2)$ . Performing the  $z$  integration, one then obtains

$$R_{Q\bar{Q}} = \frac{1}{6\pi} \int_{4m^2}^{E^2} \frac{dk^2}{k^2} \alpha_s(k^2) \left[ 1 + \frac{2m^2}{k^2} \right] \sqrt{1 - \frac{4m^2}{k^2}} n_g(E^2, k^2). \quad (10.99)$$

The predicted number of charm quark pairs per jet is shown for three values of the charm quark mass in Fig. 10.28, using a value of  $\Lambda^{(3)} = 300$  MeV. Also shown is the prediction for the number of bottom quarks per jet, with  $\Lambda^{(4)} = 260$  MeV. The OPAL data point [59] was obtained from three-jet events at LEP, by assuming that the lowest-energy jet is a gluon and lepton-tagging charm quarks in that jet.

## 10.7 Quarkonium

### 10.7.1 Quarkonium spectrum

In November 1974 a narrow vector state of mass 3.1 GeV decaying into  $e^+e^-$  and  $\mu^+\mu^-$  was discovered simultaneously at Brookhaven and SLAC [60]. At the time many explanations were given, but it was soon established that the observed particle was a bound state of a heavy quark-antiquark pair  $Q\bar{Q}$ . The particle, named the  $J/\psi$ , is an  $s$ -wave,  $J = 1$  bound state of charm quarks,  $c\bar{c}$ , described in spectroscopic notation ( ${}^{2S+1}L_J$ ) as  ${}^3S_1$ . The analogous bound state made up of  $b\bar{b}$  (and called the  $\Upsilon$ ) was discovered at Fermilab in 1977 [61]. Many levels of these  $Q\bar{Q}$  systems have subsequently been discovered and their spectra will be described below.

In 1974 the surprise was that the  $J/\psi$  had a width of only 88 keV, much narrower than one would expect for a hadronically decaying resonance of such a high mass. Early theoretical work [62] provided an explanation, suggesting that heavy quark-antiquark bound states should be narrow because of asymptotic freedom, exploiting the analogy with positronium which is a QED bound state of an electron and a positron.

To understand the correspondence of the quarkonium system with positronium it may be helpful to recall some formulae for the latter system. In these formulae  $\mu$  denotes the reduced mass,  $\mu = m_e/2$ . (The same formulae are also true for the hydrogen atom with the appropriate substitution for the reduced mass.) In natural units where  $\hbar = c = 1$ , the Bohr radius, which sets the scale of atomic sizes, is given by  $a_0 = 1/(\alpha\mu)$  where  $\alpha$  is the electromagnetic fine structure constant. The scale of the excitation energies of the atom is set by the Rydberg,  $\mathcal{R} = \frac{1}{2}\mu\alpha^2$  and energy levels are given by

$$E_n = -\frac{\mathcal{R}}{n^2}, \quad (10.100)$$

where  $n$  is the principal quantum number. In the non-relativistic limit the energy levels are determined by the principal quantum number alone. Moreover for a spherical symmetric potential of the form  $V \sim r^k$  we have from the virial theorem that the expectation values of the kinetic and potential energies are related by

$$2\langle T \rangle = k\langle V \rangle, \quad (10.101)$$

where  $T$  and  $V$  are the kinetic and potential energies respectively. Therefore for a Coulombic system we have that

$$\mu v^2 = 2\langle T \rangle = -2E_1 = \mu\alpha^2 \quad (10.102)$$

and hence that the average velocity  $v$  is of order  $\alpha$ . Therefore, in as

much as the coupling is small, the system will be non-relativistic. For a Coulomb potential the wave function is given by the product of an angular factor and a radial wave function. Thus for the lowest-lying *s*-wave state we have

$$\psi(r, \theta, \phi) = \frac{1}{\sqrt{4\pi}} R_0(r), \quad R_0(r) = 2 \left( \frac{1}{a_0} \right)^{\frac{3}{2}} \exp(-r/a_0), \quad (10.103)$$

where the subscript indicates the angular momentum quantum number, *L*. The square modulus of the radial wave function at the origin for this state is

$$|R_0(0)|^2 = \frac{4}{a_0^3} = 4\alpha^3\mu^3. \quad (10.104)$$

For the lowest-lying *p*-wave state, the derivative of the square modulus of the wave function at the origin is given by

$$|R'_1(0)|^2 = \frac{1}{24a_0^5} = \frac{1}{24}\alpha^5\mu^5. \quad (10.105)$$

The charge conjugation parity of a fermion-antifermion system is given by  $C = (-1)^{L+S}$ , so that the  ${}^1S_0$  state (parapositronium) has the shortest lifetime since it can decay into two photons. The decay rate is determined by the product of the annihilation probability at rest and the probability of finding the  $e^+$  and  $e^-$  at the same point,

$$\Gamma({}^1S_0 \rightarrow 2\gamma) = \frac{\alpha^2}{m_e^2} |R_0(0)|^2 = \frac{1}{2}\alpha^5 m_e. \quad (10.106)$$

Because of its odd *C*-parity the  ${}^3S_1$  state (orthopositronium) can only decay to an odd number of photons. The dominant contribution comes from the decay to three photons for which the decay rate is given by

$$\Gamma({}^3S_1 \rightarrow 3\gamma) = \frac{\alpha^3}{m_e^2} \frac{4(\pi^2 - 9)}{9\pi} |R_0(0)|^2 = \frac{2(\pi^2 - 9)}{9\pi} \alpha^6 m_e. \quad (10.107)$$

We shall now proceed to use these facts in our discussion of quarkonium.

The analogy with positronium has given rise to a non-relativistic potential model for quarkonium [62,63]. The model replaces photons by gluons and the electromagnetic fine structure constant by  $\alpha_s$  times colour factors. The system will be non-relativistic with the typical velocity  $v$  given by  $\alpha_s$  evaluated at a scale corresponding to the typical size of the bound state

$$v \sim \alpha_s(1/r^2), \quad r \sim \frac{1}{mv}. \quad (10.108)$$

Since the velocity  $v$  is larger than  $\alpha_s(m^2)$ , higher-order corrections to the non-relativistic approximation are potentially more important than

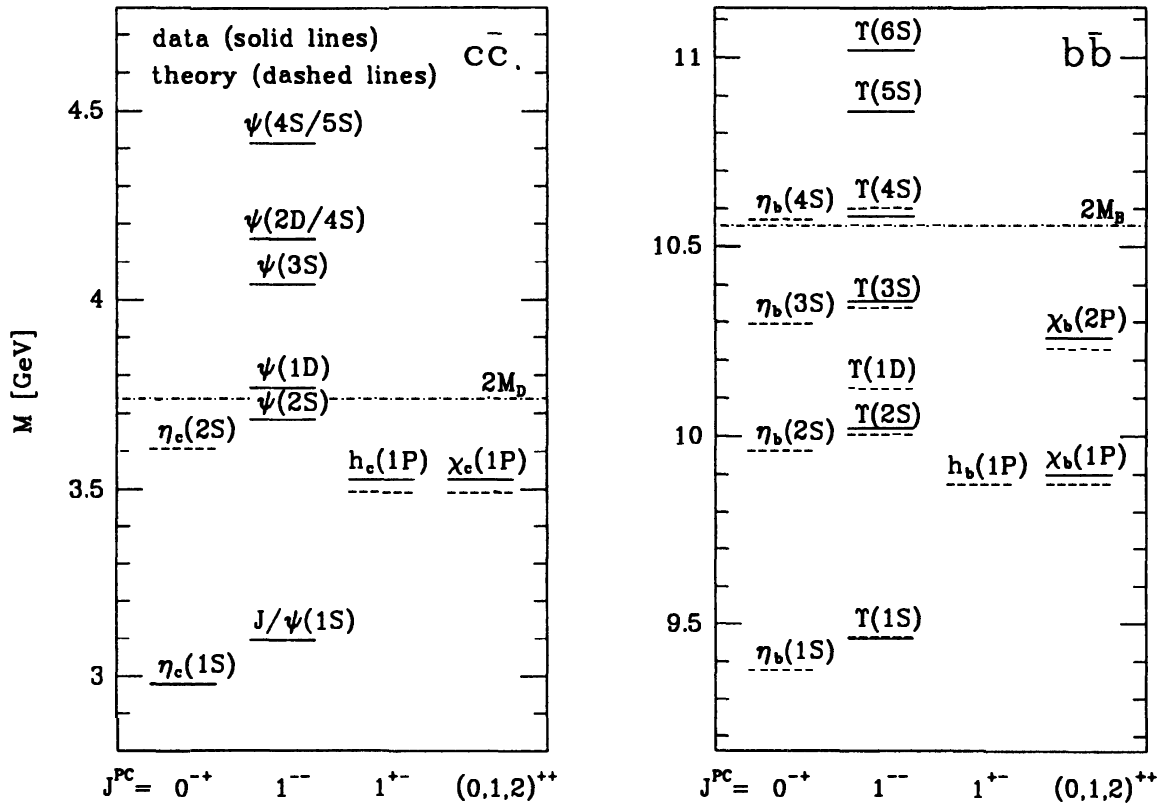


Fig. 10.29. Quarkonium spectra for charmonium and bottomonium.

higher-order perturbative corrections. Detailed results suggest that for the charmonium system  $v^2 \approx 0.23c^2$  and for bottomonium  $v^2 \approx 0.08c^2$ .

The measured states are denoted by solid lines in Fig. 10.29 which shows that the measured energy levels do not depend only on the principal quantum number,  $n$ . In particular, the  $2S$  and  $1P$  levels are split, whereas for a non-relativistic Coulombic system they would be expected to be degenerate, Eq. (10.100). Therefore a more general potential is required. This is not unexpected since the Bohr radius is of order  $a_0 \sim 1/(\alpha_s(1/r^2)\mu)$  which is too large to expect simple ideas based on one gluon exchange to apply. The spectra of charmonium and bottomonium are sensitive to the potential at radii between  $1/4 \text{ fm} < r < 1 \text{ fm}$ . The results of a calculation of the interquark potential using lattice QCD have been presented in Section 2.6.

A good description of the spectrum can be obtained using a potential which has an approximately Coulomb form at small distances,

$$V(r) \sim -\frac{4}{3} \frac{\alpha_s(1/r^2)}{r} \quad (10.109)$$

and is confining at large distances

$$V(r) \sim Kr \quad (10.110)$$

where  $K$  is the string tension.

This potential model is successful in describing the spectra of the charmonium and bottomonium states. Fig. 10.29 shows the measured spectra (solid lines) from [3] compared with the predictions [64] of the potential model (dashed lines) using a Buchmüller-Tye potential [65]. This potential satisfies the asymptotic properties specified in Eq. (10.109) and (10.110), but in addition includes the effects of two-loop running at small distances and an interpolation between the limits of small and large  $r$ .

### 10.7.2 Quarkonium decays

Generalizing Eqs. (10.107) to the case of decay to three gluons, we find in the non-relativistic potential model that the width of the  ${}^3S_1$  states,  $J/\psi$  and  $\Upsilon$ , is

$$\Gamma({}^3S_1 \rightarrow 3 \text{ gluons}) = \frac{5}{18} \frac{\alpha_s^3}{m^2} \frac{4(\pi^2 - 9)}{9\pi} |R_0(0)|^2, \quad (10.111)$$

where  $m$  is the mass of the quark. The extra colour factor with respect to Eq. (10.107) is given by

$$\frac{1}{3} \left[ \frac{1}{4} \text{Tr}\{t^A, \{t^B, t^C\}\} \right]^2 = \frac{5}{18}, \quad (10.112)$$

where Eq. (1.20) has been used in evaluating the anticommutators. The three gluons subsequently transform into light hadrons with unit probability, so Eq. (10.111) predicts the width of the  $J/\psi$  and  $\Upsilon$  into light hadrons. The corresponding formula for the  ${}^1S_0$  states,  $\eta_c$  and  $\eta_b$  is

$$\Gamma({}^1S_0 \rightarrow \text{hadrons}) = \frac{2}{3} \frac{\alpha_s^2}{m^2} |R_0(0)|^2 \quad (10.113)$$

where the colour factor is

$$\frac{1}{3} \left[ \frac{1}{2} \text{Tr}\{t^A, t^B\} \right]^2 = \frac{2}{3}. \quad (10.114)$$

Eqs. (10.113) and (10.115) lead to the prediction that the  $J/\psi$  should be narrower than the  $\eta_c$  by a factor of

$$\frac{\Gamma(J/\psi \rightarrow \text{light hadrons})}{\Gamma(\eta_c \rightarrow \text{light hadrons})} = \alpha_s \frac{5(\pi^2 - 9)}{27\pi}. \quad (10.115)$$

The wave function at the origin can be deduced from the leptonic width

$$\Gamma({}^3S_1 \rightarrow e^+ e^-) = \frac{\alpha^2 Q_f^2}{m^2} |R_0(0)|^2. \quad (10.116)$$

The above decay formulae are based on the non-relativistic potential model rather than being derived from QCD. The modern theory of

quarkonium production and decay [66] is based on a systematic approximation to the full QCD Lagrangian known as Non-Relativistic QCD, (NRQCD). Quarkonia are described in NRQCD in terms of a Fock state decomposition. Thus, for example, the wave function of an *S*-wave ortho-quarkonium vector meson may schematically be written as,

$$\begin{aligned} |\psi_Q\rangle = & O(1)|Q\bar{Q}[{}^3S_1^{(1)}]\rangle + O(v)|Q\bar{Q}[{}^3P_J^{(8)}]g\rangle + O(v^2)|Q\bar{Q}[{}^1S_0^{(8)}]g\rangle \\ & + O(v^2)|Q\bar{Q}[{}^3S_1^{(1,8)}]gg\rangle + O(v^2)|Q\bar{Q}[{}^3D_J^{(1,8)}]gg\rangle + \dots \end{aligned} \quad (10.117)$$

The spin, orbital and total angular momentum quantum numbers of the  $Q\bar{Q}$  pairs in each Fock component are indicated within the square brackets in spectroscopic notation. In each component of the wave function the  $Q\bar{Q}$  pair is either in a singlet or an octet state, denoted by the superscript in brackets. The lowest-order term in the velocity expansion corresponds to the wave function of the non-relativistic potential model and higher order terms correspond to Fock components having additional gluons. The order in the velocity expansion at which each of these Fock states participates in production or decay of the state  $\psi_Q$  is governed by simple NRQCD counting rules [66]. The consistent treatment of quarkonium decays requires a formalism which systematically includes all terms at a given order in the velocity  $v$ .

A complete treatment of the decays of quarkonium in NRQCD is beyond the scope of this book. We will discuss briefly when the non-relativistic potential model is expected to work and present the results of an analysis of *p*-wave decays in which it fails. The success of the potential model is based upon two facts. First, the dominant effect of the exchange of gluons is to produce an instantaneous interaction. Since the energy of the exchanged gluons is of order  $mv^2$  and their momentum of order  $mv$ , the typical interaction time  $\Delta t_I$  is less than the typical time associated with the interactions of the quarks

$$\Delta t_I \sim 1/(mv) \ll \Delta t_M \sim 1/(mv^2) . \quad (10.118)$$

Second, the probability of finding an extra gluon in the wave function is small, as shown in Eq. (10.117). Since these effects are suppressed by extra powers of the velocity they are relativistic corrections.

For *s*-wave decays the potential model is equivalent to NRQCD in the approximation in which only the leading terms are retained. In NRQCD, Eqs. (10.113,10.115) and (10.116) are correct if we neglect corrections of relative order  $v^2$ . The advantage of NRQCD for *s*-wave decays is that it provides a systematic method of including the relativistic corrections.

In the potential model the width for the *p*-wave decays is proportional to the derivative of the wave function at the origin, which is of order  $m^5v^5$ , as can be seen from Eq. (10.105). However in NRQCD a leading

contribution can also be obtained by taking an octet  $Q\bar{Q}$  component of the wave function, which also leads to a net contribution of order  $v^5$ . For the  $p$ -wave states the leading NRQCD results for the decay are [66]

$$\begin{aligned}\Gamma(^3P_0 \rightarrow \text{hadrons}) &= 6 \frac{\alpha_s^2}{m^4} |R'_1(0)|^2 + \frac{\alpha_s^2 \pi n_f}{3m^2} \langle \chi_{c0} | \mathcal{O}_8(^3S_1) | \chi_{c0} \rangle, \\ \Gamma(^3P_1 \rightarrow \text{hadrons}) &= \frac{\alpha_s^2 \pi n_f}{3m^2} \langle \chi_{c1} | \mathcal{O}_8(^3S_1) | \chi_{c1} \rangle, \\ \Gamma(^3P_2 \rightarrow \text{hadrons}) &= \frac{8}{5} \frac{\alpha_s^2}{m^4} |R'_1(0)|^2 + \frac{\alpha_s^2 \pi n_f}{3m^2} \langle \chi_{c2} | \mathcal{O}_8(^3S_1) | \chi_{c2} \rangle, \\ \Gamma(^1P_1 \rightarrow \text{hadrons}) &= \frac{\alpha_s^2 \pi (N^2 - 4)}{2Nm^2} \langle h_c | \mathcal{O}_8(^1S_0) | h_c \rangle.\end{aligned}\quad (10.119)$$

The above formulae are valid in order  $v^5$  and are subject to corrections of higher order in  $v$  and in  $\alpha_s$ . The symbol  $h_c$  ( $\chi_{cJ}$ ) denotes the wave function of the  $^1P_1$  ( $^3P_J$ ) state and  $\mathcal{O}_8(^1S_0)$  is an operator containing four heavy quark fields with both quark-antiquark pairs in a  $J = 0$ , colour octet state. Because of the necessity of retaining the colour octet component, the non-relativistic potential model fails to describe the complete leading term in  $P$ -state decays. Eqs. (10.119) contain four new unknown matrix elements which to leading order are related by heavy quark symmetry,

$$\langle \chi_{cJ} | \mathcal{O}_8(^3S_1) | \chi_{cJ} \rangle = \langle h_c | \mathcal{O}_8(^1S_0) | h_c \rangle (1 + O(v^2)), \quad J = 0, 1, 2. \quad (10.120)$$

As a result, at lowest order in  $v^2$ , only one non-perturbative matrix element is required, in addition to the derivative of the wave function at the origin which is already required in the non-relativistic potential model.

### 10.7.3 Quarkonium production

The production of muon pairs in hadronic collisions is of great importance because of the ease of triggering on a produced muon pair. Consequently there are many results on quarkonium production in hadronic reactions. Reviews of the data and the theory are contained in refs. [67,68]. The data come both from fixed-target experiments and from high-energy colliders. The new collider data provide information on the transverse momentum dependence of the cross section over a wide range of  $p_T$ .

Quarkonium production is also important because it is proposed as a signal for deconfinement in high-energy hadronic or nuclear collisions. For details and references to earlier literature we refer the reader to ref. [69]. After a high-energy collision, multiple interactions will thermalize the system leading to hot, strongly interacting matter. This matter can either be in a confined hadronic phase, or in a deconfined phase known as the

quark-gluon plasma. The production of quarkonium is one of the preferred places to look for evidence of the quark-gluon plasma. The idea is that, in the deconfined phase, the interquark potential will be screened, leading to a suppression of  $J/\psi$  production. Since the  $J/\psi$  has a small spatial dimension of order  $1/m$ , it emerges unscathed from the hadronic system if it is in the confined phase. Quarkonium production will therefore be sensitive to the partonic state of the medium at the moment of its creation. To calculate in detail how the observed rate of quarkonium production depends on the medium we need to understand the standard QCD production mechanisms.

The simplest diagrams which lead to the production of a  $Q\bar{Q}$  pair are the lowest-order diagrams shown in Fig. 10.8. However the quark-antiquark annihilation diagram produces a  $Q\bar{Q}$  pair in an octet state. The gluon-gluon fusion mechanism can produce a  $Q\bar{Q}$  pair in either a singlet or an octet state. The *colour evaporation model* assumes that the colour quantum numbers are adjusted by emitting a soft gluon at no cost in rate and with no dynamical effects [70]. Differential distributions for the production of a given quarkonium state are assumed to be proportional to the rate of production of heavy quarks in the appropriate mass range

$$\frac{d\sigma_H}{dx_F} = A_H \int_{2m}^{2m_D} dm_{Q\bar{Q}} \frac{d\sigma}{dm_{Q\bar{Q}} dx_F}. \quad (10.121)$$

$A_H$  is a constant independent of  $x_F$  which expresses the fact that only a fraction of the cross section in the appropriate mass range contributes to a given quarkonium state. There is little detailed theoretical justification for the colour evaporation model. Nevertheless, the model has had some success describing the  $x_F$  distributions and energy dependences of quarkonium production at fixed-target energies. It also predicts rather similar cross sections for  $J/\psi$ ,  $\psi'$  and  $\chi$  production at fixed-target energies, in accord with observations [67,71].

A more sophisticated approach is the *colour singlet model* in which the wave function of the  $Q\bar{Q}$  state is included and the number of gluons needed to arrive at a colour singlet is taken into account explicitly. At order  $\alpha_s^2$  the only diagram which can contribute is shown in Fig. 10.30(a). This diagram (with on-shell incoming gluons) cannot contribute to the production of a  $J = 1$  state. This is a consequence of Yang's theorem [74], which states that a spin-one particle cannot couple to two photons, generalized to the case of gluons. Fig. 10.30(a) is expected to be important at high energy because of the large flux of gluons [72]. The rate is calculated to be (see for example ref. [73])

$$\hat{\sigma}(gg \rightarrow {}^{2s+1}L_J) = \frac{\pi^2(2J+1)}{16m} \Gamma({}^{2s+1}L_J \rightarrow gg) \delta(\hat{s} - M^2), \quad (10.122)$$

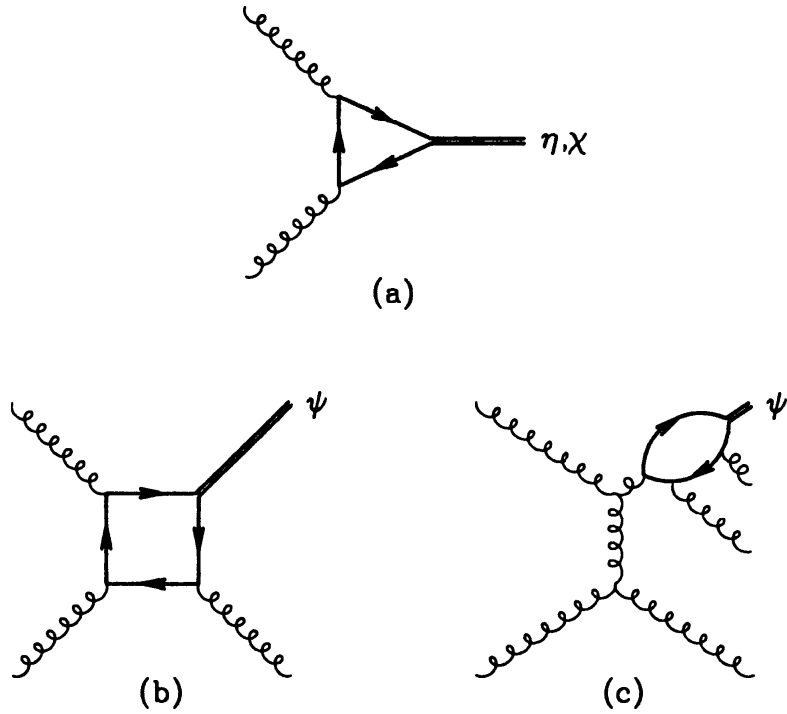


Fig. 10.30. Feynman diagrams in the colour singlet model.

where  $m$  is the mass of the quark and  $M \approx 2m$  is the mass of the  $Q\bar{Q}$  state.

From Eq. (10.113), the result in the non-relativistic potential model for production of the  ${}^1S_0$  state is therefore

$$\hat{\sigma}(gg \rightarrow \eta) = \frac{\pi^2 \alpha_s^2}{24 m^3} |R_0(0)|^2 \delta(\hat{s} - M^2). \quad (10.123)$$

This diagram can also contribute to the production of  $P$  states,  $\chi_0$  and  $\chi_2$ . From Eq. (10.119) we find that the partonic cross sections are given in the non-relativistic potential model by [75]

$$\hat{\sigma}(gg \rightarrow \chi_0) = \frac{3\pi^2 \alpha_s^2}{8m^5} |R'_1(0)|^2 \delta(\hat{s} - M^2), \quad (10.124)$$

$$\hat{\sigma}(gg \rightarrow \chi_2) = \frac{\pi^2 \alpha_s^2}{2m^5} |R'_1(0)|^2 \delta(\hat{s} - M^2). \quad (10.125)$$

The  $\chi$  states can decay to a final state containing a  $J/\psi$  and hence contribute to the observed signal for  $J/\psi$  production. In the colour singlet model the  $J/\psi$  and the  $\chi_1$  state can only be produced by higher-order diagrams and should therefore be smaller. This prediction is at variance with the data at fixed-target energies, where rather similar rates of  $J/\psi$  and  $\chi$  production are observed [67, 76].

In the light of the discussion given above for quarkonium decays, the colour singlet model should be considered to be superseded by NRQCD. The modern QCD description of quarkonium production in hadronic collisions is based on the idea of factorization [66], *i.e.* the separation of the

short and long distance pieces. Rather than discussing in detail the application of NRQCD to the total cross section we shall turn to the case of quarkonium production at large  $p_T$  which is of interest for the description of the most recent collider data [77].

In the colour singlet model at large  $p_T$  the diagrams of Fig. 10.30(b) and (c) contribute to  $J/\psi$  production [78,79]. Note however that the  $p_T$  dependences of the two diagrams is quite different. The diagram in Fig. 10.30(b) is of order  $\alpha_s^3$  but has two hard propagators in the amplitude and hence the cross section falls off like  $1/p_T^8$ . The diagram in Fig. 10.30(c) on the other hand is of  $O(\alpha_s^3)$  but leads to a cross section which falls off as  $1/p_T^4$ . In the latter diagram only the single exchanged gluon is forced far off mass shell at large  $p_T$ .

At large  $p_T$  the dominant contribution therefore comes from the diagram which describes the fragmentation of a gluon into a  $Q\bar{Q}$  pair. This fragmentation proceeds either via a colour singlet piece requiring the emission of two gluons as shown in Fig. 10.30(c) or via an octet component.

$$D(z, 2m) = d_1^{^3S_1}(z, 2m)\langle \mathcal{O}(^3S_1^{(1)}) \rangle + d_8^{^3S_1}(z, 2m)\langle \mathcal{O}(^3S_1^{(8)}) \rangle. \quad (10.126)$$

The short distance coefficient of the colour octet matrix element can be calculated from the Feynman diagram for  $g^* \rightarrow Q\bar{Q}$ . The result is [80,81],

$$d_8^{^3S_1}(z, 2m) = \frac{\alpha_s(4m^2)\pi}{24m^3}\delta(1-z). \quad (10.127)$$

The result for the colour singlet mechanism shown in Fig. 10.30(c) is given in [82,83]. Since it involves a  $Q\bar{Q}$  pair and two gluons in the final state it is more complicated than the expression in Eq. (10.127). The singlet matrix element in Eq. (10.126) can be determined by relating it to the wave function at the origin of the potential model

$$\langle 0 | \mathcal{O}(^3S_1^{(1)}) | 0 \rangle \approx \frac{3}{2\pi} |R_0(0)|^2, \quad (10.128)$$

where  $|R_0(0)|^2$  can be obtained from leptonic width, Eq. (10.116). Since  $|R_0(0)|^2$  is of order  $m^3 v^3$  the singlet piece leads to a contribution of order  $\alpha_s^3 v^3$ . The octet piece is of order  $\alpha_s v^7$ , where the suppression of four powers of  $v$  is due to the  $v^2$  suppression of the octet  $^3S_1$  piece in Eq. (10.117).

The relative numerical importance of the two mechanisms can be judged by examination of the first moment which can be calculated numerically. The total fragmentation probability is found to be [83]

$$\begin{aligned} \int_0^1 dz D(z, 2m) &= 8.28 \times 10^{-4} \frac{\alpha_s^3(4m^2)}{m^3} \langle \mathcal{O}(^3S_1^{(1)}) \rangle \\ &+ 1.31 \times 10^{-1} \frac{\alpha_s(4m^2)}{m^3} \langle \mathcal{O}(^3S_1^{(8)}) \rangle. \end{aligned} \quad (10.129)$$

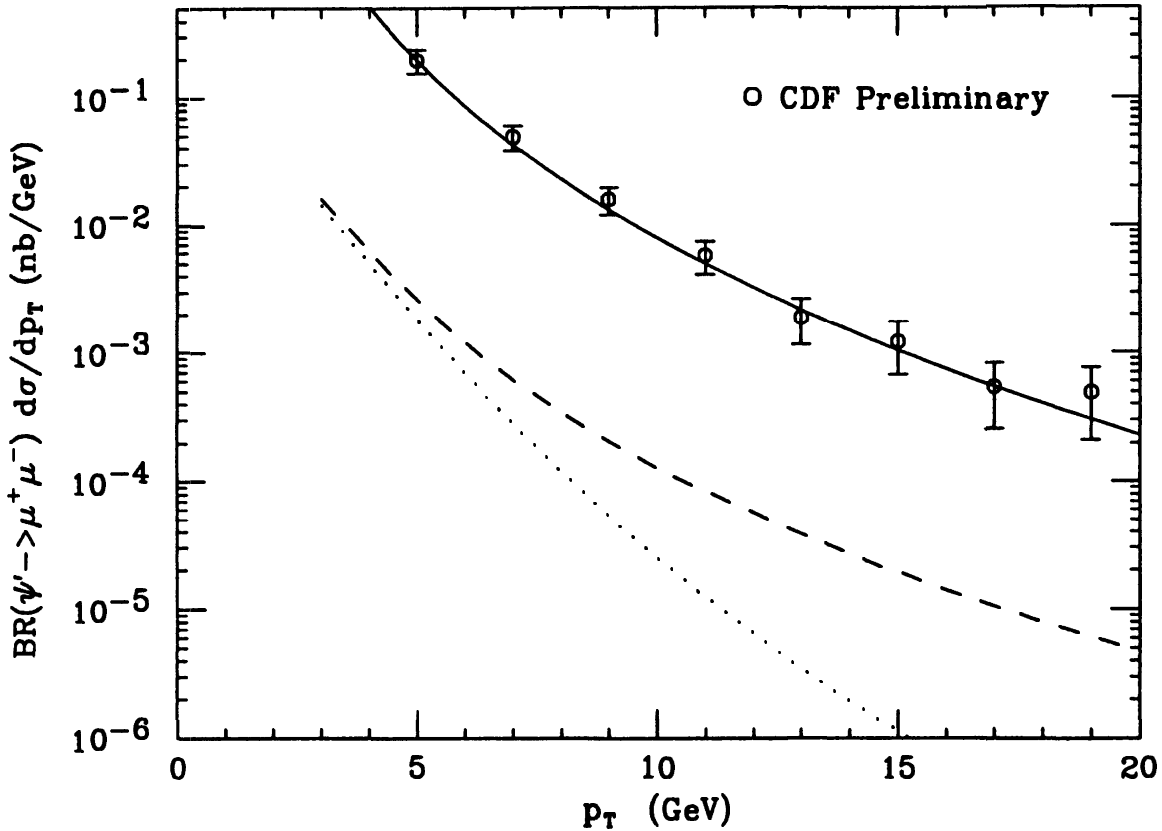


Fig. 10.31. Cross section for  $\psi'$  production with colour octet contribution adjusted to the data. Figure from ref. [81].

Fig. 10.31 shows the various contributions to  $\psi'$  production. For the  $\psi'$  the value of the singlet operator is found using Eq. (10.128) to be,

$$\langle 0 | \mathcal{O}(^3S_1^{(1)}) | 0 \rangle \approx 0.11 \text{ GeV}^3. \quad (10.130)$$

The total leading order contribution (dotted curve) and the total colour singlet fragmentation contribution (dashed curve) both lie below the CDF data, although the fragmentation contribution has the right slope in  $p_T$ . Good agreement is found by fitting the colour octet fragmentation term to the data. The value of the matrix element in Eq. (10.126) needed to fit the data is [81]

$$\langle 0 | \mathcal{O}(^3S_1^{(8)}) | 0 \rangle = 0.0042 \text{ GeV}^3 \quad (10.131)$$

which is consistent with a suppression of about  $O(v^4)$ . A full confirmation of this theory of quarkonium production will require comparison with the results from the  $\psi$  and  $\Upsilon$  systems and direct calculation of the non-perturbative matrix elements.

## References

- 1) H. Albrecht *et al.*, (ARGUS) *Phys. Lett.* **B255** (1991) 297;  
F. Bartelt *et al.*, (CLEO) *Phys. Rev. Lett.* **71** (1993) 4111.
- 2) B. Grinstein *et al.*, *Phys. Rev.* **D39** (1989) 799.
- 3) Particle Data Group, L. Montanet *et al.*, *Review of Particle Properties*, *Phys. Rev.* **D50** (1994) 1173.
- 4) P. Roudeau, Proc. XXVII Int. Conf. on High Energy Physics, Glasgow, July 1994, eds. P.J. Bussey and I.G. Knowles, Institute of Physics Publishing, Bristol (1995), Vol. I, p. 325.
- 5) Y. Nir, *Phys. Lett.* **B221** (1989) 184.
- 6) M. Athanas *et al.*, *Phys. Rev. Lett.* **73** (1994) 3503; *ibid.* **74** (1995) 3090 (erratum).
- 7) H. Schröder, *Rep. Prog. Phys.* **52** (1989) 765.
- 8) I. Bigi *et al.*, *Phys. Lett.* **B323** (1994) 408;  
G. Altarelli and S. Petrarca, *Phys. Lett.* **B261** (1991) 303.
- 9) *Future Electroweak Physics at the Fermilab Tevatron*, Report of the TeV2000 study group, Fermilab-Pub-96/046, eds. D. Amidei and R. Brock.
- 10) S. Glashow and E. Jenkins, *Phys. Lett.* **B196** (1987) 233.
- 11) V. Barger and R.J.N. Phillips, *Phys. Rev.* **D41** (1990) 884.
- 12) S. Glashow and S. Weinberg, *Phys. Rev.* **D15** (1977) 1958.
- 13) M. Gluck, J.F. Owens and E. Reya, *Phys. Rev.* **D17** (1978) 2324;  
B. Combridge, *Nucl. Phys.* **151** (1979) 429.
- 14) R.K. Ellis, *Strong Interactions and Gauge Theories*, edited by J. Tran Thanh Van, Editions Frontières, Gif-sur-Yvette, 1986, p. 339;  
R.K. Ellis, Proceedings of the 17th SLAC summer institute on particle physics, SLAC-REPORT-361, p. 45 (1989).
- 15) J.C. Collins, D.E. Soper and G. Sterman, *Nucl. Phys.* **B263** (1986) 37
- 16) S.J. Brodsky, J.C. Collins, S.D. Ellis, J.F. Gunion and A.H. Mueller, in *Proc. 1984 Summer Study on the Design and Utilization of the Superconducting Super Collider*, Fermilab, Batavia, Illinois, 1984, p. 227;  
S.J. Brodsky, J.F. Gunion and D.E. Soper, *Phys. Rev.* **D36** (1987) 2710.
- 17) P. Nason, S. Dawson and R.K. Ellis, *Nucl. Phys.* **B327** (1990) 49; *ibid.* **B335** (1990) 260 (erratum).
- 18) W. Beenakker *et al.*, *Nucl. Phys.* **B369** (1992) 543.
- 19) P. Nason, S. Dawson and R.K. Ellis, *Nucl. Phys.* **B303** (1988) 607.
- 20) W. Beenakker, H. Kuijf, W. van Neerven, J. Smith, *Phys. Rev.* **D40** (1989) 54.
- 21) G. Altarelli *et al.*, *Nucl. Phys.* **B308** (1988) 724.
- 22) S. Frixione *et al.*, *Nucl. Phys.* **B431** (1994) 453.
- 23) P. Harriman *et al.*, *Phys. Rev.* **D42** (1990) 798.
- 24) P.J. Sutton *et al.*, *Phys. Rev.* **D45** (1992) 2349.
- 25) R.K. Ellis and P. Nason, *Nucl. Phys.* **B312** (1989) 551.
- 26) E691 collaboration, J.C. Anjos *et al.*, *Phys. Rev. Lett.* **62** (1989) 513; *ibid.* **65** (1990) 2503.
- 27) NA14 collaboration, M.P. Alvarez *et al.*, *Zeit. Phys.* **C60** (1993) 53.
- 28) E687 collaboration, G. Bellini, Proceedings of 'Les Rencontres de Physique de la Vallée d'Aoste', La Thuile, 1994.
- 29) R.K. Ellis, Proc. XXIV Int. Conf. on High Energy Physics, Glasgow, August 1988, eds. R. Kotthaus and J.H. Kühn, Springer-Verlag (1988), p. 48.
- 30) S.P.K. Tavernier, *Rep. Prog. Phys.* **50** (1987) 1439.

- 31) H1 collaboration, S. Aid *et al.*, *Phys. Lett.* **B354** (1995) 494;  
ZEUS collaboration, M. Derrick *et al.*, *Phys. Lett.* **B345** (1995) 576.
- 32) UA1 collaboration, C. Albajar *et al.*, *Zeit. Phys.* **C61** (1994) 41.
- 33) CDF collaboration, F. Abe *et al.*, *Phys. Rev. Lett.* **68** (1992) 3403; *ibid.* **71** (1993) 500;  
*ibid.* **71** (1993) 2396; *ibid.* **71** (1993) 2537; *Phys. Rev.* **D50** (1994) 4252.
- 34) D0 collaboration, S. Abachi *et al.*, *Phys. Rev. Lett.* **74** (1995) 3548.
- 35) J.C. Collins and R.K. Ellis, *Nucl. Phys.* **B360** (1991) 3.
- 36) D. Schaile and P.M. Zerwas, *Phys. Rev.* **D45** (1992) 3262;  
S.L. Wu, Proceedings of the Lepton Photon Symposium, Hamburg, August 1987;  
W. Bartel *et al.*, *Phys. Lett.* **B146** (1984) 437.
- 37) D. Schaile, Proc. XXVII Int. Conf. on High Energy Physics, Glasgow, July 1994, eds.  
P.J. Bussey and I.G. Knowles, Institute of Physics Publishing, Bristol (1995), Vol. I,  
p. 27.
- 38) LEP electroweak working group, preprint CERN-PPE/95-172.
- 39) CDF collaboration, F. Abe *et al.*, *Phys. Rev. Lett.* **74** (1995) 2626.
- 40) D0 collaboration, S. Abachi *et al.*, *Phys. Rev. Lett.* **74** (1995) 2632.
- 41) A. Caner, Presented at 'Les Rencontres de Physique de la Vallée d'Aoste', March 1996.
- 42) M. Narain, Presented at 'Les Rencontres de Physique de la Vallée d'Aoste', March 1996.
- 43) V. Fadin, V. Khoze and T. Sjöstrand, *Zeit. Phys.* **C48** (1990) 613.
- 44) S. Catani *et al.*, *Phys. Lett.* **B378** (1996) 329.
- 45) R.K. Ellis, *Phys. Lett.* **B259** (1991) 492.
- 46) E. Laenen, J. Smith and W. van Neerven, *Phys. Lett.* **B321** (1994) 254.
- 47) E. Laenen, J. Smith and W. van Neerven, *Nucl. Phys.* **B369** (1992) 543.
- 48) R.K. Ellis, Proceedings of the 27th International Conference on High Energy Physics,  
Glasgow, (July 1994).
- 49) A.D. Martin, R.G. Roberts and W.J. Stirling, *Phys. Lett.* **B356** (1995) 89.
- 50) D. Bardin *et al.*, preprint CERN-TH 6443/92 (1992).
- 51) S. Eidelman and F. Jegerlehner, *Zeit. Phys.* **C67** (1995) 585.
- 52) CDF collaboration, preprint CDF/DOC/PUBLIC/3171;  
see also, 'Future Electroweak Physics at the Fermilab Tevatron, Report of the tev 2000  
Study Group', Fermilab-Pub-96/082 (1996).
- 53) S. Dawson, *Nucl. Phys.* **B249** (1985) 42;  
S. Willenbrock and D.A. Dicus, *Phys. Rev.* **D34** (1986) 155;  
S. Dawson and S. Willenbrock, *Nucl. Phys.* **B284** (1987) 449;  
C-P. Yuan, *Phys. Rev.* **D41** (1990) 42;  
S. Cortese and R. Petronzio, *Phys. Lett.* **B253** (1991) 494;  
R.K. Ellis and S. Parke, *Phys. Rev.* **D46** (1992) 3785;  
G. Bordes and B. van Eijk, *Zeit. Phys.* **C57** (1993) 81; *Nucl. Phys.* **B435** (1995) 23.
- 54) C. Peterson *et al.*, *Phys. Rev.* **D27** (1983) 105.
- 55) A.H. Mueller and P. Nason, *Phys. Lett.* **B157** (1985) 226.
- 56) A. Bassetto, M. Ciafaloni and G. Marchesini, *Phys. Rep.* **100** (1983) 201 and references  
therein.
- 57) M.L. Mangano and P. Nason, *Phys. Lett.* **B285** (1992) 160.
- 58) M.H. Seymour, *Zeit. Phys.* **C63** (1994) 99, *Nucl. Phys.* **B436** (1995) 163.
- 59) OPAL collaboration, R. Akers *et al.*, *Phys. Lett.* **B353** (1995) 595.
- 60) J.J. Aubert *et al.*, *Phys. Rev. Lett.* **33** (1974) 1404;  
J.-E. Augustin *et al.*, *Phys. Rev. Lett.* **33** (1974) 1406.
- 61) S.W. Herb *et al.*, *Phys. Rev. Lett.* **39** (1977) 252.
- 62) T. Appelquist and H.D. Politzer, *Phys. Rev. Lett.* **34** (1975) 43.

- 63) E.J. Eichten *et al.*, *Phys. Rev. Lett.* **34** (1975) 369.
- 64) E.J. Eichten and C. Quigg, *Phys. Rev.* **D49** (1994) 5845.
- 65) W. Buchmüller and S-H.H. Tye, *Phys. Rev.* **D24** (1981) 132.
- 66) G.T. Bodwin, E. Braaten and G.P. Lepage, *Phys. Rev.* **D51** (1995) 1125.
- 67) G. Schuler, preprint CERN-TH-7170-94 (1994).
- 68) E. Braaten, S. Fleming, T.C. Yuan, Ohio State preprint OHSTPY-HEP-T-96-001 (1996), submitted to *Ann. Rev. Nucl. Part. Sci.*.
- 69) H. Satz, *Nucl. Phys.* **A590** (1995) 63.
- 70) H. Fritzsch, *Phys. Lett.* **B67** (1977) 217;  
M. Glück, J.F. Owens and E. Reya, *Phys. Rev.* **D18** (1977) 162;  
J. Babcock, D. Sivers and S. Wolfram, *Phys. Rev.* **D18** (1978) 162.
- 71) M.L. Mangano, Proceedings of the Xth Topical Workshop on  $p\bar{p}$  Collider Physics, preprint CERN-TH/95-190 (1995).
- 72) S.D. Ellis and M. Einhorn, *Phys. Rev. Lett.* **34** (1975) 1190.
- 73) R. Gastmans and T.T. Wu, *The ubiquitous photon*, Oxford University Press (1990).
- 74) C.N. Yang, *Phys. Rev.* **77** (1950) 242.
- 75) R. Barbieri, R. Gatto and R. Kögerler, *Phys. Lett.* **B60** (1976) 183.
- 76) R. Gavai *et al.*, *Intl. J. Mod. Phys.* **A10** (1995) 3043.
- 77) CDF collaboration, F. Abe *et al.*, *Phys. Rev. Lett.* **69** (1992) 3704;  
K. Byrum, Proc. XXVII Int. Conf. on High Energy Physics, Glasgow, July 1994, eds. P.J. Bussey and I.G. Knowles, Institute of Physics Publishing, Bristol (1995), Vol. II, p. 989; Fermilab-Conf-94/136.
- 78) E.L. Berger and D. Jones, *Phys. Rev.* **D23** (1981) 1521;  
R. Baier and R. Rückl, *Zeit. Phys.* **C19** (1983) 251.
- 79) E. Braaten *et al.*, *Phys. Lett.* **B333** (1994) 548;  
D.P. Roy and K. Sridhar, *Phys. Lett.* **B339** (1994) 141;  
M. Cacciari and M. Greco, *Phys. Rev. Lett.* **73** (1994) 1586.
- 80) E. Braaten and T.C. Yuan, *Phys. Rev.* **D50** (1994) 3176.
- 81) E. Braaten and S. Fleming, *Phys. Rev. Lett.* **74** (1995) 3327.
- 82) E. Braaten and T.C. Yuan, *Phys. Rev. Lett.* **71** (1993) 1673.
- 83) E. Braaten and T.C. Yuan, *Phys. Rev.* **D52** (1995) 6627.

# 11

## Higgs bosons at high-energy colliders

In this chapter we will discuss how Higgs bosons can be produced and detected in high-energy hadron-hadron and  $e^+e^-$  collisions. The Higgs boson is a fundamental component of the Standard Model, and its discovery presents one of the most important challenges to present and future experimental high-energy physics. The LEP electron-positron collider provides the ideal environment for searching for a Higgs boson with a mass of less than 100 GeV. Indeed current experiments rule out a Higgs with a mass lighter than about 65 GeV. For more massive Higgs bosons, the focus of attention shifts to higher-energy colliders, in particular the Large Hadron Collider (LHC) at CERN, where  $pp$  collisions will be studied at  $\sqrt{s} = 14$  TeV. The phenomenology of Higgs searches at the LHC will be described in this chapter.

The basic properties of the Standard Model Higgs boson have already been described in Chapter 8. Since the methods for detecting the Higgs boson depend crucially on the various decay channels which are available for a given mass, these will be discussed in some detail below. We will then describe the relevant production mechanisms and corresponding cross sections at the LHC, and discuss the most important background processes. We are mainly concerned here with the minimal Standard Model which has a single Higgs boson, although many of the remarks also apply to more complicated models. A comprehensive review of all aspects of Higgs boson physics in the Standard Model and in more complicated extensions can be found in ref. [1]. At the end of this chapter we mention briefly some aspects of Higgs boson production in supersymmetric extensions of the Standard Model.

### 11.1 Higgs mass constraints

Higgs boson phenomenology is the study of the various ways in which the particle can be identified experimentally. It is a subject which has received an enormous amount of interest, principally in connection with proposals to build new high-energy colliders. One of the main difficulties is that the arbitrariness of the mass leads *a priori* to a proliferation of different production and decay scenarios — from low-energy nuclear physics to the very highest-energy hadron colliders. However, the situation has been significantly clarified by recent experimental lower bounds on the Higgs mass from LEP. From the absence of any signal from the process  $e^+e^- \rightarrow Z^*H \rightarrow f\bar{f}H$  [2], the limit

$$M_H > 65.2 \text{ GeV} \quad (95\% \text{ c.l.}) \quad (11.1)$$

has been derived [3].

There are, in addition, some theoretical arguments which suggest that the Higgs mass cannot be too large. As discussed in Section 8.5, when the Higgs mass increases the amplitude for  $WW$  scattering via Higgs exchange becomes large, and the contribution from the lowest-order diagrams exceeds the unitarity limit unless

$$M_H < \left( \frac{8\sqrt{2}\pi}{3G_F} \right)^{\frac{1}{2}} \approx 1 \text{ TeV}. \quad (11.2)$$

This is not, however, a rigorous limit — it merely states that the  $W$  sector becomes strongly interacting at this scale. It is *perturbative* unitarity, rather than unitarity itself, that breaks down. Nevertheless, it is true that very massive Higgs bosons are not narrow resonant states, and therefore their detection in invariant mass distributions becomes difficult.

Other tentative limits on  $M_H$  come from consideration of the renormalized  $\lambda$  parameter which appears in the Higgs potential, Eq. (8.15). Like all couplings in the theory, this parameter ‘runs’ with the renormalization scale  $\mu$ . Explicit calculation gives

$$\frac{\partial \lambda}{\partial \ln \mu} = \frac{3}{2\pi^2} [\lambda^2 + \frac{1}{2}g_t^2\lambda - \frac{1}{4}g_t^4 + \dots], \quad (11.3)$$

where  $g_t$  is the Higgs-top-quark Yukawa coupling (see Section 8.3.2),

$$g_t^2 = \frac{2m_t^2}{v^2} = 2\sqrt{2}G_F m_t^2. \quad (11.4)$$

On the right-hand side of Eq. (11.3) we have displayed three potentially important contributions. The first term dominates the evolution of  $\lambda$

when the parameter is large, and the solution is

$$\lambda(\mu) = \frac{\lambda(v)}{1 - \frac{3\lambda(v)}{2\pi} \ln \left( \frac{\mu}{v} \right)}, \quad (11.5)$$

with  $v = 246$  GeV. Note that the coupling increases with the scale and eventually a singularity (the Landau pole) is reached. If this singularity is to be avoided before some new physics scale  $\Lambda$  (for example, the Planck scale or the scale of some grand unification) is reached, then the coupling at low energy ( $\lambda(v)$ ) cannot be too large. This in turn translates, via Eq. (8.36), into an upper limit on the Higgs mass. In particular, for  $\Lambda = \Lambda_{\text{planck}}$  we find  $M_H < 175$  GeV, but the limit increases as  $\Lambda$  decreases. For example, if new physics sets in at the  $O(1$  TeV) scale then the upper limit on the Higgs mass is of the same order.

For a light Higgs boson, the top-quark Yukawa coupling ( $g_t$ ) terms in Eq. (11.3) become important. If  $g_t^2$  is large compared to  $\lambda$ , these contributions can change the sign of the right-hand side, thus driving  $\lambda$  to negative values. If this happens, the potential of Eq. (8.15) is no longer bounded from below, and the Higgs vacuum becomes unstable. The avoidance of this can be translated into a *lower* limit on the Higgs mass which depends on  $m_t$  and is given approximately by [4]

$$M_H > 2(m_t - 110 \text{ GeV}), \quad (11.6)$$

for top masses in a range consistent with the direct Tevatron measurements (see Chapter 10), and assuming no new physics below the Planck scale.

Further experimental information on  $M_H$  can also be obtained from electroweak radiative corrections. As an example, consider the one-loop radiative corrections to the tree-level expression which relates  $M_W$  to the fundamental parameters ( $\alpha, G_F, M_Z$ ):

$$1 - \frac{M_W^2}{M_Z^2} = \frac{1}{2} \left[ 1 - \left( 1 - \frac{4\pi\alpha}{\sqrt{2}G_F M_Z^2(1 - \Delta r)} \right)^{\frac{1}{2}} \right]. \quad (11.7)$$

An explicit calculation gives [5] (see also Section 8.2.2)

$$\Delta r \simeq \Delta\alpha + \frac{G_F}{8\sqrt{2}\pi^2} \left[ -3\cot^2\theta_W m_t^2 + \frac{11}{3} M_W^2 \ln \frac{M_H^2}{M_W^2} \right] + \dots, \quad (11.8)$$

where  $\dots$  denotes numerically less important contributions. The first term on the right-hand side,  $\Delta\alpha \simeq 1 - \alpha/\alpha(M_Z^2) \approx 0.06$ , comes from the running of the electromagnetic coupling constant. The second term comes from loop corrections involving the top quark and the Higgs boson. For given input values of  $\alpha, G_F$  and  $M_Z$ , a precise measurement of  $M_W$  (see for example Section 9.4.3) can therefore yield information on

$m_t$  (quadratic dependence) and to a lesser extent on  $M_H$  (logarithmic dependence). There are many other quantities (partial  $Z$  decay widths,  $Z$  decay asymmetries, neutrino scattering cross sections, etc.) which can be analysed in a similar way, and the most precise information comes from global fits to *all* such measurements, with  $M_H$  an unknown parameter to be fitted. Unfortunately, with the errors on the measured value of  $m_t$  still quite large at present (see Chapter 10), the information that can be extracted on  $M_H$  by this method is not yet statistically significant, although there does not appear to be any conflict with the other experimental and theoretical limits discussed above.

## 11.2 Decay channels and branching ratios

In order to devise search strategies for the Higgs boson, it is important to know the dominant decay channels for different Higgs boson masses. The ‘leading-order’ partial decay widths are readily obtained using the Feynman rules of Figs. 8.5 and 8.2.

$$\begin{aligned}\Gamma(H \rightarrow f\bar{f}) &= \frac{CG_F m_f^2 M_H}{4\pi\sqrt{2}} \left(1 - \frac{4m_f^2}{M_H^2}\right)^{\frac{3}{2}}, \\ \Gamma(H \rightarrow W^+W^-) &= \frac{G_F M_H^3}{8\pi\sqrt{2}} \left(1 - \frac{4M_W^2}{M_H^2}\right)^{\frac{1}{2}} \left(1 - \frac{4M_W^2}{M_H^2} + \frac{12M_W^4}{M_H^4}\right), \\ \Gamma(H \rightarrow ZZ) &= \frac{G_F M_H^3 M_W^2}{16\pi\sqrt{2}M_Z^2} \left(1 - \frac{4M_Z^2}{M_H^2}\right)^{\frac{1}{2}} \left(1 - \frac{4M_Z^2}{M_H^2} + \frac{12M_Z^4}{M_H^4}\right).\end{aligned}\tag{11.9}$$

where  $C$  is a colour multiplicity factor:  $C = 3$  for quarks and  $C = 1$  for leptons. The  $H \rightarrow W^+W^-$  width was derived explicitly in Section 8.2.1. The calculation of the  $H \rightarrow ZZ$  width is very similar, the main difference being an overall symmetry factor of one half for identical bosons. Note that the results in (11.9) are only valid *above* the two-particle threshold in each case. Especially for the  $W^+W^-$  and  $ZZ$ , decays which occur *below threshold*, where at least one of the final-state bosons is off mass-shell, can be important phenomenologically, see Fig. 11.1 below.

The  $H \rightarrow q\bar{q}$  decay widths have higher-order perturbative QCD corrections, and these are particularly important for the  $H \rightarrow b\bar{b}$  decay which dominates over a wide range of (light) Higgs masses. The main effect is to cause the quark mass  $m_q(\mu^2)$  to run from its ‘constituent quark’ value at  $\mu \sim m_q$  to a lower value at  $\mu \sim M_H$ , as described in Section 2.4. Since the decay width is proportional to  $m_q^2$ , this can have a significant effect on the numerical value of the decay width. Once the quark mass is replaced by its renormalized running value, the remaining perturbative corrections

are quite small.

We illustrate the above discussion for the  $H \rightarrow b\bar{b}$  decay width, which has been calculated to  $O(\alpha_s^2)$  [6]. The result is, in the  $\overline{\text{MS}}$  scheme,

$$\begin{aligned}\Gamma(H \rightarrow b\bar{b}) &= \frac{3\sqrt{2}}{8\pi} G_F M_H \bar{m}_b^2(M_H^2) \left(1 - \frac{4\bar{m}_b^2(M_H^2)}{M_H^2}\right)^{\frac{3}{2}} \\ &\times [1 + 1.803 \alpha_s(M_H^2) + 2.953 \alpha_s^2(M_H^2) + O(\alpha_s^3)] \\ &\times \left[1 + O\left(\frac{\bar{m}_b^2(M_H^2)}{M_H^2}\right)\right],\end{aligned}\quad (11.10)$$

where the running  $b$  quark mass for five flavours is given by, (cf. Eq. (2.34))

$$\begin{aligned}\bar{m}_b(M_H^2) &= \hat{m}_b [\alpha_s(M_H^2)]^{\frac{12}{23}} \\ &\times [1 + 0.3742 \alpha_s(M_H^2) + 0.1521 \alpha_s^2(M_H^2) + O(\alpha_s^3)].\end{aligned}\quad (11.11)$$

The numerical value of the integration constant  $\hat{m}_b$  is 9.13 GeV, assuming  $\Lambda_{\overline{\text{MS}}}^{(5)} = 150$  MeV and requiring  $\bar{m}_b(m_b^2) = m_b = 4.25$  GeV. The suppression of the partial width induced by the running  $b$  quark mass is significant not because the exact value for the decay rate into  $b\bar{b}$  is important *per se*, but rather because it can affect the branching ratios of rarer decay modes (see below). In particular we find that the  $H \rightarrow \gamma\gamma$  branching ratio, which is relevant for the light Higgs search at the LHC, is approximately a factor of two *higher* than the value obtained assuming a fixed  $b$  quark mass. This enhancement comes simply from the factor  $\bar{m}_b^2(M_H^2) = (150 \text{ GeV})^2 / \bar{m}_b^2(m_b^2) \simeq 0.47$  which reduces the  $H \rightarrow b\bar{b}$  partial width when the running mass is taken into account.

In addition to the ‘leading-order’ decay channels of (11.9), certain rare decay channels which appear beyond leading order can be of phenomenological importance. An example is the  $H \rightarrow \gamma\gamma$  decay, which is mediated by intermediate  $W$  and quark triangle loops:

$$\Gamma(H \rightarrow \gamma\gamma) = \frac{\alpha^2 G_F M_H^3}{128\sqrt{2}\pi^3} \left| \sum_q 3e_q^2 I_q \left( \frac{m_q^2}{M_H^2} \right) + I_W \left( \frac{M_W^2}{M_H^2} \right) \right|^2,\quad (11.12)$$

where  $I_q$  and  $I_W$  are dimensionless functions given by

$$\begin{aligned}I_q(x) &= 4x[2 + (4x - 1)F(x)] \\ I_W(x) &= -2[6x + 1 + 6x(2x - 1)F(x)] \\ F(x) &= \theta(1 - 4x) \frac{1}{2} \left[ \ln \left( \frac{1 + \sqrt{1 - 4x}}{1 - \sqrt{1 - 4x}} \right) - i\pi \right]^2 \\ &\quad - \theta(4x - 1) 2 [\sin^{-1}(1/2\sqrt{x})]^2.\end{aligned}\quad (11.13)$$

The perturbative QCD corrections to the quark-loop part of (11.12) have been calculated and found to be numerically small [7].

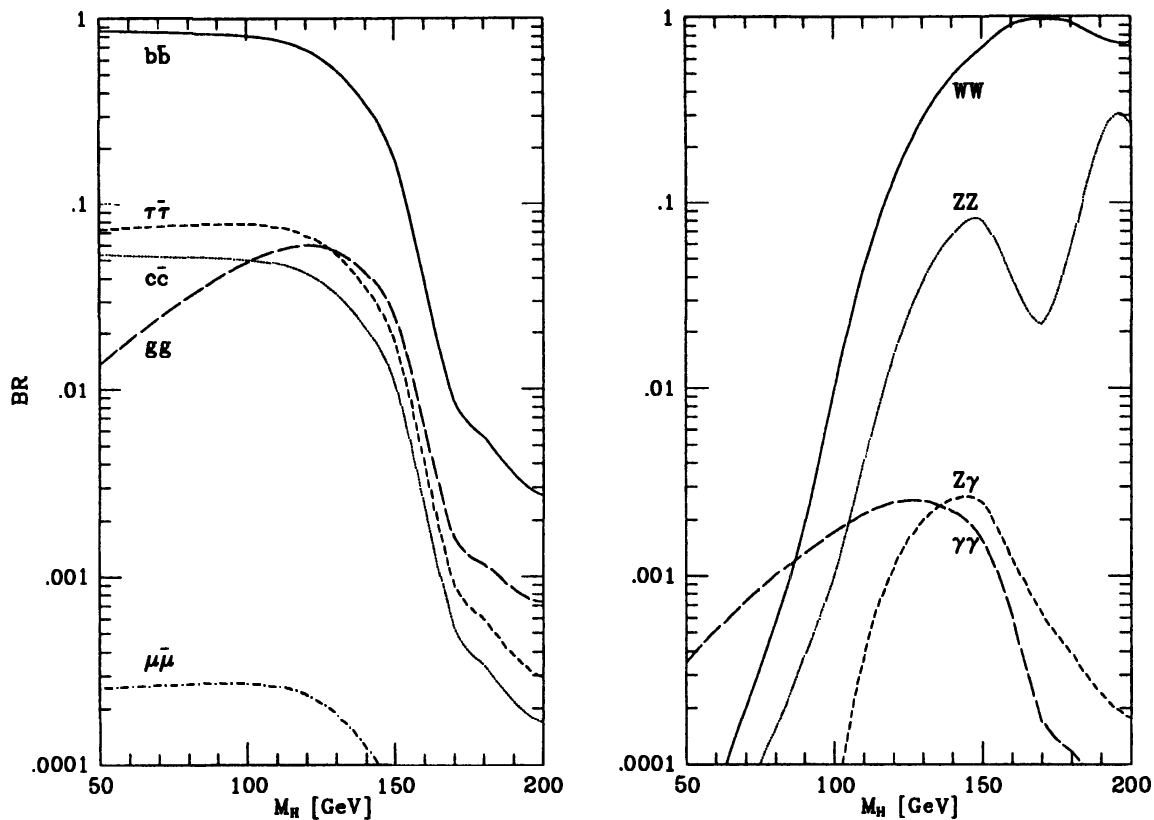


Fig. 11.1. Branching ratios of the light Standard Model Higgs boson.

The complete set of phenomenologically relevant Higgs branching ratios is shown as a function of  $M_H$  (for  $m_t = 175$  GeV) in Figs. 11.1 and 11.2, corresponding to light and heavy Higgs bosons respectively [8]. Far below the  $WW$  threshold the  $H \rightarrow b\bar{b}$  decay is dominant. This is an important signature for searches at LEP2 (see below). The next largest decay mode for a light Higgs boson is  $\tau^+\tau^-$ , with a branching ratio suppressed by a factor of  $3(m_b^2/m_\tau^2)$ . As the nominal  $W^+W^-$  threshold at  $M_H = 2M_W$  is approached from below, the off-shell  $H \rightarrow W^+W^-$ ,  $ZZ$  decays begin to dominate the decay width.

As shown in Fig. 11.2, above the  $WW$  threshold the Higgs boson decays predominantly into  $W^+W^-$  and  $ZZ$  pairs. Away from the thresholds, the branching ratios are approximately in the ratio 2:1, Eq. (11.9). The  $H \rightarrow t\bar{t}$  branching ratio is always smaller than these. Notice the dip in the  $W^+W^-$ ,  $ZZ$  branching ratios around the  $t\bar{t}$  threshold. Of course the  $W$  and  $Z$  bosons into which the Higgs boson decays are themselves unstable, and so the actual final states consist of leptons and quark jets. Table 11.1 gives the branching ratios for the various channels, for  $M_H = 500$  GeV. Final states containing hadronic jets have large backgrounds at hadron colliders. A large fraction of the decays are therefore not useful, and it is the much rarer purely leptonic final states that yield the main hope for

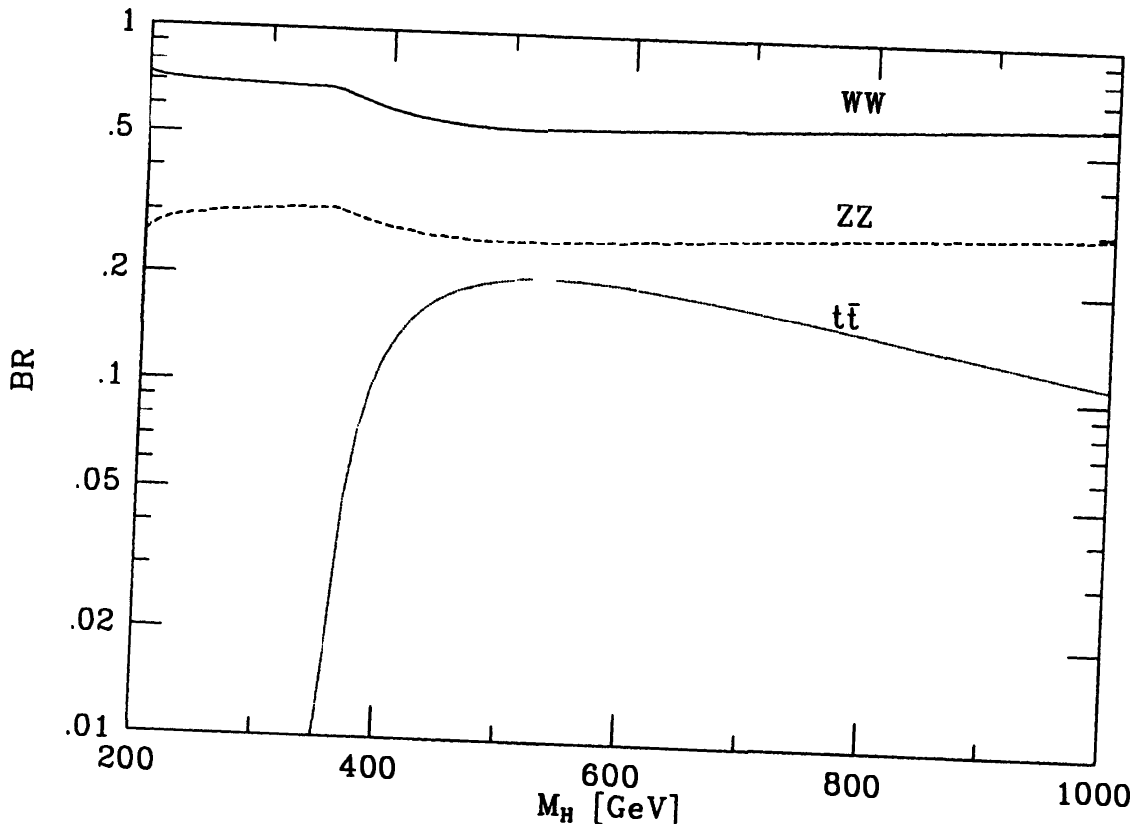


Fig. 11.2. Branching ratios of the heavy Standard Model Higgs boson. The top quark mass is 175 GeV.

discovery.

A final property of the Higgs boson which is important for hadron-collider phenomenology is the fact, already evident in Eq. (11.9), that the total Higgs boson decay width grows rapidly with  $M_H$  to become comparable with the mass at around 1.7 TeV. This is illustrated in Fig. 11.3, which shows  $\Gamma_H$  as a function of  $M_H$  for  $m_t = 175$  GeV.

### 11.3 Higgs search at LEP2

We have already noted that the current experimental lower limit on the Higgs mass comes from the LEP  $e^+e^-$  collider, via the process  $e^+e^- \rightarrow Z \rightarrow Z^*H \rightarrow f\bar{f}H$ . The LEP2 collider, with centre-of-mass energies up to  $O(200)$  GeV, extends the search to higher masses [9]. For  $\sqrt{s} > M_H + M_Z$  the final-state  $Z$  boson can be produced on mass-shell, and the cross section is

$$\sigma(e^+e^- \rightarrow ZH) = \frac{(G_F M_Z^2)^2}{3\pi} (V_e^2 + A_e^2) \frac{p}{\sqrt{s}} \frac{3M_Z^2 + p^2}{(s - M_Z^2)^2}, \quad (11.14)$$

channel	$W^+W^-$	$ZZ$	$t\bar{t}$
4 jets	24.6	12.6	
2 jets + $l\nu$	23.7		
$l^+\nu l^-\bar{\nu}$	5.7		
2 jets + $l^+l^-$		3.6	
2 jets + $\nu\bar{\nu}$		7.3	
$l^+l^-l^+l^-$		0.3	
$l^+l^-\nu\bar{\nu}$		1.1	
$\nu\bar{\nu}\nu\bar{\nu}$		1.1	
6 jets			9.1
4 jets + $l\nu$			8.8
2 jets + $l^+\nu l^-\bar{\nu}$			2.1

Table 11.1. Branching ratios (in %) of a  $M_H = 500$  GeV Higgs boson decaying into quark and lepton ( $l = e, \mu, \tau$ ) final states.

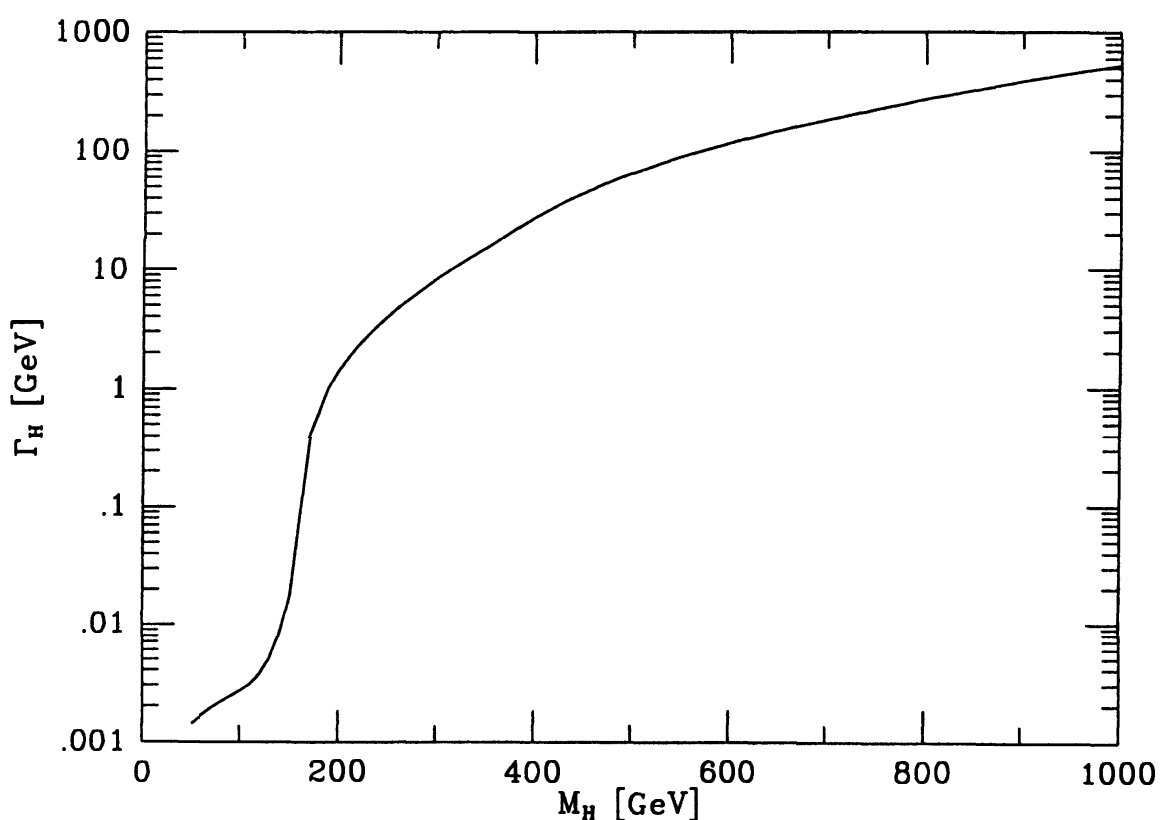


Fig. 11.3. The total Higgs decay width, for  $m_t = 175$  GeV.

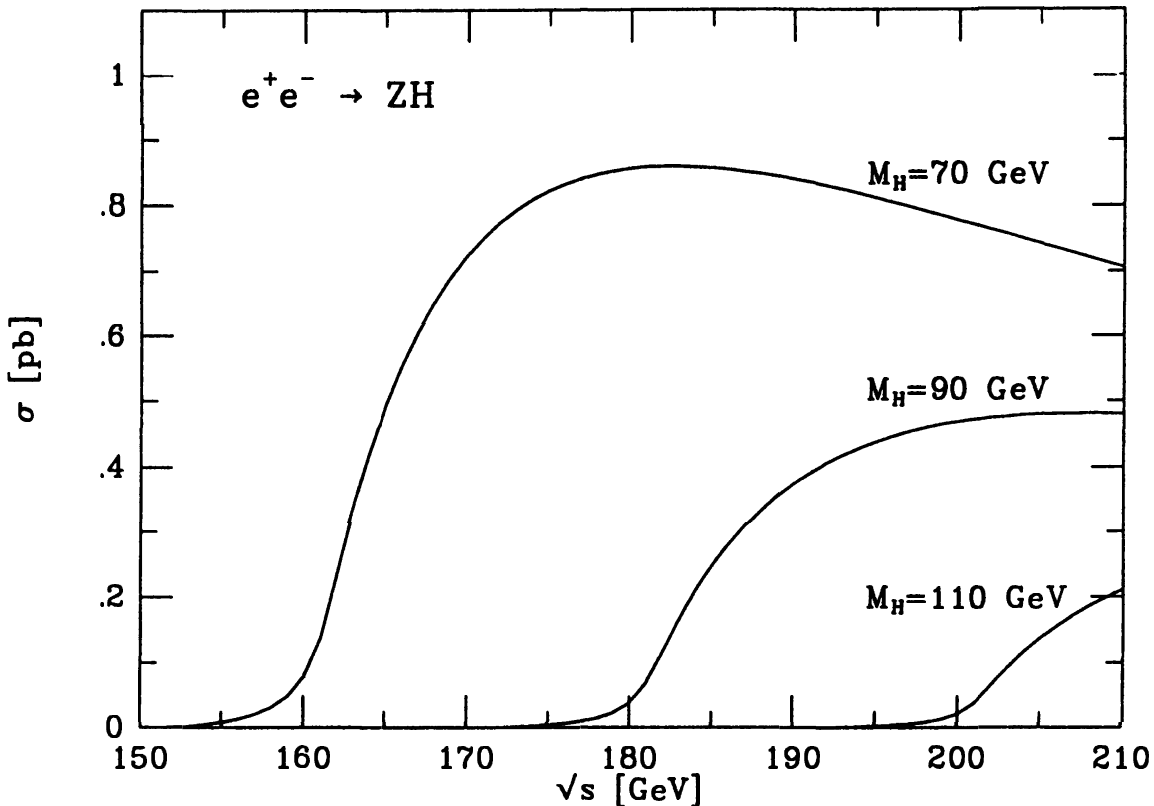


Fig. 11.4. Cross section for  $ZH$  production at LEP2.

where

$$p^2 = \frac{1}{4s} (s^2 + M_Z^4 + M_H^4 - 2sM_Z^2 - 2sM_H^2 - 2M_Z^2M_H^2) . \quad (11.15)$$

Fig. 11.4 shows this cross section as a function of  $\sqrt{s}$  for three different values of  $M_H$ . In the mass range relevant to LEP2 the Higgs decays predominantly to  $b\bar{b}$  (Fig. 11.1). Final states such as  $ZH \rightarrow \mu^+\mu^-b\bar{b}$  provide a particularly clean signature. Backgrounds from  $ZZ$  and  $W^+W^-$  production do not pose any serious problems, unless  $M_H \simeq M_Z$  when  $ZZ \rightarrow \mu^+\mu^-b\bar{b}$  can mask the Higgs signal. Even here, the ability to identify  $b$  quarks using vertex detectors allows Higgs production to be distinguished. (Recall that  $BR(Z \rightarrow b\bar{b}) \approx 0.15$  whereas  $BR(H \rightarrow b\bar{b}) \approx 0.83$  for  $M_H \simeq M_Z$ .) As a result, the Higgs boson can be discovered up to near the kinematic limit. Detailed studies [9] show that the discovery limit is approximately

$$M_H < \sqrt{s} - 97 \text{ GeV} , \quad (11.16)$$

the exact limit depending slightly on the available luminosity.

## 11.4 Higgs production at the LHC

### 11.4.1 Production mechanisms

In this section we consider the important Higgs production mechanisms at high-energy hadron colliders, in particular for the LHC proton-proton collider with  $\sqrt{s} = 14$  TeV. The overall picture is in fact quite simple — light Higgs bosons are copiously produced but suffer from severe backgrounds, while heavier Higgs bosons have smaller production cross sections with more manageable backgrounds.

There are only a limited number of production mechanisms which give cross sections large enough to be relevant at the LHC. Each makes use of the Higgs boson's preference to couple to heavy particles:

- (a) gluon-gluon fusion:  $gg \rightarrow H$ ,
- (b) vector boson fusion:  $qq \rightarrow Hqq$  via  $W^+W^-$ ,  $ZZ \rightarrow H$ ,
- (c) associated production with vector bosons:  $q\bar{q} \rightarrow WH$ ,  $ZH$ ,
- (d) associated production with top quarks:  $gg, q\bar{q} \rightarrow t\bar{t}H$ .

The leading-order Feynman diagrams for these are shown in Fig. 11.5, and each is discussed in turn below. In the cross section calculations described in the following sections, the MRS(A) parton distributions [10], defined in the  $\overline{\text{MS}}$  scheme with  $\Lambda_{\overline{\text{MS}}}^{(4)} = 230$  MeV, are used. The sensitivity of the cross sections to the choice of parton distributions is briefly discussed in Section 11.4.6.

### 11.4.2 Gluon-gluon fusion

Except possibly for very heavy Higgs bosons, the dominant production mechanism is  $gg \rightarrow H$ , via an intermediate top quark loop, Fig. 11.5(a). The matrix element summed and averaged over spins and colours is [11]

$$|\mathcal{M}(gg \rightarrow H)|^2 = \frac{\alpha_s^2(M_H^2)G_F M_H^4}{288\sqrt{2}\pi^2} \left| I\left(\frac{m_t^2}{M_H^2}\right) \right|^2, \quad (11.17)$$

where  $I(x)$  is a dimensionless function given by

$$I(x) = 3x[2 + (4x - 1)F(x)]. \quad (11.18)$$

The function  $F(x)$  is defined in Eq. (11.13). The factor  $|I(x)|^2$  vanishes as  $x \rightarrow 0$ , attains a maximum value of about 3.3 at  $x \sim 0.2$  and then decreases to unity as  $x \rightarrow \infty$ . A reasonable approximation for  $x > 1$  is

$$I(x) \approx 1 + \frac{1}{4x}. \quad (11.19)$$

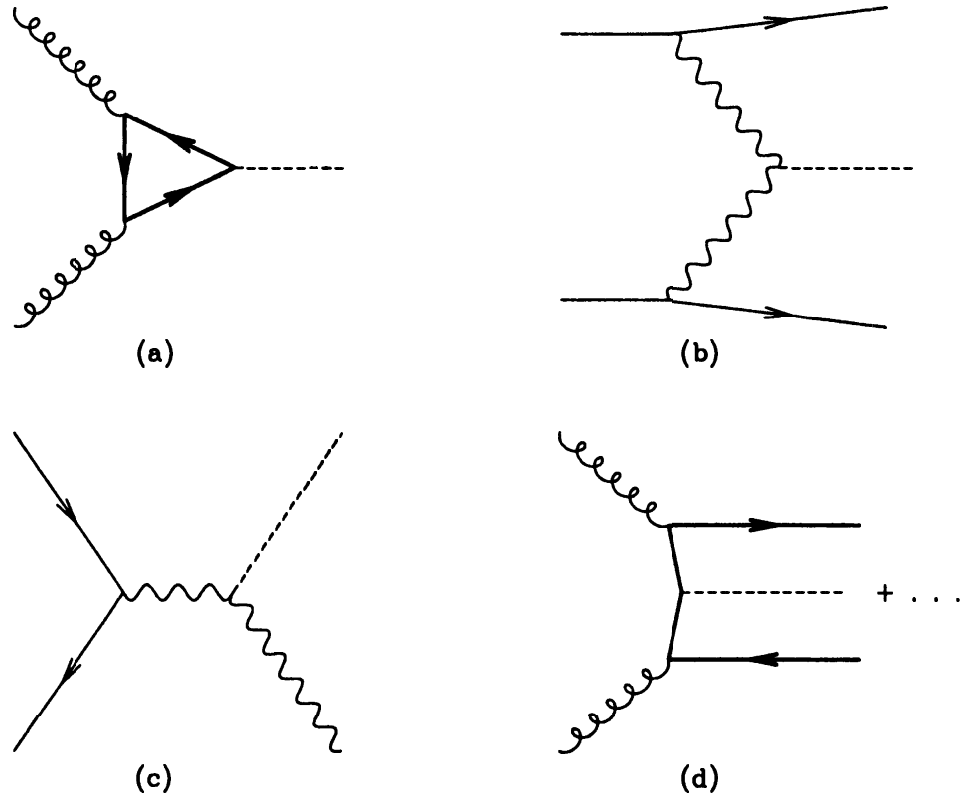


Fig. 11.5. The dominant Higgs production mechanisms at hadron colliders: (a) gluon-gluon fusion, (b) vector boson fusion, and associated production with (c)  $W, Z$  bosons and (d)  $t\bar{t}$ .

The subprocess cross section is obtained from the matrix element squared by

$$\hat{\sigma}(gg \rightarrow H) = \frac{\pi}{\hat{s}} \delta(\hat{s} - M_H^2) |\mathcal{M}(gg \rightarrow H)|^2 \equiv C_H(M_H, m_t) \delta(\hat{s} - M_H^2). \quad (11.20)$$

Note that this has a similar form to the  $W$  and  $Z$  production cross sections discussed in Section 9.4.1. The hadron-hadron cross section is obtained by convoluting (11.20) with gluon distributions in the usual way.

The next-to-leading-order corrections to the gluon-fusion subprocess cross section have been calculated in ref. [12]. Over the relevant Higgs mass range, they enhance the leading-order cross section by a factor 1.5–1.7 depending on  $M_H$ . For  $M_H^2 \ll 4m_t^2$  the corrections are calculable analytically [13]. In fact this analytic approximation is reasonable over the complete  $M_H$  range and will be used for the numerical results presented below. The cross section for Higgs production via the gluon-fusion mechanism in 14 TeV  $pp$  collisions, including the approximate next-to-leading-order corrections, is shown in Fig. 11.6 as a function of  $M_H$  for  $m_t = 175$  GeV [8].

The collider energy dependence of the cross section is illustrated in

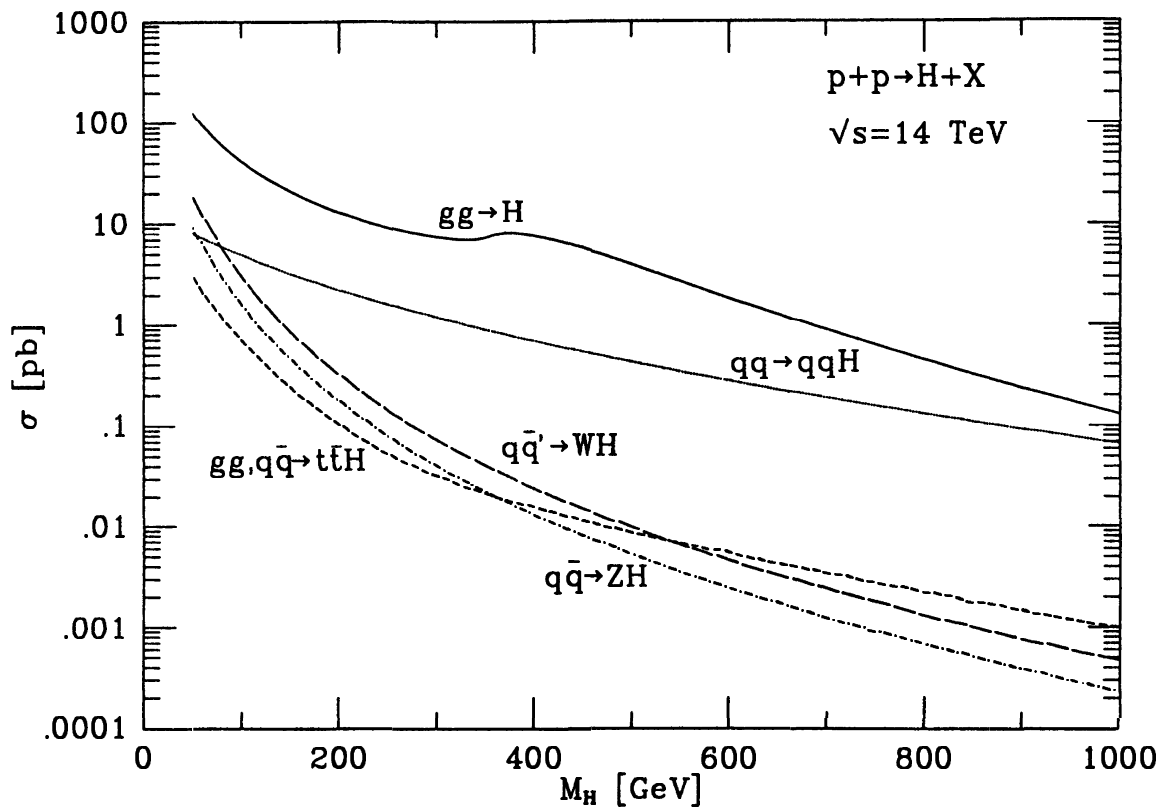


Fig. 11.6. Higgs production cross sections in  $p\bar{p}$  collisions at the LHC [8].

Fig. 11.7 for  $M_H = 100$  and  $700$  GeV. Far above threshold, the increase with  $\sqrt{s}$  is due to the rapid increase of the gluon distribution at small  $x$ . The increase is more rapid for the larger Higgs mass. In particular, the ratio  $\sigma(10 \text{ TeV})/\sigma(14 \text{ TeV})$  is 0.59 for  $M_H = 100$  GeV, falling to 0.40 for  $M_H = 700$  GeV. At this order in perturbation theory, the cross section is identical for  $p\bar{p}$  and  $p\bar{p}$  colliders. Notice also that the Tevatron  $p\bar{p}$  collider ( $\sqrt{s} = 1.8$  TeV) cross sections are not negligible, spanning the range  $0.9 - 0.02$  pb for  $M_H = 100 - 300$  GeV.

### 11.4.3 $WW$ , $ZZ$ fusion

Although gluon fusion is generally the dominant mechanism for Higgs production at the LHC, there is a comparable contribution to very heavy Higgs production from  $WW$  and  $ZZ$  fusion, Fig. 11.5(b). If the Higgs decay width is not too large compared to its mass, the cross section is calculated from the  $2 \rightarrow 3$  process  $qq \rightarrow Hqq$  with intermediate  $W$  and  $Z$  bosons.<sup>1</sup> The matrix element squared for the process  $q(p_1) + q'(p_2) \rightarrow$

<sup>1</sup> For large  $M_H$ , the large Higgs width becomes an important factor and the narrow-resonance approximation is no longer valid, see for example the discussion in ref. [15].

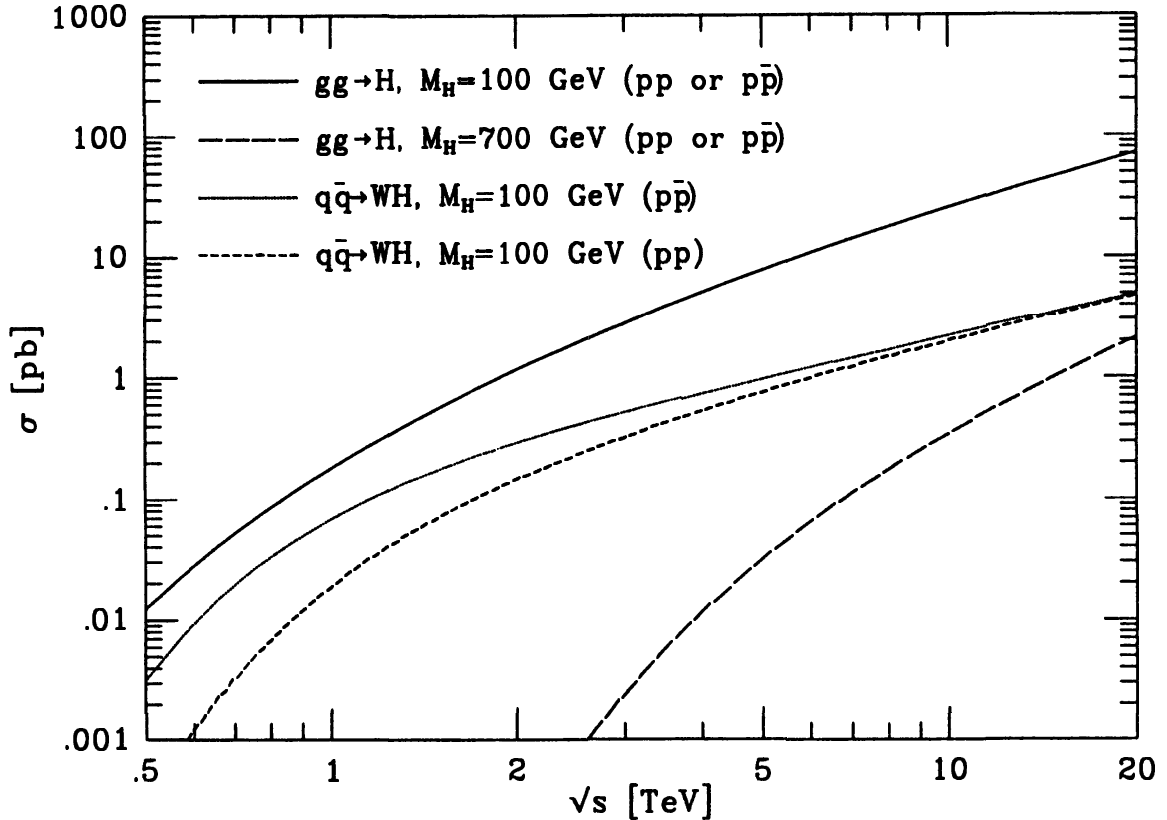


Fig. 11.7. Higgs boson production cross sections as a function the collider energy [8].

$q(p_3) + q'(p_4) + H$  via  $VV$  fusion ( $V = W, Z$ ) is [14]

$$|\mathcal{M}|^2 = 128\sqrt{2}G_F^3 M_V^8 \frac{C_1^V p_1 \cdot p_2 p_3 \cdot p_4 + C_2^V p_1 \cdot p_4 p_2 \cdot p_3}{(2p_3 \cdot p_1 + M_V^2)^2 (2p_4 \cdot p_2 + M_V^2)^2}, \quad (11.21)$$

where

$$\begin{aligned} C_1^W &= 0 \\ C_2^W &= 1 \\ C_1^Z &= \frac{1}{4} [(V_q - A_q)^2 (V_{q'} - A_{q'})^2 + (V_q + A_q)^2 (V_{q'} + A_{q'})^2] \\ C_2^Z &= \frac{1}{4} [(V_q - A_q)^2 (V_{q'} + A_{q'})^2 + (V_q + A_q)^2 (V_{q'} - A_{q'})^2], \end{aligned} \quad (11.22)$$

with the vector and axial quark couplings of Table 8.3. The next-to-leading-order QCD corrections to these processes have been calculated in ref. [16]. They give a small positive enhancement to the lowest-order cross section. The hadron-hadron cross section  $\sigma(pp \rightarrow H + X)$  is obtained by integrating the above matrix elements with three-body phase space and convoluting with the appropriate parton distributions. The resulting cross section is shown in Fig. 11.6.

#### 11.4.4 Associated production with $W, Z$ bosons

The cross sections for Higgs production in association with  $W$  and  $Z$  bosons are not large, but may be useful for detecting a light Higgs boson decaying to  $b\bar{b}$  or  $\gamma\gamma$ , since the Higgs can be ‘tagged’ by detecting the weak boson in addition. The subprocess cross sections [17] are obtained from the Feynman diagram Fig. 11.5(c) and are simply related to the  $e^+e^- \rightarrow ZH$  cross section of Eq. (11.14):

$$\begin{aligned}\hat{\sigma}(q\bar{q}' \rightarrow WH) &= \frac{(G_F M_W^2)^2}{9\pi} |V_{qq'}|^2 \frac{p_W}{\sqrt{\hat{s}}} \frac{3M_W^2 + p_W^2}{(\hat{s} - M_W^2)^2}, \\ \hat{\sigma}(q\bar{q} \rightarrow ZH) &= \frac{(G_F M_Z^2)^2}{9\pi} (V_q^2 + A_q^2) \frac{p_Z}{\sqrt{\hat{s}}} \frac{3M_Z^2 + p_Z^2}{(\hat{s} - M_Z^2)^2},\end{aligned}\quad (11.23)$$

where

$$p_V^2 = \frac{1}{4\hat{s}} (\hat{s}^2 + M_V^4 + M_H^4 - 2\hat{s}M_V^2 - 2\hat{s}M_H^2 - 2M_V^2 M_H^2) \quad (11.24)$$

for  $V = W, Z$ .

The next-to-leading-order QCD corrections are identical to those for the ‘Drell-Yan’ production of a single, massive off-shell  $W$  or  $Z$  (see Chapter 9). The lowest-order cross sections are therefore increased by  $O(20\%)$ . The cross sections at the LHC ( $\sqrt{s} = 14$  TeV) are shown in Fig. 11.6. The  $WH$  cross section is uniformly about twice as large as that for  $ZH$ .

Unlike for the dominant  $gg \rightarrow H$  mechanism, a  $p\bar{p}$  collider gives larger  $q\bar{q} \rightarrow WH, ZH$  cross sections than a  $pp$  collider. This is illustrated in Fig. 11.7 for  $q\bar{q} \rightarrow WH$  with  $M_H = 100$  GeV. The cross sections at the Tevatron  $p\bar{p}$  collider ( $\sqrt{s} = 1.8$  TeV) span the range  $0.25 - 0.002$  pb for  $M_H = 100 - 300$  GeV.

#### 11.4.5 Associated production with $t\bar{t}$

In the same spirit as the previous mechanism, a Higgs boson can be radiated off a heavy top quark produced in gluon-gluon or quark-antiquark fusion:  $gg \rightarrow t\bar{t}H$ ,  $q\bar{q} \rightarrow t\bar{t}H$  [18]. One of the Feynman diagrams is shown in Fig. 11.5(d). The cross section depends quite sensitively on the top quark mass. Although the top quark–Higgs coupling is large for large  $m_t$ , this is counterbalanced by the parton distribution suppression of the correspondingly heavier  $t\bar{t}H$  final state. The next-to-leading-order QCD corrections to  $t\bar{t}H$  production have not yet been calculated. The lowest-order cross section for  $m_t = 175$  GeV is shown in Fig. 11.6. Over most of the  $M_H$  mass range, the cross section increases as the top mass decreases.

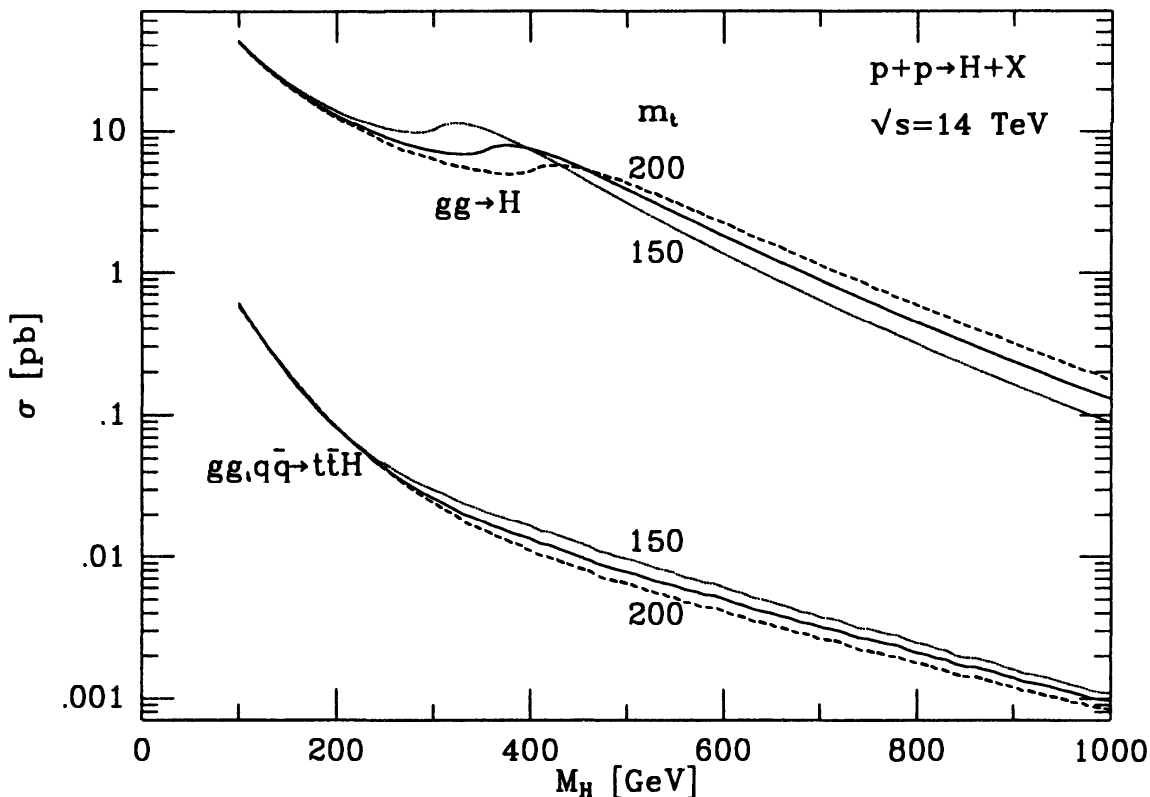


Fig. 11.8. Higgs boson production cross sections for  $m_t = 150, 175, 200$  GeV [8].

#### 11.4.6 Theoretical uncertainties in the cross sections

Apart from the obvious dependence on  $M_H$ , and to a lesser extent on  $m_t$ , there are few other uncertainties involved in the production cross section calculations. All the important Higgs cross sections, apart from associated production with  $t\bar{t}$ , are known to next-to-leading order. The various corrections are relatively modest, and there is no reason to believe that the corresponding perturbation series are anything other than well-behaved, just as for the  $W$  and  $Z$  cross sections discussed in Chapter 9. The dependence of the  $gg \rightarrow H$  and  $gg, q\bar{q} \rightarrow t\bar{t}H$  cross sections on the top quark mass is illustrated in Fig. 11.8. For the former, the behaviour is a reflection of the dependence on  $m_t/M_H$  of the function  $I$  in Eq. (11.17) — in particular, for large  $M_H$  the cross section increases with  $m_t$ . In contrast, the  $gg, q\bar{q} \rightarrow t\bar{t}H$  cross section shows the opposite behaviour, mainly due to the suppression of large final-state invariant masses from the parton distributions.

Another potential source of theoretical uncertainty comes from the quark and gluon distribution functions. The typical  $x$  value probed in these cross section calculations is  $x \sim \sqrt{\hat{s}}/s \gtrsim M_H/\sqrt{s}$ . For the LHC, therefore, Higgs boson production is sensitive to parton distributions

at  $x > O(10^{-2})$ . For quark distributions, this is precisely the region where fixed-target deep inelastic scattering experiments provide strong constraints, albeit at a lower  $\mu^2$  scale (see Chapter 4). The parton distribution uncertainty for processes like  $q\bar{q} \rightarrow q\bar{q}H$  and  $q\bar{q} \rightarrow WH, ZH, t\bar{t}H$  is therefore very small. For the dominant  $gg \rightarrow H$  process, the gluon is probed in an  $x$  region *below* that of fixed-target prompt photon production (see Chapter 7) and *above* that of  $\partial F_2/\partial \ln Q^2$  at HERA (see Chapter 4), and so the uncertainty in the Higgs cross section is larger. Using a variety of recent sets of parton distributions, one obtains a spread of no more than  $\pm 20\%$  in predictions for the  $gg \rightarrow H$  cross section [8]. Of course by the time the LHC comes into operation, it is likely that the gluon distribution will be much better determined.

## 11.5 Search strategies and backgrounds

Signals and backgrounds for a wide variety of production and decay channels have been studied [1,19,20,21]. Two channels, however, stand out from the others in that they appear to provide the ‘best’ chance for discovery of the Higgs boson at the LHC. These are

- (i)  $gg \rightarrow H \rightarrow \gamma\gamma$ , for  $M_H \lesssim 150$  GeV,
- (ii)  $gg \rightarrow H \rightarrow ZZ^{(*)} \rightarrow l^+l^-l^+l^-$ , for  $M_H \gtrsim 130$  GeV.

Certain other channels may also be useful, for example

- (iii)  $q\bar{q} \rightarrow WH \rightarrow l\bar{\nu}b\bar{b}$ ,

and, if sufficiently high luminosity is available,

- (iv)  $q\bar{q} \rightarrow WH \rightarrow l\bar{\nu}_l\gamma\gamma$ ,  $gg (q\bar{q}) \rightarrow t\bar{t}H \rightarrow WH + X \rightarrow l\bar{\nu}_l\gamma\gamma + X$ .

Note that in cases (i), (ii) and (iv) the branching ratios involved are extremely small. For example, the  $H \rightarrow 4l^\pm$  ( $l = e, \mu$ ) decay mode of a heavy Higgs has a branching ratio of only 0.12%, Table 11.1.

The total production rates are readily obtained by combining the branching ratios of Figs. 11.1, 11.2 and Table 11.1 with the cross sections of Fig. 11.6. As examples, Fig. 11.9 shows the cross section times branching ratio for ‘direct’  $pp \rightarrow H(\rightarrow \gamma\gamma) + X$  production, and Fig. 11.10 shows the cross section times branching ratio for four-charged-lepton  $pp \rightarrow H(\rightarrow ZZ \rightarrow 4l) + X$  ( $l = e, \mu$ ) production, at the LHC. Note that for the former, the effect of a rising branching ratio combined with a falling cross section yields a signal which is approximately constant as a function of  $M_H$  for  $M_H \lesssim 140$  GeV. For larger Higgs masses the event rate falls off rapidly. The  $M_H$  dependence of the  $H \rightarrow 4l^\pm$  ( $l = e, \mu$ ) event

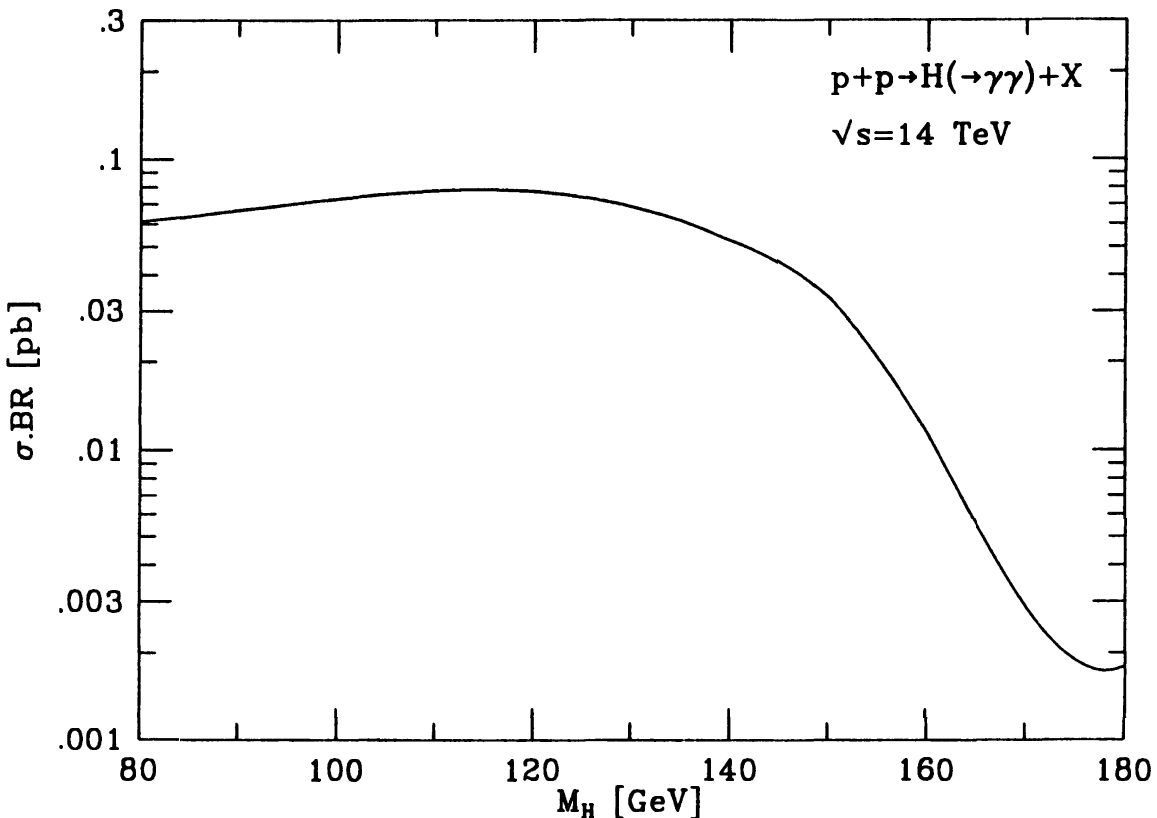


Fig. 11.9. Cross section times branching ratio for  $pp \rightarrow H(\rightarrow \gamma\gamma) + X$  as a function of  $M_H$ , at the LHC.

rate has an interesting structure. At the low mass end, the rate falls very sharply below about  $M_H = 150$  GeV — a reflection of the behaviour of the branching ratio shown in Fig. 11.1. At the high mass end, the rate falls off slowly reflecting the behaviour of the underlying production cross section. There is a dip in the rate at  $M_H \simeq 170$  GeV due to the  $W^+W^-$  threshold.

Of course, none of the above channels is free of background. The main concern is with Standard Model background processes which are *irreducible*, *i.e.* contain exactly the same set of particles in the final state as the signal. For the four classes of signal process listed above, the irreducible backgrounds come from (i)  $q\bar{q}, gg \rightarrow \gamma\gamma$ , (ii)  $q\bar{q} \rightarrow ZZ^{(*)} \rightarrow l^+l^-l^+l^-$ , (iii)  $q\bar{q} \rightarrow WZ \rightarrow l\bar{\nu}b\bar{b}$ , and (iv)  $q\bar{q} \rightarrow W\gamma\gamma \rightarrow l\bar{\nu}_l\gamma\gamma, gg(q\bar{q}) \rightarrow t\bar{t}\gamma\gamma \rightarrow l\bar{\nu}_l\gamma\gamma + X$ . Reducible backgrounds, for example where the charged lepton comes from the decay of a  $b$  quark and not a  $W$ , can generally be suppressed by additional (*e.g.* isolation and impact-parameter) cuts on the final-state particles and jets. Particularly troublesome in this respect is hadronic  $t\bar{t} \rightarrow bW^+\bar{b}W^-$  production, which is not only an irreducible background for  $H \rightarrow W^+W^-$ , but which also can mimic  $H \rightarrow 4l^\pm$  when both  $b$  quarks decay semi-leptonically. It has been shown, however, that in most cases all backgrounds can be suppressed to an acceptable level

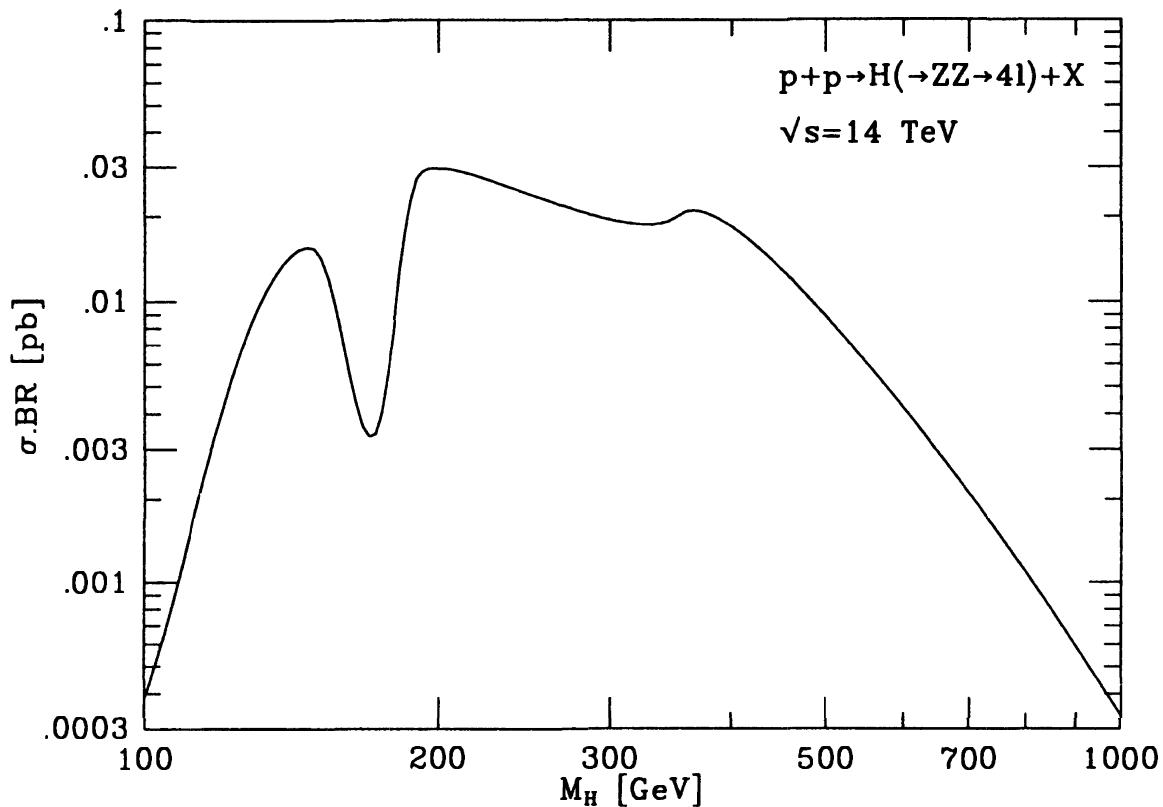


Fig. 11.10. Cross section times branching ratio for  $pp \rightarrow H(\rightarrow ZZ \rightarrow 4l) + X$  ( $l = e, \mu$ ) as a function of  $M_H$ , at the LHC.

by suitable cuts on the final-state particles, while still leaving the bulk of the signal intact [20,21]. In particular, the four-lepton channel offers the cleanest possibility of discovery, in a Higgs mass region bounded from above *and* below, the exact window depending on the available luminosity and the experimental acceptance. As a very rough guide, assuming an integrated luminosity  $\int \mathcal{L} = 10^5$  pb $^{-1}$  at  $\sqrt{s} = 14$  TeV gives a Higgs discovery window in this channel of approximately

$$130 \text{ GeV} < M_H < 800 \text{ GeV}. \quad (11.25)$$

If only  $\int \mathcal{L} = 10^4$  pb $^{-1}$  is available, the upper limit drops to around 600 GeV. An example of the detection of a heavy Higgs in this channel simulated for the ATLAS detector at the LHC is shown in Fig. 11.11.

The  $pp \rightarrow H(\rightarrow \gamma\gamma) + X$  channel allows the mass region between the LEP2 limit ( $\sim 100$  GeV) and 130 GeV to be searched. The problem here is the large irreducible continuum background from  $gg, q\bar{q} \rightarrow \gamma\gamma$  production and reducible background from hadronic jets ‘faking’ photons (in jet–jet and  $\gamma$ –jet production), both of which rise steeply as  $M_{\gamma\gamma}$  decreases. The signal can only be observed above the continuum background if the experimental  $M_{\gamma\gamma}$  resolution is very high. Fig. 11.12 shows the result of a simulation of this process for  $M_H = 120$  GeV and  $\int \mathcal{L} = 10^5$  pb $^{-1}$ ,

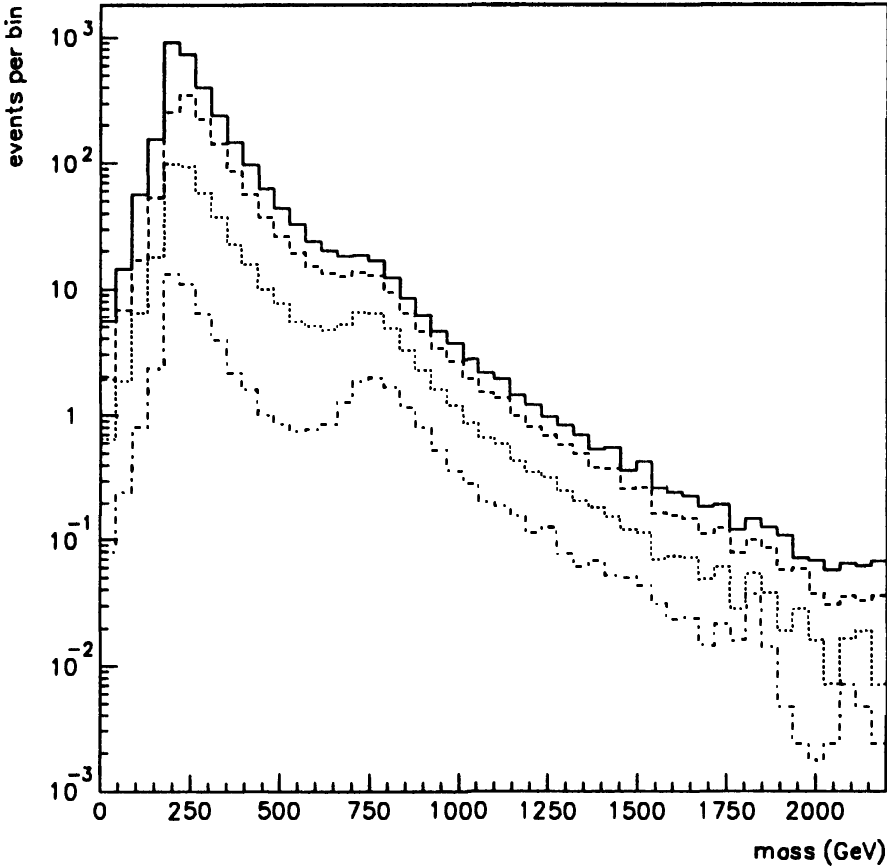


Fig. 11.11. Expected  $M_{ZZ}$  signal and background spectrum as simulated in the ATLAS detector at the LHC, for  $M_H = 800$  GeV and  $\int \mathcal{L} = 10^5 \text{ pb}^{-1}$ . Successive cuts applied: all events in acceptance (solid), events with  $p_T(Z) > \frac{1}{4}M_{ZZ}$  (dashed), events with one (dotted) and two (dot-dashed) reconstructed tag jets (see text). Figure from ref. [22].

together with the background continuum  $\gamma\gamma$  production, for the ATLAS detector at the LHC. In fact there appears to be no problem for  $M_H > O(100 \text{ GeV})$  — the main concern is with a possible window of unobservability in this channel at the low mass end.

The  $WH, t\bar{t}H$  production processes also allow the light intermediate-mass Higgs region to be covered. If high luminosity is available, one can use the decay channels  $WH \rightarrow l\nu\gamma\gamma$ , which gives a clean final state with manageable backgrounds [23]. However, the number of signal events is rather small. This is illustrated in Fig. 11.13, where the cross sections for  $pp \rightarrow t\bar{t}H, WH + X \rightarrow l\nu\gamma\gamma + X$  ( $l = e, \mu$ ) are shown as a function of  $M_H$ .

Another possibility [24] is to use the  $WH(\rightarrow b\bar{b})$  channel, which has a much higher event rate since  $H \rightarrow b\bar{b}$  is the dominant decay mode for a light Higgs. Here one would look for final states containing an isolated energetic lepton (from  $W$  decay) together with two tagged  $b$  quark jets,

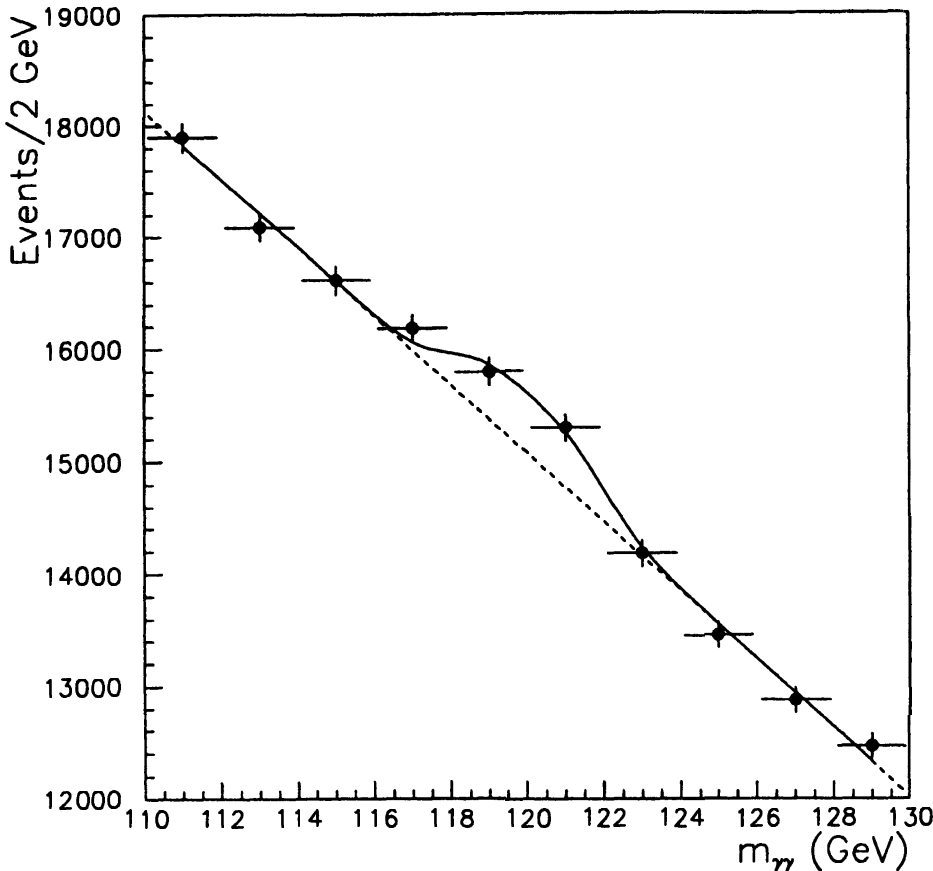


Fig. 11.12. Expected  $M_{\gamma\gamma}$  spectrum as simulated in the ATLAS detector at the LHC, for  $M_H = 120$  GeV and  $\int \mathcal{L} = 10^5$  pb $^{-1}$ . Figure from ref. [20].

whose invariant mass distribution contained a peak. This channel does not need high luminosity, but the rejection of the irreducible  $W + 2$  jets background does require a good efficiency for detecting  $b$  quark jets.

In summary, the LHC should be well able to discover a Standard Model Higgs boson in the mass range starting from the LEP2 upper limit and extending up to  $O(800)$  GeV. A considerable amount of effort has gone into investigating whether the search can be extended to  $M_H \sim 1$  TeV. Attention has focused on the heavy Higgs decay channels which have larger branching ratios (see Table 11.1), such as  $H \rightarrow WW \rightarrow l\nu jj$  and  $H \rightarrow ZZ \rightarrow l^+l^-\nu\bar{\nu}$ .

The  $H \rightarrow ZZ \rightarrow l^+l^-\nu\bar{\nu}$  signal can, in principle, be identified as a Jacobian peak in the missing transverse energy distribution, at  $E_T^{miss} \sim \frac{1}{2}M_Z$ . Aside from the irreducible  $ZZ$  continuum background, the main problem is with the much larger  $Z +$  jets background. This can only be suppressed if the detector has a large acceptance in rapidity for hadronic jets, and has a high ‘hermeticity’.

The key to utilizing the  $H \rightarrow WW \rightarrow l\nu jj$  channel is ‘jet tagging’ [25]. The idea is to use the  $WW$  and  $ZZ$  fusion production processes, which

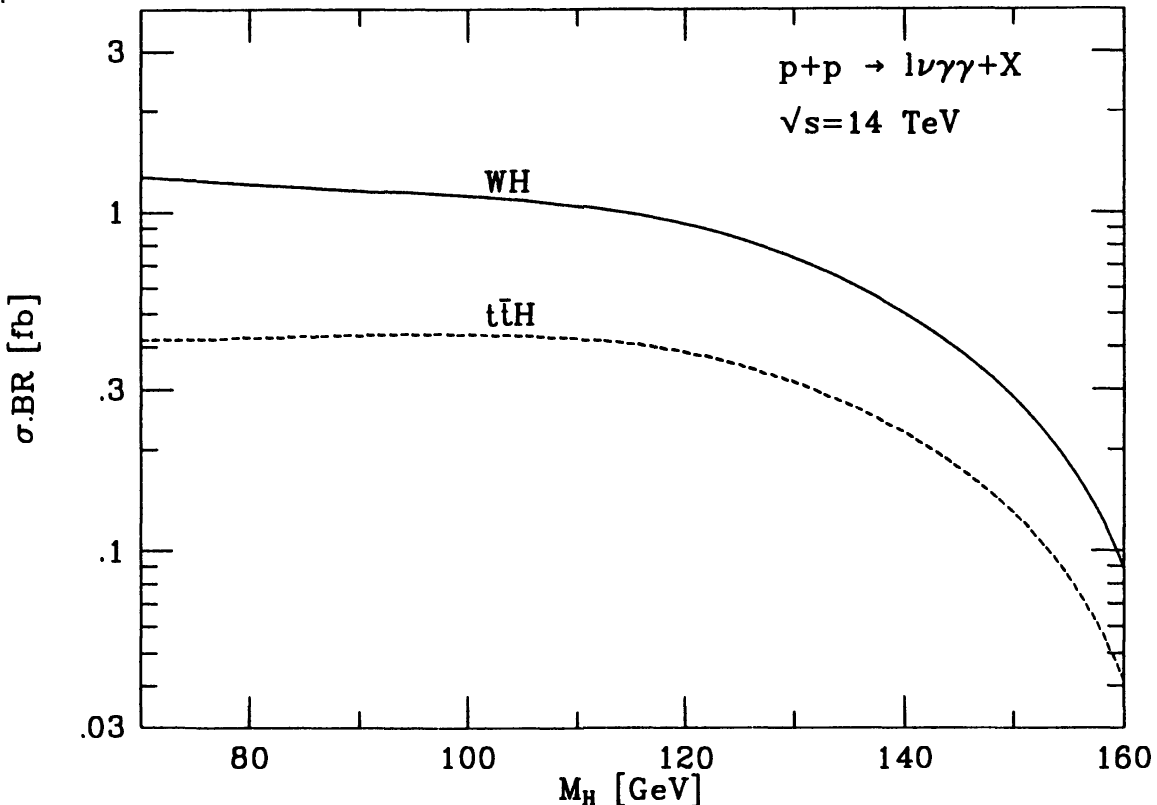


Fig. 11.13. Cross section times branching ratio for  $pp \rightarrow WH(\rightarrow l\nu\gamma\gamma) + X$  and  $pp \rightarrow t\bar{t}H(\rightarrow l\nu\gamma\gamma + \dots) + X$  ( $l = e, \mu$ ) as a function of  $M_H$ , at the LHC.

are comparable with the  $gg$  fusion process at large  $M_H$  (see Fig. 11.6) and to ‘tag’ the quark jets which are produced in association with the Higgs. These jets are energetic and are produced at large rapidity, typically  $E^j \sim 1 \text{ TeV}$  and  $p_T^j \sim \frac{1}{2}M_W$ . The probability of finding such jets in background  $W+$  jets and  $t\bar{t}$  production is small (although the ‘pile-up’ from multiple interactions in the same bunch crossing can be problematic at high luminosity), and so requiring one or two tag jets in an event provides a powerful background rejection (for a detailed discussion see refs. [20,21]). Note that jet tagging can also enhance the significance of the signal in the  $H \rightarrow ZZ \rightarrow l^+l^-l^+l^-$  and  $H \rightarrow ZZ \rightarrow l^+l^-\nu\bar{\nu}$  channels, see Fig. 11.11.

## 11.6 Summary

The Higgs boson holds the key to one of the most pressing problems in particle physics today: understanding the origin and values of the particle masses. In this chapter, we have seen that the LEP  $e^+e^-$  and LHC  $pp$  colliders are well placed to search for the Standard Model Higgs boson if, as expected, its mass is less than  $O(1 \text{ TeV})$ . Already, LEP has ruled

out a Higgs boson lighter than about 65 GeV. LEP2 will extend this search towards 100 GeV, at which point the LHC (or a future  $e^+e^-$  linear collider, see for example ref. [26]) will take over.

The Higgs mechanism, while it has many attractive features, is not without difficulties. There is, for example, a severe fine-tuning ('naturalness') problem associated with preventing the Higgs mass being renormalized up to some very high 'new-physics' or grand unification scale. Supersymmetry (SUSY) is one way of circumventing this difficulty while retaining the essential features of the Standard Model Higgs sector. In the minimal supersymmetric model, it is necessary to introduce *two* complex doublets of Higgs fields,<sup>2</sup> and the masses and couplings of the resulting five physical Higgs bosons are expressible (at leading order) in terms of just two parameters [27]. The conventional choice is the ratio of the two non-zero vacuum expectation values,  $\tan \beta = v_2/v_1$ , and the mass of the neutral CP-odd scalar boson,  $M_A$ . The key feature of the minimal SUSY model is the existence of at least one neutral, scalar Higgs boson with a mass less than  $O(150$  GeV), the exact upper bound depending weakly on the parameters of the model and on  $m_t$  [28]. In most respects, the lightest minimal SUSY Higgs boson behaves exactly like the Standard Model Higgs, and so the calculations and search strategies described in this chapter again apply. The other, heavier SUSY Higgs bosons have their own distinctive features and the phenomenology is therefore more complicated. There have been several studies in the context of future hadron colliders [29] (see also refs. [20,21]), all reaching the same conclusion that present and future experiments will together provide sensitivity to almost all of the  $(\tan \beta, M_A)$  parameter space.

## References

- 1) S. Dawson, J.F. Gunion, H.E. Haber and G.L. Kane, *The Higgs Hunter's Guide*, Addison-Wesley, Reading, MA (1990).
- 2) J.D. Bjorken, Proc. Summer Institute on Particle Physics, SLAC Report 198 (1976); J. Ellis, M.K. Gaillard and D.V. Nanopoulos, *Nucl. Phys.* **B106** (1976) 292; B.W. Lee, C. Quigg and H.B. Thacker, *Phys. Rev.* **D16** (1977) 1519; B.L. Ioffe and V.A. Khoze, *Sov. J. Part. Nucl.* **9** (1978) 50.
- 3) J.F. Grivaz, Proceedings of the International Europhysics Conference on High Energy Physics, Brussels, Belgium (1995).
- 4) N. Cabibbo, L. Maiani, G. Parisi and R. Petronzio, *Nucl. Phys.* **B158** (1979) 295; M. Sher, *Phys. Rev.* **179** (1989) 273; *Phys. Lett.* **B317** (1993) 159; *ibid.* **B331** (1994) 448; M. Lindner, M. Sher and H.W. Zaglauer, *Phys. Lett.* **B228** (1989) 139; C. Ford, D.R.T. Jones, P.W. Stephenson and M.B. Einhorn, *Nucl. Phys.* **B395** (1993) 17;

---

<sup>2</sup> A model with two complex Higgs doublets has already been considered in Section 10.2.2, in the context of unconventional top decays.

- G. Altarelli and I. Isidori, *Phys. Lett.* **B337** (1994) 141;  
 J.A. Casas, J.R. Espinosa and M. Quirós, *Phys. Lett.* **B342** (1995) 171.
- 5) M. Veltman, *Acta Phys. Pol.* **B8** (1977) 475.
- 6) S.G. Gorishny, A.L. Kataev, S.A. Larin and L.R. Surguladze, *Mod. Phys. Lett.* **A5** (1990) 2703.
- 7) H. Zheng and D. Wu, *Phys. Rev.* **D42** (1990) 3760;  
 A. Djouadi, M. Spira, J.J. van der Bij and P.M. Zerwas, *Phys. Lett.* **B257** (1991) 187;  
 S. Dawson and R.P. Kauffman, *Phys. Rev.* **D47** (1993) 1264;  
 A. Djouadi, M. Spira and P.M. Zerwas, *Phys. Lett.* **B311** (1993) 255;  
 K. Melnikov and O. Yakovlev, *Phys. Lett.* **B312** (1993) 179.
- 8) Z. Kunszt and W.J. Stirling, Proc. Large Hadron Collider Workshop, Aachen, October 1990, eds. G. Jarlskog and D. Rein, Report CERN 90-10, ECFA 90-133 (1990), Vol. II, p. 427; updated by S. Moretti, Ph.D. thesis (1995), Univ. Torino.
- 9) Report of the Higgs Working Group (conveners M. Carena and P.M. Zerwas) in *Physics at LEP2*, eds. G. Altarelli, T. Sjöstrand and F. Zwirner, Report CERN 96-01 (1996).
- 10) A.D. Martin, R.G. Roberts and W.J. Stirling, *Phys. Rev.* **D50** (1994) 6734.
- 11) H. Georgi, S.L. Glashow, M.E. Machacek and D.V. Nanopoulos, *Phys. Rev. Lett.* **40** (1978) 692.
- 12) D. Graudenz, M. Spira and P.M. Zerwas, *Phys. Rev. Lett.* **70** (1993) 1372;  
 M. Spira, A. Djouadi, D. Graudenz and P.M. Zerwas, *Nucl. Phys.* **B453** (1995) 17.
- 13) A. Djouadi, M. Spira and P.M. Zerwas, *Phys. Lett.* **B264** (1991) 440;  
 S. Dawson, *Nucl. Phys.* **B359** (1991) 283;  
 S. Dawson and R.P. Kauffman, *Phys. Rev.* **D49** (1993) 2298.
- 14) R.N. Cahn and S. Dawson, *Phys. Lett.* **B136** (1984) 196.
- 15) Z. Kunszt and D.E. Soper, *Nucl. Phys.* **B296** (1988) 253.
- 16) T. Han, G. Valencia and S. Willenbrock, *Phys. Rev. Lett.* **69** (1992) 3274.
- 17) S.L. Glashow, D.V. Nanopoulos and A. Yildiz, *Phys. Rev. D* **18** (1978) 1724.
- 18) Z. Kunszt, *Nucl. Phys.* **B247** (1984) 339;  
 See also: J.F. Gunion, H.E. Haber, F.E. Paige, Wu-Ki Tung and S. Willenbrock, *Nucl. Phys.* **B294** (1987) 621;  
 D.A. Dicus and S. Willenbrock, *Phys. Rev.* **D39** (1989) 751.
- 19) Report of the Higgs working group, in Proc. Large Hadron Collider Workshop, Aachen 1990, eds. G. Jarlskog and D. Rein, ECFA 90-133 (1990), Vol.II, p. 427.
- 20) ATLAS Technical Proposal, CERN/LHCC 94-43, LHCC/P2, 1994.
- 21) CMS Technical Proposal, CERN/LHCC 94-38, LHCC/P1, 1994.
- 22) ATLAS Letter of Intent, CERN/LHCC 92-4, LHCC/I2, 1992.
- 23) R. Kleiss, Z. Kunszt and W.J. Stirling, *Phys. Lett.* **B253** (1991) 269.
- 24) A. Stange, W. Marciano and S. Willenbrock, *Phys. Rev.* **D50** (1994) 4491;  
 J.F. Gunion and T. Han, *Phys. Rev.* **D51** (1995) 1051.
- 25) R.N. Cahn, S.D. Ellis, R. Kleiss and W.J. Stirling, *Phys. Rev.* **D35** (1987) 1626.
- 26) Proceedings of the Workshop "e<sup>+</sup>e<sup>-</sup> Collisions at 500 GeV. The Physics Potential", Munich, Annecy, Hamburg, February 1991, ed. P.M. Zerwas, DESY pub. 92-123A/B/C (1992).
- 27) H.-P. Nilles, *Phys. Rep.* **110** (1984) 1;  
 H.E. Haber and G.L. Kane, *Phys. Rep.* **117** (1985) 75;  
 R. Barbieri, *Riv. Nuovo Cimento* **11** (1988) 1.
- 28) Y. Okada, M. Yamaguchi and T. Yanagida, *Prog. Theor. Phys.* **85** (1991) 1, *Phys. Lett.* **B262** (1991) 54;  
 J. Ellis, G. Ridolfi and F. Zwirner, *Phys. Lett.* **B257** (1991) 83, *ibid.* **B262** (1991) 477;  
 A. Brignole, J. Ellis, G. Ridolfi and F. Zwirner, *Phys. Lett.* **B271** (1991) 123;  
 H.E. Haber and R. Hempfling, *Phys. Rev. Lett.* **66** (1991) 1815.
- 29) Z. Kunszt and F. Zwirner, *Nucl. Phys.* **B385** (1992) 3;  
 V. Barger, K. Cheung, R.J.N. Phillips and A.L. Stange, *Phys. Rev.* **D46** (1992) 4914;  
 H. Baer, M. Bisset, D. Dicus, C. Kao and X. Tata, *Phys. Rev.* **D47** (1993) 1062;  
 J.F. Gunion and L.H. Orr, *Phys. Rev.* **D46** (1992) 2052.

# 12

## Measurements of the strong coupling constant

A wide range of methods is available for measuring the strong coupling  $\alpha_s$ , and new measurements are continually being reported. Before reviewing the current status of  $\alpha_s$ , we should recall briefly the rather peculiar properties of this ‘fundamental constant’. The reader is referred back to Chapter 2 for a more detailed discussion.

First of all,  $\alpha_s$  is not a constant but a running quantity, whose value depends on the energy scale  $Q$  according to the equation (*cf.* Eq.(2.7))

$$Q^2 \frac{\partial \alpha_s}{\partial Q^2} = \beta(\alpha_s) = -b\alpha_s^2(1 + b'\alpha_s + \dots). \quad (12.1)$$

where  $b = (33 - 2n_f)/(12\pi)$  and  $b' = (153 - 19n_f)/(2\pi(33 - 2n_f))$  for  $n_f$  quark flavours. To this two-loop accuracy, the solution is (*cf.* Eq.(2.45))

$$\alpha_s(Q^2) = \frac{1}{bL} \left( 1 - \frac{b'}{b} \frac{\ln L}{L} \right), \quad (12.2)$$

where  $L = \ln(Q^2/\Lambda^2)$ ,  $\Lambda$  being a fundamental scale. All measurements of  $\alpha_s(Q^2)$  at different values of  $Q$  should correspond to a common value of  $\Lambda$ , or equivalently to a common value of  $\alpha_s$  at some particular scale, usually taken nowadays to be the  $Z^0$  boson mass  $M_Z$ .

In fact,  $\alpha_s$  is not itself directly observable but is an auxiliary quantity in terms of which we may represent the perturbative prediction for any dimensionless quantity in the form

$$A(Q^2) = A_0 + A_1\alpha_s(\mu^2) + A_2(Q^2/\mu^2)\alpha_s^2(\mu^2) + \dots. \quad (12.3)$$

If we could compute to all orders, the dependence on the arbitrary renormalization scale  $\mu^2$  would cancel completely between  $\alpha_s$  and the coefficients  $A_i$ . But if we choose  $\mu^2$  very different from the natural scale  $Q^2$  then large logarithms of  $Q^2/\mu^2$  remain uncancelled in any finite order, making

the prediction unreliable. In that sense we may say that an experiment at scale  $Q$  is really measuring  $\alpha_s(Q^2)$ .

Another point to remember is that  $\alpha_s$ , not being directly observable, depends in higher order not only on the scale but also on the renormalization scheme. The customary reference scheme is nowadays the modified minimal subtraction ( $\overline{\text{MS}}$ ) scheme and so the quoted scale  $\Lambda$  is usually  $\Lambda_{\overline{\text{MS}}}^{(5)}$ , the  $\overline{\text{MS}}$  scale with five active quark flavours, as appropriate at  $Q = M_Z$ . Note however that the scale  $\Lambda_{\overline{\text{MS}}}^{(5)}$  (whose value is about 200 MeV) is not a very physical quantity: it is the scale at which the five-flavour formula (12.2) would diverge if extrapolated far outside its domain of validity. Consequently it has become more usual to interpret all measurements in terms of a corresponding value of  $\alpha_s(M_Z^2)$ , which is what we shall do here.

To perform the evolution of  $\alpha_s$  from the physical scale  $Q$  to  $M_Z$ , the most common procedure is to use the two-loop truncation of Eq. (12.2), matching the formulae for different numbers of active flavours, if necessary, by imposing continuity at  $Q = m_q$  where  $m_q$  is the relevant quark mass. As discussed in Section 2.4, this matching procedure is satisfactory to two-loop order. Occasionally, for example in ref. [1], three-loop evolution of  $\alpha_s$  with the appropriate matching relation (2.41) has been used, but the differences are negligible on the scale of experimental and other theoretical uncertainties at present, being typically of the order of  $\pm 1\%$  in  $\alpha_s(M_Z^2)$ .

Before discussing particular measurements of  $\alpha_s$ , we should comment on the phenomenon of the ‘incredible shrinking error’. Since  $\alpha_s(Q^2)$  is a function of  $Q^2/\Lambda^2$ , Eq. (12.1) tells us that the error in  $\Lambda$  is related to that in  $\alpha_s$  at any scale by

$$\frac{\delta\Lambda}{\Lambda} = -\frac{1}{2} \frac{\delta\alpha_s}{\beta(\alpha_s)} . \quad (12.4)$$

Since the  $\beta$  function decreases with increasing scale like  $\alpha_s^2$ , this means that the best relative precision is obtained at the lowest possible scale, where  $\alpha_s$  is largest. In terms of  $\alpha_s(M_Z^2)$ , we have

$$\frac{\delta\alpha_s(M_Z^2)}{\alpha_s(M_Z^2)} \sim \frac{\alpha_s(M_Z^2)}{\alpha_s(Q^2)} \frac{\delta\alpha_s(Q^2)}{\alpha_s(Q^2)} . \quad (12.5)$$

Thus the relative error in  $\alpha_s$  is shrunk by the ratio of  $\alpha_s(M_Z^2)$  to  $\alpha_s(Q^2)$ . However, one must bear in mind that perturbative and non-perturbative corrections that may be negligible at high scales can become important at  $Q \ll M_Z$ , so the net gain from measuring at a low scale is not so clear. In particular, one should look very carefully at possible sources of power-suppressed corrections ( $1/Q^p$ ).

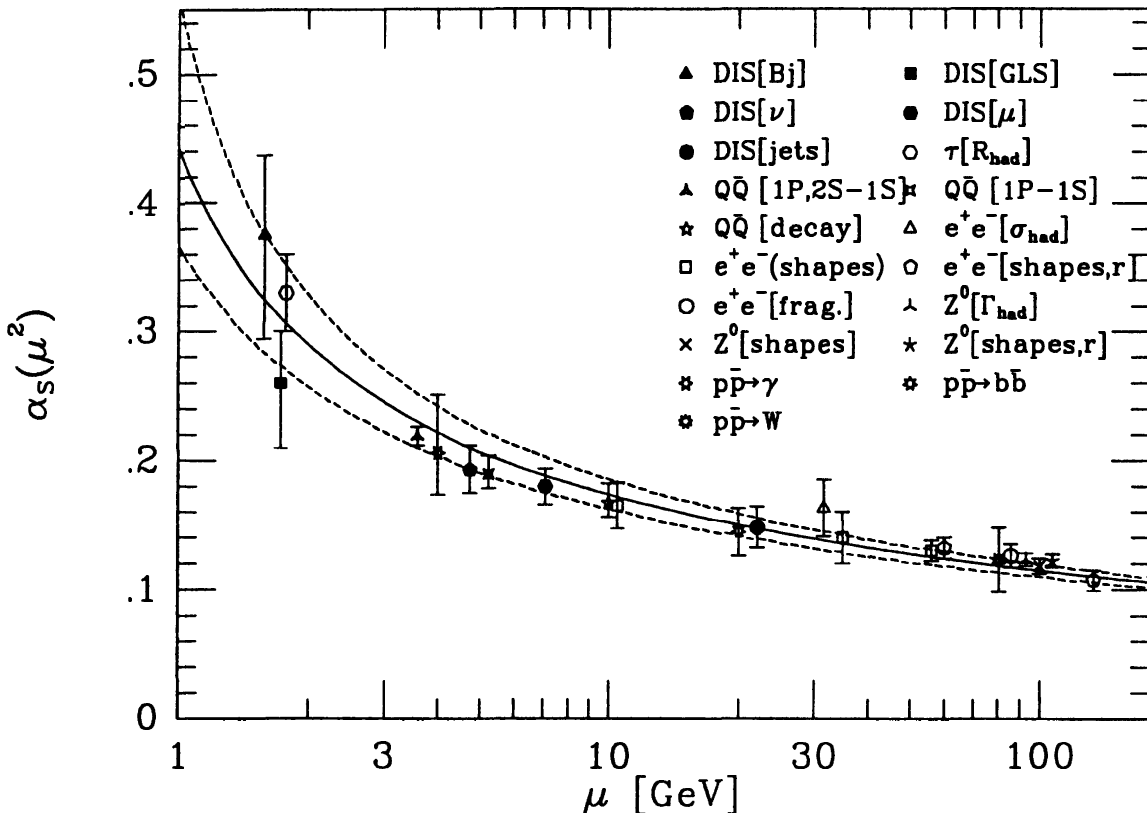


Fig. 12.1. Graphical representation of the data from Table 12.1. The curves correspond to  $\alpha_s(M_Z^2) = 0.116 \pm 0.005$ . The data points at  $\mu = 5, 58$  and  $91$  GeV have been shifted for clarity.

## 12.1 Summary of $\alpha_s$ measurements

Table 12.1, adapted and updated from a review by Bethke [1], gives a summary of  $\alpha_s$  values, averaged over various classes of measurement methods. For each measurement the typical momentum scale  $Q$  is given together with the measured value at that scale,  $\alpha_s(Q^2)$ . These results are presented in graphical form in Fig. 12.1. The running of  $\alpha_s$  may be seen clearly. The shrinking error, Eq. (12.5), is manifest in the convergence of the curves with increasing scale. The values and errors for  $\alpha_s$  extrapolated to the  $Z^0$  mass scale,  $\alpha_s(M_Z^2)$ , are also shown in Table 12.1, and will be discussed later.

In the following subsections we give some further details of the various methods for measuring  $\alpha_s$  and draw some conclusions. For a review of earlier results, see also ref. [2].

Process	$Q$ [GeV]	$\alpha_s(Q^2)$	$\alpha_s(M_Z^2)$	Theory
DIS [BjSR]	1.58	$0.375 \pm 0.062$	$0.122 \pm 0.005$	NNLO
DIS [GLS]	1.73	$0.26 \pm 0.04$	$0.108 \pm 0.006$	NNLO
DIS [ $\nu$ ]	5.0	$0.193 \pm 0.019$	$0.111 \pm 0.006$	NLO
DIS [ $\mu$ ]	7.1	$0.180 \pm 0.014$	$0.113 \pm 0.005$	NLO
DIS [jets]	22.1	$0.148 \pm 0.016$	$0.118 \pm 0.009$	NLO
$\tau$ [ $R_{\text{had}}$ ]	1.77	$0.33 \pm 0.03$	$0.118 \pm 0.004$	NNLO
$Q\bar{Q}$ [1P,2S-1S]	3.6	$0.219 \pm 0.007$	$0.115 \pm 0.002$	LGT(NR)
$Q\bar{Q}$ [1P-1S]	5.0	$0.190 \pm 0.014$	$0.112 \pm 0.004$	LGT(W)
$Q\bar{Q}$ [decay]	10.0	$0.167 \pm 0.015$	$0.113 \pm 0.007$	NLO
$e^+e^-$ [ $\sigma_{\text{had}}$ ]	31.6	$0.163 \pm 0.022$	$0.133 \pm 0.015$	NNLO
$e^+e^-$ [shapes]	10.5	$0.165 \pm 0.018$	$0.113 \pm 0.006$	NLO
$e^+e^-$ [shapes]	35.0	$0.140 \pm 0.020$	$0.119 \pm 0.014$	NLO
$e^+e^-$ [shapes]	58.0	$0.130 \pm 0.008$	$0.122 \pm 0.007$	NLO
$e^+e^-$ [shapes]	58.0	$0.132 \pm 0.008$	$0.124 \pm 0.007$	resum.
$e^+e^-$ [frag.]	22–91		$0.126 \pm 0.009$	NLO
$Z^0$ [ $\Gamma_{\text{had}}$ ]	91.2	$0.123 \pm 0.005$	$0.123 \pm 0.005$	NNLO
$Z^0$ [shapes]	91.2	$0.118 \pm 0.006$	$0.118 \pm 0.006$	NLO
$Z^0$ [shapes]	91.2	$0.122 \pm 0.005$	$0.122 \pm 0.005$	resum.
$e^+e^-$ [shapes]	133	$0.107 \pm 0.008$	$0.113 \pm 0.009$	resum.
$p\bar{p}, pp \rightarrow \gamma + X$	4.0	$0.206 \pm 0.045$	$0.112 \pm 0.012$	NLO
$p\bar{p} \rightarrow b\bar{b}X$	20.0	$0.145 \pm 0.018$	$0.113 \pm 0.011$	NLO
$p\bar{p} \rightarrow W + \text{jets}$	80.6	$0.123 \pm 0.025$	$0.121 \pm 0.024$	NNLO

Table 12.1. Summary of  $\alpha_s$  measurements.

## 12.2 Deep inelastic scattering

### 12.2.1 Sum rules

At the lowest scale in Table 12.1 comes a recent theoretical study [3] in which the CERN EMC/SMC [4] and SLAC E142/143 [5] data on polarized lepton-nucleon scattering are used to extract a value of  $\alpha_s$  from the higher-order corrections to the Bjorken sum rule for  $g_1^p - g_1^n$ , Eq. (4.237). Closely following is a similar measurement based on the Gross-Llewellyn Smith (GLS) sum rule for deep inelastic neutrino-nucleon scattering, Eq. (4.156). In both cases the perturbative corrections have been calculated [6] up to  $O(\alpha_s^3)$  (*i.e.* next-to-next-to-leading order, NNLO), Eqs. (4.157) and (4.252), and the power ('higher twist') corrections to deep inelastic scattering are relatively well understood, making this an attractive method for determining  $\alpha_s$  in spite of the low scale.

In the case of the Gross-Llewellyn Smith sum rule, for example, we have

$$\int_0^1 dx [F_3^{\nu p}(x, Q^2) + F_3^{p p}(x, Q^2)] = 6(1 - \Delta_{\text{pert.}} - \Delta_{\text{h.t.}}) \quad (12.6)$$

where the perturbative correction is, for  $n_f = 3$ ,

$$\Delta_{\text{pert.}} = \frac{\alpha_s}{\pi} + 3.58 \left(\frac{\alpha_s}{\pi}\right)^2 + 19.0 \left(\frac{\alpha_s}{\pi}\right)^3. \quad (12.7)$$

The non-perturbative (higher-twist) correction  $\Delta_{\text{h.t.}}$  has been estimated [7] using QCD sum rules [8], which yield

$$\Delta_{\text{h.t.}} = 0.032 \pm 0.016. \quad (12.8)$$

The result shown is then obtained [9] from a combined analysis of high-precision CCFR and other data at  $\langle Q^2 \rangle = 3 \text{ GeV}^2$ .

Owing to the low value of the momentum scale, the theoretical uncertainty is dominated by the higher-twist contribution. A measurement of the  $Q^2$  dependence of the sum rule would be helpful in checking the validity of the estimate (12.8). Similar remarks apply to the Bjorken sum rule.

### 12.2.2 Scaling violation in structure functions

At intermediate scales, around  $Q = 5 - 10 \text{ GeV}$ , measurements based on the violation of Bjorken scaling in deep inelastic structure functions have provided the most reliable information on  $\alpha_s$ . Here the calculations have been performed only to next-to-leading order (NLO), but again the higher-twist power corrections appear well under control.

The value listed for muon scattering comes from the combined analysis of BCDMS and SLAC charged lepton data already discussed in Section 4.4. The result for neutrino scattering is that obtained by the CCFR collaboration [10] from an analysis of the non-singlet structure function  $F_3(x, Q^2)$ , supplemented by data on  $F_2(x, Q^2)$  at large  $x$ , where non-singlet contributions are again dominant. This avoids dependence on the less well known gluon contribution. Other measurements from scaling violation are consistent with the two values quoted, with larger statistical errors.

### 12.2.3 Jets in deep inelastic scattering

A new method of  $\alpha_s$  determination at intermediate to high scales is provided by the measurements of jet production rates in deep inelastic scattering at HERA. An advantage over similar measurements in  $e^+e^-$  annihilation is that the scale, set by the momentum transfer  $Q^2$ , can be varied over a wide range in a single experiment at a single beam energy.

Results have been reported [11,12] based on the 2+1 jet rate, that is, the fraction of deep inelastic events in which one can resolve two final-state ‘current’ jets in addition to the ‘beam’ jet which carries the remnants of the incoming proton. The 2+1 jet cross section is at least first order in  $\alpha_s$ , and  $O(\alpha_s^2)$  calculations have been performed [13,14]. The jets are defined using a modified form of the JADE jet clustering algorithm defined in Section 3.3 [15].

The jet rates for a given value of  $\alpha_s$  depend on the parton distributions in the proton, and so one has to assume a set of distributions in order to deduce a value of  $\alpha_s$ . To allow for this, distributions corresponding to a range of different  $\alpha_s$  values have been provided [16].

Results from the two HERA experiments, extrapolated from the region  $Q^2 \sim 100 - 4000 \text{ GeV}^2$  to  $Q^2 = M_Z^2$ , are

$$\begin{aligned}\alpha_s(M_Z^2) &= 0.123 \pm 0.012(\text{stat.}) \pm 0.013(\text{sys.}) \quad (\text{H1}), \\ \alpha_s(M_Z^2) &= 0.117 \pm 0.005(\text{stat.}) \pm 0.009(\text{sys.}) \quad (\text{ZEUS}).\end{aligned}\quad (12.9)$$

The average of these values, combining all the errors in quadrature, is given in Table 12.1. The value given for  $\alpha_s(Q^2)$  at  $Q = 22.1 \text{ GeV}$  is the average over the range  $Q^2 = 120 - 3600 \text{ GeV}^2$  quoted in ref. [12].

## 12.3 $\tau$ lepton decay

One of the most carefully studied methods for measuring  $\alpha_s$  is based on the hadronic decays of the  $\tau$  lepton. Here not only the total hadronic

width but also spectral moments of the hadron mass distribution have been calculated to  $O(\alpha_s^3)$  [17] and measured with high precision [18,19].

The measurement is based on the ratio of the hadronic to leptonic decay widths, which is given theoretically by

$$R_\tau = \frac{\Gamma(\tau \rightarrow \nu_\tau + \text{hadrons})}{\Gamma(\tau \rightarrow \nu_\tau \bar{\nu}_e e)} = 3S_{\text{EW}}(1 + \delta_{\text{PQCD}} + \delta_{\text{NPQCD}}). \quad (12.10)$$

$S_{\text{EW}} = 1.0194$  is known from electroweak theory [20]. The perturbative contribution  $\delta_{\text{PQCD}}$  is known up to third order [21]:

$$\delta_{\text{PQCD}} = a + 5.2a^2 + 26.4a^3 (\pm 130a^4), \quad (12.11)$$

where  $a = \alpha_s(m_\tau^2)/\pi$ . The fourth-order contribution (in brackets) has the coefficient chosen by Braaten *et al.* [17] to estimate the error due to higher orders. Since  $a$  turns out to be about 0.1 it is easy to see the size of the various contributions to  $\delta_{\text{PQCD}}$ .

At the very low scale of these measurements,  $Q \sim m_\tau$ , one has to be sure that not only the perturbative correction  $\delta_{\text{PQCD}}$  but also the non-perturbative, power-suppressed contribution  $\delta_{\text{NPQCD}}$  are well under control. Fortunately, much can be inferred about power corrections from the operator product expansion (OPE) [17]. There should be terms of the form  $c_D^i \langle O(D) \rangle / m_\tau^D$  ( $D = 4, 6, \dots$ ),  $c_D^i$  is a computable coefficient for the  $i$ -th spectral moment, and the parameters  $\langle O(D) \rangle$  describe vacuum condensates of the corresponding dimension [8]. There should be no  $D = 2$  terms apart from those induced by the (current) quark masses, which are negligible except for decays to  $s\bar{u}$ . The  $D = 4$  terms should correspond to the gluon condensate  $\langle \alpha_s G^2 \rangle$  measured in other processes. All these predictions are well confirmed by the data [18,19,22], and in particular there is no evidence of power corrections outside the framework of the OPE.

In the case of the total hadronic rate  $R_\tau$ , the contribution of  $\langle \alpha_s G^2 \rangle$  vanishes at leading order in  $\alpha_s$ , and therefore the expected non-perturbative correction is particularly small, coming predominantly from  $D = 6$  four-quark operators. The estimate of ref. [17] is

$$\delta_{\text{NPQCD}} = -0.007 \pm 0.004. \quad (12.12)$$

The experimental value of  $R_\tau$  is deduced from the leptonic branching fraction  $B_l$  via the relation

$$R_\tau = \frac{1 - B_e - B_\mu}{B_l} = \frac{1}{B_l} - 1 - f_\mu \quad (12.13)$$

where  $f_\mu = 0.9726$  is a phase space correction.  $B_l$  can be measured in three independent ways: from the  $e$  and  $\mu$  leptonic branching ratios,  $B_e = B_l$  and  $B_\mu = f_\mu B_l$ , and from the lifetime  $\tau_\tau = B_l \tau_\mu (m_\mu/m_\tau)^5$ .

The result for  $\alpha_s$  shown in Table 12.1 is based on the two recent combined analyses of  $R_\tau$  and the spectral moments of the hadron mass distribution. These give [18,19]:

$$\begin{aligned}\alpha_s(m_\tau^2) &= 0.355 \pm 0.021 \text{ (ALEPH)} , \\ \alpha_s(m_\tau^2) &= 0.306 \pm 0.024 \text{ (CLEO)} .\end{aligned}\quad (12.14)$$

The slight discrepancy between the two values may be traced to different leptonic branching ratios. The hadronic mass spectra are in good agreement. In combining these results, we assign a rescaled error to take account of the discrepancy. Because of the shrinking error, the corresponding uncertainty in  $\alpha_s(M_Z^2)$  is still one of the smallest in Table 12.1.

The high precision of this determination of  $\alpha_s$  depends crucially on believing the small estimate (12.12) of the non-perturbative correction. A more cautious approach would be to allow for the possibility of a  $D = 2$  ( $1/m_\tau^2$ ) correction due to confinement effects. This would significantly increase the theoretical uncertainty [23].

## 12.4 Quarkonium

### 12.4.1 Lattice spectroscopy

The lattice formulation of QCD provides a potentially highly accurate method for determining  $\alpha_s$  because it allows the non-perturbative calculation of matrix elements which can be matched to perturbation theory. Experimental input enters in setting the scale for  $\alpha_s$ , using, for example, a hadron mass splitting. The determination requires that the lattice spacing should be small enough for perturbative behaviour to be seen at short distances, and that systematic errors in the calculated hadron masses should be under control.

There are a number of suitable definitions of  $\alpha_s$  on the lattice; for a recent review see ref. [24]. Definitions based on the static potential between heavy quarks have an appealing physical interpretation. A popular choice is  $\alpha_V$ , defined in terms of the Fourier transform of the potential,  $\tilde{V}(q)$ :

$$\alpha_V(q^2) = -\frac{q^2}{4\pi C_F} \tilde{V}(q) . \quad (12.15)$$

The running of the coupling constant from various definitions can be measured and is found to agree well with two-loop perturbation theory down to scales as low as 2 GeV. Most of these studies have used the quenched approximation, in which light quark loops are neglected.

The simplest definition of  $\alpha_s$ , but one which does not directly allow for tests of its running, is based on the average plaquette, *i.e.* the expectation

value of the  $1 \times 1$  Wilson loop operator (2.74). This quantity,  $\alpha_P$ , is chosen to agree with  $\alpha_V$  defined from the heavy quark potential to  $O(\alpha_S^2)$ . It is readily measured on both quenched and unquenched configurations and so has been used to provide a determination of  $\alpha_S$  for the physical number of light quark flavours [25, 26, 27].

To set the scale for  $\alpha_S$ , *i.e.* to measure the lattice spacing, there are also a variety of choices. A useful set of splittings are those in the spin-averaged heavy quarkonium spectrum, since they are experimentally independent of the other parameter in the theory, the heavy quark mass (see Fig. 10.29), and are relatively insensitive to the quenched approximation. The spectrum can be calculated with low statistical and systematic errors on the lattice either using the Wilson formulation, with modifications [25, 26], or by an expansion around the non-relativistic limit (NRQCD) [28, 29]. In the latter case it has been possible to show that the values of the lattice spacing obtained from comparing different splittings to experiment are more consistent when dynamical fermions are included than in the quenched approximation. This is equivalent to saying that values of  $\alpha_P$  at a fixed scale in physical units converge as  $n_f$  is increased to the physical value. Fig. 12.2 illustrates this point.

Combining a measurement of  $\alpha_P$  with a determination of the lattice spacing from the  $\Upsilon$  spectrum and extrapolating to  $n_f = 3$  gives

$$\alpha_P^{(n_f=3)} ((8.2 \text{ GeV})^2) = 0.195 \pm 0.003 , \quad (12.16)$$

where only the lattice Monte Carlo statistical error is displayed. The scale of 8.2 GeV is set by the lattice spacing. To obtain the  $\overline{\text{MS}}$  coupling one must make the conversion

$$\alpha_{\overline{\text{MS}}}^{(n_f)}(Q^2) = \alpha_P^{(n_f)}(e^{5/3}Q^2) \left[ 1 + \frac{2}{\pi} \alpha_P^{(n_f)} + O((\alpha_P^{(n_f)})^2) \right] . \quad (12.17)$$

The factor of  $\exp(5/3)$  absorbs the  $n_f$  dependence in (at least) the second term. The scale is thus converted to  $Q = 8.2e^{-5/6} = 3.6$  GeV for  $\alpha_{\overline{\text{MS}}}$ , and one obtains

$$\alpha_{\overline{\text{MS}}}^{(n_f=3)} ((3.6 \text{ GeV})^2) = 0.219 \pm 0.003 \quad (12.18)$$

(statistical error only) if the  $O(\alpha_P^2)$  term is set to zero. Estimating systematic errors due to the extrapolations in  $n_f$ , dynamical quark masses and lattice spacing, one obtains the result displayed in Table 12.1.

In fact the coefficient of the  $O(\alpha_P^2)$  term in Eq. (12.17) has been calculated for  $n_f = 0$  [30]. Using this value (0.96) instead of zero, one would obtain  $\alpha_S(M_Z^2) = 0.117$  instead of 0.115 [29].

The unquenched calculation using Wilson heavy fermions compared with charmonium data [26] obtains consistent, although somewhat lower, results with larger errors, as summarized in Table 12.1.

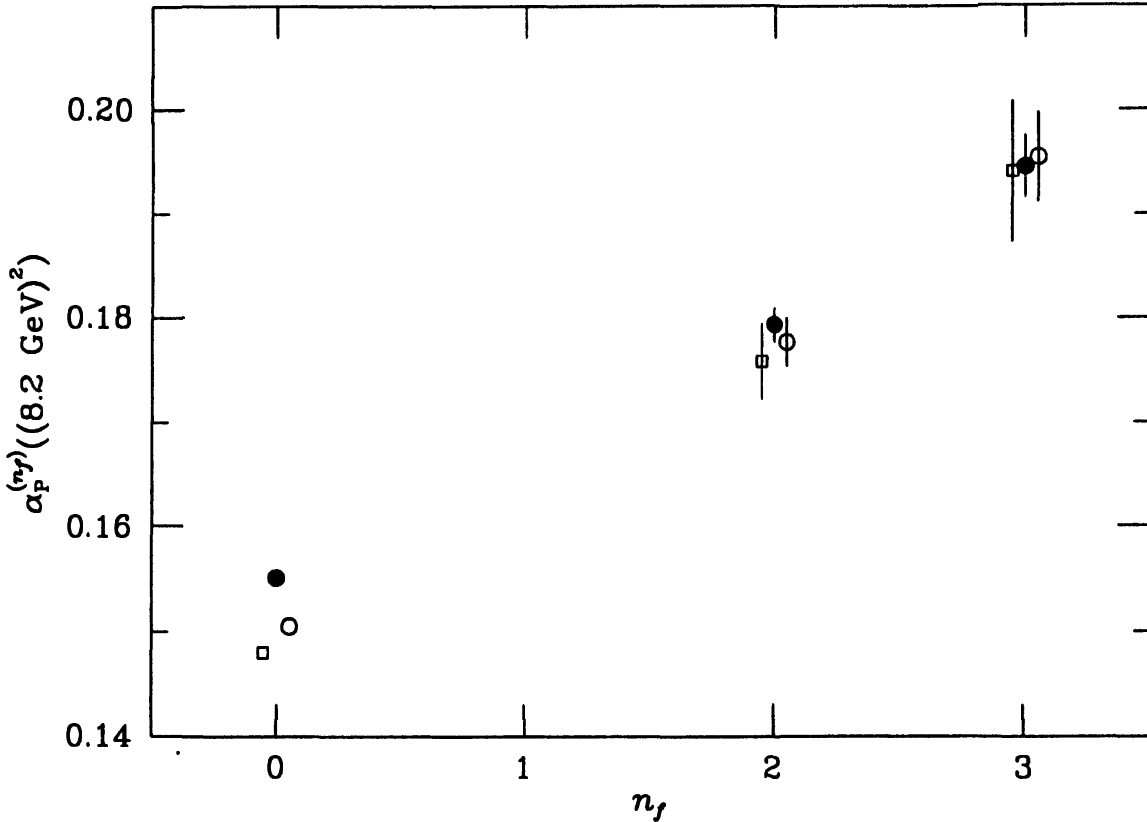


Fig. 12.2.  $\alpha_P^{(n_f)}((8.2 \text{ GeV})^2)$  versus  $n_f$  with the scale set by the  $\Upsilon$  1S-1P (full circles), the  $\Upsilon$  1S-2S (open circles) or the charmonium 1S-1P (boxes, preliminary) splitting. The points at  $n_f = 3$  are extrapolated from  $n_f = 0$  and 2. Adapted from ref. [29].

#### 12.4.2 Quarkonium decays

The other quarkonium results shown in Table 12.1 are from the decay widths of  ${}^3S_1 Q\bar{Q}$  states. If  $m_Q \gg \Lambda$  then the short- and long-distance effects on the width can be factorized, with the former calculable in perturbative QCD. The leading-order results were given in Section 10.7. In order to measure  $\alpha_s$ , one needs at least the next-to-leading order predictions [31], which for the  $\Upsilon$  are

$$\begin{aligned} \Gamma^{\mu\mu} &= \frac{1}{9} \frac{|R_0(0)|^2}{m_b^2} \alpha^2 \left[ 1 - \frac{16}{3} \frac{\alpha_s}{\pi} + \dots \right] \\ \Gamma^{\gamma gg} &= \frac{8(\pi^2 - 9)}{81\pi} \frac{|R_0(0)|^2}{m_b^2} \alpha \alpha_s^2 \left[ 1 - 7.4 \frac{\alpha_s}{\pi} + \dots \right] \\ \Gamma^{ggg} &= \frac{10(\pi^2 - 9)}{81\pi} \frac{|R_0(0)|^2}{m_b^2} \alpha_s^3 \left[ 1 - 4.9 \frac{\alpha_s}{\pi} + \dots \right], \end{aligned} \quad (12.19)$$

in the  $\overline{\text{MS}}$  scheme with  $\mu = m_b$ .

The dependence on  $R_0(0)$ , the radial wave function at the origin, can

be eliminated by forming ratios. Including the dependence on the renormalization scale explicitly, to next-to-leading order,

$$\begin{aligned} R_\mu &\equiv \frac{\Gamma^{ggg}}{\Gamma^{\mu\mu}} = \frac{10(\pi^2 - 9)}{9\pi} \frac{\alpha_s^3(\mu^2)}{\alpha^2} \left\{ 1 + \left[ 0.4 - 6.3 \ln\left(\frac{m_b^2}{\mu^2}\right) \right] \frac{\alpha_s(\mu^2)}{\pi} \right\} \\ R_\gamma &\equiv \frac{\Gamma^{\gamma gg}}{\Gamma^{ggg}} = \frac{4}{5} \frac{\alpha}{\alpha_s(\mu^2)} \left\{ 1 - \left[ 2.6 - 2.1 \ln\left(\frac{m_b^2}{\mu^2}\right) \right] \frac{\alpha_s(\mu^2)}{\pi} \right\}. \end{aligned} \quad (12.20)$$

In principle,  $R_\gamma$  provides a relatively clean measurement of  $\alpha_s$ . In practice, there are non-negligible corrections from the photon acceptance and from relativistic effects. A more complete discussion can be found in ref. [32].

## 12.5 $e^+e^-$ annihilation

### 12.5.1 Hadronic cross section

Measurements of  $\alpha_s$  have been performed using the total cross section for  $e^+e^-$  annihilation into hadrons at intermediate energies. In some cases the original analyses used obsolete values of electroweak parameters or radiative corrections; the result quoted in Table 12.1, taken from ref. [2], has been corrected for these effects as far as possible.

The result based on the hadronic width of the  $Z^0$  boson represents in fact the latest  $\alpha_s$  value from the combined fits of the LEP Electroweak Working Group [33] to LEP and SLC data. Although the data fitted include forward-backward asymmetries and partial widths for heavy quark decays, the value obtained depends essentially on the peak cross section, the total width and the leptonic branching fraction. The result is

$$\alpha_s(M_Z^2) = 0.123 \pm 0.004 \pm 0.002, \quad (12.21)$$

where the first error is that of the fit at a fixed Higgs boson mass,  $M_H = 300$  GeV, and the second is the variation in the result when the Higgs mass is varied in the range  $60 < M_H < 1000$  GeV.

At present, the LEP results on the  $Z^0$  branching fractions into charm and bottom quarks are not in good agreement with the Standard Model. The current values are [33]

$$\begin{aligned} R_b &= 0.2219 \pm 0.0017 \quad (\text{SM: } 0.2156), \\ R_c &= 0.1543 \pm 0.0074 \quad (\text{SM: } 0.1724). \end{aligned} \quad (12.22)$$

The excess of decays into  $b\bar{b}$  has led to speculation that there is new physics in this channel (see for example ref. [34]). If this were the case then of course the fitted value of  $\alpha_s$  could be modified. Note, however, that the charm decay fraction  $R_c$  deviates downwards, to such an extent that

the sum of  $R_b$  and  $R_c$  is below the Standard Model prediction, although still within two standard deviations of it:

$$R_b + R_c = 0.3762 \pm 0.0076 \quad (\text{SM: } 0.3880) . \quad (12.23)$$

Consequently it is not clear whether new physics, if present in heavy quark channels, would imply an increase or a decrease in the fitted value of  $\alpha_s$ .

### 12.5.2 Event shapes

Determinations of  $\alpha_s$  are available using  $e^+e^-$  event shape and jet rate distributions computed to next-to-leading order in  $\alpha_s$  (NLO) or with large logarithms resummed to all orders as discussed in Section 6.5. The result at 10.5 GeV is from the CLEO collaboration at CESR [35]. Results at 58 GeV are those of the TRISTAN experiments [36], the NLO value being an average taken from ref. [37]. Event shapes and jet rates in  $Z^0$  decay have been analysed by the LEP and SLC experiments to NLO [38] and including resummation [39]. Although these two methods of analysis use some of the same data, the regions of event shape distributions fitted and the associated systematic errors are rather different, so we treat them as independent measurements. For recent reviews of event shape analyses see for example refs. [1,2]. A measurement at 133 GeV by the L3 collaboration at LEP [40], based on resummed event shapes, is also shown.

The connection between the perturbative predictions of event shapes and the corresponding quantities derived from the hadrons observed experimentally is made by performing hadronization corrections, estimated by means of the models described in Section 5.6. These corrections are nominally of order  $\Lambda/Q$ , but in Monte Carlo studies are often found to be of order 10% or larger at LEP energies, their size depending on the particular observable and the range of values fitted. Typically, the NLO perturbative correction term is also about 10%. Thus the estimated uncertainty in the hadronization correction makes a substantial contribution to the systematic error in  $\alpha_s$ . Note that, despite the high energy, power-suppressed terms play a more important role here than in fully inclusive measurements at lower energies. In the  $\tau$  decay rate, for example, the leading power correction is only expected to be of order  $\Lambda^4/Q^4$ , as discussed above.

### 12.5.3 Scaling violation in fragmentation

The analysis of scaling violation in jet fragmentation in  $e^+e^-$  annihilation was discussed in Section 6.1.1. Here the errors are larger than in deep inelastic scattering because the typical scale  $Q$  is higher and high-precision data have been obtained only at  $Q = M_Z$ . The first analysis

[41] used a fixed-order matrix element model with a cut-off, while that of [42] is essentially model independent. Therefore only the latter is shown in Table 12.1.

## 12.6 Hadron-hadron scattering

Determinations of  $\alpha_s$  at hadron-hadron ( $pp$  and  $p\bar{p}$ ) colliders have been performed by comparing direct photon, heavy quark, and  $W$  boson plus jet cross sections with next-to-leading order predictions. Measurements based on pure jet production are only possible for the two-jet case, because calculations of the NLO corrections to multijet production have not yet been completed.

So far, the precision achieved in hadron-hadron determinations has been less than that in  $e^+e^-$  and lepton-hadron processes, owing to the larger experimental and theoretical uncertainties associated with incoming hadrons. First of all, there are extra uncertainties associated with the parton distributions of the incoming hadrons. The hadronic final state is also more complicated, containing not only the products of the perturbative hard subprocess but also the soft remnants of spectator partons, *i.e.* those that do not participate in the hard subprocess, and their interactions. Furthermore in most cases the nature and kinematics of the hard subprocess are less well known.

Amongst the best understood processes in hadron-hadron collisions are vector boson and vector boson plus jet production, as explained in Chapter 9. From the ratio of these two cross sections for  $W$  bosons, the UA1 [43] and UA2 [44] collaborations at CERN determined

$$\begin{aligned}\alpha_s(M_W^2) &= 0.127 \pm 0.026(\text{stat.}) \pm 0.034(\text{sys.}) \quad (\text{UA1}), \\ \alpha_s(M_W^2) &= 0.123 \pm 0.018(\text{stat.}) \pm 0.017(\text{sys.}) \quad (\text{UA2}).\end{aligned}\quad (12.24)$$

Combining these results and translating from scale  $M_W$  to  $M_Z$  gives the result shown in Table 12.1.

Direct photon production in proton-proton and proton-antiproton collisions, discussed in Section 7.9, has been used for the measurement of  $\alpha_s$  by the UA6 collaboration in ref. [45]. The hard subprocess is similar to that for  $W$  boson production at large transverse momentum. The difference  $\sigma(p\bar{p} \rightarrow \gamma X) - \sigma(pp \rightarrow \gamma X)$  is measured in order to cancel the relatively poorly known contributions of the sea quark and gluon distributions in the proton, leaving the better known valence part. The scale  $Q$  is set by the transverse momentum of the photon,  $p_T \sim 4$  GeV, giving the result shown.

Another hadronic process that has been used to determine  $\alpha_s$  is heavy quark production. The UA1 collaboration [46] obtained the results shown

from a comparison between their data on  $b\bar{b}$  production and the  $O(\alpha_s^3)$  calculation of ref. [47]. For a first attempt to extract  $\alpha_s$  from the jet-jet rate see ref. [48].

## 12.7 Conclusions

Evolving all of the  $\alpha_s$  measurements to  $Q = M_Z$ , we obtain the results given in the fourth column of Table 12.1 and shown graphically in Fig. 12.3. The indicated errors typically have large systematic and theoretical components, so it is difficult to quantify the level of agreement between the different methods of measurement. If one ignores this problem, chi-squared minimization gives a good fit ( $\chi^2/\text{d.o.f.} = 13.5/21$ ) with  $\alpha_s(M_Z^2) = 0.1162 \pm 0.0012$ . A more cautious approach to the error would be to assign an uncertainty equal to that of a typical measurement by a reliable method. This leads to our ‘global preferred value’

$$\alpha_s(M_Z^2) = 0.116 \pm 0.005 , \quad (12.25)$$

which is close to the one given in ref. [49]. The corresponding value of the five-flavour scale, defined according to Eq. (12.2), is<sup>1</sup>

$$\Lambda_{\overline{\text{MS}}}^{(5)} = 202 \pm 65 \text{ MeV} . \quad (12.26)$$

The results in Fig. 12.3, which are presented roughly in increasing order of energy scale, tend to lie slightly below the mean value (12.25) at low scales (say, up to  $Q = 20$  GeV) and above it at higher scales. This tendency is not strong enough to be taken very seriously at present. Nevertheless it is interesting to consider possible causes of such an effect.

One obvious possibility is that the running of  $\alpha_s$  is not as expected. This would be the case if new types of coloured particles were contributing to the QCD  $\beta$  function. One candidate would be a low-mass spin one-half supersymmetric partner to the gluon, a light gluino [50]. However, gluino masses in the appropriate range are disfavoured by other data [39,51]. For example, studies of  $e^+e^- \rightarrow 4$  jets have found no sign of the production of non-standard coloured particles.

Another possibility is that there is a systematic difference between hard processes in which the large momentum scale is spacelike, as in deep inelastic scattering, and those in which it is timelike, as in  $e^+e^-$  annihilation [52]. Then the association of low  $\alpha_s(M_Z^2)$  with low scales would not be significant, being merely a reflection of the fact that deep inelastic data predominate at lower scales. Data from HERA will play a crucial role in testing this hypothesis. Further results from  $\tau$  decay will also be helpful.

---

<sup>1</sup> If the definition (2.44) is used, the value becomes  $217 \pm 70$  MeV.

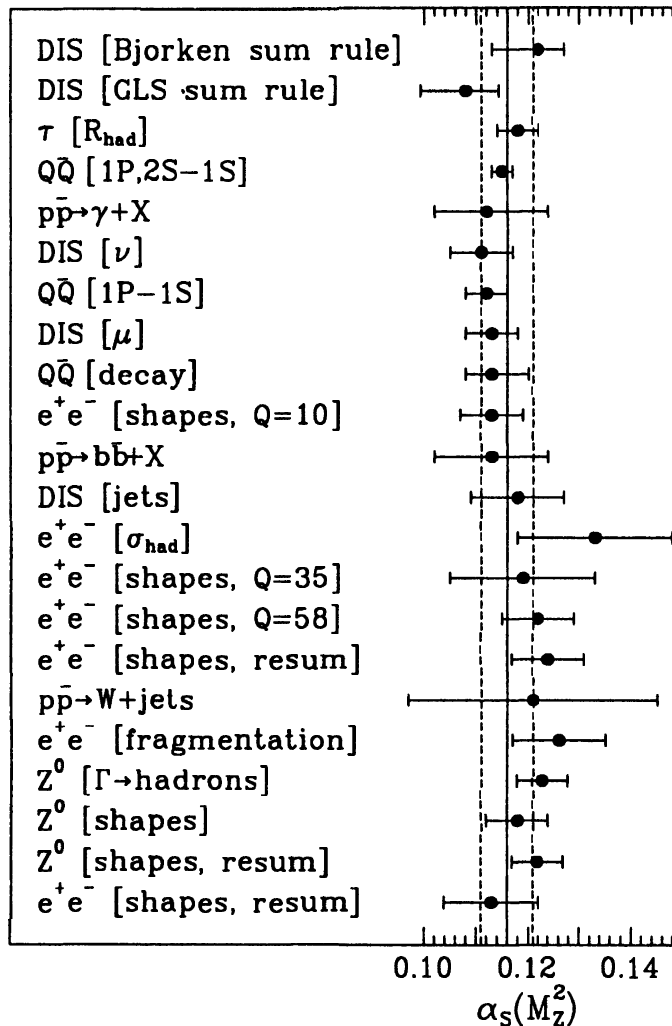


Fig. 12.3. Summary of  $\alpha_s$  measurements, evolved to the scale  $M_Z$ . The lines correspond to Eqs. (12.25,12.26).

If the running of  $\alpha_s$  is not as expected, this process should yield a low value because of its low scale. In the other scenario, it would give a high value because it is timelike.

A third possible source of discrepancy that has been suggested [1] is the effect of quark masses. The lowest  $\alpha_s$  values seem to be concentrated in the intermediate region of  $Q$  in which heavy quarks start to play a role. Most higher-order QCD corrections have been calculated only in the massless quark limit, and might therefore be unreliable in this region. An exception is the total  $e^+e^-$  hadronic rate [53], making a precision measurement of this quantity at an intermediate scale very desirable.

## References

- 1) S. Bethke, in Proc. QCD94 Conference, Montpellier, July 1994, *Nucl. Phys. B (Proc. Suppl.)* **39BC** (1995) 198.
- 2) M. Schmelling, *Physica Scripta* **51** (1995) 683.
- 3) J. Ellis and M. Karliner, *Phys. Lett.* **B341** (1995) 397.
- 4) EMC collaboration, J. Ashman *et al.*, *Phys. Lett.* **B206** (1988) 364, *Nucl. Phys.* **B328** (1989) 1;  
SMC collaboration, B. Adeva *et al.*, *Phys. Lett.* **B302** (1993) 533; *ibid.* **B320** (1994) 400; D. Adams *et al.*, *Phys. Lett.* **B329** (1994) 399.
- 5) E142 collaboration, P.L. Anthony *et al.*, *Phys. Rev. Lett.* **71** (1993) 959;  
E143 collaboration, K. Abe *et al.*, *Phys. Rev. Lett.* **74** (1995) 346; *ibid.* **75** (1995) 25.
- 6) S.A. Larin and J.A.M. Vermaasen, *Phys. Lett.* **B259** (1991) 345.
- 7) V.M. Braun and A.V. Kolesnichenko, *Nucl. Phys.* **B283** (1987) 723.
- 8) M.A. Shifman, A.I. Vainshtein and V.I. Zakharov, *Nucl. Phys.* **B147** (1979) 385, 448, 519.
- 9) CCFR-NuTeV collaboration, D.A. Harris *et al.*, in Proc. 30th Rencontres de Moriond, Meribel les Allues, France, ed. J. Trân Thanh Vân, Editions Frontières, Gif sur Yvette (1996).
- 10) CCFR collaboration, P.Z. Quintas *et al.*, *Phys. Rev. Lett.* **71** (1993) 1307.
- 11) H1 collaboration, T. Ahmed *et al.*, *Phys. Lett.* **B346** (1995) 415.
- 12) ZEUS collaboration, M. Derrick *et al.*, *Phys. Lett.* **B363** (1995) 201.
- 13) T. Brodkorb and J.G. Körner, *Zeit. Phys.* **C54** (1992) 519;  
T. Brodkorb and E. Mirkes, *Zeit. Phys.* **C66** (1995) 141;  
E. Mirkes and D. Zeppenfeld, Karlsruhe preprint TTP-95-42 (1995).
- 14) D. Graudenz, *Phys. Lett.* **B256** (1992) 518, *Phys. Rev.* **D49** (1994) 3291, *Comp. Phys. Comm.* **92** (1995) 65.
- 15) T. Brodkorb and J.G. Körner, E. Mirkes and G.A. Schuler, *Zeit. Phys.* **C44** (1989) 415.
- 16) A. Vogt, *Phys. Lett.* **B354** (1995) 145;  
A. Martin, R.G. Roberts and W.J. Stirling, *Phys. Lett.* **B356** (1995) 89.
- 17) E. Braaten, S. Narison and A. Pich, *Nucl. Phys.* **B373** (1992) 581;  
F. Le Diberder and A. Pich, *Phys. Lett.* **B289** (1992) 165.
- 18) ALEPH collaboration, D. Buskulic *et al.*, *Phys. Lett.* **B307** (1993) 209, L. Duflot, in Proc. QCD94 Conference, Montpellier, July 1994, *Nucl. Phys. B (Proc. Suppl.)* **39BC** (1995) 322.
- 19) CLEO collaboration, T. Coan *et al.*, *Phys. Lett.* **B356** (1995) 580.
- 20) W. Marciano and A. Sirlin, *Phys. Rev. Lett.* **61** (1988) 1815.
- 21) L.R. Surguladze *et al.*, *Phys. Rev. Lett.* **66** (1991) 560;  
S. Gorishny *et al.*, *Phys. Lett.* **B259** (1991) 144.
- 22) R. Stroynowski, in Proc. 27th Int. Conf. on High Energy Physics, Glasgow, July 1994, eds. P.J. Bussey and I.G. Knowles, Institute of Physics Publishing, Bristol (1995), Vol. II, p. 859.
- 23) G. Altarelli, P. Nason and G. Ridolfi, *Zeit. Phys.* **C68** (1995) 257.
- 24) P. Weisz, in Proc. Int. Symposium on Lattice Field Theory, Melbourne, July 1995.
- 25) A.X. El-Khadra, *Nucl. Phys. B (Proc. Suppl.)* **34** (1994) 141; A. El-Khadra, G. Hockney, A. Kronfeld and P. Mackenzie, *Phys. Rev. Lett.* **69** (1992) 729.
- 26) S. Aoki, M. Fukugita, S. Hashimoto, N. Ishizuka, H. Mino, M. Okawa, T. Onogi and A. Ukawa, *Phys. Rev. Lett.* **74** (1995) 22.
- 27) C.T.H. Davies, K. Hornbostel, G.P. Lepage, A. Lidsey, J. Shigemitsu and J. Sloan, *Phys. Lett.* **B345** (1995) 42.

- 28) G.P. Lepage, L. Magnea, C. Nakhleh, U. Magnea and K. Hornbostel, *Phys. Rev.* **D46** (1992) 4052.
- 29) C.T.H. Davies, A.J. Lidsey, P. McCallum, K. Hornbostel, G.P. Lepage, J. Shigemitsu and J. Sloan, in Proc. Int. Symposium on Lattice Field Theory, Melbourne, July 1-5.
- 30) M. Lüscher and P. Weisz, *Phys. Lett.* **B349** (1995) 165.
- 31) S.J. Brodsky, G.P. Lepage and P. Mackenzie, *Phys. Rev.* **D28** (1983) 228.
- 32) K. Kwong *et al.*, *Phys. Rev.* **D37** (1988) 3210.
- 33) D. Schaile, Proc. 27th Int. Conf. on High Energy Physics, Glasgow, July 1994, eds. P.J. Bussey and I.G. Knowles, Institute of Physics Publishing, Bristol (1995), Vol. I, p. 27;  
LEP Electroweak Working Group, CERN preprint PPE/95-172 (1995).
- 34) M. Shifman, *Mod. Phys. Lett.* **A10** (1995) 605.
- 35) CLEO collaboration, L. Gibbons *et al.*, Cornell preprint CLNS-95-1323 (1995).
- 36) VENUS collaboration, K. Abe *et al.*, *Phys. Lett.* **B240** (1990) 232;  
AMY collaboration, K.B. Lee *et al.*, *Phys. Lett.* **B313** (1993) 469;  
TOPAZ collaboration, Y. Ohnishi *et al.*, *Phys. Lett.* **B313** (1993) 475.
- 37) S. Bethke, in Proc. 26th Int. Conf. on High Energy Physics, Dallas, August 1992, ed. J.R. Sanford, AIP, New York (1993).
- 38) ALEPH collaboration, D. Decamp *et al.*, *Phys. Lett.* **B257** (1991) 479;  
DELPHI collaboration, P. Abreu *et al.*, *Zeit. Phys.* **C54** (1992) 55;  
L3 collaboration, O. Adriani *et al.*, *Phys. Rep.* **236** (1993) 1;  
OPAL collaboration, P.D. Acton *et al.*, *Zeit. Phys.* **C55** (1992) 1;  
Mark II collaboration, S. Komamiya *et al.*, *Phys. Rev. Lett.* **64** (1990) 987.
- 39) ALEPH collaboration, D. Decamp *et al.*, *Phys. Lett.* **B284** (1992) 163;  
DELPHI collaboration, P. Abreu *et al.*, *Zeit. Phys.* **C59** (1993) 21;  
L3 collaboration, O. Adriani *et al.*, *Phys. Lett.* **B284** (1992) 471;  
OPAL collaboration, P.D. Acton *et al.*, *Zeit. Phys.* **C59** (1993) 1, R. Akers *et al.*, *Zeit. Phys.* **C68** (1995) 519;  
SLD collaboration, K. Abe *et al.*, *Phys. Rev.* **D51** (1995) 962.
- 40) L3 collaboration, M. Acciarri *et al.*, *Phys. Lett.* **B371** (1996) 137.
- 41) DELPHI collaboration, P. Abreu *et al.*, *Phys. Lett.* **B311** (1993) 408.
- 42) ALEPH collaboration, D. Buskulic *et al.*, *Phys. Lett.* **B357** (1995) 487; *ibid.* **B364** (1995) 247(erratum).
- 43) M. Lindgren *et al.*, *Phys. Rev.* **D45** (1992) 3038.
- 44) UA2 collaboration, J. Alitti *et al.*, *Phys. Lett.* **B263** (1991) 563.
- 45) UA6 collaboration, G. Ballocchi *et al.*, *Phys. Lett.* **B317** (1993) 250.
- 46) UA1 collaboration, C. Albajar *et al.*, *Phys. Lett.* **B369** (1996) 46.
- 47) P. Nason, S. Dawson and R.K. Ellis, *Nucl. Phys.* **327** (1989) 49;  
M.L. Mangano, P. Nason and G. Ridolfi, *Nucl. Phys.* **373** (1992) 295.
- 48) W.T. Giele, E.W.N. Glover and J. Yu, *Phys. Rev.* **D53** (1996) 120.
- 49) Particle Data Group, L. Montanet *et al.*, *Review of Particle Properties*, *Phys. Rev.* **D50** (1994) 1173.
- 50) G.R. Farrar, *Phys. Rev.* **D51** (1995) 3904.
- 51) S. Banerjee, in Proc. 27th Int. Conf. on High Energy Physics, Glasgow, July 1994, eds. P.J. Bussey and I.G. Knowles, Institute of Physics Publishing, Bristol (1995), Vol. II, p. 889.
- 52) J. Ellis, D.V. Nanopoulos and D.A. Ross, *Phys. Lett.* **B267** (1991) 132.
- 53) K.G. Chetyrkin, J.H. Kühn and M. Steinhauser, *Phys. Lett.* **B371** (1996) 93.

# Index

## — A —

action  
  Euclidean, 40  
  lattice, 42  
  Wilson, 44, 419  
Adler sum rule, 127  
Altarelli-Parisi equation, 108, 167, 170, 195  
  singlet, 110, 115  
  solution, 116  
angular ordering, 179, 183  
anomalies, 281  
anomalous dimension, 30, 114, 196  
  higher-order, 196  
 $j \gg 1$ , 117  
 $j \rightarrow 1$   
  spacelike, 132  
  timelike, 203  
leading-order, 115  
resummed, 203  
antenna pattern, 179  
 $\alpha_s$ , 411  
  running, 22, 24, 172, 413  
  shrinking error, 412  
  value, 424  
asymptotic freedom, 4, 22, 26–27  
average multiplicity, 217  
  hadron, 200  
  jet, 231  
axial gauge, 11

## — B —

backward evolution, 175  
Bengtsson-Zerwas angle, 78, 163  
 $\beta$  function  
  QCD, 24  
  QED, 24  
BFKL equation, 137–139  
binomial moments, 214  
Bjorken scaling, 88  
Bjorken sum rule, 149, 415  
Bjorken  $x$ , 86  
Bloch-Nordsieck theorem, 58  
bottom quark  
  decays, 333  
  hadronic, 338  
  semi-leptonic, 334  
fragmentation function, 200, 372  
hadroproduction, 357, 360  
  cross section, 353  
  differential cross section, 360  
  transverse momentum  
    distribution, 361  
  in jets, 374  
mass, 1, 31, 357, 392  
weak isospin, 362  
bottomonium, 375  
branching  
  algorithm, 173  
  coherent, 178, 182  
  phase space, 164  
  spacelike, 165, 172  
  timelike, 158, 168

Breit frame of reference, 211  
 Breit-Wigner distribution, 312

— C —

*C*-parameter, 72  
 Cabibbo angle, 288  
 Callan-Gross relation, 91, 97  
 charm quark  
   decays, 333  
   hadronic, 338  
   semi-leptonic, 334  
 fragmentation function, 200, 372  
 hadroproduction, 357  
 in jets, 374  
 mass, 1, 357  
 parton distribution, 93  
 photoproduction, 359  
 charmonium, 375, 418  
 chiral symmetry, 15  
 Chudakov effect, 180  
 CKM matrix, 288  
 coefficient function, 107, 194  
 coherence effect, 180  
 coherent branching, 178, 182  
 colour algebra, 181  
 colour dipole, 139  
 colour factors, 6  
   measurement, 77  
 condensate  
   gluon, 417  
   quark, 16  
 cone algorithm  
    $R$ , 247  
   Sterman-Weinberg, 64  
 confinement, 4, 22, 380  
 coupling  
   fermion, 284  
   running, 22, 24, 413  
 covariant derivative  
   electroweak, 271  
   QCD, 6  
 covariant parton model, 94  
 CP violation, 288  
   strong, 13

crossing, 89, 247, 257  
 custodial symmetry, 280

— D —

dead cone, 79  
 decays  
   heavy quarks, 333  
   hadronic, 338  
   semi-leptonic, 334  
   vector bosons, 290  
 deconfinement, 380  
 deep inelastic scattering, 86  
   charged current, 92  
   data, 122  
   jet production, 211, 416  
   kinematics, 86  
   neutral current, 91  
   neutrino, 87  
   polarized, 147  
   QCD corrections, 99, 107  
   saturation, 147  
   scaling violation, 415  
   small  $x$ , 128  
 DGLAP equation, 108  
 digamma function, 145  
 dilogarithm, 67  
 dimensional regularization, 37, 57,  
   104, 308  
 dimensional transmutation, 47  
 direct photon production, 264, 423  
 down quark  
   mass, 1, 16  
 Drell-Yan process, 301

— E —

$e^+e^-$  cross section  
   heavy quark, 62  
   jets, 63, 230  
   longitudinal, 209  
   on  $Z$  pole, 55  
   radiative corrections, 56  
   total, 3, 53, 421  
 eikonal

factor, 257  
 formula, 178  
 electroweak interactions, 270  
 energy profiles of jets, 260  
 energy-energy correlation, 75  
 Euler constant, 38, 226, 325  
 event generators, 186, 191  
 event shapes, 71, 220, 422  
 evolution equation, 165, 195  
 exponentiation, 223

**— F —**

factorization, 104, 193, 239–240, 302, 309  
 classical model, 240  
 power corrections, 242  
 scale, 238–239, 351  
 scheme, 105  
 Fermi constant, 276, 287  
 fermion  
 couplings, 284  
 doubling problem, 44  
 families (generations), 281  
 Feynman gauge, 11  
 Feynman rules, 8  
 electroweak, 277, 286  
 QCD, 9  
 Feynman  $x$ , 310  
 field strength tensor, 5  
 fine structure constant, 287, 368  
 flavour excitation, 353  
 flavour symmetry, 15  
 forward evolution, 175  
 fragmentation function, 193, 195  
 asymmetric, 207  
 $b$  and  $c$  quark, 200  
 current jet, 211  
 gluon, 200, 208, 219  
 longitudinal, 207  
 non-singlet, 196  
 photon, 268  
 power corrections, 200  
 scaling violation, 422  
 singlet, 196

small- $x$ , 204  
 transverse, 207

**— G —**

$\Gamma$  function, 38  
 gauge  
 axial, 11  
 Feynman, 11  
 fixing, 5, 8  
 invariance, 7  
 Landau, 11  
 light-cone, 11  
 parameter, 8  
 physical, 12  
 unitary, 274  
 Gell-Mann SU(3) matrices, 6  
 generating function, 213  
 gluon fragmentation, 215  
 jet rates, 230  
 quark fragmentation, 214  
 ghost field, 8  
 GLAP equation, 108, 167, 170, 195  
 singlet, 110, 115  
 solution, 116  
 gluino, 424  
 gluon  
 condensate, 417  
 mass, 8  
 momentum, 92  
 parton distribution, 92  
 scalar, 58, 73, 254  
 spin, 73, 77, 254, 329  
 gluon jet  
 compared to quark, 219, 263  
 fragmentation function, 219  
 Goldstone boson, 16, 293  
 Goldstone theorem, 16, 275  
 Gottfried sum rule, 128  
 Gross–Llewellyn Smith sum rule, 126, 415

**— H —**

hadronic tensor, 94

- hadronization, 54, 157, 175, 184  
 ‘tube’ model, 185, 210  
 cluster model, 188  
 corrections, 222, 422  
 independent fragmentation, 186  
 jet rates, 230  
 string model, 187  
 hadroproduction  
     direct photon, 264  
     heavy quark, 357  
     jets, 237, 246  
         experiment, 250  
         vector bosons, 301  
 handbag diagram, 96  
 heavy quark, 332  
     decays, 333  
     hadronic, 338  
     semi-leptonic, 334  
     spectator model, 338  
 effective theory, 18  
 fragmentation, 370  
 gluon emission, 78  
 in jets, 372  
 production, 423  
     higher order, 350  
     in  $e^+e^-$  annihilation, 62  
     lowest order, 347  
 symmetry, 17  
 helicity conservation, 162–163  
 Higgs boson, 272, 388  
 branching ratios, 391  
 decays, 278, 391  
 jet tagging, 407  
 mass  
     constraints, 389  
     experimental lower bound, 389  
     upper bound, 295  
 production  
     associated with  $t\bar{t}$ , 401  
     associated with  $W, Z$ , 401  
     at LHC, 397  
     at Tevatron, 399, 401  
     gluon-gluon fusion, 397  
     irreducible background, 404  
     mechanisms, 397  
      $WW, ZZ$  fusion, 399  
     width, 278  
 Higgs field, 272  
     vacuum expectation value, 274, 276  
 Higgs mechanism, 272  
 Higgs potential, 273  
 higher twist, 123, 127, 415  
 hopping parameter, 45  
 hypercharge, weak, 271, 281
- I —
- independent fragmentation, 186  
 infinite momentum frame, 88  
 infra-red cut-off, 171, 183  
 infra-red sensitivity, 193  
 irreducible background, 404  
 Isgur-Wise function, 19  
 isospin  
     strong, 15, 127  
     weak, 271, 281
- J —
- Jacobian peak, 320  
 jet  
     deep inelastic scattering, 416  
      $e^+e^-$ , 63  
      $e^+e^-$  and  $ep$  compared, 212  
      $e^+e^-$  and  $p\bar{p}$  compared, 263  
     hadron-hadron scattering, 246  
     hadroproduction, 237, 246  
         angular distribution, 250, 252  
         experiment, 250  
          $E_T$  distribution, 251  
         kinematics, 246  
         multijet, 255, 260  
         three-jet, 258  
         two-jet, 247  
     mass distribution, 224  
     merging, 261  
     production  
         in association with  $W$ , 327  
         in association with  $Z$ , 327  
         two-jet, 250  
     profiles, 260

rates, 228, 422  
 shapes, 220  
 width, 219  
 jet algorithm  
 cluster, 66  
 cone, 247

Snowmass accord, 260

JADE, 66, 416

$k_T$  (Durham), 71

$R$ , 247

Sterman-Weinberg, 64, 219

jet fragmentation, 193, 195

in deep inelastic scattering, 211

quark-gluon differences, 219

jet multiplicity, 231

in deep inelastic scattering, 234

leading-log approximation, 232

matching to fixed-order, 234

next-to-leading logs, 233

## — K —

KLN theorem, 58

KNO scaling, 218

## — L —

Lagrangian

electroweak, 271

Higgs, 276

QCD, 5

$\Lambda$  parameter, 34

flavour dependence, 35

value, 424

Landau gauge, 11

large logarithms, 71, 129, 136, 138

large  $N$  limit, 142

lattice QCD, 39, 418

lattice simulations, 45

light-cone coordinates, 355

light-cone gauge, 11

Lipatov characteristic function, 145

$\text{Li}_2$  function, 67

local parton-hadron duality, 184

log matching, 226

luminosity  
 accelerator, 242  
 partonic, 243

## — M —

Mandelstam variables, 89

Mellin transform, 114, 195

inverse, 116, 120

minimal subtraction scheme, 38

MLLA approximation, 205

moments

binomial, 214

fragmentation function, 195

multiplicity, 216

structure function, 114

Monte Carlo simulation, 166, 170, 173, 191

multijet production, 255, 260

multiplicity

average, 217

distribution, 216

width, 218

moments, 216

## — N —

Nachtmann-Reiter angle, 78

narrow width approximation, 312, 343

neutral current, 91

neutrinos, number of, 291

non-relativistic QCD, 379, 419

## — O —

optical theorem, 294

## — P —

parallel transporter, 41

parton

branching, 158

- cascade**, 174
  - distribution**, 92, 166
  - luminosity**, 243
  - shower**, 157, 174
  - wee**, 98
  - parton model**
    - covariant**, 94
    - deep inelastic scattering**, 86
    - in field theory**, 93
    - naive**, 86, 90
    - QCD improved**, 98, 237
  - perturbative unitarity**, 293
  - Peterson function**, 370
  - phase space**
    - branching**, 164
    - multi-body**, 343
    - three-body**, 56
    - two-body**, 278
  - physical gauge**, 12
  - $\pi^0$  **decay**, 2
  - planar approximation**, 142
  - plus prescription**, 167
  - pointlike constituents**, 88
  - polarization**
    - in deep inelastic scattering**, 147
    - in parton branching**, 161–163, 174
    - in top decay**, 341
    - in vector boson production**, 295
    - in vector boson scattering**, 292
    - sum**, 101
  - pomeron**, 130
  - positronium**, 375
  - potential**
    - Higgs**, 273
    - QCD**, 49, 418
  - power corrections**, 123, 127, 200, 242, 412, 415, 417, 422
    - heavy quark mass**, 338–339, 350
  - preconfinement**, 188
  - pseudo-rapidity**, 246
  - $\psi$  **function**, 145
- Q —**
- quark**
  - condensate**, 16
  - masses**, 14, 29
  - mixing matrix**, 288
  - parton distributions**, 92
  - properties**, 1
  - sea**, 92
  - spin**, 91, 329
  - valence**, 92
  - quark-gluon plasma**, 380
  - quarkonium**, 418
    - decays**, 378, 420
    - potential**, 377
    - production**, 380
      - colour evaporation model**, 381
      - colour singlet model**, 381
    - spectrum**, 375
    - wave function**, 140
  - quenched approximation**, 45
    - corrections to**, 419
- R —**
- radiation function**, 179
  - rapidity**, 185, 246, 304
  - Regge theory**, 130
  - renormalization**
    - scale**, 37, 60, 222, 227, 351, 411
    - scheme**, 30, 36, 412
  - resolvable branching**, 171, 174
  - resummation**, 220, 228
    - event shapes**, 223, 422
    - leading logarithms**, 223
    - matching with fixed order**, 226
    - next-to-leading logarithms**, 225
    - thrust**, 227
  - jet rates**, 71, 228
  - small  $x$** 
    - deep inelastic scattering**, 138
    - jet fragmentation**, 203
  - transverse momentum distribution**, 324
  - $\rho$  **parameter**, 278
  - running coupling constant**, 22, 172, 413
  - running mass**, 30

Rutherford scattering, 254

— S —

scalar gluon, 58, 73, 254

scale

choice, 60

dependence, 59, 222, 227, 351

scaling, 88, 304

scaling violation, 108, 193, 195

deep inelastic scattering, 415

fragmentation function, 422

semileptonic branching ratio

charm, 338

shape variables, 71, 185, 220, 422

single effective subprocess

approximation, 255, 258

singularities

collinear, 57

soft, 57

small  $x$ , 128

spacelike branching, 165, 172

spectator model, 334, 338

spherocity, 72

spin

gluon, 73, 77, 254

quark, 91, 329

splitting function, 108, 195

higher order

spacelike, 111

timelike, 196

lowest order, 101, 162, 168–169, 195

polarized, 151

unregularized, 160, 163

spontaneous symmetry breaking, 16,

272, 276

strange quark

mass, 1, 17

string tension, 49, 378

strong coupling constant, 411

running, 22, 413

value, 424

strong CP problem, 13

structure constants, 6

structure function, 87

longitudinal, 91, 107

neutrino scattering, 90

parity violating, 91

polarized, 148

$SU(2) \otimes U(1)$ , 271

$SU(3)_c$ , 1

$SU(3)_f$ , 15

Sudakov form factor, 170, 172, 184,

215, 225

sum rule, 109, 126

Adler, 127

Bjorken, 149, 415

Ellis-Jaffe, 150

Gottfried, 128

Gross-Llewellyn Smith, 126, 415

momentum, 109

valence, 92

supersymmetry, 409, 424

symmetry

approximate, 14

chiral, 15

custodial, 280

exact, 12

flavour, 15

heavy quark, 17

spontaneously broken, 16, 272

— T —

$\tau$  lepton, 416

$\theta_W$ , 275

three jet production, 255

thrust, 72, 185, 220

timelike branching, 158, 168

top quark

decays, 340

CKM-disfavoured, 342

to charged Higgs, 345

to  $Wb$ , 340

mass, 1, 364

production, 362

at LHC, 368

cross section, 353, 364

single top, 370

width, 341

transverse mass, 246, 320, 349  
 trigger bias, 251  
 triple-gluon vertex, 76, 159  
 twist, 123, 415  
 two jet production, 247

### — U —

unitarity triangle, 289  
 unitarity, perturbative, 293  
 unitary gauge, 274  
 up quark  
   mass, 1, 16

### — V —

valence quark, 92  
 vector bosons  
   decay, 290  
   pair production, 295  
   production, 301, 303, 313  
     QCD corrections, 307  
   scattering, 291  
 virtual corrections, 56, 58, 65, 73,  
   103, 171, 266, 301, 307, 323, 351

### — W —

$W$  decay  
   hadronic, 291  
   width, 290  
 $W$  mass, 275  
   measurement, 319  
 $W$  production  
   cross sections, 313  
   in association with jets, 327, 423  
   pair production  
     hadronic, 298  
     in  $e^+e^-$ , 297  
   rapidity asymmetry, 315  
   transverse mass, 319  
   transverse momentum distribution,  
     321  
 weak boson

masses, 275  
 pair production, 295  
 scattering, 291  
 weak hypercharge, 271, 281  
 weak isospin, 271, 281  
 wee partons, 98  
 Weinberg angle, 275  
 Wilson action, 44, 419

### — Y —

Yang's theorem, 381  
 Yukawa couplings, 283, 389

### — Z —

$Z$  decay  
   hadronic, 291, 421  
   invisible, 291  
   to  $b$  and  $c$ , 421  
   width, 290  
 $Z$  mass, 275, 287  
 $Z$  production  
   cross sections, 313  
   in association with jets, 327  
   pair production  
     hadronic, 298  
     in  $e^+e^-$ , 298  
   rapidity distribution, 315  
   transverse momentum distribution,  
     321  
 $\zeta$  function, 59